frontiers | Research Topics

Dust and polluted aerosols: Sources, transport and radiative effects

Edited by
Zhiyuan Hu, Rui Mao, Chen Siyu, Xiao-Xiao Zhang, Zhenming Ji and Longlei Li

Published in
Frontiers in Environmental Science

ISSN 1664-8714
ISBN 978-2-83252-011-6
DOI 10.3389/978-2-83252-011-6

About Frontiers

Frontiers is more than just an open access publisher of scholarly articles: it is a pioneering approach to the world of academia, radically improving the way scholarly research is managed. The grand vision of Frontiers is a world where all people have an equal opportunity to seek, share and generate knowledge. Frontiers provides immediate and permanent online open access to all its publications, but this alone is not enough to realize our grand goals.

Frontiers journal series

The Frontiers journal series is a multi-tier and interdisciplinary set of open-access, online journals, promising a paradigm shift from the current review, selection and dissemination processes in academic publishing. All Frontiers journals are driven by researchers for researchers; therefore, they constitute a service to the scholarly community. At the same time, the *Frontiers journal series* operates on a revolutionary invention, the tiered publishing system, initially addressing specific communities of scholars, and gradually climbing up to broader public understanding, thus serving the interests of the lay society, too.

Dedication to quality

Each Frontiers article is a landmark of the highest quality, thanks to genuinely collaborative interactions between authors and review editors, who include some of the world's best academicians. Research must be certified by peers before entering a stream of knowledge that may eventually reach the public - and shape society; therefore, Frontiers only applies the most rigorous and unbiased reviews. Frontiers revolutionizes research publishing by freely delivering the most outstanding research, evaluated with no bias from both the academic and social point of view. By applying the most advanced information technologies, Frontiers is catapulting scholarly publishing into a new generation.

What are Frontiers Research Topics?

Frontiers Research Topics are very popular trademarks of the *Frontiers journals series*: they are collections of at least ten articles, all centered on a particular subject. With their unique mix of varied contributions from Original Research to Review Articles, Frontiers Research Topics unify the most influential researchers, the latest key findings and historical advances in a hot research area.

Find out more on how to host your own Frontiers Research Topic or contribute to one as an author by contacting the Frontiers editorial office: frontiersin.org/about/contact

Dust and polluted aerosols: Sources, transport and radiative effects

Topic editors

Zhiyuan Hu — Sun Yat-sen University, China
Rui Mao — Beijing Normal University, China
Chen Siyu — Lanzhou University, China
Xiao-Xiao Zhang — Xinjiang Institute of Ecology and Geography, Chinese Academy of Sciences (CAS), China
Zhenming Ji — Sun Yat-sen University, China
Longlei Li — Cornell University, United States

Citation

Hu, Z., Mao, R., Siyu, C., Zhang, X.-X., Ji, Z., Li, L., eds. (2023). *Dust and polluted aerosols: Sources, transport and radiative effects*. Lausanne: Frontiers Media SA. doi: 10.3389/978-2-83252-011-6

Table of contents

frontiers in Environmental Science

ORIGINAL RESEARCH
published: 16 September 2021
doi: 10.3389/fenvs.2021.744255

Trends of Planetary Boundary Layer Height Over Urban Cities of China From 1980–2018

Yanfeng Huo[1,2,3], *Yonghong Wang*[4,5]*, *Pauli Paasonen*[5], *Quan Liu*[6], *Guiqian Tang*[7], *Yuanyuan Ma*[8], *Tuukka Petaja*[4], *Veli-Matti Kerminen*[4] *and Markku Kulmala*[4]

[1]*Anhui Institute of Meteorological Sciences, Key Laboratory for Atmospheric Sciences & Remote Sensing of Anhui Province, Hefei, China,* [2]*Shouxian National Climate Observatory, Shouxian, China,* [3]*Huaihe River Basin Typical Farmland Ecological Meteorological Field Science Experiment Base of China Meteorological Administration, Shouxian, China,* [4]*Research Center for Eco-Environmental Sciences, Chinese Academy of Science, Beijing, China,* [5]*Institute for Atmospheric and Earth System Research/Physics, Faculty of Science, University of Helsinki, Helsinki, Finland,* [6]*Beijing Weather Modification Office, Beijing Meteorological Bureau, Beijing, China,* [7]*Institute of Atmospheric Physics, Chinese Academy of Sciences, Beijing, China,* [8]*Key Laboratory of Land Surface Process and Climate Change in Cold and Arid Regions, Northwest Institute of Eco-Environment and Resources, Chinese Academy of Sciences, Lanzhou, China*

OPEN ACCESS

Edited by:
Rui Mao,
Beijing Normal University, China

Reviewed by:
Yongjing Ma,
Institute of Atmospheric Physics (CAS), China
Xiaoyan Wang,
Fudan University, China
Miao Yu,
Chinese Academy of Meteorological Sciences, China

***Correspondence:**
Yonghong Wang
yonghongwang@rcees.ac.cn

Specialty section:
This article was submitted to Atmosphere and Climate, a section of the journal Frontiers in Environmental Science

Received: *20 July 2021*
Accepted: *01 September 2021*
Published: *16 September 2021*

Citation:
Huo Y, Wang Y, Paasonen P, Liu Q, Tang G, Ma Y, Petaja T, Kerminen V-M and Kulmala M (2021) Trends of Planetary Boundary Layer Height Over Urban Cities of China From 1980–2018. Front. Environ. Sci. 9:744255. doi: 10.3389/fenvs.2021.744255

Boundary layer height (BLH) is an important parameter in climatology and air pollution research, especially in urban city. We calculated the BLH with a bulk Richardson number (Ri) method over urban cities of China during 1980–2018 using European Centre for Medium-Range Weather Forecasts (ECMWF) ERA-interim data after carefully validation with sounding data obtained from two meteorology stations in eastern China during 2010–2018. The values of BLH between these two types of data have correlation coefficients in the range of 0.65–0.87, which indicates that it is reasonable to analyze long-term trends of the BLH from ERA data sets. Using ERA-interim calculated BLH, we found that there is an increasing trend in the daytime BLH in most cities of eastern China, particularly during the spring season. A correlation analysis between the BLH and temperature, wind speed, relative humidity and visibility revealed that the variability in meteorological parameters, as well as in aerosol concentrations over highly polluted eastern China, play important roles in the development of the BLH.

Keywords: boundary layer height, aerosol, visibility, trend, meteorology parameter

INTRODUCTION

Planetary boundary layer (PBL) is the turbulent layer of the troposphere and plays an important role influencing the concentration, transport and diffusion of atmospheric compounds (Stull, 1988). The PBL height is most commonly identified as an inversion in the potential temperature and dewpoint, or as a peak value in the low-level wind speed. Air pollutants are concentrated in the PBL, and the daily variation of the PBL is crucial in interpreting the diurnal variation of air pollutants in areas with anthropogenic emissions (Kaser et al., 2015; Petäjä et al., 2016; Sun et al., 2013; Ma et al., 2020; Xian et al., 2021). In general, the height of planetary boundary layer varies spatially and temporally, typically ranging from about a hundred meters to some kilometres. The PBL height can be as high as 5 km over a desert in mid-summer due to strong surface heating, while being as low as 50–100 m during a night over land under clear sky and light wind conditions (Zhang et al., 2013; Chen et al., 2016).

Radio sounding measurements, providing the profiles of wind, humidity and temperature, are typically used in weather stations to determine the height of PBL (Seidel et al., 2010). In general, such sounding is conducted twice a day at 08:00 and 20:00. However, the method needs a lot of man power to be conducted in long-term measurements, in addition to which it cannot provide information about the diurnal evolution of the boundary layer height due to the limited time resolution. Seidel et al (2010) compared seven methods of calculating the PBL height from a 505-station global radiosonde data set, and also attempted to quantify aspects of structural and parametric uncertainty in the values of the PBL height. Zhang et al (2013) estimated trends of the PBL height over 25 stations in Europe using radiosonde data from 1973–2010, and found significant increases in the daytime PBL height at most of the stations. Guo et al (2016) compared the PBL height between the radiosonde and reanalysis data from 2011–2015 in China, and found a good agreement between these two data sets. Remote sensing, as an alternative method, is widely used to determine the PBL height from a backscattering signal during the past decades. Wang et al (2012) derived the PBL height at two locations of Lanzhou, China, using a micro-pulse lidar and microwave radiometer, and found that these two results were consistent with each other during strong convective situations. Zhang et al (2016) compared the PBL height from CALIOP and radiosonde data in Beijing and Jinhua, and obtained correlation coefficients of 0.59 and 0.65 at Beijing and Jinhua, respectively, between these two kinds of data.

Very recently, Guo et al (2019) found an increasing trends of the PBL height over China during 1976–2003, but a non-uniform decrease after 2004. Capital cities of China suffer the most from air pollution, but the variability and trends of the PBL height are unknown in those regions.

With the rapid economic growth in China, air pollution has become an issue with large influences on climate, human health and visibility degradation during the last decades (Wang et al., 2015). Wang et al (2020), Ding et al (2016) and Petäjä et al (2016) and other work (Ma et al., 2020) found that atmospheric air pollution can be enhanced by boundary layer-aerosol interactions, characterised by higher aerosol concentrations and shallower boundary layer heights. Therefore, a better knowledge of the long-time variation of the PBL height in China is essential when evaluating variations in aerosol concentrations and effects of regional climate change. However, only a few studies reported a long-

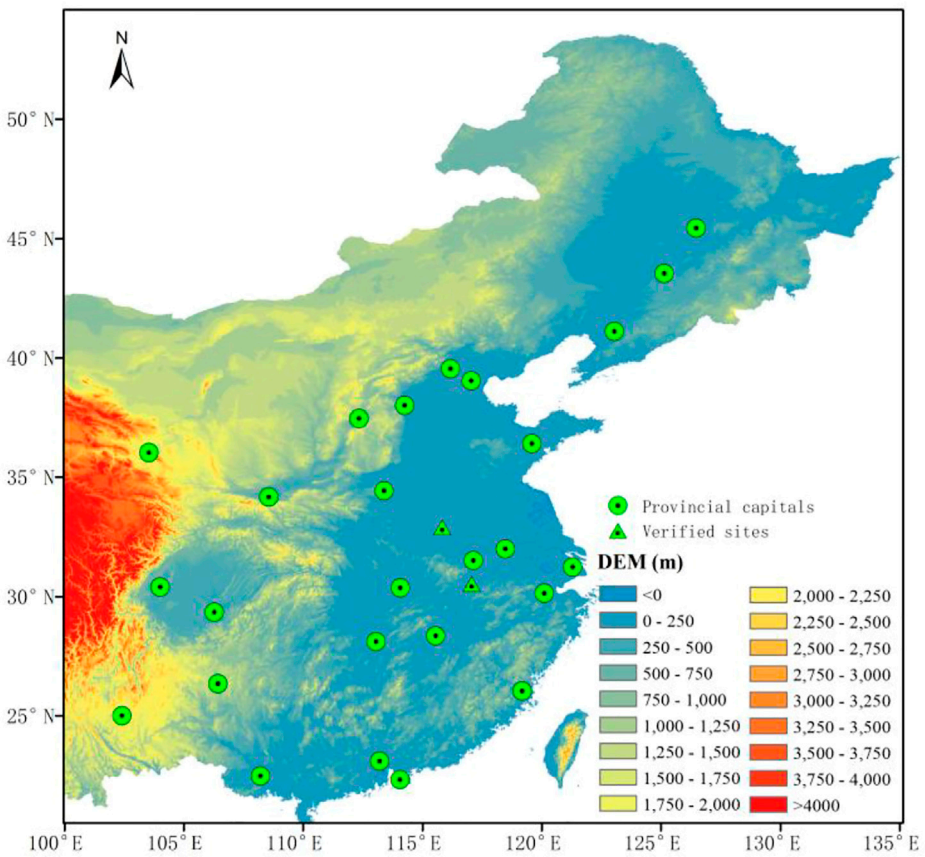

FIGURE 1 | The distribution of stations in this study. The color in the map represents altitude. The blue triangles denotes Fuyang **(upper one)** and Anqing station, respectively.

TABLE 1 | Seasonal trends in 14 BJT BLH, wind speed, temperature, cloud cover, relative humidity (z, WS, T, CC, RH with units of m, 10^{-3} m/s, 10^{-2} K, 10^{-3}, ‰, respectively) during 1980–2018. Boldfaces are significant at 95% confidence interval or greater.

Station(°N,°E)	DJF					MAM					JJA					SON				
	z	WS	T	CC	RH	z	WS	T	CC	RH	z	WS	T	CC	RH	z	WS	T	CC	RH
Beijing(40,116)	0.7	4.8	**4.5**	0.7	−0.1	**7.0**	4.8	**6.9**	**−2.2**	**−1.9**	1.7	**−9.2**	**4.4**	**−2.3**	**−1.4**	−0.5	−1.7	3.2	0.2	−0.038
Shanghai(31,121)	−0.1	−4.7	**4.1**	−1.8	−1.0	**4.7**	0.5	**10.2**	**−3.8**	**−3.3**	1.3	−7.0	**6.7**	−1.5	**−1.9**	**2.8**	−5.5	**6.8**	**−3.1**	**−16.6**
Guangzhou(23,113)	1.5	−2.3	2.1	−0.6	−1.1	**4.5**	**−8.6**	**4.5**	**−2.9**	**−2.1**	1.2	**−8.5**	**1.7**	−0.9	**−1.3**	0.7	**−16.6**	**3.0**	0.5	−0.5
Shenzhen(22,114)	−1.0	−6.8	2.6	−0.0	−1.1	0.1	**−13.0**	**4.4**	**−2.6**	**−1.7**	−1.2	**−17.5**	**1.9**	0.1	**−1.2**	-0.4	**−22.8**	**3.5**	1.0	−0.5
Tianjin(39,117)	1.3	3.3	**4.3**	0.6	0.0	2.2	3.1	**5.3**	**−1.8**	**−1.5**	−0.1	−6.2	**3.5**	**−2.1**	−1.2	-2.5	−3.6	2.5	0.2	0.1
Chongqing(29,106)	0.9	0.5	1.8	−0.6	−0.8	2.1	1.1	**6.1**	−1.2	**−1.6**	4.3	−1.2	**4.7**	−0.8	**−2.0**	**3.0**	0.7	**5.1**	**−1.9**	**−1.5**
Haerbin(45,126)	−0.8	**−14.2**	0.8	**−3.2**	−1.3	0.4	−0.8	1.4	0.9	0.6	−0.1	−7.9	**4.0**	**−2.3**	−0.9	**4.1**	**−10.9**	**6.9**	−1.0	**−1.8**
Changchun(44,125)	−1.5	**−11.7**	0.1	−1.4	−0.9	3.4	−0.6	2.8	−0.3	0.0	0.5	−6.5	**4.3**	**−2.0**	−1.1	**4.6**	**−11.2**	**6.6**	−0.5	−1.3
Shenyang(41,123)	1.1	−5.5	3.5	−0.7	**−1.6**	2.2	−2.5	3.3	−0.3	−0.3	−0.2	**−13.0**	2.6	−1.4	−0.1	0.6	−6.5	**5.1**	−0.2	−0.2
Taiyuan(37,112)	0.2	−3.0	3.1	0.8	0.0	**1.4**	8.0	**5.5**	−1.9	**−1.7**	**9.4**	**−10.5**	**3.5**	**−2.4**	−1.5	1.8	−2.7	1.8	0.8	0.1
Shijiazhuang(38,114)	0.6	5.8	2.9	0.4	0.4	5.3	6.8	**5.8**	**−2.0**	**−1.9**	1.2	−1.6	2.6	**−2.2**	−0.8	-0.9	0.6	1.4.	0.3	−0.0
Lanzhou(36,103)	**−6.1**	2.8	2.1	0.4	**3.6**	1.2	2.2	**5.6**	−0.3	1.3	−2.7	1.7	**5.1**	0.7	1.0	**-8.6**	3.0	**3.4**	4.6	**4.1**
Xian(34,108)	−1.5	−3.2	2.2	0.3	0.2	2.1	1.1	**7.4**	**−2.3**	**−1.8**	1.8	−3.5	**4.9**	**−2.5**	**−1.7**	-1.5	−0.8	**4.0**	−0.6	−0.6
Jinan(36,120)	−2.1	**−10.7**	**4.0**	0.0	−0.3	2.5	6.3	**4.4**	−0.6	−0.9	2.6	**−9.9**	2.4	−1.4	−0.6	0.3	−8.6	**3.8**	−0.4	−0.3
Zhengzhou(34,113)	−0.7	−1.7	2.6	−0.1	−0.8	0.5	**6.0**	**6.5**	**−2.2**	**−2.0**	4.3	0.0	**4.3**	**−2.5**	**−2.0**	2.2	0.9	2.8	−1.5	−1.4
Chengdu(30,104)	**3.1**	−0.0	2.9	−1.7	**−1.5**	**4.5**	**−4.3**	**6.9**	−1.0	**−1.9**	1.3	−2.7	**3.6**	−0.6	−1.2	−0.0	−1.6	**3.4**	−1.0	−0.1
Wuhan(30,114)	−0.1	−1.2	2.6	−0.4	−1.5	1.8	−0.6	**7.8**	**−2.0**	**−2.3**	1.7	1.8	**3.3**	−0.5	**−1.4**	1.3	−5.7	**4.4**	−1.4	−1.3
Hefei(31,117)	−1.1	−2.4	2.5	−0.8	−0.9	2.6	1.3	**7.8**	**−2.5**	**−2.6**	0.8	−4.5	2.6	−0.6	**−0.9**	0.4	−3.7	**4.0**	−1.8	−0.9
Nanjing(32,118)	−0.1	−3.5	3.5	−0.8	−1.1	3.2	2.3	**8.0**	**−3.2**	**−2.8**	−0.1	**−8.7**	**3.4**	−1.0	**−1.2**	1.5	−1.9	**4.9**	−2.4	−1.5
Hangzhou(30,120)	0.5	−2.4	**4.7**	−1.7	−0.9	**5.7**	−1.3	**9.7**	**−3.6**	**−3.0**	1.5	**−9.0**	**4.8**	−0.7	-1.2	1.5	**−6.8**	**6.1**	−2.1	−1.1
Guiyang(26,106)	**2.4**	−0.2	0.4	−2.1	**−1.3**	2.3	−7.3	**3.8**	−1.1	**−1.1**	1.1	−7.5	0.2	−0.1	**−0.9**	**2.5**	−0.2	**2.2**	**−1.9**	−0.8
Changsha(28,113)	0.3	−1.2	2.5	−0.5	−1.4	**2.5**	−2.9	**7.3**	**−3.0**	**−2.0**	2.9	−1.1	2.0	0.2	**−1.4**	1.5	**−8.5**	**4.3**	−2.3	−1.4
Nanchang(28,115)	−0.6	2.6	3.7	−0.1	−0.9	1.8	−1.2	**8.1**	**−3.4**	**−2.2**	−0.7	−4.2	1.6	0.4	−0.7	0.9	−3.2	**5.8**	−2.4	−1.4
Fuzhou(26,119)	0.6	−0.2	**4.8**	−1.7	−1.2	2.0	−3.3	**6.4**	**−3.2**	**−2.2**	−0.9	**−8.2**	**2.6**	−0.1	0.2	−1.1	**−11.0**	**5.0**	−0.6	−0.1
Kunming(25,102)	−1.4	−1.1	2.2	−0.2	−0.1	-3.6	**−14.2**	1.5	1.1	0.3	2.7	−4.4	**2.8**	−0.8	**−1.8**	**3.6**	2.1	**3.8**	**−3.7**	**−2.2**
Nanning(22,108)	1.8	3.5	1.2	**−3.9**	**−1.4**	2.6	−4.0	**2.8**	−1.4	**−1.2**	−0.7	−4.7	**1.8**	0.6	**−1.7**	1.1	−6.8	**3.4**	−1.3	−1.4

The boldfaces are significant at 95% confidence interval or greater.

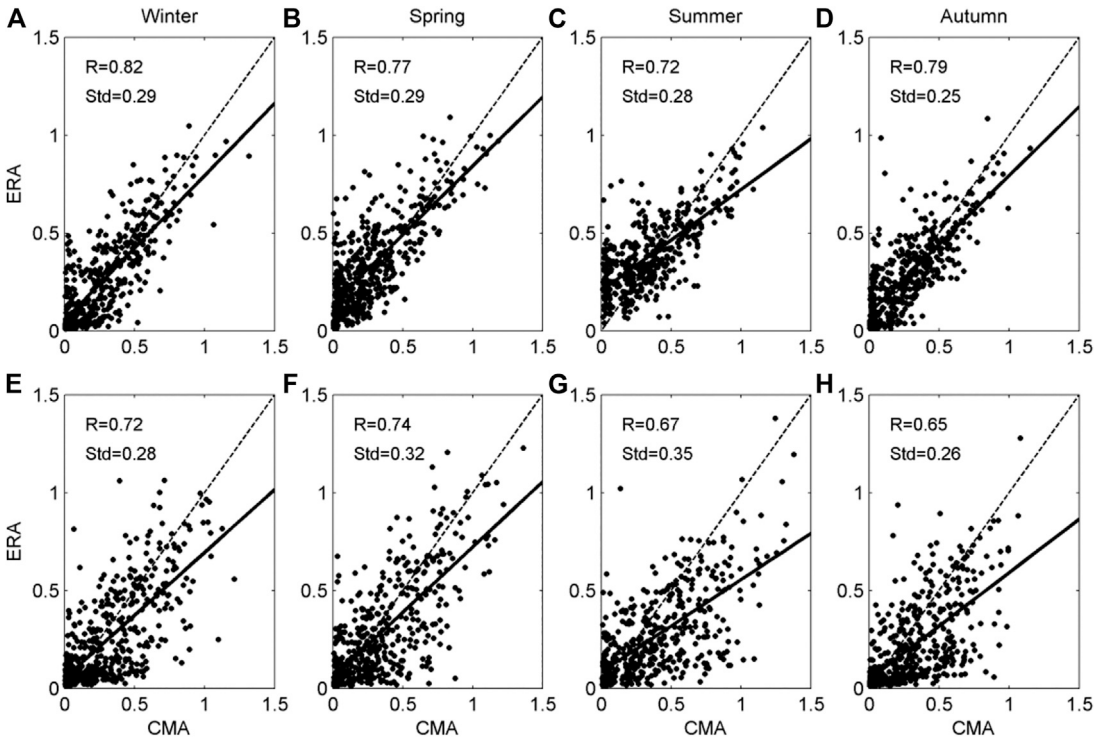

FIGURE 2 | CMA-BLH and ERA-BLH at (the **upper** panel) 0800 and (the **lower** panel) 2000 BJT in **(A,B)** winter, **(C,D)** spring, **(E,F)** summer, and **(G,H)** autumn in Anqing.

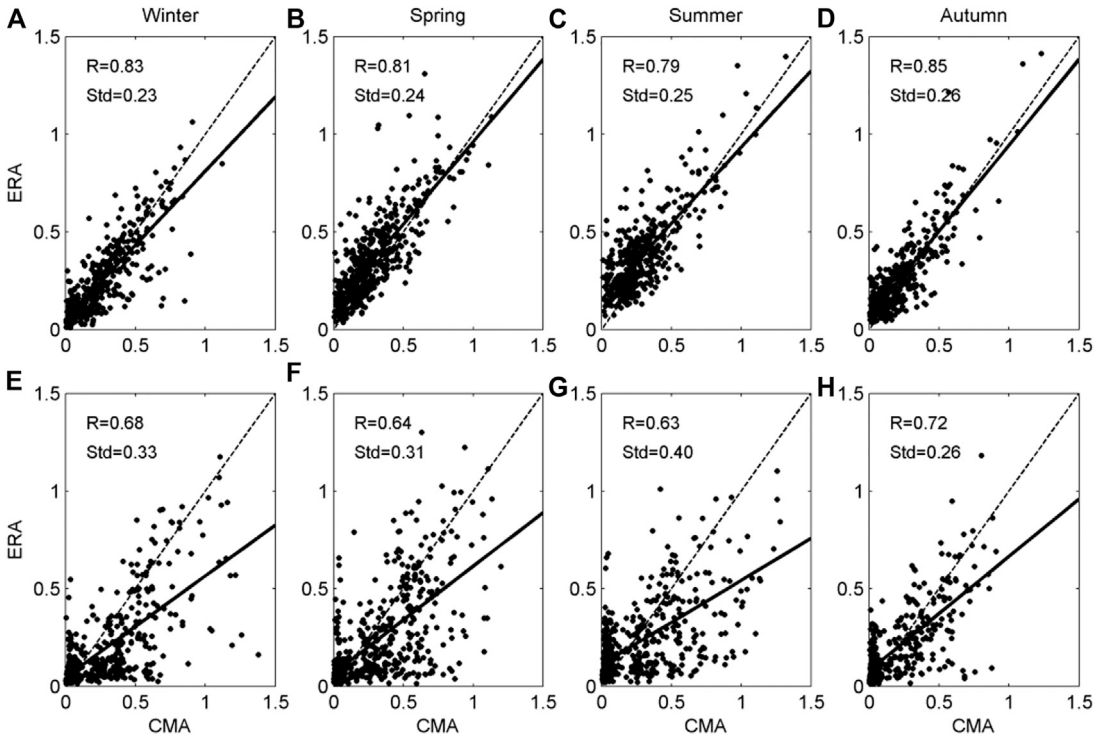

FIGURE 3 | CMA-BLH and ERA-BLH at (the **upper** panel) 0800 and (the **lower** panel) 2000 BJT in **(A,B)** winter, **(C,D)** spring, **(E,F)** summer, and **(G,H)** autumn in Fuyang.

term variation of the PBL height over highly polluted cities in China (Guo et al., 2016; Tang et al., 2016).

In this study, we used ERA-reanalysis data combined with radio sounding measurements in determining long-term trends in the BLH in the capital cities of each province in eastern China. Our results provide insights into the decadal variation of the BLH in polluted eastern China during the urbanization period. We also explored the spatial variability in the BLH over China during these years.

DATA AND METHODOLOGY

We chose 26 capital cities of each province in eastern China to analyze the boundary layer heights (BLHs) variation and made a comprehensive analysis. The detailed city list and locations are listed in **Table 1**.

Dataset

The ERA-Interim reanalysis are assimilated results, including model products and various measurements (Dee et al., 2011). Its

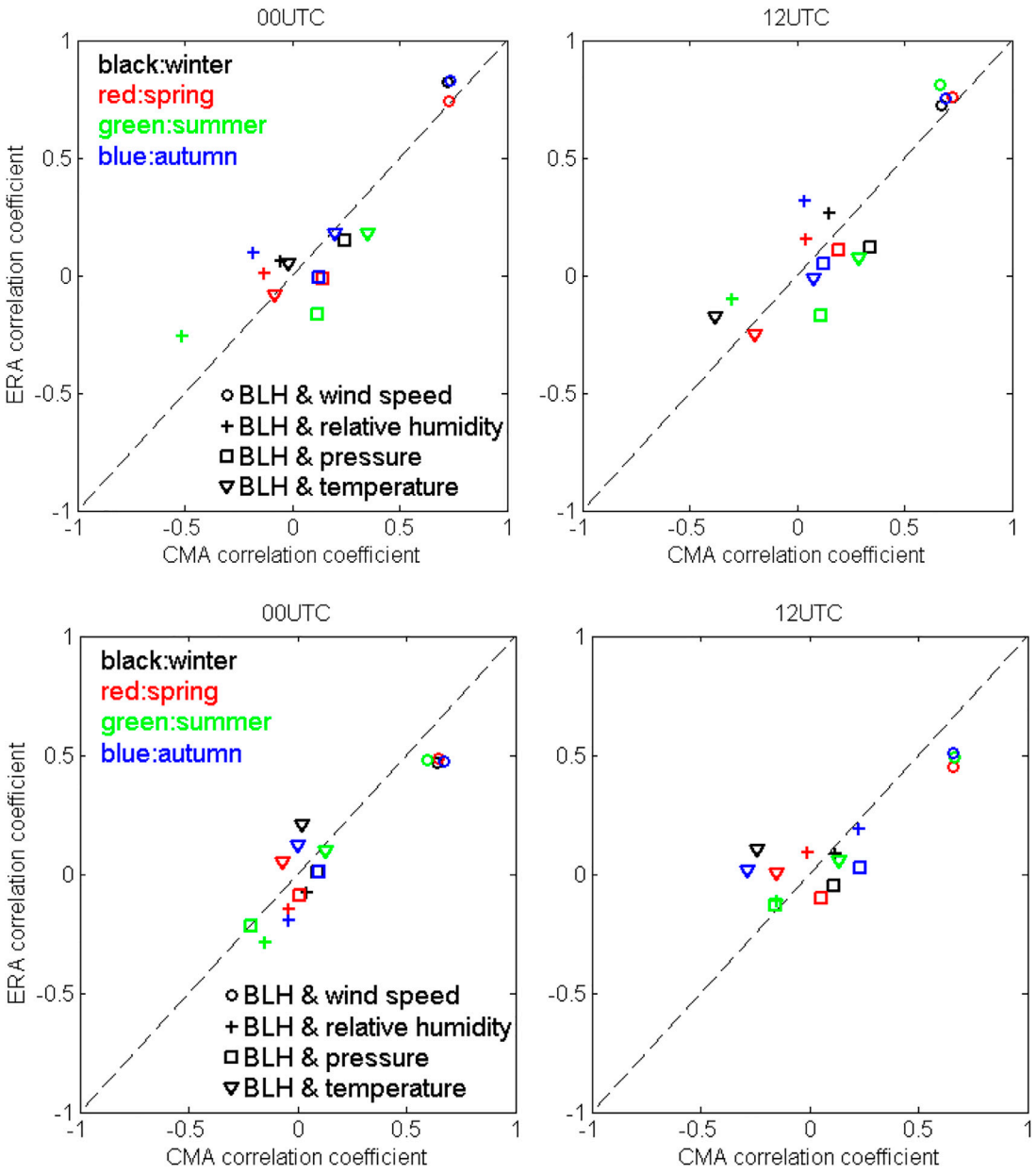

FIGURE 4 | Comparison of correlation coefficient between meteorological parameters and BLH calculated from ERA reanalysis data and measurement data, the **upper** panel is Anqing station and the **lower** panel is Fuyang station.

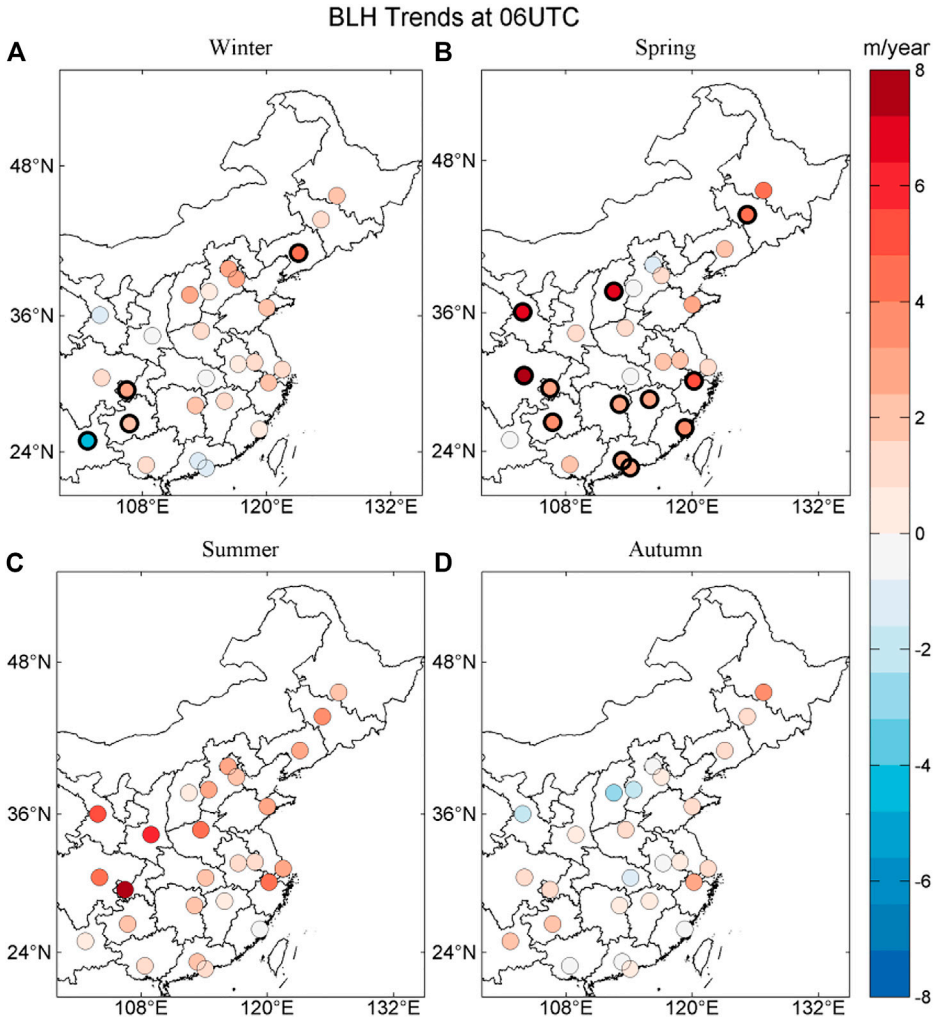

FIGURE 5 | Seasonal trends of PBL height during 14:00 BJT from 1980–2018. The thick black circle represents the trend is significant at 95% confidence interval or greater.

model-layers data contain 60 vertical layers (starting with about 25 m near surface, decreasing to about 500 m around 500 hPa), which has been used to calculate the boundary layer height (Seidel et al., 2010; Guo et al., 2016). In this work, the reanalysis data with a horizontal resolution of 0.75° × 0.75° and time resolution of 6 h were used for the BLHs calculation, after which we interpolated the BLHs to 26 city sites (**Figure 1**). In addition, the surface temperature, relative humidity and wind speed obtained from reanalysis products were used in our analysis to constrain the factors influencing the boundary layer. Visibility data from the strictly quality-controlled Chinese observational data set were also used to analyze influences of aerosols on the boundary layer height.

We applied radiosonde data at two sounding stations in central China during 2010–2018 to validate our results from the ERA-Interim reanalysis calculation. The two stations are a part of China Meteorological Administration L-band second-resolution ground-based sounding network. The instrument used for validation is a digital radiosonde sensor (GTS1), which is developed by the Shanghai Changwang Meteorological Science and Technology Company. The instrument has been used widely in China meteorology stations as routine measurements, and a comparison between the GTS1 and Vaisala RS80 shows that the instrument performance good (Bian et al., 2010). For simplicity, we hereafter call the reanalysis results and sounding results as ERA-BLH and CMA-BLH, respectively.

The Method Used to Estimate BLH

A bulk Richardson number (Ri) method was carefully applied to calculate the BLHs in this work. The Ri method was first put forward by (Vogelezang and Holtslag, 1996). The method is suitable for both stable and convective boundary layer, in which the value of Ri can be expressed as:

$$Ri(z) = \frac{(g/\theta_{vs})(\theta_{vz} - \theta_{vs})(z - z_s)}{(u_z - u_s)^2 + (v_z - v_s)^2 + bu_*^2} \quad (1)$$

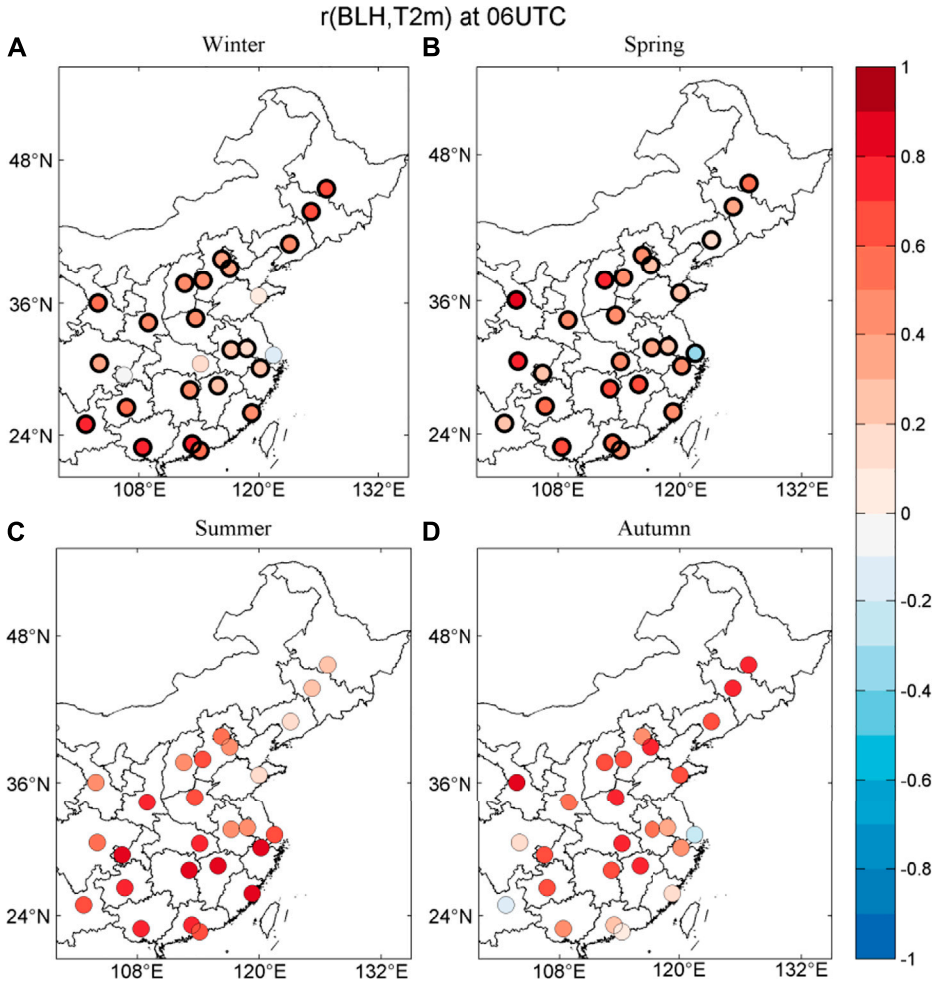

FIGURE 6 | Correlations of seasonal 14 BJT BLH and temperature during 1980–2018. Thick black circle represents the trend is significant at 95% confidence interval or greater.

Here the subscript s and z indicate the surface and specific height, respectively, the variables g and θ are gravity acceleration and potential temperature, respectively, u and v are the horizontal wind velocity components, u_* is the surface friction velocity, and b is a constant. In general, bu_* is much smaller than the bulk wind shear term (the two other terms together in the denominator) and can be neglected. In our calculations, the surface height was assumed to be 2 m and the surface wind was approximated to be zero, and the first level at which the interpolated Ri was equal to 0.25 was interpreted as the BLH. This method has been proven to be one of the best methods for the climatological analysis of the BLH because of its applicability for both stable and convective boundary layers (Seidel et al., 2010).

RESULTS AND DISCUSSION

Validation of ERA-BLH With CMA-BLH

This section presents an inter-comparison of the ERA-BLH with CMA-BLH data at the stations of Fuyang and Anqing in eastern China. The soundings were usually launched at 08:00 and 20:00 Beijing time (BJT), so the value of BLH were mainly compared at these two moments. **Figures 2**, **3** show scatter plots between the ERA-BLH with CMA-BLH in Fuyang and Anqing, respectively, the upper panels correspond to 08:00 and the lower panels to 20:00 BJT. The correlation coefficients between two kinds of BLH data were larger than 0.7° at 08:00 for most of the time, which is consistent with earlier results in the Beijing station (Guo et al., 2016). These high correlation coefficients give us confidence that ERA-BLH is an appropriate alternative approach to analyze changes in the boundary layer height. It is interesting to note that comparison results at 08:00 BJT were better than those at 20:00 BJT. A possible reason for this is that the convective boundary layer transmits to a nocturnal stable boundary layer after sunset, so that the existence of a residual layer at 20:00 may increase differences between two kinds of BLH data.

To further validate our analysis method, we compared BLH with meteorological parameters for both ERA data and measurement data from the Anqing and Fuyang stations (**Figure 4**). We found a good consistency between the

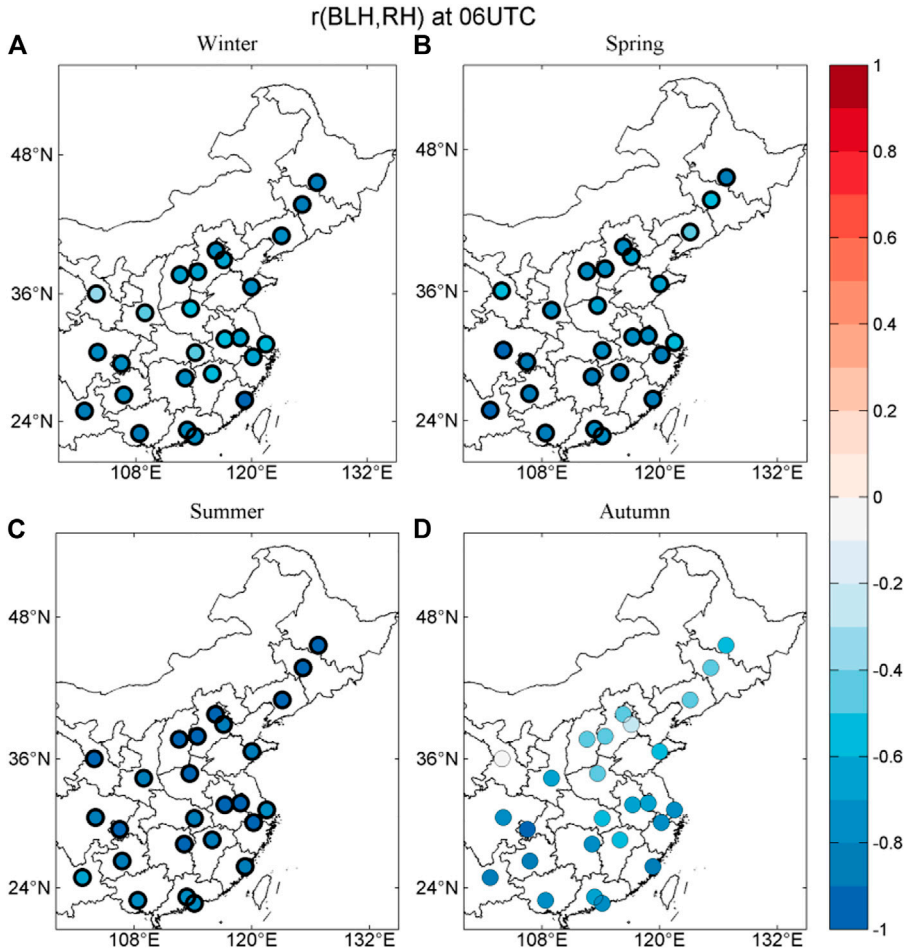

FIGURE 7 | Correlations of seasonal 14 BJT BLH and relative humidity during 1980–2018. Thick black circle represents the trend is significant at 95% confidence interval or greater.

observed and reanalysis data in terms of the couplings of meteorological conditions and BLH. The validation presented here gives confidence in applying the ERA data to the analysis of long-term interactions between the BLH and meteorological variability.

Trends of Planetary Boundary Layer Height in Urban Cities of China

The development of the day-time boundary layer height is closely related to solar radiation reaching the surface, so the surface temperature, wind speed, relative humidity, cloud cover and aerosol concentration may be factors that directly or indirectly influence the BLH. A typical daily variation of the BLH showed a maximum at around noon due to the convective activity, whereas low values occurred during nighttime, termed the nocturnal boundary layer. Early mornings and later afternoons were transition periods between a stable boundary layer and convective boundary layer. Therefore, we used the BLH at 14: 00 local time when the convective activity is the main factor influencing the BLH.

A statistical analysis of the BLH, temperature, wind speed, relative humidity and cloud cover in 26 cities in eastern China are shown in **Table 1**. The BLH showed an increasing trend at most of the cities, and especially so in spring and summer. The increasing trend was the highest in the city of Taiyuan, being equal to 11 m/year in spring and 9.4 m/year in summer. The variation of the BLH during the winter season was complex compared with the other seasons, showing an equal number of increasing and decreasing trends between the 26 cities. In every season, there were also cities having a decreasing trend of the BLH. The largest decreasing trend of the BLH was observed in Lanzhou, with a value of -8.6 m/year during the autumn season. It is also worth note that the decreasing trend of the BLH in Lanzhou, significant in summer, autumn and winter seasons, is very likely related to the significant increase of the relative humidity. Using 6.5 years of lidar measurements in Hong Kong, Yang et al. (2013) found a slight decreasing trend of the daily maximum mixing layer height from 2003 to 2009. We could also clearly see that the surface temperature at most of the cities increased during 1980–2015. The increase

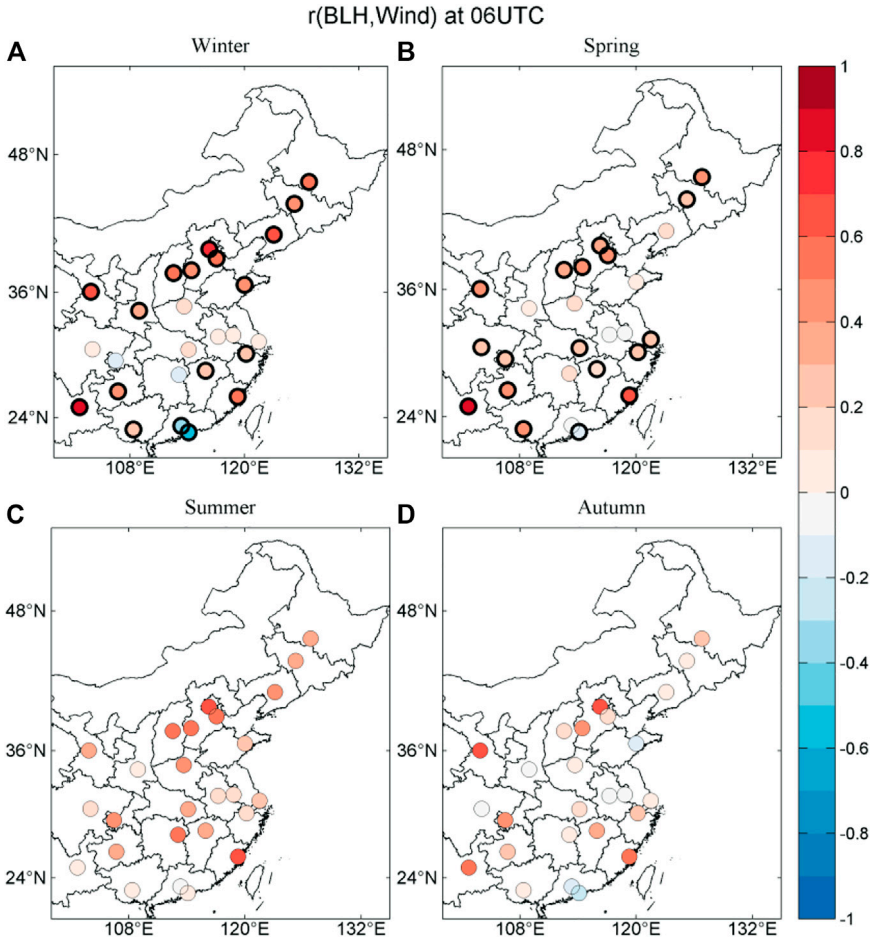

FIGURE 8 | Correlations of seasonal 14 BJT BLH and wind speed during 1980–2018. Thick black circle represents the trend is significant at 95% confidence interval or greater.

of temperature in urban cities is a combined effect of urban heat island effect and regional warming (Cao et al., 2016).

Figure 5 shows the spatial variability in the long-term trend of the BLH across eastern China. There are both positive or negative trends, as one can see, but many of the trends are not statistically significant. Based on **Table 1**, the BLH has higher increasing trends during the spring season than during the other seasons, whereas decreasing trends can be seen for nine stations during the summer seasons and for eight stations during the autumn season. The differences in the values of the BLH between the different seasons are related to differences in meteorological parameters and aerosol concentrations.

Influence of Meteorology

A boundary layer height is closely related to the atmospheric stability, which in turn is driven by the surface temperature, wind speed, relative humidity and aerosol loading (Zhang et al., 2013). **Figure 6** depicts the correlation coefficient between the BLH and surface temperate at 14:00 in 26 cities of eastern China. A positive correlation was obtained for most of the stations during the four seasons. In particular, the correlation is significant during the summer season; for example, the correlation between the BLH and surface temperature could as high as 0.6° in North China Plain and eastern China, while being lower at around 0.3°at the stations in the south area. In winter, the correlation between the BLH and surface temperature showed a different pattern, being higher in the south area and having even negative values in the north part of China. From **Table 1** we can see that the surface temperature in most of the cities have increased, which is consistent with the fast urbanization and global warming (Cao et al., 2016). Elevated surface temperatures lead to increased sensitive heat flux, and as a result, the boundary layer will develop higher during daytime. In general, higher increases in the surface temperature were associated with larger increases in the boundary layer height in China (**Figure 6**).

A high surface temperature results in a larger sensible heat flux, which lead to high boundary layer height (Stull, 1988). As presented in **Figure 7**, the relative humidity shows negative correlation with the BLH in all the urban stations considered here. **Figure 8** shows the correlation between the wind speed and BLH, with high values over the north region of China indicating

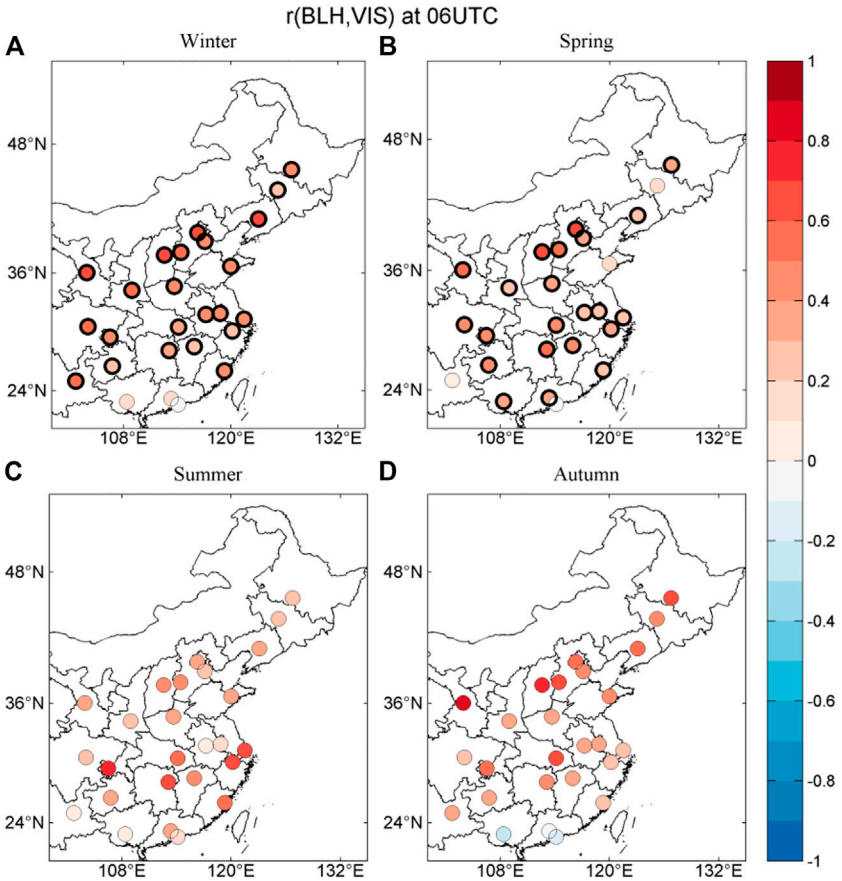

FIGURE 9 | Correlations of seasonal 14 BJT BLH and surface visibility during 1980–2018. Thick black circle represents the trend is significant at 95% confidence interval or greater.

that larger wind speeds favor the development of BLH. However, a negative correlation coefficient was observed in the stations of Guangzhou and HK. A possible explanation for this is that high wind speeds usually correspond to precipitation events in Guangdong Province, as a result of which the development of BLH is suppressed due to lack of upward turbulent kinetic energy (Back and Bretherton, 2005).

Aerosol Effect on BLH

Anthropogenic emissions of aerosol particles and their precursors have decreased the atmospheric visibility in China (Che et al., 2007; Wang et al., 2009, Wang et al., 2019). Since aerosol particles also decrease the amount of solar radiation reaching the surface, they might suppress the development of the boundary layer. The degradation of surface visibility could be a good proxy of light extinction due to atmospheric aerosol. We investigated long-term trends of visibility at 14:00 local time. **Figure 9** shows the correlation between the BLH and visibility during 1980–2015 in eastern China. In general, the correlation coefficient showed positive values, especially in the north area stations, with a clear variability between the different seasons. In particular, the boundary layer height seemed to be influenced more by aerosol particle during the cold season compared with the warm season. The highest correlation between the boundary layer height with visibility were observed at the stations in North China Plain. This indicates that aerosol pollution may have had a significant influence on the development of boundary layer height in North China Plain (Wang et al., 2020), even though it is also possible that the high correlation is due to aerosols being diluted more efficiently under high boundary layer conditions. The lowest correlations were observed in the south areas of China, suggesting more important role of meteorology parameters in determining the boundary layer height compared with aerosol particles.

CONCLUSION

In this study, we analyzed long-term trends of the boundary layer height in eastern China during the 1980–2018 period from ERA-reanalysis data, after carefully validating the boundary layer height data from ERA with sounding results. The results showed a slight increasing trends of the boundary layer height in most urban stations of eastern China, especially in the spring season. The correlations of the BLH with the surface temperature, relative humidity, wind speed and visibility were presented and discussed. The results suggest that the increased temperature is the main driving force of the variation

in the BLH, while aerosol particles also play important role. Our results revealed an increased trend of daytime boundary layer height under the warming climate, despite an increased loading of atmospheric pollutants.

DATA AVAILABILITY STATEMENT

The raw data supporting the conclusions of this article will be made available by the author, without undue reservation.

AUTHOR CONTRIBUTIONS

YW initiated the study. YH, YW, PP, GT, TP, VK and MK interpreted the data. YH, YW and VK wrote the article.

FUNDING

This work was supported by National Key Research and Development Program of China (No. 2016YFA0602001, No. 2016YFC0203302, and No. 2017YFC0209604), the National Natural Science Foundation of China (Grant No.41705014 and 41905013), and Chinese Academy of Sciences (CAS) "Light of West China" Program. The Innovation Development Program of Anhui Meteorology bureau (Grant No. CXM202102), key research and Development Program of Anhui Province (No. 202004b11020012) and Academy of Finland (311932).

ACKNOWLEDGMENTS

We acknowledge ECMWF for the high quality data.

REFERENCES

Back, L. E., and Bretherton, C. S. (2005). The Relationship between Wind Speed and Precipitation in the Pacific ITCZ. *J. Clim.* 18 (20), 4317–4328. doi:10.1175/JCLI3519.1

Bian, J., Chen, H., Vömel, H., Duan, Y., Xuan, Y., and Lü, D. (2010). Intercomparison of Humidity and Temperature Sensors: GTS1, Vaisala RS80, and CFH. *Adv. Atmos. Sci.* 28, 139–146. doi:10.1007/s00376-010-9170-8

Cao, C., Lee, X., Liu, S., Schultz, N., Xiao, W., Zhang, M., et al. (2016). Urban Heat Islands in China Enhanced by Haze Pollution. *Nat. Commun.* 7, 12509. doi:10.1038/ncomms12509

Che, H., Zhang, X., Li, Y., Zhou, Z., and Qu, J. J. (2007). Horizontal Visibility Trends in China 1981-2005. *Geophys. Res. Lett.* 34 (24). doi:10.1029/2007GL031450

Chen, X., Škerlak, B., Rotach, M. W., Añel, J. A., Su, Z., Ma, Y., et al. (2016). Reasons for the Extremely High-Ranging Planetary Boundary Layer over the Western Tibetan Plateau in Winter. *J. Atmos. Sci.* 73 (5). 2021–2038. doi:10.1175/jas-d-15-0148.1

Dee, D. P., Uppala, S. M., Simmons, A. J., Berrisford, P., Poli, P., Kobayashi, S., et al. (2011). The ERA-Interim Reanalysis: Configuration and Performance of the Data Assimilation System. *Q.J.R. Meteorol. Soc.* 137 (656), 553–597. doi:10.1002/qj.828

Ding, A. J., Huang, X., Nie, W., Sun, J. N., Kerminen, V. M., Petäjä, T., et al. (2016). Enhanced Haze Pollution by Black Carbon in Megacities in China. *Geophys. Res. Lett.* 43 (6), 2873–2879. doi:10.1002/2016GL067745

Guo, J., Li, Y., Cohen, J. B., Li, J., Chen, D., Xu, H., et al. (2019). Shift in the Temporal Trend of Boundary Layer Height in China Using Long-Term (1979-2016) Radiosonde Data. *Geophys. Res. Lett.* 46 (11), 6080–6089. doi:10.1029/2019GL082666

Guo, J., Miao, Y., Zhang, Y., Liu, H., Li, Z., Zhang, W., et al. (2016). The Climatology of Planetary Boundary Layer Height in China Derived from Radiosonde and Reanalysis Data. *Atmos. Chem. Phys.* 16 (20), 13309–13319. doi:10.5194/acp-16-13309-2016

Kaser, L., Karl, T., Yuan, B., Mauldin, R. L., III, Cantrell, C. A., Guenther, A. B., et al. (2015). Chemistry-turbulence Interactions and Mesoscale Variability Influence the Cleansing Efficiency of the Atmosphere. *Geophys. Res. Lett.* 42 (24), 810–894. doi:10.1002/2015GL066641

Ma, Y., Ye, J., Xin, J., Zhang, W., Vilà-Guerau de Arellano, J., Wang, S., et al. (2020). The Stove, Dome, and Umbrella Effects of Atmospheric Aerosol on the Development of the Planetary Boundary Layer in Hazy Regions. *Geophys. Res. Lett.* 47, e2020GL087373. doi:10.1029/2020GL087373

Petäjä, T., Järvi, L., Kerminen, V.-M., Ding, A. J., Sun, J. N., Nie, W., et al. (2016). Enhanced Air Pollution via Aerosol-Boundary Layer Feedback in China. *Sci. Rep.* 6, 18998. doi:10.1038/srep18998

Seidel, D. J., Ao, C. O., and Li, K. (2010). Estimating Climatological Planetary Boundary Layer Heights from Radiosonde Observations: Comparison of Methods and Uncertainty Analysis. *J. Geophys. Res.* 115 (16), 1–15. doi:10.1029/2009JD013680

Stull, R. B. (1988). *An Introduction to Boundary Layer Meteorology*. Dordrecht: Kluwer Academic Publishers.

Sun, Y., Song, T., Tang, G., and Wang, Y. (2013). The Vertical Distribution of PM2.5 and Boundary-Layer Structure during Summer Haze in Beijing. *Atmos. Environ.* 74, 413–421. doi:10.1016/j.atmosenv.2013.03.011

Tang, G., Zhang, J., Zhu, X., Song, T., Münkel, C., Hu, B., et al. (2016). Mixing Layer Height and its Implications for Air Pollution over Beijing, China. *Atmos. Chem. Phys.* 16, 2459–2475. doi:10.5194/acp-16-2459-2016

Vogelezang, D. H. P., and Holtslag, A. A. M. (1996). Evaluation and Model Impacts of Alternative Boundary-Layer Height Formulations. *Boundary-layer Meteorol.* 81 (3–4), 245–269. doi:10.1007/BF02430331

Wang, K., Dickinson, R. E., and Liang, S. (2009). Clear Sky Visibility Has Decreased over Land Globally from 1973 to 2007. *Science* 323 (5920), 1468–1470. doi:10.1126/science.1167549

Wang, Y. H., Liu, Z. R., Zhang, J. K., Hu, B., Ji, D. S., Yu, Y. C., et al. (2015). Aerosol Physicochemical Properties and Implications for Visibility during an Intense Haze Episode during winter in Beijing. *Atmos. Chem. Phys.* 15, 3205–3215. doi:10.5194/acp-15-3205-2015

Wang, Y., Wang, Y., Wang, L., Petäjä, T., Zha, Q., Gong, C., et al. (2019). Increased Inorganic Aerosol Fraction Contributes to Air Pollution and Haze in China. *Atmos. Chem. Phys.* 19, 5881–5888. doi:10.5194/acp-19-5881-2019

Wang, Y., Yu, M., Wang, Y., Tang, G., Song, T., Zhou, P., et al. (2020). Rapid Formation of Intense Haze Episodes via Aerosol-Boundary Layer Feedback in Beijing. *Atmos. Chem. Phys.* 20 (1), 45–53. doi:10.5194/acp-20-45-2020

Wang, Z., Cao, X., Zhang, L., Notholt, J., Zhou, B., Liu, R., et al. (2012). Lidar Measurement of Planetary Boundary Layer Height and Comparison with Microwave Profiling Radiometer Observation. *Atmos. Meas. Tech.* 5 (8), 1965–1972. doi:10.5194/amt-5-1965-2012

Xian, T., Li, Z., and Wei, J. (2021). Changes in Air Pollution Following the COVID-19 Epidemic in Northern China: The Role of Meteorology. *Front. Environ. Sci.*, 9. doi:10.3389/fenvs.2021.654651

Yang, D., Li, C., Lau, A. K.-H., and Li, Y. (2013). Long-term Measurement of Daytime Atmospheric Mixing Layer Height over Hong Kong. *J. Geophys. Res. Atmos.* 118 (5), 2422–2433. doi:10.1002/jgrd.50251

Zhang, W., Guo, J., Miao, Y., Liu, H., Zhang, Y., Li, Z., et al. (2016). Planetary Boundary Layer Height from CALIOP Compared to Radiosonde over China. *Atmos. Chem. Phys.* 16 (15), 9951–9963. doi:10.5194/acp-16-9951-2016

Zhang, Y., Seidel, D. J., and Zhang, S. (2013). Trends in Planetary Boundary Layer Height over Europe. *J. Clim.* 26 (24), 10071–10076. doi:10.1175/JCLI-D-13-00108.1

Conflict of Interest: The authors declare that the research was conducted in the absence of any commercial or financial relationships that could be construed as a potential conflict of interest.

The reviewer YM declared a shared affiliation, with no collaboration, with one of the authors GT to the handling editor at the time of the review.

Publisher's Note: All claims expressed in this article are solely those of the authors and do not necessarily represent those of their affiliated organizations, or those of the publisher, the editors, and the reviewers. Any product that may be evaluated in this article, or claim that may be made by its manufacturer, is not guaranteed or endorsed by the publisher.

frontiers in Environmental Science

ORIGINAL RESEARCH
published: 10 November 2021
doi: 10.3389/fenvs.2021.763504

Long-Term Variation in Wintertime Atmospheric Diffusion Conditions Over the Sichuan Basin

Guoyin Wang[1,2], *Wennan Leng*[3], *Shaojing Jiang*[4] *and Bangjun Cao*[5]*

[1]Department of Atmospheric and Oceanic Sciences and Institute of Atmospheric Sciences, Fudan University, Shanghai, China, [2]CMA-FDU Joint Laboratory of Marine Meteorology, Shanghai, China, [3]Gansu Weather Modification Office, Lanzhou, China, [4]Department of Geography and Spatial Information Techniques, Ningbo University, Ningbo, China, [5]Plateau Atmosphere and Environment Key Laboratory of Sichuan Province, School of Atmospheric Sciences, Chengdu University of Information Technology, Chengdu, China

Atmospheric diffusion is one of the factors affecting local air quality, dominating the evolution of air pollution episodes. Previous work has emphasized the unfavorable diffusion conditions in the Sichuan Basin resulting from its complex terrain. However, the recent spatiotemporal variation in atmospheric diffusion conditions in the basin and their effects on local air quality remain unclear. Based on the wind speed, boundary layer height, vertical potential temperature difference of ERA5 analysis, two independent metrics containing information on horizontal and vertical diffusion ability, i.e., ventilation coefficient (V_E) and the air stagnant conditions (ASI), are involved to indicate wintertime atmospheric diffusion conditions in the basin. Both V_E and ASI reveal a decrease tendency of atmospheric diffusion condition from the northwestern portion of the basin to the southeast. In terms of the long-term variation in diffusion conditions, V_E showed a broader increasing trend from 1979 to 2019, with a distinct increase in the western region. In contrast, the occurrence of air stagnation events has declined –3~–6%/decade in the basin, more significantly over the western basin. Both the increase in V_E and the decrease in air stagnation frequency indicate the improvement of atmospheric diffusion conditions in the Sichuan Basin from 1979 to 2019, which mitigates the effects of air pollutant emissions to some extent. The enhancement of diffusion conditions is due to the improvement of vertical diffusion conditions. The lowest seasonal PM2.5 concentrations occur in the northwestern basin, where V_E is highest and ASI is lowest. Atmospheric diffusion conditions can explain approximately 25–50% of the interannual variation in PM2.5 concentrations in Chengdu.

Keywords: atmospheric diffusion ability, ventilation coefficient, atmospheric boundary layer, air pollution, Sichuan Basin

OPEN ACCESS

Edited by:
Longlei Li,
Cornell University, United States

Reviewed by:
Pengfei Tian,
Lanzhou University, China
Xuanze Zhang,
Institute of Geographic Sciences and Natural Resources Research (CAS), China
Qinjian Jin,
University of Kansas, United States

***Correspondence:**
Bangjun Cao
caobj1989@163.com

Specialty section:
This article was submitted to Atmosphere and Climate, a section of the journal Frontiers in Environmental Science

Received: *24 August 2021*
Accepted: *27 October 2021*
Published: *10 November 2021*

Citation:
Wang G, Leng W, Jiang S and Cao B (2021) Long-Term Variation in Wintertime Atmospheric Diffusion Conditions Over the Sichuan Basin. Front. Environ. Sci. 9:763504. doi: 10.3389/fenvs.2021.763504

1 INTRODUCTION

Severe and frequent air pollution has become a major environmental concern in China in recent years (Dang and Liao, 2019; Hu et al., 2019; Li et al., 2019; Mu and Zhang, 2014). Pollution episodes, characterized by dense fine particles and low horizontal visibility, have many negative impacts on transportation, public health and weather/climate (Che et al., 2019; Chen H. et al., 2019; Chen S. et al., 2019; Feng and Wang, 2019; He Y. et al., 2018; Jian et al., 2018; Wang et al., 2009; Wang et al.,

2018b). Numerous studies have been conducted to reveal the mechanisms of haze formation and its long-term variation, indicating that high pollutant emissions and unfavorable meteorological conditions are two key factors (Chen et al., 2018; Ding et al., 2019; Fan et al., 2020; Huang et al., 2018; Miao et al., 2017; Hu et al., 2021). Secondary aerosol formation also contributes to the explosive growth of particulate concentrations, especially during the developing stage of each pollution episode (Guo et al., 2019; He J. et al., 2018; Ma et al., 2020; Sun et al., 2013; Zhao D. et al., 2018). Moreover, variation in East Asian winter monsoon strength, El Niño-Southern Oscillation, Arctic Sea ice extent and the phase of Pacific Decadal Oscillation change background atmospheric circulation and in turn affect the formation of air pollution at different time scales (Cai et al., 2017; Chang et al., 2020; Chen and Wang, 2015; Li et al., 2016; Wang et al., 2020; Yin et al., 2017).

There are four main regions suffering from the severe air pollution in China: the North China Plain (NCP), Yangtze River Delta (YRD), Pearl River Delta (PRD) and Sichuan Basin (Bi et al., 2016; Wang and Zhang, 2020a; Wang and Zhang, 2020b; Xia et al., 2020; Zhang and Geng, 2019; Zhao and Garrett, 2015; Zhao et al., 2020). Compared to the first three mega-regions, less attention has been given to the air quality in the Sichuan Basin, especially the long-term variation in air quality and its attribution in terms of the long-term variation. The Sichuan Basin comprises the greater part of eastern Sichuan Province and the western portion of Chongqing municipality located in southwestern China. It is surrounded by the highlands of the Tibetan Plateau to the west, the YunGui Plateau to the south, the Wu Mountains to the east and the Daba Mountains to the north (Cao et al., 2020; Liu et al., 2021; Zhong et al., 2019). The complex local topography stimulates special meteorological conditions with lower surface wind, higher relative humidity and a stable boundary layer, which is conducive to the formation of haze in the basin (Liao et al., 2018; Ning et al., 2018). Therefore, although the anthropogenic emissions in the basin are not as much as those in the other three regions, its air pollution ranks in the top four regions in China (Fan et al., 2015; Gui et al., 2019; Liu et al., 2019; Zhang et al., 2019; Zhao S. et al., 2018).

Emissions in a specific region do not normally change much over a short period, but local meteorological patterns change rapidly and can strongly affect the accumulation, removal, and transport of air pollutants and thus the day-to-day variation in air pollutants (Chen et al., 2020; Zhang, 2017; Zhang et al., 2014; Zhao C. et al., 2018). A combined metric to evaluate the effects of atmospheric conditions on air pollution is the atmospheric diffusion ability, which cannot be ignored in the quantitative evaluation of historical emission reduction effects and the development of emission reduction measures. The atmospheric ventilation coefficient (V_E) provides an indication of the ability of the atmosphere to disperse pollutants over a region and is the metric most frequently used to predict the evolution of local diffusion conditions. Generally, V_E in the basin is relatively weak due to special terrain (Ning et al., 2019; Tang et al., 2015; Zhu et al., 2018). Severe air pollution episodes are also linked to the occurrence of air stagnation conditions (Wang et al., 2016). A previous work highlighted that the Sichuan Basin experiences frequent air stagnation conditions for approximately half of the whole year, which is the worst atmospheric diffusion condition among the four severely polluted regions in China listed above. However, the work of Wang et al. (2016) has only provided an average frequency of air stagnation in the basin based on the meteorological conditions at several PM2.5 observation stations from 2013 to 2017. The thresholds for the occurrence of air stagnation events are established according to the global air pollutant concentrations, which may smooth some local air pollution information. In addition, the spatial variation in the occurrence frequency of air stagnation conditions in the basin, how atmospheric diffusion conditions have changed in recent decades, and the extent of impact of temporal and spatial variation in atmospheric diffusion conditions on local air quality remain unclear.

In this work, the long-term variation in V_E and the occurrence of air stagnation events are examined to investigate the spatial and temporal variation in atmospheric diffusion conditions in the Sichuan Basin. The regional thresholds for air stagnation conditions are defined in **Section 2**. Spatiotemporal variation in diffusion conditions and their effects on local air quality are shown in **Section 3**.

2 DATA AND METHOD

2.1 Data

Figure 1 shows the altitude distribution around the Sichuan Basin. Sixty-four air quality observation stations from the Ministry of Ecology and Environment of the People's Republic of China are located in the basin (i.e., altitude under 1,000 m). The 64 stations belong to 14 cities in Sichuan Province and Chongqing City. The PM2.5 concentrations observed from December 2013 to December 2019 at the 64 stations were used to indicate the variation in ambient air quality. The fifth-generation European Centre for Medium-Range Weather Forecasts atmospheric reanalysis data (ECMWF ERA5) with a horizontal resolution of 0.25°×0.25° from 1979 to 2019 were used to supply meteorological variables for the Sichuan Basin. The evaluation of the representation and accuracy of ERA5 over Sichuan Basin are shown in SI. The mean wind speeds at 1,000, 925, 900, 875 and 850 hPa (Wind_BL) are considered the average wind speeds in the boundary layer. The 10-m wind speed (Wind_10), potential temperature difference between 925 hPa and 850 hPa ($\Delta\theta$), boundary layer height (BLH), and total precipitation were incorporated to evaluate the atmospheric diffusion conditions in the Sichuan Basin. ERA5 BLH is diagnosed as the height where the bulk Richardson number becomes superior to 0.25 (https://apps.ecmwf.int/codes/grib/param-db?id=159). Given the relatively poor performance for the stable boundary layer in model simulation (Stull, 2012), only the 14:00 local time (6:00 UTC) air quality and meteorological dataset were used in this work. The altitude distribution around the Sichuan Basin was derived from the global digital elevation model (DEM), with a horizontal grid spacing of 30 arc seconds (approximately 1 km).

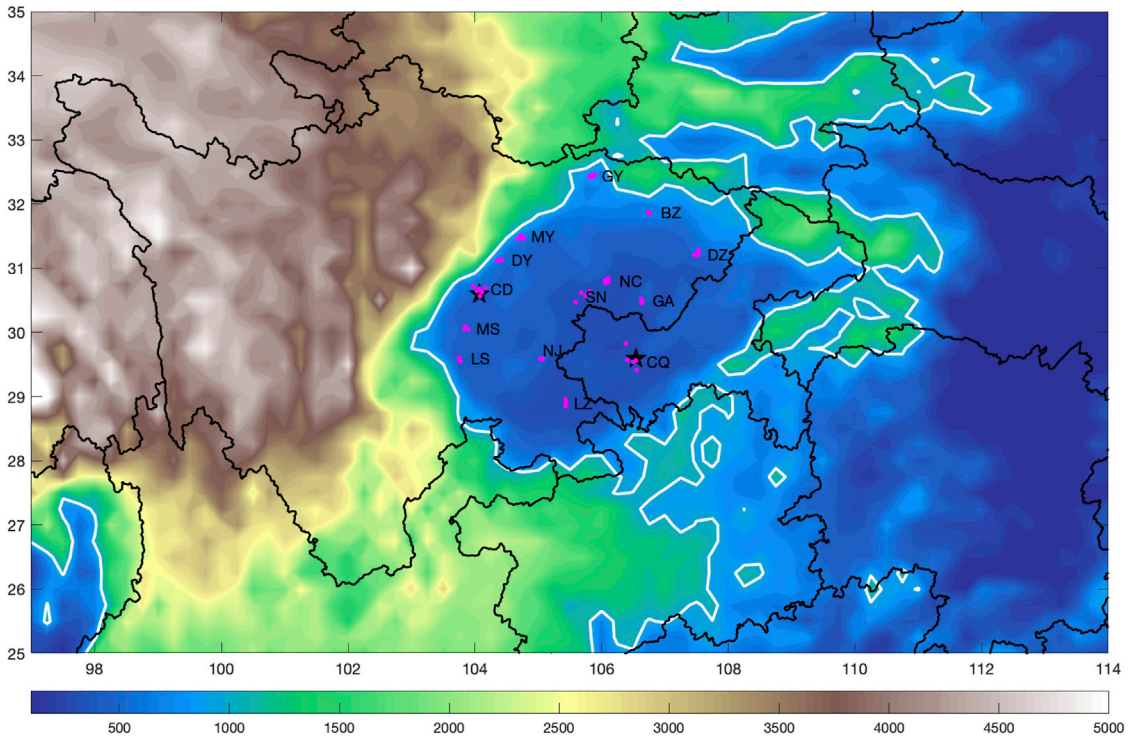

FIGURE 1 | Spatial distribution of elevation around the Sichuan Basin (unit: m) and 64 air quality observation stations in the basin. The edge of the Sichuan Basin is marked by the 1000-m contour line (white line). Magenta dots indicate the locations of the 64 air quality stations. GY (Guangyuan), BZ (Bazhong), MY (Mianyang), DY (Deyang), CD (Chengdu), MS (Meishan), LS (Leshan), NC (Nanchong), SN (Suining), NJ (Nenjiang), DZ (Dazhou), GA (Guang'an), CQ (Chongqing), and LZ (Luzhou) indicate the 14 cities in the basin. CD and CQ are marked by black stars.

2.2 Method for Calculating the Ventilation Coefficient (V_E) and Air Stagnation Index (ASI)

The ventilation coefficient (V_E) is a product of the boundary layer height and average vertical wind speed through the boundary layer. The higher the V_E is, the more efficiently the atmosphere can disperse near-surface pollutants and the better the air quality. The V_E can be calculated by (Lu et al., 2012; Liu et al., 2012; Sujatha et al., 2016):

$$V_E = \int_0^{BLH} u(z)dz = \overline{u_{BL}} \cdot BLH$$

where $\overline{u_{BL}}$ is the average wind speed in the boundary layer.

Air stagnation is considered to consist of light winds so that horizontal dispersion is at a minimum, a stable lower atmosphere that effectively prevents vertical escape, and no precipitation to wash any pollution away (Wang et al., 2018a). Severe air pollution episodes are usually related to the presence of air stagnation. There exist several types of quantitative definitions for air stagnation events based on different meteorological variables depending on the domain concerned. Previous work has shown relatively high frequency of air stagnation events in the Sichuan Basin based on a nationwide unified air stagnation threshold. However, it is essential to identify a more regionally applicable air stagnation definition due to the complicated terrain around the basin. Here, the 10 m (Wind_10) wind speed and potential temperature difference between 925 hPa and 850 hPa ($\Delta\theta$) were used to measure the atmospheric horizontal and vertical dispersion capability (Wang et al., 2016; Wang et al., 2018a). Higher $\Delta\theta$ means stronger temperature inversion in the low troposphere, which indicates lower capability of vertical diffusion and implies higher concentration of surface PM2.5. In terms of the surface wind speed, a higher wind speed indicates more effective outward transport of local air pollutants. Both vertical and horizonal diffusion control the variation in surface PM2.5 concentrations. However, how do Wind_10 and $\Delta\theta$ coordinate to manage the diffusion of air pollutants? **Figure 2** shows the seasonal average PM2.5 concentrations corresponding to the specific Wind_10 and ($\Delta\theta$) ranges. Dry-day PM2.5 concentrations at the 64 stations were used to identify the threshold of air stagnation. Generally, PM2.5 concentrations decrease with increasing wind speeds and increase with increasing $\Delta\theta$, especially in spring and winter. PM2.5 concentrations are the most sensitive to the variation in Wind_10 and $\Delta\theta$ in winter, with PM2.5 concentrations exceeding 110 $\mu g/m^3$ under the conditions of high-$\Delta\theta$ and low-Wind_10 compared to values lower than 50 $\mu g/m^3$ for the situations of low-$\Delta\theta$ and high-Wind_10. Therefore, we only focus

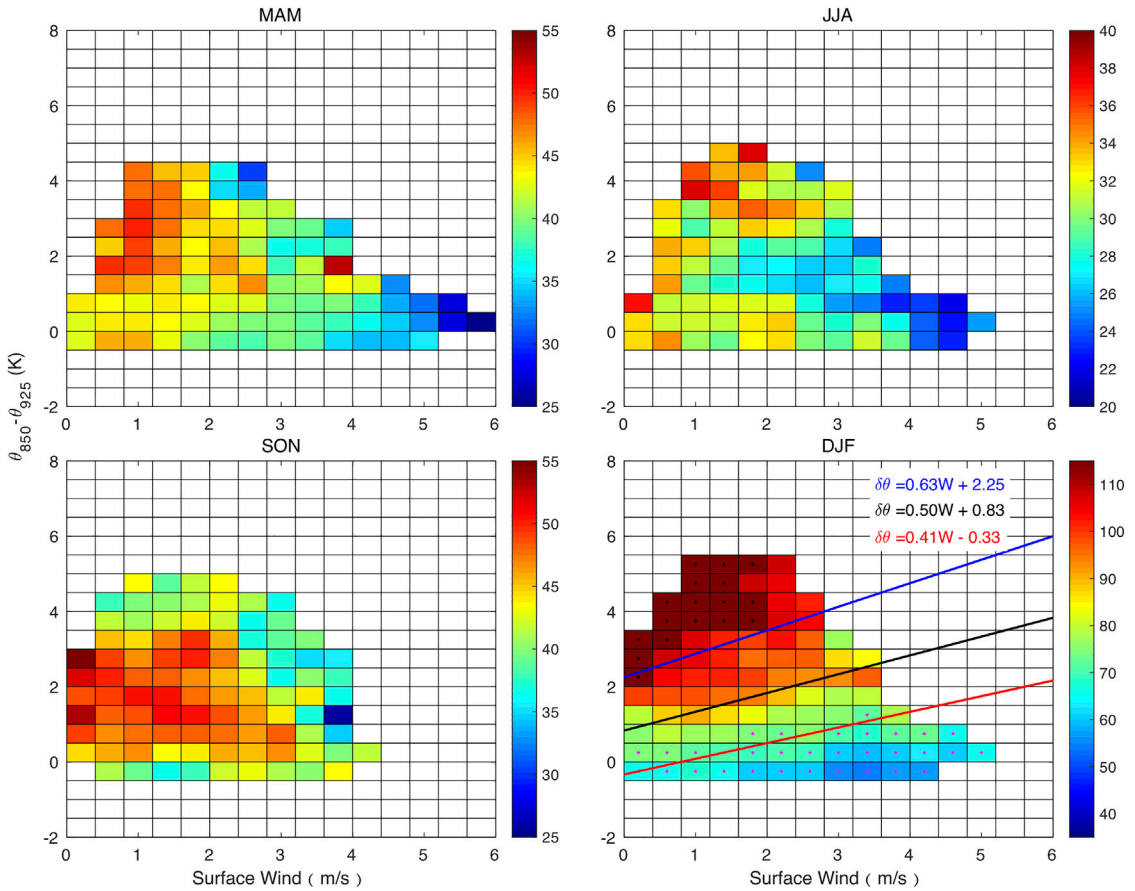

FIGURE 2 | Seasonal dependence of PM2.5 concentrations on the 10-m wind speed (Wind_10) and potential temperature difference between 925 hPa and 850 hPa ($\Delta\theta$) (unit of PM2.5 is μg/m^3). The average PM2.5 concentrations are counted according to the observed $\Delta\theta$-Wind_10. All the available dry-day PM2.5 concentrations at the 64 stations are used in this figure. Grids with sample sizes greater than 100 are shown here. Dots in winter indicate the average PM2.5 concentration of the specific grid higher than 115 (unhealthy level) or lower than 75 (moderate level) μg/m^3. The blue, black and red lines in winter indicate the thresholds for unfavorable conditions, air stagnation and favorable conditions, which are fitted based on the locations of dots in **Figures 2**, **3**, respectively.

on the wintertime atmospheric diffusion conditions hereafter. Taking the $\Delta\theta$-Wind_10 locations with PM2.5 concentrations lower than 75 (moderate level) or higher than 115 μg/m^3 (unhealthy level) as the conditions favorable or unfavorable, respectively, for air pollutant diffusion, **Figure 2** shows the $\Delta\theta$-Wind_10 thresholds for favorable and unfavorable conditions in winter. If the observed $\Delta\theta$-Wind_10 values in a region exceed the unfavorable threshold, the atmospheric diffusion condition for the specific day is considered unfavorable. Similarly, if$\Delta\theta$-Wind_10 meets the criterion of less than the favorable threshold, conditions are defined as favorable.

To eliminate the effects of seasonal, spatial, and long-term variations in PM2.5 concentration, PM2.5 concentrations on dry days were normalized by their corresponding monthly mean values. That is, if the normalized PM2.5 concentrations exceeded 100%, the original PM2.5 concentrations were higher than their monthly mean, and the corresponding atmospheric conditions were defined as air stagnation conditions. **Figure 3** displays the relationship between normalized PM2.5 concentrations and the variation in $\Delta\theta$-Wind_10. It shows the same distribution pattern for normalized PM2.5 concentrations as that of the original PM2.5 concentrations; i.e., with decreasing $\Delta\theta$ and increasing Wind_10, normalized concentrations tend to decrease. **Figure 3** shows the fitting line of the threshold of the air stagnation condition (i.e., 100% normalized concentrations) in winter. If the observed $\Delta\theta$-Wind_10 is located in the upper region of the fitting line, the atmospheric conditions will be defined as air stagnation conditions. Therefore, unfavorable conditions are somewhat extreme and severe air stagnation conditions. It is assumed that all rainy days with 4-h precipitation amounts higher than 0.5 mm are by default no-air-stagnation days because of wet deposition. If precipitation exceeds 1 mm, the atmospheric conditions are considered favorable due to the more effective wet deposition. A day can be classified as an air-stagnation or no-air-stagnation day based on the observed $\Delta\theta$-Wind_10. The monthly or seasonal occurrence of air stagnation days is defined

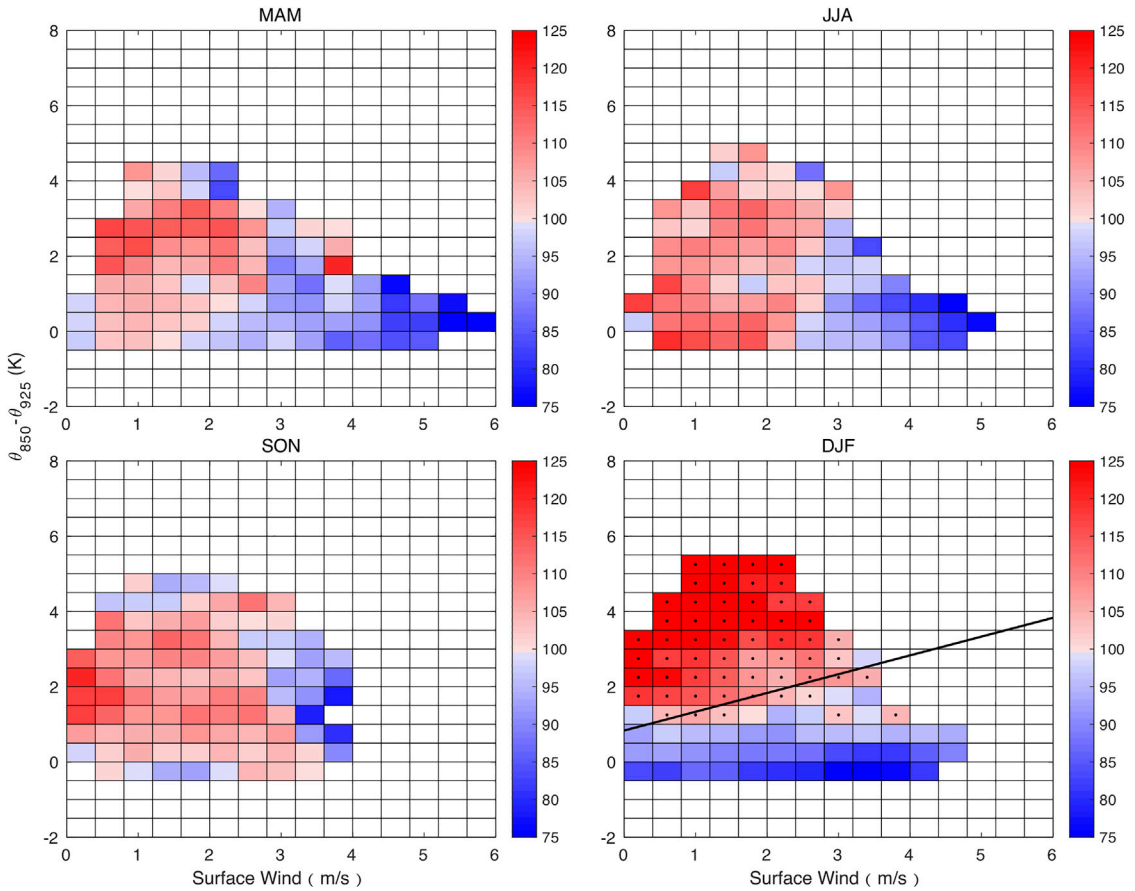

FIGURE 3 | Seasonal dependence of normalized PM2.5 concentrations on the 10-m wind speed (Wind_10) and potential temperature difference between 925 hPa and 850 hPa ($\Delta\theta$) (unit of normalized PM2.5 is %). Dots in winter indicate the normalized PM2.5 concentration of the specific grid greater than 100% (higher than its monthly mean). The black line in winter indicates the threshold of the air stagnation condition based on the locations of dots. Grids with sample sizes greater than 100 are shown here.

as the air stagnation index (ASI), which combines the horizontal and vertical atmospheric diffusion conditions.

3 RESULTS

3.1 Distribution of the Climatology of Atmospheric Diffusion Conditions in the Sichuan Basin

The wintertime climatology distributions of V_E, and frequencies of ASI, favorable and unfavorable conditions over the Sichuan Basin are shown in **Figure 4**. V_E tended to decrease from the northwest region of the basin to the southeast, with the maximum V_E exceeding 3,400 m^2/s compared to the lowest value of approximately 1,600 m^2/s. **Figure 5** shows the distribution of Wind_BL and BLH, which are used for the calculation of V_E. The BLH and average wind speed in the boundary layer were higher in the northwest portion of the basin, where the elevations are in the range of 500–1,000 m (**Figure 1**). The sloped terrain in the northwest area of the basin may increase absorption of solar radiation (Wang and Wang, 2015), enhancing the development of the daytime convective boundary layer and the downward transport of upper momentum, which leads to higher BLH and Wind_BL. In addition, the northwestern region of the basin is also a principal track of northwestern cold air to the basin, and the airflow over the northern mountain brings cold air and heavy wind to the northwestern basin. Deeper in the basin, where the elevation is lower than 500 m, both BLH and average wind speed declined by approximately 40% compared to the northwest region due to the blocking of terrain and the effect of valleys. The almost synchronous spatial variations in BLH and Wind_BL contributed to the evident regional difference in V_E in the basin.

As a metric combining the atmospheric horizontal and vertical diffusion conditions and wet deposition effect, the frequency of ASI can be used to measure the local atmospheric diffusion capacity more comprehensively. **Figure 4** shows an almost opposite spatial distribution of ASI to V_E over the basin, with an increasing tendency from the northwest to the southeast region. The spatial distribution pattern of ASI frequency

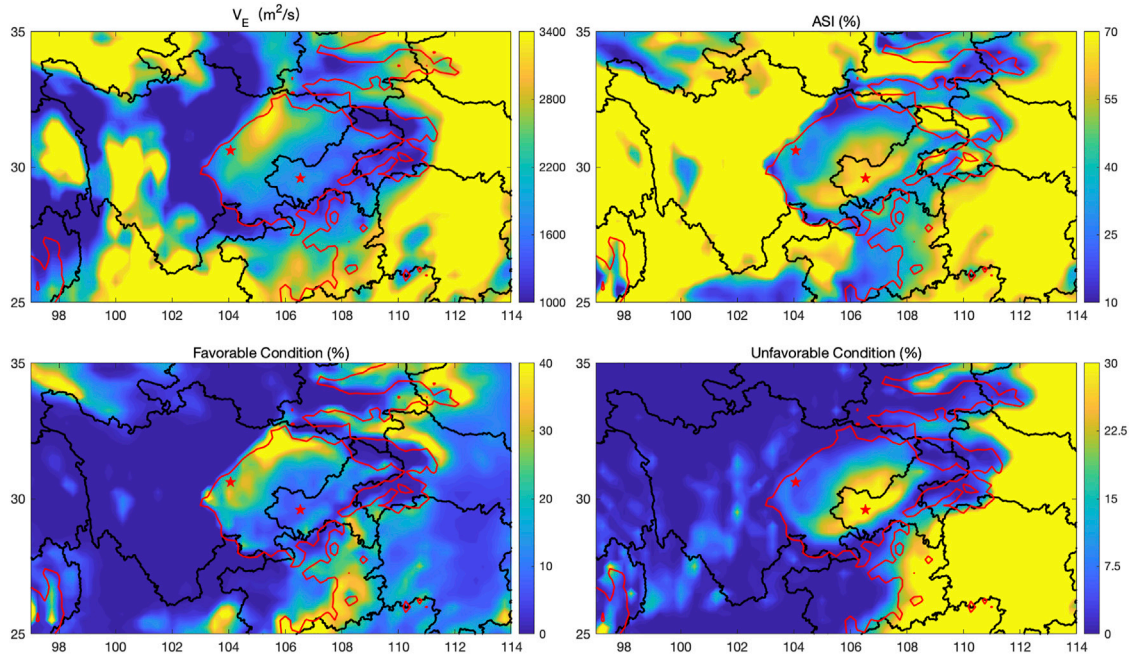

FIGURE 4 | Distributions of ventilation coefficient (V_E), frequency of air stagnation index (ASI), favorable condition and unfavorable condition during the winters from 1979 to 2019 in Sichuan Basin. Two red pentagrams indicate the locations of Chengdu and Chongqing.

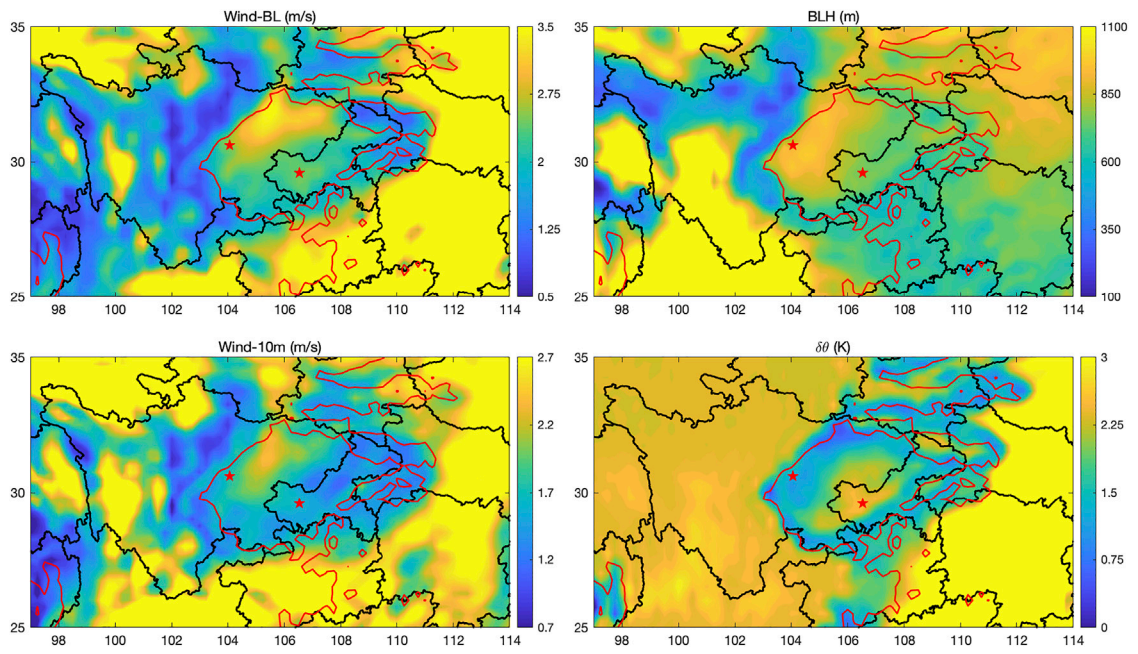

FIGURE 5 | Distributions of boundary layer wind speed (Wind_BL), boundary layer height (BLH), 10-m wind speed (Wind_10) and potential temperature difference between 925 hPa and 850 hPa ($\Delta\theta$) during the winters from 1979 to 2019 in the Sichuan Basin. Two red pentagrams indicate the locations of Chengdu and Chongqing.

climatology over the basin agrees well with the previous work (Liao et al., 2018). The wintertime ASI frequency was lower than 20% in the northwestern part of the basin, while it increased to over 60% in the southeastern low-altitude region. The spatial correlation coefficient between ASI frequency and elevation was -0.44 over the basin region, indicating that more frequent air stagnation events occurred in the low-altitude region. According to the climatology of the surface wind speed (Wind_10) and

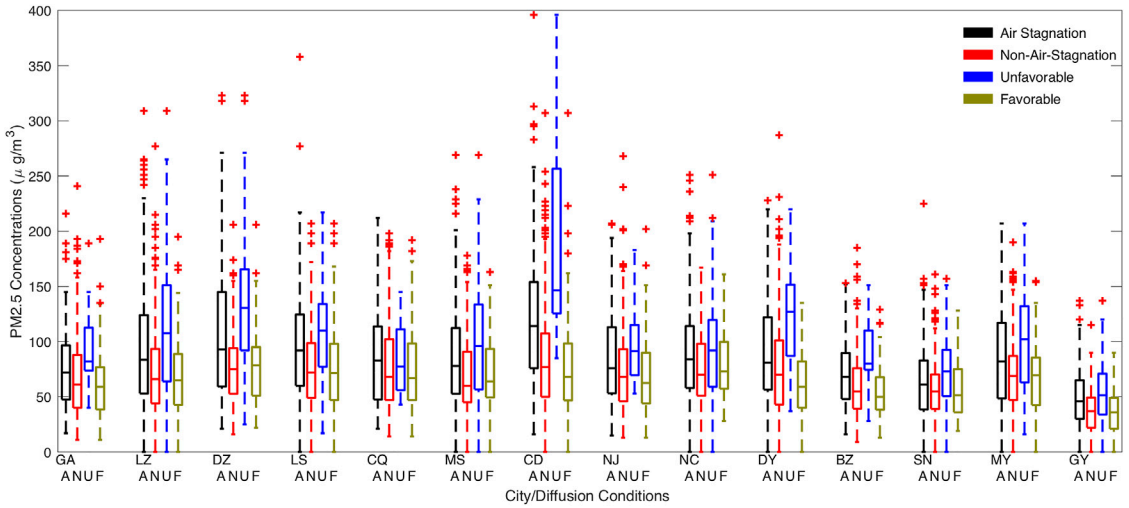

FIGURE 6 | Box plot of daily mean PM2.5 concentrations according to different metrics of atmospheric diffusion conditions in the specific cities. Abbreviations of the 14 cities are the same as in **Figure 1**. Labels of A/N/U/F in the *X*-axis indicate air stagnation, no-air-stagnation days, and unfavorable and favorable conditions, respectively.

potential temperature difference between 925 hPa and 850 hPa ($\Delta\theta$) in **Figure 5**, Wind_10 showed a decreasing tendency from the northwest to the southeast region, similar to the distribution of Wind_BL. In the vertical direction, $\Delta\theta$ was lower in the southeast low-altitude region and higher in the northwest region, in contrast to the distribution of BLH. Based on the definition of ASI, low wind_10 simultaneous with high $\Delta\theta$ indicates a condition suitable for the occurrence of air stagnation. The consistent distribution of horizontal and vertical diffusion capability in space led to the spatial differences in ASI frequency over the basin.

A day can be defined as an air-stagnation day or a no-air-stagnation day, based on the threshold of $\Delta\theta$-Wind_10 in **Figure 3**. In general, the capability for air pollutant diffusion was higher on no-air-stagnation days than on air-stagnation days. However, **Figure 6** shows a large range of observed PM2.5 concentrations on air-stagnation days and on no-air-stagnation days, which indicates that the occurrence of air stagnation is not sufficiently accurate to measure the atmospheric diffusion ability of air pollutants. Applying the thresholds of national air quality standards, the $\Delta\theta$-Wind_10 relationship corresponding to moderate (75 μg/m^3) and unhealthy (115 μg/m^3) air quality levels is used to represent very favorable and very unfavorable diffusion conditions. **Figure 6** shows a clearer distinction PM2.5 concentrations between favorable and unfavorable than that for air-stagnation and no-air-stagnation days, demonstrating a more rational measurement of atmospheric diffusion conditions based on the occurrence of favorable and unfavorable conditions. According to the distribution of favorable and unfavorable condition frequencies in **Figure 4**, more than 40% of favorable diffusion conditions occurred in the northwestern part of the basin, compared to less than 10% for unfavorable conditions. In the southeastern low-altitude region of the basin, the frequency of favorable conditions decreased to approximately 15%, and the occurrence of unfavorable conditions exceeded 30%. Because unfavorable conditions are extreme air stagnation conditions, the spatial distribution pattern of occurrence frequencies was almost identical, with an overall lower frequency of unfavorable conditions. The high frequency of unfavorable diffusion conditions in the southeastern region of the basin exacerbates local wintertime air quality.

3.2 Long-Term Variation in Atmospheric Diffusion Conditions in the Basin

The emission of air pollutants and their precursors is the initial cause of air pollution episodes, but the daily fluctuations and evolution of air quality are exacerbated by unfavorable meteorological conditions, which can be measured based on atmospheric diffusion conditions. Air pollutant emissions are thought to have increased due to anthropogenic activities in recent decades, which is the main reason for the worsening of ambient air quality. However, it remains unclear how the recent atmospheric diffusion conditions changed and what the effect of atmospheric condition variation on the air quality is. **Figure 7** shows the patterns of variation in wintertime atmospheric diffusion conditions in the basin during the period of 1979–2019. The linear trends of V_E, ASI frequency, and favorable and unfavorable condition frequencies indicate the variation in atmospheric diffusion conditions. In general, V_E showed a broadly increasing trend in the Sichuan Basin from 1979 to 2019, with a higher positive tendency in the western region and a weak negative trend in the eastern part. The V_E in Chengdu and Chongqing cities showed an almost identical weakly positive tendency of approximately 20 m^2/(s decade). Although the linear trend was insignificant, the consistent increase in V_E in the basin represents an improvement in

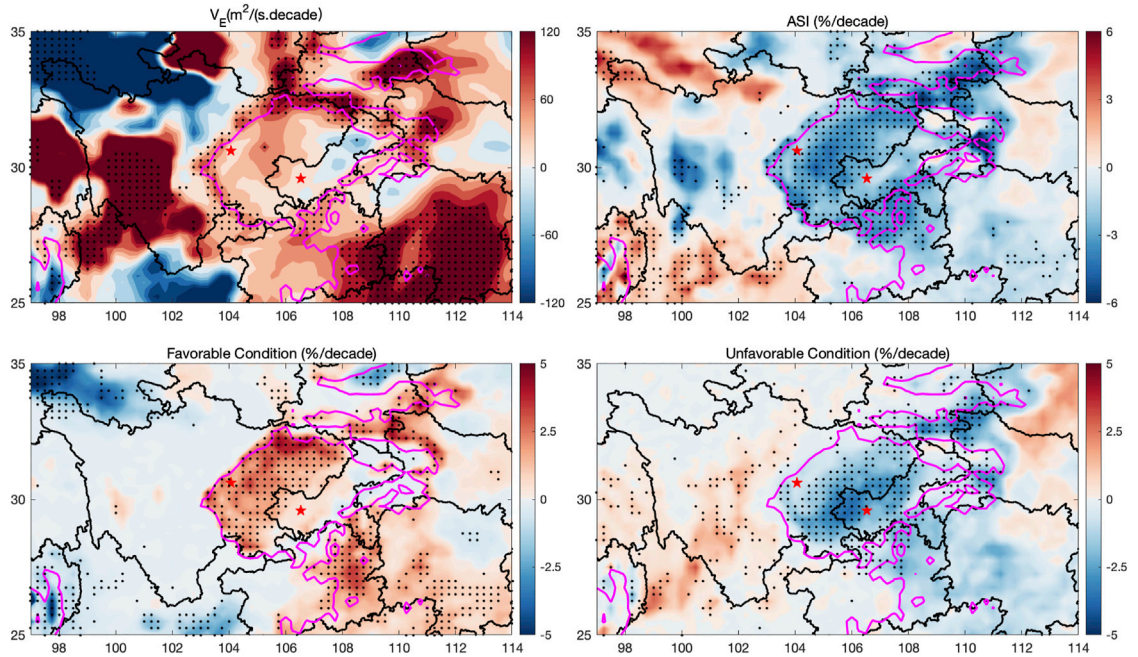

FIGURE 7 | Distribution of the long-term trends of V_E, ASI, and favorable and unfavorable condition frequencies during the winters from 1979 to 2019 in the Sichuan Basin. Dots mark the significance at 5% of the linear trends based on least square method.

atmospheric diffusion conditions in recent decades, which may alleviate to a certain extent the increase in anthropogenic emissions. The temporal variation of the two factors affecting V_E are shown in **Figure 8**. The wind speed in the boundary layer reveals a decreasing trend in the basin, with a significant negative trend in the eastern part, where the Wind_BL was lower than that in the northwestern region. That is, the already weak horizontal diffusion conditions decreased further. However, in the vertical direction, a significant increase in BLH occurred over most regions of the basin, which in part counteracts the effects of the decreasing Wind_BL and resulted in an overall increase in V_E.

Measuring the variation in diffusion conditions from another view, **Figure 7** also shows the pattern for the ASI frequency. Contrary to the increasing V_E tendency, the wintertime occurrence of air stagnation events exhibited a decreasing trend of ~3–6%/decade in the basin. The negative tendency of the ASI frequency was more significant over the western part of the basin than in the eastern region, which is similar to the pattern for V_E. A lower frequency of ASI also implies better atmospheric diffusion conditions. The variation in surface wind speed was not significant in the basin as shown in **Figure 8**. For wet deposition, precipitation frequency is considered as the main factor based on the definition of ASI. The variation in precipitation frequency was weak and insignificant, although the wintertime precipitation amount showed a significant decreasing trend during the study period. Therefore, the impact of horizonal diffusion conditions and wet deposition on ASI variation can be neglected, and the decreasing trend in ASI frequency was driven by the negative tendency of $\Delta\theta$. In sum, regardless of the increase in V_E or the decrease in ASI frequency, the two independent metrics exhibit improvements in atmospheric diffusion conditions in the Sichuan Basin from 1979 to 2019, which mitigates the effects of air pollutant emissions to some extent. Given the causes underlying variation in V_E and ASI, it is the recent better vertical diffusion conditions (i.e., higher BLH and weaker $\Delta\theta$) that have contributed to the overall improvement of atmospheric diffusion conditions.

The variation in frequencies of favorable and unfavorable conditions is also illustrated in **Figure 7**. **Figure 7** shows a large area of increasing frequency of favorable conditions in the basin, which indicates the improvement in atmospheric diffusion conditions. The occurrence of favorable conditions increased significantly by 4–5%/decade over the western part of the basin, but the tendency was not significant in the eastern region. The spatial distribution of variation in frequency of favorable conditions was consistent with that for V_E. The higher the V_E and favorable condition frequency, the better the diffusion conditions. Both V_E and favorable condition frequency indicated remarkable improvement in diffusion conditions over the western area of the basin, where the atmospheric diffusion conditions were better than in other regions. For unfavorable conditions, which are highly likely to exacerbate severe air pollution, the frequency showed a significant falling trend from 1979 to 2019 over the southeast low-altitude region. Although the increasing tendency of favorable condition frequency was not remarkable over the southeast low-altitude region, the significant decrease in the occurrence of unfavorable conditions marks an improvement in the local atmospheric diffusion conditions. Overall, a higher frequency of favorable diffusion conditions occurred over the

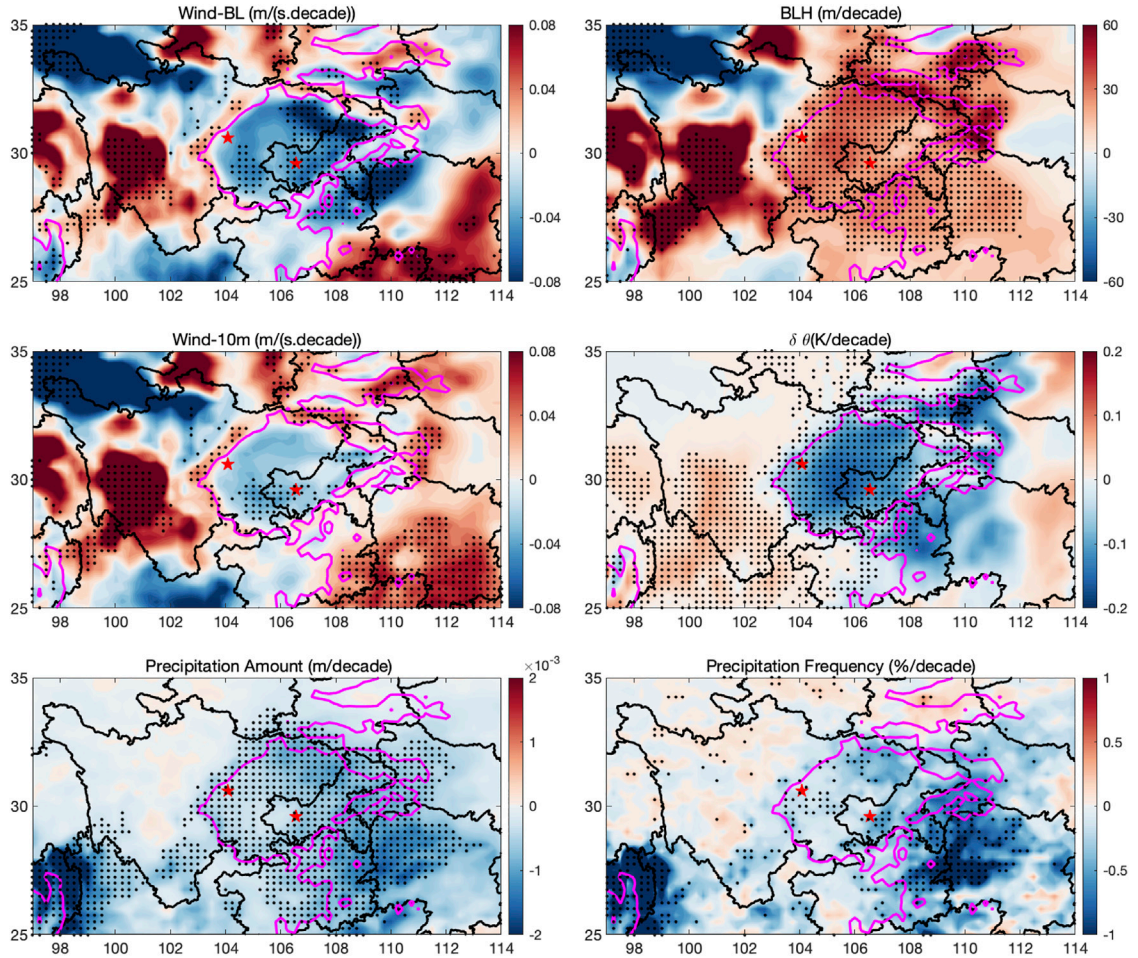

FIGURE 8 | Distribution of the long-term trends of Wind_BL, BLH, Wind_10 m, $\Delta\theta$, precipitation amount and precipitation frequency during the winters from 1979 to 2019 in the Sichuan Basin. Dots mark the significance at 5% of the linear trends based on least square method.

western better-diffusion region, and a lower frequency of unfavorable diffusion conditions took place over the eastern worse-diffusion region; both processes noticeably enhanced the atmospheric diffusion ability.

3.3 Effects of Atmospheric Diffusion Conditions on Air Quality

If the air pollutant emissions are identical for all cities, the differences in ambient air pollutant concentrations are almost determined by atmospheric diffusion conditions; i.e., better diffusion ability corresponds to low air pollutant concentrations, and vice versa. **Figure 9** shows the winter average PM2.5 concentrations varying with atmospheric diffusion conditions in the 14 cities within the basin. The cities are presented in ascending order of average V_E, with the lowest V_E in Guang'an (GA) and the highest value in Guangyuan (GY). Similar to the spatial distribution in **Figure 4**, **Figure 9** shows decreasing trends of ASI and unfavorable condition frequencies with increasing in V_E. Generally, average winter PM2.5 concentrations decline with increasing local atmospheric diffusion conditions. Guangyuan has the best air quality due to its excellent atmospheric diffusion ability. However, the atmospheric diffusion conditions are moderate in Chengdu (CD), which is the capital of Sichuan Province, and its air pollution is the most serious among the 14 cities. Located in the northwestern part of the basin, Mianyang (MY) has the second highest V_E, but its air quality is worse than in the other cities with approximately the same level of V_E. Chengdu and Mianyang are the top two cities in terms of GDP volume in Sichuan Province, which implies higher anthropogenic emission levels than other cities.

The multiyear average PM2.5 concentration showed a close relationship with atmospheric diffusion ability (**Figure 9**). Taking Chengdu and Chongqing as examples, **Figure 10** shows that the interannual air quality changed with diffusion conditions. Monthly PM2.5 concentrations exhibited a significant decreasing trend in Chengdu and Chongqing from the winter

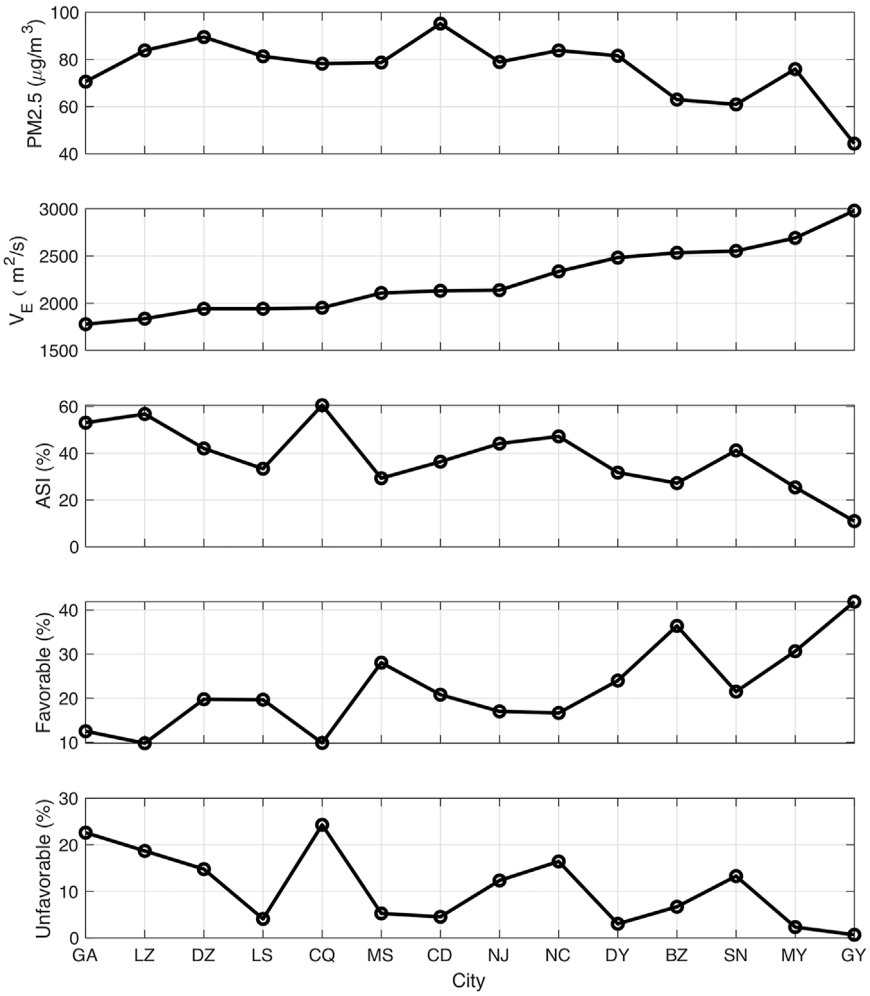

FIGURE 9 | Variation of winter average PM2.5 concentrations with V_E, frequency of ASI, and favorable and unfavorable conditions in the 14 cities in the basin. All the variables are the average values during the winters from 2013 to 2019. Cities are ranked by the value of V_E.

of 2013–2019, with negative tendencies of −11.34 and −8.93 μg/(m^3. yr). Based on the national air quality standard in China, daily mean PM2.5 concentrations lower than 35 μg/m^3 are good air quality days. **Figure 10** also shows the monthly occurrence of good air quality in the two cities from 2013 to 2019, showing significant increases of 2.12 and 2.87%/yr. The remarkable decrease in PM2.5 concentration and increase in the frequency of good air quality represent the success of emission reduction policies in recent years. The industrial and residential emissions of SO_2 in Sichuan Province and Chongqing municipality decreased from $1.29*10^6$ to $8.4*10^5$ tons from 2011 to 2017, which contributed to the significant decrease in regional PM2.5 concentrations (National Bureau of Statistics of China, 2020). To exclude the effects of emission reduction on air quality, the detrending time series of PM2.5 concentration and frequency of good air quality were used to investigate the influence of atmospheric diffusion conditions on the interannual variation in air quality. There were significant correlations between the occurrence of good air quality and VE/ASI/favorable conditions in the two cities, with correlation coefficients of 0.71/−0.5/0.6 and 0.47/−0.58/0.45 in Chengdu and Chongqing, respectively. In addition, the PM2.5 concentration was significantly negatively correlated with V_E and favorable condition frequency in Chengdu. Moreover, **Table 1** summarizes the correlation coefficients between the metrics indicating atmospheric diffusion conditions and the series of "moderate," "unhealthy for sensitive groups to unhealthy," "very unhealthy to hazardous" air quality in Chengdu and Chongqing. Only the occurrence of good or very unhealthy to hazardous air quality was closely associated with atmospheric diffusion. The frequencies of occurrence of moderate to unhealthy air quality were insensitive to variations in ambient atmospheric conditions.

4 CONCLUSIONS AND DISCUSSION

Atmospheric diffusion controls the day-to-day evolution of air pollution episodes, the long-term variation of which has

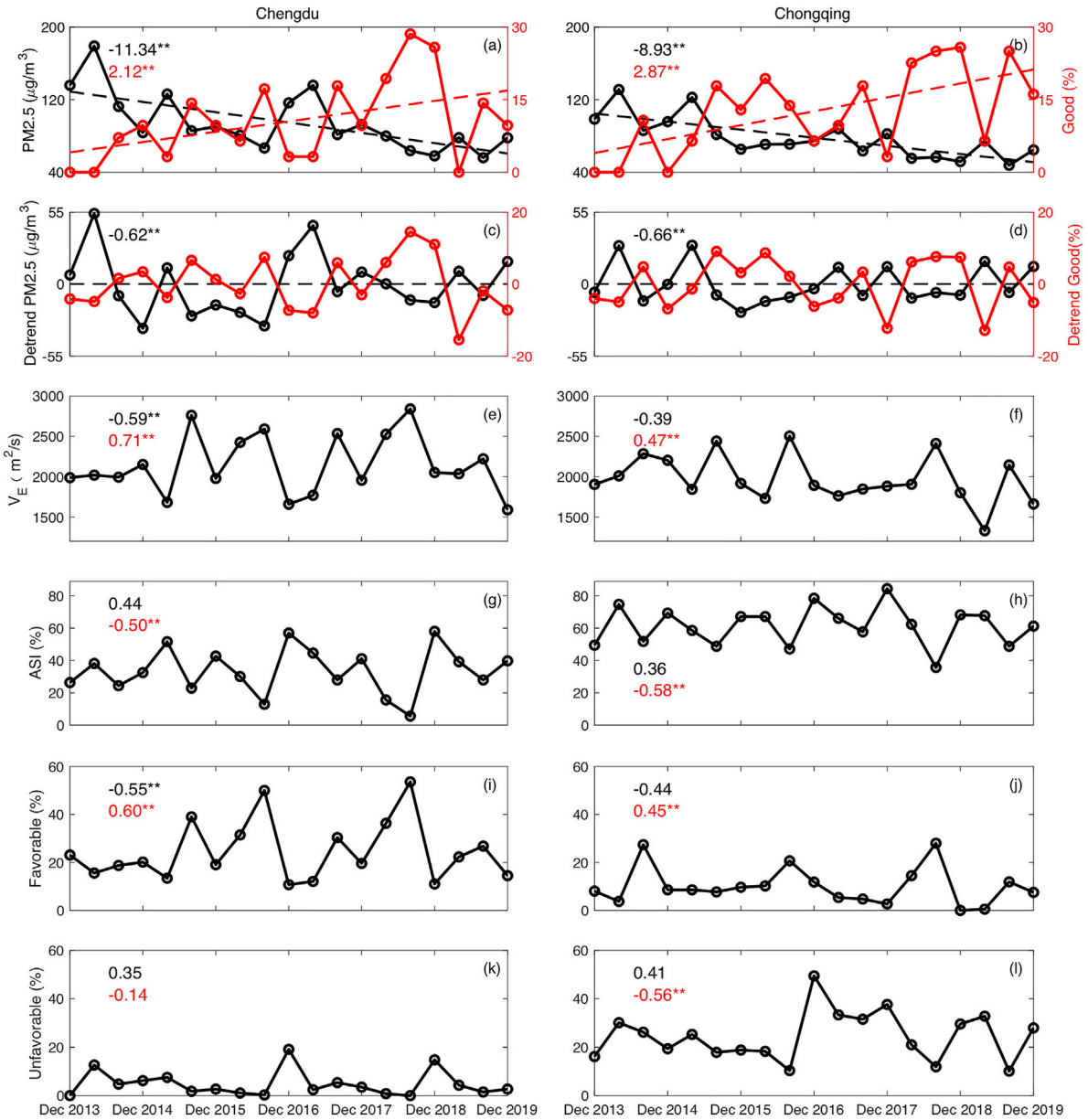

FIGURE 10 | Variation in monthly PM2.5 concentrations and good air quality frequency **(A–B)**, detrending PM2.5 concentrations and good air quality frequency **(C–D)**, V_E **(E–F)**, frequencies of ASI **(G–H)**, favorable **(I–J)** and unfavorable **(K–L)** conditions during the winters from 2013 to 2019 (19 months in total) in Chengdu and Chongqing. Detrending series were calculated by subtracting the linear trend from the original series. Values in Figs **(A–B)** are the linear trend of PM2.5 concentration (black) and good air quality (red). ** indicates significance at 0.01 of the linear trends based on least square method. Values in Figs **(C–D)** indicate the correlation coefficient of detrended PM2.5 concentrations and good air quality frequency. ** indicates that the correlation coefficient is significant at the 0.01 probability level. Values in Figs. **(E–L)** indicate the correlation coefficients between the detrended PM2.5 concentrations (black) and good air quality frequency (red) with the specific metric of atmospheric diffusion conditions. ** indicates that the correlation coefficient is significant at the 0.01 probability level.

important significance for the quantitative evaluation of historical emission reduction effects or the development of emission reduction measures. The spatial and temporal distributions of wintertime atmospheric diffusion conditions in the Sichuan Basin are examined in this work. The thresholds for occurrence of air stagnation events are established based on the relationship between PM2.5 concentrations and surface wind speed and potential temperature differences at 925 hPa and 800 hPa. V_E and the frequency of air stagnation events were incorporated to evaluate the variation in atmospheric diffusion conditions and their effects on air quality in the Sichuan Basin. Both atmospheric horizontal and vertical diffusion conditions are contained in the definitions of V_E and air stagnation events. Wind_BL/BLH/Wind_10/$\Delta\theta$, which are four independent variables, were used to indicate the capacity for horizontal and vertical diffusion ability, respectively. In terms of the spatial distribution of

TABLE 1 | Correlation coefficients between the detrend PM2.5 concentrations and the frequencies of different air quality levels with the specific metric indicating atmospheric diffusion conditions during the winter of 2013–2019 in Chengdu and Chongqing (* indicates that the correlation coefficient is significant at the 0.01 probability level).

Chengdu/Chongqing	Monthly mean	Good	Moderate	Unhealthy for sensitive groups to unhealthy	Very unhealthy to hazardous
PM2.5 (μg/m^3)	—	0–35	35–75	75–115	>115
V_E	–0.59*/–0.39	0.71*/0.48*	0.29/0.12	0.07/–0.07	–0.63*/–0.27
ASI	0.44/0.36	–0.5*/–0.58*	–0.15/–0.03	–0.31/0.09	0.54*/0.26
Favorable	–0.55*/–0.44	0.6*/0.46*	0.24/0.35	0.19/–0.20	–0.59*/–0.34
Unfavorable	0.35/0.41	–0.14/–0.56*	–0.26/–0.12	–0.34/0.15	0.47*/0.27

atmospheric diffusion conditions, V_E exhibited a decreasing tendency from the northwest of the basin to its southeast, with the highest V_E being higher than 3,400 m^2/s compared to the lowest value of approximately 1,600 m^2/s. The distribution of air stagnation event frequency is opposite to that of V_E, showing a low frequency of approximately 15% over the northwestern high-altitude basin and a higher frequency of 60% over the southeastern low-altitude region. The northwest-southeast decrease in atmospheric diffusion conditions is attributed to the consistent spatial distribution of horizontal diffusion conditions and vertical conditions, both of which showed higher ability over the northwestern basin and lower ability over the southeast. The frequency of favorable conditions showed with a spatial distribution similar to that of V_E, and the spatial variation in unfavorable conditions resembled that of air stagnation events.

Given the long-term variations in winter atmospheric diffusion conditions, V_E showed a broadly increasing trend from 1979 to 2019, with a distinct increase in the western region and a weak negative trend in the eastern basin. The significant increase in BLH explained the positive tendency of V_E over most of the basin, and the remarkable decrease in Wind_BL drove the negative tendency of V_E in the eastern basin. In contrast, the occurrence of air stagnation events showed a decreasing trend of ~3–6%/decade in the basin, which was more significant over the western part of the basin than over the eastern region. The decreasing pattern of ASI frequency was driven by the negative tendency of $\Delta\theta$. Generally, both increasing V_E and decreasing ASI frequency indicate the improvement of atmospheric diffusion conditions in the Sichuan Basin from 1979 to 2019, mitigating the effects of air pollutant emissions to some extent. The enhancement of atmospheric diffusion conditions is attributed to the improvement of vertical diffusion conditions (i.e., higher BLH and weaker $\Delta\theta$). The recent better atmospheric diffusion conditions are also reflected by the significant increasing trend of favorable conditions over the western part of the basin, and the dramatic decrease in the unfavorable condition frequency over the eastern region.

Seasonal PM2.5 concentrations declined with increasing local atmospheric diffusion conditions, with the best air quality in the northwest city of Guangyuan. Air quality in Chengdu and Mianyang were worse than in other cities with the same level of atmospheric diffusion conditions, perhaps because of their higher anthropogenic emission levels. The atmospheric diffusion conditions showed significant correlations with the occurrence of "good" and "very unhealthy to hazardous" air quality, and the occurrence frequencies of "moderate" to "unhealthy" air quality were insensitive to the variation in ambient atmospheric conditions. Atmospheric diffusion conditions were able to explain approximately 25–50% of the interannual variation in PM2.5 concentrations in Chengdu.

Long-term variation of daytime BLH have been investigated in many other studies, which shows remarkable increase trend over the past decades (Guo et al., 2016; Wang and Wang, 2016). The variation in wind speed, low tropospheric stability, surface temperature and cloud cover are considered as the dominant factors for the increase of BLH (Li et al., 2021; Guo et al., 2021). Considering the severe air pollution in the winter and poor performance of the stable BLH simulation, spatial and temporal variations in wintertime atmospheric diffusion conditions at 14:00 LST were investigated in this study. However, there were remarkable seasonal and diurnal differences in the processes in the atmospheric boundary layer (Stull, 2012; Wang and Wang, 2016), which may affect the variation in atmospheric diffusion conditions and warrant future studies.

DATA AVAILABILITY STATEMENT

The original contributions presented in the study are included in the article/**Supplementary Material**, further inquiries can be directed to the corresponding author.

AUTHOR CONTRIBUTIONS

GW and BC designed and conducted the research and analysis. WL and SJ collected data and contributed to the definition of air stagnation. GW, SJ and BC worked together on the interpretation of results and wrote the paper.

FUNDING

This study was funded by the National Natural Science Foundation of China (41975075, 42075058 and 41805117) and Shanghai International Science and Technology Partnership Project (No. 21230780200).

ACKNOWLEDGMENTS

Hourly PM2.5 real-time data in China were downloaded from the website of Ministry of Ecology and Environment of the People's Republic of China (http://106.37.208.233:20035). The fifth generation European Centre for Medium-Range Weather Forecasts atmospheric reanalysis data (ECMWF ERA5) at 97–114°E and 25–35°N with a horizontal resolution of 0.25°* 0.25° from 1979 to 2019 are downloaded from https://www.ecmwf.int/en/forecasts/datasets/reanalysis-datasets/era5.

SUPPLEMENTARY MATERIAL

The Supplementary Material for this article can be found online at: https://www.frontiersin.org/articles/10.3389/fenvs.2021.763504/full#supplementary-material

REFERENCES

Bi, J., Huang, J., Holben, B., and Zhang, G. (2016). Comparison of Key Absorption and Optical Properties between Pure and Transported Anthropogenic Dust over East and Central Asia. *Atmos. Chem. Phys.* 16 (24), 15501–15516. doi:10.5194/acp-16-15501-2016

Cai, W., Li, K., Liao, H., Wang, H., and Wu, L. (2017). Weather Conditions Conducive to Beijing Severe Haze More Frequent under Climate Change. *Nat. Clim Change* 7 (4), 257–262. doi:10.1038/nclimate3249

Cao, B., Wang, X., Ning, G., Yuan, L., Jiang, M., Zhang, X., et al. (2020). Factors Influencing the Boundary Layer Height and Their Relationship with Air Quality in the Sichuan Basin, China. *Sci. Total Environ.* 727, 138584. doi:10.1016/j.scitotenv.2020.138584

Chang, L., Wu, Z., and Xu, J. (2020). Potential Impacts of the Southern Hemisphere Polar Vortices on central-eastern China Haze Pollution during Boreal Early winter. *Clim. Dyn.* 55 (3), 771–787. doi:10.1007/s00382-020-05294-3

Che, H., Xia, X., Zhao, H., Dubovik, O., Holben, B. N., Goloub, P., et al. (2019). Spatial Distribution of Aerosol Microphysical and Optical Properties and Direct Radiative Effect from the China Aerosol Remote Sensing Network. *Atmos. Chem. Phys.* 19 (18), 11843–11864. doi:10.5194/acp-19-11843-2019

Chen, H., and Wang, H. (2015). Haze Days in North China and the Associated Atmospheric Circulations Based on Daily Visibility Data from 1960 to 2012. *J. Geophys. Res. Atmos.* 120 (12), 5895–5909. doi:10.1002/2015jd023225

Chen, H., Wang, H., Sun, J., Xu, Y., and Yin, Z. (2019a). Anthropogenic fine Particulate Matter Pollution Will Be Exacerbated in Eastern China Due to 21st century GHG Warming. *Atmos. Chem. Phys.* 19 (1), 233–243. doi:10.5194/acp-19-233-2019

Chen, J., Li, Z., Lv, M., Wang, Y., Wang, W., Zhang, Y., et al. (2018). Aerosol Hygroscopic Growth, Contributing Factors and Impact On Haze Events in a Severely Polluted Region in Northern China. *Atmos. Chem. Phys* 19 (2), 1327–1342. doi:10.5194/acp-19-1327-2019

Chen, S., Zhang, X., Lin, J., Huang, J., Zhao, D., Yuan, T., et al. (2019b). Fugitive Road Dust PM2.5 Emissions and Their Potential Health Impacts. *Environ. Sci. Technol.* 53 (14), 8455–8465. doi:10.1021/acs.est.9b00666

Chen, Z., Chen, D., Zhao, C., Kwan, M.-p., Cai, J., Zhuang, Y., et al. (2020). Influence of Meteorological Conditions on PM2.5 Concentrations across China: A Review of Methodology and Mechanism. *Environ. Int.* 139, 105558. doi:10.1016/j.envint.2020.105558

Dang, R., and Liao, H. (2019). Severe winter Haze Days in the Beijing-Tianjin-Hebei Region from 1985 to 2017 and the Roles of Anthropogenic Emissions and Meteorology. *Atmos. Chem. Phys.* 19 (16), 10801–10816. doi:10.5194/acp-19-10801-2019

Ding, A., Huang, X., Nie, W., Chi, X., Xu, Z., Zheng, L., et al. (2019). Significant Reduction of PM2.5 in Eastern China Due to Regional-Scale Emission Control: Evidence from SORPES in 2011-2018. *Atmos. Chem. Phys.* 19 (18), 11791–11801. doi:10.5194/acp-19-11791-2019

Fan, H., Zhao, C., and Yang, Y. (2020). A Comprehensive Analysis of the Spatio-Temporal Variation of Urban Air Pollution in China during 2014-2018. *Atmos. Environ.* 220, 117066. doi:10.1016/j.atmosenv.2019.117066

Fan, J., Rosenfeld, D., Yang, Y., Zhao, C., Leung, L. R., and Li, Z. (2015). Substantial Contribution of Anthropogenic Air Pollution to Catastrophic Floods in Southwest China. *Geophys. Res. Lett.* 42 (14), 6066–6075. doi:10.1002/2015gl064479

Feng, F., and Wang, K. (2019). Determining Factors of Monthly to Decadal Variability in Surface Solar Radiation in China: Evidences from Current Reanalyses. *J. Geophys. Res. Atmos.* 124 (16), 9161–9182. doi:10.1029/2018jd030214

Gui, K., Che, H., Wang, Y., Wang, H., Zhang, L., Zhao, H., et al. (2019). Satellite-derived PM2.5 Concentration Trends over Eastern China from 1998 to 2016: Relationships to Emissions and Meteorological Parameters. *Environ. Pollut.* 247, 1125–1133. doi:10.1016/j.envpol.2019.01.056

Guo, J., Miao, Y., Zhang, Y., Liu, H., Li, Z., Zhang, W., et al. (2016). The Climatology of Planetary Boundary Layer Height in China Derived from Radiosonde and Reanalysis Data. *Atmos. Chem. Phys.* 16 (20), 13309–13319. doi:10.5194/acp-16-13309-2016

Guo, J., Xu, H., Liu, L., Chen, D., Peng, Y., Yim, S. H. L., et al. (2019). The Trend Reversal of Dust Aerosol over East Asia and the North Pacific Ocean Attributed to Large-Scale Meteorology, Deposition, and Soil Moisture. *J. Geophys. Res. Atmos.* 124 (19), 10450–10466. doi:10.1029/2019jd030654

Guo, J., Zhang, J., Yang, K., Liao, H., Zhang, S., Huang, K., et al. (2021). Investigation of Near-Global Daytime Boundary Layer Height Using High-Resolution Radiosondes: First Results and Comparison with ERA-5, MERRA-2, JRA-55, and NCEP-2 Reanalyses. *Atmos. Chem. Phys. Discuss.* [in review]. doi:10.5194/acp-2021-257

He, J., Lu, S., Yu, Y., Gong, S., Zhao, S., and Zhou, C. (2018a). Numerical Simulation Study of winter Pollutant Transport Characteristics over Lanzhou City, Northwest China. *Atmosphere* 9 (10), 382. doi:10.3390/atmos9100382

He, Y., Wang, K., Zhou, C., and Wild, M. (2018b). A Revisit of Global Dimming and Brightening Based on the sunshine Duration. *Geophys. Res. Lett.* 45 (9), 4281–4289. doi:10.1029/2018gl077424

Hu, Z., Huang, J., Zhao, C., Ma, Y., Jin, Q., Qian, Y., et al. (2019). Trans-Pacific Transport and Evolution of Aerosols: Spatiotemporal Characteristics and Source Contributions. *Atmos. Chem. Phys.* 19, 12709–12730. doi:10.5194/acp-19-12709-2019

Hu, Z., Jin, Q., Ma, Y., Pu, B., Ji, Z., Wang, Y., et al. (2021). Temporal Evolution of Aerosols and Their Extreme Events in Polluted Asian Regions during Terra's 20-year Observations. *Remote Sensing Environ.* 263, 112541. doi:10.1016/j.rse.2021.112541

Huang, X., Wang, Z., and Ding, A. (2018). Impact of Aerosol-PBL Interaction on Haze Pollution: Multiyear Observational Evidences in North China. *Geophys. Res. Lett.* 45 (16), 8596–8603. doi:10.1029/2018gl079239

Jian, B., Li, J., Wang, G., He, Y., Han, Y., Zhang, M., et al. (2018). The Impacts of Atmospheric and Surface Parameters on Long-Term Variations in the Planetary Albedo. *J. Clim.* 31 (21), 8705–8718. doi:10.1175/jcli-d-17-0848.1

Li, J., Liao, H., Hu, J., and Li, N. (2019). Severe Particulate Pollution Days in China during 2013-2018 and the Associated Typical Weather Patterns in Beijing-Tianjin-Hebei and the Yangtze River Delta Regions. *Environ. Pollut.* 248, 74–81. doi:10.1016/j.envpol.2019.01.124

Li, Q., Zhang, R., and Wang, Y. (2016). Interannual Variation of the Wintertime Fog-Haze Days across central and Eastern China and its Relation with East Asian winter Monsoon. *Int. J. Climatol.* 36 (1), 346–354. doi:10.1002/joc.4350

Li, Y., Li, J., Zhao, Y., Lei, M., Zhao, Y., Jian, B., et al. (2021). Long-term Variation of Boundary Layer Height and Possible Contribution Factors: A Global Analysis. *Sci. Total Environ.* 796, 148950. doi:10.1016/j.scitotenv.2021.148950

Liao, T., Gui, K., Jiang, W., Wang, S., Wang, B., Zeng, Z., et al. (2018). Air Stagnation and its Impact on Air Quality during winter in Sichuan and Chongqing, Southwestern China. *Sci. Total Environ.* 635, 576–585. doi:10.1016/j.scitotenv.2018.04.122

Liu, Y., Tang, G., Huang, X., Wei, K., Wu, S., Wang, M., et al. (2021). Unexpected Deep Mixing Layer in the Sichuan Basin, China. *Atmos. Res.* 249, 105300. doi:10.1016/j.atmosres.2020.105300

Liu, Y., Tang, G., Zhou, L., Hu, B., Liu, B., Li, Y., et al. (2019). Mixing Layer Transport Flux of Particulate Matter in Beijing, China. *Atmos. Chem. Phys.* 19 (14), 9531–9540. doi:10.5194/acp-19-9531-2019

Lu, C., Deng, Q.-h., Liu, W.-w., Huang, B.-l., and Shi, L.-z. (2012). Characteristics of Ventilation Coefficient and its Impact on Urban Air Pollution. *J. Cent. South. Univ. Technol.* 19 (3), 615–622. doi:10.1007/s11771-012-1047-9

Ma, Y., Ye, J., Xin, J., Zhang, W., Vilà-Guerau de Arellano, J., Wang, S., et al. (2020). The Stove, Dome, and Umbrella Effects of Atmospheric Aerosol on the Development of the Planetary Boundary Layer in Hazy Regions. *Geophys. Res. Lett.* 47 (13). doi:10.1029/2020gl087373

Miao, Y., Guo, J., Liu, S., Liu, H., Li, Z., Zhang, W., et al. (2017). Classification of Summertime Synoptic Patterns in Beijing and Their Associations with Boundary Layer Structure Affecting Aerosol Pollution. *Atmos. Chem. Phys.* 17 (4), 3097–3110. doi:10.5194/acp-17-3097-2017

Mu, M., and Zhang, R. (2014). Addressing the Issue of Fog and Haze: A Promising Perspective from Meteorological Science and Technology. *Sci. China Earth Sci.* 57, 1–2. doi:10.1007/s11430-013-4791-2

National Bureau of Statistics of China (2020). https://data.stats.gov.cn/easyquery.htm?cn=C01. Accessed November 3, 2021.

Ning, G., Wang, S., Ma, M., Ni, C., Shang, Z., Wang, J., et al. (2018). Characteristics of Air Pollution in Different Zones of Sichuan Basin, China. *Sci. Total Environ.* 612, 975–984. doi:10.1016/j.scitotenv.2017.08.205

Ning, G., Yim, S. H. L., Wang, S., Duan, B., Nie, C., Yang, X., et al. (2019). Synergistic Effects of Synoptic Weather Patterns and Topography on Air Quality: a Case of the Sichuan Basin of China. *Clim. Dyn.* 53 (11), 6729–6744. doi:10.1007/s00382-019-04954-3

Stull, R. B. (2012). *An Introduction to Boundary Layer Meteorology*. Dordrecht: Springer Science & Business Media.

Sujatha, P., Mahalakshmi, D. V., Ramiz, A., Rao, P. V. N., and Naidu, C. V. (2016). Ventilation Coefficient and Boundary Layer Height Impact on Urban Air Quality. *Cogent Environ. Sci.* 2 (1), 1125284. doi:10.1080/23311843.2015.1125284

Sun, Y. L., Wang, Z. F., Fu, P. Q., Yang, T., Jiang, Q., Dong, H. B., et al. (2013). Aerosol Composition, Sources and Processes during Wintertime in Beijing, China. *Atmos. Chem. Phys.* 13 (9), 4577–4592. doi:10.5194/acp-13-4577-2013

Tang, G., Zhu, X., Hu, B., Xin, J., Wang, L., Münkel, C., et al. (2015). Impact of Emission Controls on Air Quality in Beijing during APEC 2014: Lidar Ceilometer Observations. *Atmos. Chem. Phys.* 15 (21), 12667–12680. doi:10.5194/acp-15-12667-2015

Wang, K., Dickinson, R. E., and Liang, S. (2009). Clear Sky Visibility Has Decreased over Land Globally from 1973 to 2007. *Science* 323 (5920), 1468–1470. doi:10.1126/science.1167549

Wang, L., and Wang, K. (2015). Impacts of DEM Uncertainty on Estimated Surface Solar Radiation and Extracted River Network. *Bull. Am. Meteorol. Soc.* 96 (2), 297–304. doi:10.1175/bams-d-13-00285.1

Wang, X., Dickinson, R. E., Su, L., Zhou, C., and Wang, K. (2018a). PM2.5 Pollution in China and How it Has Been Exacerbated by Terrain and Meteorological Conditions. *Bull. Am. Meteorol. Soc.* 99 (1), 105–119. doi:10.1175/bams-d-16-0301.1

Wang, X., and Wang, K. (2016). Homogenized Variability of Radiosonde-Derived Atmospheric Boundary Layer Height over the Global Land Surface from 1973 to 2014. *J. Clim.* 29 (19), 6893–6908. doi:10.1175/jcli-d-15-0766.1

Wang, X., Wang, K., and Su, L. (2016). Contribution of Atmospheric Diffusion Conditions to the Recent Improvement in Air Quality in China. *Sci. Rep.* 6, 36404. doi:10.1038/srep36404

Wang, X., Wen, H., Shi, J., Bi, J., Huang, Z., Zhang, B., et al. (2018b). Optical and Microphysical Properties of Natural mineral Dust and Anthropogenic Soil Dust Near Dust Source Regions over Northwestern China. *Atmos. Chem. Phys.* 18 (3), 2119–2138. doi:10.5194/acp-18-2119-2018

Wang, X., and Zhang, R. (2020a). Effects of Atmospheric Circulations on the Interannual Variation in PM2.5 Concentrations over the Beijing-Tianjin-Hebei Region in 2013-2018. *Atmos. Chem. Phys.* 20 (13), 7667–7682. doi:10.5194/acp-20-7667-2020

Wang, X., and Zhang, R. (2020b). How Did Air Pollution Change during the COVID-19 Outbreak in China. *Bull. Am. Meteorol. Soc.* 101 (10), E1645–E1652. doi:10.1175/bams-d-20-0102.1

Wang, Y., Meng, Z., Lyu, R., Huang, G., He, Q., and Cheng, T. (2020). Spatiotemporal Changes of Surface Solar Radiation: Implication for Air Pollution and rice Yield in East China. *Sci. Total Environ.* 739, 140361. doi:10.1016/j.scitotenv.2020.140361

Xia, X., Che, H., Shi, H., Chen, H., Zhang, X., Wang, P., et al. (2020). Advances in Sunphotometer-Measured Aerosol Optical Properties and Related Topics in China: Impetus and Perspectives. *Atmos. Res.* 249, 105286. doi:10.1016/j.atmosres.2020.105286

Yin, Z., Wang, H., and Chen, H. (2017). Understanding Severe winter Haze Events in the North China Plain in 2014: Roles of Climate Anomalies. *Atmos. Chem. Phys.* 17 (3), 1641–1651. doi:10.5194/acp-17-1641-2017

Zhang, L., Guo, X., Zhao, T., Gong, S., Xu, X., Li, Y., et al. (2019). A Modelling Study of the Terrain Effects on Haze Pollution in the Sichuan Basin. *Atmos. Environ.* 196, 77–85. doi:10.1016/j.atmosenv.2018.10.007

Zhang, Q., and Geng, G. (2019). Impact of Clean Air Action on PM2.5 Pollution in China. *Sci. China Earth Sci.* 62, 1845–1846. doi:10.1007/s11430-019-9531-4

Zhang, R., Li, Q., and Zhang, R. (2014). Meteorological Conditions for the Persistent Severe Fog and Haze Event over Eastern China in January 2013. *Sci. China Earth Sci.* 57 (1), 26–35. doi:10.1007/s11430-013-4774-3

Zhang, R. (2017). Warming Boosts Air Pollution. *Nat. Clim Change* 7 (4), 238–239. doi:10.1038/nclimate3257

Zhao, C., and Garrett, T. J. (2015). Effects of Arctic Haze on Surface Cloud Radiative Forcing. *Geophys. Res. Lett.* 42 (2), 557–564. doi:10.1002/2014gl062015

Zhao, C., Li, Y., Zhang, F., Sun, Y., and Wang, P. (2018a). Growth Rates of fine Aerosol Particles at a Site Near Beijing in June 2013. *Adv. Atmos. Sci.* 35 (2), 209–217. doi:10.1007/s00376-017-7069-3

Zhao, D., Schmitt, S. H., Wang, M., Acir, I.-H., Tillmann, R., Tan, Z., et al. (2018b). Effects of NOx and SO2 on the Secondary Organic Aerosol Formation from Photooxidation of α-pinene and Limonene. *Atmos. Chem. Phys.* 18, 1611–1628. doi:10.5194/acp-18-1611-2018

Zhao, H., Che, H., Zhang, L., Gui, K., Ma, Y., Wang, Y., et al. (2020). How Aerosol Transport from the North China plain Contributes to Air Quality in Northeast China. *Sci. Total Environ.* 738, 139555. doi:10.1016/j.scitotenv.2020.139555

Zhao, S., Yu, Y., Yin, D., Qin, D., He, J., and Dong, L. (2018c). Spatial Patterns and Temporal Variations of Six Criteria Air Pollutants during 2015 to 2017 in the City Clusters of Sichuan Basin, China. *Sci. total Environ.* 624, 540–557. doi:10.1016/j.scitotenv.2017.12.172

Zhong, J., Zhang, X., Wang, Y., Wang, J., Shen, X., Zhang, H., et al. (2019). The Two-Way Feedback Mechanism between Unfavorable Meteorological Conditions and Cumulative Aerosol Pollution in Various Haze Regions of China. *Atmos. Chem. Phys.* 19 (5), 3287–3306. doi:10.5194/acp-19-3287-2019

Zhu, X., Tang, G., Guo, J., Hu, B., Song, T., Wang, L., et al. (2018). Mixing Layer Height on the North China Plain and Meteorological Evidence of Serious Air Pollution in Southern Hebei. *Atmos. Chem. Phys.* 18 (7), 4897–4910. doi:10.5194/acp-18-4897-2018

Conflict of Interest: The authors declare that the research was conducted in the absence of any commercial or financial relationships that could be construed as a potential conflict of interest.

frontiers | Frontiers in Environmental Science

ORIGINAL RESEARCH
published: 13 April 2022
doi: 10.3389/fenvs.2022.851915

Dust Aerosol Vertical Profiles in the Hinterland of Taklimakan Desert During Summer 2019

Jianrong Bi[1,2,3], Zhengpeng Li[1,3], Dapeng Zuo[1,3], Fan Yang[1,4], Bowen Li[1,3], Junyang Ma[1,3], Zhongwei Huang[1,2,3] and Qing He[4]*

[1]Key Laboratory for Semi-Arid Climate Change of the Ministry of Education, College of Atmospheric Sciences, Lanzhou University, Lanzhou, China, [2]Collaborative Innovation Center for Western Ecological Safety, Lanzhou University, Lanzhou, China, [3]Gansu Provincial Field Scientific Observation and Research Station of Semi-Arid Climate and Environment, Lanzhou, China, [4]Taklimakan Desert Meteorology Field Experiment Station, Institute of Desert Meteorology, China Meteorological Administration (CMA), Urumqi, China

OPEN ACCESS

Edited by:
Zhiyuan Hu,
Sun Yat-sen University, China

Reviewed by:
Huizheng Che,
Chinese Academy of Meteorological Sciences, China
Wencai Wang,
Ocean University of China, China
Chao Liu,
Nanjing University of Information Science and Technology, China

***Correspondence:**
Jianrong Bi
bijr@lzu.edu.cn

Specialty section:
This article was submitted to Atmosphere and Climate, a section of the journal Frontiers in Environmental Science

Received: 10 January 2022
Accepted: 17 February 2022
Published: 13 April 2022

Citation:
Bi J, Li Z, Zuo D, Yang F, Li B, Ma J, Huang Z and He Q (2022) Dust Aerosol Vertical Profiles in the Hinterland of Taklimakan Desert During Summer 2019. Front. Environ. Sci. 10:851915. doi: 10.3389/fenvs.2022.851915

Dust aerosol vertical profiles are very essential to accurately evaluate their climate forcing and trans-subcontinental transportation to downstream areas. We initiated a joint comprehensive field experiment to investigate the vertical profiles and optical characteristics of dust aerosol in the hinterland of Taklimakan Desert (TD) during summer 2019. After smoothing the raw signals, the CHM15k ceilometer could distinctly detect a moderate intensity of dust layer, cloud layer, and subsequent rainfall process. The results showed that dust events frequently occurred in TD during the entire period; the overall mean $PM_{2.5}$, PM_{10}, $PM_{2.5}/PM_{10}$, and Ångström exponent are 110.4 ± 121.0 μg/m^3, 317.2 ± 340.0 μg/m^3, 0.35 ± 0.07, and 0.28 ± 0.12, respectively, suggesting that dust particles are predominant aerosol types in TD. There was an obvious summertime dust stagnation layer persistently hanged over the desert at 1.5–3.0-km height. A deep and intense daytime convective structure was also detected by the ceilometer, with maximum aerosol mixing layer height of ~3 km that appeared at 12:00 UTC, which was in favor of lifting the ground-generated dust particles into the upper atmosphere. The normalized range-corrected signal $\log_{10}$(RCS), aerosol extinction $\sigma(z)$, and backscattering coefficient $\beta(z)$ of the ceilometer were higher than 6.2, 0.5 km^{-1}, and 0.01 km^{-1} sr^{-1} for heavy dust storms, respectively, and the corresponding vertical optical range was smaller than 1.0 km. The aerosol lidar ratio was equal to 50 sr, which was greatly different from those of clear-sky cases. The retrieved $\sigma(z)$ values were about 2.0, 0.5, 0.14, and 0.10 km^{-1} at 200-m height, respectively, under strong dust storm, blowing dust, floating dust, and clear-sky conditions. This indicated that the aerosol extinction coefficients under dust events were about 3–10 times greater than those of clear-sky cases. The statistics of the aerosol optical parameters under different dust intensities in TD were very helpful to explore and validate dust aerosols in the application of climate models or satellite remote sensing.

Keywords: dust aerosol, aerosol extinction coefficient profile, dust stagnation layer, aerosol mixing layer height, Taklimakan Desert

INTRODUCTION

Dust aerosol is one of the major aerosol types in the troposphere, which plays a pivotal role in affecting public health, transportation safety, air quality, and climatic effects. In view of climatic impacts, airborne dust particles could modulate the redistribution of radiation energy in the atmosphere by direct scattering and absorption of solar shortwave or terrestrial longwave radiation (*i.e.*, aerosol–radiation interaction, Huang et al., 2014; Che et al., 2019a; Che et al., 2019b; Hu et al., 2020; Li et al., 2021) and acting as effective cloud condensation nuclei. They can indirectly promote or inhibit the precipitation intensity through altering cloud microphysical properties and lifetime (*i.e.*, aerosol–cloud interaction, Twomey, 1977; Huang et al., 2006a; Huang et al., 2006b); thus, they have a far-reaching influence on the energy budget of Earth's atmosphere system and relevant hydrological cycles (Rosenfeld et al., 2001; Yin and Chen, 2007; Li et al., 2016; Jin Q. et al., 2021) as well as accelerate snow melting by changing the surface albedo of snow and ice sheets (*i.e.*, snow/ice albedo mechanism, Huang et al., 2011; Wang et al., 2013; Qian et al., 2014). Furthermore, dust aerosols usually carry rich nutrients and organic matters deposited on Earth's surface and affect the biomass productivity of the Pacific Ocean and the atmosphere–ocean carbon exchange, hence exerting a crucial role in global biogeochemical cycle (Jickells et al., 2005; Maher et al., 2010; Shao et al., 2011).

The Taklimakan Desert (TD) in northwest China is an important dust source region of East Asia and frequently produces a lot of tiny soil particles every spring that are uplifted and injected into the upper atmosphere by strong surface winds and cold frontal cyclones (Ge et al., 2014; Huang et al., 2014; Chen et al., 2017a; Chen et al., 2017b; Hu et al., 2019a). These elevated dust aerosols can travel eastward over long distances on a subcontinental scale, even across the Pacific Ocean, and arrive at the west coast of North America within about 1 week *via* prevalent westerlies (Husar et al., 2001; Uno et al., 2009; Uno et al., 2011; Hu et al., 2019b). They then exert a profound effect on the ecological environment and climate change both regionally and globally. To date, there has been a great deal of intensive field campaigns (*e.g.*, ACE-Asia, ADEC, PACDEX) and ground-based aerosol monitoring networks (*e.g.*, ADNET, AERONET, CARSNET) for investigating Asian dust aerosols (Holben et al., 1998; Huebert et al., 2003; Shimizu et al., 2004; Mikami et al., 2006; Huang et al., 2008; Che et al., 2015; Che et al., 2019a; Che et al., 2019b), which are invaluable for comprehensively understanding the climatic impacts of mineral dust in East Asia. Earlier studies (Liao and Seinfeld, 1998; Huang et al., 2009; Hu et al., 2020) have demonstrated that the shortwave and longwave radiative heating rates of dust aerosols play an important role in influencing the thermal and dynamic structures of the atmosphere layer, which are significantly dependent on their optical properties and vertical profiles. The Intergovernmental Panel on Climate Change (IPCC Climate Change, 2013) indicated that the magnitude and sign of positive or negative radiative forcing of dust aerosol still remain a very big uncertainty due to lack of accurate information on their total loading, optical characteristics, and spatial and temporal distributions.

Kai et al. (2008) successfully observed the dust layer structure over the northern edge of TD during a heavy dust storm in April 2002 by using a depolarization lidar and showed that there was a dense dust layer that appeared at 5.5-km height with a depolarization ratio of 0.15–0.25. Huang et al. (2010) detected dust aerosol vertical profiles and their long-range transport with three micro-pulse lidar systems and implied that the height of the dust layer was primarily concentrated 2 to 3 km in northwest China during spring in 2008. Bi et al. (2017) indicated that a thick dust layer generally appeared below 4-km height with a depolarization ratio of 0.20–0.30 at Dunhuang, nearby the downstream of TD, during spring in 2012. The aforementioned publications mostly focused on the dust optical properties in spring but little on the dust vertical structures in summer. Jin L. et al. (2021) and Mu et al. (2021) found that, compared with spring, dust events also frequently occurred in TD during the summer season. Chen et al. (2017a) showed that the summer dust long-range transport in TD had a comparable contribution to East Asia as that in spring. Based on the Cloud–Aerosol Lidar and Infrared Pathfinder Satellite Observations (CALIPSO), Huang et al. (2007) revealed that summertime Taklimakan dust plumes transported southward and appeared over the Tibetan Plateau (about 4–7 km in altitude). Yumimoto et al. (2010) combined the ground-based lidars, CALIPSO, and numerical models and confirmed that summertime Taklimakan dust traveled eastward at 6–8 km in altitude and swept across the Pacific Ocean in mid-August 2009. Therefore, a comprehensive knowledge of summertime dust vertical profiles and uplifted height in Taklimakan Desert is vital to investigate their trans-subcontinental transport and climatic effects on a regional scale.

To elucidate the interactions among dust aerosol, cloud, and radiation budget and relevant climate influences over Taklimakan Desert, the Semi-Arid Climate and Environment Observatory of Lanzhou University (SACOL) and Institute of Desert Meteorology, China Meteorological Administration (CMA) jointly carried out an intensive field campaign in Tarim Basin during the summer of 2019. We deployed a set of state-of-the-art instruments at Tazhong site, which is located in the center of TD. The main instruments include the CHM15k ceilometer, sun/sky radiometer, an 80-m gradient meteorological tower, eddy covariance system, particulate mass monitor, and surface radiation fluxes (Bi et al., 2022). This study mainly explores the vertical profiles and optical properties of dust aerosol over TD during summer in 2019. The structure of this paper is organized as follows: **Section 2** introduces the data, instrument information, and retrieval methods to solve the Mie scattering lidar equation. **Section 3** presents the results and discussion, and the conclusion is given in **Section 4**.

DATA AND METHODS

Site Information

Taklimakan Desert is the second largest shifting sand-dune desert in the world, which covers a total area of 3.376×10^5 km^2, with an

east–west length of 1,000 km and a south–north width of 400 km. It is encompassed by huge mountains, with Tianshan Mountain to the north, Pamir Plateau to the west, Kunlun Mountains to the south, and over Lake Lop Nur and Kumtag Desert to the east (Pan et al., 2020; Bi et al., 2022). Tazhong station [38.968° N, 83.659° E, 1,100 m above mean sea level (MSL)] is situated in the hinterland of TD, and its climate pattern belongs to warm temperate continental desert climate, which gets abundant sunshine, sparse desert vegetation, and a significant diurnal temperature difference. Because of its unique topography and environmental features, the climate here is characterized by extreme drought, scarce precipitation (~38 mm), intense evaporation (~2,500–3,400 mm), frequent dust storms, and a deep boundary layer structure during daytime (Wang et al., 2016; Pan et al., 2020; Yang et al., 2021).

Dust Aerosol Measurements

The CHM15k ceilometer (Lufft, Germany) is an unattended and single-wavelength elastic lidar for continuously detecting the vertical profiles of aerosol and cloud. The ceilometer emits a solid-state laser pulse at 1,064-nm wavelength (Nd:YAG, class M1 laser) with a narrow line width of 0.38 nm, which facilitates excellent background light suppression (Heese et al., 2010). The laser has a nominal pulse energy of 8.0 μJ and a repetition frequency of 6,500 Hz, with separated-lens telescopes of 100-mm diameter for the transmitter and the receiver. The beam divergence angle and field of view are 0.33 and 0.45 mrad, respectively. An avalanche photo diode in photon counting mode is used to receive the attenuated backscattering signals from aerosol particles or cloud droplets with a 5-m vertical resolution and a 15-s temporal resolution. A fan and a heater are installed inside the device to automatically remove impurities and dewdrops from the window in real time .

A sun/sky radiometer (model CE-318, Cimel, France) is designed to automatically observe the direct solar irradiances and diffuse sky radiances at a wavelength range of 340–1,020 nm, with 1.2° full field-of-view every 15 min. These datasets are capable of retrieving the aerosol optical depth (AOD), Ångström exponent (AE), water vapor content (WVC), volume size distribution (dV/dlnR), and single scattering albedo (SSA). The inversion accuracies of AOD, dV/dlnR, and SSA are expected to be 0.01–0.02, 15–35%, and 0.03–0.05, respectively, for a newly calibrated field instrument (Holben et al., 1998; Che et al., 2015; Che et al., 2019a; Che et al., 2019b).

The CALIPSO is a polar-orbiting satellite that provides height-resolved profiles of aerosols and clouds on a global scale (Winker et al., 2007; Winker et al., 2009). It can measure the total attenuated backscattering signals at 532 and 1,064 nm, depolarization ratio at 532 nm, and attenuated color ratio with vertical resolution of 30 m below 8.2 km, which is commonly utilized to probe the three-dimensional distribution and transport of aerosol species both regionally and globally (Huang et al., 2008; Liu et al., 2008). In this study, we make use of level 1B products and vertical feature mask products, including the feature classification of cloud and aerosol types (Liu et al., 2009), to intercompare the vertical structures of dust aerosol and cloud detected by the ground-based ceilometer.

Other Ground-Based Measurements

Data on the hourly mean mass concentrations of particulate matters (*e.g.*, $PM_{2.5}$ and PM_{10}, in μg/m^3) are acquired from Chinese Environmental Protection Bureau (CEPB, www.chinaairdaily.com), which are based on electron absorption (Andersen Instruments and Wedding and Associates Beta Attenuation Monitors-BAM) or inertial mass weighing principal (R&P Tapered Element Oscillating Microbalance-TEOM) (U.S. EPA, 1991).

An 80-m gradient meteorological tower can continuously collect multiple meteorological variables at seven layers of different heights, for instance, air temperature (°C) and relative humidity (%; HMP155A, Vaisala, Finland), wind speed (ms^{-1}) and wind direction (°; WindSonic Gill 2, England), ambient pressure (hPa; CS100, Setra, United States), precipitation (mm; 52203, YOUNG, United States), and sensible heat and latent heat fluxes (W m^{-2}; CPEC310, Campbell, United States). All datasets are automatically sampled and stored in a Campbell data logger with 1- and 30-min time intervals (Yang et al., 2021). At the same time, the experimenters manually recorded the total cloud amount, cloud types, visibility, and weather conditions every 1 h during daytime, which can assist in identifying key weather processes, such as dust storm, rainy, cloudy, or clear-sky days.

Methods

The classical elastic Mie scattering lidar equation can be expressed as, follows:

$$X(z) = P(z)z^2 = CE\beta(z)\exp\left(-2\int_0^z \sigma(z)dz\right) \quad (1)$$

where z is the distance between scattered particles, ceilometer lidar $P(z)$ is the energy of backscatter signal at altitude z, $X(z)$ is normalized range-corrected backscatter signal, C is the calibration constant of lidar, E is laser-emitted pulse energy, $\beta(z)$ is backscattering coefficient (β) at z, and $\sigma(z)$ is extinction coefficient at z.

Aerosols and air molecules are two main contributors for the total extinction $\sigma(z)$ and backscattering $\beta(z)$; hence, $X(z)$ is also expressed as follows:

$$X(z) = CE\left[\beta_a(z) + \beta_m(z)\right]\exp\left(-2\int_0^z \left[\sigma_a(z) + \sigma_m(z)\right]dz\right) \quad (2)$$

where the subscripts a and m represent aerosol and air molecule (Rayleigh), respectively. It is difficult to solve the backscatter lidar equation because there are two unknown variables in one equation: $\beta(z)$ and $\sigma(z)$. Fernald method (Fernald, 1984) is generally utilized to acquire an analytical solution of the lidar equation which defines a lidar ratio as the ratio of extinction to backscattering coefficient.

$$S_a = \sigma_a(z)/\beta_a(z),\ S_m = \sigma_m(z)/\beta_m(z) = \frac{8\pi}{3} \quad (3)$$

The lidar ratio of air molecule (S_m) can be determined by the standard atmospheric profile which has a constant value of 8π/3. The aerosol lidar ratio (S_a) might vary from 10 to 150 sr, which is

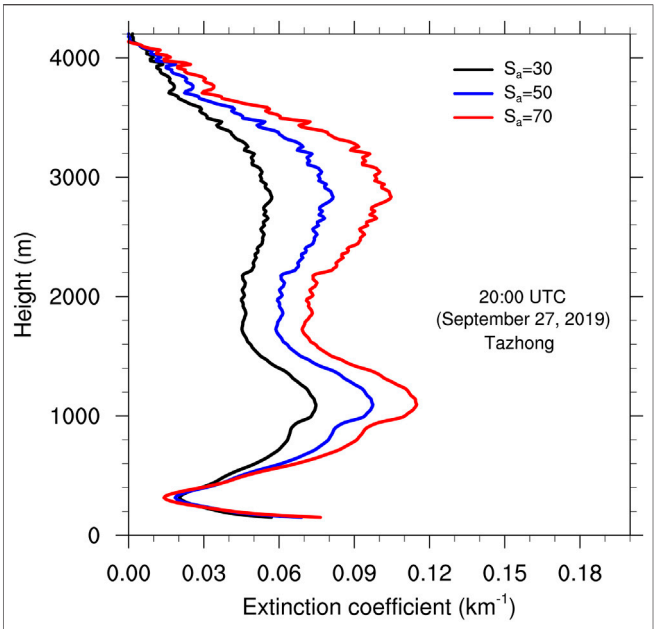

FIGURE 1 | Sensitivity study of different lidar ratio values' (S_a) influence on the inversion of aerosol extinction coefficient (km^{-1}) profiles at 20:00 UTC on September 27, 2019 at Tazhong.

primarily dependent on the aerosol species, chemical composition, size distribution, and refractive index of aerosol particles as well as on the wavelength of the incident light (Ackermann, 1998). **Figure 1** presents a sensitivity study of different lidar ratio values (S_a = 30, 50, and 70 sr) influencing the inversion of aerosol extinction coefficient profiles at 20:00 UTC on September 27, 2019 at Tazhong. That time is a clear-sky condition with low aerosol concentrations, representing typical background levels in TD. We designate S_a the value of 30 under clear-sky condition as a reference. It is evident that there are relatively small influences for different S_a values on the retrievals of $\sigma(z)$ below 500-m height, which is mainly due to the low aerosol concentrations at 500-m height range. However, those influences gradually increase with height from 500 m to 4 km and are closely linked to the aerosol concentrations—for instance, the retrieved $\sigma(z)$ values at 1.1 km are 0.075, 0.097, and 0.115 km^{-1}, respectively, for S_a of 30, 50, and 70 sr, which suggests that different S_a values (50 and 70 sr) would lead to the extinction coefficients of inversion being about 29.3 and 53.3% higher than that for the reference value (S_a = 30 sr). The corresponding $\sigma(z)$ values at 2.8 km are 0.058, 0.082, and 0.108 km^{-1}, respectively, for S_a of 30, 50, and 70 sr, resulting in errors of approximately 41.4 and 86.2%. Therefore, the calculation errors of aerosol extinction coefficient profiles strongly rely on the accuracy of the S_a value.

The volumetric aerosol lidar ratio can be effectively determined by the combination of an elastic backscatter lidar and a collocated sun/sky radiometer measurement (Huang et al., 2010). This method is mainly dependent on sky radiometer-derived high-precision AOD (~0.01–0.02) during daytime as a constraint for the inversion of ceilometer signals. The AOD is obtained by the integral of $\sigma(z)$ at atmospheric column. However, there are two major problems for the application of this method to the ceilometer. Firstly, the sun/sky radiometer only measured clear-sky AOD values during daytime, when the ceilometer signals are greatly affected by strong background light. Secondly, the lidar ratio estimated by ceilometer inversion is based on columnar AOD, which is largely influenced by the incomplete overlap height (~150 m) of the ceilometer. This problem is especially serious for the cases wherein most of the aerosol particles are concentrated in the lower atmospheric layer (Wiegner and Geiß, 2012), for instance, in desert areas with frequent emissions of high concentrations of dust particle from near-surface. Fortunately, Liu et al. (2002) directly observed the S_a values of Asian dust by using a high-spectral-resolution lidar (HSRL) and Raman elastic-backscatter lidar and indicated that the measured S_a values ranged from 42 to 55 sr, with a total mean of 51 sr. Murayama et al. (2004) showed that the S_a of lofted Asian dust varied from 43 to 49 sr at 355 and 532 nm with a dual-wavelength Raman lidar. Tesche et al. (2009) implied that the average S_a values of African dust are in the range of 53–55 sr at 355, 532, and 1,064 nm during SAMUM 2006 by using ground-based Raman lidar and an airborne HSRL. Consequently, in this study, we designate S_a = 50 sr for dust aerosols and S_a = 30 sr for clear-sky conditions to retrieve the vertical profiles of backscattering and extinction coefficients.

RESULTS AND DISCUSSION

Optical Characteristics of Dust Aerosols

Figure 2 depicts the time series of hourly average mass concentrations of $PM_{2.5}$ and PM_{10} and the ratios of $PM_{2.5}$/PM_{10} sampled at Hotan Environmental Protection Bureau from July 1 to September 30, 2019. Hotan (37.087° N, 79.927° E, 1,380 m above MSL) is about 300 km southwest of Tazhong, which is the closest environmental monitoring station to the center of TD. The results indicate that the hourly mean PM concentrations display dramatic day-to-day variations during the entire period. In about 90% of the total number days, the $PM_{2.5}$ and PM_{10} concentrations are greater than 100 and 250 μg/m^3, with maxima of 977 and 2,758 μg/m^3 (which occurred in July 26), respectively, which are 27 times and 36 times higher than the values set by the World Health Organization Air Quality Guidelines of 35 μg/m^3 for $PM_{2.5}$ and 75 μg/m^3 for PM_{10} (World Health Organization, 2005). The background levels of $PM_{2.5}$ and PM_{10} concentrations can also remain at 50 and 130 μg/m^3, respectively, under clear-sky conditions (September 20–30, 2019). Frequent dust events lead to significant variations of surface PM concentrations, for example, in July 15 and 26, August 13 and 17, and September 3 and 6. The ratio of $PM_{2.5}$ to PM_{10} is a key indicator for distinguishing the relative contributions of fine-mode and coarse-mode particles. The corresponding ratios are all smaller than 0.50, implying that the coarse-mode particles are dominant in the surface particulate matters over TD. The overall hourly mean $PM_{2.5}$, PM_{10}, and $PM_{2.5}/PM_{10}$ are 110.4 ± 121.0 μg/m^3, 317.2 ± 340.0 μg/

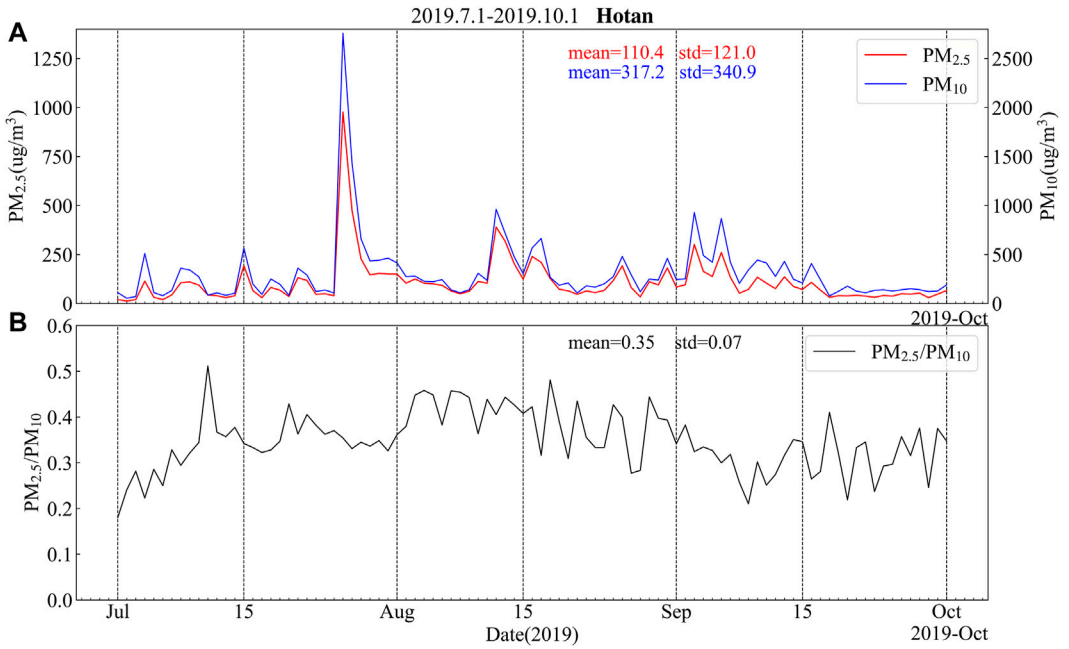

FIGURE 2 | Time series of hourly mean mass concentrations of particulate matter (PM) at Hotan from July 1 to September 30, 2019. **(A)** $PM_{2.5}$ (μg/m^3) *vs*. PM_{10} (μg/m^3). **(B)** Ratios of $PM_{2.5}/PM_{10}$. The corresponding total mean values and standard deviation are shown in the figures.

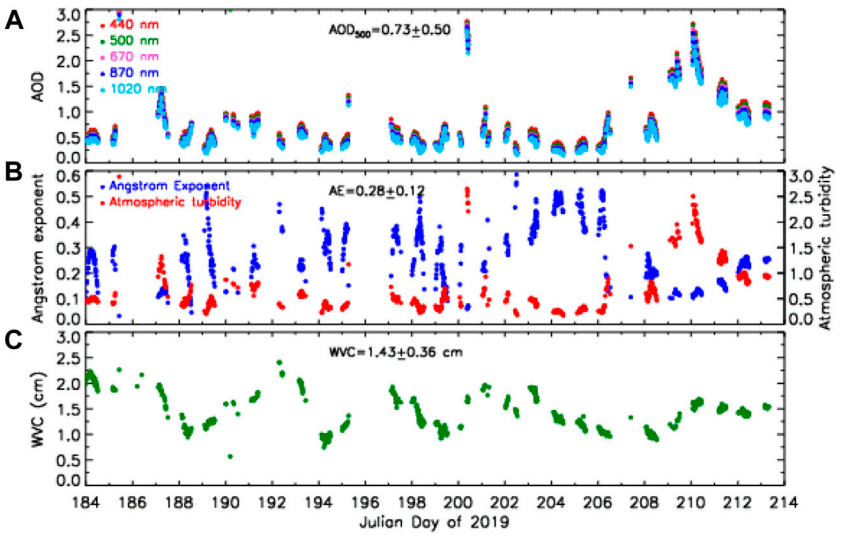

FIGURE 3 | Time evolutions of aerosol optical properties retrieved by Cimel sun/sky radiometer at Tazhong from July 2 to August 1, 2019. **(A)** Aerosol optical depth. **(B)** Ångström exponent *vs*. atmospheric turbidity. **(C)** Water vapor content in centimeters. The corresponding overall mean values and standard deviation are shown in the figures.

m^3, and 0.35 ± 0.07, respectively, during the whole period. Meanwhile, high levels of surface particulate matter concentrations persist for a long duration and cover a large spatial distribution over TD throughout the summer of 2019, which ultimately have adverse effects on human health, air quality, and traffic safety.

Figure 3 illustrates the time evolutions of AOD, AE, and WVC (in cm) derived from the sun/sky radiometer at Tazhong from July 2 to August 1, 2019. The Ångström exponent is generally used to reflect the size of aerosol particles, that is, small AE values (<0.60) indicate that coarse-mode particles are dominant, whereas large AE values (>1.0) represent the dominance of

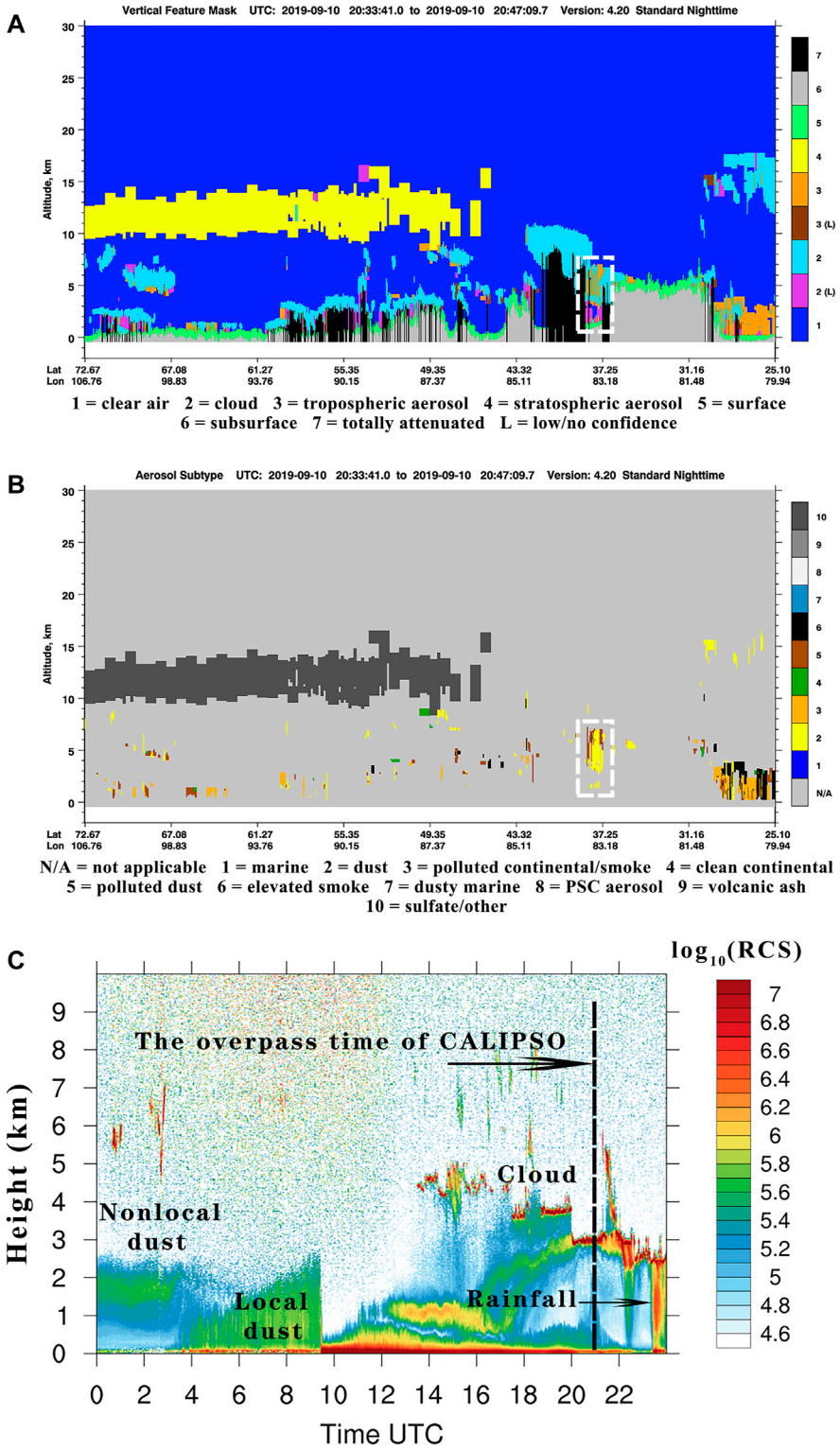

FIGURE 4 | Vertical profiles of dust aerosols and cloud layers on September 10, 2019 at Tazhong. **(A)** Purple and light blue in white dashed rectangle show the cloud layers detected by CALIPSO Vertical Feature Mask products. **(B)** Yellow in white dashed rectangle shows the dust aerosol detected by CALIPSO. **(C)** Normalized range-corrected signal in logarithmic scale observed from the ceilometer. The black dashed line denotes the passing time of CALIPSO over Tazhong station. Height is above-the-ground level in kilometers.

fine-mode particles. It is obvious that the aerosol optical properties at Tazhong also show remarkable diurnal variations, with the total averages of AOD_{500}, $AE_{440\text{-}870}$, and WVC at 0.73 ± 0.50, 0.28 ± 0.12, and 1.43 ± 0.36 cm, respectively. The AOD_{500} values vary from 0.20 to 3.0, and the $AE_{440–870}$ values range from 0.03 to 0.64, which further confirms that dust particles in the columnar atmosphere are the predominant aerosol types in the hinterland of TD, with little impacts by human activities. All AOD_{500} values are greater than 1.0, and the corresponding $AE_{440–870}$ values remain between 0.03 and 0.30 under several heavy dust events from September 26 to 30, 2019. In fact, Che et al. (2013) analyzed the multi-year (2004–2008) aerosol optical features and have also verified that coarse-mode dust aerosols are dominant in Tazhong. Thereby, it is reasonable that we specified a lidar ratio of 50 for dust aerosol to retrieve the dust extinction coefficient profiles.

Dust Aerosol Vertical Profiles

Figure 4 delineates the vertical profiles of dust aerosols and cloud layers at Tazhong on September 10, 2019 as measured by CALIPSO and the CHM15k ceilometer. The passing time of CALIPSO over Tazhong station is at 20:40 UTC, marked with a black dashed line in **Figure 4C**. The results suggest that both the ground-based ceilometer and the spaceborne CALIPSO can clearly detect the cloud layers (purple and light blue in **Figure 4A**) at 3–6 km and dust layers (yellow in **Figure 4B**) at 1–3 km height. **Figure 4C** shows the normalized range-corrected signal in logarithmic scale [$\log_{10}$(RCS)] as observed from the ceilometer. We can see that the $\log_{10}$(RCS) signals are weak below 1-km height during 00:00–04:00 UTC, and there is a lightly intense dust layer hanging at an altitude of 1–2.5 km, which is thought to be the transported dust aerosols from the surrounding areas. A moderately intense dust event begins to make an outbreak at 04:00 UTC, and locally generated dust particles are gradually lofted from the surface to the upper free atmosphere (~2.5 km), accompanied by northwestward surface wind speeds of up to 6.0–8.0 m/s. Then, the dust storm reaches its strongest peak at 09:39 UTC, and the corresponding $\log_{10}$(RCS) signals at 200-m height are greater than 7.0, when the maximum wind speed was exceeding 17.0 m/s. Meanwhile, the $\log_{10}$(RCS) signals above 1-km height are slightly weak, which is primarily attributed to the high concentrations of dust particles causing an intense attenuation of weak laser energy of the ceilometer. There are two evident layers at 15:00 UTC; in other words, a dust aerosol layer occurs at 0–1.5-km height and a cloud layer appears at 3.5–5.0-km height. It is very interesting that the dust aerosols are gradually uplifted again at 16:00 UTC and reached an altitude of 3 km at 20:00 UTC; then, they are mixed evenly with clouds, which was effectively detected by both the ceilometer and CALIPSO. High-altitude clouds and water vapor carried by westerly cold front cyclones interplay with elevated dust particles *via* a series of complex cloud microphysical processes. Finally, a rainfall event appears at 23:30 UTC, and it shows that the $\log_{10}$(RCS) signals of the ceilometer exhibit a very strong vertical profile from the ground to 3-km height, which is mainly owing to the scattering of emitted laser energy by the falling raindrops. The occurrence of a rainfall episode is also demonstrated by the simultaneous datasets of rain gauge and hourly manual records. The whole dust storm event lasted for nearly 20 h, and it would undoubtedly exert a profound impact on the energy budget and precipitation distribution over the TD region. Similar interactions among dust aerosols, cloud layers, and precipitations have taken place approximately 10 times during the entire experiment period. This is very vital to uncover the feedback mechanism of the dust–cloud–precipitation process in Taklimakan Desert, which is worthy of further investigation in the future.

As mentioned above, we collect the raw backscattering signals of the ceilometer at 5-m vertical resolution and 15-s temporal resolution. Because the emitted laser pulse energy is low (~8.0 μJ), the signal-to-noise ratio (SNR) of the ceilometer is larger than 1 at 8.5-km height during nighttime. Nevertheless, influenced by strong background sunlight, the corresponding SNR value is about 1 at up to 4 to 5 km during daytime, depending on the aerosol loading (Heese et al., 2010). **Figure 5A** characterizes the raw backscattering signals of the ceilometer [$\log_{10}$(RCS)] at 01:30 UTC on August 14, 2019. The SNR is approximately equal to 1 at 2-km height but decreases seriously with height at above 2 km. There is a distinct aerosol layer at about 1.5 km and an evident cloud layer at 5.8 km in our case. However, due to the low SNR values, the backscattering signals of aerosols and clouds are relatively not obvious in **Figure 5A**. The vertical distributions of cloud layers at 5–6.5 km are also not apparent (see **Figure 5C**). Smoothing the raw signal can effectively suppress the noise, and aerosol or cloud layers could be clearly detected, as shown in **Figures 5B, D**. In the smoothing method, we recalculate the raw backscattering signals at 15-m vertical resolution and 30-min time interval. After smoothing, the SNR values of the ceilometer have been greatly improved, and the SNR is higher than 1 at 8-km height so that aerosol layers or cloud layers in the upper troposphere would be detected by the CHM15k ceilometer. Therefore, subsequently, the $\log_{10}$(RCS) signals and retrieved backscattering and extinction coefficients from the ceilometer are processed by a smoothing algorithm, except for special declarations.

Figure 6 shows the diurnal variation of $\log_{10}$(RCS) of the ceilometer and the vertical profiles of aerosol extinction coefficient $\sigma(z)$ during a typical blowing dust event on July 26, 2019. Dust aerosols are confined in the atmospheric boundary layer of 0–1-km height at 00:00–06:00 UTC, with the strongest signal peak located at about 200–300 m. As discussed above, the peak of $\log_{10}$(RCS) signals corresponds to the maxima of PM_{10} concentration and AOD_{500} of 2,758 μg/m^3 and 3.0, respectively, as well as with $AE_{440–870}$ of 0.03. Driven by strong surface winds (~10 m/s) and the intense sensible flux heating in the afternoon, dust particles are gradually lifted upward from 06:00 UTC and dispersed over time. The dust vertical structures show an obvious stratification, and the $\log_{10}$(RCS) signal is the strongest near the ground surface and clearly drops with the increase of height. **Figure 6B** displays the vertical profiles of the aerosol extinction coefficient at various hours, and the Rayleigh extinction coefficient of air molecule is illustrated with a black line. There are no effective inversion results of $\sigma(z)$ at 0–150 m, which is the height of the incomplete overlap factor of the

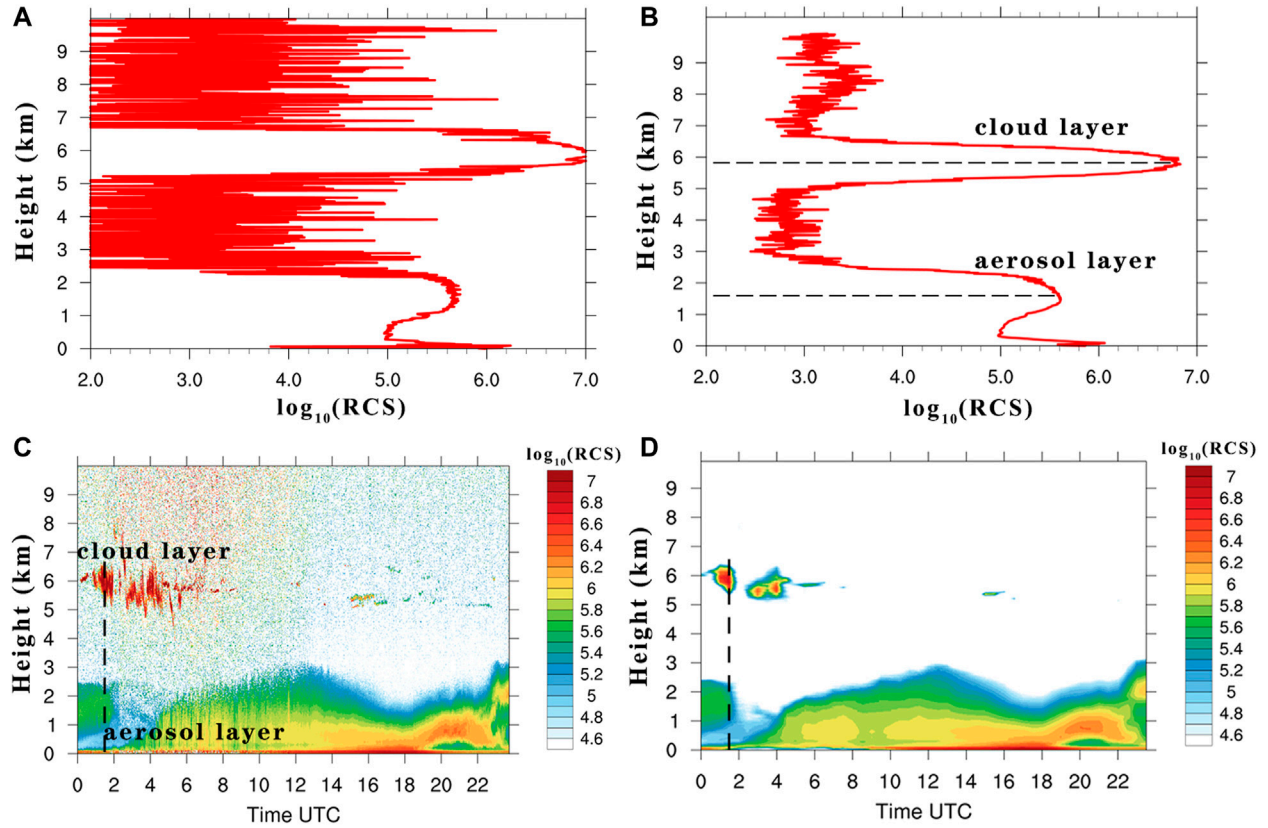

FIGURE 5 | Normalized range-corrected signal in logarithmic scale [$\log_{10}$(RCS)] of the ceilometer at 01:30 UTC on August 14, 2019. **(A)** Raw signals with 5-m vertical resolution and 15-s interval. **(B)** Smoothed signals with 15-m vertical resolution and 30-min time interval. Time evolutions of $\log_{10}$(RCS) of the ceilometer on August 14, 2019. **(C)** Raw signals. **(D)** Smoothed signals. The black dashed line denotes the corresponding time of $\log_{10}$(RCS) in **Figures 4A, B**. There is a distinct dust aerosol layer from the surface to 2 km in height, and a visible cloud layer appears at a height of 5–6.5 km.

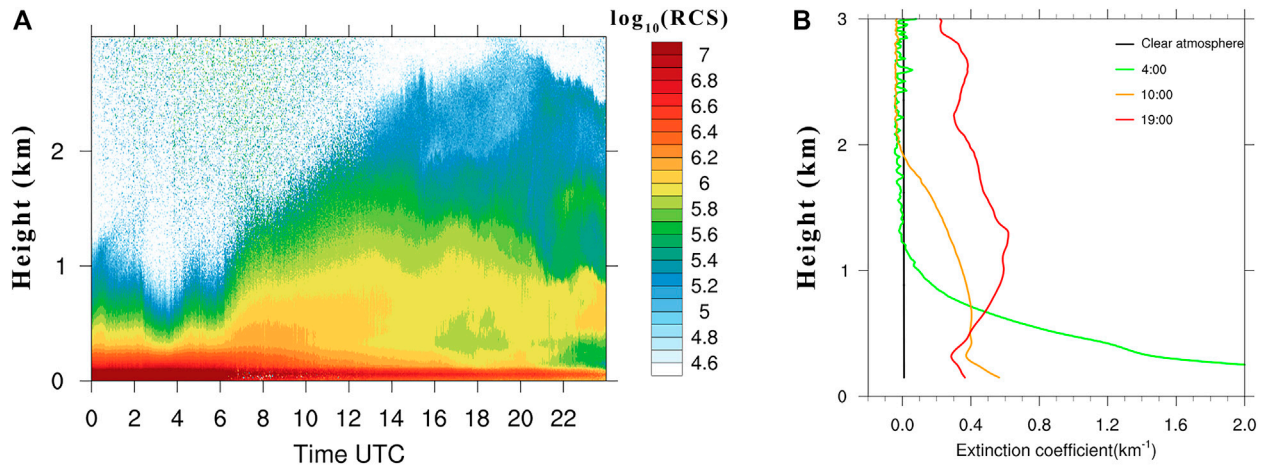

FIGURE 6 | (A) Diurnal variation of $\log_{10}$(RCS) of the ceilometer on July 26, 2019. **(B)** Vertical profiles of aerosol extinction coefficient (km^{-1}) at various hours on July 26, 2019. A distinct dust aerosol layer is lofted from 06:00 UTC. The black line illustrates the Rayleigh extinction coefficient of air molecules.

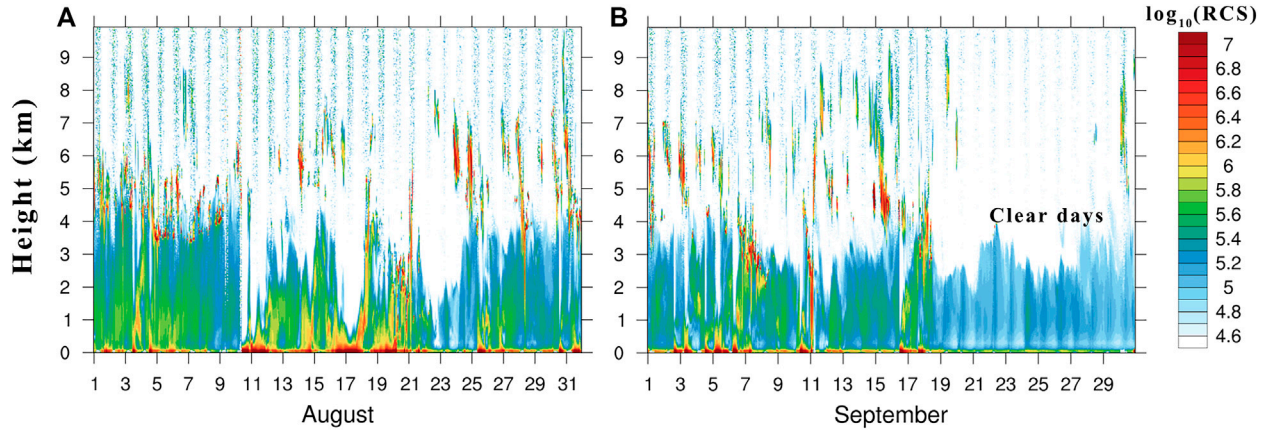

FIGURE 7 | Time series of 30-min averaged $\log_{10}$(RCS) of the ceilometer after smoothing signals at Tazhong. **(A)** August. **(B)** September. There are 12 consecutive clear-sky days since September 19, 2019.

ceilometer. It is clear that the maximum dust $\sigma(z)$ value at 04:00 UTC exceeds 2.0 km^{-1} on 300 m and almost linearly decreases with height, close to 0 km^{-1} at 1.0-km height. This majorly indicates that a great deal of high-concentration dust aerosols near the surface has strong attenuation effects on laser pulse energy, which directly leads to very weak backscattering signals in the upper atmosphere. The $\sigma(z)$ profile presents two distinct layers at 10:00 UTC along with the uplifted and diffused dust particles—that is, the $\sigma(z)$ value is about 0.6 km^{-1} at 200 m and stays around 0.4 km^{-1} at 300 m, then decreases with height from 0.30 to 1.8 km, and is equal to 0 km^{-1} at 1.8 km. The extinction coefficient $\sigma(z)$ at 19:00 UTC also shows prominent vertical variations, and there are three obvious dust layers. The $\sigma(z)$ value is about 0.3 km^{-1} at 300 m but increases with height from 300 m to 1.3 km [$\sigma(z)$ ~0.65 km^{-1}] and then slightly decreases with height from 1.3 to 3.0 km and is about 0.2 km^{-1} at 3.0 km.

Figure 7 describes the time series of dust vertical profiles in August and September 2019 at Tazhong. It is evident that dust events frequently occur in the hinterland of TD during summer in 2019, and the occurrence frequencies and intensities of dust storms in August are significantly higher than those in September. The backscattering signals of the ceilometer are greatly intense from August10 to 21, implying that heavy dust events persistently make an outbreak during this period, with a maximum uplifted height of 4 km. Moderate dust events are still active from September 1 to 18, but there are 12 consecutive clear-sky days from September 19 to 30. The $\log_{10}$(RCS) signals of the ceilometer under clear-sky conditions are relatively weak, with all values less than 5.2, which is well representative of the background levels of dust aerosols in TD. Generally, the number of dusty days accounts for about 77% of the whole period, and most of the uplifted heights of dust layers are less than 3 km, although on occasional events these could reach up to 4 km. These elevated dust particles would heat up the atmospheric layer and alter the thermal structure of the atmosphere at daytime through absorption of solar radiation. On the other hand, the airborne dust aerosols could also prevent the surface longwave radiation emitted into outer space and play a vital role in heat preservation at nighttime. Whether the summertime dust aerosols can be transported downstream for a long distance is mainly dependent on the uplifted height (4 to 5 km) and the intensity of mid-latitude westerlies (Yumimoto et al., 2010; Chen et al., 2017b). **Figure 7** also indicates that an obvious dust stagnation layer persistently hovers over the TD at 1.5–3.0-km height during summer in 2019. Affected by the surrounding huge mountains and the Mongolian cold frontal cyclone, the summertime high-altitude dust stagnation layer is not easily transported outside the Tarim Basin. After hanging over the desert for several days, most of the elevated dust particles are re-deposited in TD and nearby downstream arid regions through gravitational dry settlement or wet removal process. As a result, the transported contribution of the summertime Taklimakan dust to East Asian dust loading is relatively small.

Aerosol Mixing Layer Height

The height of the atmospheric boundary layer (ABLH) is a key quantity to reflect the complex physical processes of turbulent mixing and convective development and could directly affect the vertical exchanges of water vapor, matters, momentum, and energy between the land surface and the upper atmosphere. The potential temperature gradient method is commonly used to calculate the ABLH based on radiosonde profile measurements, which is defined as the height at which the air temperature gradient is obviously discontinuous or the diurnal variation of temperature is close to disappearing (Holzworth, 1964; Liu and Liang, 2010; Dai et al., 2014). It is well known that the concentrations of water vapor or aerosols are high in the ABL, whereas they rapidly decrease in the free atmosphere. Thus, we can define the aerosol mixing layer height (AMLH) as the height at which the humidity or aerosol concentration gradient is evidently discontinuous. The AMLH primarily represents the vertical distributions of airborne particles in the lower atmosphere, which is slightly different from the traditional ABLH. Because the backscattering signal profile $X(z) = P(z)z^2$

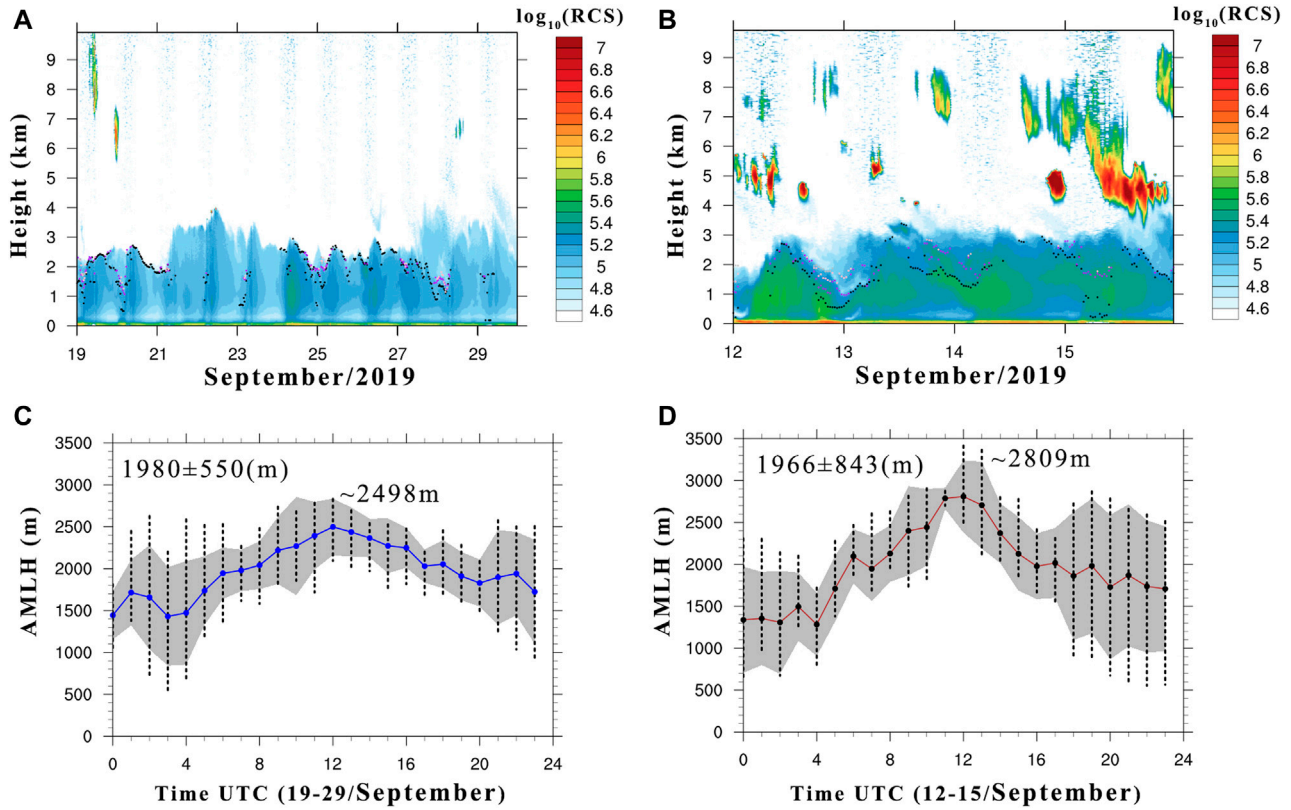

FIGURE 8 | Time evolutions of 30-min averaged $\log_{10}$(RCS) of the ceilometer at Tazhong. The black dots show the aerosol mixing layer height (AMLH). **(A)** Background levels of low aerosol concentrations under clear-sky conditions from September 19 to 30, 2019. **(B)** Vertical distributions of dust aerosols under floating dusty days from September 12 to 15, 2019. Hourly average diurnal variations of AMLH (in m) at Tazhong. The black dashed lines indicate the maximum or minimum values at the corresponding hour. The gray shades denote plus or minus one standard deviation. **(C)** Clear-sky days from September 19 to 30, 2019. **(D)** Floating dusty days from September 12 to 15, 2019. The overall means and maximum AMLH are shown in the figures.

can well reflect the vertical distribution of aerosol concentrations, the gradient method or wavelet covariance transform method is usually utilized to retrieve the AMLH based on the backscattering signals. In the gradient method, the AMLH is defined as the height at which $X(z)$ significantly decreases with z, namely, the height corresponding to the minimum of $\frac{\partial[X(z)]}{\partial z}$ (Sawyer and Li, 2013). In wavelet covariance transform method, Davis et al. (2000) defined a wavelet covariance transform function $W_f(a, b)$ related to the integral of lidar's backscattered signal, and AMLH is determined as the height corresponding to the maximum value of $W_f(a, b)$. The detailed inversion algorithms can be referred to earlier literatures (Davis et al., 2000; Kotthaus and Grimmond, 2018). In this study, we combine the gradient method with the wavelet covariance transform method to calculate the AMLH from the backscattering signal of the ceilometer, which is suitable for cases of low backscattered signal gradient or well-defined atmospheric inversion layer above the ABL.

Figures 8A, B outline the time evolutions of 30-min averaged $\log_{10}$(RCS) of the ceilometer under clear-sky and floating dusty conditions at Tazhong. The AMLH marked with black dots is superposed on the figures. It is apparent in **Figures 8A, B** that the AMLH exhibits a large fluctuating diurnal variation. Here we make use of a three standard deviation (3σ) criteria to inspect if any measurements fall within the 3σ range of the mean of AMLH for a certain whole day [*i.e.*, mean (AMLH) ± 3σ]. In other words, any point that exceeds the mean by 3σ would be regarded as highly improbable and eliminated. The clear-sky days in **Figures 8A,C** are from September 19 to 30, 2019, and the floating dusty days in **Figures 8B, D** are from September 12 to 15, 2019. The results show that AMLHs present significant structural characteristics under two weather conditions, which is highly consistent with the change of $\log_{10}$(RCS) signals. The maximum values of AMLH are almost concentrated on 2–3.5 km, which is the height of the aforementioned dust stagnation layer. The AMLHs exhibit prominent diurnal variations, namely, they are usually a low stable layer in the morning (~1.4–1.8 km) and at nighttime and are a high convective layer in the afternoon (~2.0–2.8 km). The standard deviation generally decreases with the increase of AMLH. The diel variations of AMLHs under floating dusty conditions are more significant than those of clear-sky cases, which are possibly attributed to the relatively weak backscattering signals of the ceilometer caused by the low aerosol concentrations under clear-sky conditions. There is a deep daytime AMLH (~3 km) convective structure and an obvious dust stagnation layer over the hinterland of TD during the

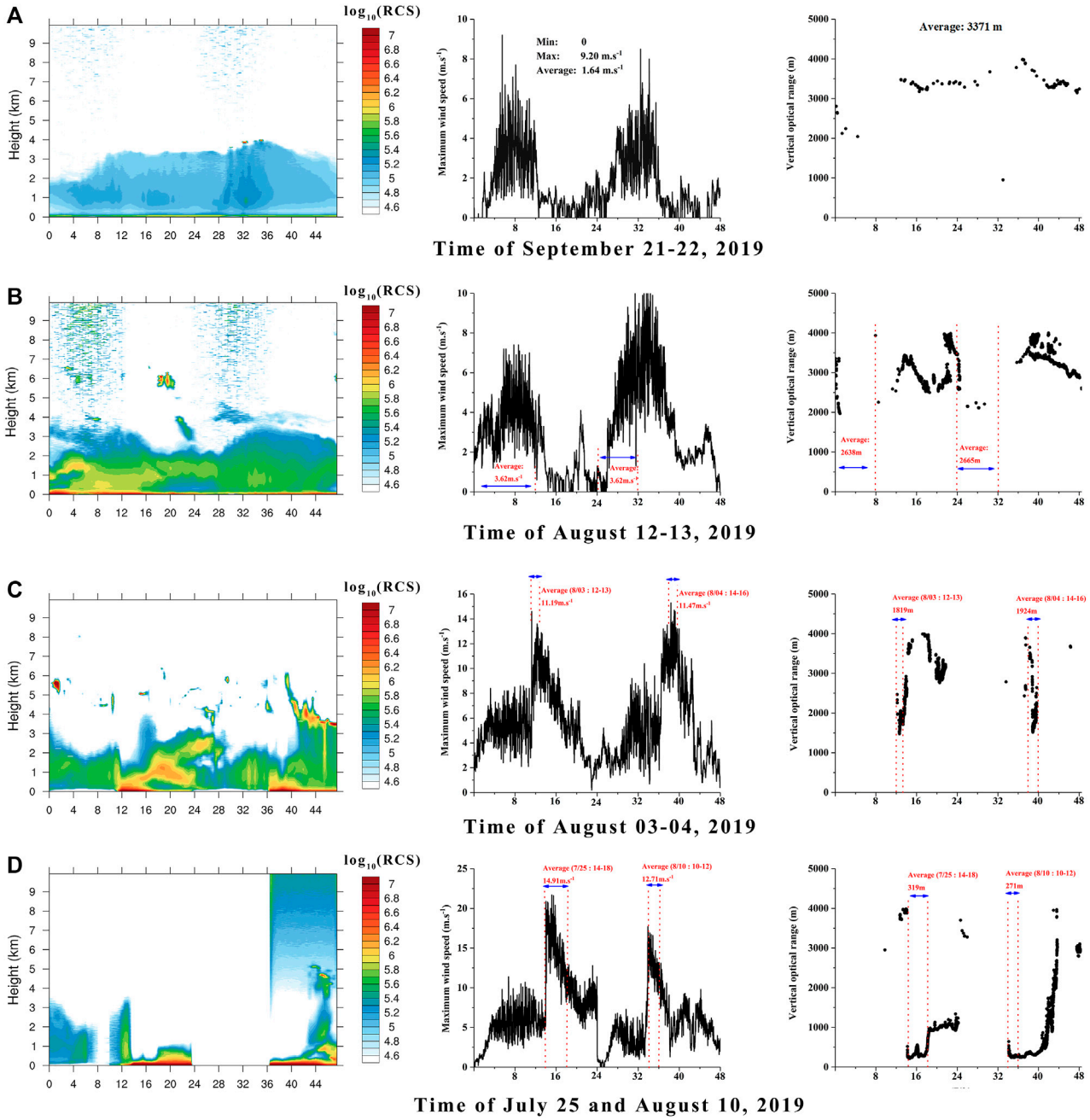

FIGURE 9 | Left panels: vertical profiles of 30-min averaged $\log_{10}$(RCS) from the ceilometer. Middle panels: time series of instantaneous maximum surface wind speed (ms^{-1}) with 1-min resolution. Right panels: time series of vertical optical range (in m) from the ceilometer. The mean values are shown in the figures. **(A)** Clear-sky days are from September 21 to 22, 2019. **(B)** Floating dusty days are from August 12 to 13, 2019. **(C)** Blowing dusty days are from August 3 to 4, 2019. **(D)** Strong dust storms are on July 25 and August 10, 2019.

whole period. The average maximum AMLHs under the two cases are about 2.5 and 2.8 km that appeared at 12:00 UTC, respectively, which is greatly consistent with the PBL height (3 to 4 km) measured from the radiosonde data (Zhang et al., 2011; Wang et al., 2016). The summertime AMLHs in Taklimakan Desert are remarkably larger than those in humid (~800 m–1.5 km) or sub-humid (~1.0–2.0 km) regions (Davis et al., 2000; Liu and Liang, 2010; Sawyer and Li, 2013; Kotthaus and Grimmond, 2018). Such a deep and intense AMLH convective structure is conducive to vertically uplift the dust particles generated from the desert surface into the upper atmosphere during summer and then exerts a far-reaching impact on the ecological environment and climate change.

Threshold of Diverse Dust Aerosol Intensities

As mentioned above, the occurrences of dust episodes have a great contribution to the surface particulate concentrations over desert areas. In this study, we propose a quantitative threshold method to distinguish the different levels of dust events based on the hourly average mass concentrations of particulate matters (*e.g.*, $PM_{2.5}$ and PM_{10}) and wind speed (ws). Note that the classification algorithm in this paper is somewhat different from the standard method of the World Meteorological Organization for identifying dust storms, which is mainly on the basis of horizontal visibility and wind speed. Therefore, the typical dust events can be classified as follows: (1) clear-sky condition: $PM_{10} < 150\ \mu g/m^3$, $PM_{2.5} < 50\ \mu g/m^3$, and ws < $2.0\ ms^{-1}$; (2) floating dust: $150\ \mu g/m^3 \leq PM_{10} < 400\ \mu g/m^3$, $PM_{2.5} \geq 50\ \mu g/m^3$, $2.0\ ms^{-1} \leq ws < 5.0\ ms^{-1}$, lasting for 3 h at least; (3) blowing dust: $400\ \mu g/m^3 \leq PM_{10} < 800\ \mu g/m^3$, $PM_{2.5} \geq 100\ \mu g/m^3$, $5.0\ ms^{-1} \leq ws < 10.0\ ms^{-1}$, lasting for 3 h at least; (4) and dust storm: $PM_{10} \geq 800\ \mu g/m^3$, $PM_{2.5} \geq 150\ \mu g/m^3$, ws ≥ $10.0\ ms^{-1}$, lasting for 3 h at least. Then, we can analyze the characteristics of the aerosol optical parameters under different dust intensities, such as normalized range-corrected signal $\log_{10}(RCS)$, aerosol extinction [$\sigma(z)$] and backscattering [$\beta(z)$] coefficients, vertical optical range (VOR), and corresponding lidar ratio (S_a). Similar to the definition of horizontal visibility, the VOR is calculated as the height at which the integral of the aerosol extinction coefficient with z is equal to 3, namely: $\int_0^{VOR} \sigma(z)dz = 3$.

Figure 9 draws the vertical profiles of $\log_{10}(RCS)$, surface wind speed, and VOR under different dust events at Tazhong. Here the clear-sky days, floating dust, blowing dust, and strong dust storms are from September 21 and 22, August 12 and 13, August 3 and 4, July 25, and August 10, 2019, respectively. The backscattering signal intensities $\log_{10}(RCS)$ and VORs of the ceilometer present pronounced diurnal variations with the increase of surface wind speed and persistence of high wind speed. The maximal AMLH values are about 4.0, 3.2, 2.5, and 1.0 km for clear-sky days, floating dust, blowing dust, and heavy dust storms, respectively, which is majorly owing to the different concentrations of dust particles produced from the surface and caused by different degrees of attenuation of emitted laser pulse energy. The $\log_{10}(RCS)$ under clear-sky conditions are all lower than 5.2 and range from 5.2 to 5.8 under floating dust and from 5.6 to 6.2 under blowing dust. The $\log_{10}(RCS)$ are higher than 6.2 for heavy dust storm cases. Affected by the lofted dust particles, the atmospheric turbidities significantly increase, and the corresponding VOR values vary from 3.2 to 4.0 km, from 2.0 to 3.5 km, from 1.5 to 3.0 km, and from 0.2 to 1.5 km, respectively. Obviously, the diurnal variations of VOR greatly fluctuate under strong dust storms and blowing dust. In comparison, the clear-sky VORs display relatively smooth variations. The overall mean VOR values are approximately 3.37, 2.64, 1.92, and 0.32 km for four typical weather types, respectively, as shown in **Figure 9**.

Figure 10 shows the averaged vertical profiles of aerosol extinction coefficient at Tazhong under clear-sky, floating dust, blowing dust, and strong dust storm conditions. The clear-sky days include from September 21 to 29, 2019. The floating dusty days include July 27 and 29, August 12 and 13, and September 13. The blowing dusty days include July 26 and August 3 and 4. The strong dusty days include July 25, August 10, 11, and 17, and September 6 and 10. The results imply that the aerosol extinction coefficients $\sigma(z)$ are all greater than $1.0\ km^{-1}$ at 150–300-m height, with maximal $\sigma(z)$ of $2.0\ km^{-1}$ for strong dust storms. The corresponding $\sigma(z)$ distinctly decreases with the increase of height, from $1.0\ km^{-1}$ at 300 m to $0.3\ km^{-1}$ at 1 km and $0.0\ km^{-1}$ at 2.0 km, and then this remains at $0.0\ km^{-1}$ from 2.0 to 5.0 km. This suggests again that the intense attenuation effects induced by massive airborne dust particles directly result in very weak backscattering signals above 2.0-km height. For the blowing dust case, the $\sigma(z)$ value is about $0.50\ km^{-1}$ at 200 m, linearly decreases with height, is $0.25\ km^{-1}$ at 300 m, and then stays at around $0.30\ km^{-1}$ from 300 m to 1.6 km; finally, it gradually decreases with height and is nearly $0.0\ km^{-1}$ at 4.0 km. The $\sigma(z)$ values are 0.10 km and $0.14\ km^{-1}$ at 200-m height for clear-sky and floating dust, respectively, and both linearly reduce with height and are about 0.04 and $0.09\ km^{-1}$ at 300 m. Then, the $\sigma(z)$ values of the two cases nonlinearly increase with height and reach a maximum of $0.20\ km^{-1}$ at 2.7 km for clear-sky case and a maximum of $0.32\ km^{-1}$ at 2.6 km for floating dust case. Finally, the corresponding $\sigma(z)$ values decrease again with height and stay at about $0.05\ km^{-1}$ from 3.4 to 5.0 km. Generally, the aerosol extinction coefficients under dust cases

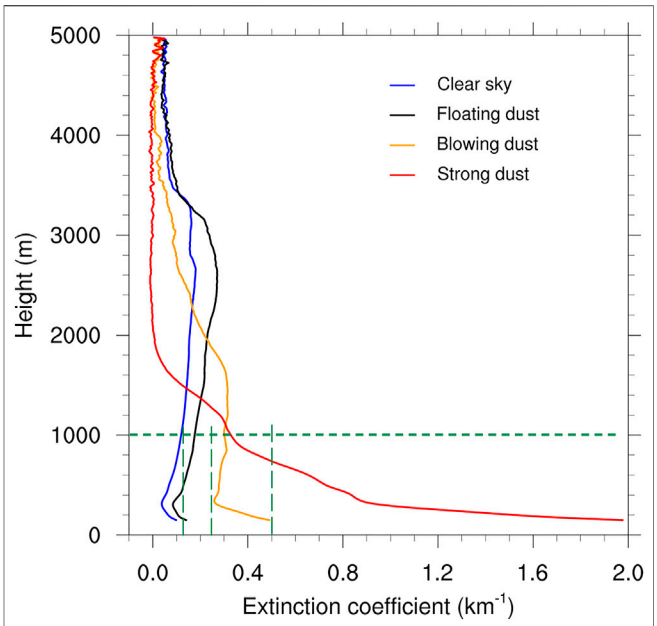

FIGURE 10 | Averaged vertical profiles of aerosol extinction coefficient (km^{-1}) at Tazhong under clear sky (blue), floating dust (black), blowing dust (orange), and strong dust storm (red) conditions. The clear-sky days were from September 21 to 29, 2019. The floating dusty days were July 27 and 29, August 12 and 13, and September 13, 2019. The blowing dusty days include July 26 and August 3 and 4, 2019. The strong dusty days include July 25, August 10, 11, and 17, and September 6 and 10, 2019.

TABLE 1 | Statistics of aerosol optical parameters under different levels of dust intensity during summer 2019 at Tazhong.

Dust intensity levels	log_{10}(normalized range-corrected signal) (0–1 km)	Vertical optical range (km)	σ (0–1 km) (km^{-1})	β (0–1 km) (km^{-1} sr^{-1})	S_a (sr)
Clear sky	<5.2	>3.0	<0.12	<0.004	30
Floating dust	5.2–5.8	2.0–3.0	0.12–0.25	0.0024–0.005	50
Blowing dust	5.6–6.2	1.0–3.0	0.25–0.50	0.005–0.01	50
Strong dust	>6.2	<1.0	>0.50	>0.01	50

log_{10}(RCS), σ(z), and β(z) are calculated as the overall average from 0 to 1 km.

are about 3–10 times higher than those in clear-sky conditions. These structural patterns reflect the influences of uplifted dust aerosols on the $\sigma(z)$ vertical profiles at different heights.

Table 1 summarizes the statistics of aerosol optical parameters under different levels of dust intensity during summer in 2019 at Tazhong. It is evident that the $\log_{10}$(RCS), $\sigma(z)$, and $\beta(z)$ are less than 5.2, 0.12 km^{-1}, and 0.004 km^{-1} sr^{-1} for clear-sky cases, respectively, and the corresponding VOR is greater than 3.0 km, while the lidar ratio S_a is 30 sr. The $\log_{10}$(RCS), $\sigma(z)$, and $\beta(z)$ are larger than 6.2, 0.5 km^{-1}, and 0.01 km^{-1} sr^{-1} for strong dust storms, respectively, and the corresponding VOR is smaller than 1.0 km, while the lidar ratio S_a is 50 sr. The $\log_{10}$(RCS), $\sigma(z)$, $\beta(z)$, and VOR vary as 5.2–5.8, 0.12–0.25 km^{-1}, 0.0024–0.005 km^{-1} sr^{-1}, and 2.0–3.0 km under floating dust, respectively, and the corresponding aerosol optical characteristics are in the ranges 5.6–6.2, 0.25–0.50 km^{-1}, 0.005–0.01 km^{-1} sr^{-1}, and 1.0–3.0 km for blowing dust. Unlike the HSRL or Raman depolarized lidar, the CHM15k ceilometer can only provide vertical profile information of aerosol optical properties at 1,064 nm, and it lacks multi-channel profiles and depolarization ratio. However, these statistical variables are very helpful to investigate and validate dust aerosols in the application of climate models or satellite remote sensing.

CONCLUSION

This study mainly examined the vertical profiles and optical properties of dust aerosol in the hinterland of Taklimakan Desert during summer in 2019. The primary findings are summarized in the following discussion.

Influenced by the abundant surface dust sources and strong wind speed, dust events frequently occurred in Taklimakan Desert during the whole inclusive period; the overall hourly mean $PM_{2.5}$, PM_{10}, $PM_{2.5}/PM_{10}$, and $AE_{440–870}$ were 110.4 ± 121.0 μg/m^3, 317.2 ± 340.0 μg/m^3, 0.35 ± 0.07, and 0.28 ± 0.12, respectively, suggesting that dust particles were the predominant aerosol types in the hinterland of TD. Both the ground-based ceilometer and spaceborne CALIPSO could distinctly detect the dust aerosol, high-altitude cloud layer, and subsequent rainfall process. Affected by the surrounding huge mountains and the intensity of mid-latitude westerlies, there was an obvious summertime dust stagnation layer persistently hovering over the TD at 1.5–3.0-km height, and most of the uplifted dust particles were re-deposited in the TD and nearby downstream arid regions after hanging over the desert for several days. The AMLH exhibited prominent diurnal variations, which were usually a low stable layer in the morning and at nighttime (~1.5 km) and a high convective layer in the afternoon (~2.8 km). There was a deep and intense daytime convective structure with maximum AMLH of ~3 km that appeared at 12:00 UTC, which was greatly consistent with the PBL height (3 to 4 km) measured from radiosonde data.

The backscattering signals $\log_{10}$(RCS), $\sigma(z)$, and $\beta(z)$ were less than 5.2, 0.12 km^{-1}, and 0.004 km^{-1} sr^{-1} for clear-sky cases, respectively, and the corresponding VOR was greater than 3.0 km, while the lidar ratio S_a was 30 sr. In comparison, the $\log_{10}$(RCS), $\sigma(z)$, and $\beta(z)$ were larger than 6.2, 0.5 km^{-1}, and 0.01 km^{-1} sr^{-1} for heavy dust storms, respectively, and the corresponding VOR was smaller than 1.0 km, while S_a was equal to 50 sr. The aerosol extinction coefficients $\sigma(z)$ were about 2.0, 0.5, 0.14, and 0.10 km^{-1} at 200-m height, respectively, under strong dust storm, blowing dust, floating dust, and clear-sky conditions, and the corresponding values were 0.30, 0.30, 0.15, and 0.11 km^{-1} at 1 km. Generally, the aerosol extinction coefficients under dust events were about 3–10 times higher than those of clear-sky cases. The statistics of aerosol optical parameters under different dust intensities at Tazhong are very helpful to investigate and validate dust aerosols in the application of climate models or satellite remote sensing.

The findings of this paper directly confirmed the existence of a dust stagnation layer and a deep daytime convective structure over Taklimakan Desert in summer, which provide an invaluable dataset for surveying the uplifted and long-distance transportation of summertime Taklimakan dust particles. The interaction among dust aerosol, cloud, and precipitation plays a pivotal role in the radiation budget of the Earth–atmosphere system and concerning the hydrological cycle, but it still remains one of the biggest uncertainties in the current climate change. To uncover the complex feedback mechanism of dust–cloud–precipitation in desert source regions, in the future, we should integrate a variety of advanced detection methods (*e.g.*, HSRL, Raman depolarized lidar, cloud radar), sophisticated satellite remote sensing algorithms (*e.g.*, CALIPSO, CloudSat), and optimal and robust climate models to acquire three-dimensional and comprehensive multi-variable information of these complicated processes.

DATA AVAILABILITY STATEMENT

The original contributions presented in the study are included in the article/Supplementary Material. Further inquiries can be directed to the corresponding author.

AUTHOR CONTRIBUTIONS

JB coordinated and supervised the project. JB, ZL, DZ, FY, BL, JM, ZH, and QH contributed to field experiment and data analysis, research framework design, and writing the first drafts. ZL prepared data and completed all figures. JB revised the manuscript. All co-authors contributed to the interpretation of the results and to the text and approved it for publication.

FUNDING

This research was founded by the National Science Foundation of China (42075126), the Project of Field Scientific Observation and Research Station of Gansu Province (18JR2RA013), the Fundamental Research Funds for the Central Universities (lzujbky-2021-kb02 and lzujbky-2021-sp04), and China 111 Project (number B13045).

ACKNOWLEDGMENTS

The authors are grateful to the NASA scientific team for the provision of CALIPSO products and the Chinese Environmental Protection Bureau for providing data on the hourly mean $PM_{2.5}$ and PM_{10} concentrations at Hotan. We would like to express special thanks to all staff of Taklimakan Desert Meteorology Field Experiment Station for supporting the field experiment. We also appreciate all reviewers and editors for their constructive and insightful comments.

REFERENCES

Ackermann, J. (1998). The Extinction-To-Backscatter Ratio of Tropospheric Aerosol: A Numerical Study. *J. Atmos. Oceanic Technol.* 15 (4), 1043–1050. doi:10.1175/1520-0426(1998)015<1043:tetbro>2.0.co;2

Bi, J., Huang, J., Shi, J., Hu, Z., Zhou, T., Zhang, G., et al. (2017). Measurement of Scattering and Absorption Properties of Dust Aerosol in a Gobi farmland Region of Northwestern China - a Potential Anthropogenic Influence. *Atmos. Chem. Phys.* 17, 7775–7792. doi:10.5194/acp-17-7775-2017

Bi, J., Zuo, D., Yang, F., Zhang, L., Huang, Z., and Wang, T. (2022). Surface Radiation Characteristics and Downward Cloud Radiative Forcing in Southern Xinjiang during Summer 2019. *Meteorol. Atmos. Phys.* 134 (1), 13–23. doi:10.1007/s00703-021-00847-5

Che, H., Wang, Y., Sun, J., Zhang, X., Zhang, X., and Guo, J. (2013). Variation of Aerosol Optical Properties over the Taklimakan Desert in China. *Aerosol Air Qual. Res.* 13, 777–785. doi:10.4209/aaqr.2012.07.0200

Che, H., Zhang, X.-Y., Xia, X., Goloub, P., Holben, B., Zhao, H., et al. (2015). Ground-based Aerosol Climatology of China: Aerosol Optical Depths from the China Aerosol Remote Sensing Network (CARSNET) 2002-2013. *Atmos. Chem. Phys.* 15, 7619–7652. doi:10.5194/acp-15-7619-2015

Che, H., Xia, X., Zhao, H., Dubovik, O., Holben, B. N., Goloub, P., et al. (2019a). Spatial Distribution of Aerosol Microphysical and Optical Properties and Direct Radiative Effect from the China Aerosol Remote Sensing Network. *Atmos. Chem. Phys.* 19, 11843–11864. doi:10.5194/acp-19-11843-2019

Che, H., Gui, K., Xia, X., Wang, Y., Holben, B. N., Goloub, P., et al. (2019b). Large Contribution of Meteorological Factors to Inter-Decadal Changes in Regional Aerosol Optical Depth. *Atmos. Chem. Phys.* 19, 10497–10523. doi:10.5194/acp-19-10497-2019

Chen, S., Huang, J., Li, J., Jia, R., Jiang, N., Kang, L., et al. (2017a). Comparison of Dust Emissions, Transport, and Deposition between the Taklimakan Desert and Gobi Desert from 2007 to 2011. *Sci. China Earth Sci.* 60, 1338–1355. doi:10.1007/s11430-016-9051-0

Chen, S., Huang, J., Kang, L., Wang, H., Ma, X., He, Y., et al. (2017b). Emission, Transport, and Radiative Effects of mineral Dust from the Taklimakan and Gobi Deserts: Comparison of Measurements and Model Results. *Atmos. Chem. Phys.* 17, 2401–2421. doi:10.5194/acp-17-2401-2017

Dai, C., Wang, Q., Kalogiros, J. A., Lenschow, D. H., Gao, Z., and Zhou, M. (2014). Determining Boundary-Layer Height from Aircraft Measurements. *Boundary-Layer Meteorol.* 152 (3), 277–302. doi:10.1007/s10546-014-9929-z

Davis, K. J., Gamage, N., Hagelberg, C. R., Kiemle, C., Lenschow, D. H., and Sullivan, P. P. (2000). An Objective Method for Deriving Atmospheric Structure from Airborne Lidar Observations. *J. Atmos. Oceanic Technol.* 17 (11), 1455–1468. doi:10.1175/1520-0426(2000)017<1455:aomfda>2.0.co;2

Fernald, F. G. (1984). Analysis of Atmospheric Lidar Observations: Some Comments. *Appl. Opt.* 23, 652–653. doi:10.1364/AO.23.000652

Ge, J. M., Huang, J. P., Xu, C. P., Qi, Y. L., and Liu, H. Y. (2014). Characteristics of Taklimakan Dust Emission and Distribution: A Satellite and Reanalysis Field Perspective. *J. Geophys. Res. Atmos.* 119 (20), 11772–11783. doi:10.1002/2014JD022280

Heese, B., Flentje, H., Althausen, D., Ansmann, A., and Frey, S. (2010). Ceilometer Lidar Comparison: Backscatter Coefficient Retrieval and Signal-To-Noise Ratio Determination. *Atmos. Meas. Tech.* 3, 1763–1770. doi:10.5194/amt-3-1763-2010

Holben, B. N., Eck, T. F., Slutsker, I., Tanré, D., Buis, J. P., Setzer, A., et al. (1998). AERONET: A Federated Instrument Network and Data Archive for Aerosol Characterization. *Remote Sensing Environ.* 66 (1), 1–16. doi:10.1016/s0034-4257(98)00031-5

Holzworth, G. C. (1964). Estimates of Mean Maximum Mixing Depths in the Contiguous United States. *Mon. Wea. Rev.* 92 (5), 235–242. doi:10.1175/1520-0493(1964)092<0235:eommmd>2.3.co;2

Hu, Z., Huang, J., Zhao, C., Bi, J., Jin, Q., Qian, Y., et al. (2019a). Modeling the Contributions of Northern Hemisphere Dust Sources to Dust Outflow from East Asia. *Atmos. Environ.* 202, 234–243. doi:10.1016/j.atmosenv.2019.01.022

Hu, Z., Huang, J., Zhao, C., Ma, Y., Jin, Q., Qian, Y., et al. (2019b). Trans-Pacific Transport and Evolution of Aerosols: Spatiotemporal Characteristics and Source Contributions. *Atmos. Chem. Phys.* 19, 12709–12730. doi:10.5194/acp-19-12709-2019

Hu, Z., Huang, J., Zhao, C., Jin, Q., Ma, Y., and Yang, B. (2020). Modeling Dust Sources, Transport, and Radiative Effects at Different Altitudes over the Tibetan Plateau. *Atmos. Chem. Phys.* 20, 1507–1529. doi:10.5194/acp-20-1507-2020

Huang, J., Lin, B., Minnis, P., Wang, T., Wang, X., Hu, Y., et al. (2006a). Satellite-based Assessment of Possible Dust Aerosols Semi-direct Effect on Cloud Water Path over East Asia. *Geophys. Res. Lett.* 33, L19802. doi:10.1029/2006GL026561

Huang, J., Minnis, P., Lin, B., Wang, T., Yi, Y., Hu, Y., et al. (2006b). Possible Influences of Asian Dust Aerosols on Cloud Properties and Radiative Forcing Observed from MODIS and CERES. *Geophys. Res. Lett.* 33, L06824. doi:10.1029/2005GL024724

Huang, J., Minnis, P., Yi, Y., Tang, Q., Wang, X., Hu, Y., et al. (2007). Summer Dust Aerosols Detected from CALIPSO over the Tibetan Plateau. *Geophys. Res. Lett.* 34, L18805. doi:10.1029/2007GL029938

Huang, J., Minnis, P., Chen, B., Huang, Z., Liu, Z., Zhao, Q., et al. (2008). Long-range Transport and Vertical Structure of Asian Dust from CALIPSO and Surface Measurements during PACDEX. *J. Geophys. Res.* 113, D23212. doi:10.1029/2008JD010620

Huang, J., Fu, Q., Su, J., Tang, Q., Minnis, P., Hu, Y., et al. (2009). Taklimakan Dust Aerosol Radiative Heating Derived from CALIPSO Observations Using the Fu-Liou Radiation Model with CERES Constraints. *Atmos. Chem. Phys.* 9, 4011–4021. doi:10.5194/acp-9-4011-2009

Huang, Z., Huang, J., Bi, J., Wang, G., Wang, W., Fu, Q., et al. (2010). Dust Aerosol Vertical Structure Measurements Using Three MPL Lidars during 2008 China-U.S. Joint Dust Field experiment. *J. Geophys. Res.* 115, D00K15. doi:10.1029/2009JD013273

Huang, J., Fu, Q., Zhang, W., Wang, X., Zhang, R., Ye, H., et al. (2011). Dust and Black Carbon in Seasonal Snow across Northern China. *Bull. Amer. Meteorol. Soc.* 92, 175–181. doi:10.1175/2010BAMS3064.1

Huang, J., Wang, T., Wang, W., Li, Z., and Yan, H. (2014). Climate Effects of Dust Aerosols over East Asian Arid and Semiarid Regions. *J. Geophys. Res. Atmos.* 119, 11398–11416. doi:10.1002/2014JD021796

Huebert, B. J., Bates, T., Russell, P. B., Shi, G., Kim, Y. J., Kawamura, K., et al. (2003). An Overview of ACE-Asia: Strategies for Quantifying the Relationships between Asian Aerosols and Their Climatic Impacts. *J. Geophys. Res.* 108 (D23), 8633. doi:10.1029/2003JD003550

Husar, R. B., Tratt, D. M., Schichtel, B. A., Falke, S. R., Li, F., Jaffe, D., et al. (2001). Asian Dust Events of April 1998. *J. Geophys. Res.* 106 (D16), 18317–18330. doi:10.1029/2000jd900788

IPCC Climate Change (2013). "The Physical Science Basis," in *Contribution of Working Group I to the Fifth Assessment Report of the Intergovernmental Panel on Climate Change*. Editors T. F. Stocker, D. Qin, G.-K. Plattner, M. Tignor, S. K. Allen, J. Boschung, et al. (Cambridge, United Kingdom and New York, NY, USA: Cambridge University Press), 1535.

Jickells, T. D., An, Z. S., Andersen, K. K., Baker, A. R., Bergametti, G., Brooks, N., et al. (2005). Global Iron Connections between Desert Dust, Ocean Biogeochemistry, and Climate. *Science* 308, 67–71. doi:10.1126/science.1105959

Jin, L., He, Q., Li, Z., Deng, M., and Abbas, A. (2021). Interannual and Seasonal Variations of Sand-Dust Events in Tarim Basin, China. *Res. Sq*. doi:10.21203/rs.3.rs-327333/v1

Jin, Q., Wei, J., Lau, W. K. M., Pu, B., and Wang, C. (2021). Interactions of Asian mineral Dust with Indian Summer Monsoon: Recent Advances and Challenges. *Earth-Science Rev.* 215, 103562. doi:10.1016/j.earscirev.2021.103562

Kai, K., Nagata, Y., Tsunematsu, N., Matsumura, T., Kim, H.-S., Matsumoto, T., et al. (2008). The Structure of the Dust Layer over the Taklimakan Deser during the Dust Storm in April 2002 as Observed Using a Depolarization Lidar. *J. Meteorol. Soc. Jpn.* 86 (1), 1–16. doi:10.2151/jmsj.86.1

Kotthaus, S., and Grimmond, C. S. B. (2018). Atmospheric Boundary-layer Characteristics from Ceilometer Measurements. Part 1: A New Method to Track Mixed Layer Height and Classify Clouds. *Q.J.R. Meteorol. Soc.* 144 (714), 1525–1538. doi:10.1002/qj.3299

Li, Z., Lau, W. K. M., Ramanathan, V., Wu, G., Ding, Y., Manoj, M. G., et al. (2016). Aerosol and Monsoon Climate Interactions over Asia. *Rev. Geophys.* 54, 866–929. doi:10.1002/2015RG000500

Li, L., Mahowald, N. M., Miller, R. L., Pérez García-Pando, C., Klose, M., Hamilton, D. S., et al. (2021). Quantifying the Range of the Dust Direct Radiative Effect Due to Source Mineralogy Uncertainty. *Atmos. Chem. Phys.* 21, 3973–4005. doi:10.5194/acp-21-3973-2021

Liao, H., and Seinfeld, J. H. (1998). Radiative Forcing by mineral Dust Aerosols: Sensitivity to Key Variables. *J. Geophys. Res.* 103, 31637–31645. doi:10.1029/1998JD200036

Liu, S., and Liang, X.-Z. (2010). Observed Diurnal Cycle Climatology of Planetary Boundary Layer Height. *J. Clim.* 23 (21), 5790–5809. doi:10.1175/2010jcli3552.1

Liu, Z., Sugimoto, N., and Murayama, T. (2002). Extinction-to-backscatter Ratio of Asian Dust Observed with High-Spectral-Resolution Lidar and Raman Lidar. *Appl. Opt.* 41 (15), 2760–2767. doi:10.1364/AO.41.002760

Liu, D., Wang, Z., Liu, Z., Winker, D., and Trepte, C. (2008). A Height Resolved Global View of Dust Aerosols from the First Year CALIPSO Lidar Measurements. *J. Geophys. Res.* 113, D16214. doi:10.1029/2007JD009776

Liu, Z., Vaughan, M., Winker, D., Kittaka, C., Getzewich, B., Kuehn, R., et al. (2009). The CALIPSO Lidar Cloud and Aerosol Discrimination: Version 2 Algorithm and Initial Assessment of Performance. *J. Atmos. Ocean Technol.* 26 (7), 1198–1213. doi:10.1175/2009jtecha1229.1

Maher, B. A., Prospero, J. M., Mackie, D., Gaiero, D., Hesse, P. P., and Balkanski, Y. (2010). Global Connections between Aeolian Dust, Climate and Ocean Biogeochemistry at the Present Day and at the Last Glacial Maximum. *Earth-Science Rev.* 99 (1-2), 61–97. doi:10.1016/j.earscirev.2009.12.001

Mikami, M., Shi, G. Y., Uno, I., Yabuki, S., Iwasaka, Y., Yasui, M., et al. (2006). Aeolian Dust experiment on Climate Impact: An Overview of Japan-China Joint Project ADEC. *Glob. Planet. Change* 52, 142–172. doi:10.1016/j.gloplacha.2006.03.001

Mu, L., Su, J., Mo, X., Peng, N., Xu, Y., Wang, M., et al. (2021). The Temporal-Spatial Variations and Potential Causes of Dust Events in Xinjiang Basin during 1960-2015. *Front. Environ. Sci.* 9, 727844. doi:10.3389/fenvs.2021.727844

Murayama, T., Müller, D., Wada, K., Shimizu, A., Sekiguchi, M., and Tsukamoto, T. (2004). Characterization of Asian Dust and Siberian Smoke with Multi-Wavelength Raman Lidar over Tokyo, Japan in spring 2003. *Geophys. Res. Lett.* 31, L23103. doi:10.1029/2004GL021105

Pan, H., Huo, W., Wang, M., Zhang, J., Meng, L., Kumar, K. R., et al. (2020). Insight into the Climatology of Different Sand-Dust Aerosol Types over the Taklimakan Desert Based on the Observations from Radiosonde and A-Train Satellites. *Atmos. Environ.* 238, 117705. doi:10.1016/j.atmosenv.2020.117705

Qian, Y., Yasunari, T. J., Doherty, S. J., Flanner, M. G., Lau, W. K. M., Ming, J., et al. (2014). Light-Absorbing Particles in Snow and Ice: Measurement and Modeling of Climatic and Hydrological Impact. *Adv. Atmos. Sci.* 32, 64–91. doi:10.1007/s00376-014-0010-0

Rosenfeld, D., Rudich, Y., and Lahav, R. (2001). Desert Dust Suppressing Precipitation: A Possible Desertification Feedback Loop. *Proc. Natl. Acad. Sci.* 98, 5975–5980. doi:10.1073/pnas.101122798

Sawyer, V., and Li, Z. (2013). Detection, Variations and Intercomparison of the Planetary Boundary Layer Depth from Radiosonde, Lidar and Infrared Spectrometer. *Atmos. Environ.* 79, 518–528. doi:10.1016/j.atmosenv.2013.07.019

Shao, Y., Wyrwoll, K.-H., Chappell, A., Huang, J., Lin, Z., McTainsh, G. H., et al. (2011). Dust Cycle: An Emerging Core Theme in Earth System Science. *Aeolian Res.* 2, 181–204. doi:10.1016/j.aeolia.2011.02.001

Shimizu, A., Sugimoto, N., Matsui, I., Arao, K., Uno, I., Murayama, T., et al. (2004). Continuous Observations of Asian Dust and Other Aerosols by Polarization Lidars in China and Japan during ACE-Asia. *J. Geophys. Res.* 109, D19S17. doi:10.1029/2002JD003253

Tesche, M., Ansmann, A., MüLLER, D., Althausen, D., Mattis, I., Heese, B., et al. (2009). Vertical Profiling of Saharan Dust with Raman Lidars and Airborne HSRL in Southern Morocco during SAMUM. *Tellus B: Chem. Phys. Meteorology* 61, 144–164. doi:10.1111/j.1600-0889.2008.00390.x

Twomey, S. (1977). The Influence of Pollution on the Shortwave Albedo of Clouds. *J. Atmos. Sci.* 34 (7), 1149–1152. doi:10.1175/1520-0469(1977)034<1149:tiopot>2.0.co;2

U.S. EPA (1991). *Technical Assistance Document for Sampling and Analysis of Ozone Precursors*. Report No. EPA 600/8-91-215. North Carolina: U. S. Environmental Protection Agency, Atmospheric Research and Exposure Assessment Laboratory. Research Triangle Park, NC.

Uno, I., Eguchi, K., Yumimoto, K., Takemura, T., Shimizu, A., Uematsu, M., et al. (2009). Asian Dust Transported One Full Circuit Around the globe. *Nat. Geosci.* 2, 557–560. doi:10.1038/NGEO583

Uno, I., Eguchi, K., Yumimoto, K., Liu, Z., Hara, Y., Sugimoto, N., et al. (2011). Large Asian Dust Layers Continuously Reached North America in April 2010. *Atmos. Chem. Phys.* 11, 7333–7341. doi:10.5194/acp-11-7333-2011

Wang, X., Doherty, S. J., and Huang, J. (2013). Black Carbon and Other Light-Absorbing Impurities in Snow across Northern China. *J. Geophys. Res. Atmos.* 118, 1471–1492. doi:10.1029/2012JD018291

Wang, M., Wei, W., He, Q., Yang, Y., Fan, L., and Zhang, J. (2016). Summer Atmospheric Boundary Layer Structure in the Hinterland of Taklimakan Desert, China. *J. Arid Land* 8 (6), 846–860. doi:10.1007/s40333-016-0054-3

Wiegner, M., and Geiß, A. (2012). Aerosol Profiling with the Jenoptik Ceilometer CHM15kx. *Atmos. Meas. Tech.* 5, 1953–1964. doi:10.5194/amt-5-1953-2012

Winker, D. M., Hunt, W. H., and McGill, M. J. (2007). Initial Performance Assessment of CALIOP. *Geophys. Res. Lett.* 34, L19803. doi:10.1029/2007GL030135

Winker, D. M., Vaughan, M. A., Omar, A., Hu, Y., Powell, K. A., Liu, Z., et al. (2009). Overview of the CALIPSO Mission and CALIOP Data Processing Algorithms. *J. Atmos. Ocean Technol.* 26 (11), 2310–2323. doi:10.1175/2009jtecha1281.1

World Health Organization (2005). *Air Quality Guidelines for Particulate Matter, Ozone, Nitrogen Dioxide and Sulfur Dioxide. Global Update, E87950*. Copenhagen: World Health Organization Regional Office for Europe.

Yang, F., He, Q., Huang, J., Ali, M., Yang, X., Huo, W., et al. (2021). Desert Environment and Climate Observations Network Over the Taklimakan Desert. *B. AM. Meteorol. Soc.* 102 (6), E1172–E1191. doi:10.1175/BAMS-D-20–0236.1

Yin, Y., and Chen, L. (2007). The Effects of Heating by Transported Dust Layers on Cloud and Precipitation: A Numerical Study. *Atmos. Chem. Phys.* 7, 3497–3505. doi:10.5194/acp-7-3497-2007

Yumimoto, K., Eguchi, K., Uno, I., Takemura, T., Liu, Z., Shimizu, A., et al. (2010). Summertime Trans-Pacific Transport of Asian Dust. *Geophys. Res. Lett.* 37, L18815. doi:10.1029/2010GL043995

Zhang, Q., Zhang, J., Qiao, J., and Wang, S. (2011). Relationship of Atmospheric Boundary Layer Depth with Thermodynamic Processes at the Land Surface in Arid Regions of China. *Sci. China Earth Sci.* 54 (10), 1586–1594. doi:10.1007/s11430-011-4207-0

Conflict of Interest: The authors declare that the research was conducted in the absence of any commercial or financial relationships that could be construed as a potential conflict of interest.

Publisher's Note: All claims expressed in this article are solely those of the authors and do not necessarily represent those of their affiliated organizations or those of the publisher, the editors, and the reviewers. Any product that may be evaluated in this article or claim that may be made by its manufacturer is not guaranteed or endorsed by the publisher.

frontiers | Frontiers in Environmental Science

ORIGINAL RESEARCH
published: 26 April 2022
doi: 10.3389/fenvs.2022.832710

Comprehensive Analysis of a Dust Storm by a Lidar Network Combined With Multiple Data

Lili Yang[1,2], Shuwen Zhang[1], Huijie Tao[2], Yanping Yang[1,2], Lina Wang[2], Yongfeng Cui[3], Yanyan Xu[4] and Xiaoyun Li[4]*

[1]Key Laboratory for Semi-Arid Climate Change of the Ministry of Education, College of Atmospheric Sciences, Lanzhou University, Lanzhou, China, [2]Forecast Department, Gansu Province Environmental Monitoring Center, Lanzhou, China, [3]Forecast Department, Wuwei Ecological Environment Monitoring Center, Wuwei, China, [4]Marketing Center, Wuxi CAS Photonics Co., Ltd., Wuxi, China

In order to improve the accuracy of dust storm prediction and reduce the damage and losses by a dust storm event, it is necessary to conduct an in-depth study on the same. The data of the national air quality stations, backward trajectories generated by the Hybrid Single-Particle Lagrangian Integrated Trajectory model (HYSPLIT), and the lidar network data from Wuwei, Baiyin, and Dingxi were used to study a large-scale dust storm event that occurred from 12 to 14 May 2019. This study explores the cause of the dust storm and physical characteristics of dust aerosols in three-dimensional space, as well as its impact on air quality. Results show that the dust storm was caused by the eastward movement of the East Asian trough and affected most cities in northern China from northwest to southeast. Consequently, the air quality deteriorated seriously, especially over the Hexi Corridor. The hourly peak concentrations of PM_{10} in Wuwei and Baiyin were close to 3,000 $\mu g \cdot m^{-3}$. The observations from the lidar network show that the dust intensities were similar at different cities, and their extinction coefficients were close. However, the depolarization ratio varied with sources and the physical characteristics of dust particles. According to the simulation results of extinction coefficients and particle concentrations, due to the impact of dust transported at high altitudes, the concentration of particles in Dingxi did not decrease with the increase in altitude. The particle concentrations from ground-based monitoring were lower than those of Baiyin and Wuwei, while particle concentrations above 0.3 km were higher than those of Baiyin and Wuwei.

Keywords: dust, lidar network, particle concentration, synoptic situation, HYSPLIT backward trajectory, extinction coefficient

OPEN ACCESS

Edited by:
Longlei Li,
Cornell University, United States

Reviewed by:
Eduardo Landulfo,
Instituto de Pesquisas Energéticas e Nucleares (IPEN), Brazil
Dipesh Rupakheti,
Nanjing University of Information Science and Technology, China

***Correspondence:**
Shuwen Zhang
zhangsw@lzu.edu.cn

Specialty section:
This article was submitted to Atmosphere and Climate, a section of the journal Frontiers in Environmental Science

Received: *10 December 2021*
Accepted: *28 February 2022*
Published: *26 April 2022*

Citation:
Yang L, Zhang S, Tao H, Yang Y, Wang L, Cui Y, Xu Y and Li X (2022) Comprehensive Analysis of a Dust Storm by a Lidar Network Combined With Multiple Data. Front. Environ. Sci. 10:832710. doi: 10.3389/fenvs.2022.832710

1 INTRODUCTION

Since 1990, with the rapid development of industries and urbanization, as a consequence of economic growth and population aggregation, China's urban ambient air quality has been seriously deteriorated, with air pollution growing into one of the most concerned environmental issues in China. Many scholars in the environmental field have been focusing on the research of $PM_{2.5}$ and O_3 (Lou et al., 2016; Maji et al., 2017; Chen et al., 2020; Jiang and Xia, 2021). In addition, in response to the severe air pollution situation, China introduced the "Air Pollution Prevention and

Control Action Plan" and the "Air Pollution Prevention and Control Law" in September 2013 and August 2015, respectively. By combining the effective measures in the field of air pollution prevention and control over the years, China has made more comprehensive regulations on the problems of pollution in various fields. With the implementation of a series of environmental protection measures, China's ambient air quality has been greatly improved during the 13th Five-Year Plan period (Zeng et al., 2019; Maji et al., 2020; Zhao et al., 2020; Hu et al., 2021), especially in a megalopolis. However, in northern China, especially in northwest China, due to the geographic proximity to several large deserts, the area is prone to be hit by dust storms, which causes heavy pollution (Wu and Kai, 2016; Guo et al., 2019; Yang et al., 2021a; Rupakheti et al., 2021; Zhang et al., 2021). According to the statistics (Yang et al., 2021b), the dust events in China decreased year by year, but the strong dust storm did not decrease during 2015–2020. Therefore, research on dust events cannot be ignored.

At present, the monitoring method of dust events is relatively limited, with ground-based monitoring stations as main approaches, which only represent the dust intensity over the ground, and cannot detect the dust intensity of high altitudes and the height of dust. With the advancement of science and technology, a series of satellites has been successfully launched, and the pieces of remote sensing equipment carried by them have realized the vertical monitoring of aerosols. Therefore, most scholars studied dust events based on the aerosol optical depth (AOD) obtained from the secondary product of satellites (Banks et al., 2013; Feng et al., 2015; Long et al., 2015; Guo et al., 2017; Reiji, 2018). However, the relationship between the temporal and spatial variability of the AOD and the ground-monitoring particulate matter varies with places (Li et al., 2014a; Li et al., 2015; Xu et al., 2021) and seasons (Schafer et al., 2008; Li et al., 2014b; Hu et al., 2016; Ma et al., 2016). Due to various uncertainty sources such as calibration, surface parameterization, and assumptions in aerosol retrieval models, there is great uncertainty in the AOD retrieved by the satellite. Therefore, if the AOD retrieved by the satellite is used to retrieve particle concentrations, the error will be further increased. Additionally, polar orbiting satellites pass through the same area twice a day in a fixed time, which cannot capture the whole process of the weather system or pollution process. On the other hand, satellites cannot detect the atmospheric conditions under the clouds.

The ground-based lidar fills the gap with higher temporal resolution, which is widely applied in fields such as urban scenarios, environment, ecology, and so on (Bai et al., 2021; Floutsi et al., 2021; Taubert et al., 2021). The aerosol lidar is widely used in the study of dust events. Salgueiro et al. (2021) studied the pollution process jointly affected by a forest fire and Saharan desert dust aerosols over southwestern Europe on June 21, 2019, by using a multi-wavelength Raman lidar and Sun photometer and summarized the different characteristics of forest fire and dust aerosol particles. Janicka et al. (2017) have conducted a similar research study by using the aerosol-polarization-Raman PollyXT-UW lidar for a serious pollution caused by forest fires and dust events in Warsaw, Central Poland, on 10 July 2013. In order to better understand the differences between dust aerosols and anthropogenic pollutants in large spatial scales in China, Banks et al. (2017) employed an elastic lidar to investigate the vertical profiles of aerosols along the Yangtze River during the Yangtze River Campaign of winter 2015. Durable Saharan dust event incursions over the city of Sofia, Bulgaria, on 15 and 23 April, and aerosol layers extraordinary in altitude (up to 15 km) were detected by an Nd:YAG-laser-based lidar (Atanaska et al., 2017).

A ground-based lidar can detect the vertical distribution of aerosols, but the monitoring of an individual lidar cannot reflect the characteristics of aerosols in three-dimensional space. In order to promote the continuous improvement of air quality in the Beijing–Tianjin–Hebei area and surrounding areas, the China National Environmental Monitoring Centre (CNEMC) established a comprehensive three-dimensional observation network of air pollution in 2017, including 37 lidars (Wang et al., 2019), which are mainly deployed in Beijing, Tianjin, Hebei, Henan, Shandong, Shanxi, and other regions. In order to obtain the characteristics of dust in three-dimensional space, reveal the source, transmission, and development trend of dust, and improve the method of dust monitoring, the Department of Ecology and Environment of Gansu Province successively built multiple lidars in Gansu Province from 2019 to 2020, filling the gap of the lidar network in northwest China.

In this study, the dust event that occurred from 11 to 14 May 2019 (all times mentioned in this study refer to Beijing time) was comprehensively analyzed based on the lidar network in northwest China, combined with the data from China's national urban air quality monitoring stations, National Centers for Environmental Prediction (NCEP) reanalysis data, and HYSPLIT backward trajectory. The dust sources and the synoptic system were thoroughly studied, as well as the changes of particle sizes and concentrations in the process of dust transmission, especially in the vertical direction. By fitting the extinction coefficient and the particle concentration, the monitoring of particle concentration was extended from the ground to a high altitude, which realized the research of lidar data from qualitative to quantitative. This study will help us to further understand the process of dust storms, provide a basis for the improvement of numerical prediction, contribute to the prediction and early warning of dust events, and reduce the harm caused by dust.

The data and methodology are introduced briefly in **Section 2**. The distribution of three-dimensional space and transmission and development of the dust event are shown in **Section 3**. **Section 4** gives the conclusion and possible further improvements to this study.

2 MATERIALS AND METHODS

2.1 Lidar Network

The stations of the three lidars for capturing the dust storm are located in Wuwei (102.65°E, 37.91°N), Baiyin (104.13°E, 36.54°N), and Dingxi (104.61°E, 35.60°N). The three lidars are of the same type, named as AGHJ-I-LIDAR, whose laser is Nd:YAG and emits wavelengths of 355 and 532 nm. The aerosols in the

atmosphere produce Mie scattering after encountering with the emitted laser, and the scattering signals with the direction of 180° (backscattering) are received and are then divided into three channels, which are 355 nm parallel, 532 nm parallel, and 532 nm vertical, respectively. The maximum pulse energy of 355 and 532 nm wavelengths reach 25 and 30 mJ, respectively. The spatial resolution of the lidar is 7.5 m, the temporal resolution is 5 min, the maximum detection distance is 10 km, and the blind zone and incomplete-overlap zone are 30 and 120 m, respectively. The characteristics of atmospheric aerosol were studied by converting the received signal into the extinction coefficient and depolarization ratio (Lee and Noh, 2015; Nishizawa et al., 2017; Niu et al., 2019; Panahifar et al., 2020). The specific algorithm was presented elsewhere (Yang et al., 2021a).

2.2 HYSPLIT Backward Trajectory

HYSPLIT (Draxler and Hess, 1998) was originally jointly developed by the Air Resources Laboratory (ARL) of the National Oceanic and Atmospheric Administration (NOAA) and the Bureau of Meteorology, Australia. HYSPLIT calculates and analyzes the transport and diffusion trajectory and settlement of air pollutants based on meteorological data and the Lagrange method. The data of the Global Data Assimilation System (GDAS) from the NCEP are used as the initial field of HYSPLIT, and the horizontal resolution is 1 × 1.

2.3 Data of Air Quality From National Stations

The observational data of $PM_{2.5}$ and PM_{10} hourly concentrations were released on the National Urban Air Quality Real-Time Release Platform of CNEMC. The data are monitored by the automatic monitoring instruments installed in the national urban air quality monitoring stations with the temporal resolution of 1h, which work continuously throughout the year, and there are 1,436 stations in China. The collection duration of $PM_{2.5}$ and PM_{10} concentrations is required to stay at least 20 h per day and at least 45 min per hour, according to the ambient air quality standard (GB 3095–2012); otherwise, the data shall be deemed invalid.

2.4 NCEP Reanalysis Data

The data used to analyze the synoptic system guiding dust storms were derived from NCEP reanalysis data, which assimilate real-time observation data such as station data, satellite observation, ships, and planes. The horizontal resolution is 2.5 × 2.5, and the time resolution is 6 h. The pressure level is divided into 17 layers (1,000, 925, 850, 700, 600, 500, 400, 300, 250, 200, 150, 100, 70, 50, 30, 20, and 10 hPa). The temperature and wind field in ground data were derived from the 0.995 sigma level.

3 RESULTS AND DISCUSSION

The dust storm that occurred from 11 to 14 May 2019 seriously affected most cities in northern China. Many studies show that the Himawari geostationary satellite has advantages in dust detection (Bessho, et al., 2016; She et al., 2018; Xia et al., 2019; Zhang et al., 2019). As shown in **Figure 1**, the Himawari-8 detection results at 09:00 a.m. on May 11 with less cloud influence were selected. It can be seen that the dust over the Taklimakan Desert was very serious, and it was transmitted eastward to the west of Hexi Corridor and Inner Mongolia.

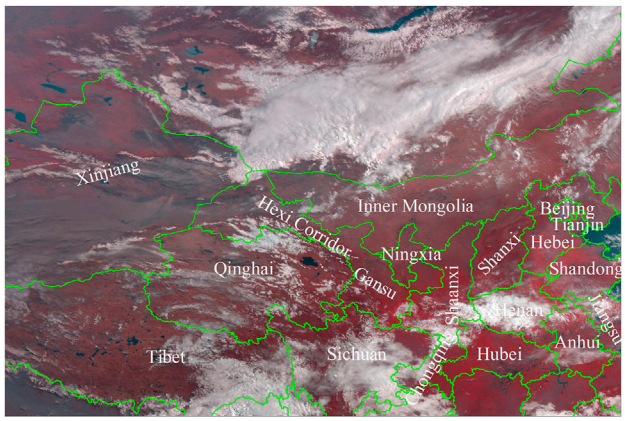

FIGURE 1 | Spatial distribution of clouds and dust storms derived from the Himawari-8 geostationary satellite at 09:00 BT on 11 May.

3.1 Distribution of Three-Dimensional Space of the Dust Storm

The dust event caused a sharp increase in the concentration of particulate matter in the atmosphere. In order to explore the impact of the dust event on the ambient air quality, the mass concentration of PM_{10} and $PM_{2.5}$ monitored on the ground was used to study the impact in the horizontal direction, and the ground-based lidar network was used to study the impact in the vertical direction.

3.1.1 Horizontal Distribution of the Dust Storm

In order to show the impact scope, intensity, and trend of the dust event, **Figure 2** shows the distribution of the hourly concentration of PM_{10} monitored on the ground from 06:00 a.m. on May 11 to 06:00 a.m. on May 13; it can be seen that the process of dust transmission takes place from west to east. Meanwhile, the hourly concentration of PM_{10} and $PM_{2.5}$ of nine cities from 00:00 a.m. on May 11 to 00:00 a.m. on May 14 was selected to have a thorough understanding of the impact of the dust process on the urban ambient air quality (**Figure 3A**). The cities arranged from top to bottom in **Figure 3A** were from west to east in the geographical location (**Figure 3B**); it also showed the process of dust transmission from west to east, and the trend of $PM_{2.5}$ and PM_{10} hourly concentrations was consistent during the dust process.

As can be seen from **Figure 2**, there was little impact of dust at 06:00 a.m. on May 11; however, the concentration of PM_{10} in Hami increased to 574 $\mu g \cdot m^{-3}$ at 08:00 a.m. (**Figure 3A**), and the air quality deteriorated to serious pollution. The north of Xinjiang and the west of the Hexi Corridor were obviously affected at 12:00

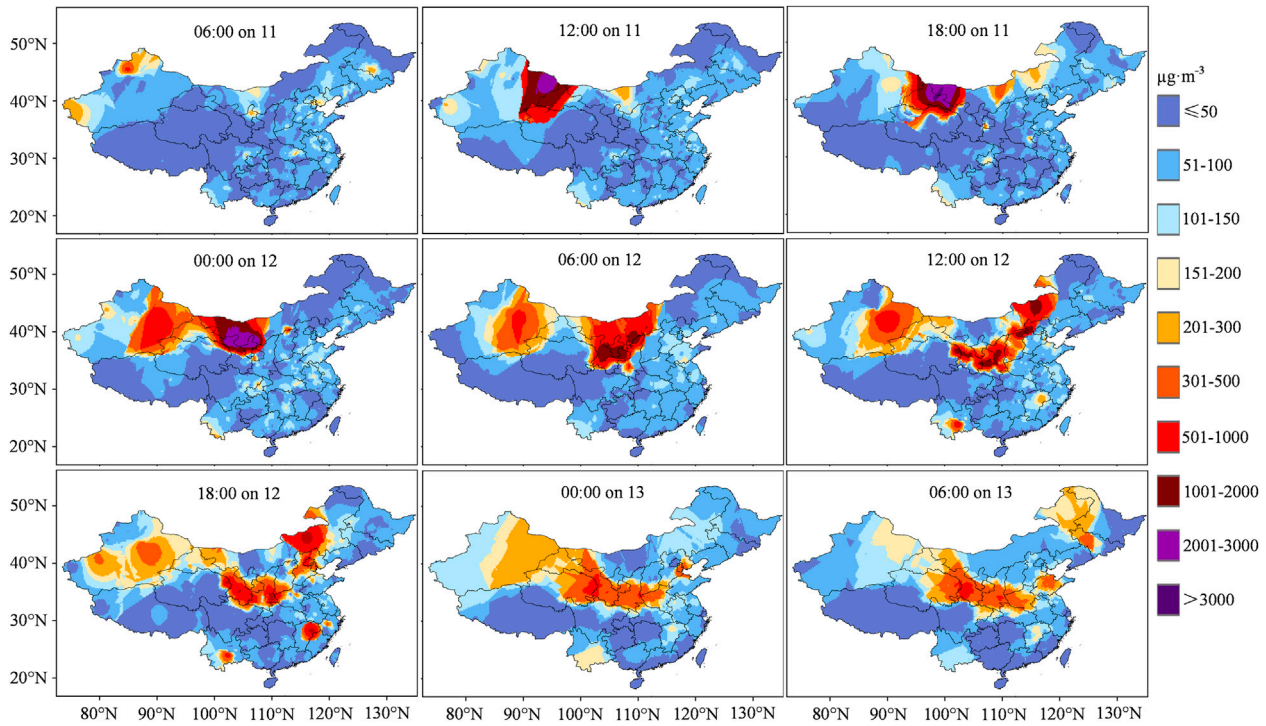

FIGURE 2 | Distribution of the hourly concentration of PM_{10} monitored on the ground from 06:00 on 11 May to 06:00 on 13 May.

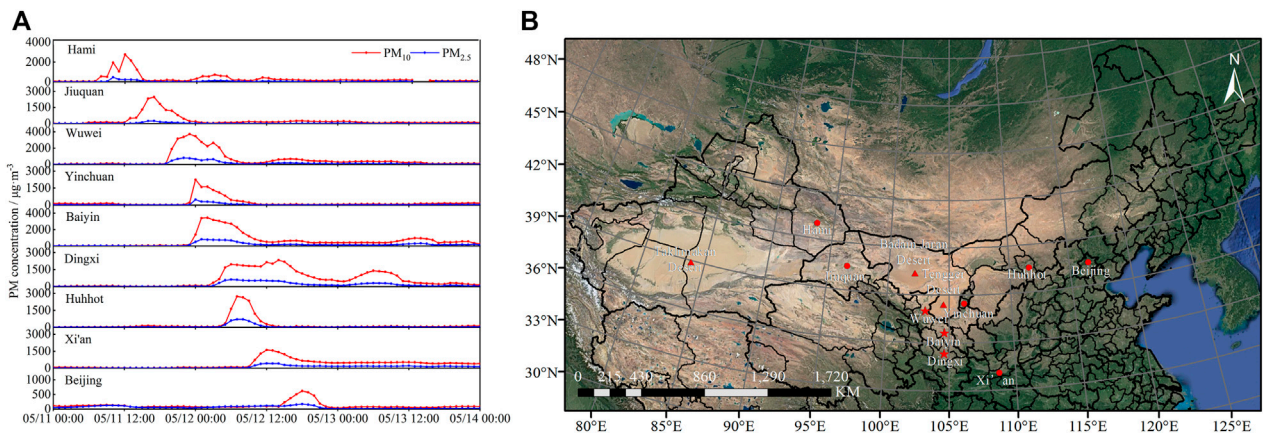

FIGURE 3 | Hourly concentration of PM_{10} and $PM_{2.5}$ of nine cities from 00:00 on 11 May to 00:00 on 14 May **(A)**; locations of the studied cities and their surrounding geomorphic characteristics, ● represents cities, ▲ represents deserts, and ★ represent lidar stations **(B)**.

p.m.; the concentration of PM_{10} in Hami reached the peak of 2,759 μg·m^{-3}, and the concentration of $PM_{2.5}$ increased to 230 μg·m^{-3}. Subsequently, the dust transmitted from west to east, and the dust intensity in Hami decreased significantly. The west of the Hexi Corridor began to be affected by dust (**Figure 2**). As a result, the concentration of PM_{10} in Jiuquan gradually increased, and the ambient air quality deteriorated into serious pollution at 13:00 (**Figure 3A**), and the PM_{10} concentration reached the peak of 2,464 μg·m^{-3} until 17:00; the $PM_{2.5}$ concentration reached the peak concentration of 244 μg·m^{-3} at the same time. Then, the dust continued to move eastward; the PM_{10} concentration in Jiuquan gradually decreased, and it was 1808 μg·m^{-3} at 18:00 and 94 μg·m^{-3} at 01:00 on May 12. The dust moved very slowly (60 km·h^{-1}) in the Hexi Corridor and did not affect Wuwei until 20:00 on May 11 (**Figure 3A**). The PM_{10} concentration in Wuwei suddenly increased from 76 μg·m^{-3} in the previous hour to 1,498 μg·m^{-3} and reached a peak of 2,703 μg·m^{-3} at 23:00; at the same time, the

$PM_{2.5}$ concentration reached 614 μg·m^{-3}. The peak concentration of PM_{10} in Wuwei was significantly higher than that in the upwind area, which might be due to the superposition of the dust in the Badain Jaran Desert. As can be seen from **Figure 2**, the air quality in the west of the Hexi Corridor improved significantly at 00:00 on 12 May, and the eastward movement of the dust affected the central and western part of Inner Mongolia, the central and eastern part of the Hexi Corridor, and the central part of Gansu and Ningxia. Yinchuan and Baiyin were hit by dust almost at the same time (**Figure 3A**); the PM_{10} concentration increased to 2,250 μg·m^{-3} and 1,407 μg·m^{-3} at 00:00 on 12 May, respectively, and the $PM_{2.5}$ concentration increased to 483 μg·m^{-3} and 514 μg·m^{-3}, respectively. Then, the PM_{10} concentration in Yinchuan gradually decreased, and the air quality improved at 12:00. Nevertheless, the dust intensity in Baiyin continued to increase after 00:00 on 12 May, and the peak concentration of PM_{10} and $PM_{2.5}$ reached 2,727 μg·m^{-3} and 614 μg·m^{-3} at 02:00, which was second to Wuwei. The influence of dust in Baiyin lasted for a long time, and the concentration of PM_{10} did not drop to 264 μg·m^{-3} until 00:00 on 14 May, which might be due to the superposition of the dust in the Tengger Desert. In addition, the dust was transmitted from Wuwei to Baiyin at an average speed of 50 km·h^{-1}. Compared with other cities, the PM_{10} concentration in Dingxi increased slowly (**Figure 3A**), with the level of 347 μg·m^{-3} at 03:00 on 12 May, and the peak concentration of PM_{10} and $PM_{2.5}$ reached 2045 μg·m^{-3} and 478 μg·m^{-3} at 06:00 on 12 May; the dust intensity was weaker than that in upwind cities, but the PM_{10} concentration decreased slowly. As a result, the heavy pollution in Dingxi lasted for a long time. It is preliminarily considered that the dust was mainly floating dust when it was transmitted to Dingxi, combined with the local topographic conditions that were not conducive to the diffusion of pollutants. Huhhot was affected by dust for a short time (**Figure 3A**), with the peak concentration of PM_{10} and $PM_{2.5}$ reaching 2,732 μg·m^{-3} and 714 μg·m^{-3} at 07:00 on 12 May, and the air quality improved after 13:00. Xi'an was slightly affected by dust (**Figure 3A**), but it lasted for a long time; the PM_{10} concentration decreased to 144 μg·m^{-3} until 13:00 on the 15th. The duration of dust influence lasted for the shortest time in Beijing, with the concentration of PM_{10} increasing to 226 μg·m^{-3} at 15:00 on 12 May, and decreased to 83 μg·m^{-3} at 22:00. When the dust was transported to Beijing (**Figure 3A**), the intensity of dust weakened significantly, and the peak concentration of PM_{10} was only 618 μg·m^{-3}.

It can be seen from **Figure 2** that most cities in northern China were affected by dust on 12 May, with the central and eastern part of Gansu, Ningxia, Shaanxi, and most parts of Inner Mongolia being hit the hardest. The front air mass of the dust reached the Beijing–Tianjin–Hebei area. The intensity of dust increased significantly, especially in Lanzhou, which is located in the center of Gansu, with a daily average concentration of PM_{10} reaching 1,275 μg·m^{-3}, which was 8.5 times the secondary standard of PM_{10} specified in GB3095-2012. The floating dust was transported to the Yangtze–Huaihe region, and the scope of dust impact was further expanded on 13 May. Gansu, Ningxia, and Shaanxi remained as the central areas of strong dust, and the daily average concentration of PM_{10} was about 500 μg·m^{-3}. Sichuan, Hubei, Henan, Shandong, Anhui, and Jiangsu were newly affected areas by floating dust, and the daily average concentration of PM_{10} was 200–300 μg·m^{-3}. The dust concentration in the Beijing–Tianjin–Hebei area decreased significantly. On 14 May, with the gradual diffusion and settlement of dust during the transportation process, the impact scope was not significantly expanded compared with the previous day. The influence of dust in upwind cities gradually ended, and the dust intensity was significantly weakened. The daily average concentration of PM_{10} in the affected cities remained at about 250 μg·m^{-3}. Subsequently, the strong cold air moved to the south and east and removed pollution obviously. The impact of the dust event gradually ended, and the ambient air quality improved after the 14th.

In summary, the strong dust event lasted for a long time and affected a wide area. The northern part of Xinjiang was first affected on 11 May, and then, the dust spread to the Beijing–Tianjin–Hebei area and the Yangtze–Huaihe region, which affected most cities in northern China. The ambient air quality deteriorated into serious pollution, and the air quality in the Hexi Corridor was the most affected. Until 14 May, the affected cities were dominated by floating dust, and the impact of dust gradually weakened. The variation trend of PM_{10} and $PM_{2.5}$ was consistent, but the concentration of PM_{10} was significantly greater than that of $PM_{2.5}$, indicating that the particles were carried mostly by coarse particles, and the proportion of coarse particles in cities near the source was higher. When dust was transmitted to downwind cities, it was mainly in the form of floating dust, and the proportion of fine particles increased slightly. In addition, the transmission speed of dust in the Hexi Corridor was about 50–60 km·h^{-1}. Combined with the moving path of dust and the distance between cities, the dust rising time of downwind cities can be effectively predicted, which plays a guiding role in the qualitative prediction of dust in downwind cities.

3.1.2 Vertical Distribution of the Dust Storm

3.1.2.1 Qualitative Analysis

The data of national air quality stations are mainly derived by ground-based monitoring, which cannot reflect the change characteristics of particles in the vertical direction. As a piece of active remote sensing equipment, the aerosol lidar makes up for the disadvantage that particle monitoring is limited to the ground. The results from the lidar can not only reflect the distribution characteristics of particles in the vertical direction but also reflect the particle size and morphological characteristics of particles. According to the development height of the dust, the detection results of the three aerosol lidars within 3 km from 12:00 on 11 May to 00:00 on 14 May are shown in **Figure 4**. In order to explore the monitoring effect of the three aerosol lidars, the curves of hourly PM_{10} concentrations (the black solid line) monitored from the ground were superimposed on the distribution of the extinction coefficient on the left side of **Figure 4**. It can be seen that the near-ground extinction coefficients were consistent with the variations of PM_{10} concentrations. During periods of strong dust, the extinction coefficients of the three lidars were all greater than 1 km^{-1}. The

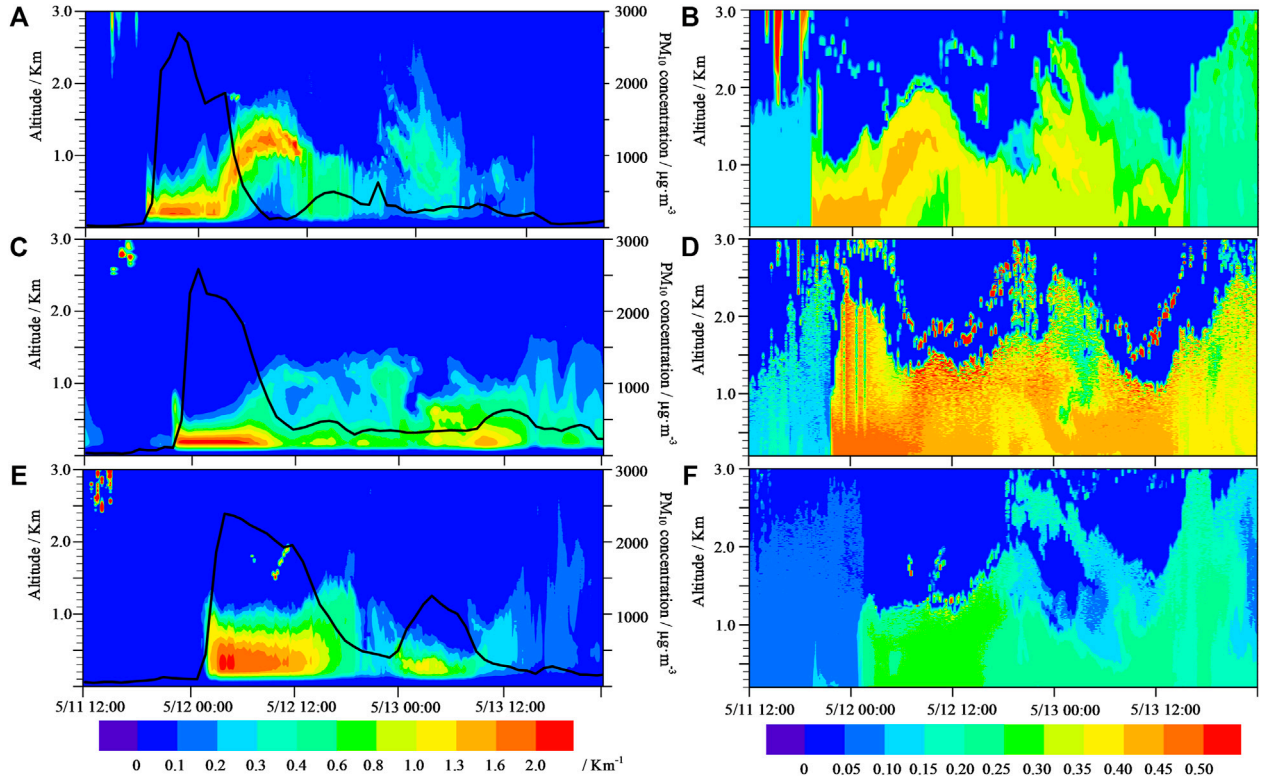

FIGURE 4 | Extinction coefficient (left panel) and depolarization ratio (right panel) of the lidar network from 12:00 on 11 May to 00:00 on 14 May (from top to bottom: Wuwei **(A, B)**, Baiyin **(C, D)**, and Dingxi **(E, F)**; black solid line: hourly PM_{10} concentrations monitored from the ground).

temporal and spatial distribution of the extinction coefficient of Wuwei (**Figure 4A**) shows that the dust in Wuwei was mainly concentrated within the height of 0.8 km from 19:00 on 11 May to 04:00 on 12 May, and the strong dust (extinction coefficient greater than 1 km^{-1}) was distributed within the height of 0.4 km; the ground PM_{10} concentration in some periods was over 2000 $\mu g \cdot m^{-3}$. From 07:00 to 12:00 on 12 May, the near-ground extinction coefficients were low, and the corresponding PM_{10} concentrations were low (less than 200 $\mu g \cdot m^{-3}$). However, there was a strong dust zone at an altitude of 1.0–1.5 km during this period; the extinction coefficients in some areas were close to 2 km^{-1}, and the strong dust zone showed a sinking trend. It was expected that the local air quality would deteriorate again during the dust deposition process, and the monitoring results showed that the near-ground extinction coefficients and corresponding PM_{10} concentrations increased again after 12:00. From the extinction coefficients of Baiyin (**Figure 4C**), it can be seen that during the dust period, the vertical height of dust development of Baiyin was mainly concentrated at the height of about 1.5 km. The strong dust of Baiyin was concentrated within 0.3 km from 22:00 on 11 May to 08:00 on 12 May, and the extinction coefficients in some periods were even greater than 2 km^{-1}, corresponding to the ground-monitoring PM_{10} concentration greater than 2000 $\mu g \cdot m^{-3}$. Then, the extinction coefficients weakened with the weakening of the dust intensity and enhanced again at 10:00–14:00 on 13 May, corresponding to the extinction coefficients greater than 1 km^{-1}. However, at this time, the corresponding PM_{10} concentration only reached about 500 $\mu g \cdot m^{-3}$, indicating that the high-altitude dust transmission was significantly increased compared with the previous period of strong dust. From the extinction coefficients of Dingxi (**Figure 4E**), it can be seen that the vertical height of dust development of Dingxi was close to that of Baiyin, but the strong dust developed to the height of 0.6 km, which was higher than that of Wuwei and Baiyin. When it comes to the duration of the dust process among the three cities, it lasted the longest in Dingxi, while Baiyin and Wuwei had undergone similar duration. Therefore, the higher the development height of strong dust was, the longer it took for aerosol particles to settle and the longer the dust events lasted.

The temporal and spatial distribution of depolarization ratios is shown in the right side of **Figure 4**. The depolarization ratios increased significantly during the dust process, and at the same lidar station, the higher the dust intensity was, the greater the extinction coefficients and the greater the depolarization ratios became. With the weakening of the dust intensity, the depolarization ratios decreased, indicating that the proportion of non-spherical particles carried in strong dust was higher than that in floating dust. Wuwei and Baiyin, as the cities near the sources, had significantly higher depolarization ratios than Dingxi over the period of strong dust. Therefore, it can be inferred that the proportion of non-spherical particles in the

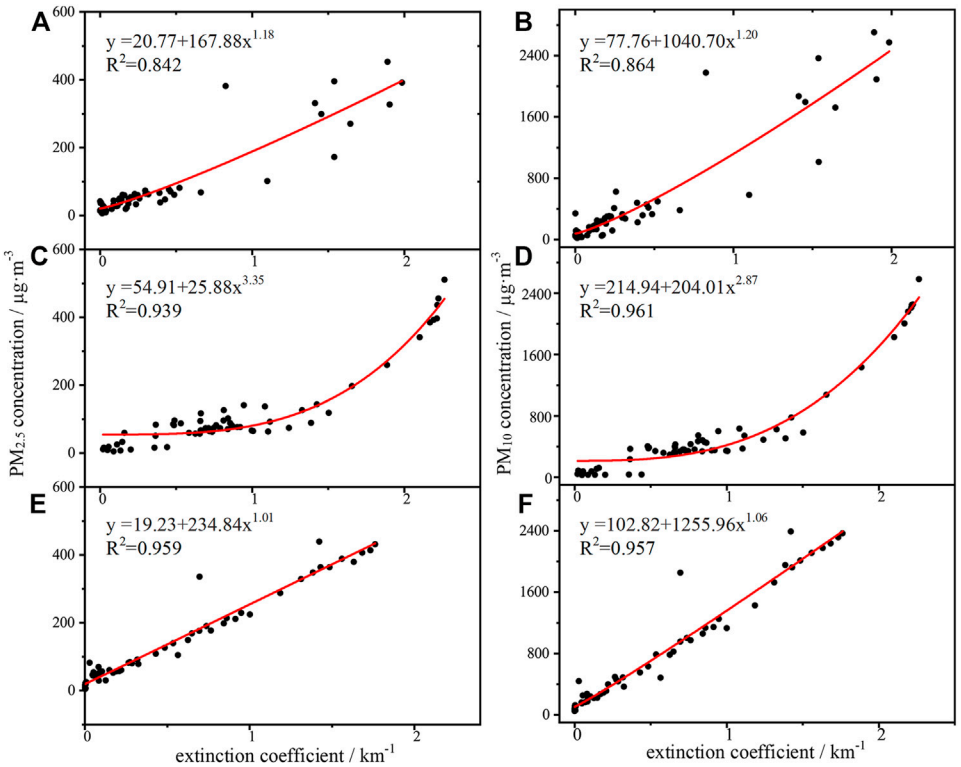

FIGURE 5 | Relationship between the extinction coefficient and $PM_{2.5}$ (left panel), PM_{10} (right panel) concentration monitored on the ground (from top to bottom: Wuwei **(A,B)**, Baiyin **(C,D)**, and Dingxi **(E,F)**.

dust near the source was higher. In the dust process of transmission to the downwind cities, the non-spherical particles were affected by both air resistance and sedimentation and settled faster than the spherical particles. Therefore, when the dust was transported to the downwind cities, the proportion of non-spherical particles decreased. In addition, the dust intensities of Baiyin and Wuwei were similar, but the depolarization ratios of Baiyin (**Figure 4D**) were significantly greater than those of Wuwei (**Figure 4B**). Combined with the backward trajectory of **Figure 8**, it showed that the depolarization ratios in different sources with similar dust intensities were not necessarily close.

The results of the lidar completely showed the development and transmission of dust, which played a positive guiding role in the nowcasting of dust in local and downwind cities. The higher the development height of strong dust was, the longer the duration of dust events lasted. The extinction coefficients with similar dust intensities were close, but the depolarization ratios were not necessarily close. The reason may be due to different sources, or that spherical particles may be easier to transport, and non-spherical particles may be easier to settle in the downwind transmission of dust.

3.1.2.2 Quantitative Analysis

In order to obtain the temporal and spatial changes of particle concentration during dust events, especially the changes in vertical height, the mass concentration of the particulate matter obtained by the aerosol lidar is the direction that many scholars (Xiang et al., 2015; Yang et al., 2021a) have been working on. The extinction coefficients at 200 m height from 12:00 on 11 May to 00:00 on 14 May were selected to fit with the ground-monitoring particle concentration, and the fitting results are presented in **Figure 5**. The relative humidity of each lidar station during the fitting period was less than 80%, so the influence of water vapor on the extinction coefficient was ignored. It was found that the extinction coefficients at 200 m height had a high correlation with the concentrations of PM_{10} and $PM_{2.5}$ monitored on the ground, and when the particle concentrations were greater, the correlation was higher, and the fitting effect was better. The fitting curves of Wuwei and Dingxi were close to linearity. However, due to the influence of meteorological conditions such as humidity (Lagrosas et al., 2017; Lv et al., 2017), when the extinction coefficients of Baiyin increased to a certain extent, the change was not obvious with the increase of particle concentration, and the reason needs to be further explored.

$y = a + bx^c$ (**Figure 5**) was selected as the best fitting formula after the comparison of various fitting formulas. The parameters c of Wuwei and Dingxi were close to 1, indicating a linear fitting, and the parameter c of Baiyin were 3.35 and 2.87 for $PM_{2.5}$ and PM_{10}, respectively. Fortunately, the fitting effect of the extinction coefficients of each lidar with the concentration of $PM_{2.5}$ and PM_{10} was very good. Compared with Baiyin and Dingxi, the fitting results of Wuwei were slightly worse, the correlation

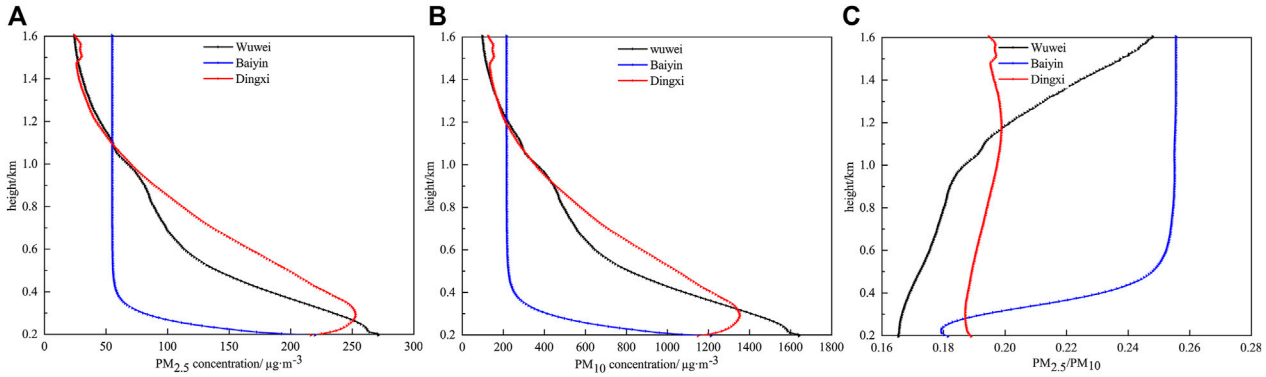

FIGURE 6 | Vertical variation of $PM_{2.5}$ and PM_{10} average concentrations over the strong dust period **(A)** $PM_{2.5}$; **(B)** PM_{10}; and **(C)** $PM_{2.5}/PM_{10}$.

coefficient (R^2) of fitting $PM_{2.5}$ and PM_{10} were 0.842 and 0.864, respectively. The R^2 of the fitted $PM_{2.5}$ of Baiyin and Dingxi were 0.939 and 0.959, and the R^2 of the fitted PM_{10} were 0.961 and 0.957, respectively.

Based on the aforementioned analysis, the greater the particle concentration, the better is the fitting effect. Therefore, the period when the PM_{10} concentrations exceeded 500 $\mu g \cdot m^{-3}$ was selected to estimate the distribution of the average concentration of $PM_{2.5}$ and PM_{10} at different heights (**Figure 6**). The selected periods for Wuwei, Baiyin, and Dingxi were 20:00 on 11 May to 06:00 on 12 May, 00:00–12:00 on 12 May, and 04:00 on 12 May to 10:00 on 13 May, respectively. The distribution of the average concentrations of $PM_{2.5}$ and PM_{10} at different heights can been seen from **Figures 6A, B**.

The concentrations of $PM_{2.5}$ and PM_{10} in Wuwei gradually decreased with the increase in altitude. The average concentration of $PM_{2.5}$ decreased from 520 $\mu g \cdot m^{-3}$ on the ground to 270 $\mu g \cdot m^{-3}$ at 0.2 km height and to 67 $\mu g \cdot m^{-3}$ at 1 km height, and the average concentration of PM_{10} decreased from 2,437 $\mu g \cdot m^{-3}$ on the ground to 1,639 $\mu g \cdot m^{-3}$ at 0.2 km height and to 364 $\mu g \cdot m^{-3}$ at 1 km height. The concentrations of $PM_{2.5}$ and PM_{10} in Baiyin decreased rapidly with the increase in altitude within 0.4 km. The average concentration of $PM_{2.5}$ decreased from 515 $\mu g \cdot m^{-3}$ on the ground to 193 $\mu g \cdot m^{-3}$ at 0.2 km height and to 59 $\mu g \cdot m^{-3}$ at 0.4 km height, and the average concentration of PM_{10} decreased from 2088 $\mu g \cdot m^{-3}$ on the ground to 1,071 $\mu g \cdot m^{-3}$ at 0.2 km height and to 255 $\mu g \cdot m^{-3}$ at 0.4 km height. Combined with **Figure 4C**, the extinction coefficients above 0.4 km height were very small, indicating that the dust intensities were very small and the fitting would lead to a large error, so it would not be analyzed. The average concentration of $PM_{2.5}$ in Dingxi decreased from 325 $\mu g \cdot m^{-3}$ on the ground to 225 $\mu g \cdot m^{-3}$ at 0.2 km height, and the average concentration of PM_{10} decreased from 1,314 $\mu g \cdot m^{-3}$ on the ground to 1,198 $\mu g \cdot m^{-3}$ at 0.2 km height. However, the difference between Wuwei and Baiyin was that within the altitude of 0.2–0.3 km, the average concentrations of $PM_{2.5}$ and PM_{10} in Dingxi gradually increased with the increase in altitude, which increased to 253 $\mu g \cdot m^{-3}$ and 1,351 $\mu g \cdot m^{-3}$, respectively at the altitude of 0.3 km. The concentrations of $PM_{2.5}$ and PM_{10} above 0.3 km gradually decreased again with the increase in altitude, and decreased to 71 $\mu g \cdot m^{-3}$ and 357 $\mu g \cdot m^{-3}$, respectively, at 1 km altitude, which was close to the average concentrations of $PM_{2.5}$ and PM_{10} at 1 km altitude in Wuwei. Also, it can be seen from **Figures 6A, B** that although the ground particle concentration in Dingxi was lower than that in Baiyin and Wuwei, the particle concentration in the height of 0.3–0.9 km was higher than that in Baiyin and Wuwei. **Figure 6C** shows the variation of the value of $PM_{2.5}/PM_{10}$ during the selected period. The value of $PM_{2.5}/PM_{10}$ of Wuwei and Baiyin increased with the increase in altitude, while the value of $PM_{2.5}/PM_{10}$ of Dingxi did not change significantly with altitude, indicating that in cities near sources, low altitude was dominated by coarse particles, and the proportion of fine particles was small and increased with the increase in height. The value of $PM_{2.5}/PM_{10}$ gradually tended to be stable in the vertical direction during transmission to the downwind. On the other hand, the value of $PM_{2.5}/PM_{10}$ of Dingxi within 0.3 km was higher than that in Baiyin and Wuwei, which further proved that coarse particles were easier to settle when the dust was transported to the downwind.

By retrieving the distribution of $PM_{2.5}$ and PM_{10} average concentrations at different heights during strong dust events, it is found that when a dust event occurred, the particle concentrations did not necessarily decrease with the increase in altitude. The ground particle concentrations in Dingxi were lower than those in Baiyin and Wuwei, but the high-altitude particle concentrations above 0.3 km were higher than those in Baiyin and Wuwei. The slow settlement of high-altitude particulate matter had a longer impact on the local ambient air quality. The average concentrations of $PM_{2.5}$ and PM_{10} in Baiyin and Wuwei gradually decreased with the increase in altitude, indicating that the dust mainly came from the surrounding sources. The maximum average concentrations of $PM_{2.5}$ and PM_{10} in Dingxi were located near the height of 0.3 km, indicating that high-altitude transmission was the main source. For Wuwei and Baiyin, the low altitude was dominated by coarse particles, and the proportion of fine particles was low. When the dust was transported to Dingxi, the value of $PM_{2.5}/PM_{10}$ in the vertical direction gradually tended to be stable and greater than that of Wuwei and Baiyin, which further proved

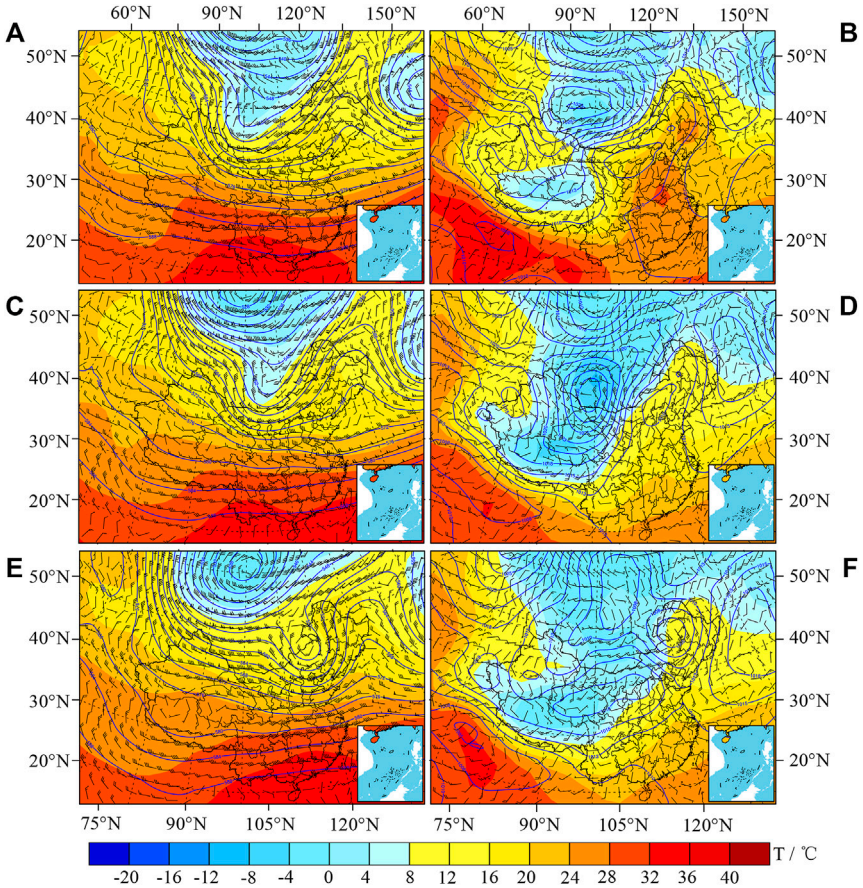

FIGURE 7 | Synoptic situation during the dust storm: **(A)** 500 hPa at 08:00 on 11 May; **(B)** surface at 08:00 on 11 May; **(C)** 500 hPa at 20:00 on 11 May; **(D)** surface at 20:00 on 11 May; **(E)** 500 hPa at 20:00 on 12 May; and **(F)** surface at 20:00 on 12 May.

that coarse particles were easier to settle during the transmission.

3.2 Synoptic System Causing the Dust Storm

An in-depth understanding of the synoptic system guiding the dust event will help to improve the accuracy of dust event forecasting and effectively reduce disasters and losses caused by the dust event. In order to explore reasons for the occurrence and development of the dust event, the synoptic system that led to the dust event was deeply analyzed (**Figure 7**). The East Asian trough moved eastward, which became even stronger under the influence of cold air in high latitudes, resulting in the dust event.

The synoptic situation of 500 hPa at 08:00 on 11 May is shown in **Figure 7A**; the trough moved to the eastern part of northern Xinjiang, the southern branch of the trough extended to 40°N, and the wind speed near the trough reached 38 $m{\cdot}s^{-1}$. There was a cold center near Sajan; the cold trough slightly lagged behind the height trough, and the cold advection after the height trough was strong, indicating that the East Asian trough was still in the strengthening stage. The east of the Hexi Corridor was dominated by a weak northwest airflow; the low-altitude water vapor was very weak, and the temperature continued to rise, which provided certain thermal conditions for the front of the cold air. Led by the East Asia trough, the strong cold air on the ground moved southeast along the northwest. The strong wind behind the front caused strong dust from the east of northern Xinjiang to the west of the Hexi Corridor. Following the East Asian trough, the cold air moved eastward, and the high-pressure center had crossed the Sajan, with strong strength, and the central strength reached more than 1,035 hPa (**Figure 7B**). The cold front was located at the border between China and Mongolia in an east–west direction, and there was an obvious thermal low pressure in the front side of the front. Due to the development of thermal low pressure, the cold front was further strengthened, the isobars behind the front were dense, and there was a wide range of gale areas. The tail of the cold front had crossed the Tianshan Mountains and affected the eastern part of northern Xinjiang. The Hexi Corridor was under the control of thermal low pressure in the front side of the front. As the East Asian trough moved eastward, it gradually turned to the north–south direction; the cold front gradually turned to the northeast–southwest direction and entered the Hexi Corridor through the northwestern path. The strong wind

behind the front caused the dust event in the Hexi Corridor from west to east.

Due to the supplement of cold air in high latitudes, the East Asian trough deepened and strengthened on 11 May, and the movement speed of the East Asian trough was relatively slow. It took 12 h until 20:00 on 11 May (**Figure 7C**) to move from the eastern part of northern Xinjiang to the west of the Hexi Corridor. The enhancement of convergence and ascending movement in the front of the East Asian trough promoted further enhancement of the ground thermal low pressure. Affected by the northwest gale after the cold front, the Hexi Corridor had experienced strong dust weather and was most obviously affected by dust. At the same time, it can be seen that there was a new trough generation and development in the north of Sajan, which blocked the cold air supplement of the East Asian trough. At this time, the cold center behind the trough had been significantly weakened, and the trough would enter a period of rapid movement toward the east. The development of the thermal low pressure in the front side of the front in central Inner Mongolia and Ningxia had created favorable conditions for the further enhancement of the cold front (**Figure 7D**), resulting in a wide range of strong wind areas in the central and western Inner Mongolia; this caused a strong dust event in the Badain Jaran Desert and Tengger Desert and further enhanced the dust in the middle and east of the Hexi corridor. Therefore, the dust became the strongest when it moved to the east of the Hexi Corridor.

It can be seen from 500 hPa at 20:00 on 12 May (**Figure 7E**) that the trough had moved to the eastern part of northern China, and the intensity was obviously weakened, and the ground cold air quickly moved eastward and weakened, resulting in floating dust in the middle and eastern parts of China, but the dust stayed for a long time. Since then, the cold air moved rapidly eastward following the East Asian trough. At the same time, due to the weakening of the East Asian trough and lack of subsequent supplement of cold air, the strength of the ground cold high pressure weakened rapidly during the eastward movement. The cold high-pressure center moved to the north of Shaanxi, and the center strength was only 1,020 hPa at 20:00 on 12 May (**Figure 7F**). Moreover, during the eastward movement of cold high pressure, in the northern section, it can follow the movement of the trough, with fast moving speed and strong intensity. However, in the south section, there is no obvious system for it to follow, leading to rapidly weakening intensity and slower movement speed. At the same time, the front end of the cold front reached the west of Shandong; therefore, the dust moved eastward to the Yangtze–Huaihe region, but the dust intensity was obviously weakened.

3.3 HYSPLIT Backward Trajectory

In order to further explore the source of the dust event, the HYSPLIT backward trajectory was used to analyze the dust transmission path at different heights of the three aerosol lidar stations. The strong dust was mainly concentrated below 1,500 m, according to the lidar detection results. Therefore, the 24-h backward trajectories of the dust transmission at three altitudes of 200 m, 500, and 1,000 m at the time of PM_{10} peak concentration in Wuwei, Baiyin, and Dingxi were selected.

Figure 8A shows the backward trajectories of Wuwei at 23:00 on 11 May. The source at 1,000 m in Wuwei was different from those at 500 and 200 m. At 02:00 on 11 May, the 1,000 m high-altitude dust was located in the Kumtag Desert and then gradually spread from the ground to a high altitude. The dust spread to a height of 1,000 m when it reached Wuwei, where the 1,000 m high-altitude dust in Wuwei originated. The dust of 500 and 200 m in Wuwei came from the 500–1,000 m altitude in the northwest of Inner Mongolia and gradually settled. Multiple sources were superimposed when the dust passed through the Badain Jaran Desert. Combined with the backward trajectory analysis of different heights, the dust of Wuwei mainly came from Kumtag Desert, deserts near northwest Inner Mongolia, and the Badain Jaran Desert, and the dust at high and low altitudes was affected along different paths.

According to the HYSPLIT backward trajectory analysis of Baiyin at 02:00 on 12 May, the sources within the height of 200–1,000 m were relatively consistent (**Figure 8B**). The dust was located near Hami at 02:00 on 11 May and then gradually diffused from the ground to the high altitude. After 14:00, the dust at 200–500 m gradually settled to the ground through the Hexi Corridor, but the dust at 1,000 m spread to the high altitude, and the dust moved to the vicinity of the Badain Jaran Desert at 20:00. Subsequently, dust at different heights was transmitted to Baiyin along the northwest path at a relatively stable altitude.

The HYSPLIT backward trajectories of Dingxi at 14:00 on 12 May are shown in **Figure 8C**. The paths of the dust were very consistent, which came from the border between China and Mongolia and were transported along the northwestern path. At about 20:00 on 11 May, the dust passed through the Badain Jaran Desert and settled here. Then, the dust at the height of 1,000 m was superimposed with the dust of the Badain Jaran Desert and diffused to the high altitude. The dust at the height of 200–500 m was transported close to the ground and diffused to the high altitude when passing through the Tengger desert at 08:00 on 12 May. Combined with the backward trajectory analysis of different heights, the dust in Dingxi mainly came from the sandy land on the border of China and Mongolia, Badain Jaran Desert, and Tengger Desert. The dust in high and low altitudes came from different sources and affects Dingxi along the same path.

HYSPLIT backward trajectory analysis shows that the high- and low-altitude dust in Wuwei had different sources and paths, which was mainly from the Kumtag Desert, near northwest Inner Mongolia, and the Badain Jaran Desert. The high-altitude dust was transmitted along the northwest by the western path, and the low-altitude dust was transmitted along the northwestern path. The sources of Baiyin were relatively consistent, which came from the desert and Gobi near Hami, superimposed with the dust of the Badain Jaran Desert, and were transmitted along the northwestern path. The high- and low-altitude dust paths in Dingxi were very consistent, but the sources were slightly different. The near surface dust mainly came from the Tengger Desert, and the high-altitude dust came from the border of China and Mongolia and the Badain Jaran Desert. Combined with the detection data from lidars, the results indicate

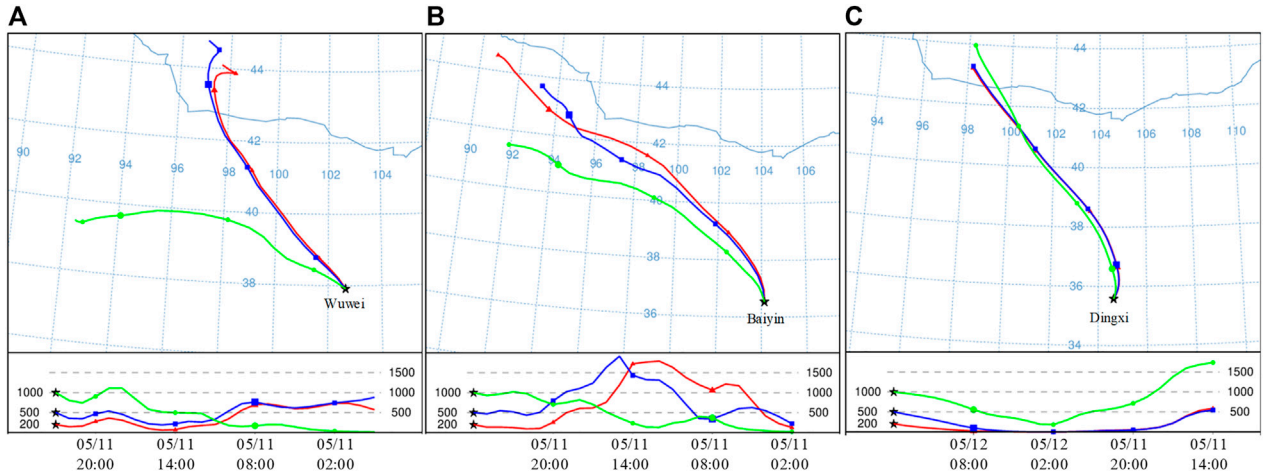

FIGURE 8 | 24-h HYSPLIT backward trajectories: **(A)** Wuwei at 23:00 on 11 May; **(B)** Baiyin at 02:00 on 12 May; and **(C)** Dingxi at 14:00 on 12 May.

that in addition to the impact of dust intensity, different sources of dust also had an impact on the lidar results, especially on the depolarization ratio.

4 CONCLUSION AND DISCUSSION

At present, dust monitoring is relatively simple, mainly relying on ground particle monitors and satellites. However, the ground particle monitors can only obtain the ground dust intensity, and the satellites are seriously affected by clouds. Therefore, there is a lack of monitoring in the vertical direction of dust, which cannot reflect the development and transmission characteristics of dust in three-dimensional space. In order to solve this problem and realize the qualitative to quantitative research of the aerosol lidar in dust detection, a dust event in China from 11 to 14 May 2019 was studied as a case. The study analyzed the horizontal and vertical characteristics of dust and the physical characteristics of dust particles in a comprehensive way; the synoptic system and the sources of dust and the following conclusions were obtained.

The East Asian trough moved eastward to lead the eastward diffusion and transmission of the dust event from the eastern part of northern Xinjiang and the western Hexi Corridor on 11 May, resulting in the deterioration of the ambient air quality in most cities in northern China, causing serious pollution, of which the Hexi Corridor was the most seriously affected. The PM_{10} hourly peak concentration of Wuwei and Baiyin was close to 3,000 $\mu g \cdot m^{-3}$, and the dust impact was significantly weakened on 14 May. The qualitative analysis of lidar network monitoring results combined with HYSPLIT backward trajectories show that when the dust intensities were the same in different cities, the extinction coefficients were close, but the depolarization ratios were not necessarily close. As cities close to the sources, the sources of Wuwei and Baiyin were not only high-altitude transmission but also superimposed with the dust of the surrounding deserts. As a city far away from the source, the source of Dingxi was mainly high-altitude transmission. In addition, for Wuwei and Baiyin, the proportion of coarse particles and non-spherical particles carried in dust was higher than that in Dingxi. It is preliminarily considered that the sedimentation velocity and resistance coefficient of non-spherical particles were greater than spherical particles; therefore, coarse particles and non-spherical particles were easier to settle. The fitting effect between the extinction coefficient and the $PM_{2.5}$ and PM_{10} concentrations monitored on the ground was very good. Through the fitting, it is found that the particle concentration in Dingxi did not necessarily decrease with the increase of height during the dust period. The ground particle concentrations in Dingxi were lower than those in Baiyin and Wuwei, but the high-altitude particle concentrations above 0.3 km were higher than those in Baiyin and Wuwei.

Using the aerosol lidar network can not only reflect the development characteristics of dust in the vertical direction but can also effectively show the change characteristics of aerosol particle sizes and morphology and realize the quantitative analysis of particle concentration in three-dimensional space, which is of significant importance for informing the forecasting of the dust event.

DATA AVAILABILITY STATEMENT

The datasets presented in this study can be found in online repositories. The names of the repository/repositories and accession number(s) can be found below: The data of P.M. and PM10 concentration for this study can be found in the National Urban Air Quality Real-Time Release Platform of the China National Environmental Monitoring Center (http://106.37.208.233:20035/). The NCEP/NCAR reanalysis data were provided by NOAA (https://psl.noaa.gov/data/gridded/data.ncep.reanalysis.html). The lidar data in the article can be directly contacted with the first author.

AUTHOR CONTRIBUTIONS

SZ conceived and designed the experiments; LY analyzed the data and wrote the manuscript; YY contributed and analyzed **Figure 4**; LW and HT reviewed and edited the manuscript; YX and YC helped with discussion; and XL processed lidar preliminary data. All authors contributed critically to the drafts and gave final approval for publication.

FUNDING

This work was jointly supported by the Foundation for National Natural Science Foundation of China (No. 42075126; No. 41975019), Natural Science Foundation of Gansu Province of China (No. 21JR7RA691; No. 20JR5RA122; No. 20JR10RA444). This work was supported by Supercomputing Center of Lanzhou University.

ACKNOWLEDGMENTS

The authors are grateful to CNEMC for providing the data on PM2.5 and PM10 concentrations and greatly appreciate NOAA for sharing the NCEP/NCAR reanalysis data. We acknowledge the reviewers and the editor for their valuable comments and suggestions.

REFERENCES

Bai, L., Li, Y., Cen, M., and Hu, F. (2021). 3D Instance Segmentation and Object Detection Framework Based on the Fusion of Lidar Remote Sensing and Optical Image Sensing. *Remote Sensing* 13 (16), 3288. doi:10.3390/rs13163288

Banks, J. R., Brindley, H. E., Flamant, C., Garay, M. J., Hsu, N. C., Kalashnikova, O. V., et al. (2013). Intercomparison of Satellite Dust Retrieval Products over the West African Sahara during the Fennec Campaign in June 2011. *Remote Sensing Environ.* 136, 99–116. doi:10.1016/j.rse.2013.05.003

Banks, J. R., Brindley, H. E., Stenchikov, G., and Schepanski, K. (2017). Satellite Retrievals of Dust Aerosol over the Red Sea and the Persian Gulf (2005-2015). *Atmos. Chem. Phys.* 17, 3987–4003. doi:10.5194/acp-17-3987-2017

Bessho, K., Date, K., Hayashi, M., Ikeda, A., Imai, T., Inoue, H., et al. (2016). An Introduction to Himawari-8/9— Japan's New-Generation Geostationary Meteorological Satellites. *J. Meteorol. Soc. Jpn.* 94, 151–183. doi:10.2151/jmsj.2016-00929

Chen, L., Zhu, J., Liao, H., Yang, Y., and Yue, X. (2020). Meteorological Influences on PM2.5 and O3 Trends and Associated Health burden since China's Clean Air Actions. *Sci. Total Environ.* 744, 140837. doi:10.1016/j.scitotenv.2020.140837

Deleva, A. D., Peshev, Z. Y., Dreischuh, T. N., and Stoyanov, D. V. (2017). "Lidar Observations of Aerosol Loadings Extended throughout the Troposphere," in Proc. SPIE 10226, 19th International Conference and School on Quantum Electronics, 5 January 2017 (Laser Physics and Applications), 102260X. doi:10.1117/12.2264235

Draxler, R. R., and Hess, G. D. (1998). An Overview of the HYSPLIT 4 Modeling System for Trajectories, Dispersion and Deposition. *Aust. Meteorol. Mag.* 47 (4), 295–308.

Feng, Q., Cui, S., and Zhao, W. (2015). Effect of Particle Shape on Dust Shortwave Direct Radiative Forcing Calculations Based on Modis Observations for a Case Study. *Adv. Atmos. Sci.* 32 (9), 1266–1276. doi:10.1007/s00376-015-4235-3

Floutsi, A. A., Baars, H., Radenz, M., Haarig, M., Yin, Z., Seifert, P., et al. (2021). Advection of Biomass Burning Aerosols towards the Southern Hemispheric Mid-latitude Station of Punta Arenas as Observed with Multiwavelength Polarization Raman Lidar. *Remote Sensing* 13 (1), 138–155. doi:10.3390/rs13010138

Guo, J., Xia, F., Zhang, Y., Liu, H., Li, J., Lou, M., et al. (2017). Impact of Diurnal Variability and Meteorological Factors on the PM2.5 - AOD Relationship: Implications for PM2.5 Remote Sensing. *Environ. Pollut.* 221, 94–104. doi:10.1016/j.envpol.2016.11.043

Guo, P., Yu, S., Wang, L., Li, P., Li, Z., Mehmood, K., et al. (2019). High-altitude and Long-Range Transport of Aerosols Causing Regional Severe Haze during Extreme Dust Storms Explains Why Afforestation Does Not Prevent Storms. *Environ. Chem. Lett.* 17, 1333–1340. doi:10.1007/s10311-019-00858-0

Hu, Z., Jin, Q., Ma, Y., Pu, B., Ji, Z., Wang, Y., et al. (2021). Temporal Evolution of Aerosols and Their Extreme Events in Polluted Asian Regions during Terra's 20-year Observations. *Remote Sensing Environ.* 263, 112541. doi:10.1016/j.rse.2021.112541

Hu, Z., Zhao, C., Huang, J., Leung, L. R., Qian, Y., Yu, H., et al. (2016). Trans-Pacific Transport and Evolution of Aerosols: Evaluation of Quasi-Global WRF-Chem Simulation with Multiple Observations. *Geosci. Model. Dev.* 9, 1725–1746. doi:10.5194/gmd-9-1725-2016

Janicka, L., Stachlewska, I. S., Veselovskii, I., and Baars, H. (2017). Temporal Variations in Optical and Microphysical Properties of mineral Dust and Biomass Burning Aerosol Derived from Daytime Raman Lidar Observations over warsaw, poland. *Atmos. Environment* 169, 162–174. doi:10.1016/j.atmosenv.2017.09.022

Jiang, B., and Xia, D. (2021). Ammonia Control Represents the Key for PM2.5 Elimination: Insights for Global Air Pollution Control Interconnected from PM2.5 Events in China. *Clean. Techn. Environ. Pol.* 23 (1), 829–841. doi:10.1007/s10098-020-01923-x

Lagrosas, N., Ong, P. M. B., Shiina, T., and Kuze, H. (2017). Diurnal Behavior of Aerosol Extinction Coefficient Based on Lidar and Ground Sampling Instruments, 35th Japanese Laser Sensing Symposium. At: National Institute of Information and Communications Technology (NICT) 4-2-1, Nukui-Kitamachi, Koganei, Tokyo 184–8795. Japan.

Lee, K.-H., and Noh, Y. M. (2015). Multi-wavelength Raman LIDAR for Use in Determining the Microphysical, Optical, and Radiative Properties of Mixed Aerosols. *ajae* 9, 91–99. doi:10.5572/ajae.2015.9.1.091

Li, J., Carlson, B. E., and Lacis, A. A. (2014a). Application of Spectral Analysis Techniques in the Intercomparison of Aerosol Data: Part III. Using Combined PCA to Compare Spatiotemporal Variability of MODIS, MISR, and OMI Aerosol Optical Depth. *J. Geophys. Res. Atmos.* 119 (7), 4017–4042. doi:10.1002/2013JD020538

Li, J., Carlson, B. E., and Lacis, A. A. (2014b). Application of Spectral Analysis Techniques in the Intercomparison of Aerosol Data. Part II: Using Maximum Covariance Analysis to Effectively Compare Spatiotemporal Variability of Satellite and AERONET Measured Aerosol Optical Depth. *J. Geophys. Res. Atmos.* 119 (1), 153–166. doi:10.1002/2013JD020537

Li, J., Carlson, B. E., and Lacis, A. A. (2015). How Well Do Satellite AOD Observations Represent the Spatial and Temporal Variability of PM 2.5 Concentration for the United States? *Atmos. Environ.* 102, 260–273. doi:10.1016/j.atmosenv.2014.12.010

Long, X., Li, N., Tie, X., Cao, J., Zhao, S., Huang, R., et al. (2016). Urban Dust in the Guanzhong basin of china, Part I: a Regional Distribution of Dust Sources Retrieved Using Satellite Data. *Sci. Total Environ.* 541, 1603–1613. doi:10.1016/j.scitotenv.2015.10.063

Lou, C.-R., Liu, H.-Y., Li, Y.-F., and Li, Y.-L. (2016). Socioeconomic Drivers of PM2.5 in the Accumulation Phase of Air Pollution Episodes in the Yangtze River Delta of China. *Ijerph* 13 (10), 928–947. doi:10.3390/ijerph13100928

Lv, L., Liu, W., Zhang, T., Chen, Z., Dong, Y., Fan, G., et al. (2017). Observations of Particle Extinction, PM2.5 Mass Concentration Profile and Flux in north China Based on mobile Lidar Technique. *Atmos. Environ.* 164, 360–369. doi:10.1016/j.atmosenv.2017.06.022

Ma, X. Y., Wang, J. Y., Yu, F. Q., Jia, H. L., and Hu, Y. N. (2016). Can MODIS AOD Be Employed to Derive PM2.5 in Beijing-Tianjin-Hebei over China? *Atmos. Res.* 181, 250–256. doi:10.1016/j.atmosres.2016.06.018

Maji, K. J., Dikshit, A. K., Arora, M., and Deshpande, A. (2017). Estimating Premature Mortality Attributable to PM2.5 Exposure and Benefit of Air Pollution Control Policies in China for 2020. *Sci. Total Environ.* 612, 683–693. doi:10.1016/j.scitotenv.2017.08.254

Maji, K. J., Li, V., and Lam, J. C. K. (2020). Effects of China's Current Air Pollution Prevention and Control Action Plan on Air Pollution Patterns, Health Risks and Mortalities in Beijing 2014-2018. *Chemosphere* 260. doi:10.1016/j.chemosphere.2020.127572

Nishizawa, T., Sugimoto, N., Matsui, I., Shimizu, A., Hara, Y., Itsushi, U., et al. (2017). Ground-based Network Observation Using Mie-Raman Lidars and Multi-Wavelength Raman Lidars and Algorithm to Retrieve Distributions of Aerosol Components. *J. Quant. Spectrosc. Ra* 188, 79–93. doi:10.1016/j.jqsrt.2016.06.031

Niu, H. W., Kang, S. C., Gao, W. N., Wang, Y. H., and Paudyal, R. (2019). Vertical Distribution of the Asian Tropopause Aerosols Detected by CALIPSO. *Environ. Pollut.* 253, 207–220. doi:10.1016/j.envpol.2019.06.111

Panahifar, H., Moradhaseli, R., and Khalesifard, H. R. (2020). Monitoring Atmospheric Particulate Matters Using Vertically Resolved Measurements of a Polarization Lidar, *In-Situ* Recordings and Satellite Data over Tehran, Iran. *Sci. Rep.* 10, 20052. doi:10.1038/s41598-020-76947-w

Reiji, K. (2018). Satellite-based Mapping of Dust Erodibility in Northeast Asia. *Nat. Hazards* 92, 19–25. doi:10.1007/s11069-016-2393-y

Rupakheti, D., Yin, X. F., Rupakheti, M., Zhang, Q. G., Li, P., Rai, M., et al. (2021). Spatio-temporal Characteristics of Air Pollutants over Xinjiang, Northwestern China. *Environ. Pollut.* 268, 115907. doi:10.1016/j.envpol.2020.115907

Salgueiro, V., Costa, M. J., Guerrero-Rascado, J. L., Couto, F. T., and Bortoli, D. (2021). Characterization of forest Fire and Saharan Desert Dust Aerosols over South-Western Europe Using a Multi-Wavelength Raman Lidar and Sun-Photometer. *Atmos. Environ.* 252, 118346. doi:10.1016/j.atmosenv.2021.118346

Schafer, K., Harbusch, A., Emeis, S., Koepke, P., and Wiegner, M. (2008). Correlation of Aerosol Mass Near the Ground with Aerosol Optical Depth during Two Seasons in Munich. *Atmos. Environ.* 42, 4036–4046. doi:10.1016/j.atmosenv.2008.01.060

She, L., Xue, Y., Yang, X. H., Guang, J., Li, Y., Che, Y. H., et al. (2018). Dust Detection and Intensity Estimation Using Himawari-8/AHI Observation. *Remote Sens.* 10, 490. doi:10.3390/rs10040490

Taubert, F., Fischer, R., Knapp, N., and Huth, A. (2021). Deriving Tree Size Distributions of Tropical Forests from Lidar. *Remote Sens.* 13 (1), 131–154. doi:10.3390/rs13010131

Wang, Y. S., Gong, Z. Y., Liu, Z. R., Tang, G. G., Cheng, L. J., Che, F., et al. (2019). Construction and Application of Comprehensive Observation Network for Air Pollution in Beijing-Tianjin-Hebei and its Surrounding Areas. *Res. Environ. Sci.* 32 (10), 1651–1663. (In Chinese). doi:10.13198/j.issn.1001-6929.2019.09.12

Wu, J., and Kai, K. (2016). Characteristics of Dust Outbreaks and Their Relation to Strong Wind and Land Surface Conditions in the Gobi Desert and Northern China, 1999-2013. *J. Arid Land.* 26, 51–57. doi:10.14976/jals.26.2_51

Xia, X. L., Min, J. Z., Wang, Y. B., Shen, F. F., Yang, C., and Sun, Z. D. (2019). Assimilating Himawari-8 AHI Aerosol Observations with a Rapid-Update Data Assimilation System. *Atmos. Environ.* 215, 116866. doi:10.1016/j.atmosenv.2019.116866

Xiang, Y., Zhang, T. S., Zhao, X. S., Liu, J. G., Dong, Y. S., Fan, G. Q., et al. (2015). "Retrieval of PM2.5 Concentration from Lidar Data," in *Light, Energy and the Environment, OSA Technical Digest (Online), Paper EM3A.6* (Washington, DC, USA: Optical Society of America). doi:10.1364/ee.2015.em3a.6

Xu, Y. L., Huang, Y., and Guo, Z. Y. (2021). Influence of AOD Remotely Sensed Products, Meteorological Parameters, and AOD-PM2.5 Models on the PM2.5 Estimation. *Stoch. Env. Res. Risk A.* 35 (3), 1–16. doi:10.1007/s00477-020-01941-7

Yang, L. L., Hu, Z. Y., Huang, Z. W., Wang, L. N., Han, W. Y., Yang, Y. P., et al. (2021a). Detection of a Dust Storm in 2020 by a Multi-Observation Platform over the Northwest China. *Remote Sens.* 13 (6), 1056–1074. doi:10.3390/rs13061056

Yang, L. L., Zhang, S. W., Huang, Z. W., Yang, Y. P., Wang, L. N., Han, W. Y., et al. (2021b). Characteristics of Dust Weather in China from 2015 to 2020. *Atmos.* 12 (8), 952–964. doi:10.3390/atmos12080952

Zeng, Y. Y., Cao, Y. F., Qiao, X., Seyler, B. C., and Tang, Y. (2019). Air Pollution Reduction in China: Recent success but Great challenge for the Future. *Sci. Total Environ.* 663, 329–337. doi:10.1016/j.scitotenv.2019.01.262

Zhang, J., Zhou, C. H., Gui, H. L., and Zhang, X. Y. (2021). Biological Crust in Sand and Dust Storm Source Areas of Asia and its Impact on Dust Emission. *Adv. Clim. Change Res.* 12 (3), 395–408. doi:10.1016/j.accre.2021.05.007

Zhang, Z. Y., Wu, W. L., Fan, M., Tao, M. H., Wei, J., Jin, J., et al. (2019). Validation of Himawari-8 Aerosol Optical Depth Retrievals over China. *Atmos. Environ.* 199, 32–44. doi:10.1016/j.atmosenv.2018.11.024

Zhao, H., Chen, K. Y., Liu, Z., Zhang, Y. X., Shao, T., and Zhang, H. L. (2020). Coordinated Control of PM2.5 and O3 Is Urgently Needed in China after Implementation of the "Air Pollution Prevention and Control Action Plan". *Chemosphere* 270. doi:10.1016/j.chemosphere.2020.129441

Conflict of Interest: Authors YX and XL were employed by Wuxi CAS Photonics Co., Ltd.

The remaining authors declare that the research was conducted in the absence of any commercial or financial relationships that could be construed as a potential conflict of interest.

Publisher's Note: All claims expressed in this article are solely those of the authors and do not necessarily represent those of their affiliated organizations, or those of the publisher, the editors, and the reviewers. Any product that may be evaluated in this article, or claim that may be made by its manufacturer, is not guaranteed or endorsed by the publisher.

frontiers | Frontiers in Environmental Science

ORIGINAL RESEARCH
published: 13 May 2022
doi: 10.3389/fenvs.2022.820452

Evolution Characteristics of Sand-Dust Weather Processes in China During 1961–2020

Haixia Duan[1], *Wei Hou*[2]*, *Hao Wu*[3], *Taichen Feng*[4] *and Pengcheng Yan*[1]

[1]*Lanzhou Institute of Arid Meteorology, China Meteorological Administration, Lanzhou, China,* [2]*Laboratory for Climate Studies, China Meteorological Administration, Beijing, China,* [3]*Hunan Climate Center, China Meteorological Administration, Changsha, China,* [4]*School of Atmospheric Sciences, Lanzhou University, Lanzhou, China*

The spring sand-dust weather can be disastrous in China. It seriously endangers agricultural production, transportation, air quality, people's lives and property, and is a subject of sustained and extensive concern. Currently, few studies have been conducted to analyze sand-dust events in North China from the perspective of sand-dust processes. Although there are a few studies on the spatio-temporal variation characteristics of sand-dust processes, they are mainly based on outdated data or case studies of major sand-dust events. In this study, the evolution characteristics of sand-dust processes in China over the last 60 years are studied based on the identification method and several characteristic quantities (including duration and impact range) of sand-dust weather processes defined in the *Operational Regulations of Monitoring and Evaluation for Regional Weather and Climate Processes* newly issued by the China Meteorological Administration in 2019. First, through statistics, we obtain the annual occurrence frequency, annual days, and the annual number of affected stations of sand-dust processes (including sand-dust storms, blowing sand, and suspended dust) from January 1961 to May 2021. Based on the Mann–Kendall test (MK) and Ensemble Empirical Mode Decomposition (EEMD), we analyzed evolution trends and probability distribution characteristics of annual occurrence frequency, annual days, and the annual number of affected stations of sand-dust processes. In addition, we investigate the start time of the first and the last dust processes in each of the past 60 years, as well as the seasonal distribution characteristics of sand-dust processes. The results show that under the background of global warming, the sand-dust weather in China tends to decrease significantly. Specifically, the annual occurrence frequency and annual days showed an upward trend before the 1980s and a significant downward trend after that, as well as the significant turnarounds in the annual number of dust processes that occurred in the 1990s and around 2010. Moreover, the sand-dust processes tend to start later and end earlier. The sand-dust processes are mainly concentrated between March and May, with the highest occurrence probability in April.

Keywords: China, sand-dust process, temporal evolution, EEMD, probability distributions

OPEN ACCESS

Edited by:
Rui Mao,
Beijing Normal University, China

Reviewed by:
Yan Yu,
Peking University, China
Jing Li,
Peking University, China
Qinjian Jin,
University of Kansas, United States

***Correspondence:**
Wei Hou
houwei298615@cma.cn

Specialty section:
This article was submitted to Atmosphere and Climate, a section of the journal Frontiers in Environmental Science

Received: *23 November 2021*
Accepted: *21 March 2022*
Published: *13 May 2022*

Citation:
Duan H, Hou W, Wu H, Feng T and Yan P (2022) Evolution Characteristics of Sand-Dust Weather Processes in China During 1961–2020. Front. Environ. Sci. 10:820452. doi: 10.3389/fenvs.2022.820452

INTRODUCTION

Sand-dust weather can be disastrous and seriously damage the ecological environment (Sun et al., 2001), causing excessive loss of soil and nutrients in source areas and aggravating land desertification (Chandler et al., 2004; Kielgaard et al., 2004; Zobeck and Pelt, 2006). In addition, it can bring serious environmental pollution (Giannadaki et al., 2013; Knippertz and Stuut, 2014; Pu et al., 2015; Guo et al., 2018; Tian et al., 2019) to downstream areas, seriously endangering human health (Mott et al., 2005; Goudie, 2014; Tong et al., 2017). Sand-dust weather can also lead to mesoscale to large-scale climate adjustment (Idso and Brazel, 1977; Littmann, 1991). Specifically, dust aerosols contribute large amounts of fine particles (Bishop et al., 2002; Evan et al., 2009; Hsu et al., 2009; Mahowald, 2011; Prospero et al., 2012) to marine and terrestrial ecosystems, thus affecting regional and global climate change (Huang et al., 2014), including changes in the hydrological cycle (Goudie, 2009; Huang et al., 2010a), marine primary productivity (Mahowald et al., 2005; Han et al., 2008), radiation balance, cloud formation (Huang et al., 2014; Li et al., 2016), glacier formation and melting (Calov et al., 2005; Krinner et al., 2006; Bar–Or et al., 2008), and global carbon and energy cycles (Mahowald et al., 2005; Jickells et al., 2006; Ling et al., 2014). Dust aerosols can also affect precipitation through aerosol-cloud-precipitation interactions (Huang et al., 2010b; Carslaw et al., 2013; Jin et al., 2016; Jin and Wang, 2018).

Arid and semi-arid areas are prone to sand-dust weather. These areas include the North American Great Plains, North Africa, the Middle East, the Mongolian Gobi Desert, and Central Asia (Ahmed et al., 1987; Chen et al., 1995; Alpert and Ganor, 2001; Natsagdorj et al., 2003; Worster, 2004; Alizadeh–Choobari et al., 2016; Beyranvand et al., 2019). As a part of the sand-dust storm area in Central Asia, northern China is one of the few areas in the world where sand-dust weather occurs frequently. Asia is the second-largest source of dust in the world due to the large deserts in the Middle East, Central Asia, and East Asia (Jin et al., 2021), and approximately 40% of the dust aerosols in the world come from Asia (Zhang et al., 2003a; Tanaka and Chiba, 2006). The sand-dust weather in northern China is mainly distributed in the Northwest and North of the country. However, the impact of sand-dust weather is not limited to these regions. Eastern China (Zhang et al., 2013; Wang and Chen, 2016; Yang et al., 2017), East Asia (Chung et al., 2005; Huang et al., 2014; Lee et al., 2014; Yumimoto and Takemura, 2015; Kashima et al., 2016), North America and Europe (Husar et al., 2001; Tratt et al., 2001; Uno et al., 2001; Bishop et al., 2002; Chun et al., 2002; Grousset et al., 2003; Grousset et al., 2003; Zhang et al., 2003b; Mukai et al., 2004; Chung et al., 2005; Yuan and Zhang, 2006; Stith et al., 2009; Creamean et al., 2013; Liu et al., 2013), and even the Arctic (Stone et al., 2005) are affected by dust from North China.

Sand-dust weather endangers the human living environment and socio-economy (Chen et al., 2004; Liu et al., 2006; Meng and Lu, 2007; Goudie, 2009; Tam et al., 2012). Dust aerosols have a significant impact on the atmospheric system, air pollution, marine and terrestrial ecosystems, and regional and global climate change (Bryant, 2013; Wang et al., 2015; Mao et al., 2019; Jin et al., 2021). Therefore, human beings increasingly recognize that sand-dust weather is not just a severe meteorological disaster, but also a considerable global ecological and environmental problem (Shao and Dong, 2006; Jin et al., 2017). Currently, numerous studies have been conducted on the spatio-temporal variations of sand-duct events in northern China, which are of great significance to improving understanding of sand-dust storms and effectively controlling their occurrence. However, most of these studies examine the statistical characteristics of sand-dust weather based on a single station (Quan et al., 2001; Kurosaki et al., 2011; Shao et al., 2013; Shao et al., 2013; Kim and Choi, 2015; Kang et al., 2016; Yong et al., 2021), and they rarely analyze sand-duct events in northern China from the perspective of sand-dust processes or focus on the local characteristics of sand-dust weather (Natsagdorj et al., 2003; Liu et al., 2004; Zhang et al., 2005; Wang et al., 2006; Tang et al., 2013; Zhao et al., 2013; Guan et al., 2014; Liu et al., 2014). Moreover, although there are a few previous studies on the spatio-temporal variations of sand-dust processes, they are mainly based on outdated data from the "China Severe Sand-Dust Storm Series and Its Supporting Dataset (1960–2007)" (Sun et al., 2001; Zhou and Wang, 2002; Guan et al., 2017; Wang et al., 2020) or case studies of major sand-dust events (Husar et al., 2001; Chung et al., 2003; Zhang et al., 2005; Shao and Mao, 2016).

To improve the monitoring and forecasting of significant regional weather and climate processes in China and establish a relatively unified index system at national and regional levels, the China Meteorological Administration issued the *Regulations of Monitoring and Evaluation for Regional Weather and Climate Processes* in 2019. Combined with the spatial distribution characteristics of the current ground-based meteorological observation network in China, this file specifies the identification methods of four important regional weather and climate processes (rainstorm, high temperature, drought, and sand-dust), as well as the calculation methods of characteristic quantities such as duration and impact range. In this study, to better understand and analyze the evolution characteristics of sand-dust processes in China in the last 60 years, we first statistically obtained sand-dust processes in China from January 1961 to May 2021 by using the regional sand-dust process identification method. We then analyzed the interdecadal, interannual, and seasonal variation characteristics of regional sand-dust processes from the perspectives of occurrence frequency, duration, and the influence range of sand-dust processes at different levels, to provide a theoretical basis for improving understanding of regional sand-dust processes in China, which can finally improve the sand-dust forecast and disaster prevention.

In this study, sand-dust weather is divided into three levels, i.e., sand-dust storm, blowing sand, and suspended dust. According to the *Operational Regulations of Monitoring and Evaluation for Regional Weather and Climate Processes*, we obtained the occurrence frequency, total duration, and the number of affected stations of sand-dust processes each year from January 1961 to May 2021, based on the Mann-Kendall test and the ensemble empirical mode decomposition (EEMD)

method. The present study then analyzes the evolution trends and probability distribution characteristics of the above three statistical indicators. Meanwhile, the start time of the first and last sand-dust weather processes for each year are investigated, and the seasonal distribution characteristics of sand-dust processes are analyzed.

DATA AND METHODS

Study Area

According to the meteorological observation standard issued by the China Meteorological Administration in 1979 (Central Meteorological Bureau, 1979), sand-dust storms, blowing sand, and suspended dust are all classified as sand-dust events. Among them, sand-dust storms are the most disastrous. They are generally defined as a storm carrying a large amount of sand and dust, which makes the air severely turbid and reduces the horizontal visibility to below 1,000 m. Note that the severe sand-dust storm with the greatest destructive power can reduce the horizontal surface visibility to below 50 m or even 0 m. Blowing sand is usually defined as a weather phenomenon with horizontal visibility of 10,000–1,000 m, which is caused by strong wind carrying a large amount of sand and dust. Suspended dust is the weakest of the three sand-dust categories. It is usually caused by airflows in the mid-upper troposphere transporting dust from the windward direction, or by some fine dust suspended in the lower troposphere (horizontal visibility below 10,000 m) after a sand-dust storm. 20:00 LST (Local Standard Time; the same below) was selected as the recording mode. If there were two or more sand-dust records before 20:00 LST in 1 day, it was considered a sand-dust day. If the sand-dust event lasts after 20:00 LST, it was considered two sand-dust days (Central Meteorological Bureau, 1979).

Through remote sensing and field observation, it has been determined that the main sand-dust source areas in China include the Tarim Basin (Taklamakan Desert), the Alxa Gobi (Badain Jaran Desert, Tengger Desert, Ulan Buh Desert and Hexi Corridor), the Junggar Basin (Gurbantunggut Desert), the Ordos Plateau and the southeastern Inner Mongolia Plateau (Duce et al., 1980; Iwasaka et al., 1983; Dong et al., 2000; Qiu et al., 2001; Sun et al., 2001; Prospero et al., 2002; Qian et al., 2004). The Tarim Basin and the Junggar Basin are both located in Xinjiang. Due to large deserts in the basins, the sand-dust weather in these two regions is quite frequent, especially in the Tarim Basin where the average annual sand-dust weather is more than 100 days, with individual areas exceeding 200 days (Qian et al., 2002; Wang et al., 2005; Wan et al., 2013). However, due to the closed terrain of these basins and the prevailing easterly wind at the opening of the eastern edge of the basin, small-scale sand-dust events often stay in basins and have little impact on the downstream areas. Thus, the sand-dust processes are often studied separately in these two areas (Goudie, 1983, 2009; Washington et al., 2003; Wang et al., 2005; Qian et al., 2007; Ganor et al., 2010; Xu et al., 2016; Yang et al., 2016; Li et al., 2018). Because the focus of this study is to reveal the evolution characteristics of regional sand-dust processes in China, the small-scale sand-dust processes in these two basins are not considered due to their limited impact. Therefore, the study area in this research does not include Xinjiang. However, the sand-dust processes originating in Xinjiang that extend and have an influence on downstream areas are still considered.

Dataset

The data of this study comes from the "dust (storm) data set (v1. 0)" established by the meteorological information center of the China Meteorological Administration in 2013, this data set contains the daily observations of dust weather phenomena (including sand-dust storms, blowing sand, and suspended dust) from more than 2,400 national surface meteorological stations in 31 provinces (cities and autonomous regions) in China since January 1954. The missing rate of daily observations of weather phenomena in the data set is less than 1%, the accuracy of element data is close to 100%, and it is automatically updated and extended every day. The observation of sand-dust storms blowing sand and suspended dust in the data set conform to the requirements of *the criterion of surface meteorological observation*, and the process of data quality control includes basic parameter check, data missing inspection, climatological limit value check, variation range inspection, internal consistency inspection, time consistency inspection, comprehensive analysis of quality control code, spatial consistency inspection and marking of quality control code.

The data used in this study range from 1 January 1961, to 31 May 2021, including the daily observations of the sand-dust storm, blowing sand, and suspended dust derived from 1945 ground-based meteorological stations in China, except for Xinjiang (**Figure 1**). These data are provided by the National Meteorological Information Center of the China Meteorological Administration. To ensure the integrity and reliability of the data, the selected stations have data records dating from least 1 January 1961. The data missing rate of all stations is less than 1%. All data can be downloaded from the China Meteorological Data Service Center (http://data. cma. cn).

Methods

According to the national standard of Classification of sand-dust weather (GB/T20480-2017, Niu et al., 2017), a sand-dust process is defined as a weather process that lasts for at least 1 day. For a sand-dust process at a single station, if a station monitors continuous sand-dust weather, it is determined that there is a sand-dust process at that station. Note that the shortest duration of a sand-dust process at a single station is 1 day. In terms of regional sand-dust weather, if there are not less than 3% of adjacent stations (adjacent distance ≤200 km) with suspended dust or severer sand-dust weather on a certain day, that day should be regarded as a regional sand-dust weather day. The distance (D) between adjacent station A and station B is calculated by the following equation **Eq. 1**.

$$D = \frac{R \times \cos^{-1}(\sin(LatA) \times \sin(LatB) + \cos(LatA) \times \cos(LatB) \times \cos(LonA - LonB)) \times \pi}{180} \quad (1)$$

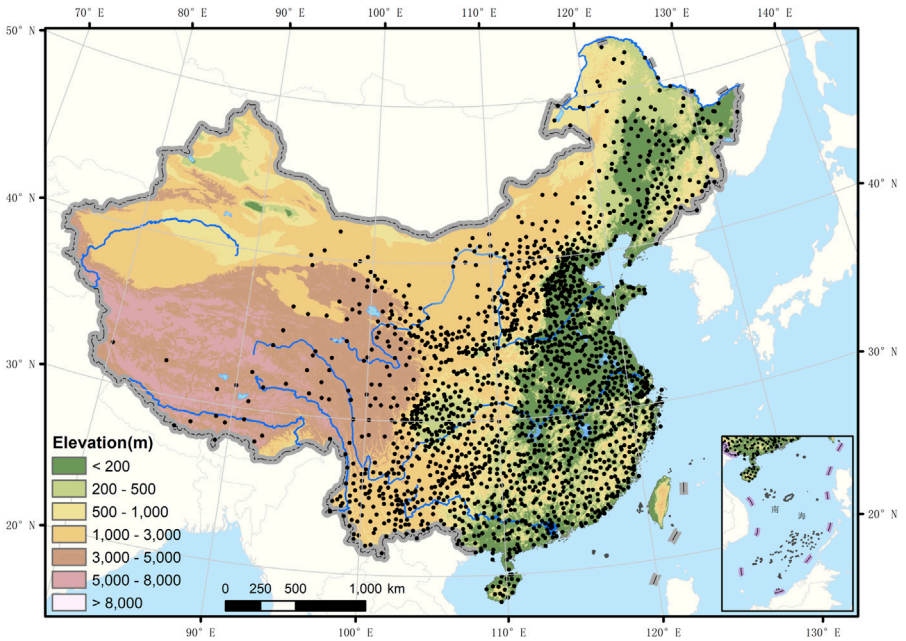

FIGURE 1 | Study area and station distribution.

where R denotes the average radius of the earth, taken as 6,371 km $\pi = 3.14$. In addition, LonA, LatA, LonB, and LatB indicate the longitude and latitude of station A and station B, respectively. For the start time of a regional sand-dust process, the first sand-dust day meeting the judgment standard of a sand-dust process is the start date of the regional sand-dust process. Similarly, after a sand-dust process is started, the last sand-dust day during continuous dust days is the end date of the regional sand-dust process. Moreover, we need to separate the regional sand-dust processes with a short time gap. That is, for the regional sand-dust process with a duration of more than 4 days determined by the above four conditions, if the average longitude position of stations where blowing sand is observed retreats westward by 4.5 longitudes or more compared with the previous day, the previous day is determined as the end date of this regional sand-dust process. The method in this paper is developed based on the Objective Identification Technique for Regional Extreme Event (OITREE, Ren et al., 2012; Li et al., 2014).

The Mann-Kendall test is a rank-based nonparametric test, which has the advantage of being able to test for linear or nonlinear trends, it is a classical technique for climate diagnosis and prediction (Mann, 1945; Kendall, 1975). The MK method can be used to determine the presence or absence of abrupt climate changes in a climate series and, when present, it can be used to determine the timing of the abrupt changes. The MK method is also often used to detect trends in the frequency of precipitation and drought under the influence of climate change. This study was used to analyze time series data for trends in dust and sand processes. The MK was used because it is distribution-free, robust to outliers, and has a high capacity for non-normally distributed data (Yue et al., 2002; Onoz and Bayazit, 2003). Our analysis shows that the annual time series of annual total frequency and total days of sand-dust processes are not significantly autocorrelated at the 90% confidence level. Therefore, the effect of autocorrelation on trend estimation can be ignored (Hu et al., 2021).

Huang et al. (1998) proposed the Empirical Mode Decomposition (EMD) method and successfully developed the Hilbert-Huang transform by combining the EMD method with the Hilbert spectrum analysis. According to the EMD method, a series of data sequences with different characteristic scales are formed by repeatedly screening and decomposing the signal into a series of fluctuations and a trend term. Each sequence is called an Intrinsic Mode Function (IMF) component, and the IMF component with the lowest frequency represents the time series of the general trend or mean value of the original signal (Huang and Wu, 2008; Wu et al., 2011). Due to the adaptability of the EMD method in signal analysis, the EMD method has been widely used in various fields. However, the signal sometimes has the phenomenon of mode mixing in the application process, which affects the analysis effect of the EMD method. To solve this problem, Wu and Huang (2009) proposed the EEMD method, in which the uncorrelated Gaussian white noise can be artificially added to the original signal to eliminate the phenomenon of mode mixing. Currently, the EEMD method has been frequently used to detect the scale variation characteristics (Guo et al., 2016; Lin et al., 2016; Sankaran, 2017; Deng and Fu, 2019; Li and Yue, 2020) and to predict the trends of climate element series (Liang and Ding, 2012; Diodato and Bellocchi, 2014; Zhang and Yan, 2014; Qi et al., 2017; Bi et al., 2018).

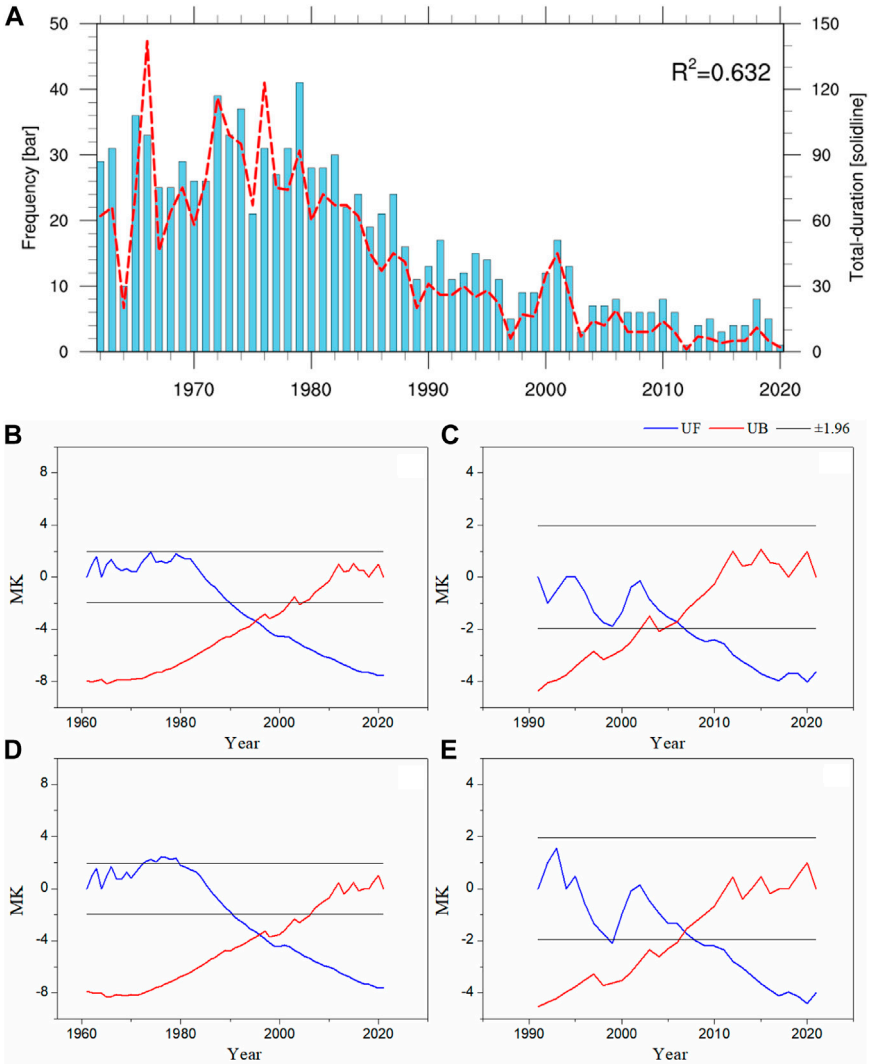

FIGURE 2 | (A) Annual total frequency (blue histogram) and total days (red solid line; unit: day) of sand-dust processes. Test results of **(B,C)** annual total frequency and **(D,E)** annual total days of sand-dust processes during 1961–2020 by the MK. The blue line represents UF in the MK method, the red line represents UB, and the black line is ±1.96 (0.05 significance). **(B)** and **(D)** are the detection of the 1961–2020 sequence, and **(C)** and **(E)** are the detection of the 1991–2020 sequence.

RESULTS

Temporal Evolution Characteristics of Sand-Dust Weather

As shown in **Figure 2A**, the annual total number and duration of sand-dust processes in China exhibit a general trend of first increasing and then decreasing from 1961 to 2020. Specifically, the annual total number of sand-dust processes gradually increased from 1961 to 1979, peaked in 1979, and then decreased rapidly until the 21st century. For the annual total days of sand-dust processes, it increased from 1961 to 1965 and reached its peak in 1965, then gradually increasing after a decrease in 1966, with two sub-peaks in 1972 and 1976. After 1976, the annual total days rapidly decreased, with a valley value of 6 days in 1997. There was a short active period of sand-dust weather between 1998 and 2002, and the annual frequency and total days of sand-dust processes increased. After 2002, they both decreased again. Compared with 1961–1999, the annual average frequency and total days of sand-dust processes in 2000–2020 decreased by 71.4 and 78%, respectively.

According to the MK results, **Figures 2B,D** are for the detection of the sequence from 1961 to 2020. The annual frequency and annual sand-dust days showed an increasing trend before the 1990s, followed by a decreasing trend, and the decreasing trend was even greater. The change trends of annual frequency and total days of sand-dust processes significantly turned around in the 1990s and around 2006. In the late 1990s, the annual frequency and the annual number of dust days dropped significantly, indicating a sudden change. Further testing of the sequence from 1991 to 2020 (**Figures**

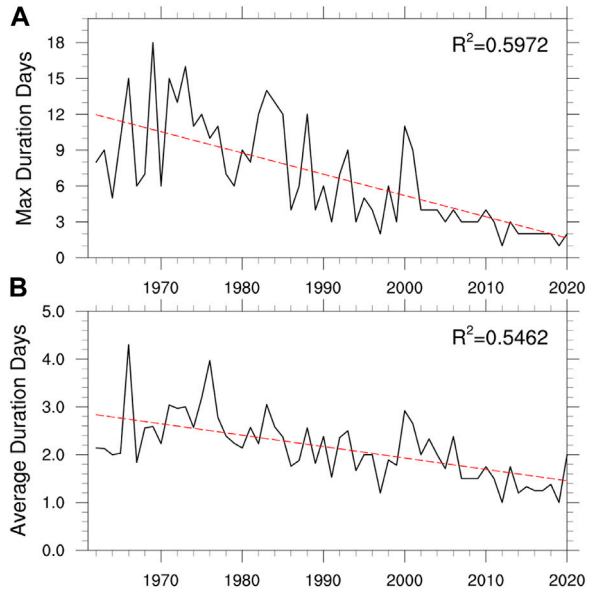

FIGURE 3 | Time evolution of **(A)** annual longest duration and **(B)** annual average duration of sand-dust processes from 1961 to 2020. The red dotted line denotes the linear trend.

2C,E) indicated that the UF values of the annual total frequency and annual total days of sand-dust processes were basically below 0 after the 1990s, indicating that the overall trend was decreasing after the 1990s. The intersection of UF and UB in the confidence interval around 2006, that is, there was an obvious mutation in 2006. That is to say, the annual total frequency and annual total days were significantly reduced after the mutation. Therefore, China's sand dust underwent significant mutations in the late 1990s and around 2006. The annual average frequency of sand-dust processes was 27 in the period 1961–1989, 10 between 1990 and 2010, and 4 between 2011 and 2020. For annual sand-dust days, the value was 69 before 1990, 20 in 1990–2010, and 5 in 2011–2020.

It is worth noting that although the data for 2021 ends in May, the frequency of sand-dust processes and total days increased sharply in 2021, reaching the maximum since 2003. The frequency and total days of sand-dust processes in 2021 were 10 and 19, respectively.

From 1961 to 2020, the annual longest duration of sand-dust processes in China increased first and then decreased (**Figure 3A**). Specifically, it tended to increase before 1973 and decrease after 1973. In addition, the annual longest duration of sand-dust processes fluctuated greatly during 1961–1973, with low values in 1964, 1967, and 1970, and high values in 1963, 1966, and 1969, reaching the peak in 1969 (18 days) and sub-peak in 1973 (16 days). After 1973, the annual longest duration of sand-dust processes began to decrease gradually. In the early 1980s (1981–1986), the duration of sand-dust processes was relatively long, but it was relatively short in the 1990s. The year 2000 is a high-value year of the longest duration (11 days), and subsequently, the longest duration of sand-dust processes decreased rapidly until 2020.

The evolution of the average duration of sand-dust processes is slightly different from that of the longest duration (**Figure 4B**), showing an overall increasing-decreasing-increasing evolution trend. Specifically, the average duration of sand-dust processes trended to increase before the 1970s, decrease from the 1970s to 1990s, increase slightly in the early 2000s, decrease in the late 2000s, and increase in 2020. Among them, the average duration of sand-dust processes was the maximum (4.3 days) in 1966, followed by 1976 (3.97 days) and 2000 (2.92 days), and the least (1 day) in 2012 and 2019. From January to May 2021, the average duration of sand-dust processes was 2 days, and the longest duration was 4 days.

In this paper, the "maximum number of stations" refers to the maximum number of stations affected by each sand-dust process in a year. The "average number of stations" refers to the average number of stations affected by each sand-dust process in a year. From trends of the maximum station number for suspended dust, blowing sand and sand-dust storms (**Figure 4A**). The annual maximum number of stations with different categories of sand-dust processes shows a decreasing-increasing-decreasing-increasing trend from 1961 to 2020. Specifically, the number of sand-dust stations for different grades of sand-dust processes decreased in the early 1960s, the maximum numbers of suspended dust and blowing-sand processes increased to the peak in the late 1970s. The maximum number of sand-dust storm stations was slightly different from suspended dust and blowing sand, it increased to its peak in the mid-1970s. After that, the maximum number of stations for the three sand-dust categories gradually decreased. It reached the valley in the late 2010s. Subsequently, it increased again in the

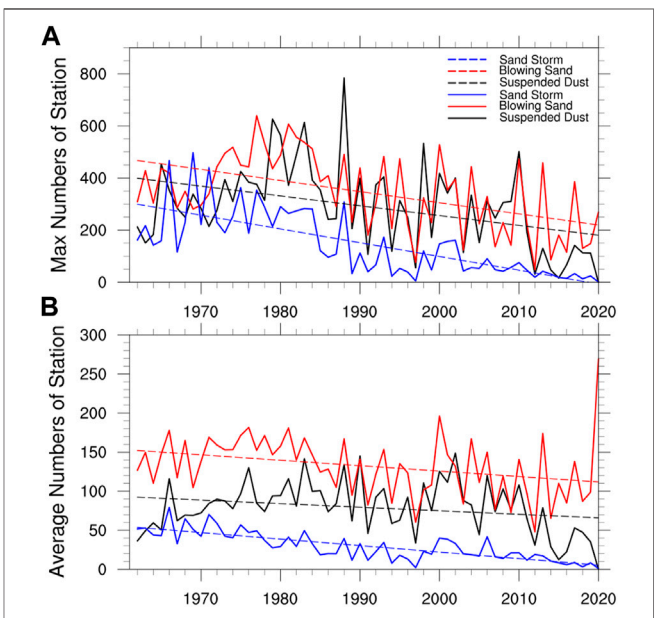

FIGURE 4 | The annual **(A)** maximum and **(B)** average number of stations (solid line) for different categories of sand-dust processes, and their linear trends (dotted line).

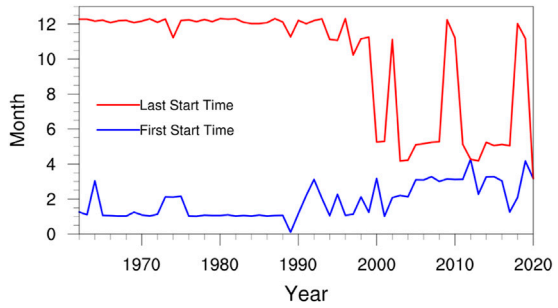

FIGURE 5 | Start time of the first (solid blue line) and last sand-dust (solid red line) processes each year.

2020s. From January to May 2021, the maximum number of stations for suspended dust, blowing sand, and sand-dust storm processes were 339, 394, and 103, respectively. Among them, the maximum numbers of suspended dust and blowing sand in 2021 were significantly more than the multi-year average values from 1961 to 2020 (288 and 345 stations, respectively), while the maximum number of sand-dust storm stations was less than the multi-year average (150 stations).

The maximum number of stations for suspended dust and blowing sand were significantly more than that of sand-dust storms during 1961–2020, except for the late 1960s to the early 1970s. In the past 60 years, the average number of maximum blowing sand stations (329 stations) was more than that of suspended dust and sand-dust storm stations.

From the average number of stations for different sand-dust processes (**Figure 4B**), it can be found that the average number of blowing sand stations is the largest, followed by suspended dust and sand-dust storms. The average number of stations for suspended dust and blowing sand show a decreasing-increasing-decreasing-increasing trend, and they both peaked in the 1970s, with two valley values in the early 1960s and the end of the 2020s. The average number of blowing sand stations in 2020 was 269, followed by 196 in 2001. Since 1961, the average number of sand-dust storm stations has shown a decreasing-increasing-decreasing-increasing trend. Specifically, the average number of sand-dust storm stations was largest in the 1960s, reaching a minimum in the early 1990s, before increasing again in the early 2000s, and then continuing to decrease until early 2020, when it increased again.

Figure 5 shows the start time of the first and last sand-dust processes each year. The first sand-dust process in China mainly occurred in early January before the 1990s. After that, the start time of the first sand-dust process was gradually delayed and postponed to March after the 2000s. The start time in 2021 was January 13. The last sand-dust process in each year tends to start earlier. Specifically, the start time was basically in December before the 1990s. After that, it gradually advanced to mid-late May after the 2000s. In other words, over the past 60 years, the start time of sand-dust processes was delayed and the end time advanced.

Table 1 lists the top 10 years with the maximum number of stations for suspended dust, blowing sand, and sand-dust storm processes during 1960–2020, as well as the months with the maximum number of sand-dust stations in 10 years. It can be seen that the top 10 years were mainly before the 1990s, including 4 years (1980, 1982, 1983, and 1988) in the 1980s. In addition, in the top 10 years, the months with the maximum number of suspended dust stations are concentrated in spring, with six instances in April, two storms in May, and only one occurrence in December. The top 10 years with the maximum number of blowing sand stations also mainly appeared before the 1990s, mostly in the 1970s–1980s. After the 1990s, only the year 2000 ranks in the top 10. In the top 10 years, the month with the maximum number of blowing sand stations was April, followed by

TABLE 1 | The top 10 years with the maximum number of sand-dust stations for different sand-dust categories during 1961–2020, and the months with the maximum number of sand-dust stations in the 10 years.

Order	Suspended-dust			Blowing sand			Sand-dust storm		
	Stations	Year	month	Stations	Year	month	Stations	Year	month
1	784	1988	4	639	1977	2	497	1969	3
2	626	1979	4	607	1981	4	467	1966	4
3	613	1983	5	557	1982	4	451	1959	4
4	564	1980	4	537	1983	3	440	1971	3
5	533	1998	4	532	1978	4	394	1961	4
6	501	2010	3	528	2000	4	373	1960	4
7	489	1982	5	518	1974	4	363	1975	4
8	454	1965	12	512	1984	2	353	1977	2
9	425	1975	4	495	1973	12	319	1958	2
10	418	2000	4	491	1988	1	308	1988	4

TABLE 2 | The top 10 years with the most sand-dust processes, the months with the most sand-dust processes in the 10 years, and the maximum number of affected stations in a sand-dust process during 1961–2020.

Order	Frequency	Year	Total duration	Maximum number of suspended-dust stations and month of occurrence	Maximum number of blowing sand stations and month of occurrence and month of occurrence	Maximum number of sand-dust storm stations and month of occurrence and month of occurrence
1	41	1979	92	626 (4)	436 (2)	214 (4)
2	39	1972	116	276 (12)	443 (12)	230 (4)
3	37	1974	95	310 (5)	518 (4)	253 (4)
4	36	1965	73	454 (12)	437 (3)	159 (12)
5	33	1966	142	353 (4)	419 (11)	467 (4)
6	33	1973	99	394 (5)	495 (12)	190 (3)
7	31	1963	87	224 (4)	428 (1)	217 (1)
8	31	1976	66	151 (4)	443 (5)	188 (5)
9	31	1978	123	384 (4)	532 (4)	288 (4)
10	30	1982	74	314 (5)	557 (4)	274 (4)

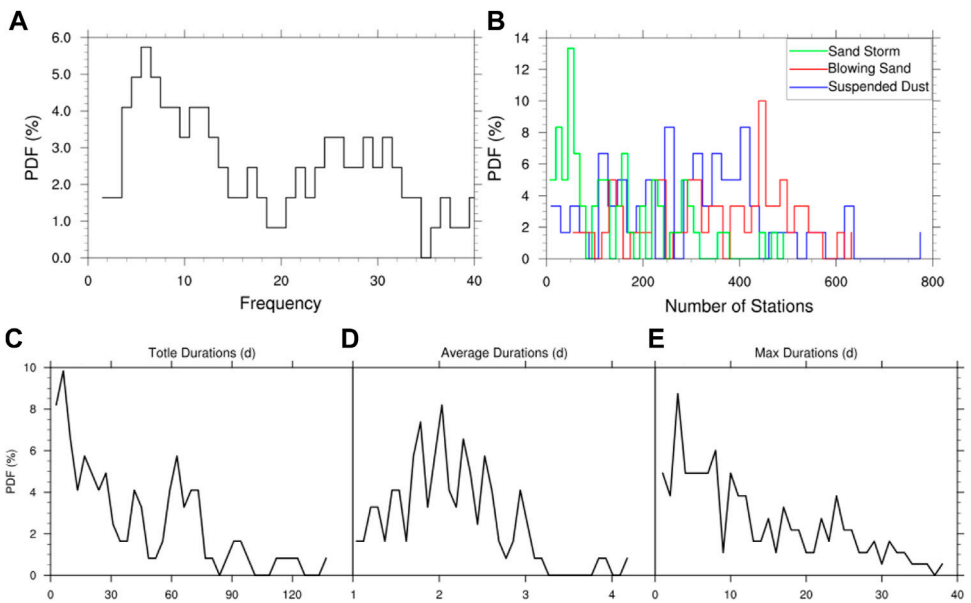

FIGURE 6 | Probability distributions of **(A)** annual total frequency, **(B)** maximum number of affected stations, **(C)** annual total days, **(D)** average days, and **(E)** maximum duration for different categories of sand-dust processes.

February, with instances only happening once in January, March, and December. The top 10 years with the maximum number of sand-dust storm stations appeared all before the 1990s, with 3 times in the 1960s, 4 times in the 1970s, and 3 times in the 1980s. In addition, for the month with the maximum number of sand-dust storm stations, April is the most frequent (7 times), followed by March (2 times) and February (1 time).

Therefore, the top 10 years with the maximum number of sand-dust stations for different sand-dust categories are mainly

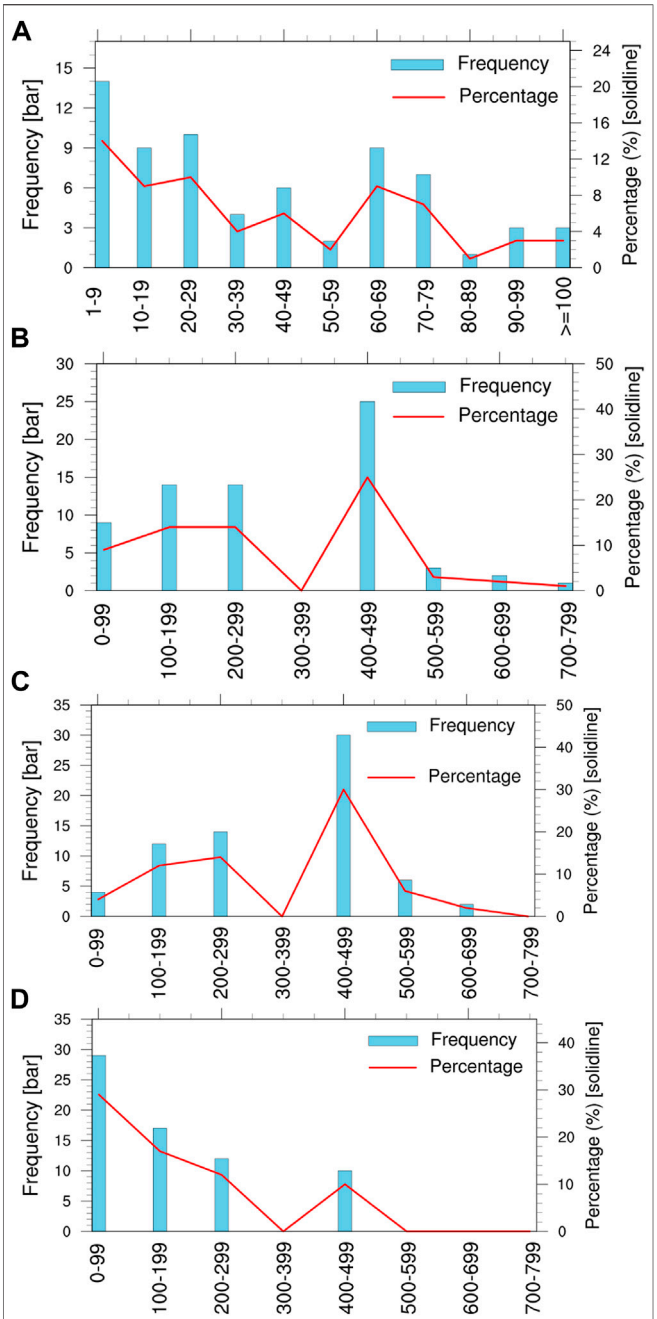

FIGURE 7 | Frequency and probability of **(A)** the number of sand-dust processes, **(B)** maximum number of suspended-dust stations, **(C)** maximum number of blowing-sand stations, and **(D)** maximum number of sand-dust storm stations.

before the 1990s, and the sand-dust processes mainly occur in April.

Table 2 lists the top 10 years with the most sand-dust processes, the months with the most sand-dust processes in the 10 years, and the maximum number of affected stations in a sand-dust process from 1961 to 2020. The top 10 years with the most suspended dust processes are mainly before the 1980s, including 3 years (1963, 1965, and 1966) in the 1960s, 6 years (1972, 1973, 1974, 1976, 1978, and 1979) in the 1970s and only 1 year (1982) after the 1980s. For the top 10 years with the most sand-dust processes, the annual total durations of sand-dust weather are all more than 60 days, with the most duration days in 1966. In addition, for the maximum number of sand-dust stations in these 10 years, the average value is 375, and the maximum is 626 in 1979. The maximum number of suspended dust stations mainly appear in April, followed by May and December (2 times). For the maximum number of blowing sand stations, the average is 471 in the 10 years, and the monthly distribution of the maximum number of blowing sand stations is relatively scattered, i.e., three times in April, twice in December, and once in January, February, March, and November. For the annual maximum number of sand-dust storm stations, the average is 248 in the 10 years, and the maximum mainly appears in spring, i.e., six times in April and once in January, March, May, and December.

Overall, the top 10 years with the most sand-dust processes are concentrated in the 1960s and 1970s, and the month with the most sand-dust processes is mainly April. In the years with more sand-dust processes, the maximum number of affected stations for different categories of sand-dust processes is also more than the average.

Probability Distributions of Sand-Dust Processes

Figure 6 shows the probability distributions of the annual frequency, the maximum number of affected stations, annual total days, average days, and maximum duration of sand-dust processes. The probability distribution of the annual frequency of sand-dust processes is mainly concentrated 5–14 times and 26–32 times. The largest probability was six occurrences (5.6%), followed by 8–12 (4%) and 26–32 (about 3%). Considering the probability distribution of the maximum number of affected stations for different categories of sand-dust processes (**Figure 6B**), the number of suspended-dust stations is mainly concentrated in stations 220–430. The probability of 220 and 430 stations is the largest (8%), followed by 120 stations (6.3%), and the probability of exceeding 600 stations was 2%. The probability distribution of the maximum number of blowing-sand stations was relatively scattered, and the maximum probability (10%) appears in about 450 stations. The probability reaches 5% when the maximum number is 130–140, 220–240, or 300–320. The probability of storms affecting more than 600 stations is 1.5%. The maximum number of dust-dust storm stations has the highest probability for 60 stations (13.5%), followed by 30 stations (8.5%) and 110–130 stations, 160 stations, 230 stations, and 280 stations (more than 5%).

The probability distribution of sand-dust process durations (**Figures 6C–E**) show that the annual total days of sand-dust processes are mainly about 5 days, followed by 10–30 days and 60–75 days (4%). The average probability of an annual total duration exceeding 100 days is 0.6%. The annual average days of sand-dust processes are mainly 1–3 days. The probability of 2 days is more than 6%, and the probability of 3 days is 3%. The

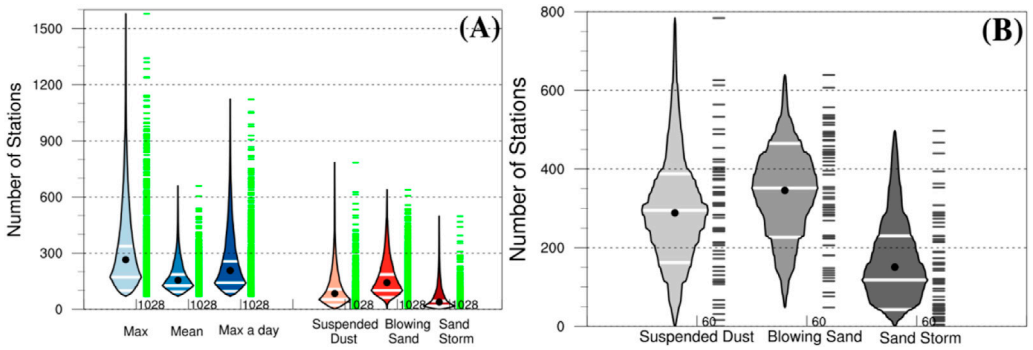

FIGURE 8 | (A) Percentile box-type diagrams of the maximum, the average number of affected stations, the maximum number of stations in a single day for all sand-dust processes, and the number of affected stations for different categories of sand-dust processes during 1961–2020. **(B)** Percentile box-type diagrams of the maximum number of affected stations for different categories of sand-dust processes during 1961–2020. Black dots in boxes are average values, and white lines from the bottom to the top in boxes are the first, second, and third quartiles, respectively.

maximum duration of sand-dust processes is mainly 1–8 days, of which the probability of 3 days is the largest (8%), followed by 10–12 days (4%). The probability with the maximum duration reaching 25 days exceeds 3%, and it is 1% for more than 30 days.

The annual total days of sand-dust processes are divided into 11 grades, i.e., 1–9, 10–19, 20–29, 30–39, 40–49, 50–59, 60–69, 70–79, 80–89, 90–99, and ≥100 (days), as shown in **Figure 7A**. The results suggest that the frequency of 1–9 is the most (14 times), accounting for 21%, followed by 20–29 (10 times; 15%). In addition, the frequency for 10–19 and 60–69 is 9 times, accounting for 13%. Overall, for the annual total days of sand-dust processes, the frequency is the most (33 times; 49%) within 30 days, followed by 60–79 (16 times; 23%). The frequency of more than 100 days is 3 times, accounting for 4%.

The maximum number of suspended-dust stations is divided into eight grades, i.e., 0–99, 100–199, 200–299, 300–399, 400–499, 500–599, 600–699, and 700–799, as shown in **Figure 7B**. The results indicate that the maximum number of suspended-dust stations is mainly concentrated in grades 100–299 and 400–499. Specifically, the highest probability is in grades 400–499 (45%), followed by grades 200–299 (15 times; 23%) and grades 100–199 (14 times; 19%). Similar to the suspended dust, the probability of the maximum number of blowing-sand stations (**Figure 7C**) is the largest in grades 400–499 (35%), followed by grades 100–199 and 200–299 (both 14 times; 20%). In addition, the frequency for grades 0–99 is 9 times, accounting for 14%. For the maximum number of sand-dust storm stations (**Figure 7D**), the probability is the highest in grades 0–99 (24 times; 38%), followed by grades 200–299 (17 times; 23%), 200–299 (13 times; 15%) and 400–499 (12 times; 14%). No sand-dust storms can affect more than 500 stations.

It can be seen that in the sand-dust processes in China, the probability of a large-scale sand-dust process is greater than the probability of a small-scale sand-dust process. Generally, during the small-scale sand-dust weather, the intensity of sand-dust is weak, mainly by suspended-dust. During the occurrence of large-scale sand-dust weather, the intensity of sand-dust is strong, mainly by blowing sand and sand storms.

Figure 8A shows the percentile box-type diagrams of the maximum number of affected stations, the average number of affected stations, the maximum number of affected stations in a single day for all the sand-dust processes (1,028 in total), and the number of affected stations for different categories of sand-dust processes from 1961 to 2020. The results show that the maximum number of affected stations for all the sand-dust processes is concentrated between 100 and 300, with an average value of 258 and a maximum value of 1,579. The average number of affected stations is concentrated between 100 and 200, with an average of 153 and a maximum value of 659. The maximum number of affected stations in a single day is concentrated between 100 and 300, with an average of 202 and a maximum of 1,122. In all the sand-dust processes, the number of suspended-dust stations is mainly concentrated between 30 and 120, with an average of 80 stations and a maximum of 784 stations. The number of blowing-sand stations is more than that of suspended-dust stations, and it is mainly concentrated between 70 and 200, with an average of 136 stations and a maximum of 639 stations. For a single sand-dust storm process, the number of affected stations is mainly concentrated between 10 and 50, with an average of 41 stations and a maximum of 497 stations.

From the percentile box-type diagrams of the maximum number of affected stations for different categories of sand-dust processes during 1961–2020 (**Figure 8B**), the maximum number of suspended-dust stations is mainly concentrated between 180 and 390, with an average of 289 and a maximum of 784. The maximum number of blowing-sand stations is mainly concentrated between 220 and 460, with an average of 346 and a maximum of 639. The maximum number of sand-dust storm stations is concentrated between 50 and 230, with an average of 150 and a maximum of 497.

Figure 9 shows the monthly frequency of the annual maximum number of affected stations for different categories of sand-dust processes. The annual maximum number of suspended-dust stations mainly appears from March to May, including 41.7% in April and 25% in March, and appears only in June during summer and only in October during autumn, and the probability is 8.3% in winter. The annual maximum number of

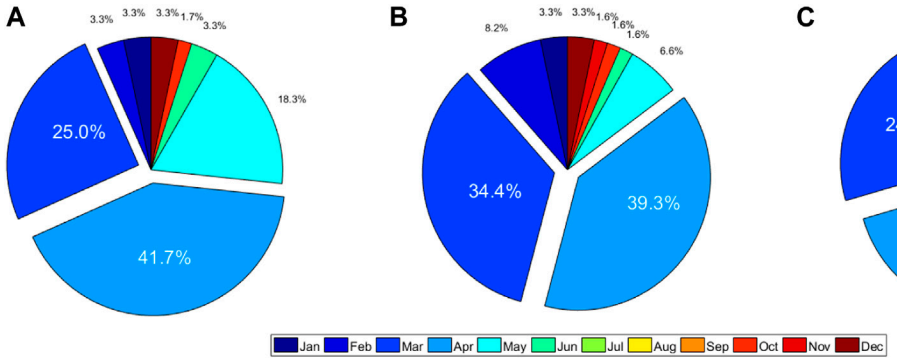

FIGURE 9 | Monthly probability of the maximum number of affected stations for **(A)** suspended-dust, **(B)** blowing sand, and **(C)** sand-dust storm processes.

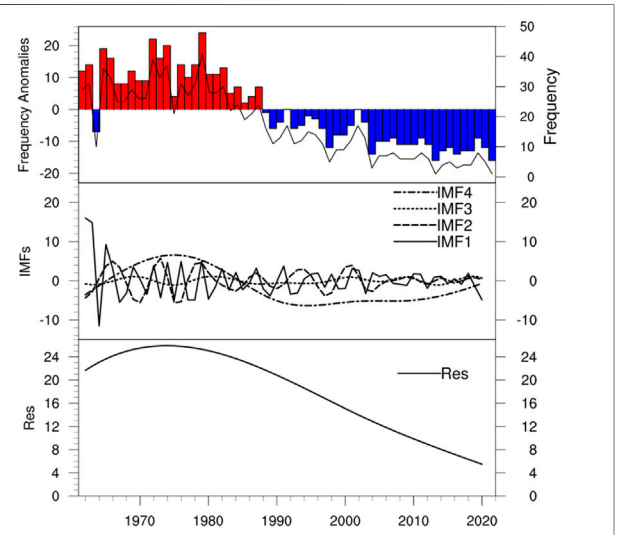

FIGURE 10 | The anomalies evolution and the EEMD results of the annual total number of sand-dust processes.

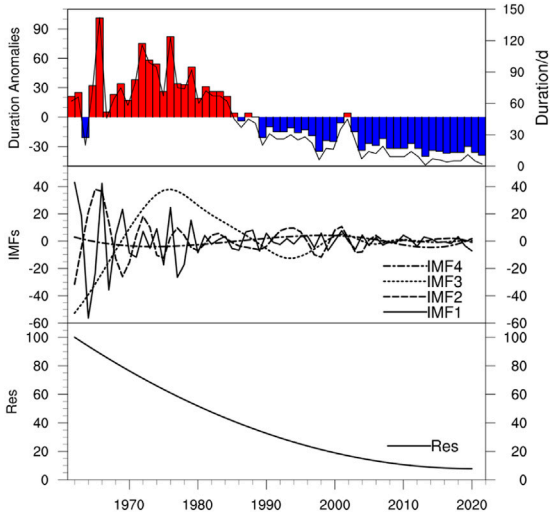

FIGURE 11 | Same as **Figure 10**, but for the annual total days of sand-dust processes.

blowing-sand stations also mainly occurs in spring (March–May), 39.3% in April, 34.4% in March, and 8.3% in February. The probability of the maximum number of blowing-sand stations in winter is 15%, which is more than that of suspended dust and sand-dust storm weather. The maximum number of blowing-sand stations never appears in summer, and the probability is 2% in October. The probability of the maximum number of sand-dust storm stations reaches 82% in spring, with 55.7% in April, 24.6% in March, and 1.6% in May. The probability of annual maximum sand-dust storm stations is 1.6% in June, 0% in autumn, and, 4.9% in January–February.

In summary, during 1961–2020, the probability of the annual total frequency of sand-dust processes is mainly concentrated 5–14 times and 26–32 times, with a maximum probability of 6 times. The annual total duration has a maximum probability of 5 days, followed by 60–70 days. The maximum numbers of suspended-dust, blowing-sand, and sand-dust storm stations are concentrated between 220 and 430, about 450 and about 60, respectively. The annual maximum numbers of affected stations for suspended dust, blowing sand and sand-dust storm are mainly concentrated in 180–390, 220–460, and 50–230, respectively. In addition, the months with the most affected stations by sand-dust processes mainly concentrate from March to May, with the highest probability in April.

Evolution Trends of Sand-Dust Processes

The EEMD is quite suitable for analyzing nonlinear and non-stationary time series. It has the advantages of local stabilization processing and no need to pre-set basis function, and it can effectively solve the problems of mode mixing in the EMD.

From **Figure 10A**, it can be found that the annual total frequency of sand-dust processes before 1986 shows positive anomalies, except for 1963, while it is a negative anomaly during 1986–2020. By the EEMD of the annual number of sand-dust processes, we obtain four IMF components and one trend component (Res). Each component is relatively

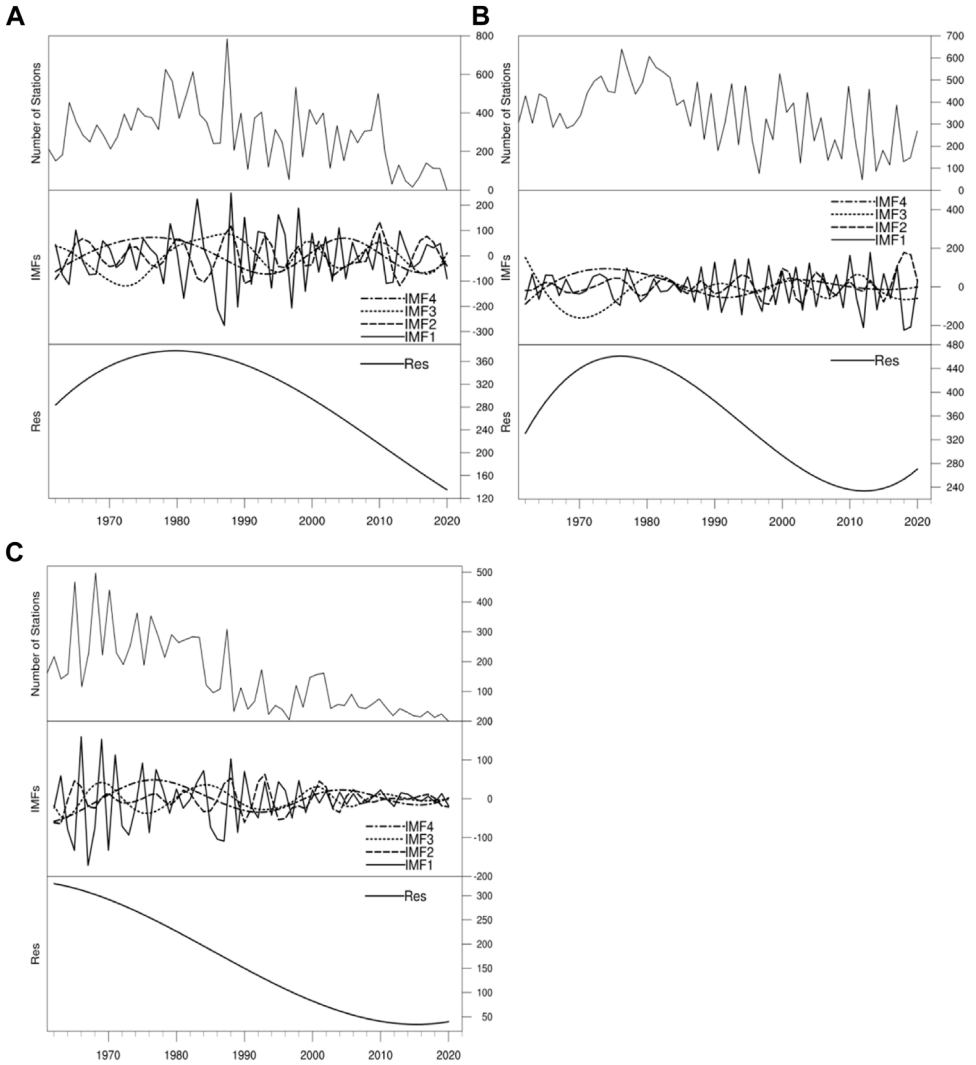

FIGURE 12 | Annual maximum number of affected stations (top) and their EEMD results (bottom) for the **(A)** suspended dust, **(B)** blowing sand, and **(C)** sand-dust storm processes.

independent and can reflect the inherent multi-time scale oscillation mode in the initial sequence.

Figure 10B shows the subsequence of the number of sand-dust processes between 1961 and 2020 using the EEMD. The results suggest that quasi-periodic oscillations of different time scales show strong or weak non-uniform changes with time in the same period. Specifically, the IMF1 component has the largest amplitude, with the highest fluctuation frequency. With time increasing, the amplitude and frequency of other IMF components decrease in turn, and corresponding fluctuation periods gradually increase. The IMF1 component has a 4–5-year periodic variation, a 6–8-year periodic variation for the IMF2 component, and a 10-year periodic variation for the IMF3 component. The trend component Res increases slightly and then decreases rapidly from 1961 to 2020.

The annual total duration of sand-dust processes and the anomaly evolution are given in **Figure 11**. There are positive anomalies before 1984, except for 1963. After 1984, there are negative anomalies, except for 1985 and 2000 when there are weak positive anomalies. This result indicates that annual total days of sand-dust processes are generally more than average before the mid-1980s and less than average thereafter. The IMF components and Res component decomposed by the EEMD show that there is a 4–5-year periodic variation for IMF1, a 6–8-year periodic variation for IMF2, and a 30-year periodic variation for IMF3. The Res component presents a significant decreasing trend from 1961 to 2020.

According to the EEMD results of the maximum number of affected stations for different categories of sand-dust processes (**Figure 12**), it can be found that the IMF1 component for the suspended-dust processes shows a 4-year periodic variation before the 1990s, and the cycle period is reduced to about 3 years from 1990s to 2010s and turns back to 4 years after 2010. There is an 8-year periodic variation for the IMF2

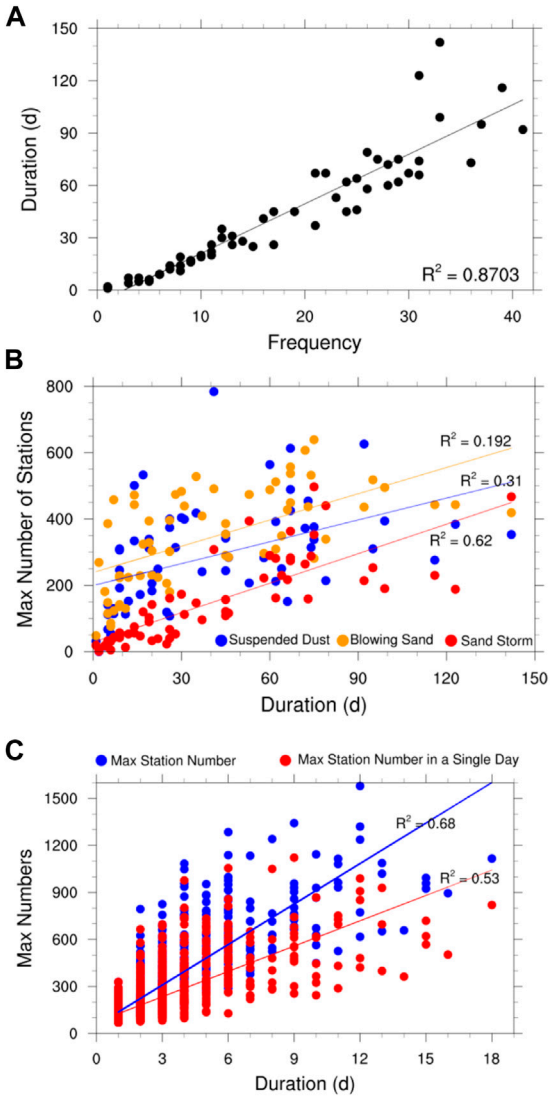

FIGURE 13 | Scatter plots of all the sand-dust processes in 1961–2020. **(A)** Annual frequency and annual total duration. **(B)** Annual total duration and the maximum number of affected stations for different categories of sand-dust processes. **(C)** maximum duration, maximum numbers of affected stations in a single process and a single day.

component, a 15–20-year periodic variation for IMF3, and a 30-year periodic variation for IMF4. Moreover, the Res component increases first and then decreases between 1961 and 2020. Specifically, it increases from 1961 to the early 1980s and decreases after the 1980s. For the maximum number of blowing-sand stations, the periodic variations of IMF components are consistent with suspended-dust processes, and its Res component shows an increase-decrease-increase trend. Specifically, it tends to increase from 1961 to 1978 and 2012–2020 and decrease from 1978 to 2012. For sand-dust storms, periodic variations of IMF components are consistent with those of the suspended-dust and blowing-sand processes. The Res component shows an overall decreasing trend, but it tends to increase slightly from the late 2010s to 2020.

The relationships between the annual frequency and the annual total duration of sand-dust processes are shown in **Figure 13A**. It suggests that there is a positive linear correlation between them, and the correlation coefficient reaches 0.87. The annual total duration of sand-dust processes increases with the increase of their frequency. From the relationships between the annual total duration and the maximum number of affected stations for different categories of sand-dust processes (**Figure 13B**), it can be seen that there is no significant linear correlation between the total duration and the maximum number of suspended-dust stations, and the correlation coefficient is only 0.19, which fails to pass the significance test at 0.01 confidence level. However, the annual total duration of sand-dust processes positively correlates with the maximum number of affected stations for blowing-sand and sand-dust storm processes, and the correlation coefficients are 0.31 and 0.62, respectively, which both pass the significance test at a 0.01 confidence level.

Figure 13C presents the scatter plots of maximum duration, the maximum number of affected stations, and the maximum number of affected stations in a single day for all the 1,028 sand-dust processes. The results show that the maximum duration of sand-dust processes has linear correlations with both the maximum number of affected stations and the maximum number of affected stations in a single day, and the squared correlation coefficients reach 0.68 and 0.53, respectively, which both pass the significance test at 0.01 confidence level. In addition, the maximum duration of a single sand-dust process is mainly within 6 days, and the number of sand-dust stations in a single day mainly ranges between 100 and 600. The maximum number of affected stations for a single process is more than that of a single day, mainly concentrating in 200–900.

Figure 14 shows the spatial distribution of the number of sand-dust processes participated by each station in each decade from 1961 to 2020. It can be seen from the figure that the stations most involved in the sand-dust process are mainly in the central and western Inner Mongolia in northern China, the central Hexi Corridor in Gansu, Ningxia, Northern Shaanxi, and central and southern Hebei. Among them, central and western Inner Mongolia and northern Ningxia are the maximum value centers involved in the sand-dust process, and central and southern Hebei is the second maximum value center. During the period from 1961 to 1990, the average number of sand-dust processes in these areas reached more than 160 times/10a, among them, the participation times of central and western Inner Mongolia and northern Ningxia reached more than 220 times/10a, and the participation times of sand and dust process in central and southern Hebei reached more than 200 times/10a. Since the 1990s, the number of stations in northern China participating in sand-dust processes has decreased rapidly. From 1991 to 2000, only some parts of central and western Inner Mongolia recorded 80 times/10a. After 2011, the participation of most sites in China reduced to less than 40 times/10a.

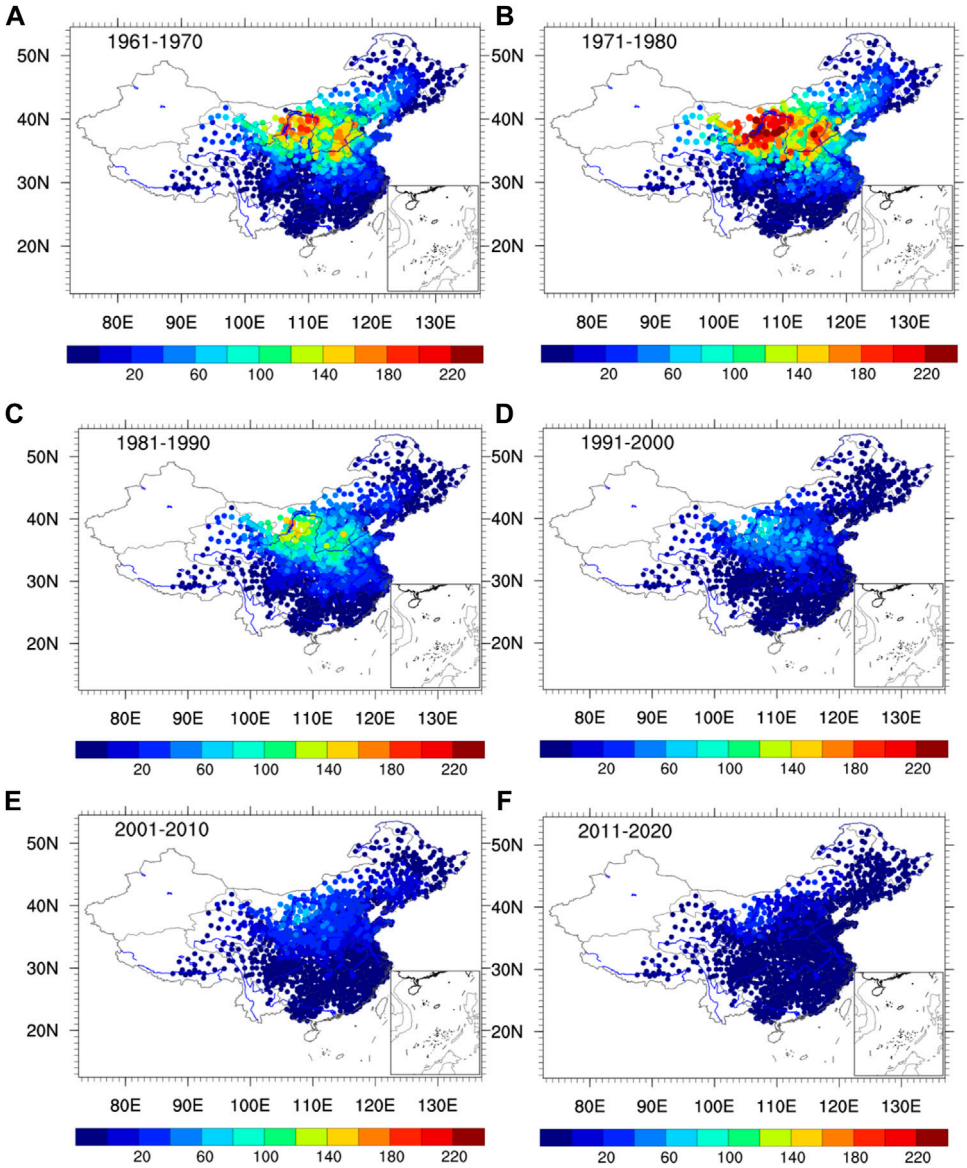

FIGURE 14 | The spatial distribution map of the number of sand-dust processes participated by each station in each decade in China from 1961 to 2020.

In summary, there are obvious interannual fluctuations in dust activity in northern China, and dust activity in China, especially in northern China, has shown a decreasing trend in general over the past 60 years, but the trend varies significantly from region to region. Our results are also in general agreement with the analysis results using the Moderate Resolution Imaging Spectroradiometer (MODIS) aerosol optical thickness product (DOD) (Wang et al., 2021), which tests the reliability of MODIS aerosol inversion data from another perspective (Yu et al., 2020). Further analysis revealed that the maximum frequency of a single station participating in sand-dust processes was 245 times/10a from 1971 to 1980, 163 times/10a from 1981 to 1990, 90 times/10a from 1991 to 2000, 63 times/10a from 2001 to 2010 and 28 times/10a from 2011 to 2020.

CONCLUSION AND DISCUSSION

Currently, most of the studies on sand-dust events in northern China are focused on the statistical characteristics of sand-dust weather at a single station, or they focus only on local features. Few studies have analyzed sand-duct events in northern China from the perspective of sand-dust processes. The few previous works on the spatio-temporal variation characteristics of the sand-dust processes are either based on outdated datasets or explore individual cases of major sand-dust events. Based on the identification methods and several characteristic quantities (including duration and impact range.) of sand-dust processes defined in the *Operational Regulations of Monitoring and Evaluation for Regional Weather and Climate Processes*, we

analyzed the annual frequency, annual total duration, and the number of affected stations for different categories of sand-dust processes (including sand-dust storm, blowing sand and suspended dust) from January 1961 to May 2021. Based on the MK test and EEMD, we further analyzed evolution trends and the probability distribution characteristics of annual frequency, annual total duration, and the number of affected stations of sand-dust processes. In addition, the start time of the first and last sand-dust processes each year, as well as the seasonal distribution characteristics of sand-dust processes, were investigated.

The results show that the annual frequency, annual duration, maximum and average number of affected stations of sand-dust processes have all decreased significantly since the 1980s. The frequency and duration of sand-dust processes have two sudden change periods in the 1990s and around 2006. There is an increasing trend in the early 1980s, a significant decreasing trend in the 1980s–1990s, and since the late 1990s, the downward trend has been slow, especially after 206. Moreover, the start time of the first sand-dust process every year has been delayed from January to February, and the start time of the last sand-dust process has been advanced from December to May. Sand-dust processes mainly occur in spring (the most in April) and are less likely to occur in the summer. Furthermore, this study found that compared with 1961–1999, the average frequency and total duration of sand-dust processes 2000–2020 have decreased by 71.4 and 78%, respectively. Since the 1990s, the number of stations in northern China participating in sand-dust processes has decreased rapidly; from 1991 to 2000, only some parts of central and western Inner Mongolia reached 80 times/10a; after 2011, the number of participation of most sites in China has been reduced to less than 40 times/10a.

It is noteworthy that in 2021, the first sand-dust process in China occurred from January 13 to 14, more than 30 days earlier than the average in 2000–2020. In March 2021, China suffered from a severe sand-dust storm rarely seen in the past 10 years, which affected 19 provinces (districts and cities) and nearly half of the country's land area. As of May 2021, the frequency and total duration of sand-dust processes in China increased sharply, reaching the maximum (10 times and 19 days) since 2003. As of October 2021, the annual amount of precipitation in northern China was the second largest in history, and rainstorms during the flood season had a high intensity and significant extremes. From July 17 to 22, an extreme rainstorm episode occurred in Henan Province of China, resulting in 292 deaths and 47 people going missing in Zhengzhou (https://www.mem.gov.cn/). In western China, the autumn rain started early, and the rainfall was highest compared to the same time of year previously. Moreover, the autumn rainfall in West China occurred significantly earlier (August 23), and was of larger intensity, with the most rainfall for the same period during other years in recent history. In September, the Weihe River experienced the largest flood for that time of year since 1935. The Yiluo River and Qin River suffered the largest floods for that time of year since 1950. Between October 3 and 6, the strongest autumn flood was recorded since meteorological records began in Shanxi Province. Meanwhile, high-temperature days were more than normal for this year, and the meteorological drought frequently occurred in the eastern part of southwest China, south China, and the eastern part of northwest China. Meanwhile, the number of landing typhoons was less, and only four typhoons landed in China, which is three fewer than in normal years (http://www.cma.gov.cn/).

Global warming has intensified the instability of the climate system and increased the possibility of extreme weather and climate events. Theoretically, water vapor will increase by 7% for every 1°C increase in temperature. This increase in water vapor makes heavy rain and rainstorms occur more frequently. Anomalies in the atmospheric circulation also cause instability in the climate system. As global warming increases, the intensity and frequency of extreme weather and climate events will be further enhanced in the future. In August 2021, the sixth assessment report of the Intergovernmental Panel on Climate Change (IPCC, 2021) revealed that all regions of the world will face intensified climate change and more severe weather extremes in the coming decades. A series of abnormal and extreme weather-climate events occurred in China in 2021. However, whether these indicate that 2021 is the beginning of a more intense period of climate change is unclear, and this issue requires further systematic research, examining the overall weather and climate characteristics and various external forcing factors in 2021.

DATA AVAILABILITY STATEMENT

The raw data supporting the conclusions of this article will be made available by the authors, without undue reservation.

AUTHOR CONTRIBUTIONS

WH initiated the study. HD, TF, WH, HW and PY interpreted the data. HD and WH wrote the article.

FUNDING

This work was supported by the National Natural Science Foundation of China (Grant: 42005058, 41675092), the Foundation of drought Meteorological Science Research (IAM202118), and the Northwest Regional Numerical Forecasting Innovation Team (grant no. GSQXCXTD-2020-02).

ACKNOWLEDGMENTS

We acknowledge the National Meteorological Information Center of China Meterological Administration for providing high quality data.

REFERENCES

Ahmed, A. S., Ali, A. A., and Alhaider, M. A. (1987). Measurement of Atmospheric Particle Size Distribution during Sand/duststorm in Riyadh, Saudi Arabia. *Atmos. Environ. (1967)* 21, 2723–2725. doi:10.1016/0004-6981(87)90205-8

Alizadeh-Choobari, O., Ghafarian, P., and Owlad, E. (2016). Temporal Variations in the Frequency and Concentration of Dust Events over Iran Based on Surface Observations. *Int. J. Climatol.* 36, 2050–2062. doi:10.1002/joc.4479

Alpert, P., and Ganor, E. (2001). Sahara mineral Dust Measurements from TOMS: Comparison to Surface Observations over the Middle East for the Extreme Dust Storm, March 14-17, 1998. *J. Geophys. Res.* 106, 18275–18286. doi:10.1029/2000JD900366

Bar-Or, R., Erlick, C., and Gildor, H. (2008). The Role of Dust in Glacial-Interglacial Cycles. *Quat. Sci. Rev.* 27, 201–208. doi:10.1016/j.quascirev.2007.10.015

Beyranvand, A., Azizi, G., Alizadeh-Choobari, O., and Darvishi Boloorani, A. (2019). Spatial and Temporal Variations in the Incidence of Dust Events over Iran. *Nat. Hazards* 97, 229–241. doi:10.1007/s11069-019-03637-w

Bi, S., Bi, S., Chen, X., Ji, H., and Lu, Y. (2018). A Climate Prediction Method Based on EMD and Ensemble Prediction Technique. *Asia-pacific J. Atmos. Sci.* 54, 611–622. doi:10.1007/s13143-018-0078-z

Bishop, J. K. B., Davis, R. E., and Sherman, J. T. (2002). Robotic Observations of Dust Storm Enhancement of Carbon Biomass in the North Pacific. *Science* 298, 817–821. doi:10.1126/science.1074961

Bryant, R. G. (2013). Recent Advances in Our Understanding of Dust Source Emission Processes. *Prog. Phys. Geogr. Earth Environ.* 37, 397–421. doi:10.1177/0309133313479391

Calov, R., Ganopolski, A., Claussen, M., Petoukhov, V., and Greve, R. (2005). Transient Simulation of the Last Glacial Inception. Part I: Glacial Inception as a Bifurcation in the Climate System. *Clim. Dyn.* 24, 545–561. doi:10.1007/s00382-005-0007-6

Carslaw, K. S., Lee, L. A., Reddington, C. L., Pringle, K. J., Rap, A., Forster, P. M., et al. (2013). Large Contribution of Natural Aerosols to Uncertainty in Indirect Forcing. *Nature* 503, 67–71. doi:10.1038/nature12674

Central Meteorological Bureau (1979). *Standard on the Surface Meteorological Observation*. Beijing, China: China Meteorological Press, 186. (in Chinese).

Chandler, D. G., Blaesing–Thompson, S., and Busacca, A. (2004). Geospatial Assessment of Agricultural Lands Critical to Air Quality on the Columbia Plateau, Washington State. *J. Soil Water Conserv.* 59, 184–189.

Chen, Y.-S., Sheen, P.-C., Chen, E.-R., Liu, Y.-K., Wu, T.-N., and Yang, C.-Y. (2004). Effects of Asian Dust Storm Events on Daily Mortality in Taipei, Taiwan. *Environ. Res.* 95 (2), 151–155. doi:10.1016/j.envres.2003.08.008

Chun, Y., Boo, K.-O., Kim, J., Park, S.-U., and Lee, M. (2001). Synopsis, Transport, and Physical Characteristics of Asian Dust in Korea. *J. Geophys. Res.* 106 (D16), 18461–18469. doi:10.1029/2001jd900184

Chung, Y.-s., Kim, H.-s., Dulam, J., and Harris, J. (2003). On Heavy Dustfall Observed with Explosive Sandstorms in Chongwon-Chongju, Korea in 2002. *Atmos. Environ.* 37 (24), 3425–3433. doi:10.1016/s1352-2310(03)00360-1

Chung, Y. S., Kim, H. S., Park, K. H., Jugder, D., and Gao, T. (2005). Observations of Dust–Storms in China, Mongolia and Associated Dust Falls in Korea in spring 2003. *Water Air Soil Pollut. Focus* 5 (3), 15–35. doi:10.1007/s11267–005–0724–1

Creamean, J. M., Suski, K. J., Rosenfeld, D., Cazorla, A., DeMott, P. J., Sullivan, R. C., et al. (2013). Dust and Biological Aerosols from the Sahara and Asia Influence Precipitation in the Western U.S. *Science* 339, 1572–1578. doi:10.1126/science.1227279

Deng, Q., and Fu, Z. (2019). Comparison of Methods for Extracting Annual Cycle with Changing Amplitude in Climate Series. *Clim. Dyn.* 52, 5059–5070. doi:10.1007/s00382-018-4432-8

Diodato, N., and Bellocchi, G. (2014). Long-term winter Temperatures in central Mediterranean: Forecast Skill of an Ensemble Statistical Model. *Theor. Appl. Climatol* 116, 131–146. doi:10.1007/s00704-013-0915-z

Dong, Z. B., Wang, X. M., and Liu, L. Y. (2000). Wind Erosion in Arid and Semiarid China: An Overview. *J. Soil Water Conserv* 55, 439–444. doi:10.3321/j.issn:1000–694X.2000.02.007

Duce, R. A., Unni, C. K., Ray, B. J., Prospero, J. M., and Merrill, J. T. (1980). Long-Range Atmospheric Transport of Soil Dust from Asia to the Tropical North Pacific: Temporal Variability. *Science* 209, 1522–1524. doi:10.1126/science.209.4464.1522

Evan, A. T., Vimont, D. J., Heidinger, A. K., Kossin, J. P., and Bennartz, R. (2009). The Role of Aerosols in the Evolution of Tropical North Atlantic Ocean Temperature Anomalies. *Science* 324, 778–781. doi:10.1126/science.1167404

Ganor, E., Osetinsky, I., Stupp, A., and Alpert, P. (2010). Increasing Trend of African Dust, over 49 years, in the Eastern Mediterranean. *J. Geophys. Res.* 115, D07201. doi:10.1029/2009JD012500

Giannadaki, D., Pozzer, A., and Lelieveld, J. (2013). Modeled Global Effects of Airborne Desert Dust on Air Quality and Premature Mortality. *Atmos. Chem. Phys.* 13 (9), 957–968. doi:10.5194/acp–14–957–2014

Goudie, A. S. (2014). Desert Dust and Human Health Disorders. *Environ. Int.* 63, 101–113. doi:10.1016/j.envint.2013.10.011

Goudie, A. S. (1983). Dust Storms in Space and Time. *Prog. Phys. Geogr. Earth Environ.* 7, 502–530. doi:10.1177/030913338300700402

Goudie, A. S. (2009). Dust Storms: Recent Developments. *J. Environ. Manage.* 90, 89–94. doi:10.1016/j.jenvman.2008.07.007

Grousset, F. E., Ginoux, P., Bory, A., and Biscaye, P. E. (2003). Case Study of a Chinese Dust Plume Reaching the French Alps. *Geophys. Res. Lett.* 30, 1277. doi:10.1029/2002GL016833

Guan, Q., Sun, X., Yang, J., Pan, B., Zhao, S., and Wang, L. (2017). Dust Storms in Northern China: Long-Term Spatiotemporal Characteristics and Climate Controls. *J. Clim.* 30 (17), 6683–6700. doi:10.1175/jcli-d-16-0795.1

Guan, Q., Yang, J., Zhao, S., Pan, B., Liu, C., Zhang, D., et al. (2014). Climatological Analysis of Dust Storms in the Area Surrounding the Tengger Desert during 1960-2007. *Clim. Dyn.* 45, 903–913. doi:10.1007/s00382-014-2321-3

Guo, B., Chen, Z., Guo, J., Liu, F., Chen, C., and Liu, K. (2016). Analysis of the Nonlinear Trends and Non-stationary Oscillations of Regional Precipitation in Xinjiang, Northwestern China, Using Ensemble Empirical Mode Decomposition. *Ijerph* 13, 345. doi:10.3390/ijerph13030345

Guo, L., Fan, B., Zhang, F., Jin, Z., and Lin, H. (2018). The Clustering of Severe Dust Storm Occurrence in China from 1958 to 2007. *J. Geophys. Res. Atmos.* 123, 8035–8046. doi:10.1029/2018JD029042

Han, Y., Fang, X., Zhao, T., and Kang, S. (2008). Long Range Trans-Pacific Transport and Deposition of Asian Dust Aerosols. *J. Environ. Sci.* 20, 424–428. doi:10.1016/s1001-0742(08)62074-4

Hsu, S.-C., Liu, S. C., Arimoto, R., Liu, T.-H., Huang, Y.-T., Tsai, F., et al. (2009). Dust Deposition to the East China Sea and its Biogeochemical Implications. *J. Geophys. Res.* 114, D15304. doi:10.1029/2008JD011223

Hu, Z., Jin, Q., Ma, Y., Pu, B., Ji, Z., Wang, Y., et al. (2021). Temporal Evolution of Aerosols and Their Extreme Events in Polluted Asian Regions during Terra's 20-year Observations. *Remote Sensing Environ.* 263, 112541. doi:10.1016/j.rse.2021.112541

Huang, J., Minnis, P., Yan, H., Yi, Y., Chen, B., Zhang, L., et al. (2010b). Dust Aerosol Effect on Semi-arid Climate over Northwest China Detected from A-Train Satellite Measurements. *Atmos. Chem. Phys.* 10, 6863–6872. doi:10.5194/acp-10-6863-2010

Huang, J., Wang, T., Wang, W., Li, Z., and Yan, H. (2014). Climate Effects of Dust Aerosols over East Asian Arid and Semiarid Regions. *J. Geophys. Res. Atmos.* 119 (19), 11398–11416. doi:10.1002/2014JD021796

Huang, J., Zhang, C., Prospero, J. M., Yi, Y., Hu, Y., SunMack, –S., et al. (2010a). African Dust Outbreaks: a Satellite Perspective of Temporal and Spatial Variability over the Tropical Atlantic Ocean. *J. Geophys. Res.* 115, D05202. doi:10.1029/2009JD012516

Huang, N. E., Shen, Z., Long, S. R., Wu, M. C., Shih, H. H., Zheng, Q., et al. (1998). The Empirical Mode Decomposition and the Hilbert Spectrum for Nonlinear and Non-stationary Time Series Analysis. *Proc. R. Soc. Lond. A.* 454, 903–995. doi:10.1098/rspa.1998.0193

Huang, N. E., and Wu, Z. (2008). A Review on Hilbert-Huang Transform: Method and its Applications to Geophysical Studies. *Rev. Geophys.* 46, RG2006. doi:10.1029/2007RG000228

Husar, R. B., Tratt, D. M., Schichtel, B. A., Falke, S. R., Li, F., Jaffe, D., et al. (2001). Asian Dust Events of April 1998. *J. Geophys. Res.* 106 (D16), 18317–18330. doi:10.1029/2000jd900788

Idso, S. B., and Brazel, A. J. (1977). Planetary Radiation Balance as a Function of Atmospheric Dust: Climatological Consequences. *Science* 198, 731–733. doi:10.1126/science.198.4318.731

Iwasaka, Y., Minoura, H., and Nagaya, K. (1983). The Transport and Spacial Scale of Asian Dust-Storm Clouds: a Case Study of the Dust-Storm Event of April 1979. *Tellus B: Chem. Phys. Meteorology* 35, 189–196. doi:10.3402/tellusb.v35i3.14594

Jin, Q., and Wang, C. (2018). The Greening of Northwest Indian Subcontinent and Reduction of Dust Abundance Resulting from Indian Summer Monsoon Revival. *Sci. Rep.* 8. doi:10.1038/s41598-018-23055-5

Jin, Q., Wei, J., Lau, W. K. M., Pu, B., and Wang, C. (2021). Interactions of Asian mineral Dust with Indian Summer Monsoon: Recent Advances and Challenges. *Earth-Science Rev.* 215, 103562. doi:10.1016/j.earscirev.2021.103562

Jin, Q., Wei, J., Yang, Z.-L., and Lin, P. (2017). Irrigation-induced Environmental Changes Around the Aral Sea: an Integrated View from Multiple Satellite Observations. *Remote Sensing* 9 (9), 900. doi:10.3390/rs9090900

Jin, Q., Yang, Z.-L., and Wei, J. (2016). Seasonal Responses of Indian Summer Monsoon to Dust Aerosols in the Middle East, India, and China. *J. Clim.* 29, 6329–6349. doi:10.1175/JCLI-D-15-0622.1

Kang, L., Huang, J., Chen, S., and Wang, X. (2016). Long-term Trends of Dust Events over Tibetan Plateau during 1961-2010. *Atmos. Environ.* 125, 188–198. doi:10.1016/j.atmosenv.2015.10.085

Kashima, S., Yorifuji, T., Bae, S., Honda, Y., Lim, Y.-H., and Hong, Y.-C. (2016). Asian Dust Effect on Cause-specific Mortality in Five Cities across South Korea and Japan. *Atmos. Environ.* 128, 20–27. doi:10.1016/j.atmosenv.2015.12.063

Kendall, M. G. (1975). *Rank Correlation Methods*. London: Griffin.

Kim, H., and Choi, M. (2015). Impact of Soil Moisture on Dust Outbreaks in East Asia: Using Satellite and Assimilation Data. *Geophys. Res. Lett.* 42 (8), 2789–2796. doi:10.1002/2015GL063325

Kjelgaard, J., Sharratt, B., Sundram, I., Lamb, B., Claiborn, C., Saxton, K., et al. (2004). PM10 Emission from Agricultural Soils on the Columbia Plateau: Comparison of Dynamic and Time-Integrated Field-Scale Measurements and Entrainment Mechanisms. *Agric. For. Meteorology* 125, 259–277. doi:10.1016/j.agrformet.2004.04.004

Knippertz, P., and Stuut, J. B. W. (2014). *Mineral Dust*. Dordrecht, Heidelberg, New York, London: Springer.

Krinner, G., Boucher, O., and Balkanski, Y. (2006). Ice-free Glacial Northern Asia Due to Dust Deposition on Snow. *Clim. Dyn.* 27, 613–625. doi:10.1007/s00382-006-0159-z

Kurosaki, Y., Shinoda, M., and Mikami, M. (2011). What Caused a Recent Increase in Dust Outbreaks over East Asia? *Geophys. Res. Lett.* 38, a–n. doi:10.1029/2011GL047494

Lee, H., Honda, Y., Lim, Y.-H., Guo, Y. L., Hashizume, M., and Kim, H. (2014). Effect of Asian Dust Storms on Mortality in Three Asian Cities. *Atmos. Environ.* 89, 309–317. doi:10.1016/j.atmosenv.2014.02.048

Li, J., Wang, S., Chu, J., Wang, J., Li, X., Yue, M., et al. (2018). Characteristics of Air Pollution Events over Hotan Prefecture at the Southwestern Edge of Taklimakan Desert, China. *J. Arid Land* 10, 686–700. doi:10.1007/s40333-018-0096-9

Li, Y.-z., and Yue, C.-f. (2020). Prediction and Analysis of Non-stationary Runoff Extreme Sequence Based on ESMD Combination Prediction Model. *Water Supply* 20 (4), 1439–1452. doi:10.2166/ws.2020.058

Li, Y., Ren, F., Li, Y., Wang, P., and Yan, H. (2014). Characteristics of the Regional Meteorological Drought Events in Southwest China during 1960-2010. *J. Meteorol. Res.* 28 (3), 381–392. doi:10.1007/s13351-014-3144-1

Li, Z., Lau, W. K. M., Ramanathan, V., Wu, G., Ding, Y., Manoj, M. G., et al. (2016). Aerosol and Monsoon Climate Interactions over Asia. *Rev. Geophys.* 54, 866–929. doi:10.1002/2015RG000500

Liang, P., and Ding, Y. H. (2012). Extended Range Forecast Experiment Based on Intraseasonal Oscillation. *Chin. J. Atmos. Sci.* 36 (1), 102–116. doi:10.3878/j.issn.1006–9895.2012.01.09

Lin, D., Bueh, C., and Xie, Z. (2016). Relationship between Summer Rainfall over North China and India and its Genesis Analysis. *Chin. J. Atmos. Sci.* 40 (1), 201–214. doi:10.3878/j.issn.1006–9895.1503.14339

Ling, X., Guo, W., and Fu, C. (2014). Composite Analysis of Impacts of Dust Aerosols on Surface Atmospheric Variables and Energy Budgets in a Semiarid Region of China. *J. Geophys. Res. Atmos.* 119 (6), 3107–3123. doi:10.1002/2013JD020274

Littmann, T. (1991). Dust Storm Frequency in Asia: Climatic Control and Variability. *Int. J. Climatol.* 11, 393–412. doi:10.1002/joc.3370110405

Liu, C.-M., Young, C.-Y., and Lee, Y.-C. (2006). Influence of Asian Dust Storms on Air Quality in Taiwan. *Sci. Total Environ.* 368 (2–3), 884–897. doi:10.1016/j.scitotenv.2006.03.039

Liu, L. Y., Shi, P. J., Gao, S. Y., Zou, X. Y., Erdon, H., Yan, P., et al. (2004). Dustfall in China's Western Loess Plateau as Influenced by Dust Storm and Haze Events. *Atmos. Environ.* 38, 1699–1703. doi:10.1016/j.atmosenv.2004.01.003

Liu, Q., Liu, Y., Yin, J., Zhang, M., and Zhang, T. (2014). Chemical Characteristics and Source Apportionment of PM10 during Asian Dust Storm and Non-dust Storm Days in Beijing. *Atmos. Environ.* 91, 85–94. doi:10.1016/j.atmosenv.2014.03.057

Liu, Z., Fairlie, T. D., Uno, I., Huang, J., Wu, D., Omar, A., et al. (2013). Transpacific Transport and Evolution of the Optical Properties of Asian Dust. *J. Quantitative Spectrosc. Radiative Transfer* 116, 24–33. doi:10.1016/j.jqsrt.2012.11.011

Mahowald, N. (2011). Aerosol Indirect Effect on Biogeochemical Cycles and Climate. *Science* 334, 794–796. doi:10.1126/science.1207374

Mahowald, N. M., Baker, A. R., Bergametti, G., Brooks, N., Duce, R. A., Jickells, T. D., et al. (2005). Atmospheric Global Dust Cycle and Iron Inputs to the Ocean. *Glob. Biogeochem. Cycles* 19, a–n. doi:10.1029/2004GB002402

Mahowald, N. M., Muhs, D. R., Levis, S., Rasch, P. J., Yoshioka, M., Zender, C. S., et al. (2006). Change in Atmospheric mineral Aerosols in Response to Climate: Last Glacial Period, Preindustrial, Modern, and Doubled Carbon Dioxide Climates. *J. Geophys. Res.* 111, a–n. doi:10.1029/2005JD006653

Mann, H. B. (1945). Nonparametric Tests against Trend. *Econometrica* 13, 245–259. doi:10.2307/1907187

Mao, R., Hu, Z., Zhao, C., Gong, D.-Y., Guo, D., and Wu, G. (2019). The Source Contributions to the Dust over the Tibetan Plateau: A Modelling Analysis. *Atmos. Environ.* 214, 116859. doi:10.1016/j.atmosenv.2019.116859

Meng, Z., and Lu, B. (2007). Dust Events as a Risk Factor for Daily Hospitalization for Respiratory and Cardiovascular Diseases in Minqin, China. *Atmos. Environ.* 41 (33), 7048–7058. doi:10.1016/j.atmosenv.2007.05.006

Mott, J. A., Mannino, D. M., Alverson, C. J., Kiyu, A., Hashim, J., Lee, T., et al. (2005). Cardiorespiratory Hospitalizations Associated with Smoke Exposure during the 1997 Southeast Asian forest Fires. *Int. J. Hyg. Environ. Health* 208, 75–85. doi:10.1016/j.ijheh.2005.01.018

Mukai, M., Nakajima, T., and Takemura, T. (2004). A Study of Long-Term Trends in mineral Dust Aerosol Distributions in Asia Using a General Circulation Model. *J. Geophys. Res.* 109 (19), D19204. doi:10.1029/2003JD004270

Natsagdorj, L., Jugder, D., and Chung, Y. S. (2003). Analysis of Dust Storms Observed in Mongolia during 1937-1999. *Atmos. Environ.* 37, 1401–1411. doi:10.1016/s1352-2310(02)01023-3

Niu, R. Y., Tian, C. Y., Zhang, H. D., and Zong, Z. P. (2017). *The Dust Weather Grade, GB/T20480-2017*. Beijing, China: Standards Press of China. (in Chinese).

Onoz, B., and Bayazit, M. (2003). The Power of Statistical Tests for Trend Detection. *Turkish J. Eng. Environ. Sci.* 27 (4), 247–251.

Prospero, J. M., Bullard, J. E., and Hodgkins, R. (2012). High-Latitude Dust over the North Atlantic: Inputs from Icelandic Proglacial Dust Storms. *Science* 335 (6072), 1078–1082. doi:10.1126/science.1217447

Prospero, J. M., Ginoux, P., Torres, O., Nicholson, S. E., and Gill, T. E. (2002). Environmental Characterization of Global Sources of Atmospheric Soil Dust Identified with the Nimbus 7 Total Ozone Mapping Spectrometer (TOMS) Absorbing Aerosol Product. *Rev. Geophys.* 40 (1), 2–1. doi:10.1029/2000RG000095

Pu, W., Zhao, X., Shi, X., Ma, Z., Zhang, X., and Yu, B. (2015). Impact of Long-Range Transport on Aerosol Properties at a Regional Background Station in Northern China. *Atmos. Res.* 153, 489–499. doi:10.1016/j.atmosres.2014.10.010

Qi, Y., Qian, C., and Yan, Z. (2017). An Alternative Multi-Model Ensemble Mean Approach for Near-Term Projection. *Int. J. Climatol.* 37, 109–122. doi:10.1002/joc.4690

Qian, W., Quan, L., and Shi, S. (2002). Variations of the Dust Storm in China and its Climatic Control. *J. Clim.* 15, 1216–1229. doi:10.1175/1520-0442(2002)015<1216:votdsi>2.0.co;2

Qian, Y.-B., Wu, Z.-N., Yang, Q., Zhang, L.-Y., and Wang, X.-Y. (2007). Ground-surface Conditions of Sand-Dust Event Occurrences in the Southern Junggar

Basin of Xinjiang, China. *J. Arid Environments* 70 (1), 49–62. doi:10.1016/j.jaridenv.2006.12.001

Qian, Y. B., Wu, Z. N., Zhang, L. Y., Shi, Q., and Wang, X. (2004). Ground–surface Conditions Resulting in Sand–Dust Storms in the South Junggar Basin. *Arid Land Geogr.* 27 (4), 540–542. doi:10.1117/12.528072

Quan, L., Shi, S., Zhu, Y., and Qian, W. (2001). Temporal–spatial Distribution Characteristics and Causes of Dust–Day in China. *Acta Geogr. Sin.* 4, 477–485. doi:10.11821/xb200104011

Ren, F., Cui, D., Gong, Z., Wang, Y., Zou, X., Li, Y., et al. (2012). An Objective Identification Technique for Regional Extreme Events. *J. Clim.* 25, 7015–7027. doi:10.1175/JCLI-D-11-00489.1

Sankaran, A. (2017). Unveiling the Multiscale Teleconnection between Pacific Decadal Oscillation and Global Surface Temperature Using Time-dependent Intrinsic Correlation Analysis. *Int. J. Climatol.* 37, 548–558. doi:10.1002/joc.4713

Shao, J., and Mao, J. (20162016). Dust Particle Size Distributions during Spring in Yinchuan, China. *Adv. Meteorology* 2016, 1–8. doi:10.1155/2016/6940502

Shao, Y., and Dong, C. H. (2006). A Review on East Asian Dust Storm Climate, Modelling and Monitoring. *Glob. Planet. Change* 52, 1–22. doi:10.1016/j.gloplacha.2006.02.011

Shao, Y., Klose, M., and Wyrwoll, K.-H. (2013). Recent Global Dust Trend and Connections to Climate Forcing. *J. Geophys. Res. Atmos.* 118, 107–111. doi:10.1002/jgrd.50836

Stith, J. L., Ramanathan, V., Cooper, W. A., Roberts, G. C., DeMott, P. J., Carmichael, G., et al. (2009). An Overview of Aircraft Observations from the Pacific Dust Experiment Campaign. *J. Geophys. Res.* 114 (D5), D05207. doi:10.1029/2008jd010924

Stone, R., Anderson, G., and Andrews, E. (2005). "Asian Dust Signature at Barrow: Observed and Simulated Incursions and Impact of Asian Dust over Northern Alaska," in Proc. Workshop on Remote Sensing of Atmospheric Aerosols (Tucson, AZ: IEEE), 74–79.

Sun, J., Zhang, M., and Liu, T. (2001). Spatial and Temporal Characteristics of Dust Storms in China and its Surrounding Regions, 1960-1999: Relations to Source Area and Climate. *J. Geophys. Res.* 106 (10), 10325–10333. doi:10.1029/2000JD900665

Tam, W. W. S., Wong, T. W., Wong, A. H. S., and Hui, D. S. C. (2012). Effect of Dust Storm Events on Daily Emergency Admissions for Cardiovascular Diseases. *Circ. J.* 76 (3), 655–660. doi:10.1253/circj.cj-11-0894

Tanaka, T. Y., and Chiba, M. (2006). A Numerical Study of the Contributions of Dust Source Regions to the Global Dust Budget. *Glob. Planet. Change* 52 (1–4), 88–104. doi:10.1016/j.gloplacha.2006.02.002

Tang, Y., Han, G., Wu, Q., and Xu, Z. (2013). Use of Rare Earth Element Patterns to Trace the Provenance of the Atmospheric Dust Near Beijing, China. *Environ. Earth Sci.* 68, 871–879. doi:10.1007/s12665-012-1791-z

Tian, R., Ma, X., Jia, H., Yu, F., Sha, T., and Zan, Y. (2019). Aerosol Radiative Effects on Tropospheric Photochemistry with GEOS-Chem Simulations. *Atmos. Environ.* 208, 82–94. doi:10.1016/j.atmosenv.2019.03.032

Tong, D. Q., Wang, J. X. L., Gill, T. E., Lei, H., and Wang, B. (2017). Intensified Dust Storm Activity and Valley Fever Infection in the Southwestern United States. *Geophys. Res. Lett.* 44, 4304–4312. doi:10.1002/2017GL073524

Tratt, D. M., Frouin, R. J., and Westphal, D. L. (2001). April 1998 Asian Dust Event: a Southern California Perspective. *J. Geophys. Res.* 106 (D16), 18371–18379. doi:10.1029/2000JD900758

Uno, I., Amano, H., Emori, S., Kinoshita, K., Matsui, I., and Sugimoto, N. (2001). Trans-Pacific Yellow Sand Transport Observed in April 1998: A Numerical Simulation. *J. Geophys. Res.* 106 (D16), 18331–18344. doi:10.1029/2000jd900748

IPCC (2021). "Summary for Policymakers," in *Climate Change 2021: The Physical Science Basis. Contribution of Working Group I to the Sixth Assessment Report of the Intergovernmental Panel on Climate Change*. Editors V. MassonDelmotte, P. Zhai, A. Pirani, S. L. Connors, C. Péan, S. Berger, et al. (Cambridge University Press).

Wan, D., Mu, G., Jin, Z., and Lei, J. (2013). The Effects of Oasis on Aeolian Deposition under Different Weather Conditions: a Case Study at the Southern Margin of the Taklimakan Desert. *Environ. Earth Sci.* 68, 103–114. doi:10.1007/s12665-012-1719-7

Wang, H.-J., and Chen, H.-P. (2016). Understanding the Recent Trend of Haze Pollution in Eastern China: Roles of Climate Change. *Atmos. Chem. Phys.* 16, 4205–4211. doi:10.5194/acp-16-4205-2016

Wang, H., Jia, X., Li, K., and Li, Y. (2015). Horizontal Wind Erosion Flux and Potential Dust Emission in Arid and Semiarid Regions of China: A Major Source Area for East Asia Dust Storms. *Catena* 133, 373–384. doi:10.1016/j.catena.2015.06.011

Wang, S., Wang, J., Zhou, Z., and Shang, K. (2005). Regional Characteristics of Three Kinds of Dust Storm Events in China. *Atmos. Environ.* 39, 509–520. doi:10.1016/j.atmosenv.2004.09.033

Wang, S., Yu, Y., Zhang, X.-X., Lu, H., Zhang, X.-Y., and Xu, Z. (2021). Weakened Dust Activity over China and Mongolia from 2001 to 2020 Associated with Climate Change and Land-Use Management. *Environ. Res. Lett.* 16, 124056. doi:10.1088/1748-9326/ac3b79

Wang, X., Hua, T., and Che, H. (2020). Temporal Variation of Dust Aerosol Pollution in Northern China. *Arab J. Geosci.* 13, 108. doi:10.1007/s12517-020-5073-x

Wang, Y., Zhuang, G., Sun, Y., and An, Z. (2006). The Variation of Characteristics and Formation Mechanisms of Aerosols in Dust, Haze, and clear Days in Beijing. *Atmos. Environ.* 40, 6579–6591. doi:10.1016/j.atmosenv.2006.05.066

Washington, R., Todd, M., Middleton, N. J., and Goudie, A. S. (2003). Dust-Storm Source Areas Determined by the Total Ozone Monitoring Spectrometer and Surface Observations. *Ann. Assoc. Am. Geogr.* 93 (2), 297–313. doi:10.1111/1467-8306.9302003

Weinan, C., Zuotao, Y., and Zhibao, D. (1995). Vertical Distribution of Grain-Size Parameters of Drifting Particles during Sand Storms in the Taklamakan Desert, Central Asia. *Phys. Geogr.* 16, 503–523. doi:10.1080/02723646.1995.10642568

Worster, D. (2004). *Dust Bowl: The Southern Plains in the 1930s*. USA: Oxford University Press.

Wu, Z., and Huang, N. E. (2009). Ensemble Empirical Mode Decomposition: a Noise-Assisted Data Analysis Method. *Adv. Adapt. Data Anal.* 01 (1), 1–41. doi:10.1142/S1793536909000047

Wu, Z., Huang, N., Wallace, J., Smoliak, B., and Chen, X. (2011). On the Time–Varying Trend in Global–Mean Surface Temperature. *Clim. Dyn.* 37 (3), 759–773. doi:10.1007/s00382-011-1128-8

Xin-fa, Q., Yan, Z., and Qi-long, M. (2001). Sand-dust Storms in China: Temporal-Spatial Distribution and Tracks of Source Lands. *J. Geogr. Sci.* 11, 253–260. doi:10.1007/BF02892308

Xu, L., Mu, G., He, J., Yang, F., Ren, X., Wan, D., et al. (2016). Variability of Dust Mass Concentrations and Deposition Rates under Different Weather Conditions in Cele Oasis, Southern Tarim Basin. *Environ. Earth Sci.* 75, 639. doi:10.1007/s12665-016-5430-y

Yang, X., Shen, S., Yang, F., He, Q., Ali, M., Huo, W., et al. (2016). Spatial and Temporal Variations of Blowing Dust Events in the Taklimakan Desert. *Theor. Appl. Climatol* 125, 669–677. doi:10.1007/s00704-015-1537-4

Yang, Y., Russell, L. M., Lou, S., Liao, H., Guo, J., Liu, Y., et al. (2017). Dust-wind Interactions Can Intensify Aerosol Pollution over Eastern China. *Nat. Commun.* 8, 15333–15338. doi:10.1038/ncomms15333

Yong, M., Shinoda, M., Nandintsetseg, B., Bi, L., Gao, H., and Wang, Y. (2021). Impacts of Land Surface Conditions and Land Use on Dust Events in the Inner Mongolian Grasslands, China. *Front. Ecol. Evol.* 9, 664900. doi:10.3389/fevo.2021.664900

Yu, H., Yang, Y., Wang, H., Tan, Q., Chin, M., Levy, R. C., et al. (2020). Interannual Variability and Trends of Combustion Aerosol and Dust in Major continental Outflows Revealed by MODIS Retrievals and CAM5 Simulations during 2003-2017. *Atmos. Chem. Phys.* 20 (1), 139–161. doi:10.5194/acp-20-139-2020

Yuan, W., and Zhang, J. (2006). High Correlations between Asian Dust Events and Biological Productivity in the Western North Pacific. *Geophys. Res. Lett.* 33 (07), L07603. doi:10.1029/2005GL025174

Yue, S., Pilon, P., Phinney, B., and Cavadias, G. (2002). The Influence of Autocorrelation on the Ability to Detect Trend in Hydrological Series. *Hydrol. Process.* 16 (9), 1807–1829. doi:10.1002/hyp.1095

Yumimoto, K., and Takemura, T. (2015). Long-term Inverse Modeling of Asian Dust: Interannual Variations of its Emission, Transport, Deposition, and Radiative Forcing. *J. Geophys. Res. Atmos.* 120 (4), 1582–1607. doi:10.1002/2014JD022390

Zhang, J., Dong, W. J., and Fu, C. B. (2005). Impact of Land Surface Deg-Radation in Northern China and Southern Mongolia on Re-gional Climate. *Chin. Sci Bull* 50, 75–81. doi:10.1360/04wd0054

Zhang, R., Jing, J., Tao, J., Hsu, S.-C., Wang, G., Cao, J., et al. (2013). Chemical Characterization and Source Apportionment of PM_{2.5} in Beijing: Seasonal Perspective. *Atmos. Chem. Phys.* 13, 7053–7074. doi:10.5194/acp-13-7053-2013

Zhang, X., and Yan, X. (2014). A Novel Method to Improve Temperature Simulations of General Circulation Models Based on Ensemble Empirical Mode Decomposition and its Application to Multi-Model Ensembles. *Tellus A: Dynamic Meteorology and Oceanography* 66, 24846. doi:10.3402/tellusa.v66.24846

Zhang, X. Y., Gong, S. L., Shen, Z. X., Mei, F. M., Xi, X. X., Liu, L. C., et al. (2003b). Characterization of Soil Dust Aerosol in China and its Transport and Distribution during 2001 ACE-Asia: 1. Network Observations. *J. Geophys. Res.* 108 (9), a–n. doi:10.1029/2002jd002632

Zhang, X. Y., Gong, S. L., Zhao, T. L., Arimoto, R., Wang, Y. Q., and Zhou, Z. J. (2003a). Sources of Asian Dust and Role of Climate Change versus Desertification in Asian Dust Emission. *Geophys. Res. Lett.* 30 (24), 2272. doi:10.1029/2003GL018206

Zhao, Y., Li, H., Huang, A., He, Q., Huo, W., and Wang, M. (2013). Relationship between thermal Anomalies in Tibetan Plateau and Summer Dust Storm Frequency over Tarim Basin, China. *J. Arid Land* 5, 25–31. doi:10.1007/s40333-013-0138-2

Zijiang, Z., and Xiwen, W. (2002). Analysis of the Severe Group Dust Storms in Eastern Part of Northwest China. *J. Geogr. Sci.* 12 (3), 357–362. doi:10.1007/BF02837557

Zobeck, T. M., and Van Pelt, R. S. (2006). Wind-induced Dust Generation and Transport Mechanics on a Bare Agricultural Field. *J. Hazard. Mater.* 132, 26–38. doi:10.1016/j.jhazmat.2005.11.090

Conflict of Interest: The authors declare that the research was conducted in the absence of any commercial or financial relationships that could be construed as a potential conflict of interest.

Publisher's Note: All claims expressed in this article are solely those of the authors and do not necessarily represent those of their affiliated organizations, or those of the publisher, the editors and the reviewers. Any product that may be evaluated in this article, or claim that may be made by its manufacturer, is not guaranteed or endorsed by the publisher.

frontiers | Frontiers in Environmental Science

ORIGINAL RESEARCH
published: 20 May 2022
doi: 10.3389/fenvs.2022.875365

Dust Aerosol's Deposition and its Effects on Chlorophyll-A Concentrations Based on Multi-Sensor Satellite Observations and Model Simulations: A Case Study

Wencai Wang[1,2]*, *Zhizheng He*[2], *Shangfei Hai*[2], *Lifang Sheng*[2], *Yongqing Han*[3,4]* and *Yang Zhou*[2]

[1]Key Laboratory of Physical Oceanography, Ocean University of China, Qingdao, China, [2]College of Oceanic and Atmospheric Sciences, Ocean University of China, Qingdao, China, [3]Laboratory for Meteorological Disaster Prevention and Mitigation of Shandong, Jinan, China, [4]Shandong Meteorological Observatory, Jinan, China

OPEN ACCESS

Edited by:
Zhiyuan Hu,
Sun Yat-sen University, China

Reviewed by:
Yong Han,
Sun Yat-sen University, China
Yuanjian Yang,
Nanjing University of Information Science and Technology, China
Jingjing Liu,
Xi'an University of Technology, China

***Correspondence:**
Wencai Wang
wangwc@ouc.edu.cn
Yongqing Han
qingyonghan@163.com

Specialty section:
This article was submitted to Atmosphere and Climate, a section of the journal Frontiers in Environmental Science

Received: 14 February 2022
Accepted: 11 April 2022
Published: 20 May 2022

Citation:
Wang W, He Z, Hai S, Sheng L, Han Y and Zhou Y (2022) Dust Aerosol's Deposition and its Effects on Chlorophyll-A Concentrations Based on Multi-Sensor Satellite Observations and Model Simulations: A Case Study. Front. Environ. Sci. 10:875365. doi: 10.3389/fenvs.2022.875365

Asian dust deposition is an important source of nutrients to the Pacific Ocean, when aerosol dust is deposited into the ocean, it will affect the biological productivity and hence climate. In this paper, we analyzed a dust process that occurred in the Taklimakan Desert during 21–25 May 2019 by employing multi-sensor satellite observations and the WRF-Chem model. It is found that dust aerosols rise in the Taklimakan Desert, moving eastward at high altitudes under the role of the westerly winds, passing over the downwind regions, and deposition in the Pacific Ocean. Dust aerosol deposition results in an increase of chlorophyll-a (Chl-a) concentrations and particulate organic carbon (POC) after 2 days, Chl-a concentrations and POC increase by 175 and 873%, respectively. Moreover, the values of Chl-a concentrations and POC are 256 and 644% higher than the 5-years average during the same period.

Keywords: dust aerosol, CALIPSO, HAMAWARI-8, chlorophyll-a concentration, WRF-chem model

1 INTRODUCTION

Dust aerosol is an important aerosol type in the atmosphere, it plays an important role in the climate system, the marine and terrestrial ecosystem, and the environment in general (Zhao et al., 2020; Hu et al., 2021). On the one hand, dust aerosol can affect the radiation budget of climate by direct effect on thermal radiation and solar radiation (Sokolik and Toon, 1996; Wang et al., 2013). On the other hand, dust aerosol can affect cloud properties and precipitation by participating in cloud and precipitation processes (Wang et al., 2010; Huang et al., 2014; Wang et al., 2015; Tao et al., 2020). Moreover, when dust aerosol settles into the ocean, it can affect the growth of marine phytoplankton by providing nutrients, then affect the marine primary productivity, even the ocean surface carbon cycle.

Since the 'iron hypothesis' was proposed in 1991 (Martin et al., 1991), researchers have conducted numerous experiments on iron in various High Nutrient-Low Chlorophyll (HNLC) regions (Frost and Morel, 1991), which have successfully induced algal blooms and reduced the partial pressure of carbon dioxide at the sea surface (Emerson, 2019). In the natural environment, soluble iron in HNLC areas of mid-latitude North Pacific mainly depends on aerosols' deposition (Moore and Braucher, 2008).

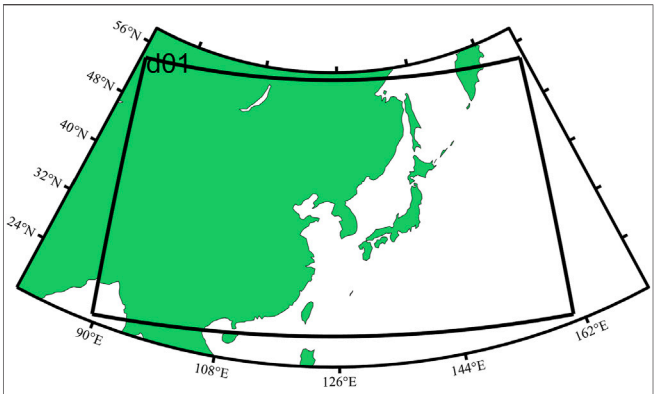

FIGURE 1 | The WRF-Chem model domain (area surrounded by solid black lines).

Yue et al. (2009) simulated the global distribution of dust sources by a global transport model and showed that the Middle East and Central Asia are the major sources of aerosol dust in the Northern Hemisphere. Many studies have shown that Asian dust aerosols can be transported over thousands of kilometers to the Pacific Ocean (Uno et al., 2009; Hu et al., 2019; Hu et al., 2020). Moreover, previous studies note that Asian dust plays a very important role in global oceanic biogeochemical cycles and hence climate since it can provide nutrients to the marine ecosystems (Bishop et al., 2002; Hsu et al., 2009; Mahowald et al., 2010).

Multi-sensor satellite observations provide valuable products to investigate dust aerosol's transport and its effect on phytoplankton blooms. For example, the 8-year analysis of the SeaWIFS and BSC-DREAM8b model (the Barcelona Supercomputing Center, Spain- The Dust Regional Atmospheric Model) shows that the deposition of mineral dust from dust sources in the deserts of North Africa and the Middle East correlates well with the chlorophyll-a concentration in large areas of the Mediterranean Sea (Varenik and Kalinskaya, 2021). Tan et al. (2011); Tan and Shi (2012) find that Asian dust aerosol is positively correlated with Chl-a concentrations in the open sea of China by using long-term satellite observation. Luo et al. (2020) find that both Chl-a concentrations and particulate organic carbon (POC) increase after the dust deposition by using multi-sensor satellite data.

These results above prove the substantial importance of Asian dust deposition in the potential stimulation of phytoplankton production over Earth's remote and spatially extensive ocean, especially over the Pacific Ocean. However, there are still some uncertainties in understanding the impact of dust aerosol on plankton growth due to the limited observations over the Pacific Ocean (Luo et al., 2020). Moreover, the amount of nutrients contained in aerosols is affected by aerosol type, aerosol source, aerosol transport path, and other factors (Luo et al., 2020; Wang et al., 2021), so multi-source data are needed to study the effect of aerosol on Chl-a concentration, especially the valuable observations from satellites in geostationary orbit which have a higher temporal and spatial resolution.

The purpose of this research is to analyze a dust case during 21–25 May 2019 and dust aerosol's effect on Chl-a concentrations by using multi-sensor satellite data combined with other data and the WRF-Chem model.

2 DATE AND METHODS

2.1 Satellite Data and Meteorological Data

2.1.1 CALIPSO

The CALIPSO satellite is launched on 28 April 2006 (Li et al., 2015). CALIPSO L2 vertical feature mask (VFM) products can provide the spatial and temporal distributions of cloud and aerosol. Moreover, VFM can provide the type of aerosols, such as dusty marine, elevated smoke, polluted smoke, dust, polluted dust, clean continental, and clean marine.

In this paper, we obtain the CALIPSO L2 VFM data during May 21–25, 2019 (Version 4.20) over East Asia from the CALIPSO website (https://www-calipso.larc.nasa.gov/products/) to research aerosol type and its transport characters.

2.1.2 HIMAWARI-8

The Himawari-8 satellite was launched on 7 October 2014, which has higher temporal, spatial, and spectral resolution than previous satellites in geostationary orbit (Bessho et al., 2016). The Advanced Himawari Imager (AHI) onboard the Himawari-8 satellite has 16 observation bands from visible channel to infrared channel, and it can provide multi-spectral images over East Asia, Southeast Asia, and Oceania. Moreover, the AHI sensor offers distinct advantages for tracking dust aerosol movement since it can provide a full-disk picture every 10-min (She et al., 2018).

In this paper, AHI Level-2 calibrated data (AOT_L2_Mean, AHI equal latitude-longitude map Data-Daily Combined Aerosol, grid interval = 0.05) with the spatial resolution of 2 km are employed to study the temporal and spatial distribution of dust aerosol. Murakami (2016) proves that the Chl-a concentrations with a time resolution of 10 min derived by Himawari-8 have uncertainties due to noise interference, but the hourly and daily Chl-a concentration effectively reduce the error, so we use L3 daily data with the horizontal resolution of 5 km in our study to research the effect of dust deposition on plankton growth (http://www.eorc.jaxa.jp/ptree/index.html).

2.1.3 Meteorological Data

The wind components, geopotential height, temperature, and sea surface temperature (SST) data sets from the European Centre for Medium-Range Weather Forecasts (ECMWF) Reanalysis 5 data (ERA5) are used to analyze the meteorological conditions for dust aerosol transport and evaluate SST's effect on phytoplankton growth for this case (https://cds.climate.copernicus.eu).

2.1.4 Other Data

The merged L3 global ocean color products are used to provide POC information and the observations of photosynthetic active radiation (PAR), the POC and PAR with the spatial resolution of 5 km × 5 km are used in our study. Merged observations from

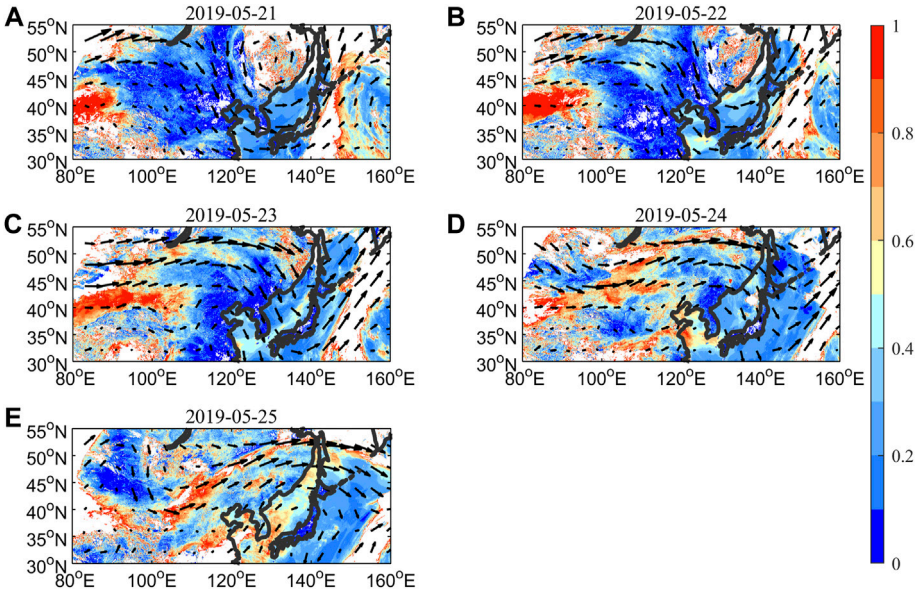

FIGURE 2 | The average daily AOD observed by the Himawari-8 is superimposed with a wind field of 500 hPa (Black arrow) on 21 **(A)**, 22 **(B)**, 23 **(C)**, 24 **(D),** and 25 **(E)** May 2019.

multi-sensors can improve both the spatial and temporal coverage of the data (Wang et al., 2021).

The Global Ocean Forecasting System (GOFS) product (version 3.1) is used to analyze seawater velocity in the surface layer of the ocean in this study, the temporal resolution and spatial resolution for seawater velocity are 3-h and 0.08 × 0.04°.

The Simple Ocean Data Assimilation ocean reanalysis (SODA) product (version 3.4) is employed to study the upwelling velocity of the ocean in this study. The spatial resolution and temporal resolution for upwelling velocity are 0.5 × 0.5° and 5-days.

The Modern-Era Retrospective analysis for Research and Applications version 2 (MERRA-2) tavg1_2d_adg_Nx: 2d,1-Hourly, Time-averaged, Single-Level, Assimilation, Aerosol Diagnostics (extended) product (V5.12.4) are provided by Goddard Earth Sciences Data and Information Services Center (GES DISC). This data, with a temporal resolution of 1 h and a spatial resolution of 0.5 × 0.625°, was used to evaluate the dust deposition simulated by the WRF-Chem model.

2.2 The Model

The HYSPLIT model provided by the Australian Meteorological Agency and the National Oceanic and Atmospheric Administration Air Resources Laboratory is performed to study dust aerosol's transport path. In this paper, the meteorological data input for the HYSPLIT model is derived from the Climate Data Center 1 (CDC1) meteorological data, and other information such as the transport altitudes of dust aerosol is obtained from the products of CALIPSO VFM.

The WRF-Chem model (Weather Research and Forecasting model coupled to Chemistry, version 3.9.1) is widely used in simulating the transport and the deposition amount of dust aerosols (Chen et al., 2017). In this paper, to cover the major source of dust aerosol (Taklimakan desert) and the deposition area for dust aerosol (the Northwestern Pacific Ocean), we set the model domain with 300 × 180 grids, the center of the domain is geographically located at 125°E and 40°N (black box in **Figure 1**), the vertical grid has 30 levels from 50 hPa to the ground. The meteorological fields input for the WRF-Chem model are provided by NCEP Climate Forecast System Version 2, the spatial and temporal resolution for meteorological data are 0.5 ° × 0.5 ° and 6-hourly. The chemical species' initial and boundary conditions are derived from Community Atmosphere Model with Chemistry, and the anthropogenic emissions were set based on Emissions Database for Global Atmospheric Research inventory data. The simulation period in our study is 9–30 May 2019, and we set the first 7 days of simulation as a model spin-up for the dust case in our research.

In this study, we calculated the vertical sub-grid-scale turbulent flux caused by vortex transport using the boundary layer scheme of Yonsei University, and combined the Monin-Obukhov surface scheme with the Noah land surface scheme (Liu et al., 2016). Morrison's two-moment microphysics scheme and Grell-Freitas integration scheme are used to simulate cloud microphysics and convection processes. We used GOCART scheme (Ginoux et al., 2001) to simulate and calculate dust emissions, and adopted four-dimensional assimilation method in the process of model simulation to reduce meteorological simulation errors. The mean bias is 1.30 m s^{-1}, which is within the acceptable range (Kumar et al., 2014). The model simulation results were adopted to determine the consistency between the increase of Chl-a concentration and dust deposition in the study area.

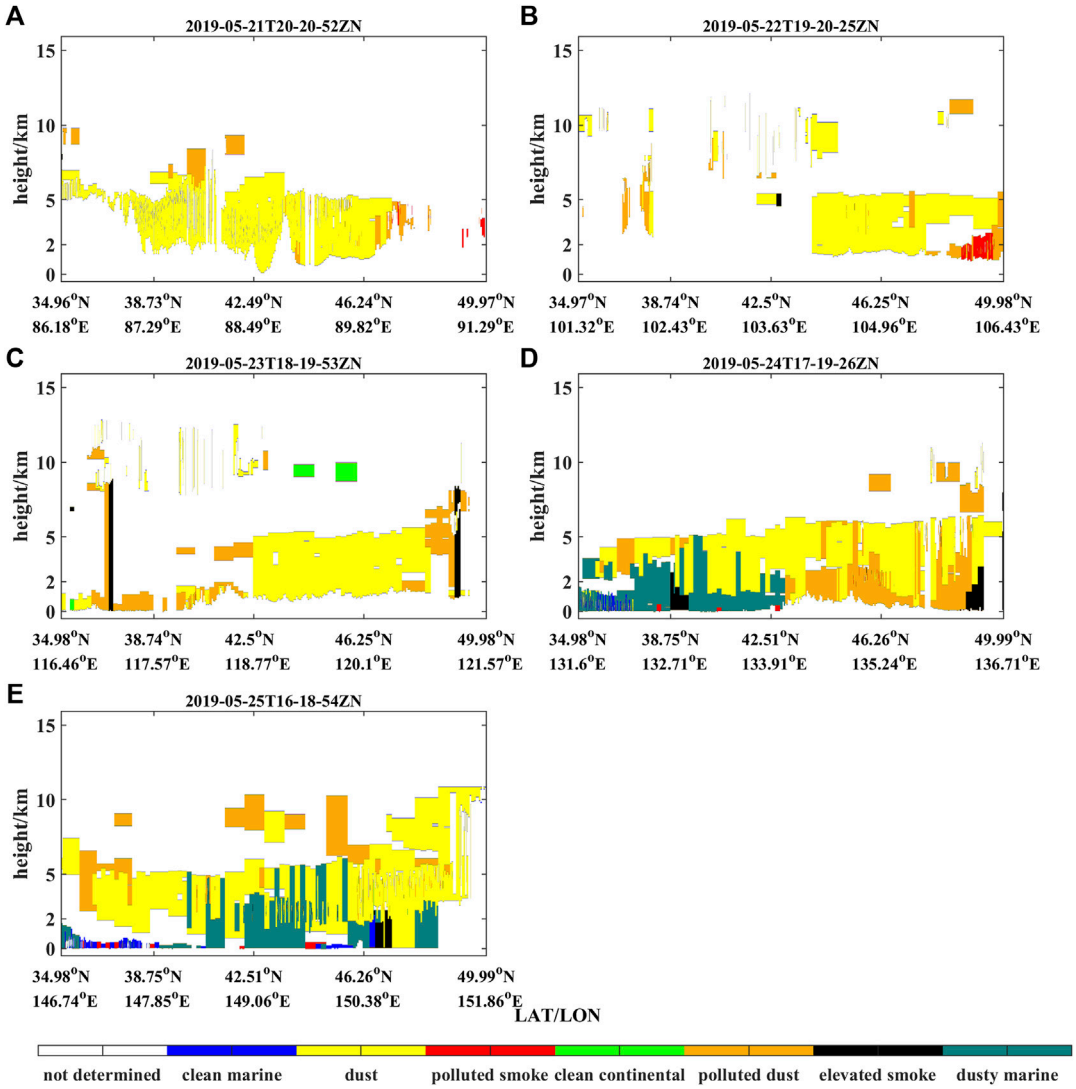

FIGURE 3 | Vertical profiles of aerosol on 21 **(A)**, 22 **(B)**, 23**(C)**, 24 **(D),** and 25 **(E)** May 2019 provided by CALIPSO VFM products.

3 RESULTS AND DISCUSSION

3.1 Dust Aerosol Transport

Aerosol optical depth (AOD) can present the spatial distribution of atmospheric aerosol, especially dust (Liu et al., 2013; Zhang et al., 2019). **Figure 2** shows the distribution of daily AOD observed by Himawari-8 satellite, we can see that there is a severe aerosol event in the Taklimakan Desert beginning on 21 May 2019 according to the AOD data (shading areas in **Figure 2**), aerosol layers with AOD greater than 0.8 move eastward with the wind according to the distribution of wind fields at 500 hPa (black arrow in **Figure 2**), passing over the Sea of Japan, and reach the northwest Pacific Ocean on 24 and 25 May as shown in **Figure 2**. During the whole period, the maximum value of AOD can reach 1.2 observed by the Himawari-8 satellite.

Figure 3 is the vertical distributions of aerosol types obtained by CALIPSO VFM products during 21–25 May 2019, its scan trajectory during this process is shown in **Figure 4**. As shown in **Figure 3**, dust aerosols distribute from 1 km to about 7 km over the dust source region (Taklimakan Desert). In the downwind region, dust aerosols distribute from 1 km to about 6 km. When dust aerosols transport to the Pacific Ocean, they distribute from 0 km to about 10 km. Based on the CALIPSO VFM results, dust aerosols account for more than 85% of all aerosols during 21–25 May 2019. Thus, dust particles are the dominant aerosol type in the whole process, the values of AOD in **Figure 2** can be related to dust concentration in the atmosphere.

A forward trajectory analysis simulated by the HYSPLIT model is conducted to find the transport paths of dust aerosols during 21–25 May 2019. The duration for the model is 93-h, and the initial height for the case is 1.5, 2.5, and 3.5 km

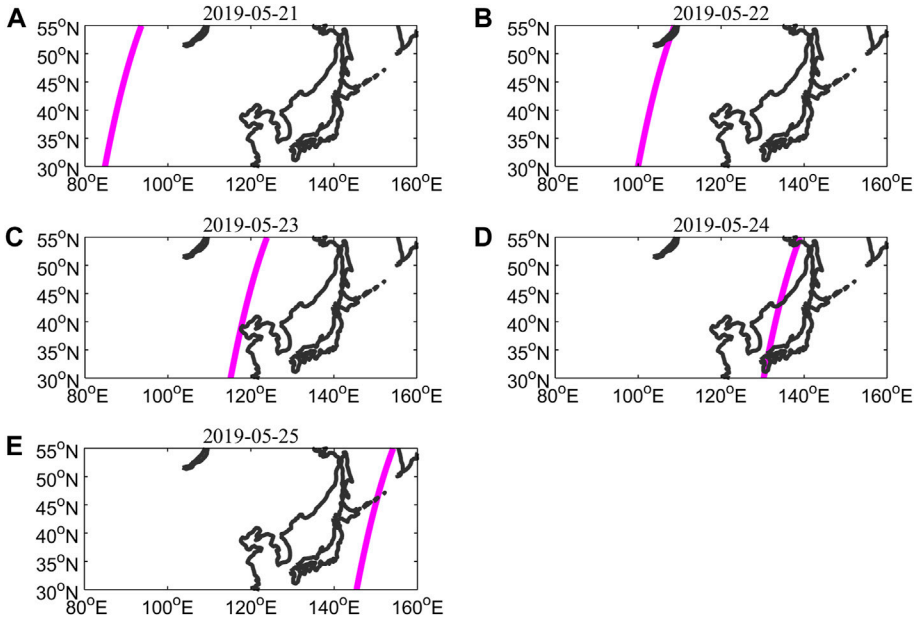

FIGURE 4 | Trajectories of CALIPSO satellite (magenta line) on 21 **(A)**, 22 **(B)**, 23 **(C)**, 24 **(D),** and 25 **(E)** May 2019 provided by CALIPSO VFM products.

where dust aerosols are observed on 21 May according to the results in **Figure 3A**. The CDC1 is used as the meteorological input at 20:00 UTC on 21 May. The model simulation shows that dust aerosols originate from the Taklimakan Desert on 21 May 2019, then spread eastward, passed over the east of China, and reach the western part of the Pacific Ocean on 24 and 25 May 2019, consistent with the results in **Figure 2**.

Meteorological condition plays an important role in dust aerosol horizontal transport (Uno et al., 2009). **Figures 6A–E** presents the potential height field and temperature field at 500 hPa during 21–25 May 2019. We can see that there is a strong cold advection at the height of 500 hPa, which is conducive for sweeping dust aerosol from the northwestern region across Northeast China, and reaching the Pacific Ocean.

To sum up, based on the results in **Figures 2**,**3**, **Figures 5**,**6**, dust aerosols rise in the Taklimakan Desert, moving eastward at high altitudes under the effect of the westerly winds, passing over the downwind regions, and deposition in the Pacific Ocean.

3.2 Effects of Dust Aerosol Deposition on Ocean Primary Productivity

The spatial distribution of Chl-a concentrations from 24–30 May 2019 is studied with the observations from the Himawari-8 satellite which is in geostationary earth orbit (GEO). The satellite in GEO can provide high temporal resolution of Chl-a concentrations compared to polar orbit satellites. **Figure 7** shows the spatial distribution of Chl-a concentrations from 24–30 May 2019. It is obvious that Chl-a concentrations massively increase on 26 May due to the deposition of dust, and lasted until 28 May. However, there are some missing values of Chl-a concentrations because of the existence of clouds, because Himawari-8 observes the Chl-a concentrations in the visible band. To better investigate the dust aerosol's effect on Chl-a concentrations, we define a relatively small region (45–50°N, 145–155°E) as shown in **Figure 7** (Black box) with data relatively integrity as the research region.

The seawater velocity represents the horizontal movement of the ocean. To investigate the oceanic transport effect on the position of deposition dust aerosols, we use seawater velocity derived from the GOFS3.1 product to calculate the longitudinal and latitudinal displacement for the research region. **Figure 8** shows the eastward and northward seawater velocity in the surface ocean (depth <100 m) from 12 May to 4 June 2019. The positive value means seawater flows eastward or northward. The total longitudinal and latitudinal displacement from 24 May to 4 June is about 80 km based on the results in **Figure 8**, respectively. Thus, the change in longitude and latitude caused by seawater movement is less than 6.7 km/day. However, the area for the research region is roughly 550 km (longitude length) and 750 km (latitudinal length). Therefore, we conclude that the movement range of dust deposition carried by seawater movement is far smaller than that of the research region, so we assume that dust deposition remains in the research region and provide nutrients for phytoplankton.

Besides nutrient input present in the aerosols, PAR and SST also can impact the Chl-a concentrations (Luo et al., 2020; Wang et al., 2021). To evaluate those factors' effect on Chl-a concentrations, the variation of the daily mean values of those factors (such as PAR, dust deposition amount, SST) are drawn over the research region using the Himawari-8 data, ERA-5 datasets, and the merged L3 global ocean color products during 24 May to 4 June 2019 (**Figure 9**).

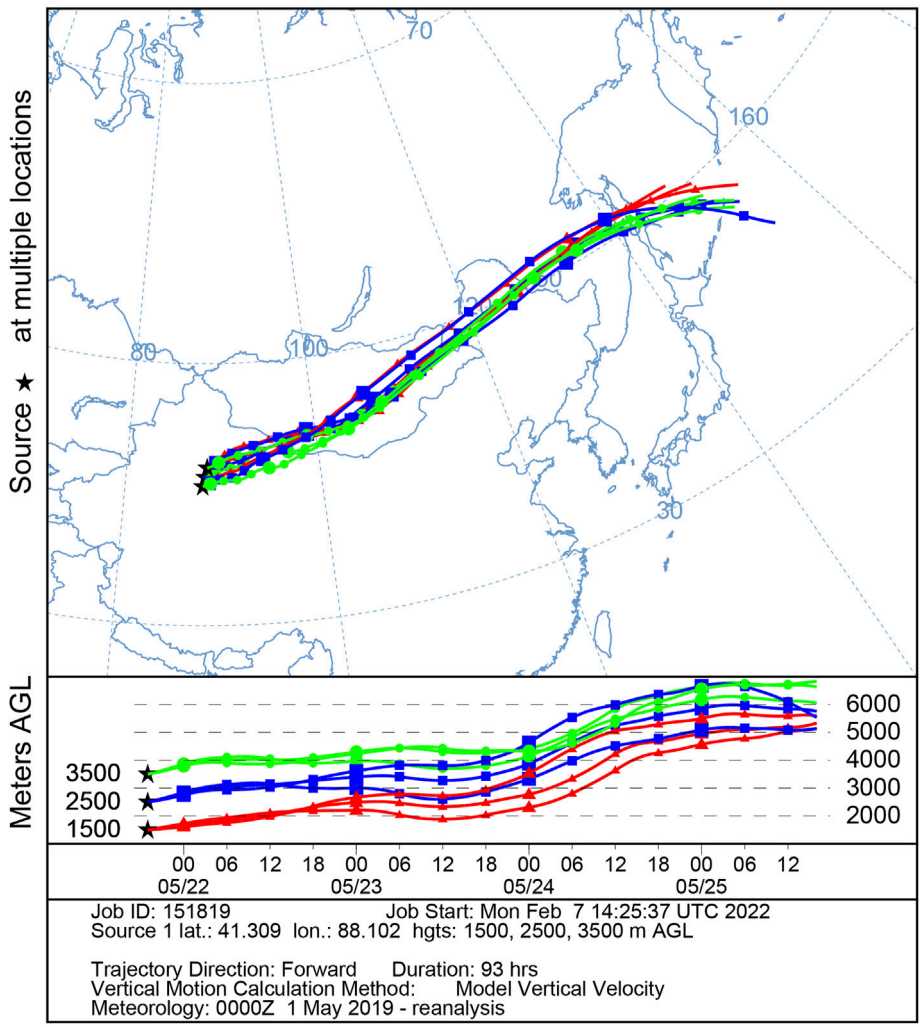

FIGURE 5 | The particle forward trajectories (93 h) beginning at 20:00 UTC 21 May 2019 by CDC1 meteorological data using the online HYSPLIT model. The begin point is set in Taklimakan Desert at 40.596°N/87.8723°E, 41.309°N/88.102°E and 42.023°N/88.336°E position. The beginning point height is set to 1.5 km (red), 2.5 km (blue), and 3.5 km (green).

In **Figure 9**, the dotted lines are the 5-year averaged values for Chl-a concentrations (black) and POC (blue) over the same period in the research region. The WRF-Chem model simulate that the average dust deposition is 179.79 μg m^{-2} (**Table 1**) on 24 May, and the simulation results began to decrease on 25 May (463.84 μg m^{-2}), which was consistent with the change of Himawari-8 AOD from 24 May (0.22) to 25 May (0.36). We also can see that the Chl-a concentrations increased on 26 May after the dust deposition on 24 May as shown in **Figure 9**. The response time is 2 days, which is similar to the iron enrichment experiment (Tsuda et al., 2003). However, dust aerosols continuously deposit into the ocean from 24 to 30 May, and the Chl-a concentrations only increase from 26 to 28 May as shown in **Figure 9** and **Table. 1**. One reason for this phenomenon is the missing observation of Chl-a concentrations due to clouds and other factors on 29 May, another reason is that the nutrient needed by the phytoplankton is oversaturated, so Chl-a concentrations do not increase after 30 May. We also can see that Chl-a concentrations have two peaks during this period, this is due to the missing values of Chl-a concentrations. Furthermore, during the response process, Chl-a concentrations increase from 0.56 mg m^{-3} (25 May) to 1.54 mg m^{-3} (26 May), which is an increase of nearly 175%. Moreover, the Chl-a concentrations (1.54 mg m^{-3}) are 256% larger than their mean values during the same periods from 2016 to 2019 (0.433 mg m^{-3}). After 29 May, the values of Chl-a concentrations decrease to less than 0.45 mg m^{-3}.

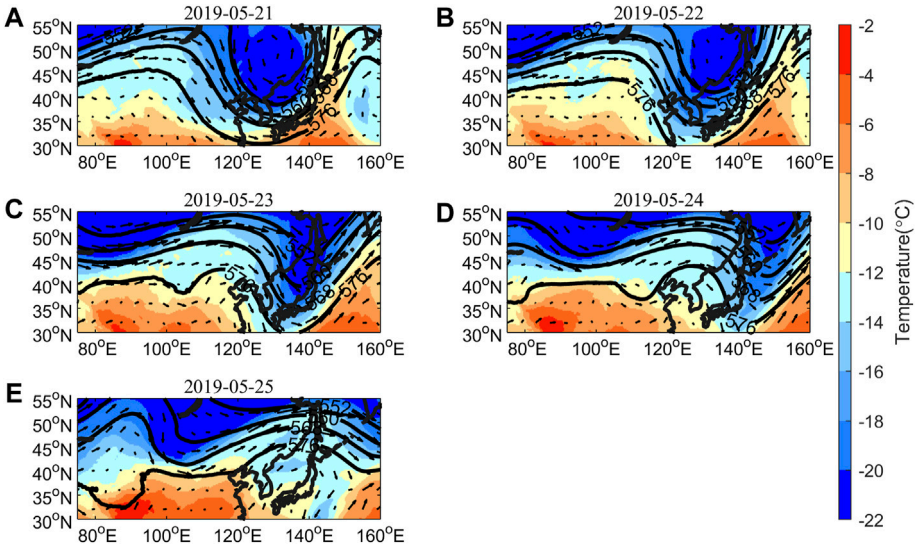

FIGURE 6 | The potential height field (black line), temperature field, and wind field at 500 hPa on 21 **(A)**, 22 **(B)**, 23 **(C)**, 24 **(D),** and 25 **(E)** May 2019 as observed by ERA5.

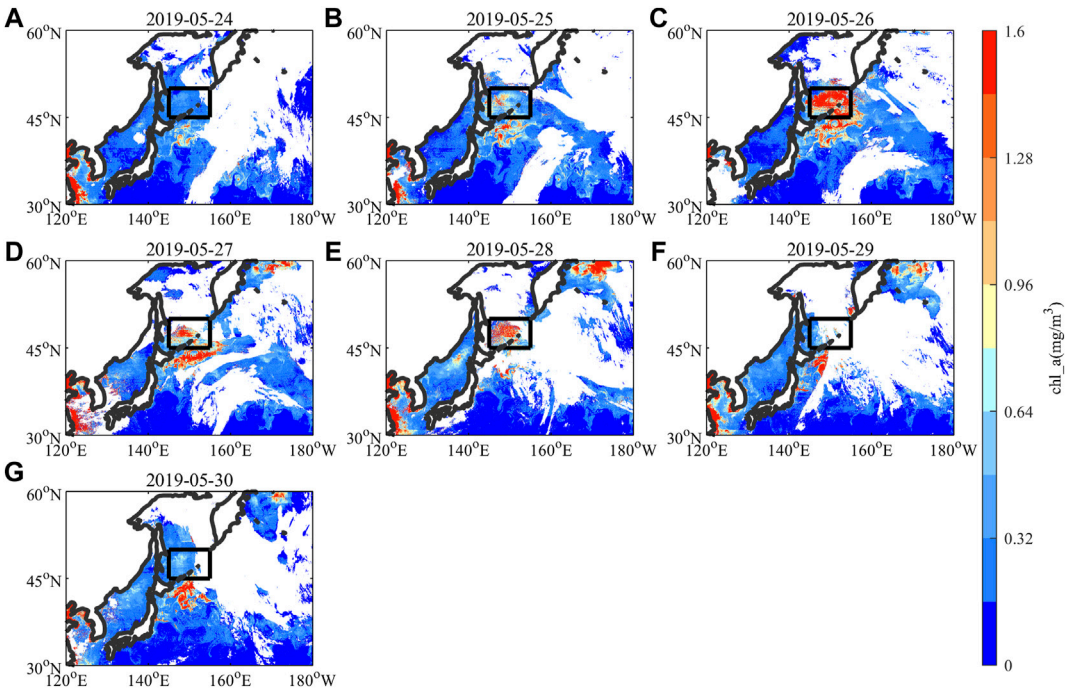

FIGURE 7 | Spatial pattern of daily mean Chlorophyll-a concentration on 24 **(A)**, 25 **(B)**, 26 **(C)**, 27 **(D)**, 28 **(E)**, 29 **(F),** and 30 **(G)** May 2019.

Suitable SST is also helpful in increasing Chl-a concentrations. In our case, the mean values of SST are 4.13, 4.01, 3.78, and 3.97 during 25–28 May. It is noted that SST shows a downward trend during Chl-a concentrations increase, the decrease in SST could easily be associated with oceanic upwelling, which can bring nutrients to the surface ocean. To investigate the possible contribution of upwelling in this case, we analyzed the upwelling velocity from SODA 3.4. Our results indicate that the mean value of upwelling velocity is about 0.053 m/d from 24 May to 28 May, which is lower than the mean value of upwelling velocity (0.085 m/d) in May 2019. Thus, the nutrient provided by the rising movement of seawater is lower

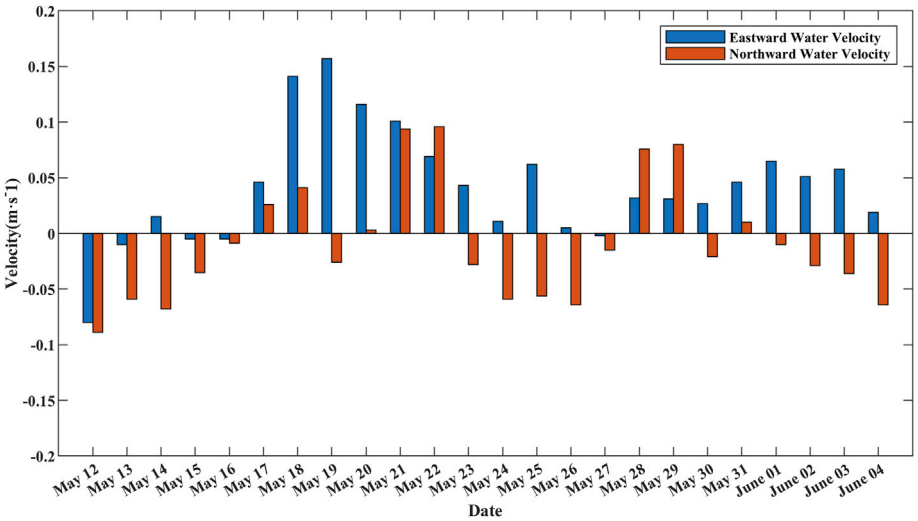

FIGURE 8 | The eastward and northward seawater velocity during 12 May to 4 June 2019.

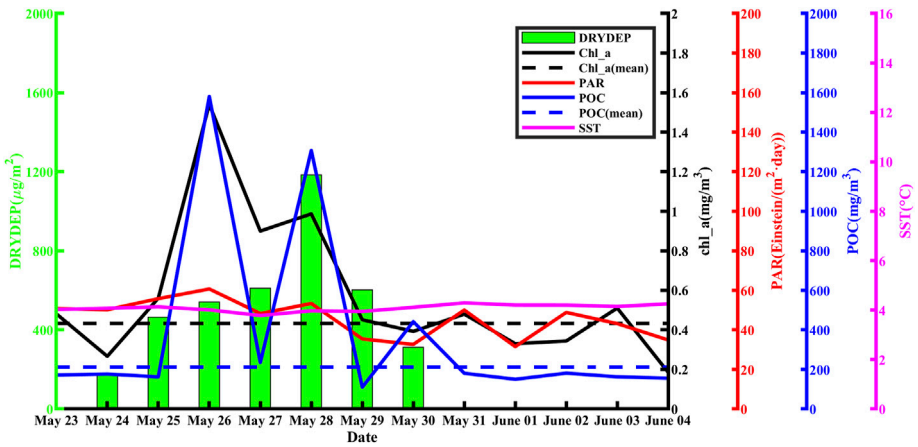

FIGURE 9 | Temporal variation of Chl-a concentrations (black), SST (magenta), PAR (red) and POC (blue) from 24 May to 4 June 2019. Dotted lines illustrate the averaged value in this period over a 5-year period in the research region with colors representing different variables. The green bar is the dust deposition simulated by the WRF-Chem model.

TABLE 1 | The values of Chl-a concentrations, POC, SST, PAR, and dust deposition as simulated by WRF-Chem model during 24–30 May.

Data	Chl-a Concentrations ($mg \cdot m^{-3}$)	POC ($mg \cdot m^{-3}$)	SST (°C)	PAR (Einstein/($m^2 \cdot day$))	Dust Deposition ($\mu g/m^2$)	AOD
24 May	0.27	175.69	4.08	50.19	179.79	0.22
25 May	0.56	162.36	4.13	55.76	463.84	0.36
26 May	1.54	1580.52	4.01	60.66	540.15	0.52
27 May	0.90	234.89	3.78	48.29	611.16	0.49
28 May	0.99	1307.11	3.97	53.34	1184.15	0.58
29 May	0.45	110.00	3.95	35.45	602.45	0.53
30 May	0.39	441.85	4.11	32.67	311.53	0.23

than the mean values of nutrients in May 2019. Therefore, both the nutrients transported by oceanic upwelling and SST are not the main factors that lead to the increase in Chl-a concentrations.

Iwasaki (2020) indicate that typhoon also can directly or indirectly affect the Chl-a concentration in the Pacific Ocean through precipitation and strong sea surface winds. However, there was no typhoon process during May 21 to 25 May 2019 as shown in **Figure 6**, thus typhoon is not a factor that lead to the change in Chl-a concentrations for this case.

On the other hand, PAR presents a slight increase trend on 26 May compared with the value on 25 May, then shows a decreasing trend during 26 May to 30 May. During this period, the maximum value of Chl-a concentrations occur on 26 May, which means that dust deposition and PAR both promote the growth of phytoplankton on 26 May. However, the value of PAR on 25 May (55.76 Einstein/(m^2·day)) is larger than that on 27 May (48.29 Einstein/(m^2·day)), while the value of Chl-a concentrations on 25 May (0.56 mg m^{-3}) is smaller than that on 27 May (0.90 mg m^{-3}) as shown in **Table. 1**, suggesting PAR is not the main factor that leads to the increase in Chl-a concentrations for this case. To sum up, based on the results discussed above, dust aerosol deposition could be the major reason for the increase in Chl-a concentrations in this case.

When dust deposition stimulates the growth of phytoplankton, it can trigger ocean biological pumps, leading to more absorption of CO_2 from the atmosphere to the ocean (Pan et al., 2011). In this paper, we use the variations in POC to assess marine biological pumps caused by dust aerosol deposition. As shown in **Figure 9**, POC shows a similar trend to those of Chl-a concentrations. the POC increased on 26 May after the dust deposition on 24 May. The response time is 2 days, which is similar to the iron enrichment experiment (Tsuda et al., 2003). In addition, the POC has two peaks during this period, which is consistent with Chl-a concentrations. During the response process, POC increased from 162.36 mg m^{-3} (25 May) to 1,580.52 mg m^{-3} (26 May), increasing nearly 873%. Moreover, the value of POC (1,580.52 mg m^{-3}) was 644% higher than its mean value in this period from 2016 to 2019 (212.25 mg m^{-3}).

4 CONCLUSIONS AND PERSPECTIVES

Dust aerosols settling into the ocean can promote marine phytoplankton by supplying nutrients, leading to more absorption of CO_2 from the atmosphere to the ocean, and even have an influence on planetary climate.

This paper research a dust episode during 21–25 May 2019, analyzes the transport and deposition of dust aerosols, quantify dust aerosol deposition on marine primary productivity by using multi-sensor satellite data and the WRF-Chem model. Model simulation and observation show that dust aerosol originated from Taklimakan Desert passing over the eastern of China and reach the research region during 24–30 May 2019, dust deposition led to an increase in Chl-a concentrations and POC after 2 days, Chl-a concentrations increase 256% compared with the 5-year average values, POC shows the similar trend as the Chl-a concentrations which increase 644% compared with the 5-year average values.

The previous studies mainly use polar orbit satellite products to study the change of Chl-a concentration due to dust aerosol deposition (Tan et al., 2016; Luo et al., 2020), so the missing observations are relatively more compared with geostationary orbit satellite products. In our study, we use the Himawari-8 satellite which has higher temporal, spatial, and spectral resolution than previous satellites in geostationary orbit, so the products can better reflect the change in Chl-a concentration due to dust deposition. However, the case in our study is a comprehensive demonstration that dust aerosol's deposition leads to the growth of phytoplankton which in turn triggers marine biological pump action. In the future work, we will use long-term data including observation over the ocean to investigate dust aerosol's effect on marine primary productivity.

DATA AVAILABILITY STATEMENT

The raw data supporting the conclusions of this article will be made available by the authors, without undue reservation.

AUTHOR CONTRIBUTIONS

WW and YH designed and write the paper. ZH and SH contributed to data processing and model simulation. LS and YZ contributed to the review and edit.

FUNDING

This work is jointly supported by the National Natural Science Foundation of China (Nos. 41875174, 41505013). We acknowledge NASA for providing the CALIPSO data, Japan Meteorological Agency for providing Himawari-8 data, and NASA and the ESA for providing Merged Ocean Color.

REFERENCES

Bessho, K., Date, K., Hayashi, M., Ikeda, A., Imai, T., Inoue, H., et al. (2016). An Introduction to Himawari-8/9— Japan’s New-Generation Geostationary Meteorological Satellites. *J. Meteorological Soc. Jpn.* 94, 151–183. doi:10.2151/jmsj.2016-009

Bishop, J. K. B., Davis, R. E., and Sherman, J. T. (2002). Robotic Observations of Dust Storm Enhancement of Carbon Biomass in the North Pacific. *Science* 298, 817–821. doi:10.1126/science.1074961

Chen, S., Huang, J., Kang, L., Wang, H., Ma, X., He, Y., et al. (2017). Emission, Transport, and Radiative Effects of Mineral Dust from the Taklimakan and Gobi Deserts: Comparison of Measurements and Model Results. *Atmos. Chem. Phys.* 17, 2401–2421. doi:10.5194/acp-17-2401-2017

Emerson, D. (2019). Biogenic Iron Dust: A Novel Approach to Ocean Iron Fertilization as A Means of Large Scale Removal of Carbon Dioxide from the Atmosphere. *Front. Mar. Sci.* 6, 22. doi:10.3389/fmars.2019.00022

Frost, B. W., and Morel, F. M. (1991). The Role of Grazing in Nutrient-Rich Areas of the Open Sea. *Limnol. Oceanogr.* 36, 1616–1630. doi:10.4319/lo.1991.36.8.1616

Ginoux, P., Chin, M., Tegen, I., Prospero, J. M., Holben, B., Dubovik, O., et al. (2001). Sources and Distributions of Dust Aerosols Simulated with the GOCART Model. *J. Geophys. Res.* 106, 20255–20273. doi:10.1029/2000JD000053

Hsu, S.-C., Liu, S. C., Arimoto, R., Liu, T.-H., Huang, Y.-T., Tsai, F., et al. (2009). Dust Deposition to the East China Sea and its Biogeochemical Implications. *J. Geophys. Res.* 114, D15304. doi:10.1029/2008JD011223

Hu, Z., Huang, J., Zhao, C., Ma, Y., Jin, Q., Qian, Y., et al. (2019). Trans-Pacific Transport and Evolution of Aerosols: Spatiotemporal Characteristics and Source Contributions. *Atmos. Chem. Phys.* 19, 12709–12730. doi:10.5194/acp-19-12709-2019

Hu, Z., Huang, J., Zhao, C., Jin, Q., Ma, Y., and Yang, B. (2020). Modeling Dust Sources, Transport, and Radiative Effects at Different Altitudes over the Tibetan Plateau. *Atmos. Chem. Phys.* 20, 1507–1529. doi:10.5194/acp-20-1507-2020

Hu, Z., Jin, Q., Ma, Y., Pu, B., Ji, Z., Wang, Y., et al. (2021). Temporal Evolution of Aerosols and Their Extreme Events in Polluted Asian Regions during Terra's 20-year Observations. *Remote Sens. Environ.* 263, 112541. doi:10.1016/j.rse.2021.112541

Huang, J., Wang, T., Wang, W., Li, Z., and Yan, H. (2014). Climate Effects of Dust Aerosols over East Asian Arid and Semiarid Regions. *J. Geophys. Res. Atmos.* 119, 11398–11416. doi:10.1002/2014JD021796

Iwasaki, S. (2020). Daily Variation of Chlorophyll-A Concentration Increased by Typhoon Activity. *Remote Sens.* 12, 1259. doi:10.3390/rs12081259

Kumar, R., Barth, M. C., Pfister, G. G., Naja, M., and Brasseur, G. P. (2014). WRF-chem Simulations of a Typical Pre-monsoon Dust Storm in Northern India: Influences on Aerosol Optical Properties and Radiation Budget. *Atmos. Chem. Phys.* 14, 2431–2446. doi:10.5194/acp-14-2431-2014

Li, J., Huang, J., Stamnes, K., Wang, T., Lv, Q., and Jin, H. (2015). A Global Survey of Cloud Overlap Based on CALIPSO and CloudSat Measurements. *Atmos. Chem. Phys.* 15, 519–536. doi:10.5194/acp-15-519-2015

Liu, L., Huang, X., Ding, A., and Fu, C. (2016). Dust-Induced Radiative Feedbacks in North China: A Dust Storm Episode Modeling Study Using WRF-Chem. *Atmos. Environ.* 129, 43–54. doi:10.1016/j.atmosenv.2016.01.019

Liu, X. G., Li, J., Qu, Y., Han, T., Hou, L., Gu, J., et al. (2013). Formation and Evolution Mechanism of Regional Haze: A Case Study in the Megacity Beijing, China. *Atmos. Chem. Phys.* 13, 4501–4514. doi:10.5194/acp-13-4501-2013

Luo, C., Wang, W., Sheng, L., Zhou, Y., Hu, Z., Qu, W., et al. (2020). Influence of Polluted Dust on Chlorophyll-A Concentration and Particulate Organic Carbon in the Subarctic North Pacific Ocean Based on Satellite Observation and the WRF-Chem Simulation. *Atmos. Res.* 236, 104812. doi:10.1016/j.atmosres.2019.104812

Mahowald, N. M., Kloster, S., Engelstaedter, S., Moore, J. K., Mukhopadhyay, S., McConnell, J. R., et al. (2010). Observed 20th Century Desert Dust Variability: Impact on Climate and Biogeochemistry. *Atmos. Chem. Phys.* 10, 10875–10893. doi:10.5194/acp-10-10875-2010

Martin, J. H., Gordon, M., and Fitzwater, S. E. (1991). The Case for Iron. *Limnol. Oceanogr.* 36, 1793–1802. doi:10.4319/lo.1991.36.8.1793

Moore, J. K., and Braucher, O. (2008). Sedimentary and Mineral Dust Sources of Dissolved Iron to the World Ocean. *Biogeosciences* 5, 631–656. doi:10.5194/bg-5-631-2008

Murakami, H. (2016). Ocean Color Estimation by Himawari-8/AHI. *Proc. SPIE* 9878, 987810. doi:10.1117/12.2225422

Pan, A., Pourziaei, B., and Huang, H. (2011). Effect of Ocean Iron Fertilization on the Phytoplankton Biological Carbon Pump. *Adv. Appl. Math. Mech.* 3, 52–64. doi:10.4208/aamm.10-m1023

She, L., Xue, Y., Yang, X., Guang, J., Li, Y., Che, Y., et al. (2018). Dust Detection and Intensity Estimation Using Himawari-8/AHI Observation. *Remote Sens.* 10, 490. doi:10.3390/rs10040490

Sokolik, I. N., and Toon, O. B. (1996). Direct Radiative Forcing by Anthropogenic Airborne Mineral Aerosols. *Nature* 381, 681–683. doi:10.1038/381681a0

Tan, S.-C., and Shi, G.-Y. (2012). Transport of a Severe Dust Storm in March 2007 and Impacts on Chlorophyll a Concentration in the Yellow Sea. *SOLA* 8, 85–89. doi:10.2151/sola.2012-022

Tan, S.-C., Shi, G.-Y., Shi, J.-H., Gao, H.-W., and Yao, X. (2011). Correlation of Asian Dust with Chlorophyll and Primary Productivity in the Coastal Seas of China during the Period from 1998 to 2008. *J. Geophys. Res.* 116, G02029. doi:10.1029/2010JG00145610.1029/2010jg001456

Tan, S., Li, J., Gao, H., Wang, H., Che, H., and Chen, B. (2016). Satellite-Observed Transport of Dust to the East China Sea and the North Pacific Subtropical Gyre: Contribution of Dust to the Increase in Chlorophyll during Spring 2010. *Atmosphere* 7, 152. doi:10.3390/atmos7110152

Tao, M., Wang, J., Li, R., Chen, L., Xu, X., Wang, L., et al. (2020). Characterization of Aerosol Type over East Asia by 4.4 Km MISR Product: First Insight and General Performance. *J. Geophys. Res. Atmos.* 125, e2019JD031909. doi:10.1029/2019JD031909

Tsuda, A., Takeda, S., Saito, H., Nishioka, J., Nojiri, Y., Kudo, I., et al. (2003). A Mesoscale Iron Enrichment in the Western Subarctic Pacific Induces a Large Centric Diatom Bloom. *Science* 300, 958–961. doi:10.1126/science.1082000

Uno, I., Eguchi, K., Yumimoto, K., Takemura, T., Shimizu, A., Uematsu, M., et al. (2009). Asian Dust Transported One Full Circuit Around the Globe. *Nat. Geosci.* 2, 557–560. doi:10.1038/ngeo583

Varenik, A. V., and Kalinskaya, D. V. (2021). The Effect of Dust Transport on the Concentration of Chlorophyll-A in the Surface Layer of the Black Sea. *Appl. Sci.* 11, 4692. doi:10.3390/app11104692

Wang, W., Huang, J., Minnis, P., Hu, Y., Li, J., Huang, Z., et al. (2010). Dusty Cloud Properties and Radiative Forcing over Dust Source and Downwind Regions Derived from A-Train Data during the Pacific Dust Experiment. *J. Geophys. Res.* 115, D00H35. doi:10.1029/2010JD014109

Wang, W., Huang, J., Zhou, T., Bi, J., Lin, L., Chen, Y., et al. (2013). Estimation of Radiative Effect of a Heavy Dust Storm over Northwest China Using Fu-Liou Model and Ground Measurements. *J. Quantitative Spectrosc. Radiat. Transf.* 122, 114–126. doi:10.1016/j.jqsrt.2012.10.018

Wang, W., Sheng, L., Jin, H., and Han, Y. (2015). Dust Aerosol Effects on Cirrus and Altocumulus Clouds in Northwest China. *J. Meteorol. Res.* 29, 793–805. doi:10.1007/s13351-015-4116-9

Wang, W., Luo, C., Sheng, L., Zhao, C., Zhou, Y., and Chen, Y. (2021). Effects of Biomass Burning on Chlorophyll-A Concentration and Particulate Organic Carbon in the Subarctic North Pacific Ocean Based on Satellite Observations and WRF-Chem Model Simulations: A Case Study. *Atmos. Res.* 254, 105526. doi:10.1016/j.atmosres.2021.105526

Yue, X., Wang, H., Wang, Z., and Fan, K. (2009). Simulation of Dust Aerosol Radiative Feedback Using the Global Transport Model of Dust: 1. Dust Cycle and Validation. *J. Geophys. Res.* 114, D10202. doi:10.1029/2008JD010995

Zhang, Z., Fan, M., Wu, W., Wang, Z., Tao, M., Wei, J., et al. (2019). A Simplified Aerosol Retrieval Algorithm for Himawari-8 Advanced Himawari Imager over Beijing. *Atmos. Environ.* 199, 127–135. doi:10.1016/j.atmosenv.2018.11.023

Zhao, L., Wang, W., Hao, T., Qu, W., Sheng, L., Luo, C., et al. (2020). The Autumn Haze-Fog Episode Enhanced by the Transport of Dust Aerosols in the Tianjin Area. *Atmos. Environ.* 237, 117669. doi:10.1016/j.atmosenv.2020.117669

Conflict of Interest: The authors declare that the research was conducted in the absence of any commercial or financial relationships that could be construed as a potential conflict of interest.

frontiers | Frontiers in Environmental Science

ORIGINAL RESEARCH
published: 23 May 2022
doi: 10.3389/fenvs.2022.839691

Influence of Dust Aerosols on Snow Cover Over the Tibetan Plateau

Dan Zhao, Siyu Chen, Yu Chen, Yongqi Gong, Gaotong Lou, Shanling Cheng and Hongru Bi*

Key Laboratory for Semi-Arid Climate Change of the Ministry of Education, Lanzhou University, Lanzhou, China

Dust in the atmosphere and snow on the Tibetan Plateau (TP) remarkably influence the Asian climate, which can influence snow cover by changing radiative forcing. In this study, we investigated the spatial and temporal distributions of dust and snow cover over the TP from 2009 to 2018 and estimated the relative contributions of atmospheric dust and dust-on-snow to the change in snow cover over the northern TP through the use of reanalysis datasets and satellite retrievals. The results show that the high and low centers of aerosol and dust aerosol optical depth (AOD) are roughly similar. Dust concentrations over the TP generally decrease from north to south and from west to east, showing decreasing trends in the winter half-year (December to May). The correlation coefficients between the dust concentration and snow cover over the northern TP are –0.6 in spring. Dust in the atmosphere and on snow over the TP could significantly influence snow cover by changing the radiative forcing, and the influence of dust deposited on snow is greater than that in the atmosphere. Atmospheric dust reduces the surface net solar radiation by –3.84 W m^{-2} by absorbing shortwave radiation, decreasing the surface temperature by –2.27°C, and finally increasing the snow cover by 1.04%. However, dust deposited on snow can decrease the surface albedo by –0.004 by reducing the surface optical properties, induce surface warming at 0.42°C, and reduce snow cover by –2.00% by rapid snowmelt in the northern TP.

Keywords: dust aerosol, Tibetan Plateau, aerosol radiative forcing, snow albedo, snow darkening, surface radiation

OPEN ACCESS

Edited by:
Yang Gao,
Ocean University of China, China

Reviewed by:
Xianwen Jing,
Hubei Normal University, China
Jiandong Wang,
Nanjing University of Information Science and Technology, China

****Correspondence:***
Siyu Chen
chensiyu@lzu.edu.cn

Specialty section:
This article was submitted to Atmosphere and Climate, a section of the journal Frontiers in Environmental Science

Received: *20 December 2021*
Accepted: *19 April 2022*
Published: *23 May 2022*

Citation:
Zhao D, Chen S, Chen Y, Gong Y, Lou G, Cheng S and Bi H (2022) Influence of Dust Aerosols on Snow Cover Over the Tibetan Plateau. Front. Environ. Sci. 10:839691. doi: 10.3389/fenvs.2022.839691

1 INTRODUCTION

As the "sensitive area" of climate change (Wu et al., 2005; Xu et al., 2015a), snow/ice is the largest seasonal variable of land cover over the Tibetan Plateau (TP) (Smith and Bookhagen, 2018; Lievens et al., 2019). The snow and ice systems over the TP are very fragile, have experienced widespread melting, and retreat in the last 20 years (Kang et al., 2015), besides the extent of ablation retreat being still gradually increasing (Yao et al., 2012). In addition, the enhanced warming over the TP has also caused widespread concern (Wu et al., 2017; Zhou and Zheng, 2021). The warming rate over the TP in the last 50 years has reached 0.3–0.4°C/decade, which is twice the global average of the same period (Shen et al., 2015). The Intergovernmental Panel on Climate Change (IPCC) (2021) pointed out that even if global warming was to be controlled within 1.5°C by the end of this century, TP warming is likely to exceed 2.1°C (Duan and Xiao, 2015). The surface albedo of glaciers over the TP has declined significantly in recent decades (Liu and Chen, 2000; Wang et al., 2014; Zhang et al., 2021). In addition to the notably rapid warming over the TP (Qin et al., 2006; Wang et al., 2008; Kang et al., 2010; Bolch et al., 2012), factors such as land use change, water vapor feedback, cloud properties, and the radiation forcing of light-absorbing aerosols (LAAs) can also significantly influence warming (Kang et al., 2000; Flanner et al., 2009; Xu et al., 2009).

Dust aerosols are mainly emitted from drylands through wind erosion (Chen et al., 2014; Huang et al., 2016; Wang et al., 2012; Bi et al., 2016). The atmosphere, hydrosphere, and cryosphere are closely related to the physical process of dust aerosols, including dust emission, transport, and wet/dry deposition (Niemand et al., 2012). Through direct and indirect effects, dust has a significant regulating effect on the Earth's radiative budget and hydrological cycle. Due to human activities, the aggravation of desertification, and vegetation degradation in recent years, the TP has become a new source of dust emissions that cannot be ignored (Ma et al., 2014). Moreover, sufficient evidence has proved that in addition to local dust emissions, a large quantity of dust particles over the TP come from external transport (Mao et al., 2019). Feng et al. (2020) found that the atmospheric dust in the top of the troposphere above the TP in spring of the 2000s increased by 34% compared with that in the 1990s, which is related to increasing dust aerosols from East Asia, South Asia, and the Middle East since the 2000s. Moreover, the results of the MISR retrievals showed that the correlation between the TP and Taklimakan Desert (TD) aerosol optical depth (AOD) is lower in spring than in summer (Xia et al., 2008). Chen et al. (2013), Chen et al. (2014) and Yuan et al. (2019) investigated the dynamic and thermal transport mechanisms of dust aerosols from the TD to the northern TP. By the weakening and northward movement of the East Asian westerly jet and the increase in surface-sensible heat over the TD in summer, abundant TD dust particles are transported to the northern slope of the TP. These results were also supported by ice cores and aerosol products from the total ozone mapping spectrometer (TOMS), as well as the coupled model intercomparison project (Phase 6) (CMIP6) and community earth system model (CESM) (Feng et al., 2020). As a crucial natural aerosol, the TP dust deposited on ice and snow is much larger than black carbon (BC). Dust can lead to significant climate effects by influencing slight initial changes in snow albedo, with rapid subsequent adjustment and feedback (Cong et al., 2015; Ji et al., 2016; Xie et al., 2018; Shi et al., 2019). The magnitude of dust deposition and its spatial distributions over the TP diverge from BC (Flanner et al., 2009), which causes the climate effect of dust-on-snow in spring to be more complex. For example, dust deposited on snow and ice could reduce snow depths by 5–25 mm in the Himalayas and western TP (Zhang et al., 2017). Qu et al. (2014) found that dust is an important factor in Zhadang Glacier melting, with an average radiative forcing weakened by dust-on-snow of 1.1–8.6 W m^{-2}. Dust deposited on snow in the Himalaya–TP also increases the surface temperature and the lower atmospheric temperature over the TP and strengthens the southwest wind in the lower layer through reducing snow albedo during the premonsoon, which, in turn, increases dust over the Indo-Gangetic Plain-Himalayas (Lau and Kim, 2018).

In this study, we used satellite retrievals and reanalysis datasets to obtain the spatial distributions of aerosols, especially dust aerosols and snow cover over the TP, and analyzed the correlation between dust and snow cover. This study mainly evaluates the relative impacts of atmospheric dust and dust-on-snow over the TP in spring and winter from 2009 to 2018. We hope to provide a reference and basis for the causes of ice and snow melting and regional warming over the TP. The datasets used in the study are presented in **Section 2**. **Section 3.1** analyzes the spatial and temporal distributions of aerosols over the TP. **Section 3.2** focuses on spatial and temporal distributions of snow cover over the TP. In **Section 3.3**, the influence mechanism of dust aerosols on snow over the TP is discussed. **Section 4** shows the conclusion and discussion.

2 DATASETS AND METHODS

2.1 MODIS

The Moderate-Resolution Imaging Spectroradiometer (MODIS) installed on the Terra and Aqua satellites is one of the most widely used remote sensing platforms in earth science research (Parkinson, 2003). The Terra and Aqua satellites feature 5-min temporal and 36-channel spectral resolutions, 2330-km viewing swath widths, wide spectral ranges (0.412–14.24 μm), and near-global coverage every 1–2 days. Thus, MODIS not only provides reliable and extensive retrieval data products on aerosols and clouds but also offers an ideal solution for aerosol model development and validation, dynamic analysis of atmospheric pollution, and air quality monitoring with a spatial resolution of 1–10 km (Levy et al., 2007; Remer et al., 2008). Dark target (DT) and deep blue (DB) are the two major algorithms applied to the MODIS instrument for retrieving AOD. DT manifests its excellent performance over high vegetation coverage regions such as farmlands or forests, while DB was developed to retrieve the aerosol properties over Gobi, deserts, or snow-covered areas. The retrieval deviation can be reduced in the estimation of surface albedo and further in AOD over the regions of bright surface with a weaker blue-band reflectance (Hsu et al., 2006). In this study, snow cover and AOD at 550 nm were derived from MODIS-Aqua version 6.1. The resolution of snow cover is 0.05° × 0.05° (lat x lon), and the AOD at 550 nm is 1° × 1° (lat x lon).

2.2 MISR

The Multiangle Imaging SpectroRadiometer (MISR) onboard Terra was launched on 18 December 1999. The sensors can measure particles with medium spatial resolution and can cover almost the whole world. MISR products have made significant progress in retrieving aerosols. However, the predictability of MISR aerosol products for $PM_{2.5}$ concentrations has not improved (Liu et al., 2007). Both MISR and MODIS are onboard the Terra satellite. Statistical comparisons were made with coincident AOD retrieved by MODIS and MISR. The correlation coefficient between MISR and MODIS is approximately 0.9 over the ocean and approximately 0.7 over land (Kahn et al., 2009). Compared to AERONET, marine stations have the highest correlation coefficient (0.9), and dusty sites have the lowest correlation coefficient (0.7) (Kahn et al., 2005). Although MISR has these biases, MISR can still represent the spatial and temporal variations in aerosols. In this study, 550 nm AOD at 550 nm

with a horizontal resolution of 0.5° × 0.5° (lat x lon) was derived from the MISR Level 3 Data.

2.3 MERRA-2 Reanalysis Data

The Modern-Era Retrospective Analysis for Research and Applications, version 2 (MERRA-2) is produced by the NASA Global Modeling and Assimilation Office (GMAO), which provides datasets dating back to 1980 (Gelaro et al., 2017). Previous studies have evaluated MERRA-2. Compared with models and observations, the MERRA-2 AOD is larger than the simulated AOD, but observations are larger than the MERRA-2 AOD (Randles et al., 2017). Furthermore, previous studies compared observed AOD based on AERONET and found that the MERRA-2 AOD better matches that of AERONET (Randles et al., 2017). Liu et al. (2019) combined the AAI and several satellite datasets to check the reliability of long-term changes in the MERRA-2 dust concentration. Moreover, MERRA-2 underestimates the daily temperature and overestimates the latent heat flux in summer (Draper et al., 2017). Although MERRA-2 still presented these biases, MERRA2 could represent the spatial and temporal variations in aerosols. In this study, we used AOD, dust aerosol optical depth (DAOD), and surface albedo with a horizontal resolution of 0.5° × 0.625°(lat x lon) to analyze the impacts of dust over the TP.

2.4 ERA5 Reanalysis Data

The European Centre for Medium-range Weather Forecasting Reanalysis V5 (ERA5) is a global atmospheric reanalysis dataset (Hersbach et al., 2019) dating back to 1950, with a horizontal resolution of 0.25° × 0.25° (Hersbach et al., 2018). Compared with ERA-Interim, ERA5 was significantly improved. The assimilation method uses the ensemble 4DVar data assimilation scheme with 10 ensemble members, with a horizontal resolution of 31 km × 31 km and a vertical stratification of 137 layers with a top pressure of 1 Pa. The integrated forecast system version was upgraded to Cy41r2, the radiative transfer mode was upgraded to RTTOV-v11, and the temporal resolution was improved to 1 h. The ERA5 reanalysis datasets are better than MERRA-2 in estimating solar irradiance, but there are some biases in cloudy conditions. ERA5 overestimates solar radiation, while MERRA-2 underestimates solar radiation in most areas. In terms of wind speed, ERA5 is superior to MERRA-2 compared to the observation data. In terms of precipitation, ERA-5 performs better on the monthly scale, followed by JRA-55, MERRA-2, and CFS-2 (Taszarek et al., 2021) in terms of thermodynamic theoretical parameters, low-altitude decrement rate, low-altitude wind shear, etc. (Maa et al., 2021). Both ERA5 and MERRA-2 data better represent variables such as temperature, moderateness, mid-tropospheric decrement rate, and mean wind. However, ERA5 has a higher correlation and lower mean error compared to MERRA-2 (Taszarek et al., 2021). In general, ERA5 is better than MERRA-2 data in terms of solar radiation, precipitation, temperature, and wind speed. However, ERA5 excludes aerosol data; we use MERRA-2 data for analyzing aerosols in this article. For the analysis of temperature and radiation, ERA5 data are used. In this study, we used surface temperature and surface net solar radiation (clear) with a horizontal resolution of 0.25° × 0.25° (lat x lon).

2.5 Correlation Analysis Method

By using the correlation analysis method, this article analyzes the correlation relationship between MERRA-2 AOD and MODIS, MISR AOD, verifying the feasibility of MERRA-2 AOD in the study area. The correlation coefficient as defined by Pearson can be used to characterize the correlation between two different variables. Assuming a sample size of n for variables x and y, the correlation coefficient formula is as follows:

$$r = \frac{\sum_{i=1}^{n}\left[(x_i - \bar{x})(y_i - \bar{y})\right]}{\sqrt{\sum_{i=1}^{n}(x_i - \bar{x})^2 \times \sum_{i=1}^{n}(y_i - \bar{y})^2}} \tag{1}$$

where $\bar{x}$ and $\bar{y}$ represent the average of x and y, respectively.

The significance test for the correlation coefficient r can be performed using the t-test method, assuming that the two variables are not correlated, with the statistic t:

$$t = r\sqrt{\frac{n-2}{1-r^2}} \tag{2}$$

n is the sample size and n-2 is the degree of freedom. The significance level is assumed to be α. If $t < t_\alpha$, the linear correlation is insignificant. If $t > t_\alpha$, the linear correlation is significant.

2.6 Climate Trends

Assuming a sample size of n for a certain climate variable xi, and ti represents the time corresponding to xi, establishing a one-dimensional linear regression equation between xi and ti:

$$\hat{x}_i = a + bt_i, i = 1, 2, \cdots, n \tag{3}$$

In **Eq. 3**, a is the regression constant and b is the regression coefficient. For the observed data xi and the time ti, the least-squares estimates of the regression coefficient b and the constant a are:

$$\begin{cases} b = \dfrac{\sum_{i=1}^{n} x_i t_i - \frac{1}{n}\left(\sum_{i=1}^{n} x_i\right)\left(\sum_{i=1}^{n} t_i\right)}{\sum_{i=1}^{n} t_i^2 - \frac{1}{n}\left(\sum_{i=1}^{n} t_i\right)^2} \\ a = \bar{x} - b\bar{t} \end{cases} \tag{4}$$

where

$$\bar{x} = \frac{1}{n}\sum_{i=1}^{n} x_i, \bar{t} = \frac{1}{n}\sum_{i=1}^{n} t_i$$

Using the relationship between the regression coefficient b and the correlation coefficient a, finding the correlation coefficient between time ti and the variable xi:

$$r = \sqrt{\frac{\sum_{i=1}^{n} t_i^2 - \frac{1}{n}\left(\sum_{i=1}^{n} t_i\right)^2}{\sum_{i=1}^{n} x_i^2 - \frac{1}{n}\left(\sum_{i=1}^{n} x_i\right)^2}} \tag{5}$$

The correlation coefficient r indicates the closeness of the linear correlation between the variable x and time t. When r = 0, the regression coefficient b is 0, and the regression line determined by the least-squares estimation is parallel to the

x-axis, indicating that the change of x is independent of time t; when r > 0, b > 0, indicating an upward trend of x with time t; when r < 0, b < 0, indicating a downward trend of x with time t. In this article, we mainly use this method to calculate the linear trend of snow and dust aerosols.

2.7 Rate of Dust Change

This article focuses on calculating the rate of dust change by using statistical methods. The difference between the dust concentrations of two adjacent days (the latter-day minus the previous day) is calculated using dust concentration data from MERRA-2 reanalysis datasets, and the rate of dust change concentration is obtained by dividing the difference by the dust concentration of the day. The main calculation formula is as follows:

$$Dust_{rate}(i) = \frac{Dust(i+1) - Dust(i)}{Dust(i)} \quad (6)$$

where Dust is the atmospheric dust concentration and $Dust_{rate}$ is the diurnal rate of atmospheric dust concentration. i represents the time series, i represents the current day, and i+1 represents the next day.

The dust concentration is influenced by the season; the effect of seasonal variability of dust concentration needs to be removed for a clearer analysis of the effect of dust on snow. We use the difference transform to remove the seasonal variability. To specifically analyze the effect of high and low values of dust variability on snow, the rates of dust change data from 2009 to 2018 were arranged from smallest to largest in spring, and the high and low values were selected using the 5% and 95% quartiles. In this article, we calculated the 5% and 95% quartiles as $-0.63\ mg\ m^{-3}\ d^{-1}$ and $0.65\ mg\ m^{-3}\ d^{-1}$. Therefore, all dates greater than $0.65\ mg\ m^{-3}\ d^{-1}$ are identified as high-value days, while dates less than $-0.63\ mg\ m^{-3}\ d^{-1}$ are identified as low-value days. Furthermore, the highest diurnal rates of atmospheric dust concentration and the lowest diurnal rates of atmospheric dust concentration are usually located next to each other. When the diurnal rate of atmospheric dust is high, the dust concentration in the atmosphere gradually increases at this time, mainly because most of dust is released into the atmosphere. When the diurnal rate of atmospheric dust is low, the dust deposits on snow at this time. Thus, the high values represent the atmospheric dust and the low values represent dust-on-snow. High and low-value days are analyzed separately for radiation, temperature, and snow distribution to comprehend the mechanism of the effect of dust to snow.

3 RESULTS

3.1 Spatial and Temporal Distributions of Aerosols Over the Tibetan Plateau

As a major aerosol over the TP, dust in the atmosphere and snow on the TP remarkably influence the Asian climate. In this article, we choose the most dominant absorbing aerosols (dust aerosols) to estimate the relative contributions of atmospheric dust and dust-on-snow to the change in snow cover over the TP through the use of reanalysis datasets and satellite retrievals. We use three aerosol-related datasets, MERRA-2 reanalysis datasets, MODIS, and MISR retrievals. The MERRA-2 reanalysis datasets include dust-related variables, which are used to investigate the association between dust aerosols and snow cover, and they further analyze the influence of atmospheric dust and dust-on-snow to the change in snow cover over the TP. Due to differences in models and emissions, MERRA-2 AOD shows specific uncertainties in different regions and should be evaluated before use. We need to analyze the applicability of MERRA-2 reanalysis datasets on the TP. To evaluate the feasibility of MERRA-2 reanalysis datasets over the TP, the aerosol products from MERRA-2 are compared with those derived from MODIS and MISR retrievals. Overall, MERRA-2 captures the spatial and temporal distributions of 550 nm AOD over the TP for 2009–2018. The monthly mean AOD distribution from MERRA-2 is similar to that from the MODIS and MISR retrievals. The TP AOD from MERRA-2, MODIS, and MISR has the largest values in April (0.31 ± 0.03, 0.36 ± 0.04, and 0.23 ± 0.03), and December (0.09 ± 0.01, 0.08 ± 0.01, and 0.06 ± 0.01) has the smallest (**Figures 1A–C**). The MERRA-2 AOD, MODIS AOD, and MISR AOD have the largest values in the northern TP (0.25 ± 0.1, 0.30 ± 0.12, and 0.20 ± 0.08) and gradually decrease from the periphery of the TP to the inside and from north to south over the TP. Meanwhile, the TP AOD from MERRA-2 has been found to be greater than that from MODIS and MISR retrievals. The differences between MERRA-2 and MODIS may be related to cloud contamination effects and emission uncertainty in each model system (Liu and Chen, 2020) (**Figures 1D–F**). The cloud contamination effects are a source of bias in the MODIS retrieval of AOD, and the emission uncertainty refers to the MERRA-2 reanalysis.

Moreover, the MERRA-2 reanalysis datasets are consistent with the MODIS and MISR retrievals, which could reflect the seasonal and monthly variations in the TP AOD during 2009–2018 (**Figure 2**). **Figure 2** shows that the values of the TP AOD from the MERRA-2 reanalysis datasets, MODIS, and MISR retrievals are 0.20 ± 0.08, 0.16 ± 0.09, and 0.14 ± 0.07 from 2009 to 2018, respectively. The TP AOD from the MERRA-2 reanalysis datasets has the largest values of 0.29 ± 0.03 in spring, followed by 0.23 ± 0.03 in summer, and the lowest AOD of 0.12 ± 0.02 in winter, which are consistent with the MODIS AOD values (0.31 ± 0.05, 0.15 ± 0.04, and 0.12 ± 0.02) and MISR AOD values (0.21 ± 0.02, 0.19 ± 0.03, and 0.08 ± 0.01) (**Figure 2A**). Although MERRA-2 AOD has been found to be greater than that from MODIS and MISR retrievals, the seasonal and monthly variation characteristics of three datasets are basically consistent. MERRA-2 AOD data can be used to reflect the variation characteristics of AOD in the TP. **Figures 2B,C** show the comparison between monthly MERRA-2 AOD and MISR AOD, MODIS AOD from 2009 to 2018. The comparison results show better correlations and smaller errors among the MERRA-2 reanalysis datasets, MISR, and MODIS retrievals, with correlation coefficients (R) of 0.90 and 0.76 and root-mean-square errors (RMSEs) of 0.03 and 0.06 (**Figures 2B,C**). Overall, the MERRA-2 monthly average AOD is in good agreement with MISR and MODIS.

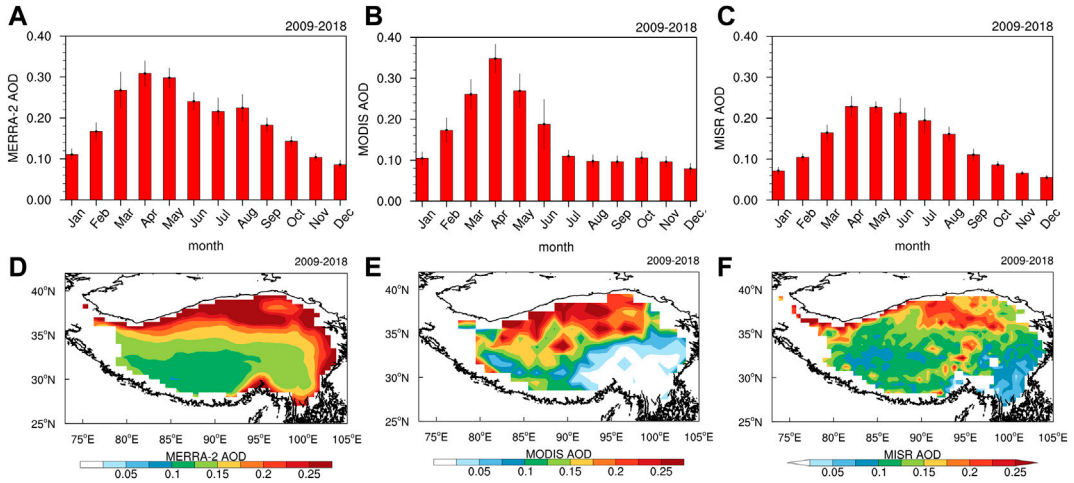

FIGURE 1 | Monthly variations in the TP AOD from the **(A)** MERRA-2, **(B)** MODIS, and **(C)** MISR retrievals during 2009–2018 and spatial distributions of the averaged AOD over the TP from the **(D)** MERRA-2, **(E)** MODIS, and **(F)** MISR retrievals during 2009–2018. Note that the error bars represent the standard deviation of the corresponding variables.

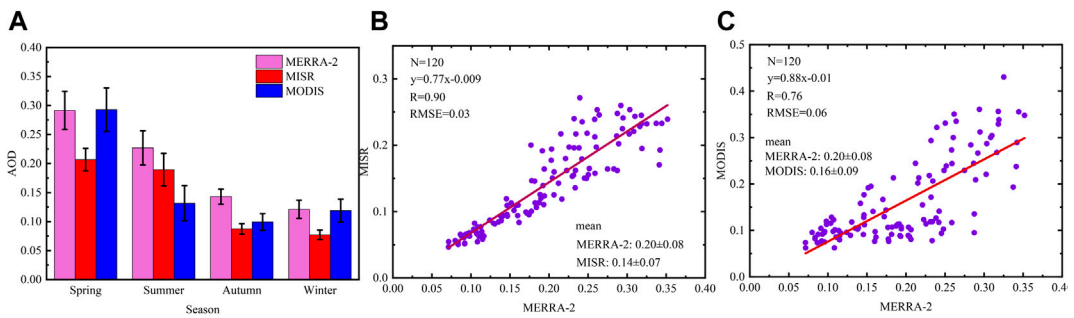

FIGURE 2 | (A) Seasonal variations in the TP AOD from the MERRA-2. MODIS and MISR retrievals during 2009–2018 and comparison of MERRA-2 AOD, **(B)** MISR AOD, and **(C)** MODIS AOD over the TP (70–110°E, 25–45°N) for 2009–2018. The red line is the fit line.

As the main type of aerosol over the TP, dust AOD has the largest value of 0.15 ± 0.02 in spring and the lowest value of 0.03 ± 0.007 in winter, showing gradual decreases from the northern to southern regions of the TP (**Figure 3A**). The temporal and spatial distributions of DAOD (**Figures 3A,C**) and dust concentration (**Figures 3B,D**) are similar to that of AOD over the TP (**Figure 1**). DAOD (0.15 ± 0.02) and dust concentration (0.2 ± 0.06 mg m^{-3}) had the largest values from March to June, while DAOD (0.03 ± 0.007) and dust concentration (0.04 ± 0.01 mg m^{-3}) had the lowest values from October to February (**Figures 3A,B**). The monthly variations in DAOD in the northern TP diverge from those in the southern TP, with the DAOD in the northern TP having the largest values in May (0.28 ± 0.03) and the DAOD in the southern TP having the largest values in May (0.11 ± 0.016) (**Figure 3**).

The dust occurrence frequency in the northern TP is higher than that in the southern TP. The DAOD (0.25 ± 0.1) and dust concentration (0.35 ± 0.2 mg m^{-3}) in the Qaidam Basin are higher than those in other regions over the TP. The difference between the northern TP and southern TP is closely related to the atmospheric circulation and aerosol emissions in the surrounding areas (**Figures 3C,F**). The results are consistent with those from Xu et al. (2015b), who showed the three-dimensional structure of aerosols over the TP based on MISR and Cloud-aerosol Lidar and Infrared Pathfinder Satellite (CALIPSO) retrievals. They further found that the spatial distribution of dust aerosols in the northern TP is significantly different from that in the southern TP, which can be seen clearly from 6 to 8 km above sea level, especially in spring and summer. Chen et al. (2013) and Yuan et al. (2020) also investigated the meridional transport path of dust from the TD to the northern slope of the TP and found that the westerly jet weakens and moves northward providing dynamic and thermal conditions for meridional transport.

The spatial distribution of dust concentration in spring and winter (**Figures 4A,C**) is similar to that of MERRA2 DAOD (**Figures 1D**, **4B**,D). The dust concentration in the northern TP (0.5 ± 0.1 mg m^{-3}) was higher than that in the southern TP (0.15 ± 0.05 mg m^{-3}) in spring from 2009 to 2018. A large dust concentration value (0.6 ± 0.1 mg m^{-3}) occurred in the Qaidam

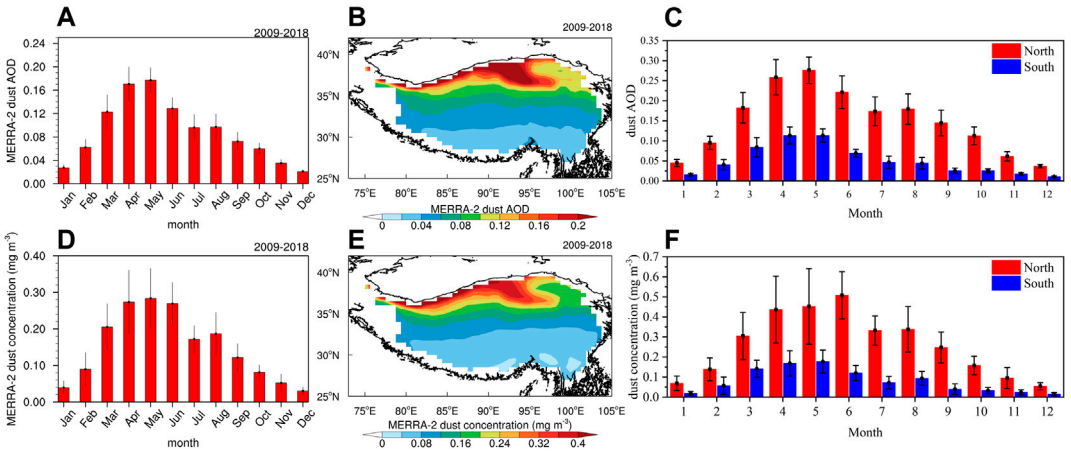

FIGURE 3 | (A) Monthly dust AOD (DAOD), **(B)** spatial distributions of DAOD, and **(C)** monthly dust AOD in the north and south over the TP for 2009–2018 from the MERRA-2 reanalysis datasets. **(D)** Monthly dust concentration (units: mg m^{-3}), **(E)** spatial distributions of dust concentration (units: mg m^{-3}), and **(F)** monthly dust concentration (units: mg m^{-3}) in the north and south over the TP for 2009–2018 from the MERRA-2 reanalysis datasets. The error bars represent the standard deviation of the corresponding variables.

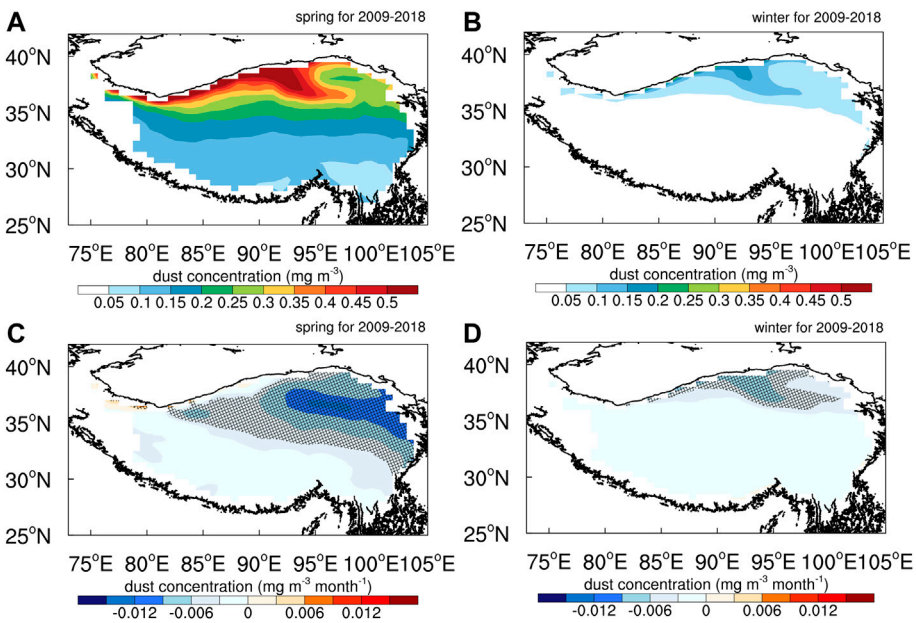

FIGURE 4 | Spatial distributions of dust concentration over the TP in **(A)** MAM and **(B)** DJF for 2009–2018 derived from MERRA-2 reanalysis datasets; spatial distributions of dust concentration linear trends (units: mg m^{-3} $month^{-1}$) over the TP in **(C)** MAM and **(D)** DJF for 2009–2018 from MERRA-2 reanalysis datasets. Regions passing the 95% significance level are highlighted by stipple. Significance is assessed through the t value of the ensemble trend.

Basin, and a small ±value (0.05 ± 0.01 mg m^{-3}) was located east of 95°E and south of 30°N on the TP based on MERRA-2 reanalysis datasets (**Figure 4A**). The spatial distribution in winter is similar to that in spring; due to the frequent dust storms in spring, the dust concentration in winter (0.15 ± 0.02 mg m^{-3}) is smaller than that in spring (**Figure 4B**). In addition, based on **Eq. 3**, the regression coefficients of monthly data with time series were calculated for spring and winter from 2009 to 2018 to obtain the long-term trend of dust concentration. The long-term trend of dust concentration shows a decreasing trend over the TP, with domain-mean values of −0.012 mg $m^{-3}$$month^{-1}$ in spring and −0.003 mg m^{-3} $month^{-1}$ in winter at the 95% significance level. The maximum values of −0.015 mg m^{-3} $month^{-1}$ in spring and −0.006 mg m^{-3} $month^{-1}$ in winter are located in the northern TP, which was related to the reduction of dust storms over the TD and Gobi Desert (GD) in recent years (**Figures 4C,D**).

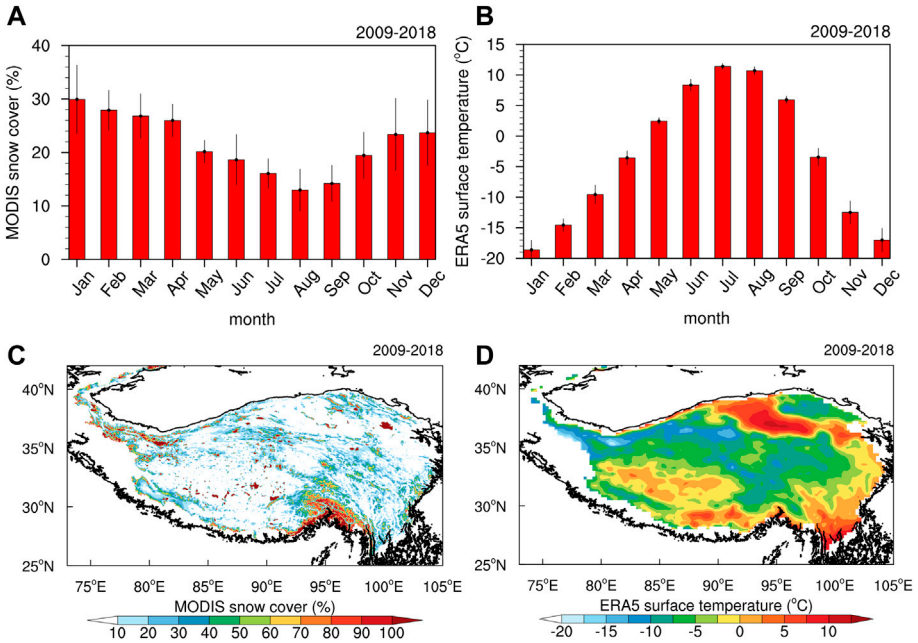

FIGURE 5 | (A) Monthly snow cover (units: %) and **(C)** spatial distributions of snow cover (units: %) over the TP for 2009–2018 derived from the MODIS retrievals. **(B)** Monthly surface temperature (units: °C) and **(D)** spatial distributions of surface temperature (units: °C) over the TP for 2009–2018 derived from ERA5 reanalysis datasets. The error bars represent the standard deviation of the corresponding variables.

3.2 Spatial and Temporal Distributions of Snow Cover Over the Tibetan Plateau

Snow cover is mainly located in the western TP (Kunlun Mountains) southeast of the TP, especially in the Hengduan Mountains, the Himalayas, and Qilian Mountains, and snow cover is difficult to melt due to the complex terrain. The snow cover in the hinterland of the TP and the Qaidam Basin with a dry climate and scarce precipitation belongs to instantaneous snow, and the snow cover is lower (10% ± 2) (**Figure 5C**). Both the fraction of coverage and duration of snow cover over the TP are lower than those at high latitudes, which leads to rapid changes in seasonal snow cover over the TP. Due to the influence of local temperature and precipitation, the changes in snow cover are more active in the cold season (**Figures 5A,C**). The snow cover accumulates gradually during the accumulation period from October to January, which causes the snow cover to have the highest values in January (30% ± 6) and lasts until spring (**Figure 5A**).

The spatial distributions of surface temperature are opposite to snow cover (**Figures 5B,D**). The monthly variability of snow on the TP is opposite to surface temperature, with snow reaching minimum values in July and August while surface temperature is at a maximum and snow reaching a maximum in December and January while surface temperature is at a minimum. With increased surface temperature, snow cover will decrease. The surface temperature has larger values in the northern TP, especially the Qaidam Basin, with the maximum value being 11.4°C, and the lowest values mainly occur in the middle, west, and southeast of the TP (−6.3°C ± 0.83, −8.8°C ± 1.15, and −5.0°C ± 1.30, respectively) (**Figure 5D**). The surface temperature over the TP has the highest value in summer (10.2°C ± 0.69) and the lowest value in winter (−16.7°C ± 1.52), with the highest value in July (11.4°C ± 0.47) and the lowest value in January (−18.6°C ± 1.58) (**Figure 5B**). The surface temperature has a larger value over the TP in summer; thus, the snow cover of only 15% indicates that most of the snow cover has melted and supplied water to the lake (Zhang et al., 2012), and the minimum snow cover appears in August (12.97% ± 3.92) (**Figures 5A,B**).

To compare the snow with dust, the snow cover was interpolated to a spatial resolution of 0.5° × 0.625° of MERRA-2. With the lower surface temperature and higher dust concentration over the TP in the winter half-year (December to May), we further investigated the influence of dust aerosols on snow cover over the TP. The distribution of snow cover in spring and winter is consistent with the annual snow cover (**Figures 6A,B**). In the eastern 90°E of the TP, snow cover increases in spring and decreases in winter. In the western 90°E of the TP, snow cover increases in spring and winter (**Figures 6C,D**), but the variation trend of dust concentration is opposite to that of snow cover in spring (**Figures 4C,D**). May dust lead to significant melting of snow in spring and winter, causing most of them at risk of rapid mass loss? We will further discuss the relationship between dust and snow cover. However, due to the accumulation of snow, the relationship between snow cover and dust concentration is not clear (**Figures 7C,D**).

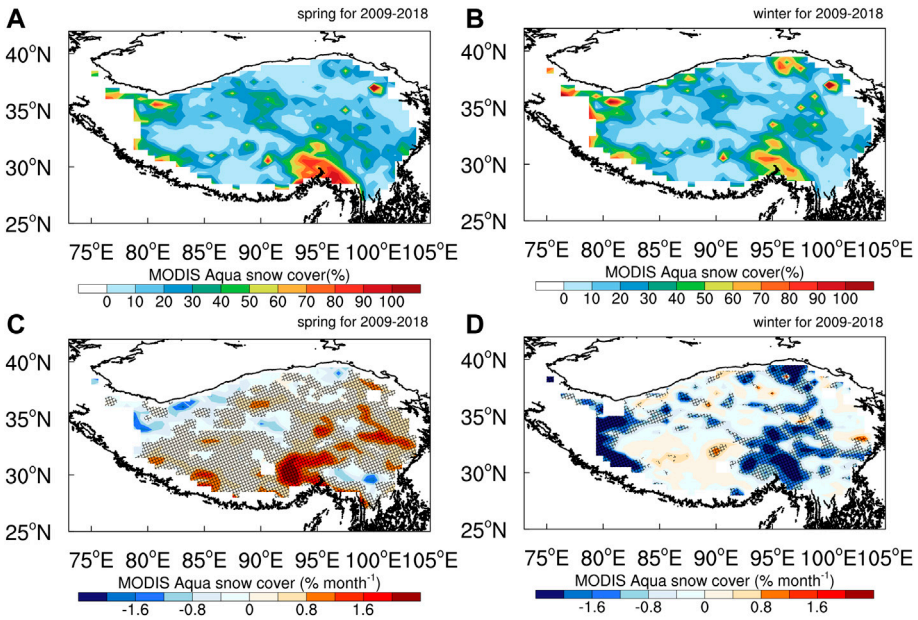

FIGURE 6 | Spatial distributions of snow cover (units: %) over the TP in **(A)** MAM and **(B)** DJF for 2009–2018 derived from MODIS retrievals. Spatial distributions of snow cover trends (units: % month^{-1}) over the TP in **(C)** spring (MAM) and **(D)** winter (DJF) for 2009–2018 derived from MODIS retrievals. Regions passing the 95% significance level are highlighted by stipple. Significance is assessed through the t value of the ensemble trend.

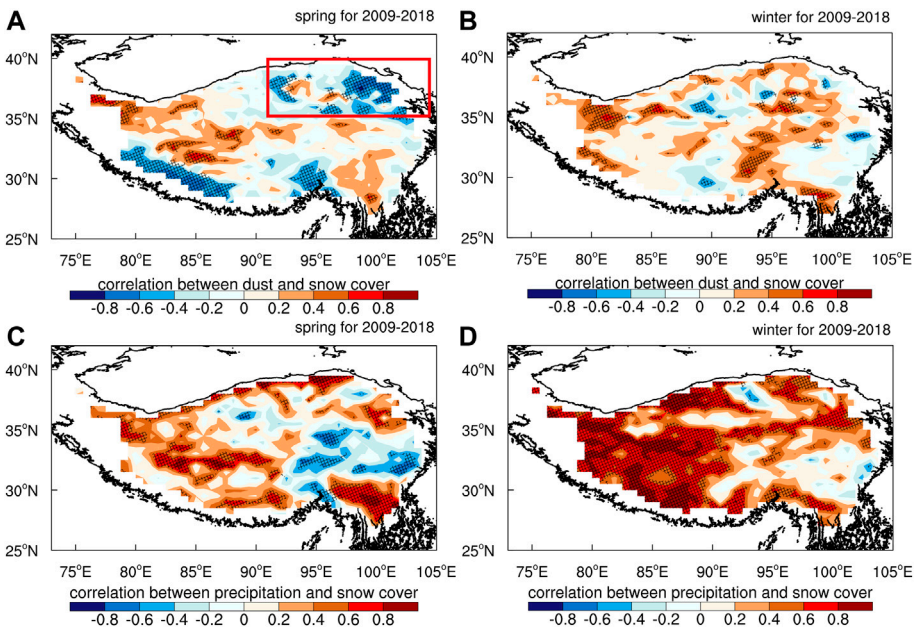

FIGURE 7 | Spatial distributions of correlation between dust concentration (units: mg m^{-3}) and snow cover (units: %) over the TP in **(A)** MAM and **(B)** DJF for 2009–2018. Spatial distributions of correlation between precipitation (units: mm) and snow cover (units: %) over the TP in **(C)** MAM and **(D)** DJF for 2009–2018. Regions passing the 85% significance level are highlighted by stipple. Significance is assessed through the t value of the ensemble trend.

Snow cover has a larger value (80% ± 12) in the southeastern TP in spring from 2009 to 2018, and the lower values (10% ± 1) are mainly in the center of the TP, including the Kunlun Mountains and Qaidam Basin (**Figure 6A**). The spatial distribution of snow cover in winter is almost equal to that in spring, while for the entire domain, snow cover in winter is lower

than that in spring, and the maximum values (70% ± 8) are mainly located in the southeastern TP. The value of snow cover is 60% ± 4 in Qinghai Lake (**Figure 6B**). There is an obviously increasing trend of snow cover in the southern TP in spring from 2009 to 2018. The maximum value was mainly located in the southeastern TP, with a maximum value of up to 1.6% month^{-1}; the snow cover in the northeastern TP shows a decreasing trend (−1.2% month^{-1}). However, whether this change is due to dust will be discussed further below. With the deposition of dust aerosols from the TD in the northern TP, dust aerosols mainly influence fresh snow in the northern TP (**Figure 6C**). The variation trend of snow cover in winter is significantly different from that in spring. Most areas of the TP show decreasing trends and are mainly located in the west, southeast, and northeast of the TP, with a maximum value of up to −2% month^{-1}. Could dust have caused the decrease in snow cover in regions of maximum snow cover? We will use the rate of dust to analyze. The snow cover shows an increasing trend in the southwestern TP, which is mainly caused by the influence of precipitation (**Figure 7D**).

Due to the influence of precipitation and temperature, the correlation between snow and dust is uncertainty. Therefore, positive correlation will occur in the case of low precipitation, and inverse phase deposition of dust in snow will occur when the dust concentration is large, while the influence of dust in the atmosphere and dust in snow is different, so the correlation results are different. Therefore, we cannot get an obvious signal from the climatic state, so we use the rate of dust change to analyze.

To explain the influence of dust on snow over the TP, this study analyzed the temporal and spatial correlations between dust concentration and snow cover. Dust has a significant correlation with snow cover in most regions of the TP at an 85% significance level of the t test. In particular, dust has a greater influence on snow cover duration in the regions of maximum snow cover (**Figure 7**). In spring, there is a significant negative correlation between dust and snow cover in the northern 35°N and eastern 90°E of the TP, with the highest correlation coefficients being −0.6. However, in winter, there is a significant positive correlation between dust and snow cover in the TP, with the highest correlation coefficients being 0.5. In the northwest and the hinterland of the TP, there is a significant positive correlation between dust and snow cover, with values of 0.4 in spring and 0.5 in winter, which are mainly influenced by precipitation more than dust aerosols (**Figures 7C,D**).

In spring, there is a significant negative correlation between dust and snow cover in the northern 35°N and eastern 90°E of the TP. Surface temperature and precipitation are two direct factors that can affect snow, while dust usually affect the snow by affecting surface temperature. The influence of precipitation will lead to a non-significant correlation in some areas. Therefore, we select the northern region of the TP (35–40°N, 87–105°E) and calculate the rate of dust and the variability characteristics of precipitation and select the high and low values of dust rate in the case of precipitation less than 0.0049 mm, so as to reduce the influence of precipitation on snow and then analyze the influence of dust on snow in the northern region of the TP (35–40°N, 87–105°E).

3.3 The Influence of Dust in the Atmosphere and Deposition in Snow Over the Tibetan Plateau

We select the northern region of the TP (35–40°N, 87–105°E) and calculate the rate of dust and the variability characteristics of precipitation and select the high and low values of dust rate in the case of precipitation less than 0.0049 mm, so as to reduce the influence of precipitation on snow and then analyze the influence of dust on snow in the northern region of the TP (35–40°N, 87–105°E). Dust physical processes, including dust emissions, long-term transport, and dry/wet deposition, are closely related to the climatic effects of dust aerosols. The study of the climate effect of dust is always very complex. It is difficult to separately analyze the effect of dust in the atmosphere and snow for observations, which leads to the lack of observational facts in the climate effects of dust aerosols over the TP. We distinguished between atmospheric dust and dust-on-snow by calculating the diurnal rate of dust concentration in the northern region of the TP (35–40°N, 87–105°E) in this study (**Figure 8**). The highest (red dots, >0.65 mg m^{-3} d^{-1}) and the lowest diurnal rates of atmospheric dust concentration (blue dots, <−0.63 mg m^{-3} d^{-1}) are usually located next to each other in **Figure 8**. In particular, the dust concentration is higher during high events (red dots) due to local dust emissions and transport from other sources. However, dust aerosols settle quickly to snow due to dry/wet deposition, which leads to dust concentrations in the atmosphere decreasing rapidly in low events (blue dots). The pattern of surface dust concentration in high and low events is almost the opposite in the northern TP (**Figures 8**, **9**). Therefore, the high and low values of the diurnal rates of atmospheric dust represent atmospheric dust and dust-on-snow over the TP, respectively. Furthermore, we investigate the influencing mechanism of atmospheric dust and dust-on-snow on snow cover over the TP based on high and low events.

Based on high and low values of dust variability, using radiation data from MERRA-2 and meteorological element data from ERA5, we analyze the characteristics of changes in solar radiation, surface temperature, and snow cover. Through analyzing the distribution characteristics of radiation, surface temperature, and snow cover in the northern region of the TP (35–40°N, 87–105°E) based on the high and low values of the rate of dust, we can analyze the influence of atmospheric dust and dust-on-snow on snow cover in the northern region of the TP (35–40°N, 87–105°E). The solar radiation anomaly and surface temperature anomaly are mainly obtained by calculating the average values of solar radiation and surface temperature in the high and low values to subtract the average values from 2009 to 2018 in spring. Dust can affect solar radiation directly, while the variation of solar radiation directly affects surface temperature. The radiation anomaly and surface temperature anomaly can be interpreted as being caused by dust. The precipitation is lower in the high and low events; thus, we can

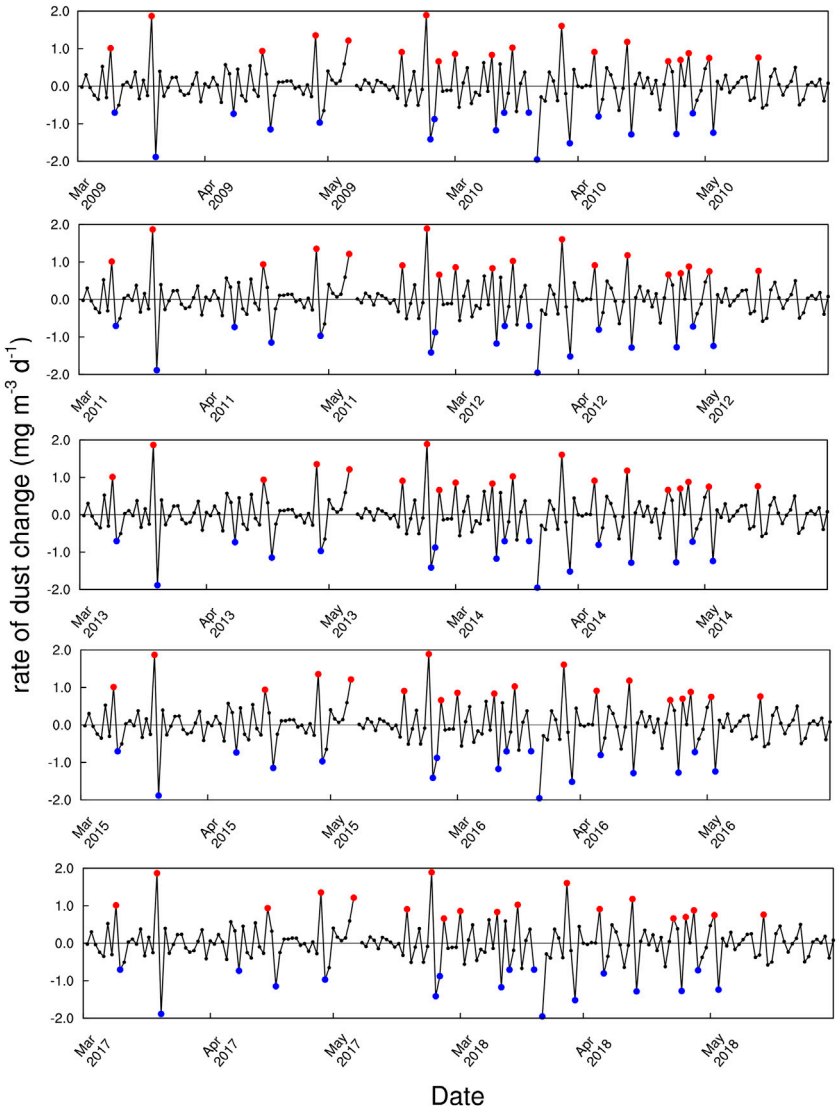

FIGURE 8 | Time variation of dust concentration (units: mg m^{-3} d^{-1}) over the TP in spring for 2009–2018 and selected cases representing atmospheric dust (red dots) and dust-on-snow (blue dots).

ignore the influence of precipitation on snow over the northern TP (**Figures 9C,D**).

Atmospheric dust reduces the surface net solar radiation (−3.84 W m^{-2}) through absorbing shortwave radiation, decreases the surface temperature (−2.27°C), and finally increases the snow cover (−1.04%). The high events occur mainly from March to May, which are mainly from local dust emissions and external transport. During high events, surface dust concentration anomaly has negative values (−0.026 mg m^{-3}), and the minimum value is −0.05 mg m^{-3}. During this time, surface dust aerosols are emitted to the atmosphere. As one of the major LAAs, dust aerosols can significantly absorb solar radiation. Due to the influence of atmospheric dust, the surface net solar radiation anomaly has lower values of −3.84 W m^{-2} in the northern TP (**Figure 10C**), which caused a negative surface temperature anomaly of −2.27°C in the northern TP during the high events (**Figure 11A**). The surface temperature can significantly influence snow cover, and the snow cover anomaly shows higher values of 3% in the eastern 90°E of the north TP and lower values of 2% in the western 90°E of the north TP. The spatial distribution of surface albedo is similar to that of snow cover; a positive surface albedo anomaly mainly occurs in the northern TP (0.0004).

The dust deposited on snow reduces the surface albedo by −0.004, induces surface warming (0.42°C), and reduces snow cover (−2.00%) by rapid snowmelt in the northern TP. The positive surface dust concentration anomaly is high over the northern TP (0.057 mg m^{-3}), and the negative values of −0.01 mg m^{-3} are located on the southern 37°N and eastern 98°E of the northern TP during low events (**Figure 9B**). Dust deposited on snow can reduce surface albedo;

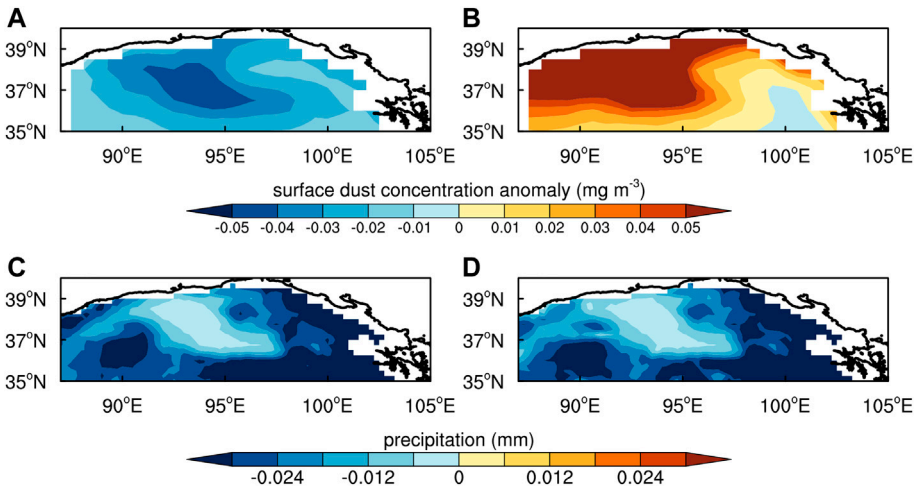

FIGURE 9 | Spatial distributions of **(A,B)** surface dust concentration (units: mg m^{-3}) and **(C,D)** precipitation (units: mm) on (first column) the difference between high and normal days and (second column) the difference between low and normal days.

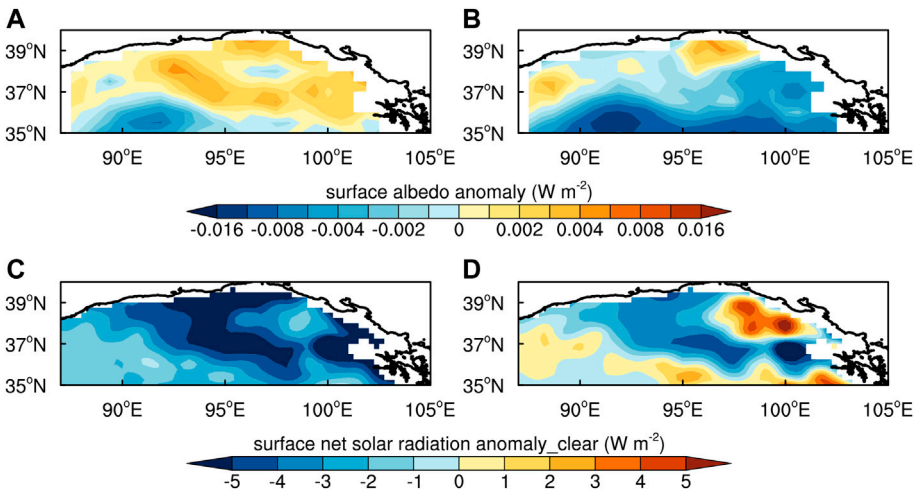

FIGURE 10 | Spatial distribution of **(A,B)** surface albedo and **(C,D)** surface net solar radiation (units: W m^{-2}) on (first column) the difference between high and normal days and (second column) the difference between low and normal days.

thus, the surface albedo anomaly has lower values of −0.004 in the northern TP, with minimum values down to −0.016. (**Figure 10B**). The spatial distribution of the surface net solar radiation anomaly is contrary to that of the surface albedo, and the larger values of 3 W m^{-2} are located in the south of northern TP (**Figure 10D**). The surface temperature has a larger value of 2°C, mainly in the west of the northern TP (**Figure 11B**). The spatial distribution of snow cover is almost opposite to that of surface temperature, while for the entire snow cover domain, the lower values of snow cover of −2.00% are mainly located north of the TP (**Figure 11D**). The significant decreasing snow cover over the TP is induced due to the snow darkening effect. Dust-on-snow increases the surface solar shortwave radiation by decreasing the surface albedo, which further strengthens the surface temperature, weakens the snow cover, and further increases dust emissions. Hence, TP dust can create a positive feedback loop, which decreases snow cover. In the same period, snow cover can partially block the upward longwave radiation from the ground and affect the ground thermal regime. When the snow cover decreases, the upward longwave radiation from the ground increases, which weakens the surface temperature. The effect of snow darkening is higher than the thermal regime of snow cover, which finally increases surface temperature and decreases snow cover. **Figure 12B** shows the significant increase in the surface latent heat flux by the dust-on-snow. This is due to the increased soil moisture induced by a rise in the amount of snowmelt over the northern TP in spring. The warming of the northern TP also increases the regional surface sensible heat flux in **Figure 12C**. The total surface heat flux (latent + sensible heat flux) shows a

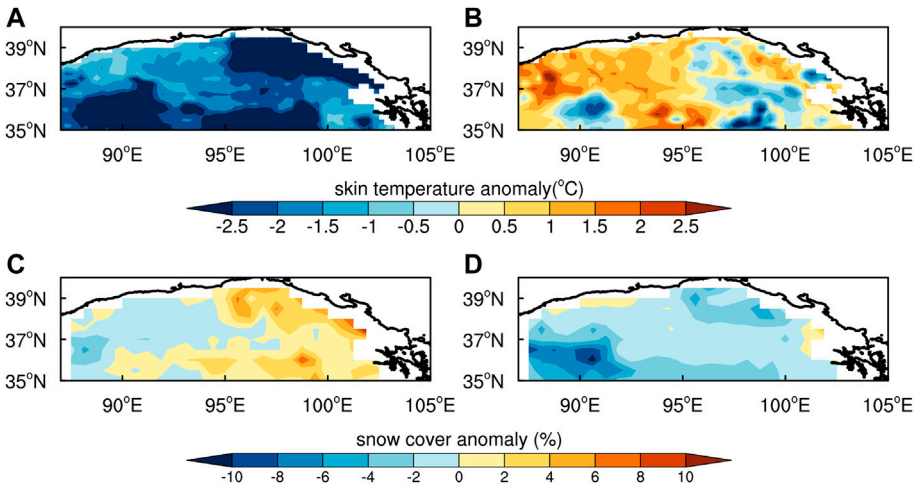

FIGURE 11 | Spatial distribution of **(A,B)** skin temperature (units: °C) and **(C,D)** snow cover (units: %) on (first column) the difference between high and normal days and (second column) the difference between low and normal days.

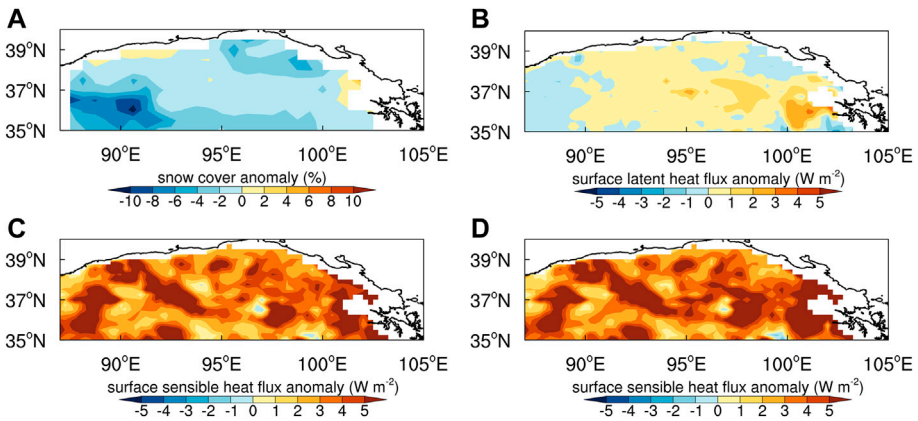

FIGURE 12 | Spatial distribution of **(A)** snow cover (units: %), **(B)** surface latent heat flux (units: W m^{-2}), **(C)** surface sensible heat flux (units: W m^{-2}), and **(D)** the surface latent + sensible heat flux (units: W m^{-2}) on the difference between low and normal days.

larger value over the northern TP (4.29 W m^{-2}). Hence, dust-on-snow over the TP can warm the TP and enhance its thermal effects by increasing the surface latent heat flux and sensible heat flux, thereby affecting the Asian climate.

4 DISCUSSION AND CONCLUSION

In addition to local dust emissions, a large number of dust particles over the TP come from external transport. Furthermore, both atmospheric dust and dust-on-snow over the TP affect snow over the TP by influencing the net surface radiation. Previous studies have mainly analyzed the effect of absorbing aerosols in the atmosphere and snow on snow cover from simulation models. This study evaluated the relative impacts of atmospheric dust and dust-on-snow over the TP in spring from 2009 to 2018 based on satellite data (MODIS) and reanalysis data (MERRA-2, ERA5).

The results showed that MERRA-2 captures the spatial and temporal distributions of aerosols over the TP well during 2009–2018. The seasonal distributions of AOD from the MERRA-2 reanalysis datasets are similar to those from MODIS and MISR retrievals. The climatic effects of dust on the energy budget and water cycle of the TP and surrounding areas cannot be ignored. Dust aerosols show decreasing trends over the TP from December to May, and snow cover shows increasing trends. Dust can absorb shortwave radiation, which can further affect snow cover over the TP.

By calculating the diurnal rate of dust concentration over the northern TP in the case of precipitation less than 0.049 mm, the extreme values of dust concentration were used to analyze the influencing mechanism of atmospheric dust and dust-on-snow

over the TP. The results show that the influence mechanism of atmospheric dust is different from that of dust-on-snow over the TP. Atmospheric dust reduces the surface temperature (−2.27°C) by weakening the net surface solar radiation (-3.84 W m-2) and increases the snow cover (1.04%). Dust-on-snow reduces the surface albedo (-0.004) and removes the snow cover (−2.00%) and expands the dust source region area by increasing snowmelt, resulting in an increase in dust emissions, which creates a significant positive feedback loop.

However, we ignore the effects of dry/wet deposition of dust on snow over the TP; as the influence of dry/wet deposition of dust on snow cover is different, the results might not be accurate. Additionally, we analyzed only dust aerosols and other types of aerosols mixed with dust aerosols in the atmosphere, which will result in different radiative characteristics (Bauer et al., 2007). We will discuss this in subsequent studies (Herman et al., 1997; Torres et al., 1998; Diner et al., 2002; Levelt et al., 2006a; Levelt et al., 2006b; Yao et al., 2010; Olauson, 2018; Tian et al., 2018; Kang et al., 2019; Sun et al., 2020; Allan et al., 2021; Liu et al., 2021).

DATA AVAILABILITY STATEMENT

The raw data supporting the conclusion of this article will be made available by the authors without undue reservation.

AUTHOR CONTRIBUTIONS

SYC conceived the idea. SYC and DZ designed the experiments. DZ, YC, and YG performed the analysis. DZ, SYC, GL, and SLC interpreted the results and wrote this article. All authors participated in the revision and editing of this article.

FUNDING

This work was supported by the Foundation for National Natural Science Foundation of China (91837103 and 41775003) and the Fundamental Research Funds for the Central Universities (lzujbky-2020-ct03).

ACKNOWLEDGMENTS

The data of M-ODIS AOD and snow cover from https://ladsweb.modaps.eosdis.nasa.gov/search/, the data of MISR AOD from https://l0dup05.larc.nasa.gov/L3Web/view, the data of MERRA-2 AOD from https://disc.gsfc.nasa.gov/datasets?keywords=MERRA2&page=1, and the data of ERA surface temperature and surface net solar radiation from https://cds.climate.copernicus.eu/cdsapp#!/dataset/reanalysis-era5-pressure-levels?tab=form.

REFERENCES

Allan, R. P., Arias, P. A., Berger, S., Canadell, J. G., Cassou, C., and Chen, D. (2021). *IPCC Climate Change 2021: The Physical Science Basis*.

Bauer, S. E., Mishchenko, M. I., Lacis, A. A., Zhang, S., Perlwitz, J., and Metzger, S. M. (2007). Do sulfate and Nitrate Coatings on Mineral Dust Have Important Effects on Radiative Properties and Climate Modeling? *J. Geophys. Res.* 112, D06307. doi:10.1029/2005JD006977

Bi, J. R., Huang, J. P., Holben, B., and Zhang, G. L. (2016). Comparison of Key Absorption and Optical Properties Between Pure and Transported Anthropogenic Dust over East and Central Asia *Atmos. Chem. Phys.* 16, 15501–15516. doi:10.5194/acp-16-15501-2016

Bolch, T., Kulkarni, A., Kääb, A., Huggel, C., Paul, F., Cogley, J. G., et al. (2012). The State and Fate of Himalayan Glaciers. *Science* 336 (6079), 310–314. doi:10.1126/science.1215828

Chen, S., Huang, J., Zhao, C., Qian, Y., Leung, L. R., and Yang, B. (2013). Modeling the Transport and Radiative Forcing of Taklimakan Dust over the Tibetan Plateau: A Case Study in the Summer of 2006. *J. Geophys. Res. Atmos.* 118, 797–812. doi:10.1002/jgrd.50122

Chen, S., Zhao, C., Qian, Y., Leung, L. R., Huang, J., Huang, Z., et al. (2014). Regional Modeling of Dust Mass Balance and Radiative Forcing over East Asia Using WRF-Chem. *Aeolian Res.* 15, 15–30. doi:10.1016/j.aeolia.2014.02.001

Cong, Z., Kang, S., Kawamura, K., Liu, B., Wan, X., Wang, Z., et al. (2015). Carbonaceous Aerosols on the South Edge of the Tibetan Plateau: Concentrations, Seasonality and Sources. *Atmos. Chem. Phys.* 15 (3), 1573–1584. doi:10.5194/acp-15-1573-2015

Diner, D. J., Beckert, J. C., Bothwell, G. W., and Rodriguez, J. I. (2002). Performance of the MISR Instrument during its First 20 Months in Earth Orbit. *IEEE Trans. Geosci. Remote Sens.* 40 (7), 1449–1466. doi:10.1109/TGRS.2002.801584

Draper, C. S., Reichle, R. H., and Koster, R. D. (2018). Assessment of MERRA-2 Land Surface Energy Flux Estimates. *J. Clim.* 31 (2), 671–691. doi:10.1175/jcli-d-17-0121.1

Duan, A., and Xiao, Z. (2015). Does the Climate Warming Hiatus Exist over the Tibetan Plateau? *Sci. Rep.* 5 (1), 13711. doi:10.1038/srep13711

Feng, X., Mao, R., Gong, D. Y., Zhao, C., Wu, C., Zhao, C., et al. (2020). Increased Dust Aerosols in the High Troposphere over the Tibetan Plateau from 1990s to 2000s. *J. Geophys. Res. Atmos.* 125, 807. doi:10.1029/2020JD032807

Flanner, M. G., Zender, C. S., Hess, P. G., Mahowald, N. M., Painter, T. H., Ramanathan, V., et al. (2009). Springtime Warming and Reduced Snow Cover from Carbonaceous Particles. *Atmos. Chem. Phys.* 9, 2481–2497. doi:10.5194/acp-9-2481-2009

Gelaro, R., McCarty, W., Suárez, M. J., Todling, R., Molod, A., Takacs, L., et al. (2017). The Modern-Era Retrospective Analysis for Research and Applications, Version 2 (MERRA-2). *J. Clim.* 30 (14), 5419–5454. doi:10.1175/JCLI-D-16-0758.1

Herman, J. R., Bhartia, P. K., Torres, O., Hsu, C., Seftor, C., and Celarier, E. (1997). Global Distribution of UV-Absorbing Aerosols from Nimbus 7/TOMS Data. *J. Geophys. Res.* 102 (D14), 16911–16922. doi:10.1029/96JD03680

Hersbach, H., Rosnay, P. D., Bell, B., Schepers, D., Simmons, A., Soci, C., et al. (2018). *Operational Global Reanalysis: Progress, Future Directions and Synergies with NWP*. doi:10.21957/tkic6g3wm

Hersbach, H., Bell, W., Berrisford, P., Horányi, A., Nicolas, J., Radu, R., et al. (2019). Global Reanalysis: Goodbye ERA-Interim, Hello ERA5. *ECMWF Newsl.* 159, 17–24. doi:10.21957/vf291hehd7

Hsu, N. C., Tsay, S.-C., King, M. D., and Herman, J. R. (2006). Deep Blue Retrievals of Asian Aerosol Properties during ACE-Asia. *IEEE Trans. Geosci. Remote Sens.* 44 (11), 3180–3195. doi:10.1109/TGRS.2006.879540

Huang, J., Yu, H., Guan, X., Wang, G., and Guo, R. (2016). Accelerated Dryland Expansion under Climate Change. *Nat. Clim. Change* 6 (2), 166–171. doi:10.1038/nclimate2837

Ji, Z., Kang, S., Zhang, Q., Cong, Z., Chen, P. F., Chen, P., et al. (2016). Investigation of Mineral Aerosols Radiative Effects over High Mountain Asia in 1990-2009 Using a Regional Climate Model. *Atmos. Res.* 178-179, 484–496. doi:10.1016/j.atmosres.2016.05.003

Kahn, R. A., Gaitley, B. J., Martonchik, J. V., Diner, D. J., Crean, K. A., and Holben, B. (2005). Multiangle Imaging Spectroradiometer (MISR) Global Aerosol Optical Depth Validation Based on 2 Years of Coincident Aerosol Robotic Network (AERONET) Observations. *J. Geophys. Res.* 110 (D10), D10S04. doi:10.1029/2004JD004706

Kahn, R. A., Nelson, D. L., Garay, M. J., Levy, R. C., Bull, M. A., Diner, D. J., et al. (2009). MISR Aerosol Product Attributes and Statistical Comparisons with MODIS. *IEEE Trans. Geosci. Remote Sens.* 47 (12), 4095–4114. doi:10.1109/TGRS.2009.2023115

Kang, S., Wake, C. P., Qin, D. H., Paul A, M., and Yao, T. D. (2000). Monsoon and Dust Signals Recorded in Dasuopu Glacier, Tibetan Plateau. *J. Glaciol.* 46 (153), 222–226. doi:10.3189/172756500781832864

Kang, S., Xu, Y., You, Q., Flügel, W.-A., Pepin, N., and Yao, T. (2010). Review of Climate and Cryospheric Change in the Tibetan Plateau. *Environ. Res. Lett.* 5 (1), 015101. doi:10.1088/1748-9326/5/1/015101

Kang, S., Wang, F., Morgenstern, U., Zhang, Y., Grigholm, B., Kaspari, S., et al. (2015). Dramatic Loss of Glacier Accumulation Area on the Tibetan Plateau Revealed by Ice Core Tritium and Mercury Records. *Cryosphere* 9 (3), 1213–1222. doi:10.5194/tc-9-1213-2015

Kang, S., Zhang, Q., Qian, Y., Ji, Z., Li, C., Cong, Z., et al. (2019). Linking Atmospheric Pollution to Cryospheric Change in the Third Pole Region: Current Progress and Future Prospects. *Nati. Sci. Rev.* 6 (4), 796–809. doi:10.1093/nsr/nwz031

Lau, W., and Kim, K.-M. (2018). Impact of Snow Darkening by Deposition of Light-Absorbing Aerosols on Snow Cover in the Himalayas-Tibetan Plateau and Influence on the Asian Summer Monsoon: A Possible Mechanism for the Blanford Hypothesis. *Atmosphere* 9, 438. doi:10.3390/atmos9110438

Levelt, P. F., Hilsenrath, E., Leppelmeier, G. W., van den Oord, G. H. J., Bhartia, P. K., Tamminen, J., et al. (2006a). Science Objectives of the Ozone Monitoring Instrument. *IEEE Trans. Geosci. Remote Sens.* 44 (5), 1199–1208. doi:10.1109/TGRS.2006.872336

Levelt, P. F., Van Den Oord, G. H. J., Dobber, M. R., Malkki, A., Huib Visser, H., Johan de Vries, J. D., et al. (2006b). The Ozone Monitoring Instrument. *IEEE Trans. Geosci. Remote Sens.* 44 (5), 1093–1101. doi:10.1109/TGRS.2006.872333

Levy, R. C., Remer, L. A., Mattoo, S., Vermote, E. F., and Kaufman, Y. J. (2007). Second-generation Operational Algorithm: Retrieval of Aerosol Properties over Land from Inversion of Moderate Resolution Imaging Spectroradiometer Spectral Reflectance. *J. Geophys. Res.* 112, D13211. doi:10.1029/2006JD007811

Lievens, H., Demuzere, M., Marshall, H.-P., Reichle, R. H., Brucker, L., Brangers, I., et al. (2019). Snow Depth Variability in the Northern Hemisphere Mountains Observed from Space. *Nat. Commun.* 10 (1), 4629. doi:10.1038/s41467-019-12566-y

Liu, L., Guo, J., Gong, H., Li, Z., Chen, W., Wu, R., et al. (2019). Contrasting Influence of Gobi and Taklimakan Deserts on the Dust Aerosols in Western North America. *Geophys. Res. Lett.* 46, 9064–9071. doi:10.1029/2019GL083508

Liu, H., Yan, R., and Yang, J. (2021). Credibility and Statistical Characteristics of CAMSRA and MERRA-2 AOD Reanalysis Products over the Sichuan Basin during 2003-2018. *Atmos. Environ.* 244, 117980. doi:10.1016/j.atmosenv.2020.117980

Liu, X., and Chen, B. (2000). Climatic Warming in the Tibetan Plateau during Recent Decades. *Int. J. Climatol.* 20 (14), 1729–1742. doi:10.1002/1097-0088(20001130)20:14<1729::aid-joc556>3.0.co;2-y

Liu, Y., Franklin, M., Kahn, R., and Koutrakis, P. (20072007). Using Aerosol Optical Thickness to Predict Ground-Level PM2.5 Concentrations in the St. Louis Area: A Comparison between MISR and MODIS. *Remote Sens. Environ.* 107, 33–44. doi:10.1016/j.rse.2006.05.022

Ma, Y., Zhu, Z., Zhong, L., Wang, B., Han, C., Wang, Z., et al. (2014). Combining MODIS, AVHRR and *In Situ* Data for Evapotranspiration Estimation over Heterogeneous Landscape of the Tibetan Plateau. *Atmos. Chem. Phys.* 14, 1507–1515. doi:10.5194/acp-14-1507-2014

Maa, B., Ma, X. Y., Yin, J., Ullah, W., Liu, M. Y., and Ullah, I. (2021). Performance Evaluation of ERA-5, JRA-55, MERRA-2, and CFS-2 Reanalysis Datasets, Over Diverse Climate Regions of Pakistan. *Weather and Climate Extremes* 33 (2), 100373. doi:10.1016/j.wace.2021.100373

Mao, R., Hu, Z., Zhao, C., Gong, D.-Y., Guo, D., and Wu, G. (2019). The Source Contributions to the Dust over the Tibetan Plateau: A Modelling Analysis. *Atmos. Environ.* 214, 116859. doi:10.1016/j.atmosenv.2019.116859

Niemand, M., Möhler, O., Vogel, B., Vogel, H., Hoose, C., Connolly, P., et al. (2012). A Particle-Surface-Area-Based Parameterization of Immersion Freezing on Desert Dust Particles. *J. Atmos. Sci.* 69 (10), 3077–3092. doi:10.1175/JAS-D-11-0249.1

Olauson, J. (2018). ERA5: The New Champion of Wind Power Modelling? *Renew. Energy* 126, 322–331. doi:10.1016/j.renene.2018.03.056

Parkinson, C. L. (2003). Aqua: an Earth-Observing Satellite Mission to Examine Water and Other Climate Variables. *IEEE Trans. Geosci. Remote Sens.* 41 (2), 173–183. doi:10.1109/TGRS.2002.808319

Qin, D. H., Shi, Y. L., and Li, P. J. (2006). Snow Cover Distribution, Variability, and Response to Climate Change in Western China. *J. Clim.* 19 (9), 1820–1833. doi:10.1175/JCLI3694.1

Qu, B., Ming, J., Kang, S.-C., Zhang, G.-S., Li, Y.-W., Li, C.-D., et al. (2014). The Decreasing Albedo of the Zhadang Glacier on Western Nyainqentanglha and the Role of Light-Absorbing Impurities. *Atmos. Chem. Phys.* 14 (20), 11117–11128. doi:10.5194/acp-14-11117-2014

Randles, C. A., Da Silva, A. M., Buchard, V., Colarco, P. R., Darmenov, A., Govindaraju, R., et al. (2017). The MERRA-2 Aerosol Reanalysis, 1980 Onward. Part I: System Description and Data Assimilation Evaluation. *J. Clim.* 30 (17), 6823–6850. doi:10.1175/JCLI-D-16-0609.1

Remer, L. A., Kleidman, R. G., Levy, R. C., Kaufman, Y. J., Tanré, D., Mattoo, S., et al. (2008). Global Aerosol Climatology from the MODIS Satellite Sensors. *J. Geophys. Res.* 113, D14S07. doi:10.1029/2007JD009661

Shen, M., Piao, S., Jeong, S.-J., Zhou, L., Zeng, Z., Ciais, P., et al. (2015). Evaporative Cooling over the Tibetan Plateau Induced by Vegetation Growth. *Proc. Natl. Acad. Sci. U.S.A.* 112 (30), 9299–9304. doi:10.1073/pnas.1504418112

Shi, Z., Xie, X., Ren, X., Li, X., Yang, L., Lei, J., et al. (2019). Radiative Effect of Mineral Dust on East Asian Summer Monsoon during the Last Glacial Maximum: Role of Snow-Albedo Feedback. *Geophys. Res. Lett.* 46 (19), 10901–10909. doi:10.1029/2019gl084211

Smith, T., and Bookhagen, B. (2018). Changes in Seasonal Snow Water Equivalent Distribution in High Mountain Asia (1987 to 2009). *Sci. Adv.* 4 (1), e1701550. doi:10.1126/sciadv.1701550

Sun, G., Hu, Z., Ma, Y., Xie, Z., Yang, S., and Wang, J. (2020). Analysis of Local Land-Atmosphere Coupling in Rainy Season over a Typical Underlying Surface in Tibetan Plateau Based on Field Measurements and ERA5. *Atmos. Res.* 243 (2020), 105025. doi:10.1016/j.atmosres.2020.105025

Taszarek, M., Pilguj, N., Allen, J. T., Gensini, V., Brooks, H. E., and Szuster, P. (2021). Comparison of Convective Parameters Derived from ERA5 and MERRA2 with Rawinsonde Data over Europe and North America. *J. Clim.* 34 (8), 3211–3237. doi:10.1175/JCLI-D-20-0484.1

Tian, X., Xie, P., Xu, J., Li, A., Wang, Y., Qin, M., et al. (2018). Long-term Observations of Tropospheric NO2, SO2 and HCHO by MAX-DOAS in Yangtze River Delta Area, China. *J. Environ. Sci.* 71, 207–221. doi:10.1016/j.jes.2018.03.006

Torres, O., Bhartia, P. K., Herman, J. R., Ahmad, Z., and Gleason, J. (1998). Derivation of Aerosol Properties from Satellite Measurements of Backscattered Ultraviolet Radiation: Theoretical Basis. *J. Geophys. Res.* 103 (D14), 17099–17110. doi:10.1029/98JD00900

Wang, B., Bao, Q., Hoskins, B., Wu, G., and Liu, Y. (2008). Tibetan Plateau Warming and Precipitation Changes in East Asia. *Geophys. Res. Lett.* 35 (14), L14702. doi:10.1029/2008GL034330

Wang, H. B., Zhang, L., Cao, X. J., Zhang, Z. W., and Liang, J. N. (2012). A-Train Satellite Measurements of Dust Aerosol Distributions Over Northern China. *J. Quantitat. Spectr. Radiat. Transf.* 122, 170–179. doi:10.1016/j.jqsrt.2012.08.011

Wang, Q., Jacob, D. J., Spackman, J. R., Perring, A. E., Schwarz, J. P., Moteki, N., et al. (2014). Global Budget and Radiative Forcing of Black Carbon Aerosol: Constraints from Pole-To-Pole (HIPPO) Observations across the Pacific. *J. Geophys. Res. Atmos.* 119, 195–206. doi:10.1002/2013JD020824

Wu, G. X., Liu, Y. M., Liu, X., Duan, A. M., and Liang, X. Y. (2005). How the Heating over the Tibetan Plateau Affects the Asian Climate in Summer. *Chin. J. Atmos. Sci.* 29 (1), 47–56. (in Chinese).doi:10.3878/j.issn.1006-9895.2005.01.06

Wu, G., He, B., Duan, A., Liu, Y., and Yu, W. (2017). Formation and Variation of the Atmospheric Heat Source over the Tibetan Plateau and its Climate Effects. *Adv. Atmos. Sci.* 34 (10), 1169–1184. doi:10.1007/s00376-017-7014-5

Xia, X., Wang, P., Wang, Y., Li, Z., Xin, J., Liu, J., et al. (2008). Aerosol Optical Depth over the Tibetan Plateau and its Relation to Aerosols over the Taklimakan Desert. *Geophys. Res. Lett.* 35, L16804. doi:10.1029/2008gl034981

Xie, X., Liu, X., Che, H., Xie, X., Li, X., Shi, Z., et al. (2018). Radiative Feedbacks of Dust in Snow over Eastern Asia in CAM4-BAM. *Atmos. Chem. Phys.* 18, 12683–12698. doi:10.5194/acp-18-12683-2018

Xu, B. Q., Wang, M., Joswiak, D. R., Cao, J. J., Yao, T. D., Wu, G. J., et al. (2009). Deposition of Anthropogenic Aerosols in a Southeastern Tibetan Glacier. *J. Geophys. Res. Atmos.* 114, 1510. doi:10.1029/2008jd011510

Xu, C., Ma, Y. M., You, C., and Zhu, Z. K. (2015a). The Regional Distribution Characteristics of Aerosol Optical Depth over the Tibetan Plateau. *Atmos. Chem. Phys.* 15 (20), 12065–12078. doi:10.5194/acp-15-12065-2015

Xu, X. D., Zhao, T. L., Shi, X. H., and Lu, C. G. (2015b). A Study of the Role of the Tibetan Plateau's Thermal Forcing in Modulating Rainband and Moisture Transport in Eastern China. *Acta Meteorol. Sin. (in Chin.* 73 (1), 20–35.

Yao, T., Li, Z., Yang, W., Guo, X., Zhu, L., Kang, S., et al. (2010). Glacial Distribution and Mass Balance in the Yarlung Zangbo River and its Influence on Lakes. *Chin. Sci. Bull.* 55 (20), 2072–2078. doi:10.1007/s11434-010-3213-5

Yao, T., Thompson, L., Yang, W., Yu, W., Gao, Y., Guo, X., et al. (2012). Different Glacier Status with Atmospheric Circulations in Tibetan Plateau and Surroundings. *Nat. Clim. Change* 2, 663–667. doi:10.1038/nclimate1580

Yuan, T., Chen, S., Huang, J., Wu, D., Lu, H., Zhang, G., et al. (2019). Influence of Dynamic and Thermal Forcing on the Meridional Transport of Taklimakan Desert Dust in Spring and Summer. *J. Clim.* 32 (3), 749–767. doi:10.1175/JCLI-D-18-0361.1

Yuan, T. G., Chen, S. Y., Wang, L., Yang, Y., Bi, H., Zhang, X., et al. (2020). Impacts of Two East Asian Atmospheric Circulation Modes on Black Carbon Aerosol over the Tibetan Plateau in Winter. *J. Geophys. Res.* 125 (12), e2020JD032458. doi:10.1029/2020jd032458

Zhang, G., Xie, H., Yao, T., Liang, T., and Kang, S. (2012). Snow Cover Dynamics of Four Lake Basins over Tibetan Plateau Using Time Series MODIS Data (2001-2010). *Water Resour. Res.* 48 (10), 1–22. doi:10.1029/2012WR011971

Zhang, Y., Kang, S., Sprenger, M., Cong, Z., Gao, T., Li, C., et al. (2017). "BC and Mineral Dust in Snow Cover on the Third Pole," in *The Cryosphere Discussions*, 1–26. doi:10.5194/tc-2017-111

Zhang, Y. L., Gao, T. G., Kang, S. C., Shanggua, D. h., and Luo, X. (2021). Albedo Reduction as an Important Driver for Glacier Melting in Tibetan Plateau and its Surrounding Areas. *Earth Sci. Rev.* 22, 103735. doi:10.1016/J.EARSCIREV.2021.103735

Zhou, T., and Zhang, W. (2021). Anthropogenic Warming of Tibetan Plateau and Constrained Future Projection. *Environ. Res. Lett.* 16 (4), 044039. doi:10.1088/1748-9326/abede8

Conflict of Interest: The authors declare that the research was conducted in the absence of any commercial or financial relationships that could be construed as a potential conflict of interest.

frontiers | Frontiers in Environmental Science

ORIGINAL RESEARCH
published: 27 June 2022
doi: 10.3389/fenvs.2022.856438

Meteorological Influence of Mineral Dust Distribution Over South-Western Africa Deserts Using Reanalysis and Satellite Data

Lerato Shikwambana[1,2]* *and Mahlatse Kganyago*[1,2]

[1]Earth Observation Directorate, South African National Space Agency, Pretoria, South Africa, [2]School of Geography, Archaeology and Environmental Studies, University of the Witwatersrand, Johannesburg, South Africa

This study investigated the meteorological influence of mineral dust in the south-western African region using satellite and reanalysis datasets by studying 1) the seasonal transport and distribution of mineral dust in the region; 2) the relationship between precipitation, wind and desert dust, and 3) the long-term trends of dust column density, precipitation rate and surface wind speed. The results show that the Namib desert is the main source of dust in the region, with the density and distribution varying by seasons. The study found that the greatest dust distribution occurs in the June-July-August (JJA) season, attributed to the southwesterly winds which transport the dust into the interior of the region. Moreover, small dust aerosols less that 20 µm are observed at highest altitudes between 7 and 10.28 km. Favourable meteorological such as strong and fast winds and low precipitation, and low vegetation played a vital role in the production and distribution of dust aerosols. Over a long time (i.e., from 1990 to 2020), dust column density trend increased, while precipitation and surface wind speed trends decreased. This study provides significant basis for assessing and monitoring of the desertification processes and their effect on regional climate variability and change in Southwest Africa, where data is ground-based data is scarce and related efforts are rare.

Keywords: dust aerosols, dust—extinction, CALIPSO, wind, MODIS, NDVI

OPEN ACCESS

Edited by:
Zhenming Ji,
Sun Yat-sen University, China

Reviewed by:
Jose M. Baldasano,
Universitat Politecnica de Catalunya, Spain
Shani Tiwari,
Council of Scientific and Industrial Research (CSIR), India

***Correspondence:**
Lerato Shikwambana
lshikwambana@sansa.org.za

Specialty section:
This article was submitted to Atmosphere and Climate, a section of the journal Frontiers in Environmental Science

Received: *17 January 2022*
Accepted: *31 May 2022*
Published: *27 June 2022*

Citation:
Shikwambana L and Kganyago M (2022) Meteorological Influence of Mineral Dust Distribution Over South-Western Africa Deserts Using Reanalysis and Satellite Data. Front. Environ. Sci. 10:856438. doi: 10.3389/fenvs.2022.856438

1 INTRODUCTION

Tropospheric aerosols ascend from natural sources such as sea-spray, volcanoes and mineral dust. Other sources of tropospheric aerosols occur from anthropogenic activities such as biomass burning, combustion of fossil fuels and from gas-to-particles conversion processes (Feiyu et al., 2008). Aerosols have substantial ability to influence the radiation transfer through the atmosphere and atmosphere water cycle, thus influence the Earth's climate directly and indirectly (Hui et al., 2005).

Mineral dust is a major component of atmospheric aerosol loading with the strongest source regions in the Saharan Desert (Caquineau et al., 2002; Washington et al., 2003; Papayannis et al., 2005; Adams et al., 2012; Ginoux et al., 2012; Chouza et al., 2016; Shikwambana and Sivakumar 2018). These dust aerosols fluctuate in space and time, with variability in mass of more than 4 orders of magnitude (Mahowald et al., 2009; Mahowald et al., 2014). Due to its specific optical properties, airborne mineral dust can absorb and scatter both terrestrial and solar radiation with direct and indirect effects on the climate (Li et al., 1996; Buseck and Mihaly 1999; Sokoliket al. 2001; Dufresne et al., 2002; Johnson and Osborne 2011; Gehlot et al., 2015). Mineral dust aerosols are accountable for

substantial climate forcing through their indirect effects on cloud and precipitation processes and their direct effects on solar and thermal radiation. The transport of mineral dust by prevailing winds from the Saharan Desert (Prospero 1996; Prospero 1999; Kallos et al., 2006; Knippertz and Todd 2012; Ridley et al., 2014), and from the Arabian desert (Prakash et al., 2015; Shalaby et al., 2015; Francis et al., 2017) have been extensively reported. However, in southern Africa only a few studies concerning mineral dust have been reported by authors such as Tesfaye et al. (2015), Dansie et al. (2017) to name a few. Bryant et al. (2007) conducted a study that focused on dust emissions from the Makgadikgadi Pans of Botswana using various satellite data such as the Total Ozone Mapping Spectrometer (TOMS) and Moderate Resolution Imaging Spectrometer (MODIS) for the period of 1980–2000. In their study they found that surface wind speed variability, sediment inflows, the extent and frequency of lake inundation intermittently influenced the desert dust loadings. Furthermore, Bhattachan et al. (2012) showed that vegetation loss and dune remobilization in the Southern Kalahari can promote dust emissions comparable to those observed from major contemporary dust sources in the Southern African region. An update dust plume source inventory for southern Africa was presented by Vickery et al. (2013). In this work they detected 328 distinct daytime dust plumes which were attributed to 101 point sources. The point sources consisted largely of ephemeral inland lakes, coastal pans as well as dry river valleys originating from Namibia, Botswana, and South Africa. Furthermore, the plume observations identified sub-basin scale source clusters for the Etosha Pan, Makgadikgadi Pans as well as the south western Kalahari pan belt.

Over the past years, the use of satellites and reanalysis datasets have proven to being amongst the best methods to use for large continuous area coverage and long-time monitoring. Some of the disadvantages of satellites is that they have limited use of optical sensors in cloudy conditions. However, in this work satellite and reanalysis datasets are of great advantage since they offer the ability to view broad areas which is important for studying the distribution of dust aerosols. Mineral dust aerosol data from the Cloud-Aerosol Lidar and Infrared Pathfinder Satellite Observations (CALIPSO) (Amiridis et al., 2013; Huang et al., 2015; Zhao et al., 2015) and the Modern-Era Retrospective analysis for Research and Applications, Version 2 (MERRA-2) (Schepanski et al., 2016; Provençal et al., 2017) have been used in the past by several researchers. CALIPSO can identify the different types of aerosols such as dust and can further provide vertical height profiles of dust. MERRA-2 provides the spatial distribution of dust extinction and wind vector data.

This research aims to 1) study the seasonal distribution of mineral dust, 2) study the seasonal distribution of meteorological parameters that impact on the mineral dust, 3) study the seasonal vertical height profiles of dust and 4) study the trend analysis of dust and some meteorological parameters that influence the dust distribution. The study presented here is organised as follows: the study region is discussed in **Section 2** while details of the data used is given in **Section 3**. **Section 4** contains a discussion of the results and conclusions are given in **Section 5**.

2 STUDY SITE

Figure 1 shows the two main deserts in southern Africa, i.e. the Namib and Kalahari. The Namib is a costal desert which stretches <2000 km along the Atlantic coasts of South Africa, Namibia and Angola. The descent of dry air of the Hadley Cell cooled by the cold Benguela current along the coast causes the Namib's aridity. In central Namib, the desert extends for approximately 140 km inland (Lancaster et al., 1984), becoming narrower at its northern and southern extremities (Lancaster et al., 1984). Within the desert, coastal plains are characterised by high air humidity, no rain and mild air temperatures. On the other hand, eastern part of the desert is characterized by low air humidity, high air temperatures, and summer rainfall prevail (Hachfeld and Jürgens 2000).

The Kalahari Desert (a large semi-arid sandy savannah) is located approximately 600 km east of the Namib desert. It occupies the northernmost part of the Northern Cape province in South Africa, the eastern third of Namibia, the southeastern parts of Angola and almost all of Botswana. The longest north-south extent is ~1,600 km, and its greatest east-west distance is ~970 km. Precipitation in the northern Kalahari can reach ~635 mm annually and the precipitation in the southern Kalahari can reach ~254 mm annually.

3 DATA AND METHODS

3.1 Data

3.1.1 CALIPSO

CALIPSO has been in orbit since 2006 and has been collecting data ever since. The specifications of CALIPSO are discussed in detail by Winker et al. (2003, 2010). One the objectives for CALIPSO is to provide measurements on the spatial and vertical distribution of aerosols globally. There are three basic types of Level 2 data products: profile products, layer products, and the vertical feature mask (VFM), and these data products are provided at various spatial resolutions. The level 2 processing involves three major steps which are discussed in detail by Winker et al. (2009).

Level 3 aerosol profile product reports monthly averaged statistics based on quality-screened level 2 aerosol extinction profiles at 532 nm below 12 km in altitude, vertically gridded to mean-sea-level. Further details on the methodology used for the generation of the Level 3 products can be found in Winker et al. (2013), Tackett et al. (2018). The mean bias becomes much larger for altitudes lower that 3 km (of the order of 60%) which is attributed to the decrease of the CALIOP signal-to-noise ratio, as well as to the incomplete overlap height region of the ground based lidar and finally to the distance between the two instruments, resulting to the observation of possibly different air masses. The data, used in this study, is the all-sky dust extinction coefficients at 532 nm available from the CALIOP Level 3 aerosol profile monthly products with a horizontal resolution of $2^{\circ} \times 5^{\circ}$ (latitude/longitude) and a vertical resolution of 60 m.

3.1.2 MERRA-2

The Modern-Era Retrospective analysis for Research and Applications, Version 2 (MERRA-2) was introduced to replace and extend the original MERRA dataset (Rienecker et al., 2011). It

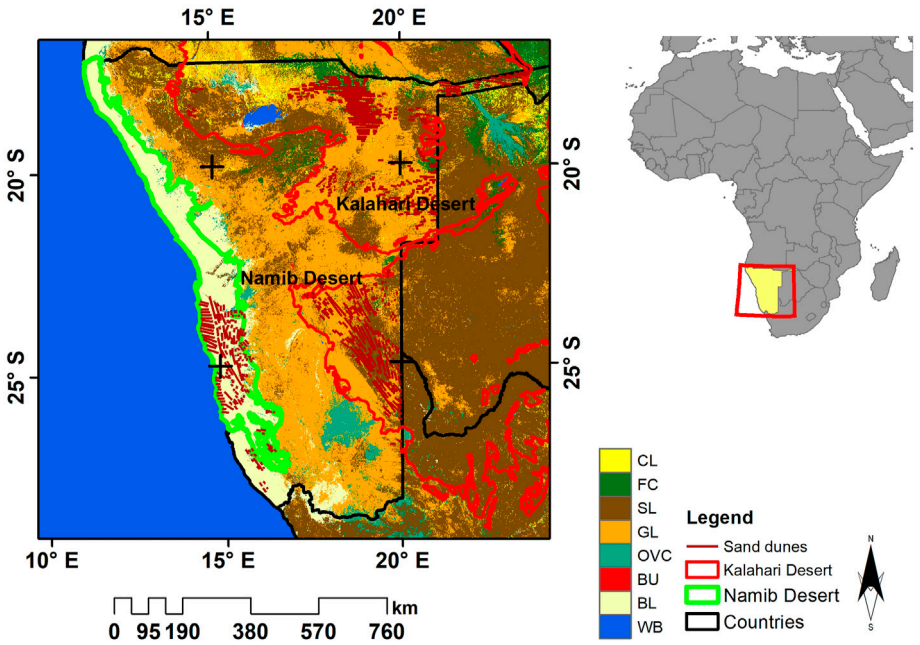

FIGURE 1 | Locations of deserts and selected pans in southern Africa.

is produced using version 5.12.4 of the Goddard Earth Observing System Model (GEOS) Data Assimilation System (DAS). Gridded data are released at a 0.625° longitude × 0.5° latitude resolution on 72 sigma–pressure hybrid layers between the surface and 0.01 hPa. MERRA-2 contains the assimilation of bias-corrected AOD from the Advanced Very High Resolution Radiometer (AVHRR) and MODIS, AOD over bright surfaces obtained from the Multiangle Imaging SpectroRadiometer (MISR), and AOD from the AErosol RObotic NETwork (AERONET) (Randles et al., 2016). More details on MERRA and MERRA-2 can be found in Rienecker et al. (2008, 2011), Buchard et al. (2015, 2016), respectively. The data used in this study are the dust column density products.

3.1.3 AIRS

The Atmospheric Infrared Sounder (AIRS) instrument was launched on 4 May 2002 on the Earth Observing System (EOS) Aqua Platform. It collects information on the different layers of the atmosphere and provides hyperspectral imagery through applying various processing algorithms. The instrument collects climate data and turns it into 3-D maps of water vapour, cloud properties, and air/surface temperature. Moreover, AIRS can measure the atmospheric temperature in the troposphere with precision of ~1 K over 1 km-thick layers under cloudy and clear conditions. AIRS also has 4 visible (VIS) and near-IR (NIR) channels between 0.40 and 0.94 μm, which are utilized for the detection of clouds in the IR FOV. The IR resolution for AIRS is 1 km in the vertical and 13.5 km in the horizontal. The VIS/NIR spatial resolution, on the other hand, is ~2.3 km. The uncertainty of estimate for temperature profiles are 1) between 1 and 2 K/km in the troposphere and 2) between 2 and 3 K/km above the troposphere. More details of the instrument are discussed by Hartmut et al. (1995), Chahine et al. (2006), Menzel et al. (2018). In this study, we use the air temperature product.

3.1.4 TRMM

In November 1997 the Tropical Rainfall Measuring Mission (TRMM) was launched. TRMM has 5 instruments onboard namely, the Lightning Imaging Sensor (LIS), TRMM Microwave Imager (TMI), Visible and Infrared Scanner (VIRS), the Precipitation Radar (PR), Clouds and the Earth's Radiant Energy System (CERES). Kummerow et al. (2000), Liu et al. (2012) provide comprehensive details on the specifications of the TMI, PR, VIRS and LIS instruments. The overall objective of TRMM was to use 1) to obtain and study multi-year science data sets of tropical and subtropical rainfall measurements, 2) to understand how interactions between the sea, air and landmasses produce changes in global rainfall and climate, 3) to improve modelling of tropical rainfall processes and their influence on global circulation to predict rainfall and variability at various periods, and 4) to test, evaluate and improve satellite rainfall measurement techniques. The relative bias of preceipitation has been calculated elevation wise, and the values have been characterized under three categories as under-estimation (bias <10%), overestimation (bias >10%), and approximately equal (bias range from 10% to 10%) (Yang and Luo, 2014). In this study, the precipitation rate product was used.

3.1.5 MODIS Normalised Difference Vegetation Index

The Normalised Difference Vegetation Index (NDVI) products (MOD13Q1) collection 6 (C6) product, from Moderate Imaging Spectroradiometer (MODIS) sensors onboard Aqua satellites, were averaged by season, i.e., DJF, MAM, JJA, and SON, in

TABLE 1 | Summary of the data used in this study.

Input data source (temporal resolution, spatial resolution)	Products used	Period of analysis	Output data
Merra-2 (monthly; 0.5° × 0.625°)	(a) Dust surface mass concentration (μg.m^{-3})	1990–2020	Seasonal distribution maps of dust surface mass concentration
	(b) Surface wind speed and wind vectors (m.s^{-1})	1990–2020	Seasonal distribution maps of wind speed and wind direction
CALIPSO (monthly, 2° × 5°)	Dust extinction coefficients at 532 nm (Mm^{-1})	2007–2020	Dust extinction coefficient vertical seasonal profiles
AIRS (monthly, 13.5 km at nadir, 1 km vertical)	Air temperature (°C)	2002–2020	Seasonal distribution maps of air temperature
TRMM (monthly, 0.25° × 0.25°)	Precipitation rate (mm/month)	2000–2020	Seasonal distribution maps of the precipitation rate
MODIS Vegetation Indices (MOD13Q1.006)	Normalised Difference Vegetation Index (NDVI)	2000–2020	Seasonal vegetation variation maps

Google Earth Engine (GEE). The products have a spatial resolution of 250 m and spanned from 2000–2020, thus were suitable to analyse the seasonal vegetation variations in this study. The NDVI quantifies vegetation by measuring the difference between near-infrared (where there is high scattering by vegetation structure) and red light (where vegetation biochemistry causes intense absorption). Generally, NDVI values <0.1 indicate no green vegetation, values between 0.2 and 0.4 correspond to areas with sparse vegetation, values between 0.4 and 0.6 indicate moderate vegetation, while values >0.6 indicate a high density of green vegetation. The MOD13Q1 C6 product has achieved Stage 3 validation, i.e., uncertainties have been rigorously quantified over global sites. Its uncertainties are within ±0.025 (https://modis-land.gsfc.nasa.gov/ValStatus.php?ProductID=MOD13, accessed: 12/05/2022). Errors in the red band associated with residual atmospheric effects are the main source of the NDVI errors.

The summary of the data used is given in **Table 1**.

3.2 Method

3.2.1 Statistical Analysis

Sneyers (1990) produced a statistical test to identify abrupt changes in significant trends. The Sequential Mann-Kendall (SQMK) test sets up two series, a progressive (forward) and a retrograde (backward) series (Sneyers, 1997; Sneyers et al., 1998; Lu et al., 2004). If the progressive and retrograde series intersect each other and diverge beyond some base value, then there is a statistically significant trend. The point where they intersect each other shows the approximate year at which the trend starts (Mosmann et al., 2004). **Supplementary Appendix A1** gives the SQMK test steps in detail.

4 RESULTS AND DISCUSSION

4.1 Seasonal Spatial and Vertical Distribution of Dust

Figure 2 shows an averaged seasonal spatial distribution of dust surface concentration overlay with 2-m wind vectors in the study region. The results clearly show that the Namib desert is the main source of dust in the region seasonally. In their study, Vickery et al. (2013) show that the Namib desert produces the highest number of plumes ~85 compared to other dust sources in Southwest Africa. This is one of the reasons why a high dust concentration is observed in that region seasonally. **Figure 2** results further show that the Kalahari Desert does not contribute significantly to the overall emission of dust in the southern African region. However, at a local scale, the Kalahari Desert could be the major contributor to the dust emissions. This is because the Kalahari is made up of biomes which is likely to trap the dust, especially during the rainy (DJF) season. The higher precipitation rate in the Kalahari also dampens the soil which reduces the formation of dust and sand. The low wind speeds also reduce the lifting and transport of sand and dust aerosols. The highest dust concentration between 0.25 and 0.30 μg m^{-3} in the Namib Desert is observed in the JJA season, followed up by the SON, DJF and MAM seasons, respectively. The high wind speeds in the JJA season (see **Figure 2C**) are the main source of the high concentration of dust. The strong winds lift large amounts of sand and dust from bare, dry soils into the atmosphere. The low precipitation seasonally also ensures that the sand and dust is always dry thus making it easier for the lifting process. This process also applies to moderate wind speeds in the SON season (see **Figure 2D**). In the SON season, a moderate dust concentration of between 0.15 and 0.23 μg m^{-3} is observed. A low dust concentration between 0.1 and 0.15 μg m^{-3} is observed in the DJF and MAM seasons, **Figures 2A,B**, respectively. The low wind speed is one of the factors that influence the low concentration of dust.

Dust aerosols exert a significant effect on the global radiative budget by scattering and absorbing longwave and shortwave radiation thereby impacting the vertical profile of temperature, atmospheric stability and precipitation (Denjean et al., 2016). It is for this reason that the knowledge of the vertical distribution of dust is important. **Figure 3** shows dust extinctions profiles averaged in a latitude-longitude box. The largest dust extinction coefficients value of ~2.7 Mm^{-1} is observed at the surface during the DJF season. This large extinction coefficient

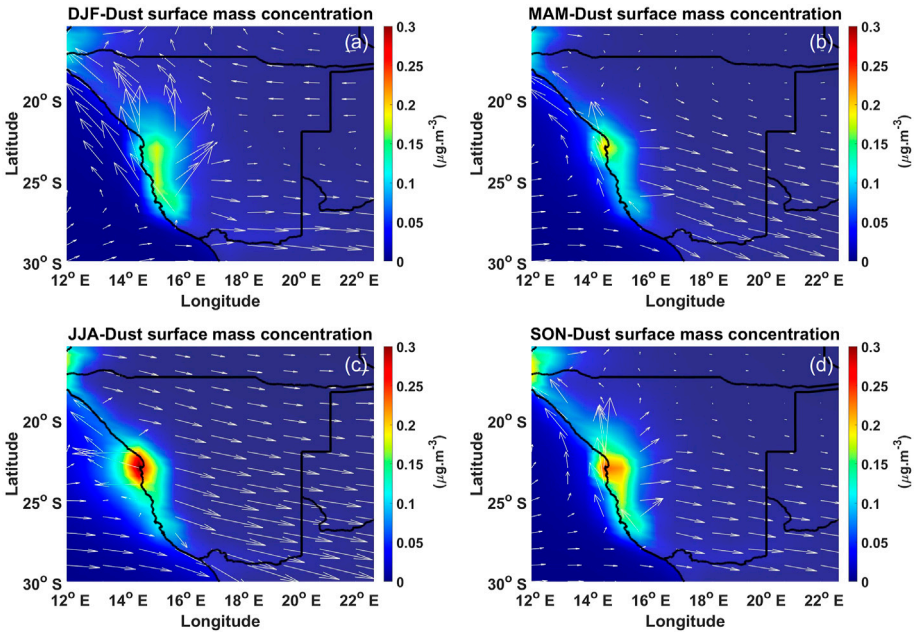

FIGURE 2 | Seasonal averaged dust surface mass concentration overlay with wind vectors for the period 1998–2020 in **(A)** DJF, **(B)** MAM, **(C)** JJA and **(D)** SON, obtained from MERRA-2.

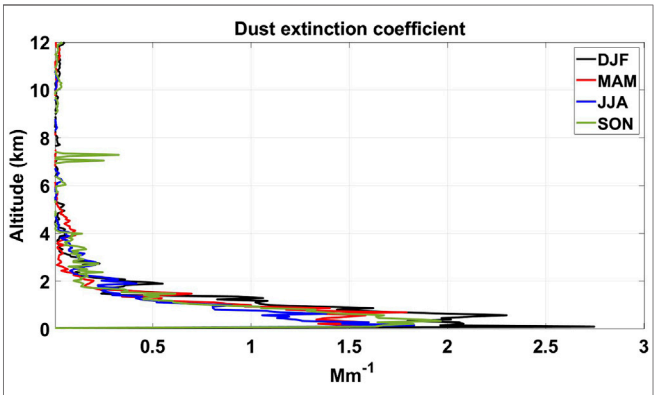

FIGURE 3 | Seasonal mean dust extinction coefficient profiles from CALIPSO over the period 2007–2020, obtained from CALIPSO.

value implies a high dust aerosol loading at the surface. However, the dust extinction coefficients values decrease with increasing altitude indicating that most of the dust aerosols are concentrated at the surface and elevate at an altitude less than 4 km. The suppression of dust aerosols on ths surface might be due to higher precipitation rates and low wind speeds. On the other hand, elevated dust aerosols are observed during the SON season. Three distinct peaks at 7.05 km (0.25 Mm^{-1}), 7.29 km (0.33 Mm^{-1}) and 10.28 km (0.037 Mm^{-1}) are observed during this period. The synthesis and elevation of these dust aerosols are due to the dry soil conditions and high wind speeds (Aili et al., 2016) experienced during this season. The high temperatures and lack of precipitation contribute favourably to the drying of the soil, which allows for the production of dust particles, and allows strong winds to transport the dust particles into the upper troposphere. Alfaro et al. (1998) showed that strong winds force particles of about 100–200 μm diameter to move in ballistic trajectories ("saltation") close to the surface. These saltating particles can break apart or eject smaller soil particles upon impacting the soil. These smaller particles (<~50 μm) are entrained into the boundary layer, after which they can be transported long distances.

4.2 Seasonal Meteorological Conditions Over the Deserts

Meteorological parameters such as wind speed and wind direction are important to understand the dispersion and propagation directions of dust aerosols. Wind in the desert also has a vast effect on the formation of sand dunes. Wind speed and wind direction seasonal results obtained from MERRA-2 are presented in **Figure 4**. Although wind speed and wind direction show seasonal variations, the only consistency is the prevailing westerlies, from the Atlantic Ocean, travelling at high wind speeds of between 8.5 and 10 m s^{-1} every season. Moreover, the longshore southerly winds in the central coastline region are also present and are maintained by a strong pressure gradient between a permanent high-pressure cell over the ocean, the South Atlantic Anticyclone (SAA), and a thermal low over the hot, arid continental landmass (Shannon, 1985; Peard, 2007). The lowest wind speeds of between 4 and 6 m s^{-1} are observed over the Namib and Kalahari deserts in the DJF, MAM and SON seasons (see **Figures 4A,B,D**). The dominant wind directions in these seasons are the westerlies and

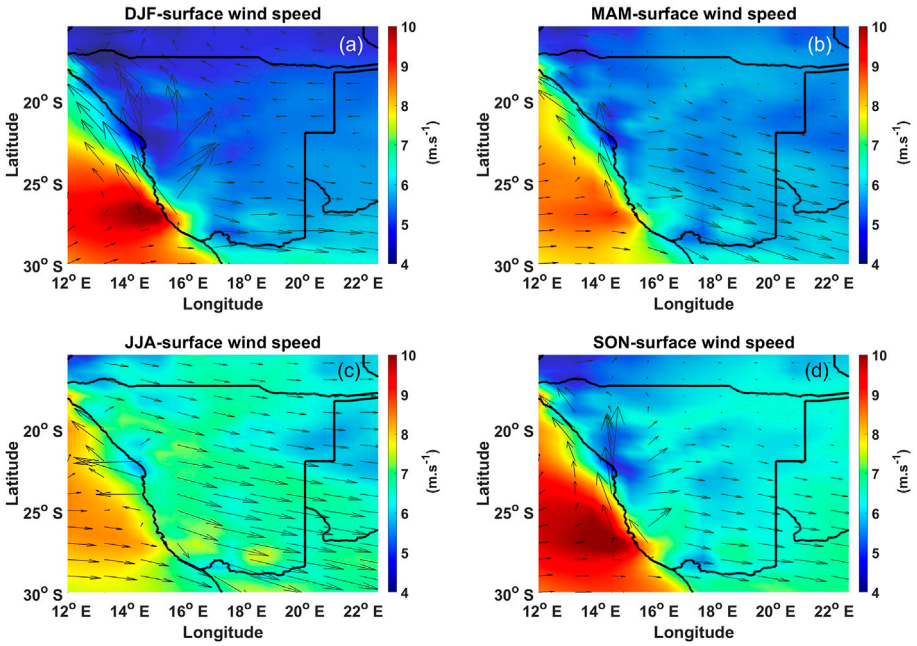

FIGURE 4 | Seasonal averaged wind speed overlay with wind vectors from 1998 to 2020 in **(A)** DJF, **(B)** MAM, **(C)** JJA and **(D)** SON, obtained from MERRA-2.

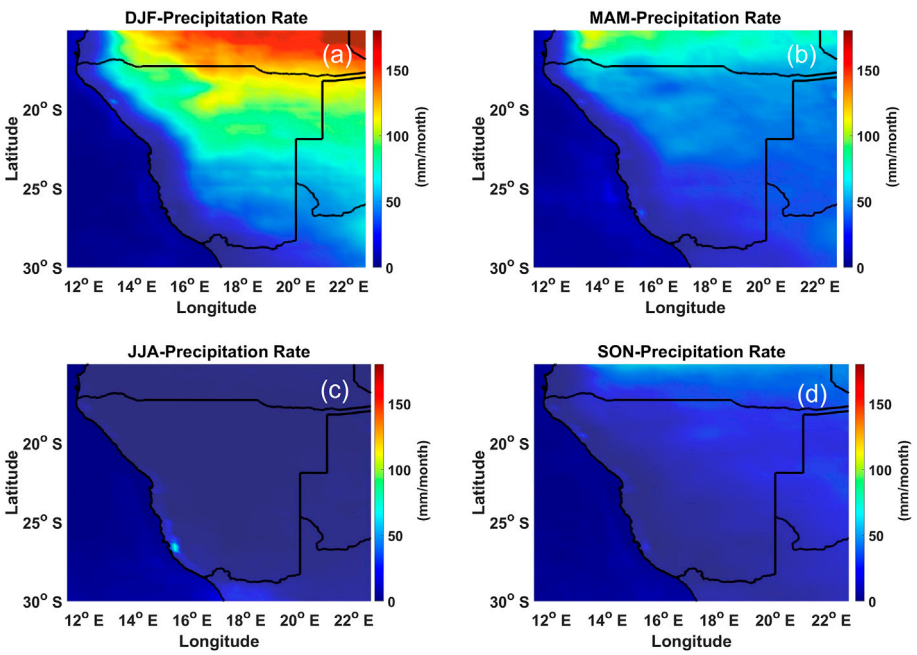

FIGURE 5 | Seasonal averaged precipitation rate from 1998 to 2020 in **(A)** DJF, **(B)** MAM, **(C)** JJA and **(D)** SON, obtained from TRMM.

southerlies. However, moderate wind speeds of between 7 and 8 m s^{-1} with dominant westerlies and easterlies winds are observed in the JJA season.

Figure 5 shows the averaged seasonal precipitation rate over the study area. Overall, the precipitation over the Namib desert is extremely low, less than 50 mm/month. However, in the JJA season (see **Figure 3C**) the is an area (23°S, 15°E) on the southern part of the desert with a precipitation rate of ~80 mm/month, which is the highest in the Namib Desert. On the other hand, the Kalahari Desert shows a precipitation rate variability for the

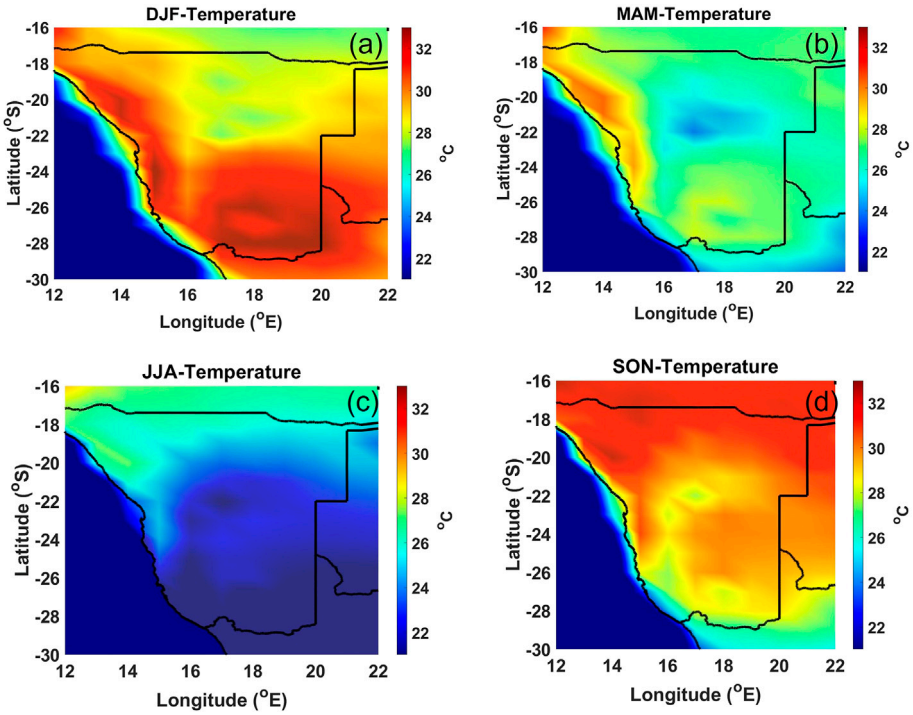

FIGURE 6 | Seasonal averaged temperature for the period of 1998–2020 in **(A)** DJF, **(B)** MAM, **(C)** JJA and **(D)** SON, obtained from AIRS.

different seasons. A high precipitation rate of ~120 mm/month is observed in the DJF season (see **Figure 5A**) while the lowest precipitation rate of >50 mm/month is observed in the JJA and SON seasons (see **Figures 5C,D**). The MAM season shows a moderate precipitation rate of ~80 mm/month. The low precipitation can be attributed to increased dust aerosol concentration. Lohmann and Feichter (2005) showed that dust aerosol can suppress precipitation by promoting the formation of small cloud droplets that do not lead to any rainfall. Furthermore, Brooks (2000) also showed that the increase in dust concentration leads to increasing atmospheric stability and reducing convection which results in decreasing rainfall. Therefore, increase concentrations of dust aerosols in the atmosphere lead to less precipitation in these deserts. Precipitation is important especially in the Kalahari Desert which has some biomes, which require some amount of water to survive.

The average seasonal air temperature is shown in **Figure 6**. The highest average temperature of ~33°C is observed over the Namib and Kalahari Deserts during the DJF season (see **Figure 6A**). The SON season also shows slightly high temperatures between 30 and 33°C over the Namib and Kalahari Deserts (see **Figure 6D**). The lowest temperature between 22 and 26°C over these deserts are observed in the JJA season (see **Figure 6C**), while moderate temperatures of between 26 and 30°C are observed in the MAM season (see **Figure 6B**). These results also show that the Namib Desert is generally warmer than the Kalahari Desert in every season. However, in the JJA season, winter fogs produced by upwelling cold currents, frequently blanket coastal deserts (such as the Namib Desert) and block solar radiation, thus making the JJA season cold. Overall, coastal deserts are relatively complex because they are at the juncture of terrestrial, oceanic, and atmospheric systems.

4.3 Seasonal and Spatial Variation of Vegetation

Figure 7 shows the seasonal distribution of NDVI over the study area. The Namib Desert shows NDVI values of <0.1 for all seasons, indicating that no vegetation is present at any time of the season over the area. This area is dominated by bare sand and dust. However, during the DJF and MAM seasons (see **Figures 7A,B**), high NDVI values >0.7 are observed in the northern parts of the Kalahari Desert. This indicates that these seasons have some vegetation. The higher precipitation rates in these seasons (see **Figures 5A,B**) aid in providing the water needed for the growth of the plants. Rainfall is the main determinant for the growth of plants in this area. Vegetation coverage in the Kalahari Desert is a crucial factor affecting wind erosion and airborne dust accumulation. High vegetation coverage traps the dust fall and thus reduces the transport and dispersion of the dust. This study does not aim to quantify the amount of dust trapped, but there are interesting studies aiming to quantify the trapping effect of different vegetation coverages on the aeolian dust to better understand the role of vegetation in aeolian dust accumulation in arid and semi-arid regions (Yan et al., 2011). The JJA and SON seasons (see **Figures 7C,D**) in the

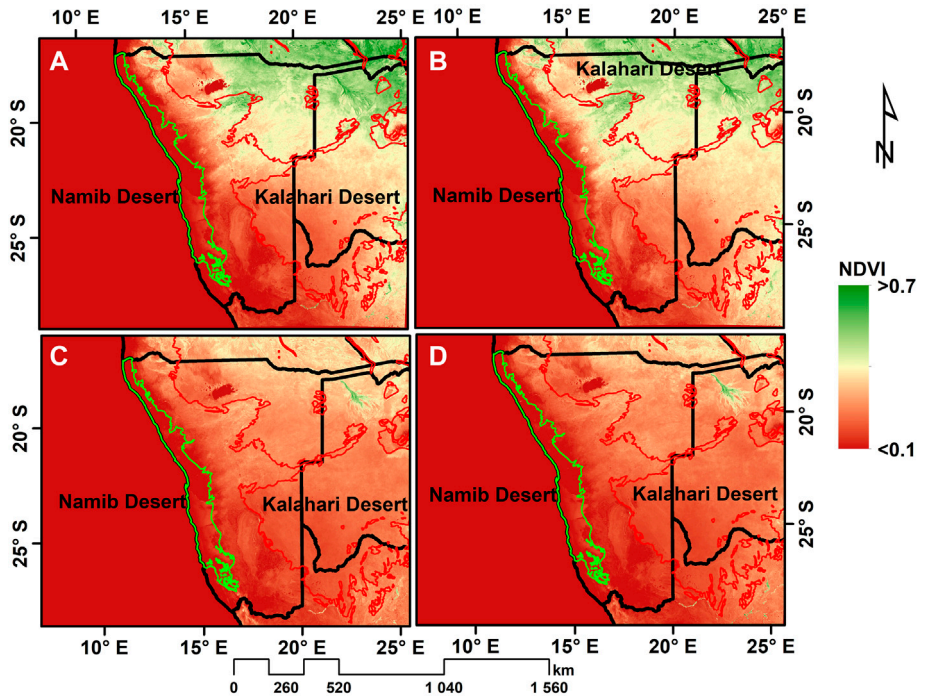

FIGURE 7 | Seasonal NDVI map distribution in **(A)** DJF, **(B)** MAM, **(C)** JJA and **(D)** SON seasons, obtained from MODIS MOD13Q1 product.

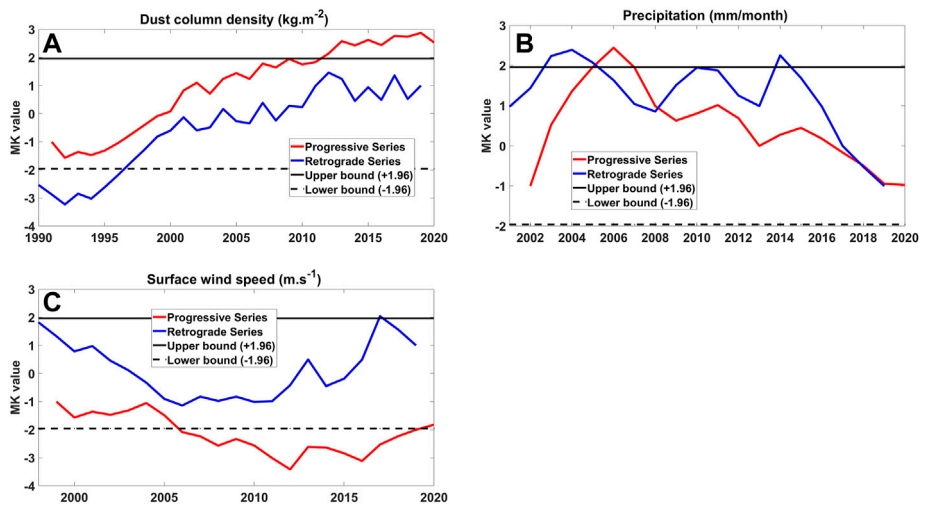

FIGURE 8 | Progressive series and retrograde series trends from the SQMK test for **(A)** dust column density, **(B)** precipitation rate and **(C)** surface wind speed.

Kalahari Desert show low to moderate values of NDVI between 0.2 and 0.4. The northern parts of the Kalahari Desert show values of ~0.4, while the southern parts of the Kalahari Desert show values of ~0.2. These values indicate that during these seasons the area comprises sparse vegetation which is due to a lack of rainfall. Furthermore, with sparse vegetation, it is anticipated that slightly more dust would be removed from the soil and transported into the atmosphere. In fact, the NDVI for JJA and SON are consistent with the seasonally averaged dust surface mass concentration results (**Figure 5**).

4.4 Trend Analysis Observations

The SQMK test is applied to detect the trends in the dust column density, precipitation rate and surface wind speeds. One of the reasons the SQMK test is used in this study is that it is not very sensitive to outliers (Mondal et al., 2015). Furthermore, the

precipitation rate and wind speed parameters were selected because they have some influence on the dust column density, therefore correlating the parameters can explain why the trend of the dust column density is observed. **Figure 8A** shows an increasing trend of the dust column density from the year 1990 to the year 2020. An increasing dust column density over time means an increase in dust aerosol loading which leads to the degradation in air quality. A decrease in precipitation over time would lead to dry soil conditions and great chances for the creation of dust from the bare soil. **Figure 8B** shows a decreasing precipitation rate from the year 2006 to the year 2020. This is the period with the highest/increasing dust column density. High wind speeds are responsible for 1) lifting the dust from the surface and 2) higher wind speeds would be responsible for the transport and distribution of the dust. **Figure 8C** shows a decreasing surface wind speed trend over time. This result means less of the dust is being transported to distant places but rather more dust particles are being removed from the bare soil thus increasing the column density of the dust. Overall, the precipitation and wind speed observations support the observation of the increasing dust density over time.

4.5 Relationship Between Precipitation, Wind and Desert Dust

Rosenfeld et al. (2001) showed that the reduction of precipitation affected by desert dust can cause drier soil, which in turn raises more dust, thus providing a possible feedback loop to further decrease precipitation. The elevated dust is then transported to various places by the wind. The transport of dust particles by wind occurs in several modes, which depend predominantly on particle size and wind speed. The dust particles are not normally directly lifted by wind because their inter-particle cohesive forces are large compared to aerodynamic forces, instead, these small particles are predominantly ejected from the soil by the impacts of saltating particles (Gillette et al., 1974). Following the ejection, dust particles are susceptible to turbulent fluctuation and thus usually enter short-term (~20–70 μm diameter) or long-term (<20 μm diameter) suspension (Kok et al., 2012). Long-term suspended dust can remain in the atmosphere for up to several weeks and can thus be transported thousands of kilometres from source regions (Kok et al., 2012). However, the acceleration of particles with diameters over ~500 μm is strongly limited by their large inertia, and these particles generally do not saltate (Shao, 2008).

5 CONCLUSION

The study uses a multi-dataset approach to study the relationship between meteorological parameters and desert dust aerosols. The study specifically looks at the deserts in south-western Africa as this is the least studied region. This study further closes the knowledge gap that exists in dust aerosols in south-western Africa, where the ground data are scarce and monitoring efforts are rare. The results clearly show that the Namib desert is the main source of dust in the Southwest African region seasonally. The greatest distribution of dust is observed in the JJA season and the southwesterly winds are accountable for the transport of dust into the interior. However, winds in the northerly direction are responsible for the transport of dust over the Atlantic Ocean. Furthermore, the highest dust aerosols were observed at ~7 and 10 km which suggests that the dust particles are <20 μm in diameter (Kok et al., 2012). This study demonstrated that meteorological parameters play an important role in the production and distribution of dust aerosols. High temperatures and lack of precipitation contribute to the drying of the bare soil creating an enabling condition to produce dust. Strong winds lift the dust from the soil and distribute the dust. This study is important because it could be used as a basis to investigate desertification, primarily from a climate change point of view, in Southwest Africa. Moreover, the study can be expanded to study the transport of dust aerosol to other areas and how this dust impacts the local cloud fraction and precipitation in those areas.

DATA AVAILABILITY STATEMENT

Publicly available datasets were analyzed in this study. This data can be found here: giovanni.gsfc.nasa.gov/.

AUTHOR CONTRIBUTIONS

LS and MK contributed to conception and design of the study. LS and MK carried out the investigation. LS and MK carried out the formal analysis. LS wrote the first draft of the manuscript. MK wrote sections of the manuscript. All authors contributed to manuscript revision, read, and approved the submitted version.

ACKNOWLEDGMENTS

The author acknowledges the GES-DISC Interactive Online Visualization and Analysis Infrastructure (Giovanni) for providing the MERRA-2, TRMM and AIRS. The author thanks the NASA Langley Research Centre Atmospheric Science Data Centre for the CALIPSO data.

SUPPLEMENTARY MATERIAL

The Supplementary Material for this article can be found online at: https://www.frontiersin.org/articles/10.3389/fenvs.2022.856438/full#supplementary-material

REFERENCES

Adams, A. M., Prospero, J. M., and Zhang, C. (2012). CALIPSO-derived Three-Dimensional Structure of Aerosol over the Atlantic Basin and Adjacent Continents. *J. Clim.* 25, 6862–6879. doi:10.1175/JCLI-D-11-00672.1

Aili, A., Kim Oanh, N. T., and Abuduwaili, J. (2016). Variation Trends of Dust Storms in Relation to Meteorological Conditions and Anthropogenic Impacts in the Northeast Edge of the Taklimakan Desert, China. *Ojap* 05, 127–143. doi:10.4236/ojap.2016.54010

Alfaro, S. C., Gaudichet, A., Gomes, L., and Maillé, M. (1998). Mineral Aerosol Production by Wind Erosion: Aerosol Particle Sizes and Binding Energies. *Geophys. Res. Lett.* 25, 991–994. doi:10.1029/98gl00502

Amiridis, V., Wandinger, U., Marinou, E., Giannakaki, E., Tsekeri, A., Basart, S., et al. (2013). Optimizing CALIPSO Saharan Dust Retrievals. *Atmos. Chem. Phys.* 13, 12089–12106. doi:10.5194/acp-13-12089-2013

Bhattachan, A., D'Odorico, P., Baddock, M. C., Zobeck, T. M., Okin, G. S., and Cassar, N. (2012). The Southern Kalahari: a Potential New Dust Source in the Southern Hemisphere? *Environ. Res. Lett.* 7, 024001. doi:10.1088/1748-9326/7/2/024001

Bou Karam Francis, D., Flamant, C., Chaboureau, J.-P., Banks, J., Cuesta, J., Brindley, H., et al. (2017). Dust Emission and Transport over Iraq Associated with the Summer Shamal Winds. *Aeolian Res.* 24, 15–31. doi:10.1016/j.aeolia.2016.11.001

Brooks, N. (2000). *Environmental Change and Land-Atmosphere Interactions in Northern Africa: The Role of Saharan Dust*. Norwich, U. K: Ph.D. thesis, Clim. Res. Unit, Univ. of East Anglia.

Bryant, R. G., Bigg, G. R., Mahowald, N. M., Eckardt, F. D., and Ross, S. G. (2007). Dust Emission Response to Climate in Southern Africa. *J. Geophys. Res.* 112, D09207. doi:10.1029/2005JD007025

Buchard, V., da Silva, A. M., Colarco, P. R., Darmenov, A., Randles, C. A., Govindaraju, R., et al. (2015). Using the OMI Aerosol Index and Absorption Aerosol Optical Depth to Evaluate the NASA MERRA Aerosol Reanalysis. *Atmos. Chem. Phys.* 15, 5743–5760. doi:10.5194/acp-15-5743-2015

Buchard, V., da Silva, A. M., Randles, C. A., Colarco, P., Ferrare, R., Hair, J., et al. (2016). Evaluation of the Surface PM2.5 in Version 1 of the NASA MERRA Aerosol Reanalysis over the United States. *Atmos. Environ.* 125, 100–111. doi:10.1016/j.atmosenv.2015.11.004

Buseck, P. R., and Pósfai, M. (1999). Airborne Minerals and Related Aerosol Particles: Effects on Climate and the Environment. *Proc. Natl. Acad. Sci. U.S.A.* 96, 3372–3379. doi:10.1073/pnas.96.7.3372

Caquineau, S., Gaudichet, A., Gomes, L., and Legrand, M. (2002). Mineralogy of Saharan Dust Transported over Northwestern Tropical Atlantic Ocean in Relation to Source Regions. *J. Geophys. Res.* 107, 247. doi:10.1029/2000JD000247

Chahine, M. T., Pagano, T. S., Aumann, H. H., Atlas, R., Barnet, C., Blaisdell, J., et al. (2006). Airs. *Bull. Amer. Meteor. Soc.* 87, 911–926. doi:10.1175/bams-87-7-911

Chouza, F., Reitebuch, O., Benedetti, A., and Weinzierl, B. (2016). Saharan Dust Long-Range Transport across the Atlantic Studied by an Airborne Doppler Wind Lidar and the MACC Model. *Atmos. Chem. Phys.* 16, 11581–11600. doi:10.5194/acp-16-11581-2016

Dansie, A. P., Wiggs, G. F. S., Thomas, D. S. G., and Washington, R. (2017). Measurements of Windblown Dust Characteristics and Ocean Fertilization Potential: The Ephemeral River Valleys of Namibia. *Aeolian Res.* 29, 30–41. doi:10.1016/j.aeolia.2017.08.002

Denjean, C., Cassola, F., Mazzino, A., Triquet, S., Chevaillier, S., Grand, N., et al. (2016). Size Distribution and Optical Properties of Mineral Dust Aerosols Transported in the Western Mediterranean. *Atmos. Chem. Phys.* 16, 1081–1104. doi:10.5194/acp-16-1081-2016

Dufresne, J.-L., Gautier, C., Ricchiazzi, P., and Fouquart, Y. (2002). Longwave Scattering Effects of Mineral Aerosols. *J. Atmos. Sci.* 59, 1959–1966. doi:10.1175/1520-0469(2002)059<1959:lseoma>2.0.co;2

Feiyu, M., Wei, G., Zhongmin, Z., and Pingxiang, L. (2008). The Ground-Based Lidar Combined with Sunphotometer for Aerosol Optical Depth Retrieval. *Proc. SPIE* 7145, 71452R. doi:10.1117/12.813083

Gehlot, S., Minnett, P. J., and Stammer, D. (2015). Impact of Sahara Dust on Solar Radiation at Cape Verde Islands Derived from MODIS and Surface Measurements. *Remote Sens. Environ.* 166, 154–162. doi:10.1016/j.rse.2015.05.026

Gillette, D. A., Blifford, I. H., Jr., and Fryrear, D. W. (1974). The Influence of Wind Velocity on the Size Distributions of Aerosols Generated by the Wind Erosion of Soils. *J. Geophys. Res.* 79, 4068–4075. doi:10.1029/JC079i027p04068

Ginoux, P., Prospero, J. M., Gill, T. E., Hsu, N. C., and Zhao, M. (2012). Global-scale Attribution of Anthropogenic and Natural Dust Sources and Their Emission Rates Based on MODIS Deep Blue Aerosol Products. *Rev. Geophys.* 50, RG3005. doi:10.1029/2012RG000388

Hachfeld, B., and Jürgens, N. (2000). Climate Patterns and Their Impact on the Vegetation in a Fog Driven Desert: The Central Namib Desert in Namibia. *phyto* 30, 567–589. doi:10.1127/phyto/30/2000/567

Hartmut, H., Aumann, H., and Miller, C. R. (1995). "Atmospheric Infrared Sounder (AIRS) on the Earth Observing System," in *Proc. SPIE 2583, Advanced and Next-Generation Satellites*. Paris, France

Huang, J., Guo, J., Wang, F., Liu, Z., Jeong, M.-J., Yu, H., et al. (2015). CALIPSO Inferred Most Probable Heights of Global Dust and Smoke Layers. *J. Geophys. Res. Atmos.* 120, 5085–5100. doi:10.1002/2014jd022898

Hui, Y., Wenqing, L., Yihuai, L., Jianguo, L., Qingnong, W., Dexi, W., et al. (2005). Tropospheric Aerosol Observations by Lidar at Naqu, Optical Technologies for Atmospheric, Ocean, and Environmental Studies. *Proc. SPIE* 5832, 148–155. doi:10.1117/12.619550

Jish Prakash, P., Stenchikov, G., Kalenderski, S., Osipov, S., and Bangalath, H. (2015). The Impact of Dust Storms on the Arabian Peninsula and the Red Sea. *Atmos. Chem. Phys.* 15, 199–222. doi:10.5194/acp-15-199-2015

Johnson, B. T., and Osborne, S. R. (2011). Physical and Optical Properties of Mineral Dust Aerosol Measured by Aircraft during the GERBILS Campaign. *Q. J. R. Meteorol. Soc.* 137, 1117–1130. doi:10.1002/qj.777

Kallos, G., Papadopoulos, A., Katsafados, P., and Nickovic, S. (2006). Transatlantic Saharan Dust Transport: Model Simulation and Results. *J. Geophys. Res.* 111, D09204. doi:10.1029/2005JD006207

Knippertz, P., and Todd, M. C. (2012). Mineral Dust Aerosols over the Sahara: Meteorological Controls on Emission and Transport and Implications for Modeling. *Rev. Geophys.* 50, RG1007. doi:10.1029/2011RG000362

Kok, J. F., Parteli, E. J. R., Michaels, T. I., and Karam, D. B. (2012). The Physics of Wind-Blown Sand and Dust. *Rep. Prog. Phys.* 75, 106901. doi:10.1088/0034-4885/75/10/106901

Kummerow, C., Simpson, J., Thiele, O., Barnes, W., Chang, A. T. C., Stocker, E., et al. (2000). The Status of the Tropical Rainfall Measuring Mission (TRMM) after Two Years in Orbit. *J. Appl. Meteor.* 39, 1965–1982. doi:10.1175/1520-0450(2001)040<1965:tsottr>2.0.co;2

Lancaster, J., Lancaster, N., and Seely, M. K. (1984). Climate of the Central Namib Desert. *Madoqua* 14, 5

Li, X., Maring, H., Savoie, D., Voss, K., and Prospero, J. M. (1996). Dominance of Mineral Dust in Aerosol Light-Scattering in the North Atlantic Trade Winds. *Nature* 380, 416–419. doi:10.1038/380416a0

Liu, Z., Ostrenga, D., Teng, W., and Kempler, S. (2012). Tropical Rainfall Measuring Mission (TRMM) Precipitation Data and Services for Research and Applications. *Bull. Am. Meteorol. Soc.* 93, 1317–1325. doi:10.1175/bams-d-11-00152.1

Lohmann, U., and Feichter, J. (2005). Global Indirect Aerosol Effects: A Review. *Atmos. Chem. Phys.* 5, 715–737. doi:10.5194/acp-5-715-2005

Lu, A., He, Y., Zhang, Z., Pang, H., and Gu, J. (2004). Regional Structure of Global Warming across China during the Twentieth Century. *Clim. Res.* 27, 189–195. doi:10.3354/cr027189

Mahowald, N., Albani, S., Kok, J. F., Engelstaeder, S., Scanza, R., Ward, D. S., et al. (2014). The Size Distribution of Desert Dust Aerosols and its Impact on the Earth System. *Aeolian Res.* 15, 53–71. doi:10.1016/j.aeolia.2013.09.002

Mahowald, N. M., Engelstaedter, S., Luo, C., Sealy, A., Artaxo, P., Benitez-Nelson, C., et al. (2009). Atmospheric Iron Deposition: Global Distribution, Variability, and Human Perturbations. *Annu. Rev. Mar. Sci.* 1, 245–278. doi:10.1146/annurev.marine.010908.163727

Menzel, W. P., Schmit, T. J., Zhang, P., and Li, J. (2018). Satellite-Based Atmospheric Infrared Sounder Development and Applications. *Bull. Am. Meteorol. Soc.* 99, 583–603. doi:10.1175/bams-d-16-0293.1

Mondal, A., Khare, D., and Kundu, S. (2015). Spatial and Temporal Analysis of Rainfall and Temperature Trend of India. *Theor. Appl. Climatol.* 122, 143–158. doi:10.1007/s00704-014-1283-z

Papayannis, A., Balis, D., Amiridis, V., Chourdakis, G., Tsaknakis, G., Zerefos, C., et al. (2005). Measurements of Saharan Dust Aerosols over the Eastern Mediterranean Using Elastic Backscatter-Raman Lidar, Spectrophotometric and Satellite Observations in the Frame of the EARLINET Project. *Atmos. Chem. Phys.* 5, 2065–2079. doi:10.5194/acp-5-2065-2005

Prospero, J. M. (1999). Long-range Transport of Mineral Dust in the Global Atmosphere: Impact of African Dust on the Environment of the Southeastern United States. *Proc. Natl. Acad. Sci. U.S.A.* 96, 3396–3403. doi:10.1073/pnas.96.7.3396

Prospero, J. M. (1996). "Saharan Dust Transport over the North Atlantic Ocean and Mediterranean: An Overview," in *The Impact of Desert Dust across the Mediterranean*. Editors S. Guerzoni and R. Chester (Dordrecht: Springer), 133–151. doi:10.1007/978-94-017-3354-0_13

Provençal, S., Kishcha, P., da Silva, A. M., Elhacham, E., and Alpert, P. (2017). AOD Distributions and Trends of Major Aerosol Species over a Selection of the World's Most Populated Cities Based on the 1st Version of NASA's MERRA Aerosol Reanalysis. *Urban Clim.* 20, 168–191. doi:10.1016/j.uclim.2017.04.001

Randles, C. A., da Silva, A. M., Buchard, V., Darmenov, A., Colarco, P. R., Aquila, V., et al. (2016). "The MERRA-2 Aerosol Assimilation," in *NASA Technical Report Series on Global Modeling and Data Assimilation*, 143. NASA/TM-2016-104606 45.

Rienecker, M. M., Suarez, M. J., Gelaro, R., Todling, R., Bacmeister, J., Liu, E., et al. (2011). MERRA: NASA's Modern-Era Retrospective Analysis for Research and Applications. *j. Clim.* 24, 3624–3648. doi:10.1175/jcli-d-11-00015.1

Rienecker, M. M., Suarez, M. J., Todling, R., Bacmeister, J., Takacs, L., Liu, H. –C., et al. (2008). *Technical Report Series on Global Modeling and Data Assimilation*, 27. NASA/TM–2008–104606, 92.

Schepanski, K., Mallet, M., Heinold, B., and Ulrich, M. (2016). North African Dust Transport toward the Western Mediterranean Basin: Atmospheric Controls on Dust Source Activation and Transport Pathways during June-July 2013. *Atmos. Chem. Phys.* 16, 14147–14168. doi:10.5194/acp-16-14147-2016

Shalaby, A., Rappenglueck, B., and Eltahir, E. A. B. (2015). The Climatology of Dust Aerosol over the Arabian Peninsula. *Atmos. Chem. Phys. Discuss.* 15, 1523–1571. doi:10.5194/acpd-15-1523-2015

Shannon, L. V. (1985). "The Benguela Ecosystem. 1. Evolution of the Benguela, Physical Features and Processes," in *Oceanography and Marine Biology*. Editor M. Barnes, An Annual Review 23, 105

Shao, Y. P. (2008). *Physics and Modelling of Wind Erosion*. Netherlands: Springer.

Shikwambana, L., and Sivakumar, V. (2018). Global Distribution of Aerosol Optical Depth in 2015 Using CALIPSO Level 3 Data. *J. Atmos. Solar-Terrestrial Phys.* 173, 150–159. doi:10.1016/j.jastp.2018.04.003

Sneyers, R. (1997). Climate Chaotic Instability: Statistical Determination and Theoretical Background. *Environmetrics* 8, 517–532. doi:10.1002/(sici)1099-095x(199709/10)8:5<517::aid-env267>3.0.co;2-l

Sneyers, R. (1990). On the Statistical Analysis of Series of Observations. *Tech. Note*, 143, 192

Sneyers, R., Tuomenvirta, H., and Heino, R. (1998). Observations Inhomogeneities and Detection of Climate Change the Case of the Oulu (Finland) Air Temperature Series. *Transp. Res. Rec.* 34, 159

Sokolik, I. N., Winker, D. M., Bergametti, G., Gillette, D. A., Carmichael, G., Kaufman, Y. J., et al. (2001). Introduction to Special Section: Outstanding Problems in Quantifying the Radiative Impacts of Mineral Dust. *J. Geophys. Res.* 106, 18015–18027. doi:10.1029/2000jd900498

Tackett, J. L., Winker, D. M., Getzewich, B. J., Vaughan, M. A., Young, S. A., and Kar, J. (2018). CALIPSO Lidar Level 3 Aerosol Profile Product: Version 3 Algorithm Design. *Atmos. Meas. Tech.* 11, 4129–4152. doi:10.5194/amt-11-4129-2018

Tesfaye, M., Tsidu, G. M., Botai, J., Sivakumar, V., and deW. RautenbachRautenbach, C. J. (2015). Mineral Dust Aerosol Distributions, its Direct and Semi-direct Effects over South Africa Based on Regional Climate Model Simulation. *J. Arid Environ.* 114, 22–40. doi:10.1016/j.jaridenv.2014.11.002

Vickery, K. J., Eckardt, F. D., and Bryant, R. G. (2013). A Sub-basin Scale Dust Plume Source Frequency Inventory for Southern Africa, 2005-2008. *Geophys. Res. Lett.* 40, 5274–5279. doi:10.1002/grl.50968

Washington, R., Todd, M., Middleton, N. J., and Goudie, A. S. (2003). Dust-storm Source Areas Determined by the Total Ozone Monitoring Spectrometer and Surface Observations. *Ann. Assoc. Am. Geogr.* 93, 297–313. doi:10.1111/1467-8306.9302003

Winker, D. M., Pelon, J., Coakley, J. A., Jr., Ackerman, S. A., Charlson, R. J., Colarco, P. R., et al. (2010). The CALIPSO Mission. *Bull. Am. Meteor Soc.* 91, 1211–1230. doi:10.1175/2010bams3009.1

Winker, D. M., Pelon, J. R., and McCormick, M. P. (2003). "The CALIPSO Mission: Spaceborne Lidar for Observation of Aerosols and cloudsProceedings. SPIE 4893," in *Lidar Remote Sensing for Industry and Environment Monitoring III*. Hangzhou, China. doi:10.1117/12.466539

Winker, D. M., Tackett, J. L., Getzewich, B. J., Liu, Z., VaughanRogers, M. A. R. R., and Rogers, R. R. (2013). The Global 3-D Distribution of Tropospheric Aerosols as Characterized by CALIOP. *Atmos. Chem. Phys.* 13, 3345–3361. doi:10.5194/acp-13-3345-2013

Winker, D. M., Vaughan, M. A., Omar, A., Hu, Y., Powell, K. A., Liu, Z., et al. (2009). Overview of the CALIPSO Mission and CALIOP Data Processing Algorithms. *J. Atmos. Ocean. Technol.* 26, 2310–2323. doi:10.1175/2009jtecha1281.1

Yan, Y., Xu, X., Xin, X., Yang, G., Wang, X., Yan, R., et al. (2011). Effect of Vegetation Coverage on Aeolian Dust Accumulation in a Semiarid Steppe of Northern China. *CATENA* 87, 351–356. doi:10.1016/j.catena.2011.07.002

Yang, Y., and Luo, Y. (2014). Evaluating the Performance of Remote Sensing Precipitation Products CMORPH, PERSIANN, and TMPA, in the Arid Region of Northwest China. *Theor. Appl. Climatol.* 118, 429–445. doi:10.1007/s00704-013-1072-0

Zhao, S., Yin, D., and Qu, J. (2015). Identifying Sources of Dust Based on CALIPSO, MODIS Satellite Data and Backward Trajectory Model. *Atmos. Pollut. Res.* 6, 36–44. doi:10.5094/APR.2015.005

Conflict of Interest: The authors declare that the research was conducted in the absence of any commercial or financial relationships that could be construed as a potential conflict of interest.

frontiers | Frontiers in Environmental Science

TYPE Original Research
PUBLISHED 26 September 2022
DOI 10.3389/fenvs.2022.983048

OPEN ACCESS

EDITED BY
Rui Mao,
Beijing Normal University, China

REVIEWED BY
Bangjun Cao,
Chengdu University of Information Technology, China
Qinjian Jin,
University of Kansas, United States

*CORRESPONDENCE
Zhaohui Lin,
lzh@mail.iap.ac.cn

SPECIALTY SECTION
This article was submitted to Atmosphere and Climate, a section of the journal Frontiers in Environmental Science

RECEIVED 30 June 2022
ACCEPTED 24 August 2022
PUBLISHED 26 September 2022

CITATION
Kamal A, Lin Z and Wu C (2022), Decadal change of spring dust activity in western Iran and its mechanism.
Front. Environ. Sci. 10:983048.
doi: 10.3389/fenvs.2022.983048

Decadal change of spring dust activity in western Iran and its mechanism

Alireza Kamal[1,2], Zhaohui Lin[1,2,3]* and Chenglai Wu[1,3]

[1]International Center for Climate and Environment Sciences, Institute of Atmospheric Physics, Chinese Academy of Sciences, Beijing, China, [2]College of Earth and Planetary Sciences, University of Chinese Academy of Sciences, Beijing, China, [3]China-Pakistan Joint Research Center on Earth Sciences, CAS-HEC, Islamabad, Pakistan

Western Iran is an important dust source region in Middle East, with strong dust activities occurring in springtime. Based on a three-hourly meteorological station data, remarkable decadal change of dust frequency in the spring season has been found in the west and southwest of Iran, with less dust activities during 1992–2005 (hereafter as "P1") and more frequent dust activities occurring during 2006–2015 (hereafter as "P2"). The decadal change signal in dust activities is closely associated with the corresponding decadal difference in precipitation and atmospheric moisture transportation in the region. Compared with P1 period during 1992–2005, anomalous moisture divergence over the center of Middle East can be found in P2 period during 2006–2015, suggesting less moisture transport to the western Iran from the Arabian Sea, Red Sea, and the Persian Gulf, hence there is relatively less precipitation and dry soil moisture over the main dust source regions in the study region, which is favorable for more frequent dust emissions in P2 period. Meanwhile, westerly anomaly in P2 period can also be found in western Iran and upstream regions, such as Iraq and Syria, which is favorable for more dust transport to western Iran from upstream dust source region in Middle East. Furthermore, negative SST anomalies in central and western North Pacific and positive SST anomalies in the eastern North Pacific can be found in P1 period, which is corresponding to positive phase of Pacific Decadal Oscillation (PDO). Conversely, a negative phase of PDO can be found during P2 period. This suggests that PDO is the key influential factor for the decadal change of spring dust activities in western Iran.

KEYWORDS

spring dust activity, decadal change, moisture transport, pacific decadal oscillation, western Iran

1 Introduction

Dust aerosol plays a pervasive role in the Earth system (Goudie and Middleton 2006; UNEP, 2016). Large amounts of dust emit in the dust source areas of the Earth, which can be transported over thousands of kilometers and deposited far away from the source regions (Shao et al., 2011; Van der Does et al., 2018). The main dust sources of the world

are mostly located in dry and semi-dry lands with sparse vegetation, and alluvial plains (Prospero et al., 2002; Ginoux et al., 2012).

Middle East is one of the key dust sources in the world (Prospero et al., 2002; Ginoux et al., 2012; Wu et al., 2020). Air quality in the Middle East is strongly affected by dust aerosol, posing a serious threat to human health (Fountoukis et al., 2020). There are large regions prone to dust emission in Middle East, with the Iraqi Alluvial plain, the Syrian Desert, and Rub al-Khali and Ad-Dahna deserts in Saudi Arabia being identified as major dust sources (Draxler et al., 2001; Goudie and Middleton, 2001; Léon and Legrand, 2003). In general, dust emissions strongly depend on meteorological factors (precipitation, near-surface winds, etc.) and land surface conditions (soil moisture, soil properties, and surface vegetation cover, etc.) (Qian et al., 2002; Shao et al., 2011; Wu et al., 2018). The meteorological factors are subject to the large-scale circulations and they vary greatly with time, which leads to the strong temporal variations of dust activity in Middle East.

Previous studies have shown that there is remarkable variability in dust activity in Middle East in interannual to decadal time scale, which are closely associated with the variation in large-scale circulation and sea surface temperature (SST) (e. g., Yu et al., 2015; Pu and Ginoux, 2016; Kamal et al., 2020). In particular, there is a significant decadal enhancement of dust activity in Saudi Arabia, which is suggested to be linked to prolonged drought and the consequent reduction in vegetation cover across the Saudi Arabia and upstream region in Sahel (e.g., Piccarreta et al., 2006; Zoljoodi et al., 2013). A relatively high dust period is found in late 1980s and early 1990s, indicating there is a 10-to-16-years cycle in dust activity in Saudi Arabia (Yu et al., 2015). However, few studies have been conducted to investigate the decadal variations of dust activity in other countries of Middle East other than Saudi Arabia. Since there is large difference in the temporal variations of dust activity in different regions of Middle East due to the different influencing factors (Furman, 2003), it is unclear whether there is also a decadal change in dust activity in other countries as Saudi Arabia. As found in East Asia and North Africa, the occurrence of dust storms is closely associated with an anomalous atmospheric circulation pattern (e.g., Fan and Wang, 2004; Ding et al., 2005; Gong et al., 2006; Fan et al., 2016; Francis et al., 2018). So, if the decadal variation of dust activities in Middle East is driven by similar large-scale circulation, it is likely that the dust activity might show similar decadal variations as in Saudi Arabia (Yu et al., 2015; Jin et al., 2021).

As a key dust source region in Middle East, Western and southwestern Iran is a regional belt of high-frequency dust outbreaks (Alizadeh-Choobari, et al., 2016; Kamal et al., 2020; Broomandi et al., 2021). It is found that dust activity is this region shows different variability from other regions in Iran (e.g., Alizadeh-Choobari, et al., 2016; Rashki et al., 2021). The main reason is that this region can be affected not only by the local dust events, but also by dust aerosols transported from upstream regions, such as Saudi Arabia and Syria (e.g., Boloorani et al., 2014; Alizadeh-Choobaril et al., 2016; Alizadeh-Choobaril and Najafi 2018; Namdari et al., 2018; Kamal et al., 2020). Taking this region as the focus domain, we will try to investigate whether there also exists decadal change of dust activity in western Iran, and what is the roles of local meteorological factors and the associated atmospheric circulation on these possible decadal changes, as well as its possible linkages to the sea surface temperature (SST) anomaly signals.

The paper is organized as follows. Section 2 introduces the research data and methodology. In Section 3 the results of decadal dust variations and underlying mechanisms are presented. Finally, conclusions and discussions are given in Section 4.

2 Data and methodology

2.1 Observation data

The dust weather data were extracted based on the code of the present meteorological observation, i.e., a description of the weather phenomena present at the time of observation. The three-hourly weather code from 10 meteorological stations across western Iran during 1979–2018 are used in this study, which are provided by the Islamic Republic of Iran Meteorological Organization (IRIMO). The dust-related weather codes are listed in Table 1. The spatial distribution of these stations is illustrated in Figure 1.

In this study, a day was considered a “dusty day” if any dust-related weather code (06–09, 30–35, 98) is reported once during the day, following Shao and Wang (2003). Dust events are further classified into two categories: dust outbreak (present weather code 07–09; 30–35; 98) and dust-in-suspension (present weather code 06). The numbers of days for either category and all dust events are also derived. Then three types of dusty day frequency (DDFs) were derived: 1) Dust Outbreak Day Frequency (DODF), 2) Dust-in-Suspension Day Frequency (DiSDF), and 3) Dust Event Day Frequency (DEDF). Following Kamal et al. (2020), for a given station, the monthly frequency of dust day for each category is calculated by dividing the number of dust days for a specific category by the total number of days with available weather observations in a specific month. The months with missing observations more than 5 days were excluded. The regional mean DDF time series is based on the average of the 10 observation stations. The interannual variations of DDF is very consistent with the MODIS dust optical depth in the

TABLE 1 Phenomena related to dust according to the World Meteorological Organization (WMO) weather codes.

Synoptic code	Weather description
06	Widespread dust in suspension in the air, not raised by wind at or near the station at the time of observation
07	Dust or sand raised by wind at or near the station at the time of observation, but no well-developed dust or sand whirl, and no dust storm or sandstorm seen
08	Well-developed dust or sand whirl seen at or near the station during the preceding hour or at the time of observation, but no dust storm or sandstorm
09	Dust storm or sandstorm within sight at the time of observation or at the station during the preceding hour
30–32	Slight or moderate dust storm or sandstorm
33–35	Severe dust storm or sandstorm
98	Thunderstorm combined with dust storms or sandstorms at time of observation, thunderstorm at time of observation

recent 2 decades when MODIS observations (Song et al., 2021) are available (Supplementary Figure S1).

As we focus on the decadal variation of spring dust activities over western Iran, the linear trend has been removed from the original DDFs dataset, then a 9-years running mean is further applied to the time series of all DDFs. The spring season in this study refers to the months of March, April, and May.

Time series data of monthly accumulated precipitation at 10 synoptic stations over western Iran during the period of 1979–2018 are obtained from IRIMO. In addition, monthly precipitation dataset from the Global Precipitation Climatology Centre (GPCC) Version 7, with a spatial resolution of 1° × 1° (Schneider et al., 2017), is also used to calculate precipitation anomalies.

In order to investigate the role of vegetation cover change, we also use leaf area index (LAI) from Moderate-Resolution Imaging Spectroradiometer (MODIS) during 2000–2018 (Myneni et al., 2015). MODIS LAI is provided continuously every 8-days on a 0.05° × 0.05° grid. Note that although MODIS observation is only available in a shorter period (i.e., after year 2000) compared to dust and precipitation observations, vegetation cover difference between two periods of high dust and low dust activity, respectively, can be calculated and thus is also shown to demonstrate its role in dust variations.

2.2 Reanalysis data

To demonstrate the variations of meteorological conditions associated with decadal changes of DDF, we also use the ERA5 reanalysis, which is the fifth ECMWF atmospheric reanalysis of the global climate (Hersbach et al., 2020). For this study, we use specific humidity (q), zonal (u) and meridian (v) wind at the 27 different atmospheric levels, sea level pressure (SLP), sea surface temperature (SST), and geopotential at 850 hPa from ERA5. ERA5 reanalysis is provided originally at ~30 km grid and is interpolated to 0.25° × 0.25° for public use.

We also use the soil moisture from ERA5-Land. ERA5-Land is generated by replaying the land component of the ERA5 climate reanalysis but at a higher-resolution (~9 km) and with an elevation correction for the thermodynamic near-surface state (Muñoz-Sabater et al., 2021). The data is interpolated to 0.1° × 0.1° for public use. Soil moisture in the topsoil level (0–7 cm) is used. To identify the decadal change of the atmospheric water vapor transport, the vertically integrated moisture flux (VIMF) is also calculated by the following equation (Li et al., 2009):

$$VIMF = -\frac{1}{g} \cdot \int_{Psurf}^{Ptop} \left(\frac{\partial uq}{\partial x} + \frac{\partial vq}{\partial y} \right) \cdot dp$$

where q is the specific humidity; u and v are the x- and y-components of the wind, respectively; p is the pressure; Psurf is the surface pressure; Ptop is the pressure at the top of the atmospheric layer; and g is the acceleration due to gravity. VIMF is calculated by integrating the horizontal moisture flux convergence over the lower to middle layers of troposphere (1,000–700 hPa). Note values of VIMF is expressed in units of 10^{-5} kg $m^{-2}s^{-1}$.

To remove the long-term trend signal, all calculations are based on the linear detrended data for the period 1979 to 2018. We use the *t*-test to determine the significance of the correlation coefficient between climatic factors and dust-day frequency, as well as the significance of the difference between two selected periods, as shown in Section 3.

3 Results

3.1 Decadal change of spring dust activity

Figure 2 shows the time series of spring dust days' frequency for DODF, DiSDF, and DEDF in western Iran from 1979 to 2018, and their corresponding 9-years running means. There are apparent interannual variations of DDF in the region, which

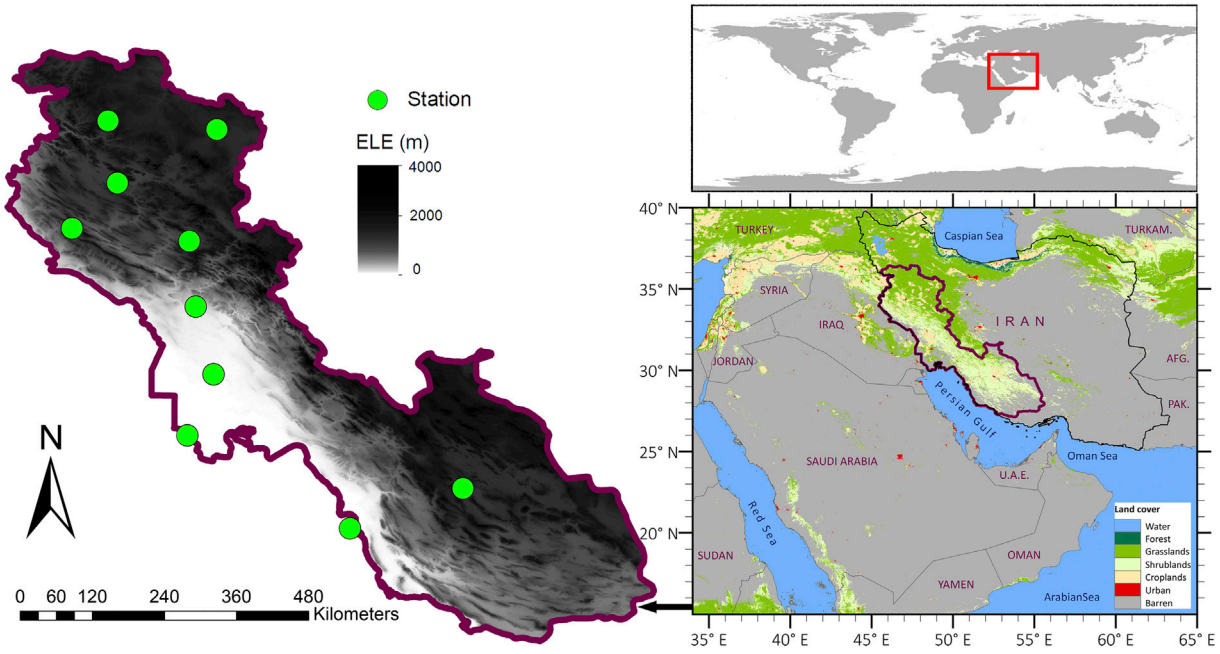

FIGURE 1
Map of Iran in the Middle East with the shaded land cover product of MODIS (MCD12Q1; Friedl and Sulla-Menashe 2015) and the topographic map of western and southwestern Iran. The stations used for three-hourly dust observations in this study are shown with green circles.

is also presented in Kamal et al. (2020). The interannual variations are underlain by the strong decadal variations. It is found that dust activities are relatively weaker during 1992–2005 (hereafter P1), with negative anomalies of dust day frequency, but strong positive anomalies of dust day frequency from 2006 to 2015 (hereafter P2) can also be found, suggesting that dust activities are stronger during 2006–2015. The most extreme DiSDF (normalized anomalies = 1.5–2.0) occurred in western Iran during 2007–2012, which is consistent with the peak of dust activities in Saudi Arabia (Yu et al., 2015) and Syria (Pu and Ginoux, 2016). DODF shows similar variations with DiSDF in most years, but they differ greatly during 2009–2018 when DiSDF shows significantly decreasing trends while there is no apparent decreasing trend in DODF. This can be explained by the fact that DODF indicates local dust emission while DiSDF indicates dust transport from upstream regions in addition to dust suspension after local dust emission. According to the temporal variations, we can identify two periods, with relatively weak dust activities in P1 during 1992–2005, and relatively strong dust activities in P2 during 2006–2015.

As precipitation is an important factor not only for the suppression of dust emission but also for the wet deposition of dust, it greatly modulates the dust activities (e.g., Zoljoodi et al., 2013; Kamal et al., 2020). In western Iran, in P1 (P2), positive (negative) precipitation anomaly corresponds well with weaker (stronger) dust activities. This suggests that both the DODF and DiSDF are regulated by spring precipitation on the decadal time scale. The correlations between dust days' frequency and precipitation are strong with the correlation coefficients −0.58 and −0.51, respectively for DODF and DiSDF in western Iran. In next sections we will further examine the role of climatic factors and atmospheric circulation in the Middle East on the decadal DiSDF changes.

3.2 Decadal differences in climatic factor and associated atmospheric circulation

Figure 3 shows the anomalies of precipitation and soil moisture in spring during P1 and P2 relative to the climatological mean from ERA5 and ERA5-Land, respectively. We can find that there is a notable decadal difference of precipitation over western Iran and surrounding regions between P1 and P2. The anomaly of spring precipitation is positive (+2 mm/month) in most parts of the region, especially in western Iran and upwind areas (Iraq and Arabian Peninsula) for P1, while precipitation anomaly is negative (−1.8 mm/month) for P2 in this region (Figures 3A,B). The soil moisture in the topsoil layer also shows a similar pattern of anomalies as precipitation (Figures 3C,D) in

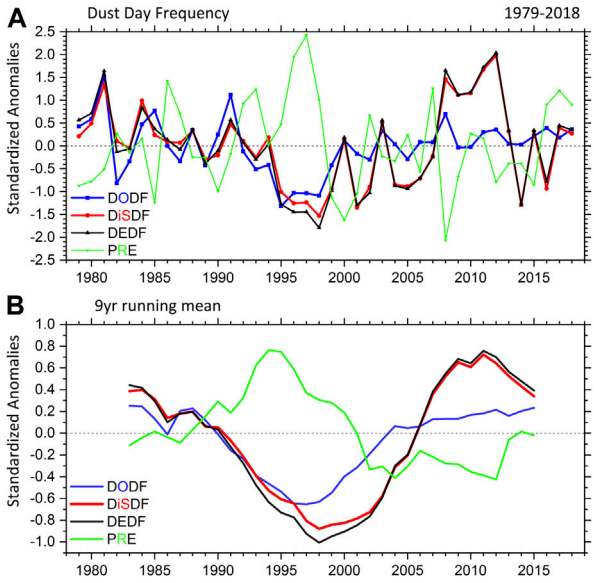

FIGURE 2
Time series of spring **(A)** dust days' frequency; Dust Outbreak Day Frequency (DODF; blue line), Dust-in-Suspension Day Frequency (DiSDF; red line), and Dust Event Day Frequency (DEDF; black line) along with precipitation (PER; green line) from 1979 to 2018 and **(B)** their corresponding 9-yr running means in western Iran (1983–2015).

most regions, with regional averages + 1.5 and −1.5 m^3 m^{-3} for P1 and p2, respectively. Note that in the southwestern part of Iran, there is some difference between precipitation anomaly and soil moisture anomaly. In this region, there is only weak dry anomaly in precipitation in P2, but there is large soil moisture deficit in the region, which may be due to enhanced evaporation during the period compared to P1 due to the increase of surface temperature.

The less precipitation and smaller soil moisture in P2 have led to a smaller vegetation cover (in terms of LAI) in P2 (Supplementary Figure S2). Although LAI data is not available for a whole period of P1, compared to the period of 2000–2005 (a part of P1) when MODIS LAI data is available, LAI is significantly smaller in western Iran and surrounding regions in P2, which can also contribute to the fact that DiSDF is larger in P2 than in P1. This is consistent with conclusions from previous studies (e.g., Kelley et al., 2015; Notaro et al., 2015), which pointed out that the reduced vegetation covers and agricultural collapse across these regions after 2007 was favorable for dust generation and transport to neighboring regions.

Atmospheric water vapour transport is the moisture source for western Iran. Figure 4 shows the mean of vertical profiles of water vapor flux in P1, P2, and climatology for the whole period (1979–2018). The results revealed that during the weak dust period, low level westerlies are strengthened at about 700 hPa which displaces the meridional transport to lower to lower levels. Hence, the strong water vapour transport (1.5×10^{-5} kg m^{-2} s^{-1}) induced by westerlies is associated with enhanced precipitation during P1 over the Middle East. Conversely, the P2 period is characterized by weak water vapour transport (1.3×10^{-5} kg m^{-2} s^{-1}) than climatology. Hence, the observed precipitation deficit over the region during P2.

Figure 5 further shows the climatology of vertically integrated moisture flux (VIMF) and its convergence/divergence and their anomalies corresponding to the decadal variation of spring DiSDF over western Iran. In general, atmospheric moisture sources for Iran are mainly Mediterranean Sea in the northwest, oceans to the south such as Red Sea, Arabic Sea, and Persian Gulf, and water vapor is transported toward Iran by Saudi Arabia Dynamic High-Pressure System and Sudan's Low-Pressure System (e.g., Heydarizad et al., 2018; Darand and Pazhoh 2019) (Figure 5A). In P1, the VIMF convergence flux flow is much higher in western Iran and upwind areas of Iraq and Arabian Peninsula in the lower to middle layers of the troposphere (VIMF: 0.03×10^{-5} kg m^{-2} s^{-1}), which is consistent to the positive precipitation anomalies in this period (Figure 5B). In P1, water vapor transported into Middle East from the Arabian Sea and Red Sea is enhanced, leading to more convergence in western Iran. Unlike P1, in P2 the northward and eastward water vapour transport to

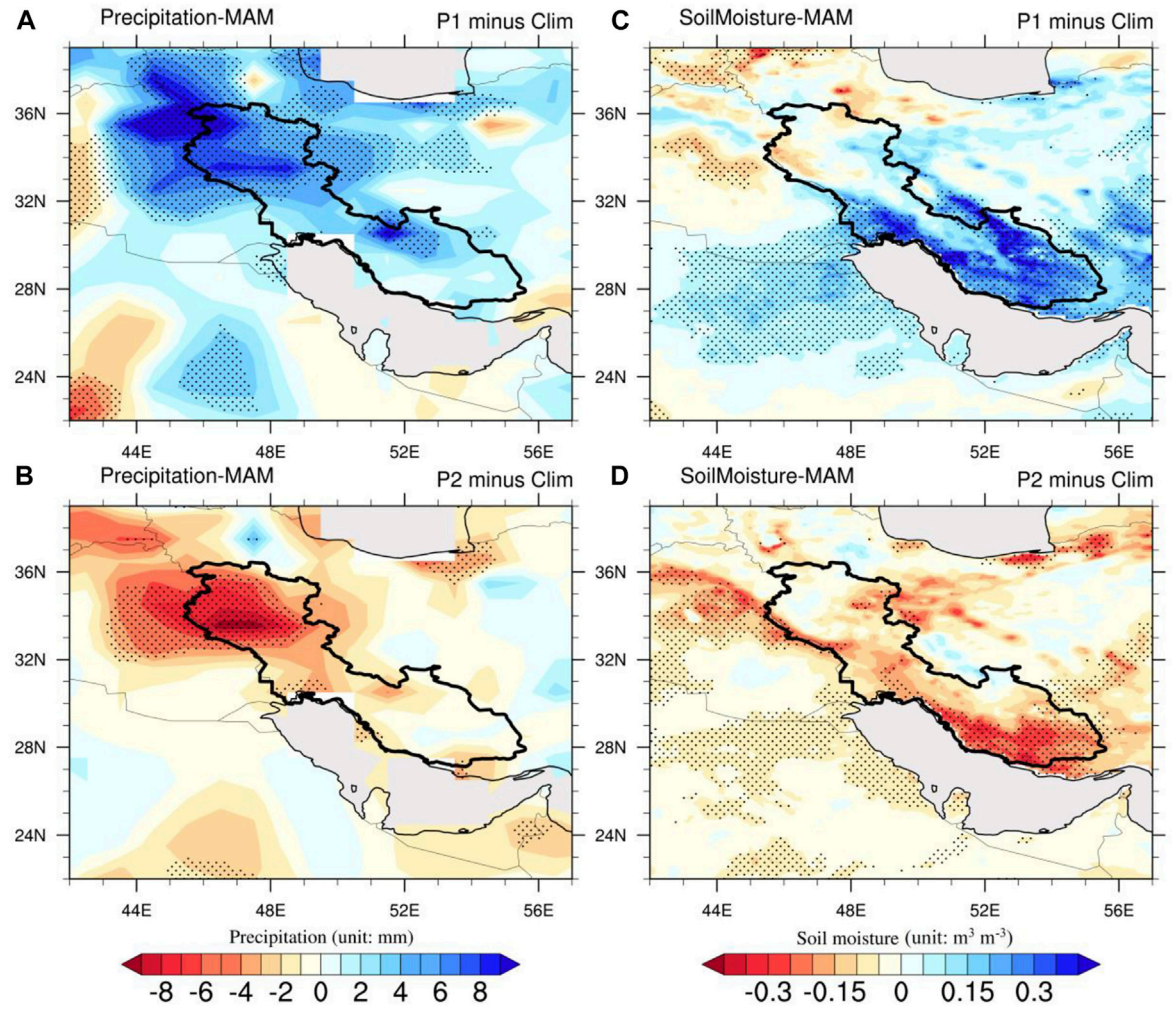

FIGURE 3
The anomalous spring precipitation (unit: mm) and soil moisture (unit: $m^3\ m^{-3}$) corresponding to the decadal variation of spring DiSDF over western Iran for the **(A,C)** P1 (1992–2005) and **(B,D)** P2 (2006–2015) periods. The climatology (Clim) of precipitation and soil moisture is calculated for the 1979–2018 and 1981–2018 periods, respectively. The black dots indicate the statistical significance at the 95% confidence level.

western Iran is reduced (VIMF: 0.01×10^{-5} kg m^{-2} s^{-1}), leading to less water vapour convergence and thus less precipitation over western Iran and surrounding regions in this period (Figure 5C).

In addition to precipitation, surface wind is another factor that strongly affects dust emission. In the spring, predominant wind direction is west over most parts of western Iran, northwest over the alluvial plain in Iraq, and east over Rub al-Khali and Ad Dahna Desert in Arabian Peninsula (Figure 6A). Figures 6B,C shows the anomaly of UV-wind in lower layers of the troposphere (averaged at the levels of 1,000, 975, 950, 925, 900, 875, 850 hPa) over center of the Middle East in the periods P1&P2. Compared to climatology during 1979–2018, the spring wind speed over the Shamal region is relatively lower in P1, while it is relatively higher in northern Iraq, Syria, and west part of Iran in P2, which leads to both greater dust transport from upstream regions to western Iran and larger local dust emission in western Iran. From the upstream dust sources for western Iran is mainly the Tigris-Euphrates basin in Iraq (Rezazadeh et al., 2013; Notaro et al., 2015; Mohammadpour et al., 2021), Syrian desert in Syria and Jordon (Zoljoodi et al., 2013; Sotoudeheian et al., 2016).

3.3 Linkage with decadal change of sea surface temperature

The decadal shift in atmospheric circulation can be closely linked to the variations of sea surface temperature. As shown in Figure 7A, associated with the low DiSDF in P1,

there exist negative SST anomalies in central and western North Pacific and positive SST anomalies in the eastern North Pacific, which is corresponding to positive phase of Pacific Decadal Oscillation (PDO). In P2 period, the pattern of SST anomaly is almost opposite to that in P1 (Figure 7B), with positive SST anomalies found in central and western North Pacific, and negative SST anomalies found in the eastern North Pacific. The pattern of SST anomalies in Pacific Ocean during P2 period resembles that for negative phase of PDO. Besides the SST anomaly signal in Pacific Ocean, opposite SST anomalies can also be found in Indian ocean for P1 and P2 period, with positive SST anomalies found in Indian Ocean and Arabian Sea in P1 period, and opposite anomalies found for P2 period.

Figure 8 shows the time series of Pacific Decadal Oscillation (PDO), Indian Ocean Basin Mode (IOBM) and Indian Ocean Dipole (IOD) indices in MAM and DiSDF over western Iran, as well as their 9-years running mean. From Figure 8A, we can find the correlation coefficient between PDO and DiSDF is about −0.34 in interannual time scale, which is statistically significance at 95% confidence level.

In decadal time scale, the variation of PDO and DiSDF are quite opposite (Figure 8B), with correlation coefficient of −0.54, which is statistically significant at the 99% confidence level (Table 2). This implies that PDO is a key influential factor for the decadal change of dust activities in western Iran. During negative PDO phase in P2 period, it is also the high dust period, while in the low dust period in P1, the PDO is in its positive phase (Figure 8B). Pu and (Ginoux et al., 2012) has revealed that there exists a significantly negative correlation between the dust activities in Syrian and the PDO in spring at interannual time scale from 2003 to 2015. The results from our study further demonstrate that, at the interdecadal time scale, PDO also play an important role in modulating the dust variations in Middle East.

For the impacts of Indian Ocean, we can find from Figure 8A that the correlation between DiSDF and IOBM is −0.29, and correlation between DiSDF and IOD is 0.19. Both of them are not exceeding the 90% significance level, suggesting that the DiSDF is not affected by IOD and IOBM in interannual time scale.

The correlation between DiSDF and IOBM, IOD at decadal time scale are shown in Table 2, and we can find that the correlation coefficient between IOBM and DiSDF is −0.43, which is statistically significant at the 99% confidence level, although it is lower than the correlation coefficient for PDO. The correlation coefficient between IOD index and DiSDF is weak, with the value of −0.29, which is not statistically significance at the 90% confidence level. This result suggests that in addition to Pacific Ocean, decadal variation of IOBM might also play an important role in modulating the decadal dust variations in western Iran.

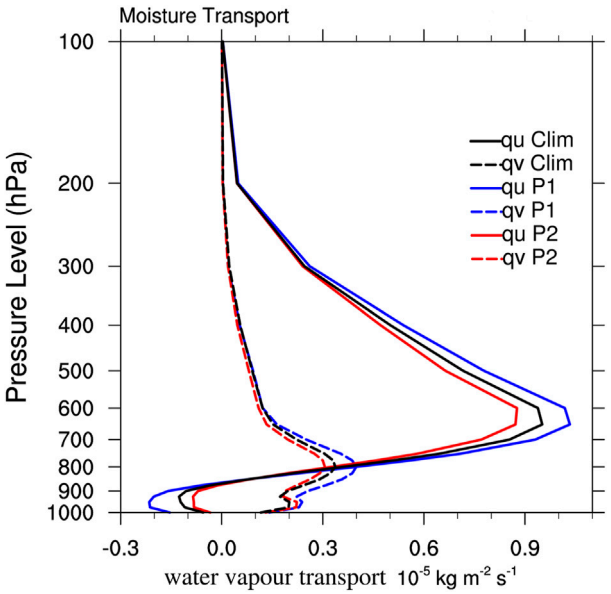

FIGURE 4
Climatology of vertical profile of water vapour transport (unit: 10^{-5} kg m^{-2} s^{-1}) over Middle East (22–38°N; 42–56°E) corresponding to the decadal variation of spring DiSDF over western Iran for the P1 (1992–2005; blue lines) and P2 (2006–2015; red lines) periods. The climatology of water vapour transport (black lines) was calculated for the 1979–2018 period. The solid lines indicate zonal transportation, while the dashed lines represent the meridional.

Previous studies have suggested that the decadal IOBM variations may be a response to the remote forcing from North Pacific Ocean and thus modulated by PDO (Han, Meehl et al., 2014; Han, Vialard et al., 2014; Dong et al., 2016). From Table 2, a strong positive correlation between PDO and IOBM is found, with correlation coefficient reaching 0.61, which is at statistically 99% confidence level. In order to distinguish whether the impact of IOBM on dust variations in western Iran in decadal time scale is distinct from that for PDO, we further use partial cross-correlation analysis (Yuan et al., 2015) to re-calculate the correlation among PDO, IOBM, and DiSDF. The results show that, after removing the influence of PDO, there is no significant correlation between DiSDF and IOBM in decadal time scale (R = −0.14). However, after excluding the IOBM signal, the correlation between DiSDF and PDO in decadal time scale is kept strong and significant (-0.39; statistically significant at the 95% confidence level). These results imply that POD plays a determining role on both IOBM and DiSDF, and IOBM may serve as an intermediary between PDO and DiSDF in western Iran.

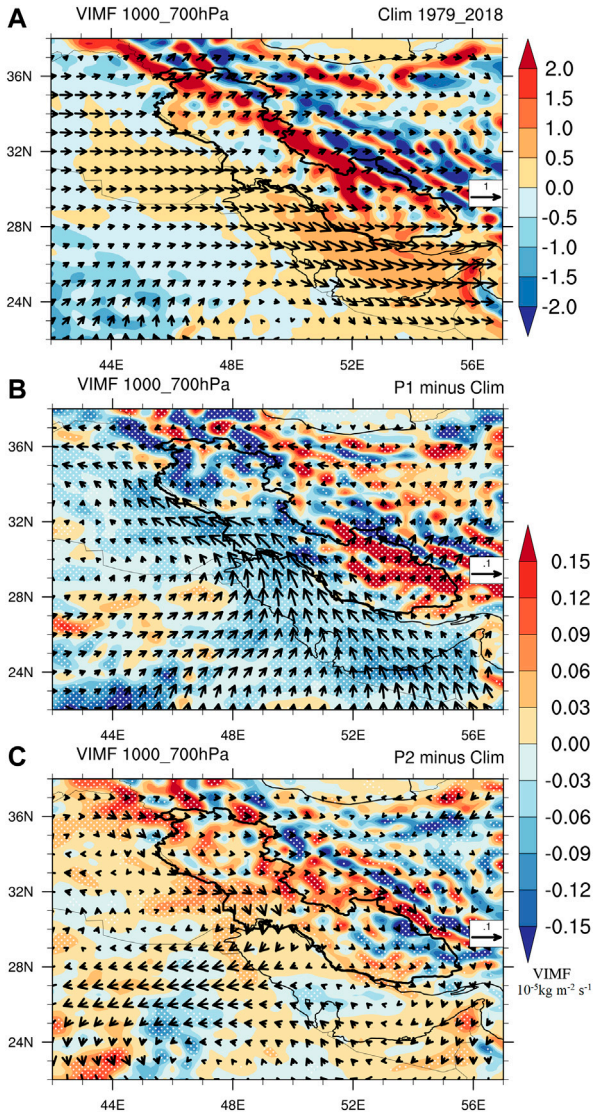

FIGURE 5
Vertically integrated moisture flux convergence/divergence (VIMF, shaded, unit: 10^{-5} kg m^{-2} s^{-1}) over the lower-middle layers of troposphere (1,000–700 hPa), superimposed with vertically integrated moisture transportation vector (arrows, Unit: kg $m^{-1}s^{-1}$) during MAM season **(A)** climatology averaged over 1979–2018; **(B)** anomalies for P1 period (1992–2005) from the climatology and **(C)** anomalies for P2 period (2006–2015) from climatology, corresponding to the decadal variation of spring DiSDF over western Iran. The reference arrow for moisture transportation vector is 1 kg $m^{-1}s^{-1}$ for climatology and 0.1 kg $m^{-1}s^{-1}$ for anomalies. The white dots **(B,C)** indicate the statistical significance at the 95% confidence level.

Figure 9 shows the anomalies of geopotential height and wind at 850hpa over the Arabian Peninsula for P1 and P2 period respectively. We can find that there exist negative anomalies of geopotential height at 850 hpa over most part of the Arabian Peninsula in negative PDO phase during 2006–2015 (P2 period) as shown in Figure 9B, while positive anomalies of 850 hpa geopotential height in the same region can be found in positive PDO phase during 1992–2005 (Figure 9A). This is consistent with previous findings that negative PDO will be favorable for the negative anomalies of geopotential height at 850 hPa in this region, and lower geopotential height over the Middle East and Africa will facilitate the formation of the cyclones that are important for the spring peak of dust storms (e.g., Dayan et al., 2008; Pu and Ginoux 2016). The opposite pattern can be found for the P1, with positive anomalies of geopotential over the Arabian Peninsula, and this is favorable for the weaking of spring dust activities in the region.

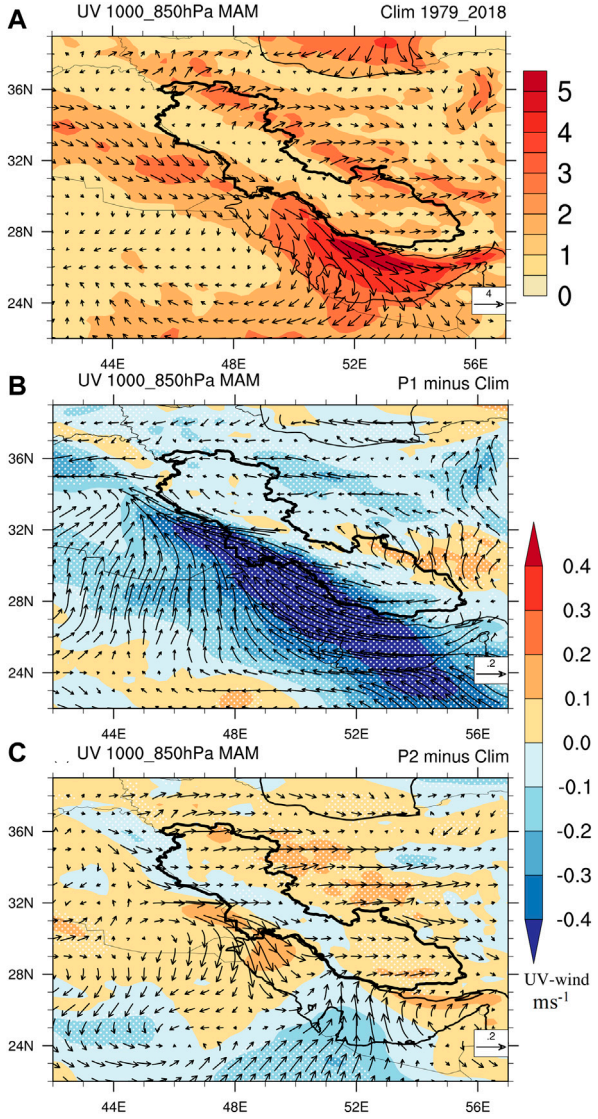

FIGURE 6
The UV-wind climatology and anomalies at 1,000–850 hPa (averaged at the seven levels: 1,000, 975, 950, 925, 900, 875, 850 hPa available from ERA5 reanalysis) during MAM season **(A)** climatology averaged over 1979–2018; **(B)** anomalies for P1 period (1992–2005) from the climatology and **(C)** anomalies for P2 period (2006–2015) from climatology, corresponding to the decadal variation of spring DiSDF over western Iran. Colored shading indicates the wind speed (unit: ms^{-1}) and is superimposed with wind vector. The reference arrow for wind vector is 4 ms^{-1} for climatology and 0.2 ms^{-1} for anomalies. The white dots **(B,C)** indicate the statistical significance at the 95% confidence level.

4 Conclusion and discussion

Based on station observation data, we revealed a decadal change of dust in-suspension day frequency over western Iran, and further pointed out that the atmospheric circulation may play an important role in modulating this decadal variation. Two periods with strong (P2: 2006–2015) and weak (P1: 1992–2005) dust activities are identified, then the surface wind, precipitation, soil moisture, water vapor transport and divergence during P1 and P2 are compared. The results show the northwesterly winds, which can either enhance the dust emission locally or transport dust from the main dust source areas to western Iran, predominate in P2 than P1.

There is anomalous convergence in the lower to middle troposphere over the western Iran in P1, resulting in more moisture transport from southern seas to the upper region and thus more precipitation in this period. The moisture

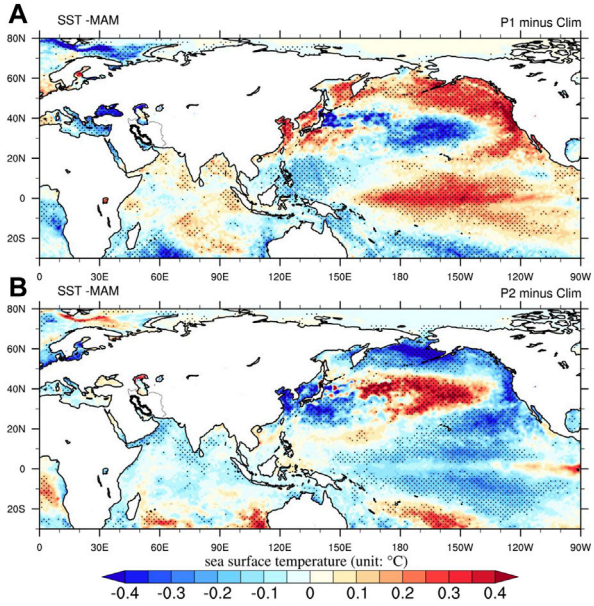

FIGURE 7
Anomalies of decadal sea surface temperature (unit: °C) for **(A)** P1 (1992–2005) and **(B)** P2 (2006–2015), relative to climatological mean corresponding to the decadal variation of spring DiSDF over western Iran. The climatology (Clim) is calculated for the 1979–2018 period. The black dots indicate the statistical significance at the 95% confidence level.

transport is closely relatively to the large-scale circulations including subtropical high-pressure system on Saudi Arabia as pointed out (Darand and Pazhoh 2019). In contrast, in P2 the negative anomalies of spring precipitation and soil moisture are evident over the region because of anomalous water vapor divergence. The negative anomalies of spring precipitation and evident has also led to the deteriorated vegetation cover in P2 in the western Iran, which also partly contributes to the high dust frequency in P2. In addition, the SST anomalies show distinct differences between the decadal change of DiSDF in P1&P2. The findings showed that a negative PDO is connected with circulation and geopotential height patterns favorable to high dust frequency in P2 in the western Iran. Previous studies have shown the PDO influences the climate factors and thus on dust in Arabian Peninsula and Syria at interannual scales (e.g., Notaro et al., 2015; Pu and Ginoux 2016). The periods of their analysis are relative short, and our study further give direct evidence on the dominant impacts of PDO on dust variations in western Iran on decadal scales. Even the significant decadal correlation between DiSDF and IOBM can be found, this correlation is no longer significant after removing the influence of PDO, and this suggests that IOBM may serve as an intermediary for the impact of PDO on DiSDF in western Iran.

With respect to various sources of dust in the Middle East, western Iran is affected by local and transported dust storms. In general, western Iran shows similar decadal changes in dust activity with Saudi Aria during 1988–2012, which suggests that decadal dust activities in both western Iran and Saudi Arabia are all associated with decadal changes in regional climate and circulations. However, whether other regions of Middle East other than Saudi Arabia and western Iran, such as Syria, Iraq and Sudan, experienced similar decadal variations need further confirmation with dust observations in these regions. In particular, as dust particles in these regions can be transported to affect western Iran, it is desirable to separate the contributions of these upstream areas to the decadal variations of dust activities in western Iran, as revealed in this study. Numerical simulation with meteorological models could be conducted to quantify the impacts of dust transportation and local dust emission on the dust storm episode, as well as the variation of dust activities in different time scales (e.g., Ledari et al., 2022). In addition to western Iran, other parts of Iran, in particular eastern Iran which is regarded as one of the most dusty regions in Middle East, also suffer from heavy dust pollution (Rashki et al., 2021), and it is desirable to conduct similar analysis as in this study for these regions to enhance our understanding of dust variations in Middle East.

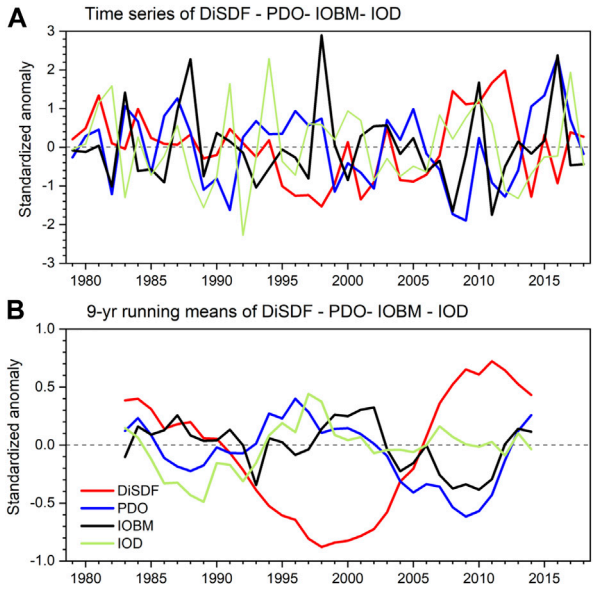

FIGURE 8
(A) Time series of spring DiSDF, PDO, IOBM, and IOD from 1979 to 2018 and **(B)** their corresponding 9-yr running means (1983–2014). The monthly standardized PDO index is derived from the leading principal component of monthly sea surface temperature anomalies in the northern Pacific Ocean (20° N) after the global average sea surface temperature has been removed. The IOBM index is defined as SST anomalies over the tropical Indian Ocean (40°E–120°E, 20°S–25°N). The IOD index is defined as the difference in SST anomalies between the west region (50°E-70°E and 10°S-10°N) and the east region (90°E-110°E and 10°S-0) in the Indian Ocean.

TABLE 2 The correlation coefficients among DiSDF, PDO, IOBM, and IOD in spring based on 9-yr running means of original series.

Variables	DiSDF	PDO	IOBM	IOD
DiSDF	1	−0.54***	−0.43***	−0.29
PDO	—	1	0.61***	0.31*
IOBM	—	—	1	−0.11
IOD	—	—	—	1

*statistically significant at the 90% level. **statistically significant at the 95% level. ***statistically significant at the 99% level.

Data availability statement

Meteorological data are available on the Islamic Republic of Iran Meteorological Organization (IRIMO) website: https://data.irimo.ir. MODIS DOD retrieval data are available at https://doi.org/10.5194/acp-21-13369-2021 (Song et al., 2021). Reanalysis data from ERA-5 is available at the following website: https://cds.climate.copernicus.eu. Precipitation dataset from GPCC V7 is available at the following website: https://www.esrl.noaa.gov/psd/data/gridded/data.gpcc.html. PDO index is available at the NOAA Climate Prediction Center website: http://www.esrl.noaa.gov/psd/data/climateindices/list.

Author contributions

All authors equally collaborated in the research presented in this publication by making the following contributions: research conceptualization, AK, ZL, and CW; methodology, AK, ZL, and CW; formal analysis, AK, ZL, and CW; data curation, AK, ZL, and CW; writing original draft preparation, AK, ZL, and CW; writing review and editing, AK, ZL, and CW; supervision, ZL

Funding

This study is jointly supported by the National Key Research and Development Program of China (grant 2020YFA0607801)

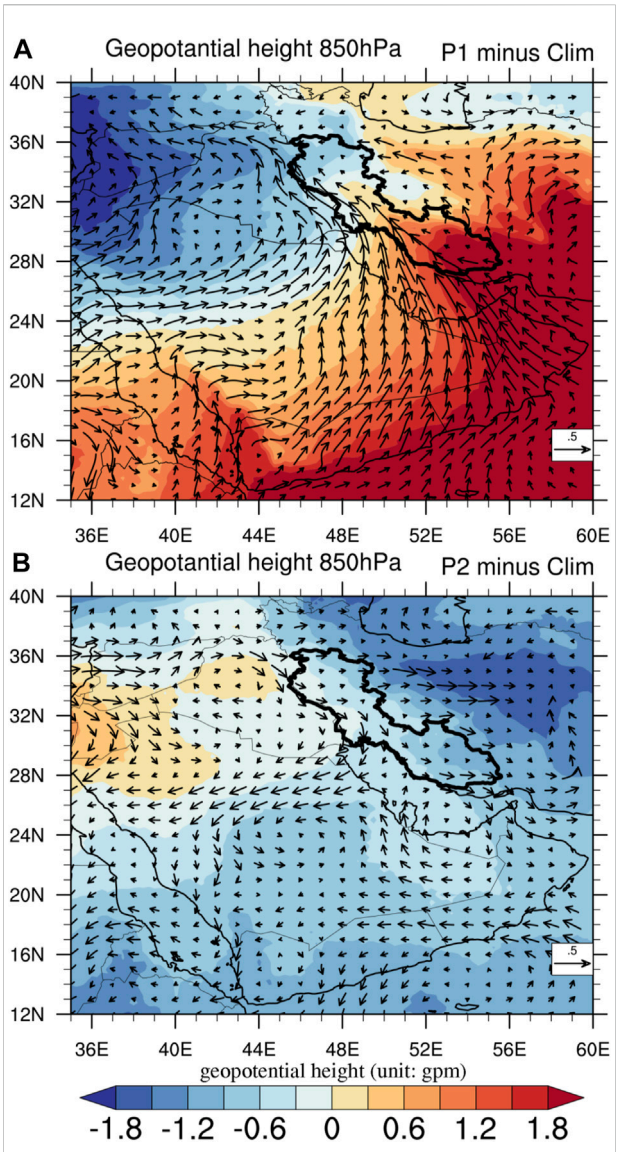

FIGURE 9
Anomalies of decadal geopotential height (colored shading; unit: gpm) and UV-wind (vectors; ms^{-1}) at 850 hPa during **(A)** P1 (1992–2005) and **(B)** P2 (2006–2015), relative to climatological mean. The climatology (Clim) is calculated for the 1979–2018 period. The reference arrow for wind vector is 0.5 ms^{-1} for anomalies.

and the National Natural Science Foundation of China (grant nos. 42075166 and 41975119). The authors acknowledge the support of the CAS-TWAS President Fellowship (No. 2017CTF116).

Acknowledgments

We would like to thank the Islamic Republic of Iran Meteorological Organization (IRIMO) for providing weather data. We also thank the European Centre for Medium-Range Weather Forecasts (ECMWF) reanalysis project for providing wind field and soil moisture data, and the Global Precipitation Climatology Centre (GPCC) for providing precipitation data over Middle East.

Conflict of interest

The handling editor RM declared a past co-authorship with the authors CW and ZL.

The authors declare that the research was conducted in the absence of any commercial or financial relationships that could be construed as a potential conflict of interest.

Publisher's note

Supplementary material

The Supplementary Material for this article can be found online at: https://www.frontiersin.org/articles/10.3389/fenvs.2022.983048/full#supplementary-material

References

Alizadeh-Choobari, O., Ghafarian, P., and Owlad, E. (2016). Temporal variations in the frequency and concentration of dust events over Iran based on surface observations. *Int. J. Climatol.*, 36(4), 2050–2062. doi:10.1002/joc.4479

Alizadeh-Choobari, O., and Najafi, M. S. (2018). Extreme weather events in Iran under a changing climate. *Clim. Dyn.*, 50(1-2), 249–260. doi:10.1007/s00382-017-3602-4

Boloorani, A. D., Nabavi, S. O., Bahrami, H. A., Mirzapour, F., Kavosi, M., Abasi, E., et al. (2014). Investigation of dust storms entering Western Iran using remotely sensed data and synoptic analysis. *J. Environ. Health Sci. Eng.*, 12(1), 124. doi:10.1186/s40201-014-0124-4

Broomandi, P., Karaca, F., Guney, M., Fathian, A., Geng, X., and Kim, J. R. (2021). Destinations frequently impacted by dust storms originating from southwest Iran. *Atmos. Res.*, 248, 105264. doi:10.1016/j.atmosres.2020.105264

Darand, M., and Pazhoh, F. (2019). Vertically integrated moisture flux convergence over Iran. *Clim. Dyn.*, 53(5-6), 3561–3582. doi:10.1007/s00382-019-04726-z

Dayan, U., Ziv, B., Shoob, T., and Enzel, Y. (2008). Suspended dust over southeastern Mediterranean and its relation to atmospheric circulations. *Int. J. Climatol.*, 28(7), 915–924. doi:10.1002/joc.1587

Ding, R., Li, J., Wang, S., and Ren, F. (2005). Decadal change of the spring dust storm in northwest China and the associated atmospheric circulation. *Geophys. Res. Lett.*, 32, L02808(2). doi:10.1029/2004GL021561

Dong, L., Zhou, T., Dai, A., Song, F., Wu, B., and Chen, X. (2016). The footprint of the inter-decadal Pacific oscillation in Indian Ocean sea surface temperatures. *Sci. Rep.*, 6(1), 21251–21258. doi:10.1038/srep21251

Draxler, R. R., Gillette, D. A., Kirkpatrick, J. S., and Heller, J. (2001). Estimating PM10 air concentrations from dust storms in Iraq, Kuwait and Saudi Arabia. *Atmos. Environ.*, 35(25), 4315–4330. doi:10.1016/S1352-2310(01)00159-5

Fan, K., and Wang, H. (2004). Antarctic oscillation and the dust weather frequency in North China. *Geophys. Res. Lett.*, 31 10. doi:10.1029/2004GL019465

Fan, K., Xie, Z. M., and Xu, Z. Q. (2016). Two different periods of high dust weather frequency in northern China. *Atmos. Ocean. Sci. Lett.*, 9(4), 263–269. doi:10.1080/16742834.2016.1176300

Fountoukis, C., Harshvardhan, H., Gladich, I., Ackermann, L., and Ayoub, M. A. (2020). Anatomy of a severe dust storm in the Middle East: Impacts on aerosol optical properties and radiation budget. *Aerosol Air Qual. Res.*, 20, 155–165. doi:10.4209/aaqr.2019.04.0165

Francis, D., Eayrs, C., Chaboureau, J. P., Mote, T., and Holland, D. M. (2018). Polar jet associated circulation triggered a Saharan cyclone and derived the poleward transport of the African dust generated by the cyclone. *J. Geophys. Res. Atmos.*, 123(21), 11,899–11,917. doi:10.1029/2018jd029095

Friedl, M., and Sulla-Menashe, D. (2015). MCD12Q1 MODIS/Terra+ aqua land cover type yearly L3 global 500m SIN grid V006 [data set]. *NASA EOSDIS Land Process. DAAC*, 10, 200. doi:10.5067/MODIS/MCD12Q1.006

Furman, H. K. H. (2003). Dust storms in the Middle East: Sources of origin and their temporal characteristics. *Indoor Built Environ.*, 12(6), 419–426. doi:10.1177/1420326X03037110

Ginoux, P., Prospero, J. M., Gill, T. E., Hsu, N. C., and Zhao, M. (2012). Global-scale attribution of anthropogenic and natural dust sources and their emission rates based on MODIS Deep Blue aerosol products. *Rev. Geophys.*, 50 3005 (3). doi:10.1029/2012RG000388

Gong, D. Y., Mao, R., and Fan, Y. D. (2006). East asian dust storm and weather disturbance: Possible links to the arctic oscillation. *Int. J. Climatol.*, 26(10), 1379–1396. doi:10.1002/joc.1324

Goudie, A., and Middleton, N. (2001). Saharan dust storms: Nature and consequences. *Earth-science Rev.*, 56(1-4), 179–204. doi:10.1016/S0012-8252(01)00067-8

Goudie, A. S., and Middleton, N. J. (2006). *Desert dust in the global system*. Springer Science & Business Media, Germany.

Han, W., Meehl, G. A., Hu, A., Alexander, M. A., Yamagata, T., Yuan, D., et al. (2014). Intensification of decadal and multi-decadal sea level variability in the Western tropical Pacific during recent decades. *Clim. Dyn.*, 43(5), 1357–1379. doi:10.1007/s00382-013-1951-1

Han, W., Vialard, J., McPhaden, M. J., Lee, T., Masumoto, Y., Feng, M., et al. (2014). Indian ocean decadal variability: A review. *Bull. Am. Meteorol. Soc.*, 95(11), 1679–1703. doi:10.1175/BAMS-D-13-00028.1

Hersbach, H., Bell, B., Berrisford, P., Hirahara, S., Horányi, A., Muñoz-Sabater, J., et al. (2020). The ERA5 global reanalysis. *Q. J. R. Meteorol. Soc.*, 146(730), 1999–2049. doi:10.1002/qj.3803

Heydarizad, M., Raeisi, E., Sori, R., and Gimeno, L. (2018). The identification of Iran's moisture sources using a Lagrangian Particle Dispersion Model. *Atmosphere*, 9(10), 408. doi:10.3390/atmos9100408

Jin, Q., Wei, J., Lau, W. K., Pu, B., and Wang, C. (2021). Interactions of Asian mineral dust with Indian summer monsoon: Recent advances and challenges. *Earth-Science Rev.*, 215, 103562. doi:10.1016/j.earscirev.2021.103562

Kamal, A., Wu, C., and Lin, Z. (2020). Interannual variations of dust activity in Western Iran and their possible mechanisms. *Big Earth Data*, 4(2), 175–190. doi:10.1080/20964471.2019.1685825

Kelley, C. P., Mohtadi, S., Cane, M. A., Seager, R., and Kushnir, Y. (2015). Climate change in the Fertile Crescent and implications of the recent Syrian drought. *Proc. Natl. Acad. Sci. U. S. A.*, 112(11), 3241–3246. doi:10.1073/pnas.1421533112

Ledari, D. G., Hamidi, M., and Shao, Y. (2022). Numerical simulation of the 18 February 2017 frontal dust storm over southwest of Iran using WRF-Chem, satellite imagery, and PM10 concentrations. *J. Arid Environ.*, 196, 104637. doi:10.1016/j.jaridenv.2021.104637

Léon, J. F., and Legrand, M. (2003). Mineral dust sources in the surroundings of the north Indian Ocean. *Geophys. Res. Lett.*, 30(6). doi:10.1029/2002GL016690

Li, H., Lin, Z., and Chen, H. (2009). Interdecadal variability of spring precipitation over South China and its associated atmospheric water vapor transport. *Atmos. Ocean. Sci. Lett.*, 2(2), 113–118. doi:10.1080/16742834.2009.11446783

Mohammadpour, K., Sciortino, M., and Kaskaoutis, D. G. (2021). Classification of weather clusters over the Middle East associated with high atmospheric dust-AODs in West Iran. *Atmos. Res.*, 259, 105682. doi:10.1016/j.atmosres.2021.105682

Muñoz-Sabater, J., Dutra, E., Agustí -Panareda, A., Albergel, C., Arduini, G., Balsamo, G., et al. (2021). Era5-land: A state-of-the-art global reanalysis dataset for land applications. *Earth Syst. Sci. Data.*, 13, 4349–4383. doi:10.5194/essd-13-4349-2021

Myneni, R., Knyazikhin, Y., and Park, T. (2015). *MOD15A2H MODIS/Terra leaf area Index/FPAR 8-Day L4 global 500m SIN grid V006*. NASA EOSDIS Land Processes DAAC, South Dakota. doi:10.5067/MODIS/MOD15A2H.006

Namdari, S., Karimi, N., Sorooshian, A., Mohammadi, G., and Sehatkashani, S. (2018). Impacts of climate and synoptic fluctuations on dust storm activity over the Middle East. *Atmos. Environ.*, 173, 265–276. doi:10.1016/j.atmosenv.2017.11.016

Notaro, M., Yu, Y., and Kalashnikova, O. V. (2015). Regime shift in Arabian dust activity, triggered by persistent Fertile Crescent drought: *J. Geophys. Res. Atmos.*, 120(19), 10–229. doi:10.1002/2015JD023855

Piccarreta, M., Capolongo, D., Boenzi, F., and Bentivenga, M. (2006). Implications of decadal changes in precipitation and land use policy to soil erosion in Basilicata, Italy. *Catena*, 65(2), 138–151. doi:10.1016/j.catena.2005.11.005

Prospero, J. M., Ginoux, P., Torres, O., Nicholson, S. E., and Gill, T. E. (2002). Environmental characterization of global sources of atmospheric soil dust identified with the Nimbus 7 Total Ozone Mapping Spectrometer (TOMS) absorbing aerosol product. *Rev. Geophys.*, 40(1), 2-1-2-31. doi:10.1029/2000RG000095

Pu, B., and Ginoux, P. (2016). The impact of the Pacific Decadal Oscillation on springtime dust activity in Syria. *Atmos. Chem. Phys.*, 16(13), 13431–13448. doi:10.5194/acp-16-13431-2016

Qian, W., Quan, L., and Shi, S. (2002). Variations of the dust storm in China and its climatic control. *J. Clim.*, 15(10), 1216–1229. doi:10.1175/1520-0442(2002)015<1216:VOTDSI>2.0.CO;2

Rashki, A., Middleton, N. J., and Goudie, A. S. (2021). Dust storms in Iran–Distribution, causes, frequencies and impacts. *Aeolian Res.*, 48, 100655. doi:10.1016/j.aeolia.2020.100655

Rezazadeh, M., Irannejad, P., and Shao, Y. (2013). Climatology of the Middle East dust events. *Aeolian Res.*, 10, 103–109. doi:10.1016/j.aeolia.2013.04.001

Schneider, U., Finger, P., Meyer-Christoffer, A., Rustemeier, E., Ziese, M., and Becker, A. (2017). Evaluating the hydrological cycle over land using the newly-corrected precipitation climatology from the Global Precipitation Climatology Centre (GPCC). *Atmosphere*, 8(3), 52. doi:10.3390/atmos8030052

Shao, Y., and Wang, J. (2003). A climatology of Northeast Asian dust events. *metz.*, 12(4), 187–196. doi:10.1127/0941-2948/2003/0012-0187

Shao, Y., Wyrwoll, K. H., Chappell, A., Huang, J., Lin, Z., McTainsh, G. H., et al. (2011). Dust cycle: An emerging core theme in Earth system science. *Aeolian Res.*, 2(4), 181–204. doi:10.1016/j.aeolia.2011.02.001

Song, Q., Zhang, Z., Yu, H., Ginoux, P., and Shen, J. (2021). Global dust optical depth climatology derived from CALIOP and MODIS aerosol retrievals on decadal timescales: Regional and interannual variability. *Atmos. Chem. Phys.*, 21(17), 13369–13395. doi:10.5194/acp-21-13369-2021

Sotoudeheian, S., Salim, R., and Arhami, M. (2016). Impact of middle eastern dust sources on PM_{10}in Iran: Highlighting the impact of Tigris-Euphrates basin sources and lake urmia desiccation: *J. Geophys. Res. Atmos.*, 121(23), 14,018–14,034. doi:10.1002/2016JD025119

Unep, W. U. N. C. C. D. (2016) *Global assessment of sand and dust storms*. United Nations Environment Programme, Nairobi.

Van Der Does, M., Knippertz, P., Zschenderlein, P., Giles Harrison, R., and Stuut, J. B. W. (2018). The mysterious long-range transport of giant mineral dust particles. *Sci. Adv.*, 4(12), eaau2768. doi:10.1126/sciadv.aau2768

Wu, C., Lin, Z., Liu, X., Li, Y., Lu, Z., and Wu, M. (2018). Can climate models reproduce the decadal change of dust aerosol in East Asia? *Geophys. Res. Lett.*, 45(18), 9953–9962. doi:10.1029/2018GL079376

Wu, C., Lin, Z., and Liu, X. (2020). The global dust cycle and uncertainty in CMIP5 (Coupled Model Intercomparison Project phase 5) models. *Atmos. Chem. Phys.*, 20(17), 10401–10425. doi:10.5194/acp-20-10401-2020

Yu, Y., Notaro, M., Liu, Z., Wang, F., Alkolibi, F., Fadda, E., et al. (2015). Climatic controls on the interannual to decadal variability in Saudi Arabian dust activity: Toward the development of a seasonal dust prediction model. *J. Geophys. Res. Atmos.*, 120(5), 1739–1758. doi:10.1002/2014JD022611

Yuan, N., Fu, Z., Zhang, H., Piao, L., Xoplaki, E., and Luterbacher, J. (2015). Detrended partial-cross-correlation analysis: A new method for analyzing correlations in complex system. *Sci. Rep.*, 5(1), 8143–8147. doi:10.1038/srep08143

Zoljoodi, M., Didevarasl, A., and Saadatabadi, A. R. (2013). Dust events in the Western parts of Iran and the relationship with drought expansion over the dust-source areas in Iraq and Syria. *Atmos. Clim. Sci.*, 3(03), 321–336. doi:10.4236/acs.2013.33034

frontiers | Frontiers in Environmental Science

TYPE Original Research
PUBLISHED 13 October 2022
DOI 10.3389/fenvs.2022.1015723

OPEN ACCESS

EDITED BY
Zhiyuan Hu,
School of atmospheric sciences, Sun Yat-sen University, China

REVIEWED BY
Zhicong Yin,
Nanjing University of Information Science and Technology, China
Yongjing Ma,
Institute of Atmospheric Physics (CAS), China
Bing Pu,
University of Kansas, United States

*CORRESPONDENCE
Xiaoyan Wang,
wangxyfd@fudan.edu.cn

SPECIALTY SECTION
This article was submitted to Atmosphere and Climate, a section of the journal Frontiers in Environmental Science

RECEIVED 10 August 2022
ACCEPTED 30 September 2022
PUBLISHED 13 October 2022

CITATION
Sun Y and Wang X (2022), Meteorological factor contributions to the seesaw concentration pattern between $PM_{2.5}$ and O_3 in Shanghai. *Front. Environ. Sci.* 10:1015723. doi: 10.3389/fenvs.2022.1015723

Meteorological factor contributions to the seesaw concentration pattern between $PM_{2.5}$ and O_3 in Shanghai

Yongzhao Sun[1] and Xiaoyan Wang[1,2,3]*

[1]Department of Atmospheric and Oceanic Sciences and Institute of Atmospheric Sciences, Fudan University, Shanghai, China, [2]CMA-FDU Joint Laboratory of Marine Meteorology, Shanghai, China, [3]Shanghai Institute of Pollution Control and Ecological Security, Shanghai, China

With the implementation of various stringent emission reduction measures since 2013 in China, significant declines in fine particle ($PM_{2.5}$) concentrations have occurred nationwide. However, China has suffered from increasing levels of ozone pollution in eastern urban areas. Many studies focus on the chemical interaction between $PM_{2.5}$ and O_3, but the meteorological mechanisms of the seesaw variation pattern between them are still unclear. Taking the megacity Shanghai (SH) as an example, we explored the meteorological causes of two types of $PM_{2.5}$-O_3 concentration variation seesaw events, i.e., high $PM_{2.5}$ concentration with low O_3 concentration (Type-one) events and low-PM-high-O_3 (Type-two) seesaw events. The backward trajectories of the 144 Type-one events are divided into three clusters. Among the three clusters of Type-one seesaw events, the boundary layer height decreases by 20.53%–53.58%, and the wind speed decreases by 17.99%–28.29%, which is unfavorable for the diffusion of local air pollutants and contributes to the accumulation of $PM_{2.5}$. Additionally, a backward air mass with a high content of $PM_{2.5}$ plays an important role in the Type-one events, especially in the case of cluster one. In terms of cluster two, the increase in cloud cover, decrease in solar radiation and increase in relative humidity also promote the hygroscopic growth of aerosols and suppress the production of O_3. As for cluster three, higher cloud cover and relative humidity contribute to the seesaw pattern of PM and O_3. The 64 Type-two seesaw events are divided into two clusters. O_3-rich air masses from the nearby east sea surface and remote northeast China increase the local O_3 of SH. Moreover, in cluster one, high boundary layer depth and wet deposition contribute to the decrease in $PM_{2.5}$ concentration. In cluster two, a obvious decrease in cloud cover and increase in solar radiation are also favorable for the photochemical production of ozone. The results will provide suggestions for the government to use to take measures to improve the air quality of SHs.

KEYWORDS

$PM_{2.5}$, O_3, meteorological mechanisms, Shanghai, backward trajectory

Introduction

In recent years, cities in eastern China have been facing severe air pollution. $PM_{2.5}$ (particles with aerodynamic diameters less than 2.5 μm) and ozone concentrations often exceed air quality standards (Ministry of Ecology and Environment, 2013). Air pollution is one of the main environmental problems in urban areas, particularly in megacities, such as Shanghai (SH). Exposure to high levels of $PM_{2.5}$ has adverse effects on human health and ecosystem productivity (Yue et al., 2017; Wang et al., 2019a). Thus, in September 2013, the State Council issued the Action Plan on the Prevention and Control of Air Pollution, known as the Clean Air Actions (CAA), to aggressively control anthropogenic emissions. The Yangtze River Delta region was required to reduce its $PM_{2.5}$ concentrations by 20% within 5 years (Ministry of Ecology and Environment, 2013). Starting that year, $PM_{2.5}$ data from a nationwide monitoring network of approximately 1000 sites became available from the China National Environmental Monitoring Center (CNEMC) of the Ministry of Ecology and Environment of China (MEE). Afterward, in a three-year action plan to fight air pollution (State Council of the People's Republic of China, 2018), sulfur dioxide, nitrogen oxides and $PM_{2.5}$ were further restricted. With joint efforts, the average annual $PM_{2.5}$ concentration in China decreased by 44% in 2019 compared with 2013 (Zhong et al., 2021). However, at the same time, the surface ozone concentration in China continues to rise (Liu et al., 2018; Dang and Liao, 2019, 2012–2017), which partially offsets the health benefits brought by the decrease in $PM_{2.5}$ concentration. Stage II of the CAA plan began in 2018 (State Council of the People's Republic of China, 2018), and new emission control measures were implemented for surface ozone.

Given the seesaw variation between $PM_{2.5}$ and O_3, i.e., the decrease in O_3 concentrations with the increase in $PM_{2.5}$ contents, many studies have been conducted to investigate the chemical mechanisms (Shao et al., 2022; Wu et al., 2022). The interaction between $PM_{2.5}$ and O_3 is closely related and very complicated. NOx and VOCs (volatile organic compounds) in the atmosphere are able to generate ozone under light conditions in photochemical reactions (Carrillo-Torres et al., 2017). In this process, NOx, SO_2 and VOCs are also oxidized to form secondary $PM_{2.5}$ (Zhu et al., 2015). At nighttime and in the immediate vicinity of large NO emissions, ozone concentrations are depressed through the process of NOx titration. The result is the net conversion of O_3 to NO_2 (Gillani and Pleim, 1996). In regions with high NOx emissions, O_3 formation can be VOC-limited (Sillman et al., 1990; Kleinman et al., 2003). As a result of CAA, NOx decreased obviously (Silver et al., 2018, 2015–2017). Thus, due to the nonlinear relationship between O_3 production and NOx (Simon et al., 2015), the concentration of O_3 in VOC-limited areas in eastern China increases to some extent.Through heterogeneous chemical reactions, $PM_{2.5}$ can indirectly affect O_3. In winter on the North China Plain, formaldehyde is produced by the oxidation of reactive VOCs. The fast production of ozone is driven by HOx radicals from the photolysis of formaldehyde, overcoming radical titration from the decreased NOx emissions (Li et al., 2021). Research has demonstrated an ~40% decrease in $PM_{2.5}$, slowing the aerosol sink of hydroperoxyl (HO2) radicals

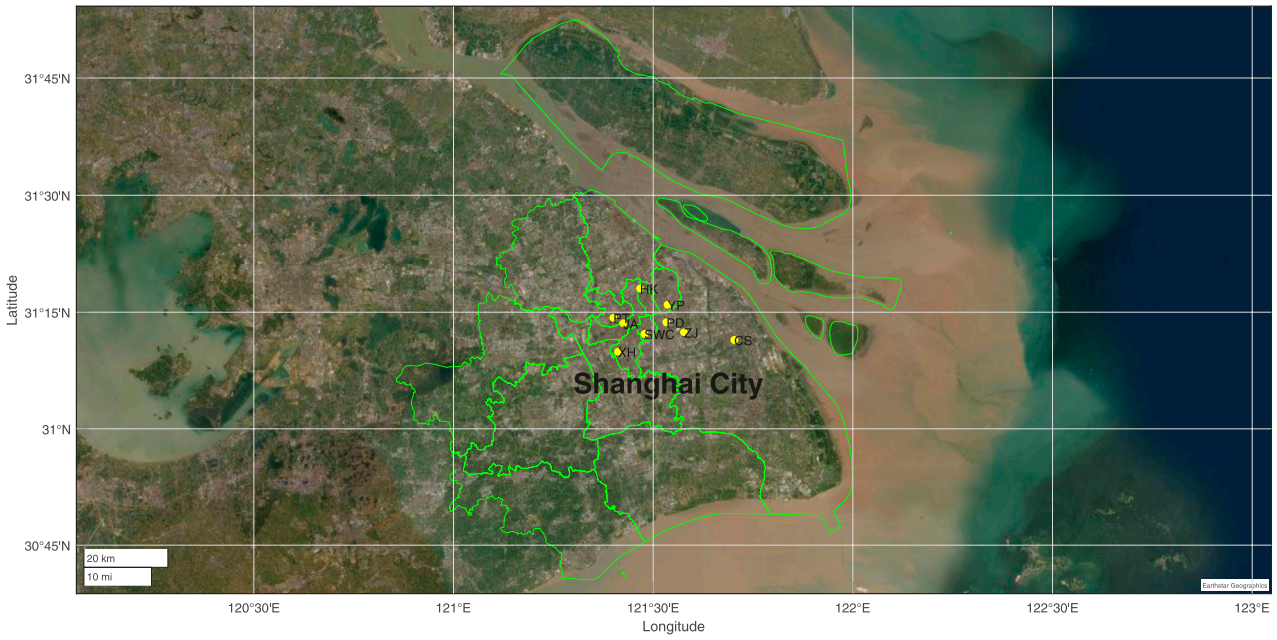

FIGURE 1
The detailed geographical distribution of 9 observational stations in the Shanghai region. The points in the figure represent the latitude and longitude of the Shanghai air quality monitoring station. Air quality monitoring station locations can be obtained from the website of Ministry of Ecology and Environment of the People's Republic of China (http://106.37.208.233:20035). Capital letters in the figure represent abbreviations of site names.

and thus stimulating ozone production at 0.6–1 ppbv a^{-}1 in Beijing–Tianjin–Hebei (Li et al., 2019). Using the WRF-CMAQ model, Liu and Wang also uncovered a similar and substantial effect of HO2 uptake on increases in O_3 levels due to changes in PM concentrations (Liu and Wang, 2020a). Although many studies have been performed to evaluate the quantitative contributions of photolysis rates and heterogeneous chemical reactions to the production of O_3, their relative importance is still unclear (He and Carmichael, 1999; Sillman, 1999).

The absorption and scattering of shortwave radiation by $PM_{2.5}$ can attenuate incident solar shortwave radiation and change the radiation balance in the atmosphere (Charlson et al., 1992; Bond et al., 2013). The attenuation of short-wave radiation will reduce the photolysis rate of O_3 and precursors (J [O_3^{1}D] and J [NO_2], etc.), which will decrease the photochemical reaction intensity, and then reduce the net chemical production of O_3 (Jacobson, 1998; Li et al., 2011; Deng et al., 2012). Wang et al. (2019b) analyzed the photolysis rate data in Beijing from 2012 to 2015, and found that aerosols caused J[NO_2] and J[O_3^{1}D] near the ground in Beijing to decrease by 24%–30% and 27%–33%, respectively, which led to a decrease of photochemical generation rate in the local ozone in summer by approximately 25%.

Previous studies on the interaction between $PM_{2.5}$ and O_3 have mostly focused on chemical mechanisms. However, meteorological conditions also have great effects on the formation, transportation and deposition processes of $PM_{2.5}$ and O_3 and their precursors (Finlayson-Pitts and Pitts, 1986; Cox and Chu, 1996; Xu et al., 1996; Mu and Zhang, 2014; Zhang et al., 2014; Hu et al., 2015; Yin et al., 2017; Zhang, 2017; Wang et al., 2021). For example, by altering the chemical reaction rates directly and the biogenic emissions of VOCs indirectly, higher temperatures can enhance ozone formation in most instances (Guenther et al., 2006; Lu et al., 2019b). The response of $PM_{2.5}$ concentrations to temperature was largely the result of competing changes in sulfate and nitrate concentrations with a smaller role played by organics (Dawson et al., 2007). Increasing relative humidity will increase the water content of fine particles, thus increasing the $PM_{2.5}$ concentration (Dawson et al., 2007). Water vapor is able to react with the excited oxygen atom O(^{1}D) and generate OH radicals, which eventually lead to a reduction in the reaction between O(^{1}D) and O_2 (Johnson et al., 1999). Thus, the increase in water vapor can lead to a decrease in surface ozone concentrations (Camalier et al., 2007; He et al., 2017).Pollutant distributions are strongly affected by the wind field (Chen et al., 2020). $PM_{2.5}$ concentrations typically decrease by an order of magnitude between polluted regions and the diluting background air, whereas for ozone concentrations may actually increase or decrease, affected by upwind regions (Jacob and Winner, 2009; Gu et al., 2020b). Precipitation decreases both $PM_{2.5}$ and O_3 concentrations *via* wet removal (Shan et al., 2008). An increase in the planetary boundary layer height can decrease pollutant levels *via* dilution of primary pollutants into a larger volume of air (Su et al., 2018)

However, most of the existing studies focused on the meteorological condition contributions to the individual pollution of $PM_{2.5}$ or O_3 (He et al., 2017; Wang et al., 2018; Lu et al., 2019a; Zhai et al., 2019; Li et al., 2020; Yin et al., 2020). In terms of the synergetic seesaw pattern between $PM_{2.5}$ and O_3, its meteorological mechanism has been poorly understood. Individual meteorological factors will have the same or adverse effects on the concentration of $PM_{2.5}$ and O_3. What is the net contribution of meteorological conditions to the seesaw concentrations pattern between $PM_{2.5}$ and O_3. This study will take the seesaw concentration events of $PM_{2.5}$ and O_3 in Shanghai as a case to reveal their meteorological causes, which will benefit the prediction of future synergetic pollution of $PM_{2.5}$ and O_3.

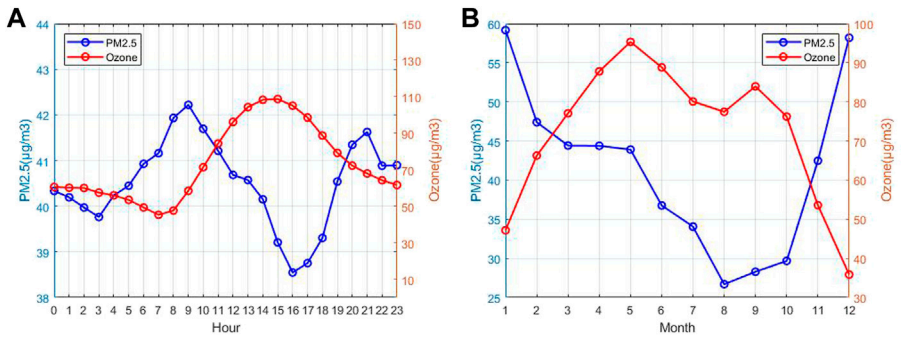

FIGURE 2
The hourly and seasonal means of $PM_{2.5}$ and ozone concentrations in Shanghai, **(A)** diurnal changes and **(B)** monthly changes from 2014 to 2020.

Data and method

Air pollution dataset

Hourly surface observations of O_3, $PM_{2.5}$ and nitrogen dioxide (NO_2) were all obtained from the CNEMC network (http://106.37.208.233:20035/, last access: 28 December 2020). As part of the CAA, the network started in 2013 with 496 sites in 74 major cities across the country, growing to more than 2500 sites in 366 cities by 2020. At each monitoring site, the concentration of O_3 was measured using ultraviolet absorption spectrometry and differential optical absorption spectroscopy. $PM_{2.5}$ mass concentrations are measured using the micro-oscillating balance method and/or the β absorption method. NO_2 concentrations are measured by the molybdenum converter method, which is known to have positive interferences from NO_2 oxidation products (Ministry of Ecology and Environment, 2012). Instrumental operation, maintenance, data assurance, and quality control were conducted based on the most recent revisions of China's environmental protection standards (Ministry of Ecology and Environment, 2013). In terms of time, all the data we used are from 13 May 2014 to 7 November 2020.

Air quality data were measured at 9 sites in the Shanghai region, and each site has distinct representation for different influences from urban air pollutant emissions. Figure 1 shows the locations of the nine sites, i.e., Putuo Station, No.15 Factory

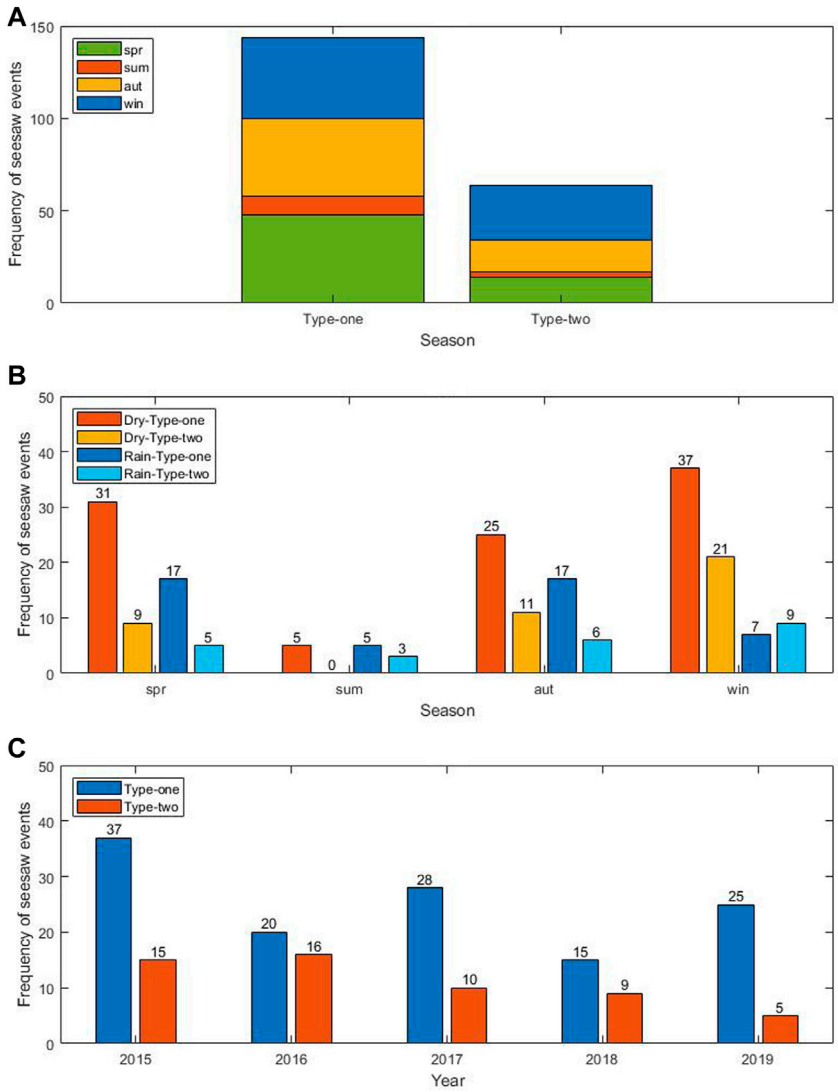

FIGURE 3
The seasonal distribution **(A)**, precipitation distribution **(B)** and annual distribution **(C)** of seesaw events in Shanghai during 2013–2020. If the hourly precipitation of any grid exceeds 0.5 mm, it is considered that there is an obvious wet cleaning process in this study.

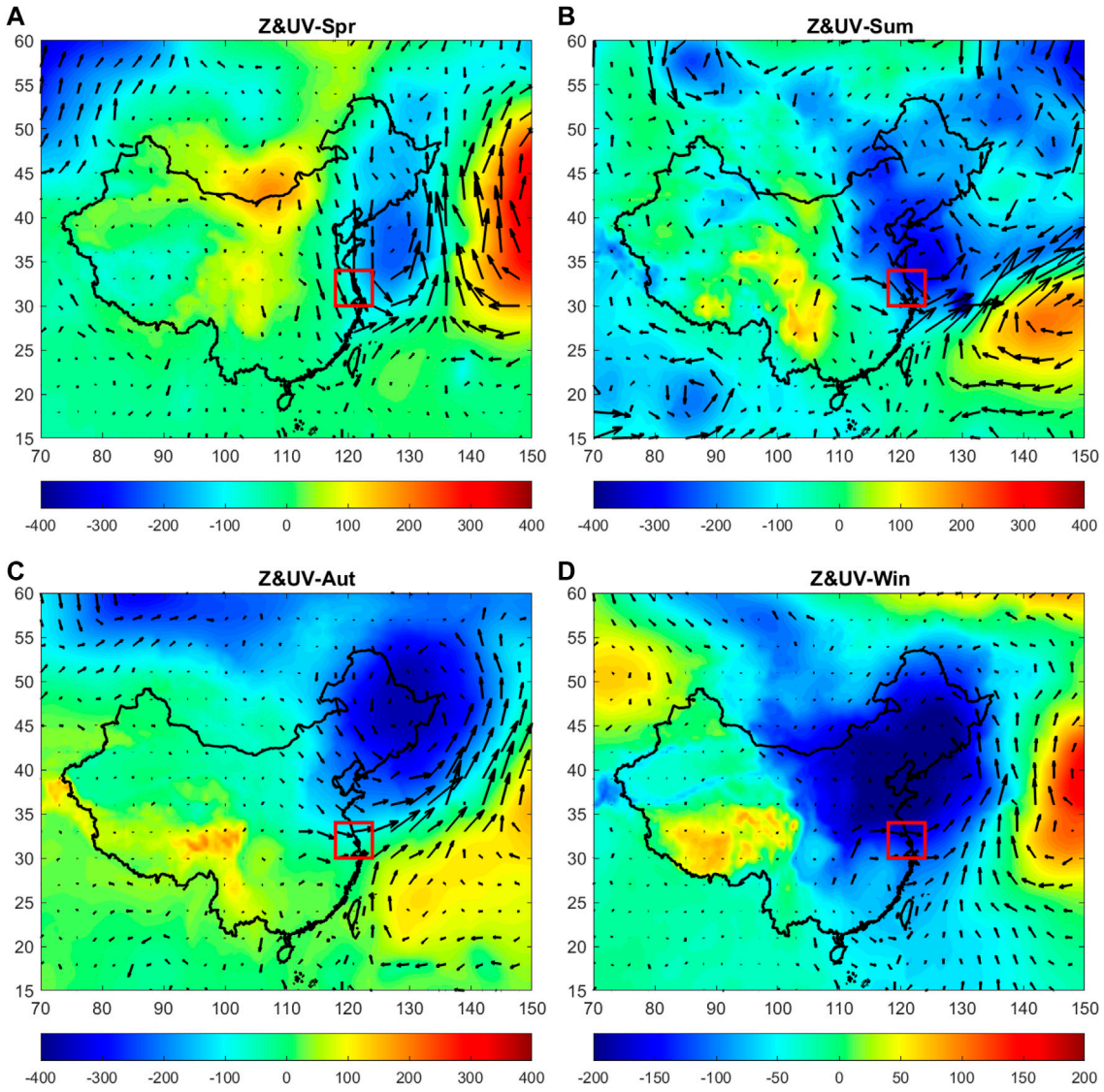

FIGURE 4
Seasonal anomaly of atmospheric circulation at 925 hPa for the Type-one seesaw events. The shading indicates the anomaly of geopotential height (unit: $m^2 \cdot s^{-2}$). The black arrow is the wind anomaly. The solid red box marks the location of Shanghai. And the results are shown for **(A)** spring, **(B)** summer, **(C)** autumn, **(D)** winter.

Station, Hongkou Station, Xuhui Shanghai Normal University Station, Yangpu Sipiao Station, Jing'an Monitoring Station, Pudong Chuansha Station, Pudong New Area Monitoring Station and Pudong Zhangjiang Station. As the observation system is being developed and gradually improved, the duration of available data varies from station to station. The concentration unit of air quality data provided by the official website of MEE is micrograms per cubic meter ($\mu g \cdot m^{-3}$). Before 31 August 2018, the concentration was under the standard condition (273 K, 1013 hPa). From 1 September 2018 and on, the reference gas concentration was changed to 298 K and 1013 hPa, and the $PM_{2.5}$ concentration was changed to the measured local environmental conditions. Additionally, we removed invalid values and abnormal values from the hourly CNEMC data due to instrument calibration issues.

Meteorological dataset

The hourly dataset of the fifth-generation European Centre for Medium-Range Weather Forecasts (ECMWF ERA5) atmospheric reanalysis dataset with a resolution of 0.25° was

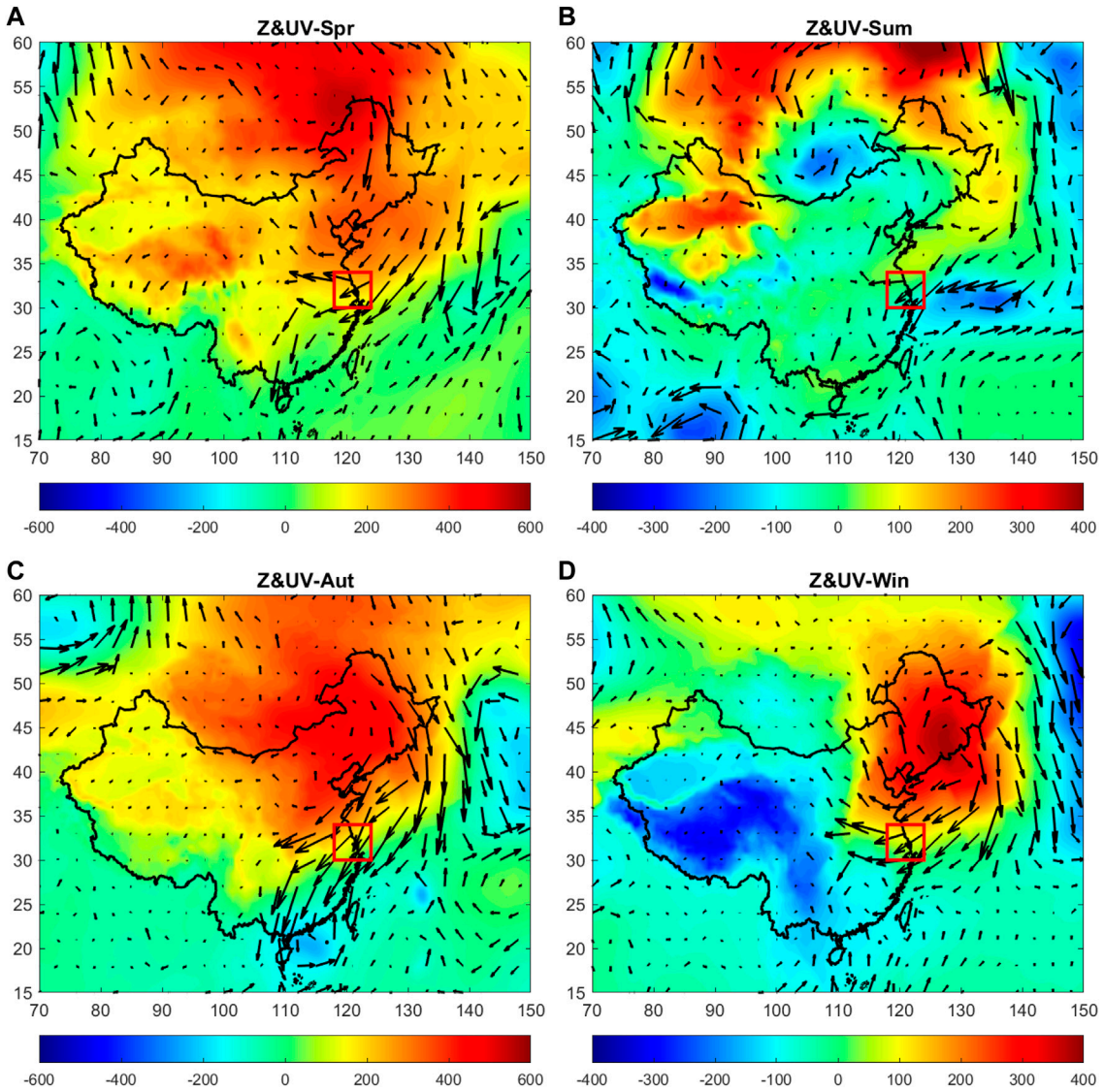

FIGURE 5
The same as in Figure 4 but for the Type-two events. The solid red box marks the location of Shanghai. And the results are shown for **(A)** spring, **(B)** summer, **(C)** autumn, **(D)** winter.

used to describe the meteorological characteristics in this research (https://cds.climate.copernicus.eu/cdsapp#!/dataset/reanalysis-era5-pressure-levels?tab=overview, https://cds.climate.copernicus.eu/cdsapp□!/dataset/reanalysis-era5-single-levels?tab=overview, last access: 18 May 2022). The U and V components of 10 m wind, 2 m air temperature, relative humidity, boundary layer height (BLH), mean surface downward longwave radiation flux (Longwave), mean surface downward shortwave radiation flux (Shortwave), total precipitation, fraction of cloud cover, surface net solar radiation (SSR), and the vertical distribution of vertical velocity, geopotential, and ozone mass mixing ratio are involved in this study. In order to find out the statistical difference between meteorological variable values of five clusters, *t*-test is used to examine significance. The *t*-test is a popular statistical tool used to test differences between the means of two groups, or the difference between one group's mean and a standard value. Running t-tests help us to understand whether the differences are statistically significant (Box, 1987).

Additional information on ozone in ERA5 is that the heterogeneous ozone chemistry is updated and the interaction between ozone and the atmosphere is one-way. Ozone is advected by the atmospheric flow. However, the

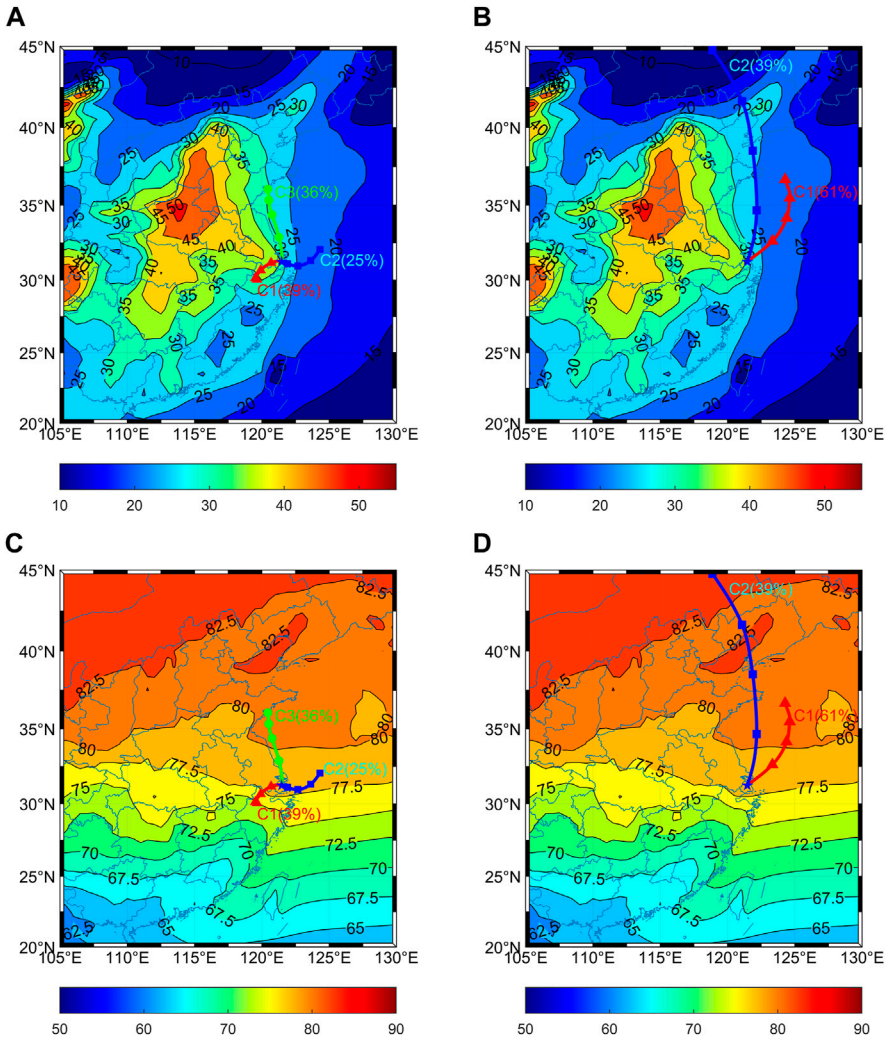

FIGURE 6
Transport pathways of air masses in 5 clusters with **(A,B)** $PM_{2.5}$ mean concentration and **(C,D)** O_3 mean concentration (ppb). The background $PM_{2.5}$ concentration is the annual average from 2014 to 2020, sourced from MERRA-2. The background ozone concentration is the annual average from 2014 to 2020, sourced from ERA5.

ERA5 prognostic ozone has no feedback on the atmosphere *via* the radiation scheme (Hersbach et al., 2020).

Since it has a relatively high temporal and spatial resolution (1 hour averages and 0.5° × 0.625°), we also obtain surface $PM_{2.5}$ concentrations in the Modern-Era Retrospective Analysis for Research and Applications, version 2 (MERRA-2). Using fields from the 2D aer_Nx collection, the concentration of particulate matter can be computed using the following formula:

$PM_{2.5}$ = DUSMASS25 + OCSMASS+ BCSMASS + SSSMASS25 + SO4SMASS* (132.14/96.06)Because the species tracer in MERRA-2 is the sulfate ion, sulfate requires a multiplication factor (https://gmao.gsfc.nasa.gov/reanalysis/MERRA-2/FAQ/). In addition to the lack of nitrate aerosols in MERRA-2, the bias in MERRA-2 mainly comes from the uncertainties of the emission inventory and meteorological simulation in GOES-5(Geostationary Operational Environmental Satellite-5) models (Buchard et al., 2016; He et al., 2019).

Definition of seesaw events of $PM_{2.5}$ and O_3

As shown in Figure 2, the $PM_{2.5}$ concentration and O_3 concentration in SH have obvious seasonal and diurnal seesaw variation characteristics. Figure 2 shows the climatology of

TABLE 1 Absolute anomalies and relative anomalies of $PM_{2.5}$, O_3 and NO_2 concentrations in each backward trajectory cluster of the two seesaw events in Shanghai. Units: μg/m^3. The anomalies are with respect to their average value of every hour in every month.

Pollutants	Cluster1	Cluster2	Cluster3
Type-one			
$PM_{2.5}$	+49.84	+40.45	+45.22
O_3	−33.19	−39.49	−33.63
NO_2	+41.06	+30.61	+22.77
Type-two			
$PM_{2.5}$	−33.88	−40.34	
O_3	+25.77	+22.65	
NO_2	−22.83	−33.87	

TABLE 2 Relative anomaly percent changes in $PM_{2.5}$, O_3 and NO_2 concentrations in each backward trajectory cluster of the two seesaw events in Shanghai. Units: %. The relative anomalies are with respect to the average value of every hour in every month.

Pollutants	Cluster1	Cluster2	Cluster3
Type-one			
$PM_{2.5}$	+107.54%	+95.92%	+105.65%
O_3	−58.45%	−54.70%	−54.56%
NO_2	+82.88%	+71.88%	+51.81%
Type-two			
$PM_{2.5}$	−67.97%	−71.09%	
O_3	+53.18%	+64.25%	
NO_2	−46.61%	−57.64%	

diurnal and seasonal variations in $PM_{2.5}$ and O_3 concentrations. It shows higher $PM_{2.5}$ concentrations during the morning rush hour and lower concentrations in the afternoon; while O_3 shows lower concentrations at 7–8 a.m. and higher concentrations at 2–3 p.m. In terms of seasonal variation, the $PM_{2.5}$ concentration in winter is the highest, but winter is the cleanest season for O_3 pollution in SH. The chemical and physical mechanisms of the diurnal and seasonal seesaw pattern between $PM_{2.5}$ and O_3 in Figure 2 have been revealed in previous studies from the perspective of the variation in emission and meteorological factors. In short, ozone has a strong correlation with high temperatures, so it peaks at midday and during mid-spring to early summer in SH (Gu et al., 2020a; Chang et al., 2021). The reason that ozone concentration of Shanghai in spring is higher than summer is the photochemical reaction of ozone affected by plum-rain in summer (Gao et al., 2017). Deep and persistent cloud cover impedes solar radiation to reach the surface of the Earth, affecting the photochemical generation of ozone Affected by human activities, household heating in winter and vehicle emissions in the morning and evening are able to increase $PM_{2.5}$ (Xiao et al., 2015; Zhang and Cao, 2015). Outbreaks of haze generally occur during the winter as a result of temperature inversions. During an inversion warm air settles above a layer of cool air near the surface. The lid-like warm air traps pollutants near the surface. Lower PM in afternoon can be explained by the enhanced emission for heating and relatively low the boundary layer (Zhang and Cao, 2015).However, there are still some seesaw events of $PM_{2.5}$ and O_3 under the background of diurnal and seesaw patterns shown in Figure 2, the mechanisms of which are still unclear. This study will focus on the meteorological causes of these seesaw events.

To eliminate the influence of seasonal variation, diurnal variation and interannual variation, the original data are classified according to different years, months and hours, and the mean, first quartile and third quartile are calculated. The original data of $PM_{2.5}$ and O_3 are compared with the corresponding quartile. If the hourly concentration of $PM_{2.5}$ is greater than the corresponding third quartile, and O_3 is less than the corresponding first quartile, we call it High-PM-Low-O_3 seesaw hour (Type-one for short). Similarly, if the hourly concentration of O_3 is greater than the corresponding third quartile, and $PM_{2.5}$ is less than the corresponding first quartile, it is defined as Low-PM-High-O_3 hour (Type-two). The quartiles are not fixed, but change with the specific year, month and hour. The above three influencing factors, together with the original data of pollutant concentration, any change in four variables will affect the quartiles. That is, the relatively high/low air pollutant concentrations are used to define the seesaw cases instead of their absolute values. To ensure the spatial and temporal continuity of the two types of cases, a seesaw event was defined as at least 12 consecutive seesaw hours occurring at more than half of the available observation stations in Shanghai.

HYSPLIT model and clustering analysis

Backward trajectory analysis essentially follows a parcel of air backward in hourly time steps for a specified length of time. The Hybrid–Single Particle Lagrangian Integrated Trajectory (HYSPLIT) model (Draxler et al., 2009) developed by the National Oceanic and Atmospheric Administration (NOAA) was used in this study to identify potential source regions of $PM_{2.5}$ or O_3 for a specific city of SH and capture the horizontal movement of the air masses from the source region. The model uses internal terrain following sigma coordinates and meteorological element fields are interpolated linearly to the corresponding coordinates.

To show the origins of air masses arriving at SH, 48-hour backward trajectories were computed every 6 h (at 00:00, 06:00, 12:00, and 18:00 UT) for the years 2014–2020 for 100 m above ground over SH using the HYSPLIT- 4 model (Draxler et al., 2009.). Meteorological archive data used for the HYSPLIT model are from NCEP (National Centers for Environmental Prediction), at a horizontal resolution of 2.5° (latitude) × 2.5° (longitude).

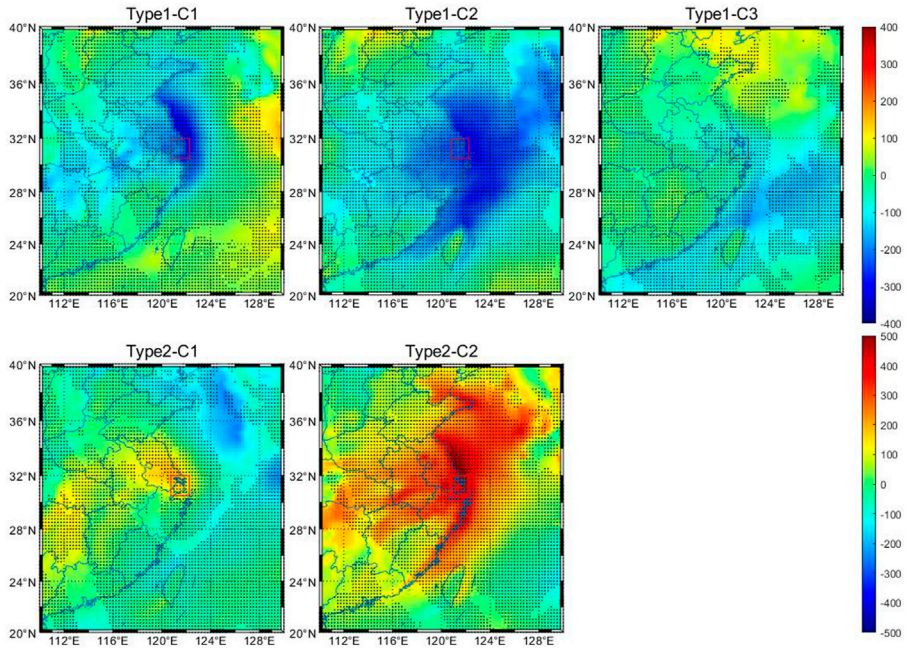

FIGURE 7
Anomalies of boundary layer height in 5 clusters. The solid blue line in the background indicates the provincial boundaries of China. Different subtitles represent different clusters. The black dots indicate that the grids are above the 99% confidence level ($p < 0.01$). The solid red box marks the location of Shanghai. Unit: m.

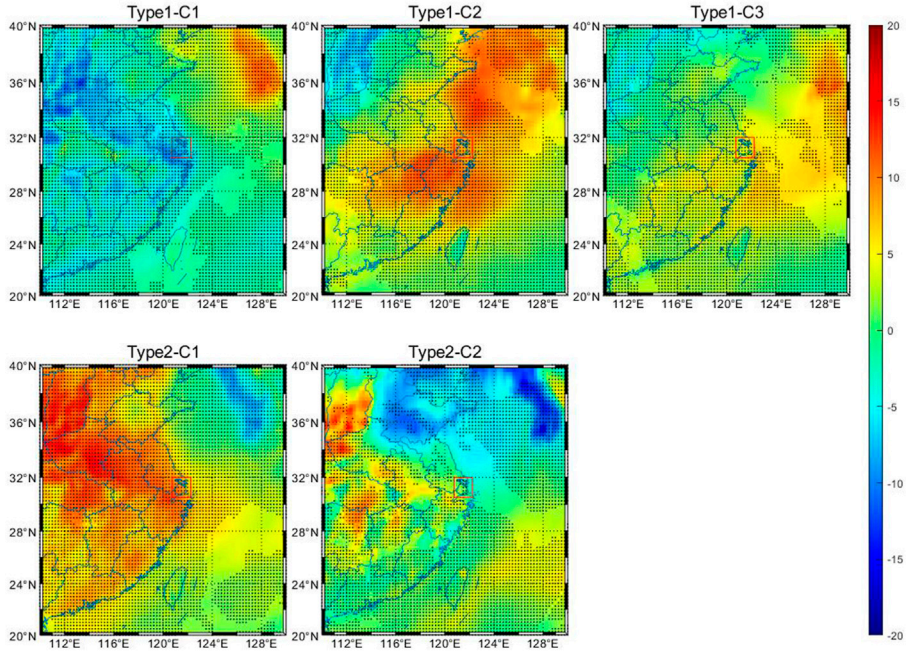

FIGURE 8
Anomalies of relative humidity in 5 clusters. The solid blue line in the background indicates the provincial boundaries of China. Different subtitles represent different clusters. The black dots indicate that the grids are above the 99% confidence level ($p < 0.01$). The solid red box marks the location of Shanghai. Unit: %.

TABLE 3 Meteorological factor percent changes in 5 clusters. The bold font indicates an important influencing factor. Units: % Data source: ERA5-1000 hPa & Surface. The relative anomalies are with respect to the average value of every hour in every month. Bold fonts indicate the main factors influencing the specific seesaw cluster.

Variable	Cluster1	Cluster2	Cluster3
Type-one			
Temperature	−3.27%	+11.18%	−0.27%
BLH	**−53.58%**	**−48.13%**	−20.53%
Shortwave	+2.91%	**−20.96%**	**−9.67%**
Longwave	−3.15%	+6.75%	+0.95%
SSR	+1.78%	−15.70%	−6.48%
Precipitation	−32.76%	**+32.25%**	−33.55%
Windspeed	−28.29%	**−39.11%**	−17.99%
Cloud Cover	+2.62%	**+24.92%**	+8.69%
Relative Humidity	−9.89%	**+12.78%**	**+5.80%**
Type-two			
Temperature	**+21.75%**	−22.80%	
BLH	+45.63%	**+100.02%**	
Shortwave	−18.87%	**+6.27%**	
Longwave	+7.08%	+0.84%	
SSR	−13.94%	+3.90%	
Precipitation	**+136.85%**	−40.58%	
Windspeed	**+38.35%**	**+38.88%**	
Cloud Cover	+37.10%	**−51.40%**	
Relative Humidity	+13.22%	+1.60%	

TrajStat software is used to classify the backward trajectories arriving at SH to better determine the transportation of $PM_{2.5}$ and O_3. The trajectories were assigned to distinct clusters according to their moving speed and direction using Ward's hierarchical method based on the Euclidean distance between all pairs of trajectories (Sirois and Bottenheim, 1995). Major transport pathways leading to elevated or dropped $PM_{2.5}$ concentrations and ozone concentrations were identified by combining trajectories with the corresponding mean concentrations of the pollutant.

Results

Occurrence frequency of the seesaw events

Figure 3A shows the seasonal distribution of the two types of $PM_{2.5}$ and O_3 seesaw events during the 2013–2020 period. Obviously, the frequency of Type-one seesaw events is higher than Type-two in total. There were 144 cases in Type-one and 64 cases in Type-two. In terms of seasons, most of the two types of seesaw events occur in winter. Both seesaw events show the lowest frequency in summer, which is approximately 22.73% and 10% of that in winter for Type-one and Type-two, respectively.

Considering the wet deposition, the physical mechanisms of the seesaw events are supposed to be different from those on dry days. We reclassified the seesaw events with the occurrence of precipitation in Figure 3B. In summer, more than half of the seesaw events occurred on rainy days, which is different from other seasons. The sample size is 5 for both dry and rainy Type-one events in summer, but all the Type-two events occur on rainy days. The positive correlation between PM2.5 and O3 in summer results in the lowest event frequency occurring in summer. High O3 concentrations in a strong oxidative air condition promoted the formation of secondary particles in summer. During plum-rain in summer, under most circumstances PM2.5 concentrations and O3 concentrations decrease at the same time due to precipitation (Jia et al., 2017; Zhu et al., 2019). The interannual variation in the seesaw event frequency is shown in Figure 3C.

Atmospheric circulation anomalies of the seesaw events

The roles of meteorology on pollutants are complex and varying. To further explore the meteorological causes behind the seesaw incidents, we calculated the anomalies of meteorological variables under the seesaw events in different seasons, including geopotential height (Z) and U/V components at 925 hPa, 850 hPa and 500 hPa. Figure 4 indicates the seasonal average of Z&UV anomalies at 925 hPa for Type-one seesaw events (i.e., high $PM_{2.5}$ with low O_3 concentrations). It shows almost the same atmospheric circulation pattern in the four seasons, with a cyclonic anomaly over North China and the Northeast China region, which brings northwest or west winds to SH. For the case of Type-two seesaw events in Figure 5 (i.e., high O_3 with low $PM_{2.5}$ concentrations), the circulation anomalies are also the same in spring, autumn and winter. SH is located at the edge of the west positive and east negative pressure, and the prevailing wind of SH comes from the northeast. In terms of the summertime, the sample size of Type-two is small, which leads to the vague distribution of its circulation anomaly pattern. The atmospheric circulation anomalies at 850 hPa and 500 hPa also show the same pattern for each type of seesaw event (figures not shown here). According to Figures 4, 5, there is almost no difference in the seasonal circulation anomalies, therefore, we investigate the mechanisms of seesaw events without considering their seasonal difference hereafter.

Regional transport contributes to the seesaw events

Although it shows a consistent seasonal circulation anomaly distribution for each type of seesaw events in Figures 4, 5, it

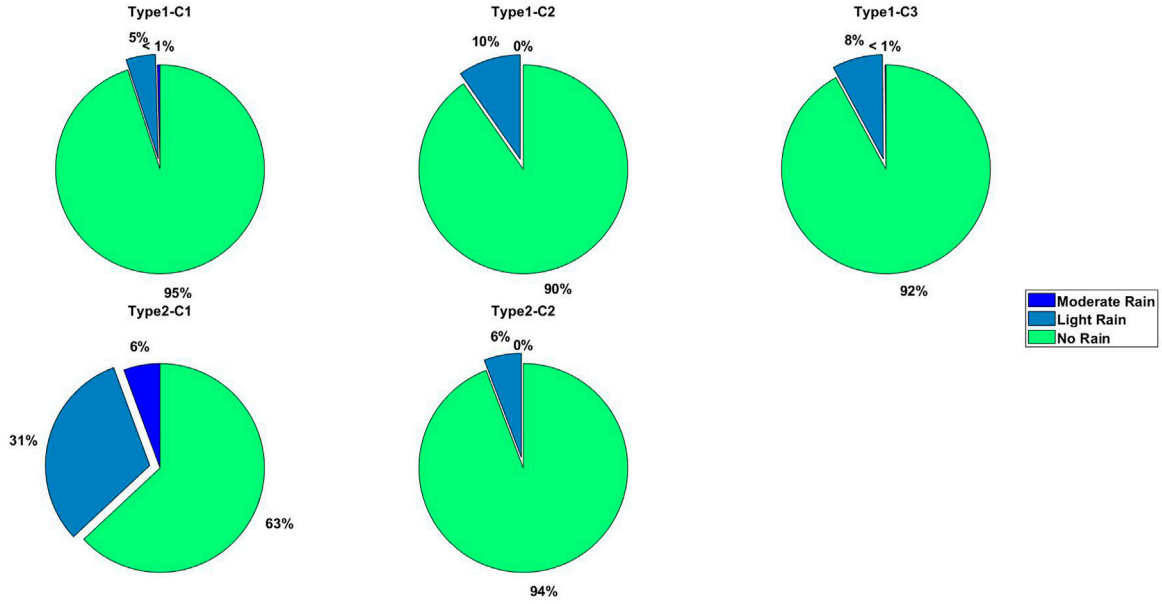

FIGURE 9
Precipitation intensities in 5 clusters of Shanghai seesaw events. No rain: the rate of fall varying between a trace and 0.5 mm per hour. Light rain: the rate of fall varying between 0.5 mm and 2.5 mm per hour. Mild rain: the rate of fall varying between 2.5 mm and 7.6 mm per hour (American Meteorological Society).

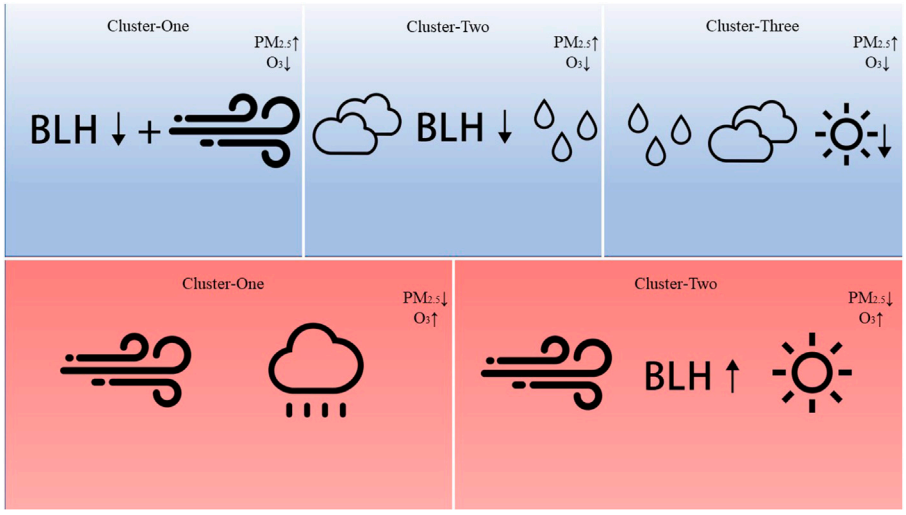

FIGURE 10
Diagram of the impacts of meteorology on both the O_3 and $PM_{2.5}$ concentrations in Shanghai during seesaw events.

indicates an average pattern of atmospheric circulation. To reveal the mechanism of the specific seesaw event, the 48 h backward trajectory of each seesaw events is calculated and clustered, which can provide the information on the origins and transport pathways of air masses. As shown in Figure 6, cluster analysis yielded a total of three air-mass clusters for the 144 Type-one seesaw events, and two air-mass clusters for the 64 Type-two events.

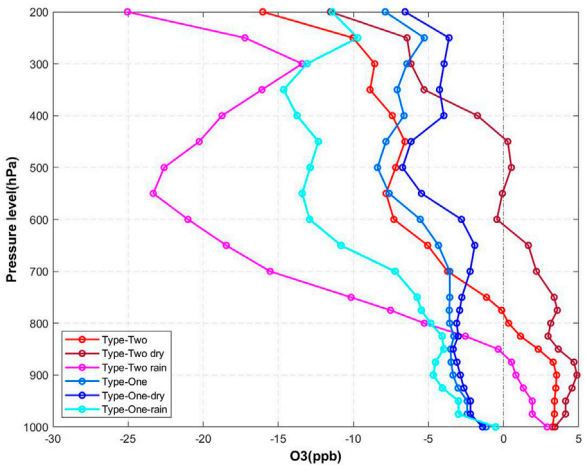

FIGURE 11
Vertical profile of the O_3 mass mixing ratio in Shanghai in autumn. The horizontal axis is the anomalies. Data source: ERA5.

For the case of Type-one events, the three kinds of air masses in SH come from the eastern ocean, north China and southwest of SH. The frequencies of these three kinds of air masses are almost the same. There are 56 samples in C1, 36 samples in C2 and 52 samples in C3. Tables 1, 2 summarize the anomalies of $PM_{2.5}$, O_3 and NO_2 concentrations in each backward trajectory cluster. For Type-one seesaw events, the magnitudes of $PM_{2.5}$ anomalies are higher in cluster-one (C1 for short) (+107%) and cluster-three (C3) (+105%) than cluster-two (+95%), which may be due to the higher $PM_{2.5}$ background concentrations transported from the north and southwest upwind regions of SH (as shown in Figure 6). Moreover, the NO_2 concentration increased by 83% and 52% in C1 and C3 in the Type-one events, respectively, which can also imply the regional transportation of aerosols and precursors.

In terms of Type-two seesaw events, the air mass in SH mainly comes from the nearby east sea surface (61% of events, 39 samples) with minor influence from the remote northeast China (39% of events, 25 samples) Compared to the average pollutant concentrations, the $PM_{2.5}$ concentrations of the two types of clusters decreased by 67.97% and 71.07%, respectively. Correspondingly, the ozone concentration increased by 53.18% and 64.25%, respectively. Based on the climatology of O_3 and $PM_{2.5}$ in Figure 6, it shows higher O_3 concentrations and lower $PM_{2.5}$ contents in the east sea surface. The easterly wind brings O_3-rich and low $PM_{2.5}$ air masses to SH, and leads to high O_3 and low $PM_{2.5}$ pollution for the two clusters of Type-two events. Several studies have found that ozone tends to be continuously produced in the downwind regions of major cities (Kleinman et al., 2003; Tie et al., 2009, 2013). O_3 formation usually occurs under strong VOC-limited conditions in coastal megacities, which inhibits O_3 chemical production. In the downwind region, O_3 formation shifts to NOx-limited conditions gradually on the contrary to the sea surface, which results in pronounced O_3 production (Kley, 1997). O_3 precursors emitted from a coastal city are advected to the ocean by land breezes and produce O_3 over the ocean, the O_3-rich air mass can be advected back to the city by sea breezes.

Meteorological cause for the seesaw events

The meteorological influence on the pollutant varied by region and could be comparable to or even more significant than the impact of changes in anthropogenic emissions (Liu and Wang, 2020b). The relative anomalies of air temperature, BLH, shortwave, longwave, SSR, precipitation, 10 m wind, cloud cover and relative humidity are involved to reveal the meteorological effects on seesaw events. Figures 7, 8 show the spatial distribution of BLH and RH relative anomalies in the five clusters. Table 3 summarizes the regional mean relative anomalies of the above nine meteorological factors of SH in the five clusters. For the case of C1 in Type-one events, it shows lower than normal BLH around SH and the East Ocean, with a significant negative BLH relative anomaly of 199.41 m (-54%). The BLH indicates the vertical diffusion ability of the local atmosphere, which has been demonstrated to have a negative relationship with ambient $PM_{2.5}$ concentrations (Wang and Wang, 2014; Wang and Wang, 2016). The lower $PM_{2.5}$ in C1 of Type-one events can be attributed to the repression of vertical diffusion to some extent. Considering that the wind speed drops by 0.93 m/s (−28%), stable and stagnant circulation may also increase the concentration of pollutants.

For C2 in Type-one, the height of the boundary layer decrease by 48.13% and the relative humidity increased by 12.78%, which is the most significant among the three clusters (Figure 8). Figure 9 shows the occurrence frequency of precipitation during the five clusters. Due to the positive precipitation anomaly (Table 3) and easterly backward trajectory (Figure 6), there is a positive relative humidity anomaly in C2 of Type-one events, which is beneficial for the hygroscopic growth of aerosols and leads to an increase in $PM_{2.5}$ concentration (Wang et al., 2019b; Won et al., 2021). The scavenging process and physical removal mechanism of PM are determined by different precipitation intensities (Andronache, 2003; Chate et al., 2003; Wang et al., 2010). According to the definition of the American Meteorological Society, precipitation can be classified as light rain, mild rain and heavy rain (American Meteorological Society American Meteorological Society, 2022). Using this definition, Figure 9 shows the distribution of no rain, light rain and mild rain under the five clusters. The precipitation in C2 is primarily light rain, and the deposition ability is weak compared to moistening the air mass. The stable air mass also contributes to the accumulation of

surface air pollutants. In addition, based on the regional mean meteorological factor anomalies in Table 3, the significant increase in cloud cover (+25%) and decrease in shortwave radiation (−21%) on the rainy days also caused the weakening of ozone photochemical production, which led to the decrease in surface ozone concentration in Shanghai.

For C3 in Type-one, the magnitudes of the regional mean meteorological anomalies are not as obvious as those in C1 and C2. However, the obvious increase in relative humidity (+5.8%) and decrease in solar radiation (−9.7%) can be considered a beneficial meteorological background for the increase of $PM_{2.5}$ and decrease of O_3, respectively. Notably, the C3 air mass comes from the North China Plain where the concentration of fine particles is generally high (Figure 6). This may indicate that the high concentration of $PM_{2.5}$ in C3 is related to transport. In brief, it is the comprehensive influence of transport, shortwave radiation and relative humidity resulting in C3 (Figure 10).

As described in the previous section, regional transport is undoubtedly the main influencing factor of the Type-two seesaw events. The trajectory in Figure 6 also shows that the air masses originate from areas with higher ozone and lower PM concentrations. Apart from that, other meteorological factors also make sense. In C1 of Type-two, the simple size of the dry-day case is small, and only the rainy cases are involved. Apparently, it shows a obvious positive anomaly of precipitation (Table 3) and relative humidity (Figure 8). Compared with the case of C2 in Type-one, the frequency of moderate rain in C1 of Type-two is much higher. The effects of wet deposition are more pronounced than the hygroscopic growth of aerosols in a humid environment, which results in a decrease in $PM_{2.5}$ (Jacob and Winner, 2009).

In C2 of Type-two events, a 51% decrease in cloud cover along with a 6.27% increase in shortwave radiation contributes to the photochemical formation of ozone. Moreover, the increase in solar radiation prompts the development of boundary layer, which results in the positive BLH anomaly by 403.28 m (+100%) and the improvement in atmospheric vertical diffusion conditions. The surface wind speed, which is regularly considered the metric of horizontal diffusion ability, increases by 39% in C2 of Type-two events. The significant improvement of vertical and horizontal diffusion conditions led to a decrease in the $PM_{2.5}$ concentration (Wang et al., 2016, Wang et al., 2018; Wang and Zhang, 2020).

Conclusions and discussion

This study explored the impact of meteorological factors on the seesaw concentration pattern between $PM_{2.5}$ and O_3 in Shanghai from 2014 to 2020. On the basis of the variation in $PM_{2.5}$ and O_3 concentrations, we divided the seesaw events into two types, Type-one (High-PM-Low-O_3) and Type-two (Low-PM- High-O_3). The trajectories of the seesaw events were assigned to distinct clusters according to their moving speed and direction using the HYSPLIT model. The specific number of clusters is given as follows: three clusters in Type-one and two clusters in Type-two.

In Type-one seesaw events, the boundary layer height in three clusters obviously decreased, C1 (−53.58%) and C2 (−48.13%). Obviously, worse diffusion conditions lead to an increase in the $PM_{2.5}$ concentration. The $PM_{2.5}$ concentration in C1 upwind direction is higher than that in SH, while the ozone concentration is lower. The transport of C1 upwind also contributes. In C2, the relative humidity increased by 12.78% which contributed to the hygroscopic growth of $PM_{2.5}$ and a decrease in O_3 production. Less SSR (−20.96%) and higher cloud cover (+24.92%) in C2 were not conducive to the formation of ozone photochemical reactions. The same conditions were found in C3, but it was less obvious than C2, +8.69% for cloud cover and −9.67% for SSR. Thus, transportation and increased relative humidity were also factors that cannot be ignored in C3.

The cause of another seesaw event is not as complicated as that of Type-one events. Figure 6 and Tables 1, 3 show that the moist oceanic air mass with rich O_3 from the northeast sea enters Shanghai and reduces the concentration of $PM_{2.5}$ at the same time in two clusters of Type-two events. Transport is undoubtedly the main influencing factor in both clusters of Type-two events. Adequate precipitation also contributes to the wet removal of fine particles in C1. A doubled BLH (+100.02%) was beneficial to the diffusion of $PM_{2.5}$ in C2. A 6.27% increase in SSR contributed to the photochemical production of O_3 under clear sky conditions.

Except for the production of ozone from photochemical reactions occurring within the troposphere, the presence of ozone in the troposphere is understood to arise from another basic process. Tropospheric-stratospheric exchange can cause the transport of stratospheric air, rich in ozone, into the troposphere (Langford, 1999). Ni et al. suggested that stratospheric ozone intrusion acts as an additional source of the near-surface tropospheric ozone concentration, which deteriorates O_3 pollution in China (Ni et al., 2019).

Therefore, we also made a vertical profile of the ozone mass mixing ratio in autumn (Figure 11). The scavenging process of precipitation can be clearly seen in this figure. Note that when the seesaw events occurred, the near-surface ozone concentration increased, but the ozone concentration in the upper levels decreased. During the precipitation, strong convective weather with obvious downward flow may have affected stratospheric-tropospheric exchange of air masses and ozone concentrations. Therefore, it is also suspected that the near-surface tropospheric ozone concentration is closely related to transport from the upper layer or stratosphere. However, there are currently no further data supporting this hypothesis. Besides autumn, the transport of ozone in the upper and lower layers is not obvious in other seasons.

Data availability statement

The original contributions presented in the study are included in the article/Supplementary Material, further inquiries can be directed to the corresponding author.

Author contributions

XW and YS designed the research. YS performed the analyses and wrote the paper. Both authors contributed to the final version of the paper.

Funding

This research has been supported by the National Natural Science Foundation of China (Grant Nos. 42075058, 41790470 and 41805117) and Shanghai International Science and Technology Partnership Project (No. 21230780200).

Acknowledgments

Daily pollutant concentration observations in Shanghai were obtained from the website of the Ministry of Ecology and Environment of the People's Republic of China (http://106.37.208.233:20035; MEEPRC, 2022). The 4-hourly ECMWF ERA5 dataset from 2014 to 2020 was downloaded from https://www.ecmwf.int/en/forecasts/datasets/reanalysis-datasets/era5 (ECMWF, 2022). Backward trajectory analysis was conducted using Hybrid–Single Particle Lagrangian Integrated Trajectory (HYSPLIT), which can be downloaded at https://www.ready.noaa.gov/HYSPLIT.php.

Conflict of interest

The authors declare that the research was conducted in the absence of any commercial or financial relationships that could be construed as a potential conflict of interest.

Publisher's note

All claims expressed in this article are solely those of the authors and do not necessarily represent those of their affiliated organizations, or those of the publisher, the editors and the reviewers. Any product that may be evaluated in this article, or claim that may be made by its manufacturer, is not guaranteed or endorsed by the publisher.

References

American Meteorological Society American Meteorological Society (2022). Rain".Glossary of meteorology. Available at: https://glossary.ametsoc.org/wiki/Rain (Accessed July 16, 2022).

Andronache, C. (2003). Estimated variability of below-cloud aerosol removal by rainfall for observed aerosol size distributions. *Atmos. Chem. Phys.* 13, 131–143. doi:10.5194/acp-3-131-2003

Bond, T. C., Doherty, S. J., Fahey, D. W., Forster, P. M., Berntsen, T., DeAngelo, B. J., et al. (2013). Bounding the role of black carbon in the climate system: A scientific assessment. *J. Geophys. Res. Atmos.* 118, 5380–5552. doi:10.1002/jgrd.50171

Box, J. F. (1987). Guinness, gosset, Fisher, and small samples. *Stat. Sci.* 2, 13437. doi:10.1214/ss/1177013437

Buchard, V., da Silva, A. M., Randles, C. A., Colarco, P., Ferrare, R., Hair, J., et al. (2016). Evaluation of the surface PM2.5 in version 1 of the NASA MERRA aerosol reanalysis over the United States. *Atmos. Environ. X.* 125, 100–111. doi:10.1016/j.atmosenv.2015.11.004

Camalier, L., Cox, W., and Dolwick, P. (2007). The effects of meteorology on ozone in urban areas and their use in assessing ozone trends. *Atmos. Environ. X.* 41, 7127–7137. doi:10.1016/j.atmosenv.2007.04.061

Carrillo-Torres, E., Hernández-Paniagua, I., and Mendoza, A. (2017). Use of combined observational- and model-derived photochemical indicators to assess the O3-NOx-VOC system sensitivity in urban areas. *Atmosphere* 8, 22. doi:10.3390/atmos8020022

Chang, L., He, F., Tie, X., Xu, J., and Gao, W. (2021). Meteorology driving the highest ozone level occurred during mid-spring to early summer in Shanghai, China. *Sci. Total Environ.* 785, 147253. doi:10.1016/j.scitotenv.2021.147253

Charlson, R. J., Schwartz, S. E., Hales, J. M., Cess, R. D., Coakley, J. A., Hansen, J. E., et al. (1992). Climate forcing by anthropogenic aerosols. *Science* 255, 423–430. doi:10.1126/science.255.5043.423

Chate, D. M., Rao, P. S. P., Naik, M. S., Momin, G. A., Safai, P. D., and Ali, K. (2003). Scavenging of aerosols and their chemical species by rain. *Atmos. Environ. X.* 37, 2477–2484. doi:10.1016/S1352-2310(03)00162-6

Chen, L., Zhu, J., Liao, H., Yang, Y., and Yue, X. (2020). Meteorological influences on PM2.5 and O3 trends and associated health burden since China's clean air actions. *Sci. Total Environ.* 744, 140837. doi:10.1016/j.scitotenv.2020.140837

Cox, W. M., and Chu, S.-H. (1996). Assessment of interannual ozone variation in urban areas from a climatological perspective. *Atmos. Environ. X.* 30, 2615–2625. doi:10.1016/1352-2310(95)00346-0

Dang, R., and Liao, H. (2019). Radiative forcing and health impact of aerosols and ozone in China as the consequence of clean air actions over 2012–2017. *Geophys. Res. Lett.* 46, 12511–12519. doi:10.1029/2019GL084605

Dawson, J. P., Adams, P. J., and Pandis, S. N. (2007). Sensitivity of PM2.5 to climate in the eastern US: A modeling case study. *Atmos. Chem. Phys.* 15, 4295–4309. doi:10.5194/acp-7-4295-2007

Deng, X., Zhou, X., Tie, X., Wu, D., Li, F., Tan, H., et al. (2012). Attenuation of ultraviolet radiation reaching the surface due to atmospheric aerosols in Guangzhou. *Chin. Sci. Bull.* 57, 2759–2766. doi:10.1007/s11434-012-5172-5

Draxler, R., Stunder, B., Rolph, G., Stein, A., Taylor, A., Zinn, S., et al. (2009). *HYSPLIT User's Guide*, 315. https://www.ready.noaa.gov/hysplitusersguide/S000.htm.

Finlayson-Pitts, B. J., and Pitts, J. (1986). Atmospheric chemistry. Fundamentals and experimental techniques. Available at: https://www.osti.gov/biblio/6379212 (Accessed June 20, 2022).

Gao, W., Tie, X., Xu, J., Huang, R., Mao, X., Zhou, G., et al. (2017). Long-term trend of O3 in a mega City (Shanghai), China: Characteristics, causes, and interactions with precursors. *Sci. Total Environ.* 9, 425–433. doi:10.1016/j.scitotenv.2017.06.099

Gillani, N. V., and Pleim, J. E. (1996). Sub-grid-scale features of anthropogenic emissions of NOx and VOC in the context of regional eulerian models. *Atmos. Environ. X.* 30, 2043–2059. doi:10.1016/1352-2310(95)00201-4

Gu, Y., Li, K., Xu, J., Liao, H., and Zhou, G. (2020a). Observed dependence of surface ozone on increasing temperature in Shanghai, China. *Atmos. Environ. X.* 221, 117108. doi:10.1016/j.atmosenv.2019.117108

Gu, Y., Yan, F., Xu, J., Qu, Y., Gao, W., He, F., et al. (2020b). A measurement and model study on ozone characteristics in marine air at a remote island station and its interaction with urban ozone air quality in Shanghai, China. *Atmos. Chem. Phys.* 20, 14361–14375. doi:10.5194/acp-20-14361-2020

Guenther, A., Karl, T., Harley, P., Wiedinmyer, C., Palmer, P. I., and Geron, C. (2006). Estimates of global terrestrial isoprene emissions using MEGAN (model of emissions of gases and aerosols from nature). *Atmos. Chem. Phys.* 30, 3181–3210. doi:10.5194/acp-6-3181-2006

He, J., Gong, S., Yu, Y., Yu, L., Wu, L., Mao, H., et al. (2017). Air pollution characteristics and their relation to meteorological conditions during 2014–2015 in major Chinese cities. *Environ. Pollut.* 223, 484–496. doi:10.1016/j.envpol.2017.01.050

He, L., Lin, A., Chen, X., Zhou, H., Zhou, Z., and He, P. (2019). Assessment of MERRA-2 surface PM2.5 over the Yangtze River basin: Ground-based verification, spatiotemporal distribution and meteorological dependence. *Remote Sens. (Basel).* 11, 460. doi:10.3390/rs11040460

He, S., and Carmichael, G. R. (1999). Sensitivity of photolysis rates and ozone production in the troposphere to aerosol properties. *J. Geophys. Res.* 104, 26307–26324. doi:10.1029/1999JD900789

Hersbach, H., Bell, B., Berrisford, P., Hirahara, S., Horányi, A., Muñoz-Sabater, J., et al. (2020). The ERA5 global reanalysis. *Q. J. R. Meteorol. Soc.* 146, 1999–2049. doi:10.1002/qj.3803

Hu, J., Wu, L., Zheng, B., Zhang, Q., He, K., Chang, Q., et al. (2015). Source contributions and regional transport of primary particulate matter in China. *Environ. Pollut.* 207, 31–42. doi:10.1016/j.envpol.2015.08.037

Jacob, D. J., and Winner, D. A. (2009). Effect of climate change on air quality. *Atmos. Environ. X.* 43, 51–63. doi:10.1016/j.atmosenv.2008.09.051

Jacobson, M. Z. (1998). Studying the effects of aerosols on vertical photolysis rate coefficient and temperature profiles over an urban airshed. *J. Geophys. Res.* 103, 10593–10604. doi:10.1029/98JD00287

Jia, M., Zhao, T., Cheng, X., Gong, S., Zhang, X., Tang, L., et al. (2017). Inverse relations of PM2.5 and O3 in air compound pollution between cold and hot seasons over an urban area of east China. *Atmosphere* 8, 59. doi:10.3390/atmos8030059

Johnson, C. E., Collins, W. J., Stevenson, D. S., and Derwent, R. G. (1999). Relative roles of climate and emissions changes on future tropospheric oxidant concentrations. *J. Geophys. Res.* 104, 18631–18645. doi:10.1029/1999JD900204

Kleinman, L. I., Daum, P. H., Lee, Y.-N., Nunnermacker, L. J., Springston, S. R., Weinstein-Lloyd, J., et al. (2003). Photochemical age determinations in the phoenix metropolitan area: Photochemical age determinations in phoenix. *J. Geophys. Res.* 108, 2621. doi:10.1029/2002JD002621

Kley, D. (1997). Tropospheric chemistry and transport. *Science* 276, 1043–1044. doi:10.1126/science.276.5315.1043

Langford, A. O. (1999). Stratosphere-troposphere exchange at the subtropical jet: Contribution to the tropospheric ozone budget at midlatitudes. *Geophys. Res. Lett.* 26, 2449–2452. doi:10.1029/1999GL900556

Li, G., Bei, N., Tie, X., and Molina, L. T. (2011). Aerosol effects on the photochemistry in Mexico City during MCMA-2006/MILAGRO campaign. *Atmos. Chem. Phys.* 11, 5169–5182. doi:10.5194/acp-11-5169-2011

Li, K., Jacob, D. J., Liao, H., Qiu, Y., Shen, L., Zhai, S., et al. (2021). Ozone pollution in the North China Plain spreading into the late-winter haze season. *Proc. Natl. Acad. Sci. U. S. A.* 118, e2015797118. doi:10.1073/pnas.2015797118

Li, K., Jacob, D. J., Liao, H., Shen, L., Zhang, Q., and Bates, K. H. (2019). Anthropogenic drivers of 2013–2017 trends in summer surface ozone in China. *Proc. Natl. Acad. Sci. U. S. A.* 116, 422–427. doi:10.1073/pnas.1812168116

Li, K., Jacob, D. J., Shen, L., Lu, X., De Smedt, I., and Liao, H. (2020). Increases in surface ozone pollution in China from 2013 to 2019: Anthropogenic and meteorological influences. *Atmos. Chem. Phys.* 20, 11423–11433. doi:10.5194/acp-20-11423-2020

Liu, H., Liu, S., Xue, B., Lv, Z., Meng, Z., Yang, X., et al. (2018). Ground-level ozone pollution and its health impacts in China. *Atmos. Environ. X.* 173, 223–230. doi:10.1016/j.atmosenv.2017.11.014

Liu, Y., and Wang, T. (2020a). Worsening urban ozone pollution in China from 2013 to 2017 – Part 1: The complex and varying roles of meteorology. *Atmos. Chem. Phys.* 20, 6305–6321. doi:10.5194/acp-20-6305-2020

Liu, Y., and Wang, T. (2020b). Worsening urban ozone pollution in China from 2013 to 2017 – Part 2: The effects of emission changes and implications for multi-pollutant control. *Atmos. Chem. Phys.* 20, 6323–6337. doi:10.5194/acp-20-6323-2020

Lu, X., Zhang, L., Chen, Y., Zhou, M., Zheng, B., Li, K., et al. (2019a). Exploring 2016–2017 surface ozone pollution over China: Source contributions and meteorological influences. *Atmos. Chem. Phys.* 19, 8339–8361. doi:10.5194/acp-19-8339-2019

Lu, X., Zhang, L., and Shen, L. (2019b). Meteorology and climate influences on tropospheric ozone: A review of natural sources, chemistry, and transport patterns. *Curr. Pollut. Rep.* 5, 238–260. doi:10.1007/s40726-019-00118-3

Ministry of Ecology and Environment (2013). Ministry of Ecology and Environment: Technical Specifications for Installation and Acceptance of Ambient air Quality Continuous Automated Monitoring System for SO_2, NO_2, O_3 and CO. Available at: http://www.mee.gov.cn/ywgz/fgbz/bz/bzwb/jcffbz/201308/W020130802493970989627.pdf (Accessed July 16, 2022).

Ministry of Ecology and Environment (2022). Technical Specification for Environmental Air Quality Assessment (Trial). Available at: http://www.mee.gov.cn/ywgz/fgbz/bz/bzwb/jcffbz/201309/t20130925_260809.shtml (Accessed July 16, 2022).

Ministry of Ecology and Environment (2012). Ministry of Ecology and environment: Ambient air quality standards. Available at: https://english.mee.gov.cn/Resources/standards/Air_Environment/quality_standard1/201605/t20160511_337502.shtml (Accessed July 16, 2022).

Mu, M., and Zhang, R. (2014). Addressing the issue of fog and haze: A promising perspective from meteorological science and technology. *Sci. China Earth Sci.* 57, 1–2. doi:10.1007/s11430-013-4791-2

Ni, Z.-Z., Luo, K., Gao, X., Gao, Y., Fan, J.-R., Fu, J. S., et al. (2019). Exploring the stratospheric source of ozone pollution over China during the 2016 Group of Twenty summit. *Atmos. Pollut. Res.* 10, 1267–1275. doi:10.1016/j.apr.2019.02.010

Shan, W., Yin, Y., Zhang, J., and Ding, Y. (2008). Observational study of surface ozone at an urban site in East China. *Atmos. Res.* 89, 252–261. doi:10.1016/j.atmosres.2008.02.014

Shao, P., Xin, J., Zhang, X., Gong, C., Ma, Y., Wang, Y., et al. (2022). Aerosol optical properties and their impacts on the co–occurrence of surface ozone and particulate matter in Kunming City, on the Yunnan–Guizhou Plateau of China. *Atmos. Res.* 266, 105963. doi:10.1016/j.atmosres.2021.105963

Sillman, S., Logan, J. A., and Wofsy, S. C. (1990). The sensitivity of ozone to nitrogen oxides and hydrocarbons in regional ozone episodes. *J. Geophys. Res.* 95, 1837. doi:10.1029/JD095iD02p01837

Sillman, S. (1999). The relation between ozone, NOx and hydrocarbons in urban and polluted rural environments. *Atmos. Environ.* 25.

Silver, B., Reddington, C. L., Arnold, S. R., and Spracklen, D. V. (2018). Substantial changes in air pollution across China during 2015–2017. *Environ. Res. Lett.* 13, 114012. doi:10.1088/1748-9326/aae718

Simon, H., Reff, A., Wells, B., Xing, J., and Frank, N. (2015). Ozone trends across the United States over a period of decreasing NOx and VOC emissions. *Environ. Sci. Technol.* 49, 186–195. doi:10.1021/es504514z

Sirois, A., and Bottenheim, J. W. (1995). Use of backward trajectories to interpret the 5-year record of PAN and O_3 ambient air concentrations at Kejimkujik National Park, Nova Scotia. *J. Geophys. Res.* 100, 2867. doi:10.1029/94JD02951

State Council of the People's Republic of China (2018). State Council of the People's republic of China: Notice of the state Council on printing and distributing the three-year action plan for winning the blue sky defense war. Available at: http://www.gov.cn/zhengce/content/2018-07/03/content_5303158.htm (Accessed July 16, 2022).

Su, T., Li, Z., and Kahn, R. (2018). Relationships between the planetary boundary layer height and surface pollutants derived from lidar observations over China: Regional pattern and influencing factors. *Atmos. Chem. Phys.* 18, 15921–15935. doi:10.5194/acp-18-15921-2018

Tie, X., Geng, F., Guenther, A., Cao, J., Greenberg, J., Zhang, R., et al. (2013). Megacity impacts on regional ozone formation: Observations and WRF-chem modeling for the MIRAGE-shanghai field campaign. *Atmos. Chem. Phys.* 13, 5655–5669. doi:10.5194/acp-13-5655-2013

Tie, X., Madronich, S., Li, G., Ying, Z., Weinheimer, A., Apel, E., et al. (2009). Simulation of Mexico City plumes during the MIRAGE-Mex field campaign using the WRF-Chem model. *Atmos. Chem. Phys.* 18, 4621–4638. doi:10.5194/acp-9-4621-2009

Wang, X., and Wang, K. (2016). Homogenized variability of radiosonde-derived atmospheric boundary layer height over the global land surface from 1973 to 2014. *J. Climate* 29 (19), 6893–6908. doi:10.1175/JCLI-D-15-0766.1

Wang, X., and Wang, K. (2014). Estimation of atmospheric mixing layer height from radiosonde data. *Atmos. Measurement Tech.* 7 (2). doi:10.5194/amt-7-1701-2014

Wang, W., Li, X., Shao, M., Hu, M., Zeng, L., Wu, Y., et al. (2019a). The impact of aerosols on photolysis frequencies and ozone production in Beijing during the 4-year period 2012–2015. *Atmos. Chem. Phys.* 19, 9413–9429. doi:10.5194/acp-19-9413-2019

Wang, X., Dickinson, R. E., Su, L., Zhou, C., and Wang, K. (2018). PM2.5 pollution in China and how it has been exacerbated by terrain and meteorological conditions. *Bull. Am. Meteorol. Soc.* 99, 105–119. doi:10.1175/BAMS-D-16-0301.1

Wang, X., Wang, K., and Su, L. (2016). Contribution of atmospheric diffusion conditions to the recent improvement in air quality in China. *Sci. Rep.* 6, 36404. doi:10.1038/srep36404

Wang, X., Zhang, L., and Moran, M. D. (2010). Uncertainty assessment of current size-resolved parameterizations for below-cloud particle scavenging by rain. *Atmos. Chem. Phys.* 10, 5685–5705. doi:10.5194/acp-10-5685-2010

Wang, X., and Zhang, R. (2020). How did air pollution change during the COVID-19 outbreak in China? *Bull. Am. Meteorol. Soc.* 101, E1645–E1652. doi:10.1175/BAMS-D-20-0102.1

Wang, X., Zhang, R., Tan, Y., and Yu, W. (2021). Dominant synoptic patterns associated with the decay process of $PM_{2.5}$ pollution episodes around Beijing. *Atmos. Chem. Phys.* 21, 2491–2508. doi:10.5194/acp-21-2491-2021

Wang, X., Zhang, R., and Yu, W. (2019b). The effects of $PM_{2.5}$ concentrations and relative humidity on atmospheric visibility in beijing. *J. Geophys. Res. Atmos.* 124, 2235–2259. doi:10.1029/2018JD029269

Won, W.-S., Oh, R., Lee, W., Ku, S., Su, P.-C., and Yoon, Y.-J. (2021). Hygroscopic properties of particulate matter and effects of their interactions with weather on visibility. *Sci. Rep.* 11, 16401. doi:10.1038/s41598-021-95834-6

Wu, X., Xin, J., Zhang, W., Gao, W., Ma, Y., Ma, Y., et al. (2022). Variation characteristics of air combined pollution in Beijing City. *Atmos. Res.* 274, 106197. doi:10.1016/j.atmosres.2022.106197

Xiao, Q., Ma, Z., Li, S., and Liu, Y. (2015). The impact of winter heating on air pollution in China. *PLOS ONE* 10, e0117311. doi:10.1371/journal.pone.0117311

Xu, D., Yap, D., and Taylor, P. A. (1996). Meteorologically adjusted ground level ozone trends in Ontario. *Atmos. Environ. X.* 30, 1117–1124. doi:10.1016/1352-2310(95)00331-2

Yin, Z., Li, Y., and Cao, B. (2020). Seasonal prediction of surface O3-related meteorological conditions in summer in North China. *Atmos. Res.* 246, 105110. doi:10.1016/j.atmosres.2020.105110

Yin, Z., Wang, H., and Chen, H. (2017). Understanding severe winter haze events in the north China plain in 2014: Roles of climate anomalies. *Atmos. Chem. Phys.* 17, 1641–1651. doi:10.5194/acp-17-1641-2017

Yue, X., Unger, N., Harper, K., Xia, X., Liao, H., Zhu, T., et al. (2017). Ozone and haze pollution weakens net primary productivity in China. *Atmos. Chem. Phys.* 17, 6073–6089. doi:10.5194/acp-17-6073-2017

Zhai, S., Jacob, D. J., Wang, X., Shen, L., Li, K., Zhang, Y., et al. (2019). Fine particulate matter ($PM_{2.5}$) trends in China, 2013–2018: Separating contributions from anthropogenic emissions and meteorology. *Atmos. Chem. Phys.* 19, 11031–11041. doi:10.5194/acp-19-11031-2019

Zhang, R., Li, Q., and Zhang, R. (2014). Meteorological conditions for the persistent severe fog and haze event over eastern China in January 2013. *Sci. China Earth Sci.* 57, 26–35. doi:10.1007/s11430-013-4774-3

Zhang, R. (2017). Warming boosts air pollution. *Nat. Clim. Chang.* 7, 238–239. doi:10.1038/nclimate3257

Zhang, Y.-L., and Cao, F. (2015). Fine particulate matter (PM2.5) in China at a city level. *Sci. Rep.* 5, 14884. doi:10.1038/srep14884

Zhong, Q., Tao, S., Ma, J., Liu, J., Shen, H., Shen, G., et al. (2021). PM2.5 reductions in Chinese cities from 2013 to 2019 remain significant despite the inflating effects of meteorological conditions. *One Earth* 4, 448–458. doi:10.1016/j.oneear.2021.02.003

Zhu, B., Kang, H., Zhu, T., Su, J., Hou, X., and Gao, J. (2015). Impact of Shanghai urban land surface forcing on downstream city ozone chemistry: Urban land-surface forcing on ozone. *J. Geophys. Res. Atmos.* 120, 4340–4351. doi:10.1002/2014JD022859

Zhu, J., Chen, L., Liao, H., and Dang, R. (2019). Correlations between PM2.5 and ozone over china and associated underlying reasons. *Atmosphere* 10, 352. doi:10.3390/atmos10070352

frontiers | Frontiers in Environmental Science

TYPE Original Research
PUBLISHED 02 December 2022
DOI 10.3389/fenvs.2022.1055673

OPEN ACCESS

EDITED BY
Longlei Li,
Cornell University, United States

REVIEWED BY
Cenlin He,
National Center for Atmospheric Research (UCAR), United States
Chaoliu Li,
State Key Laboratory of Cryospheric Science (CAS), China

*CORRESPONDENCE
Jinsen Shi,
shijs@lzu.edu.cn

SPECIALTY SECTION
This article was submitted to Atmosphere and Climate, a section of the journal Frontiers in Environmental Science

RECEIVED 28 September 2022
ACCEPTED 21 November 2022
PUBLISHED 02 December 2022

CITATION
Zhang H, Tian P, Kang C, Guo Y, Yu Z, Lu G, Tang C, Du T, Wang J, Zhang Z, Cao X, Liang J and Shi J (2022), Regional organic matter and mineral dust are the main components of atmospheric aerosols over the Nam Co station on the central Tibetan Plateau in summer. *Front. Environ. Sci.* 10:1055673. doi: 10.3389/fenvs.2022.1055673

Regional organic matter and mineral dust are the main components of atmospheric aerosols over the Nam Co station on the central Tibetan Plateau in summer

Haotian Zhang[1], Pengfei Tian[1], Chenliang Kang[1], Yumin Guo[1], Zeren Yu[1], Gefei Lu[1], Chenguang Tang[1], Tao Du[1], Jiayun Wang[1], Zhida Zhang[1], Xianjie Cao[1], Jiening Liang[1] and Jinsen Shi[1,2]*

[1]Key Laboratory for Semi-Arid Climate Change of the Ministry of Education, College of Atmospheric Sciences, Lanzhou University, Lanzhou, China, [2]Collaborative Innovation Center for Western Ecological Safety, Lanzhou University, Lanzhou, China

The transport of air pollutants from areas surrounding the Tibetan Plateau (TP) has recently been studied. However, the major sources of atmospheric total suspended particulate matter (TSP) on the central TP remain unclear due to a lack of *in-situ* observations on aerosol physico-chemical properties. Therefore, to quantitatively investigate the physico-chemical properties and reveal the major sources of atmospheric aerosols, a comprehensive field campaign was conducted at the site of Nam Co from August 6 to September 11, 2020. Aerosol loading was low during the campaign with average TSP mass concentration, scattering coefficient at 550 nm, and absorption coefficient at 670 nm being 10.11 ± 5.36 μg m^{-3}, 1.71 ± 1.36 Mm^{-1}, and 0.26 ± 0.20 Mm^{-1}, respectively. Organic matter (63.9%) and mineral dust (27.8%) accounted for most of the TSP mass concentrations. The average scattering Ångström exponent of 0.59 ± 0.14 reflected the influence of mineral dust, and the elemental fractions and the results of enrichment factor illustrated that crustal materials were the main contributors of mineral dust. The organic to elemental carbon ratio of 15.33 is probably caused by the aging that occurs during the transport of aerosols. The strong correlation between organic carbon and Ca^{2+} and the results of the electron microscopy analysis of single particles indicated that organic carbon and mineral dust had the same sources; however, the weak relation between mineral dust and wind speed indicated that local wind erosion was not the main contributor to the mineral dust. The potential source contribution function further illustrated that the summertime TSP in the central TP was mainly characterized by background biomass and mineral dust aerosols originating regionally from the ground within the TP.

KEYWORDS

atmospheric aerosols, sources, mineral dust, in-situ observation, Tibetan Plateau

Introduction

The Tibetan Plateau (TP), known as the "Third Pole," covers a large area with altitudes of over 4000 km (Kang et al., 2010a; Yao et al., 2012; Bian et al., 2020). It is a region that exerts an important influence on weather, climate, environment, and ecosystems both regionally and globally (Qiu, 2008). Its unique topography (high altitude and lack of oxygen), relatively low population density, and low rate of industrialization make the TP a climate-sensitive region that facilitates studies on the interactions between natural and anthropogenic activities (Lawrence, 2011). Atmospheric aerosols directly and indirectly modulate the energy budget of the Earth-atmosphere system by scattering and absorbing solar radiation (Tian et al., 2018; IPCC, 2021). For example, small amounts of absorbing aerosols in this region may lead to greater warming because the troposphere is thinner over the plateau (Qiu, 2008).

A quantitative estimation of the radiative effects of atmospheric aerosols requires detailed information regarding their optical properties (such as the extinction and absorption coefficients and single scattering albedo), which are related to their size distribution and chemical composition. It is known that the elemental carbon (EC) of carbonaceous aerosols is the second largest contributor to global warming after CO_2 (Ramanathan and Carmichael, 2008), and major water-soluble ions such as sulfate, nitrate, and ammonium have an impact on the hygroscopic quality and acidity of aerosols, which in turn affects aerosol optical properties (Lau et al., 2006; Pathak et al., 2009; Gao et al., 2011). Therefore, it is necessary to conduct field campaigns on atmospheric aerosols in the TP region to better understand their physico-chemical properties, conduct reasonable source analyses, and to accurately estimate their radiative effects.

Sources of atmospheric aerosols over the TP have been studied over the past few decades. Mountains with high altitudes are considered barriers to the transport of air pollutants from the surrounding regions (Wang and French, 1994). However, studies have suggested that transport of aerosols from the surrounding regions to the Tibetan Plateau occurs (Hindman and Upadhyay, 2002; Zheng et al., 2017; Dhungel et al., 2018; Xu J. et al., 2018; Zheng et al., 2020; Zhang L. et al., 2021; Li et al., 2021; Xiang et al., 2021). For example, it is known that during the pre-monsoon season, South Asia and West Asia are the main sources of pollutants from the Himalayas (Gul et al., 2022), and the results from a WRF-Chem model simulation indicated that black carbon (BC) emissions from residential areas in South Asia contributed the most to BC on the TP (Yang et al., 2020). In addition, field observations have shown that approximately 64.2% of the BC in the non-monsoon Qomolangma-Everest region originated in India and Nepal in South Asia (Xiang et al., 2021). However, carbon isotopic composition studies conducted at remote sites on the eastern TP have reflected an important local emissions contribution (Li et al., 2022). Other studies have revealed local emissions from urban vehicles and residential activities (Hu et al., 2017). Secondary aerosol formation has also been suggested to be an important aerosol source in the TP region (Wu et al., 2020).

The physico-chemical properties and composition of atmospheric aerosols have been the key focus of research conducted on plateaus. Previous research has shown that the main components of aerosols over plateaus are dust, BC, and sulfate/nitrate; however, the main composition varies based on location (Tian et al., 2017; Zhao et al., 2020). Field observations are essential to quantitatively study the physico-chemical properties of atmospheric aerosols. Despite the high altitude and harsh environment, attempts have been made to conduct field observations in the Tibetan Plateau. For example, the aerosol mass concentration and chemical species have been quantitatively estimated by collecting offline filter samples from different sites in the Tibetan Plateau region (Decesari et al., 2010; Zhao et al., 2013; Cong et al., 2015; Xu et al., 2015; Shang et al., 2018; Arun et al., 2019), and the concentrations and sources of black carbon in the TP region have been studied (Ming et al., 2010; Li et al., 2016; Li et al., 2017), and the chemical species of submicron aerosols have also been revealed using high-resolution time-of-flight aerosol mass spectrometry at a few sites (Xu et al., 2015; Zheng et al., 2017). Several field observation studies have also been conducted in the Central Highlands region. For example, the column aerosol optical properties were investigated using sun photometer measurements at Nam Co (Cong et al., 2009), and advanced instruments (Arun et al., 2019). Studies on aerosol elements (Cong et al., 2007; Li et al., 2007), analysis of sources of water-soluble organic carbon (Li et al., 2021), and studies on the effects of cow dung combustion aerosols on the local atmospheric environment have been conducted (Chen et al., 2015). However, combined *in-situ* observations of the physical parameters and chemical compositions are insufficient for making accurate calculations and analyzing the sources and the radiative effects (Zhang L. et al., 2021).

Although, the physical properties, chemical compositions, and sources of fine ($PM_{2.5}$) and submicron (PM_1) aerosols have been studied in detail within the TP region, those of total suspended particulate matter (TSP) remain unknown. In addition, most current studies on pollutant sources on the TP have focused on urban stations, and few observations of inland areas have been made, which limit our understanding of regional background atmospheric and aerosol sources on the TP. Therefore, to better understand the physico-chemical properties and reveal the sources of atmospheric aerosols in the central TP region, a comprehensive field campaign of the physical and chemical properties of TSP was conducted at Nam Co from August 6, 2020, to September 11, 2020.

Data and methodology

Site description

The experiments were conducted at the Nam Co Station for Multisphere Observation and Research, Chinese Academy of

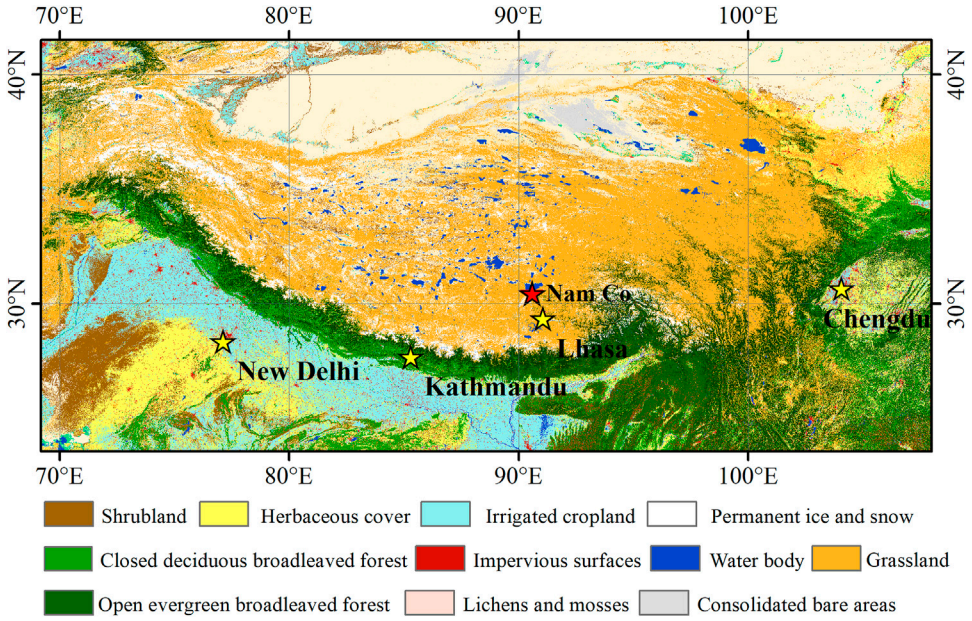

FIGURE 1
Nam Co Station (red), land cover data from the Global Land Cover with Fine Classification System at 30 m in 2020 (GLC_FCS30-2020) of the Institute of Spatial Information Innovation (Zhang et al., 2021b), Chinese Academy of Sciences.

Sciences (30.46° N, 90.58° E, 4730 m.a.s.l.), which is located in the central region of the Tibetan Plateau and is a typical station of the area because of its high altitude, low anthropogenic activity, and absence of industry (Wu et al., 2018). The Nam Co region has typical geomorphological features, such as glaciers, lakes, rivers, and meadows (Figure 1), dominated by alpine meadows and barren areas. Nam Co Station is located southeast of Nam Co Lake, which is in the northern boundary of the Nyainqentanglha mountain range, and is the second largest inland lake in the Tibet Plateau (TP) region.

The aerosol levels are very low at the Nam Co station (annual mean AOD of 0.029 at 500 nm) and the local population is also low (approximately 1000) because of the harsh climate; the population density within 25 km of the station is less than one person/km^2 (Cong et al., 2009). The nearest town to the Nam Co station is Dangxiong, which is located approximately 70 km from the station (Xu J. et al., 2018). Pollutant transport from Lhasa and Dangxiong is limited by the high mountain ridges (Xu X. et al., 2018). Residents within the region use both simple stoves without chimneys and chimney stoves for cooking and heating, and cow dung is the only biomass fuel used in tents or houses in the region (Xiao et al., 2015). Pollution from anthropogenic sources is low, which makes this site ideal for studying the physicochemical properties of background atmospheric aerosols and pollution on the plateau associated with both natural and anthropogenic emissions. In spring, Nam Co Station is affected by dust transport from the upwind sand zone (Fang, 2004), and from June to September by the Indian monsoon system (Kang et al., 2010b). During the observation period, the overall climate was cold and windy, with southerly winds and northwesterly winds dominating during the night and day, respectively.

Online instrumentation

This experiment utilized a set of instruments with online observation capability at the Semi-Arid Climate and Environment Observatory of Lanzhou University (Supplementary Table S1) to conduct online observations of aerosols in the Nam Co region from August 6, 2020, to September 11, 2020. The instrument included a multi-angle absorption photometer (MAAP, model 5012), which can directly measure the concentration of black carbon at 670 nm. The absorption coefficient was calculated by measuring the absorption and scattering of light at 670 nm through the filter membrane. The detection limit of MAAP was 3.5 × 10^{-4} absorbance units, and the uncertainty of the absorbance was ±12% (Petzold and Schönlinner, 2004). Integrating a nephelometer (model 3563, TSI Inc.) can measure the scattering coefficients of atmospheric TSP at 450, 550, and 700 nm wavelengths online. The scattering angle of aerosols observed by the nephelometer ranged from 7° to 170°, with blind areas of <7° and >170°;

therefore, the scattering coefficients observed by the instrument had truncation errors, which can be calibrated according to Anderson's method (Anderson and Ogren, 1998). The uncertainty in the measurement of the air scattering coefficient for the integrating nephelometer was 0.24% (Anderson et al., 1996). All the online instruments were placed in a room at a temperature of approximately 20°C to ensure stable operation.

Offline instrumentation

TSP samples were collected approximately 2 m above the ground using a Laoshan Electronic Instrument Factory Model 2030 medium-flow air sampler and aerosol samples were collected on 90 mm quartz fiber filters (model 1851-090, Whatman Inc.). The sampling period was from August 5, 2020, to September 14, 2020, starting at 09:00 a.m., with a flow rate of 100 L/min for 47 h. The accuracy of sampling flow is no more than ±2%, the uncertainty of flow repeatability is less than 2%, and the uncertainty of flow stability is less than 5%. The total suspended particulate concentration is obtained from offline sampling data and is calculated as (weight of filter membrane after sampling - weight of filter membrane before sampling)/volume of gas flow at the time of collection. A total of 24 TSP samples and four blank samples were collected for this experiment.

The inorganic water-soluble ions (Na^+, NH_4^+, K^+, Ca^{2+}, Mg^{2+}, Cl^-, NO_3^-, and SO_4^{2-}) were determined with an ion chromatograph (Dionex ICS-600). Organic carbon (OC) and elemental carbon (EC) were measured using a Desert Research Institute Model 2001 thermo-optical carbon analyzer following the IMPROVE A program. Metallic elements (Ca, Al, Mg, Fe, and Ti) were measured using inductively coupled plasma atomic emission spectrometry (ICP-AES).

Calculation method

The extinction of aerosol particles, including scattering and absorption, can affect atmospheric visibility and climate (Ackerman et al., 2000). The particle single scattering albedo (SSA) is a key parameter used to study the optical and microphysical properties of atmospheric aerosols, and scattering (B_{scat}) and absorption coefficients (B_{abs}) are two important optical parameters describing the scattering and absorption cross-sections per unit volume of air at wavelength λ. Where the sum of B_{scatt} and B_{absis} is the particle extinction coefficient (B_{ext}), which determines light. The SSA is defined as the ratio of B_{scat}/B_{ext} (Bodhaine, 1995

$$SSA = B_{scat}/B_{ext} = B_{scat}/(B_{scat} + B_{abs}) \quad (1)$$

Therefore, in this study, the absorption and scattering coefficients at 670 nm were used to calculate the SSA.

The aerosol scattering Ångström index (α_{sp}) was used to characterize the wavelength-dependent variation in the absorption coefficient σ_{sp} (Anderson and Ogren, 1998; Pandolfi et al., 2018), and it was calculated as follows,

$$\alpha_{sp} = -\frac{log\left(\frac{\sigma_{sct}^{450}}{\sigma_{sct}^{700}}\right)}{log\left(\frac{450}{700}\right)} \quad (2)$$

where σ_s^{λ} is the aerosol scattering coefficient at wavelength λ.

Potential source contribution function model

A (PSCF analysis was performed using the GIS-based software TrajStat, to estimate pollutant pathways by analyzing pollution trajectories at high concentrations, where Euclidean or angular distances were employed as a clustering model to identify potential pollutant source areas (Wang et al., 2009) using the following,

$$PSCF_{ij} = \frac{m_{ij}}{n_{ij}} \quad (3)$$

where ij is a grid point, n_{ij} indicates the total number of trajectory endpoints in that grid point, m_{ij} is the number of trajectory endpoints with pollutant concentration higher than the threshold value, and the median concentration is set as the threshold value in this study. After calculating the PSCF value, the weighting function was used to reduce the uncertainty caused by trajectories with fewer endpoints (Polissar, 1999). The meteorological field data were obtained from the Global Data Assimilation Forecast System used by the National Centers for Environmental Prediction Global Forecast System model. It is also possible to use a potential source factor analysis in the plateau region. Past studies have used the PSCF method to identify heavy metal sources in the Yaze region of the southeastern TP (Xu et al., 2022) and to analyze the potential source area of perfluoroalkyl acids in precipitation on the TP (Chen et al., 2021).

Enrichment factor

To determine the source of elements in aerosols, the EF of elements in aerosols relative to crustal material was calculated (Zoller et al., 1974). The EF of an element is defined as,

$$EF_x = \frac{(c_x/c_R)_{aerosol}}{(c_x/c_R)_{crust}} \quad (4)$$

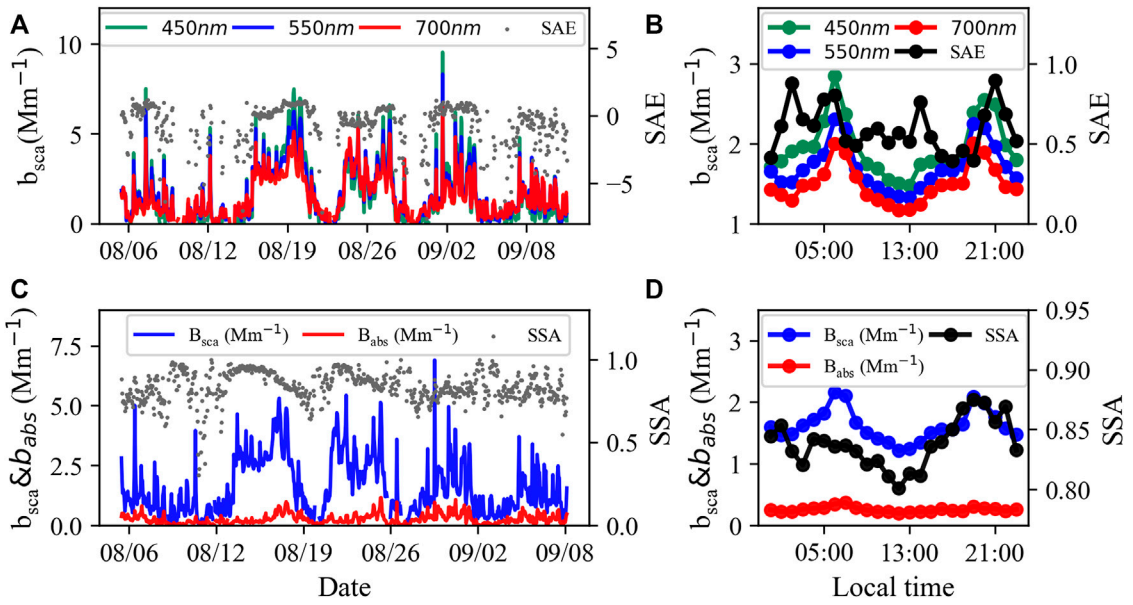

FIGURE 2
Time series of aerosol scattering coefficient and SAE at 450, 550 and 700 nm **(A)** and diurnal variation **(B)** time series of aerosol scattering coefficient, absorption coefficient and SSA at 670 nm **(C)** and diurnal variation **(D)**.

where x is the element of interest, R is the reference element, C_X is the concentration of X, C_R is the concentration of the reference element, EF_X is the EF of X, and aerosol and crustal subscripts refer to the elements in aerosol samples and in the crust, respectively. Elements with an EF close to one are usually considered to be strongly influenced by natural components, whereas EF values greater than one indicate possible anthropogenic influences (Cong et al., 2007). A reference element is often selected as a crustal element, because the pollution level is low, aluminum (Al) was chosen as the reference element in the EF calculation in this study, and its average upper continental crustal component was chosen as the crustal element.

Results and discussion

Aerosol scattering and absorption properties

The mean values of the atmospheric aerosol scattering coefficients of TSP at 450, 550, and 700 nm during the observation period were 1.97 ± 1.63, 1.71 ± 1.36, and 1.50 ± 1.14 Mm^{-1}, respectively. The mean SAE derived from the 450 nm and 700 nm scattering coefficients was 0.59 ± 0.14. The standard deviation of the scattering coefficients was large, and the diurnal variation showed a clear bimodal pattern (Figure 2A), with two peaks in the morning (06:00) and evening (19:00) and one trough in the afternoon. No peak was observed for the absorption coefficient at night.

The aerosol scattering Ångström index (SAE) is related to the average particle size of aerosols, and it ranges from 4 (Rayleigh atmosphere) to 0 (large particles), with negative values for large dust particles. The SAE of Gobi Desert aerosols is 0.52 ± 0.31 (Wang et al., 2018), and the SAE of the Granada region in Spain is 1.1 ± 0.03 for dust weather and 1.6 ± 0.03 for non-dust weather (Valenzuela et al., 2015). An East Asian tropospheric aerosol study in Beijing, China, showed that the SAE of dust, biomass burning, fresh (industrial) stack plume, other coal combustion pollution, and relatively clean (background) air are 0.59 ± 0.41, 1.52 ± 0.18, 1.49 ± 0.11, 1.39 ± 0.20, and 1.58 ± 0.18, respectively (Yang et al., 2009). The SAE for biomass combustion and relatively clean (background) air are similar. The SAE in this study was similar to that of sand aerosols, and this shows that mineral dust (MD) at the Nam Co station is likely the largest contributor to the SAE.

The average particle single scattering albedo (SSA) of TSP was 0.84 ± 0.02 at 670 nm, and the average absorption and scattering coefficients of TSP at this wavelength were 0.26 ± 0.20 Mm^{-1} and 1.61 ± 1.18 Mm^{-1}, respectively. The wavelength dependence of SSA depends on the particle size, chemical composition, and mixing state (Gyawali et al., 2012). In general, the SSA of urban aerosols ranges from 0.80 to 0.98 and that of fresh biomass combustion smoke ranges from 0.72 to 0.88. Fine mode aerosols measured using an aircraft were

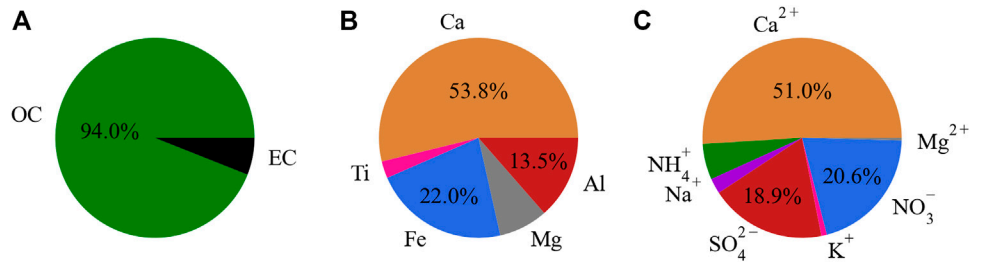

FIGURE 3
The relative mass contributions of mass concentrations of **(A)** OC, EC, **(B)** metallic elements, and **(C)** WSII.

found to have moderate absorption (single scattering albedo at 550 nm of 0.88 ± 0.03) and moderate hygroscopicity, whereas coarse-mode dust was found to have very low absorption (SSA = 0.96 ± 0.01) and almost no hygroscopicity (Anderson, 2003). Thus, the SSA in the present study was representative of a mixture of fresh biomass burning and coarse-mode dust. From the diurnal variation, SSA reached the lowest value at 12:00 and showed an increasing trend from 16:00 to 20:00, but was still less than 0.85 (Figure 2D). This was probably due to the anthropogenic activities in the area that generated the burning of fresh biomass, which increased the SSA.

Aerosol chemical compositions

The optical properties of aerosols at the Nam Co station, the influence of dust aerosols on the region was large, but the composition of aerosols in the central plateau was complex; Optical properties alone were not enough to explain the aerosol composition. To clarify the components, nature, and sources of aerosols in the Nam Co region, off-line sampling was conducted in the region for 1 month, and the chemical composition of the collected aerosol samples was analyzed. During the study period, the mean mass concentration of TSP in the region was 10.11 ± 5.36 μg m^{-3}, whereas that measured in the Himalayas was 20.65 ± 11.17 μg m^{-3} (Arun et al., 2019), and that measured at the Shiquanhe station in the Ali region was 15.71 ± 5.92 μg m^{-3} (Zhang L. et al., 2021). The Nam Co station is located, at a higher altitude than other areas on the Tibetan Plateau (TP), and there is no industrial activity in the surrounding region. The TSP concentration was lower than that at other areas on the TP; however, this could be attributed to the surrounding mountains hindering aerosol transport. A low TSP concentration was characteristic of the TP region, which is characterized by low background pollution and sensitive changes. Therefore, studying the aerosol composition and sources in this region can help to clarify the effects of natural and anthropogenic emissions and external transport within the central TP.

Carbonaceous aerosols are an important component of atmospheric aerosols and consist of elemental carbon and organic carbon, which affect the incident solar radiation by scattering and absorption (Sun et al., 2007). OC can be either released directly into the atmosphere from anthropogenic and biogenic sources, and biomass combustion, and secondary formation in the atmosphere, whereas EC is mainly derived from biomass and incomplete combustion of fossil fuels (Pachauri et al., 2013). Owing to the remote location and high altitude of the Tibet Plateau, carbonaceous aerosols may have significant climatic impacts in this region. The average mass concentrations of OC and EC at Nam Co station in the summer were 1.84 ± 0.83 and 0.12 ± 0.13 μg m^{-3}, (Figure 3A) respectively.

OC/EC ratios are often used to distinguish the relative contributions of fossil fuel or biomass combustion sources, where lower OC/EC ratios (<2.0) are characteristic of a higher share of vehicle and industrial emissions. OC/EC ratios of 3.8–13.2 indicate the predominance of biomass combustion, a greater abundance of carbonaceous aerosols in OC from biomass combustion sources, results in much higher OC/EC values. The value of OC/EC in the Nam Co area in this study was 15.33, which is much higher than that in Lhasa (6.5), an urban plateau (Zhang et al., 2008), and that at the Yulong Snow Mountain station on the southern slope of the plateau (2.06) (Niu et al., 2018). Higher OC/EC values indicate a more significant impact of biomass burning in the region, and because the study site is located in a near-pristine environment, local residential emissions in the area may be an important contributor to biomass burning. The relatively similar OC/EC values of cow dung aerosols in the Nam Co area also indicate that the local source is not negligible (Chen et al., 2015). On the other hand, the aging that occurs with the transport process of aerosols also increases the OC/EC values (Arun et al., 2019). In addition, a higher OC/EC (>2.0) is generally considered to indicate the presence of secondary organic aerosols (SOA) (Chow et al., 1996). Therefore, biomass aerosols in the region are likely to be dominated by combustion emissions from the generation of OC and the secondary generation of aerosols.

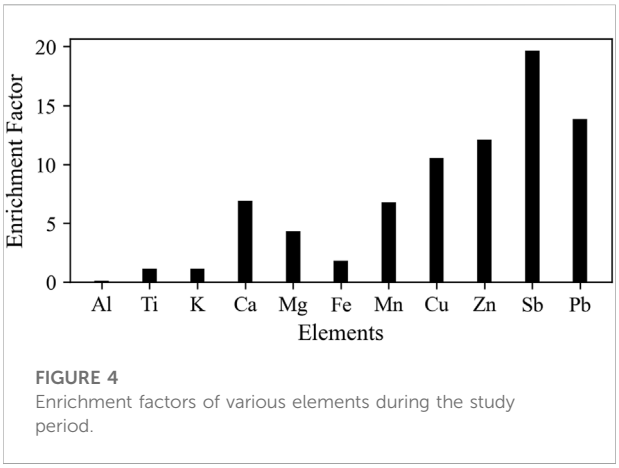

FIGURE 4
Enrichment factors of various elements during the study period.

Previous studies have considered that mineral dust was considered one of the main aerosol components in the central Himalayas (Decesari et al., 2010) and in the central TP (Cong et al., 2007; Kang et al., 2016). The mean mass concentrations of metallic elements Ca, Ti, Fe, Al, and Mg measured in the present study were 0.27 ± 0.17, 0.014 ± 0.02, 0.11 ± 0.07, 0.067 ± 0.05, and 0.039 ± 0.03 μg m^{-3}, respectively. Ca accounted for the majority of the metallic elements by mass (53.8%), followed by Fe (22.0%), Al (13.5%), Mg (7.9%), and Ti (2.8%). Everest station has 34.8% of Fe and 23.1% of Ca as metallic elements (Arun et al., 2019). Ca, Fe, and Si are major fractions of crustal elements; the values obtained for Ca and Fe in this study prove that Nam Co station is similar to Everest station and mineral dust is an important component of aerosols in the region.

The EFs of each element in the TSP samples from the Nam Co station are shown in Figure 4. The EFs of Al, Ti and K were approximately one, which indicates that they were primarily derived from natural sources, such as soil and dust. However, the values of Cu, Zn, and Sb were significantly higher (Buzica et al., 2006, which indicates that some of these elements may have originated from human activities, such as fossil fuel combustion, industrial metallurgical processes, and traffic emissions, and that they may have been deposited in the Nam Co region *via* long-distance transport.

K^+, Mg^{2+}, and Ca^{2+} are the main components of atmospheric aerosols, and their contribution to $PM_{2.5}$ (particulate matter with an aerodynamic diameter ≤2.5 μm) can reach 77% (Xu et al., 2019). In the present study, the mean mass concentrations of SO_4^{2-}, NO_3^-, Mg^{2+}, Ca^{2+}, NH_4^+, Na^+, and K^+ were 0.70 ± 0.38, 0.77 ± 0.22, 0.01 ± 0.01, 1.90 ± 0.83, 0.22 ± 0.15, 0.09 ± 0.04, and 0.03 ± 0.02 μg m^{-3}, respectively. The main contributions of the inorganic ions were Ca^{2+} (51.0%), NO_3^- (20.6%), SO_4^{2-} (18.9%), and NH_4^+(5.8%). The main ion sources in the central plateau have been identified in previous studies; for example, SO_4^{2-} and Ca^{2+} are considered typical ions from combustion emissions and mineral dust, respectively (Kang et al., 2010b). Compared to the Nepal Climate Observatory-Pyramid Station (Decesari et al., 2010) on the southern slope of the Himalayas, where the Ca^{2+} concentration during the monsoon was 0.34 μg m^{-3}, The relative concentration of Ca^{2+} in the TSP samples in this study (1.90 ± 0.83 μg m^{-3}) was higher than that in the Nepal Climate Observatory-Pyramid Station (0.50 μg m^{-3}) and that at the Everest station during the monsoon (Cong et al., 2015), reflecting a heavier dust impact in the central plateau. Furthermore, the higher mass concentrations of SO_4^{2-} and NO_3^- indicate that anthropogenic combustion emissions have less of an impact than dust emissions on the central plateau.

Discussion on aerosol sources

To clarify the composition of aerosols at the Nam Co station and further analyze the source of aerosols in the region, a reconstruction of the mass concentration of aerosols at the Nam Co station was conducted using organic matter (OM), EC, MD, and water-soluble inorganic ions (nd-WSII) of non-sand dust. The water-soluble inorganic ion concentration of non-sand dust was the sum of the SO_4^{2-}, NO_3^-, NH_4^+, and K^+ concentrations. It is necessary to determine the OM/OC ratio of to calculate the OM mass concentration (Guinot et al., 2007), and that measured at the Nam Co station from May to July 2015 was 2.28 (Xu J. et al., 2018); as this study was conducted within a relatively short time period (August to September 2020), the OM/OC value of 2.28 was used to calculate the OM mass.

Calculations of the MD concentration are commonly more accurate when multiple metallic and nonmetallic elements are combined with weighting factors (Marcazzan et al., 2001), and the equation for MD was thus revised to consider the effect of carbonates present in ionic equilibrium (Zhang L. et al., 2021).

$$MD = 1.15 \cdot (1.89 \cdot [Al] + 2.14 \cdot [Si] + 1.67 \cdot [Ti] + 1.36 \cdot [Fe] + 1.2 \cdot [K] + 1.4 \cdot [Ca]) + 1.1 \cdot [Ca] + 1.83 \cdot [Mg] \quad (5)$$

where [Si] = 4 [Al] (Wang et al., 2018), [K] = 0.6 [Fe] (Malm et al., 1994), and the factor 1.15 represents the mass of the other metal oxides that compensate for not being measured. The mass concentration of MD in the region was calculated using this equation was 1.02 μg m^{-3}, whereas that at Shiquanhe station in the Ali region was 4.61 μg m^{-3}, the mass MD concentration measured at a background site in the western Himalayas was 3.1 μg m^{-3} (Arun et al., 2019).

The reconstructed mass concentrations correlated well with the measured mass (Supplementary Figure S1). Concentrations of r = 0.89 indicated that the reconstructed mass concentrations were reasonable, and reconstructed mass concentrations of OM, EC, MD, and nd-WSII were 4.20 ± 1.90, 0.12 ± 0.13, 1.83 ± 1.24, and 0.42 ± 0.15 μg·m-3, respectively, with the largest contribution from OM (63.9%), followed by MD (27.8%), and the smallest contribution (Figure 5) from EC (1.8%).

To better understand the sources of aerosols on the central plateau, the correlations between aerosol chemicals were

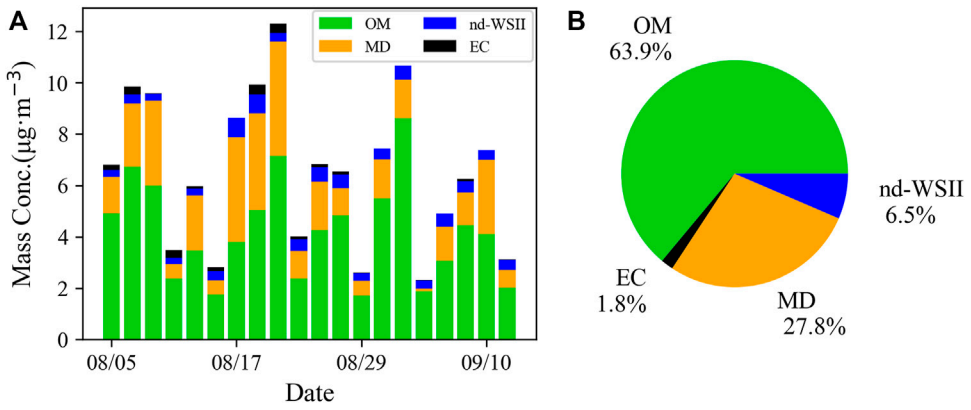

FIGURE 5
(A) The time series of mass concentrations of OM, EC, nd-WSII, and MD; **(B)** Proportion of each component of reconstructed mass concentration.

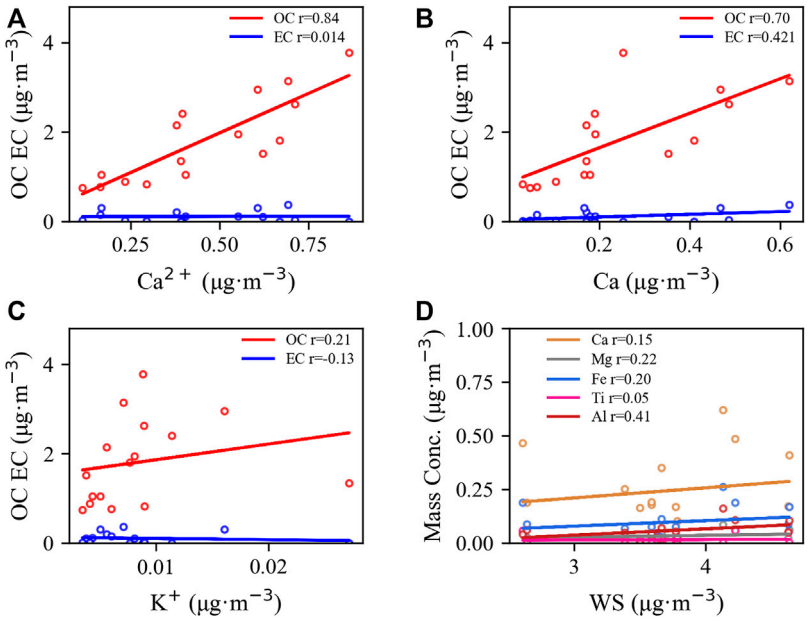

FIGURE 6
(A) Fitting curves of OC, EC, and K^+; **(B)** Fitting curves of OC, EC, and Ca; **(C)** Fitting curves of OC, EC, and Ca^{2+}; **(D)** Fitting curves of WS and metallic elements.

investigated. K^+ is a tracer of biomass combustion emissions (Zhang et al., 2018); EC had almost no linear correlation with K^+ (r = −0.06), while OC had a higher correlation coefficient with K^+ (r = 0.22) (Figure 6C). Because K^+ is often considered to come from plant burning, the weak correlation between OC and K^+ may be since most of the biomass aerosols in the region come from cattle dung burning or exotic transport. Ca^{2+} is often used as a tracer of mineral dust and represents the influence of mineral dust, with a correlation of 0.32 between OC and Ca^{2+} was measured at the Shiquanhe station in the Ali region during summer (Supplementary Figure S2) and only a slight correlation measured year-round at the eastern Himalayas remote high-altitude station (Arun et al., 2019). The correlation between WSOC and Ca^{2+} was measured by

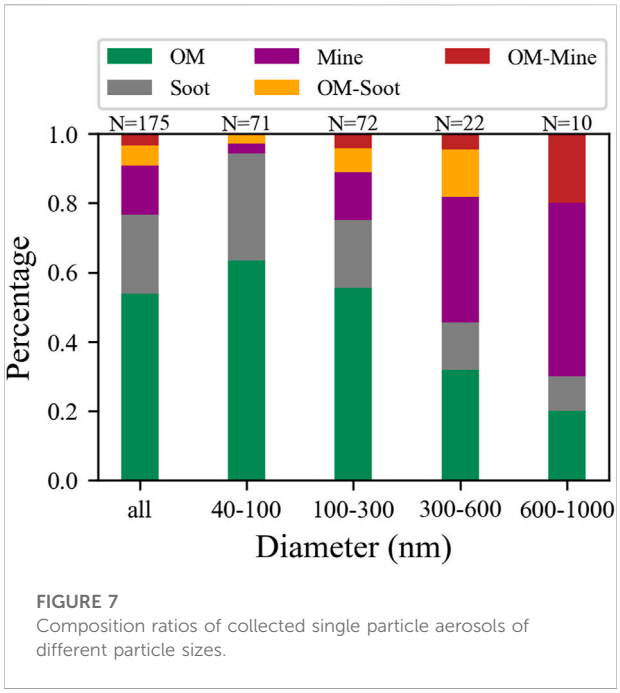

FIGURE 7
Composition ratios of collected single particle aerosols of different particle sizes.

year-round offline sampling at the Nam Co station was 0.59 (Li et al., 2021). The strong correlation between OC and Ca^{2+} and Ca in this study indicates that they are homologous.

To verify whether the MD aerosols in the region were dominated by local influences, a metal elements and wind speed correlation analysis was conducted and the results showed a very low correlation coefficient between the two. When the wind speed increased, the metal element concentration increased, but the results were not significantly, indicating that the aerosol impact of the local wind-induced sand rising on the Nam Co station is small. According to previous studies at the Nam Co station, the size distribution of OC and EC concentrations showed a bimodal variation, with the main peak of OC occurring in coarse particles, which may be due to dust particles and bioaerosols, whereas the main peak of EC in coarse particles may be caused by the resuspension of soil/dust particles containing EC (Wan et al., 2015). Another study also suggested that WSOC in the TSP during the monsoon period is influenced by fine surface soil particles within the TP (Li et al., 2021). Therefore, the same source of OC and Ca at the Nam Co station indicates that OC is primarily derived from soil OM transported with dust.

Single-particle sampling was conducted from August 16 to 18, 2020 using a DKL-2 single-particle sampler. The results showed (Figure 7) that during the sampling period, OM and MD accounted for 53.7% and 14.3% of particles, respectively. In addition, mixed particles of dust and biomass were observed (Supplementary Figure S4), which also provides evidence for the homology between biomass aerosols and dust.

To determine the sources of OC and Ca, the potential source regions of both components were analyzed using PSCF (Figure 8). The higher PSCF values in the interior of the plateau indicated that OC and Ca had similar source area distributions, and both originated primarily from the interior of the plateau, which explains the high correlation between OC and Ca in the TSP. Some studies have also suggested that dust from the Ali region of the plateau can be transported to the central part of the southern section. The strong influence of local emissions from the southeastern part of the plateau can also be demonstrated using isotope-tracing methods. These results also prove the non-negligible presence of local emission sources in the plateau region.

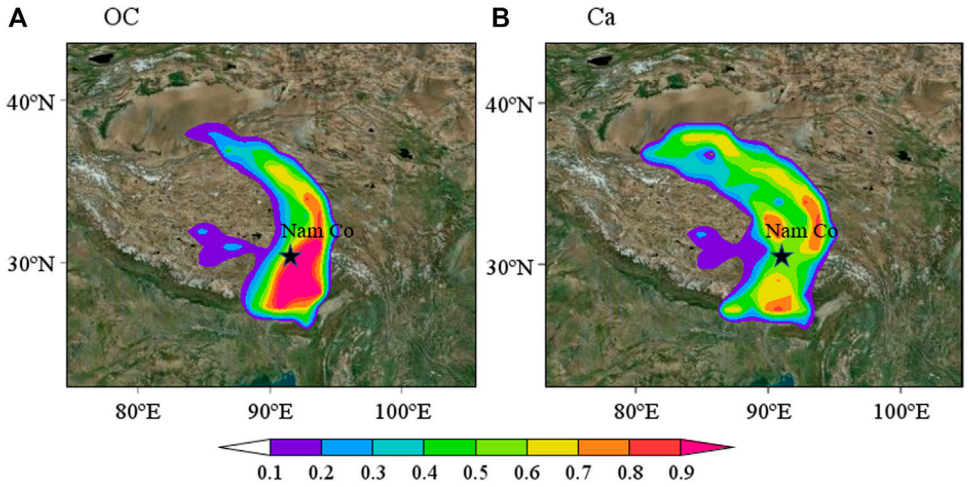

FIGURE 8
Potential source regions of OC **(A)** and Ca **(B)** in aerosols at Nam Co.

Summary and conclusions

This study studied the optical properties, chemical composition, and sources of total suspended particulate matter (TSP) at the Nam Co station in the central Tibetan Plateau (TP) region. The main results of this study are as follows:

1) The mean mass concentration of TSP was 10.11 ± 5.36 μg m^{-3}, the mean single scattering albedo (SSA) was 0.84 ± 0.09, and the mean aerosol scattering Ångström index (SAE) was 0.59 ± 0.14. The SAE of mineral dust aerosols was relatively close, indicating that aerosols in the Nam Co area are affected by sand; however, dust lowers the SAE.
2) The average mass concentrations of organic carbon (OC) and elemental carbon (EC) were 1.84 ± 0.83 μg m^{-3} and 0.12 ± 0.13 μg m^{-3}, respectively, and the mass concentration of carbonaceous aerosols was dominated by OC, which accounted for 94% of the total carbon (TC). In addition, the EC content was low, which indicated that the biomass aerosols in the region were primarily composed of OC and the secondary generation of aerosols. The OC/EC ratio of 15.33 is probably caused by the aging that occurs during the transport of aerosols.
3) Of the metallic elements, calcium accounted for most of the metallic elements by mass (53.8%), followed by iron (22.0%), and aluminum (13.5%), with mean mass concentrations of 0.27 ± 0.17 μg m^{-3}, 0.11 ± 0.07 μg m^{-3}, and 0.067 ± 0.05 μg m^{-3}, respectively. This suggests that crustal materials are the main contributors to the TSP in this region. The enrichment factor EF of elements such as Al, Ti and K was approximately one, indicating that the natural sources in the Nam co region are a major source of aerosols. And the EF values of elements such as Cu, Zn and Sb were obviously high, which shows that pollution from human activities may reach the area through long-distance transport.
4) With respect to the composition of water-soluble ions, Ca^{2+} comprised the largest inorganic ion concentration (51.0%), followed by NO_3^- (20.6%), and SO_4^{2-} (18.9%), with average mass concentrations of 1.90 ± 0.83 μg m^{-3}, 0.77 ± 0.22 μg m^{-3}, and 0.70 ± 0.38 μg m^{-3}, which reflects the influence of heavy mineral dust on the central part of the plateau and indicates that the influence of natural dust in the region is greater than that of anthropogenic fossil fuel combustion.
5) Based on the offline sampling mass reconstruction of aerosols at the Nam Co station, the mass concentrations of organic matter (OM), elemental carbon (EC), sand dust (MD), and water-soluble ions (nd-WSII) removed from sand dust were 4.20 ± 1.90, 0.12 ± 0.13 μg m^{-3}, 1.83 ± 1.24 μg m^{-3}, and 0.42 ± 0.15 μg m^{-3}, respectively, with the largest contribution from OM (63.9%), followed by MD (27.8%) and the smallest contribution from EC (1.8%). Therefore, OM and MD accounted for 91.7% of the TSP mass and were the main components of summer TSP in the Nam Co region.
6) The correlation coefficient between OC and K^+ was low (r = 0.22), and this was probably due to the low percentage of plant material being burned in the area. The strong correlation between OC and Ca^{2+} indicated that OM and MD had the same sources, and the electron microscopy images of single particles also showed the mixed transport of biomass with sand and dust. The low correlation between metal elements and wind speed indicated that the TSP did not originate locally, and the PSCF analysis illustrated that OM and mineral dust originated within the TP.

Based on the results of this study, we can conclude that the summertime TSP in the central TP is primarily characterized by background biomass and mineral dust aerosols originating regionally from the ground within the TP. These results provide a better understanding of atmospheric aerosols and will contribute to estimations of aerosol radiative effects on the TP. However, future studies are required to quantitatively estimate the contribution of internal and external sources of atmospheric aerosols in the TP region.

Data availability statement

The datasets presented in this study can be found in online repositories. The names of the repository/repositories and accession number(s) can be found below: https://data.tpdc.ac.cn/zh-hans/data/2f32c881-3ed0-45c3-83c8-86fc2a5deddb/.

Author contributions

HZ: Methodology, Software, Validation, Data Curation, Visualization, Formal analysis, Writing—Original Draft, Writing—Review and Editing. PT: Conceptualization, Funding acquisition, Supervision, Investigation, Validation, Formal analysis, Resources, Project administration, Writing—Original Draft, Writing—Review and Editing. CK: Data Curation, Investigation. YG: Data Curation, Investigation. ZY: Data Curation, Investigation. GL: Data Curation, Investigation. CT: Investigation. TD: Investigation. JW: Investigation. ZZ: Investigation. XC: Investigation, Supervision JL: Investigation, Supervision JS: Data curation, Resources, Project administration. Conceptualization, Funding acquisition, Supervision, Investigation, Validation, Formal analysis, Resources, Project administration, Writing—Original Draft, Writing—Review and Editing.

Funding

This research was supported by the Second Tibetan Plateau Scientific Expedition and Research Program (STEP), Grant no. 2019QZKK0602. PT was also funded by the National Natural Science Foundation of China (42175093 and 41905017).

Acknowledgments

We would like to thank the staff of Nam Co Station for Multisphere Observation and Research and Chinese Academy of Sciences for their help during the field campaign. The Semi-Arid Climate and Environment Observatory of Lanzhou University (SACOL) is acknowledged for the mobile aerosol observation system. The original data used in this research are available at the National Tibetan Plateau Data Center (https://data.tpdc.ac.cn/en/).

Conflict of interest

The authors declare that the research was conducted in the absence of any commercial or financial relationships that could be construed as a potential conflict of interest.

Publisher's note

All claims expressed in this article are solely those of the authors and do not necessarily represent those of their affiliated organizations, or those of the publisher, the editors and the reviewers. Any product that may be evaluated in this article, or claim that may be made by its manufacturer, is not guaranteed or endorsed by the publisher.

Supplementary material

The Supplementary Material for this article can be found online at: https://www.frontiersin.org/articles/10.3389/fenvs.2022.1055673/full#supplementary-material

References

Ackerman, A. S., Toon, O. B., Stevens, D. E., Heymsfield, A. J., Ramanathan, V. V., and Welton, E. J. (2000). Reduction of tropical cloudiness by soot. *Science* 288, 1042–1047. doi:10.1126/science.288.5468.1042

Anderson, T. L., Covert, D. S., Marshall, S. F., Laucks, M. L., Charlson, R. J., Waggoner, A. P., et al. (1996). Performance characteristics of a high-sensitivity, three-wavelength, total scatter/backscatter nephelometer. *J. Atmos. Ocean. Technol.* 13 (5), 967–986. doi:10.1175/1520-0426(1996)013<0967:pcoahs>2.0.co;2

Anderson, T. L., and Ogren, J. A. (1998). Determining aerosol radiative properties using the TSI 3563 integrating nephelometer. *Aerosol Sci. Technol.* 29, 57–69. doi:10.1080/02786829808965551

Anderson, T. L. (2003). Variability of aerosol optical properties derived from *in situ* aircraft measurements during ACE-Asia. *J. Geophys. Res.*, 108(D23). doi:10.1029/2002jd003247

Arun, B. S., Aswini, A. R., Gogoi, M. M., Hegde, P., Kumar Kompalli, S., Sharma, P., et al. (2019). Physico-chemical and optical properties of aerosols at a background site (~4 km a.s.l.) in the Western Himalayas. *Atmos. Environ.* 218, 117017. doi:10.1016/j.atmosenv.2019.117017

Bian, J., Li, D., Bai, Z., Li, Q., Lyu, D., and Zhou, X. (2020). Transport of Asian surface pollutants to the global stratosphere from the Tibetan Plateau region during the Asian summer monsoon. *Natl. Sci. Rev.* 7, 516–533. doi:10.1093/nsr/nwaa005

Bodhaine, B. A. (1995). Aerosol absorption measurements at barrow, mauna loa and the south pole. *J. Geophys. Res.* 100, 8967. doi:10.1029/95jd00513

Buzica, D., Gerboles, M., Borowiak, A., Trincherini, P., Passarella, R., and Pedroni, V. (2006). Comparison of voltammetry and inductively coupled plasma-mass spectrometry for the determination of heavy metals in PM10 airborne particulate matter. *Atmos. Environ.* 40, 4703–4710. doi:10.1016/j.atmosenv.2006.04.015

Chen, M., Wang, C., Gao, K., Wang, X., Fu, J., Gong, P., et al. (2021). Perfluoroalkyl substances in precipitation from the Tibetan Plateau during monsoon season: Concentrations, source regions and mass fluxes. *Chemosphere* 282, 131105. doi:10.1016/j.chemosphere.2021.131105

Chen, P., Kang, S., Bai, J., Sillanpää, M., and Li, C. (2015). Yak dung combustion aerosols in the Tibetan Plateau: Chemical characteristics and influence on the local atmospheric environment. *Atmos. Res.* 156, 58–66. doi:10.1016/j.atmosres.2015.01.001

Chow, J. C., Watson, J. G., Lu, Z., Lowenthal, D. H., Frazier, C. A., Solomon, P. A., et al. (1996). Descriptive analysis of PM2.5 and PM10 at regionally representative locations during SJVAQS/AUSPEX. *Atmos. Environ.* 30, 2079–2112. doi:10.1016/1352-2310(95)00402-5

Cong, Z., Kang, S., Kawamura, K., Liu, B., Wan, X., Wang, Z., et al. (2015). Carbonaceous aerosols on the south edge of the Tibetan plateau: Concentrations, seasonality and sources. *Atmos. Chem. Phys.* 15, 1573–1584. doi:10.5194/acp-15-1573-2015

Cong, Z., Kang, S., Liu, X., and Wang, G. (2007). Elemental composition of aerosol in the Nam Co region, Tibetan Plateau, during summer monsoon season. *Atmos. Environ.* 41, 1180–1187. doi:10.1016/j.atmosenv.2006.09.046

Cong, Z., Kang, S., Smirnov, A., and Holben, B. (2009). Aerosol optical properties at Nam Co, a remote site in central Tibetan Plateau. *Atmos. Res.* 92, 42–48. doi:10.1016/j.atmosres.2008.08.005

Decesari, S., Facchini, M. C., Carbone, C., Giulianelli, L., Rinaldi, M., Finessi, E., et al. (2010). Chemical composition of PM₁₀ and PM₁ at the high-altitude Himalayan station Nepal Climate Observatory-Pyramid (NCO-P) (5079 m a.s.l.). *Atmos. Chem. Phys.* 10, 4583–4596. doi:10.5194/acp-10-4583-2010

Dhungel, S., Kathayat, B., Mahata, K., and Panday, A. (2018). Transport of regional pollutants through a remote trans-Himalayan valley in Nepal. *Atmos. Chem. Phys.* 18 (2), 1203–1216. doi:10.5194/acp-18-1203-2018

Fang, X. (2004). Dust storms and loess accumulation on the Tibetan plateau: A case study of dust event on 4 march 2003 in Lhasa. *Chin. Sci. Bull.* 49, 953. doi:10.1360/03wd0180

Gao, X., Yang, L., Cheng, S., Gao, R., Zhou, Y., Xue, L., et al. (2011). Semi-continuous measurement of water-soluble ions in PM2.5 in Jinan, China: Temporal variations and source apportionments. *Atmos. Environ.* 45, 6048–6056. doi:10.1016/j.atmosenv.2011.07.041

Guinot, B., Cachier, H., and Oikonomou, K. (2007). Geochemical perspectives from a new aerosol chemical mass closure. *Atmos. Chem. Phys.* 7, 1657–1670. doi:10.5194/acp-7-1657-2007

Gul, C., Kang, S., Puppala, S. P., Wu, X., He, C., Xu, Y., et al. (2022). Measurement of light-absorbing particles in surface snow of central and Western himalayan glaciers: Spatial variability, radiative impacts, and potential source regions. *Atmos. Chem. Phys.* 22 (13), 8725–8737. doi:10.5194/acp-22-8725-2022

Gyawali, M., Arnott, W. P., Zaveri, R. A., Song, C., Moosmüller, H., Liu, L., et al. (2012). Photoacoustic optical properties at UV, VIS, and near IR wavelengths for laboratory generated and winter time ambient urban aerosols. *Atmos. Chem. Phys.* 12, 2587–2601. doi:10.5194/acp-12-2587-2012

Hindman, E. E., and Upadhyay, B. P. (2002). Air pollution transport in the Himalayas of Nepal and Tibet during the 1995–1996 dry season. *Atmos. Environ.* 36 (4), 727–739. doi:10.1016/s1352-2310(01)00495-2

Hu, Z., Kang, S., Li, C., Yan, F., Chen, P., Gao, S., et al. (2017). Light absorption of biomass burning and vehicle emission-sourced carbonaceous aerosols of the Tibetan Plateau. *Environ. Sci. Pollut. Res.* 24, 15369–15378. doi:10.1007/s11356-017-9077-3

IPCC (2021). *Climate change 2021: The physical science basis. Contribution of working group I to the sixth assessment report of the intergovernmental panel on climate change S. L. Connors, C. Péan, S. Berger, N. Caud, Y. Chen, L. Goldfarb, M. I. Gomis, M. Huang.* Cambridge: Cambridge University Press.

Kang, S., Chen, P., Li, C., Liu, B., and Cong, Z. (2016). Atmospheric aerosol elements over the inland Tibetan plateau: Concentration, seasonality, and transport. *Aerosol Air Qual. Res.* 16, 789–800.

Kang, S., Xu, Y., You, Q., Flügel, W.-A., Pepin, N., and Yao, T. (2010a). Review of climate and cryospheric change in the Tibetan Plateau. *Environ. Res. Lett.* 5, 015101. doi:10.1088/1748-9326/5/1/015101

Kang, S., Zhang, Y., Zhang, Y., Grigholm, B., Kaspari, S., Qin, D., et al. (2010b). Variability of atmospheric dust loading over the central Tibetan Plateau based on ice core glaciochemistry. *Atmos. Environ.* 44, 2980–2989. doi:10.1016/j.atmosenv.2010.05.014

Lau, K. M., Kim, M. K., and Kim, K. M. (2006). Asian summer monsoon anomalies induced by aerosol direct forcing: The role of the Tibetan plateau. *Clim. Dyn.* 26, 855–864. doi:10.1007/s00382-006-0114-z

Lawrence, M. G. (2011). Asia under a high-level Brown cloud. *Nat. Geosci.* 4, 352–353. doi:10.1038/ngeo1166

Li, C., Bosch, C., Kang, S., Andersson, A., Chen, P., Zhang, Q., et al. (2016). Sources of black carbon to the Himalayan-Tibetan Plateau glaciers. *Nat. Commun.* 7, 12574. doi:10.1038/ncomms12574

Li, C., Kang, S., and Cong, Z. (2007). Elemental composition of aerosols collected in the glacier area on Nyainqêntanglha Range, Tibetan Plateau, during summer monsoon season. *Chin. Sci. Bull.* 52, 3436–3442. doi:10.1007/s11434-007-0445-0

Li, C., Yan, F., Kang, S., Chen, P., Han, X., Hu, Z., et al. (2017). Re-Evaluating black carbon in the Himalayas and the Tibetan plateau: Concentrations and deposition. *Atmos. Chem. Phys.* 17 (19), 11899–11912. doi:10.5194/acp-17-11899-2017

Li, C., Zhang, C., Yan, F., Kang, S., Xu, Y., Liu, Y., et al. (2022). Importance of local non-fossil sources to carbonaceous aerosols at the eastern fringe of the Tibetan plateau, China: Δ14C and δ13C evidences. *Environ. Pollut.* 311, 119858. doi:10.1016/j.envpol.2022.119858

Li, Y., Yan, F., Kang, S., Zhang, C., Chen, P., Hu, Z., et al. (2021). Sources and light absorption characteristics of water-soluble organic carbon (WSOC) of atmospheric particles at a remote area in inner Himalayas and Tibetan Plateau. *Atmos. Res.* 253, 105472. doi:10.1016/j.atmosres.2021.105472

Marcazzan, G. M., Vaccaro, S., Valli, G., and Vecchi, R. (2001). Characterisation of PM10 and PM2.5 particulate matter in the ambient air of Milan (Italy). *Atmos. Environ.* 35, 4639–4650. doi:10.1016/s1352-2310(01)00124-8

Ming, J., Xiao, C., Sun, J., Kang, S., and Bonasoni, P. (2010). Carbonaceous particles in the atmosphere and precipitation of the Nam Co region, central Tibet. *J. Environ. Sci.* 22 (11), 1748–1756. doi:10.1016/s1001-0742(09)60315-6

Niu, H., Kang, S., Wang, H., Zhang, R., Lu, X., Qian, Y., et al. (2018). Seasonal variation and light absorption property of carbonaceous aerosol in a typical glacier region of the southeastern Tibetan Plateau. *Atmos. Chem. Phys.* 18, 6441–6460. doi:10.5194/acp-18-6441-2018

Pachauri, T., Singla, V., Satsangi, A., Lakhani, A., and Kumari, K. M. (2013). Characterization of carbonaceous aerosols with special reference to episodic events at Agra, India. *Atmos. Res.* 128, 98–110. doi:10.1016/j.atmosres.2013.03.010

Pandolfi, M., Alados-Arboledas, L., Alastuey, A., Andrade, M., Angelov, C., Artiñano, B., et al. (2018). A European aerosol phenomenology – 6: Scattering properties of atmospheric aerosol particles from 28 ACTRIS sites. *Atmos. Chem. Phys.* 18, 7877–7911. doi:10.5194/acp-18-7877-2018

Pathak, R. K., Wu, W. S., and Wang, T. (2009). Summertime PM_{2.5} ionic species in four major cities of China: Nitrate formation in an ammonia-deficient atmosphere. *Atmos. Chem. Phys.* 9, 1711–1722. doi:10.5194/acp-9-1711-2009

Petzold, A., and Schönlinner, M. (2004). Multi-angle absorption photometry—A new method for the measurement of aerosol light absorption and atmospheric black carbon. *J. Aerosol Sci.* 35 (4), 421–441. doi:10.1016/j.jaerosci.2003.09.005

Polissar, A. (1999). The aerosol at barrow, Alaska: Long-term trends and source locations. *Atmos. Environ.* 33, 2441–2458. doi:10.1016/s1352-2310(98)00423-3

Qiu, J. (2008). China: The third pole. *Nature* 454, 393–396. doi:10.1038/454393a

Ramanathan, V., and Carmichael, G. (2008). Global and regional climate changes due to black carbon. *Nat. Geosci.* 1, 221–227. doi:10.1038/ngeo156

Shang, D., Hu, M., Zheng, J., Qin, Y., Du, Z., Li, M., et al. (2018). Particle number size distribution and new particle formation under the influence of biomass burning at a high altitude background site at Mt. Yulong (3410 m), China. *Atmos. Chem. Phys.* 18 (21), 15687–15703. doi:10.5194/acp-18-15687-2018

Sun, H., Biedermann, L., and Bond, T. C. (2007). Color of Brown carbon: A model for ultraviolet and visible light absorption by organic carbon aerosol. *Geophys. Res. Lett.* 34, L17813. doi:10.1029/2007gl029797

Tian, P., Cao, X., Zhang, L., Sun, N., Sun, L., Logan, T., et al. (2017). Aerosol vertical distribution and optical properties over China from long-term satellite and ground-based remote sensing. *Atmos. Chem. Phys.* 17, 2509–2523. doi:10.5194/acp-17-2509-2017

Tian, P., Zhang, L., Ma, J., Tang, K., Xu, L., Wang, Y., et al. (2018). Radiative absorption enhancement of dust mixed with anthropogenic pollution over East Asia. *Atmos. Chem. Phys.* 18, 7815–7825. doi:10.5194/acp-18-7815-2018

Valenzuela, A., Olmo, F. J., Lyamani, H., Antón, M., Titos, G., Cazorla, A., et al. (2015). Aerosol scattering and absorption Angström exponents as indicators of dust and dust-free days over Granada (Spain). *Atmos. Res.* 154, 1–13. doi:10.1016/j.atmosres.2014.10.015

Wan, X., Kang, S., Wang, Y., Xin, J., Liu, B., Guo, Y., et al. (2015). Size distribution of carbonaceous aerosols at a high-altitude site on the central Tibetan Plateau (Nam Co Station, 4730ma.s.l.). *Atmos. Res.* 153, 155–164. doi:10.1016/j.atmosres.2014.08.008

Wang, B., and French, H. M. (1994). Climate controls and high-altitude permafrost, qinghai-xizang (tibet) Plateau, China. *Permafr. Periglac. Process.* 5, 87–100. doi:10.1002/ppp.3430050203

Wang, X., Wen, H., Shi, J., Bi, J., Huang, Z., Zhang, B., et al. (2018). Optical and microphysical properties of natural mineral dust and anthropogenic soil dust near dust source regions over northwestern China. *Atmos. Chem. Phys.* 18, 2119–2138. doi:10.5194/acp-18-2119-2018

Wang, Y., Zhang, X., and Draxler, R. R. (2009). TrajStat: GIS-based software that uses various trajectory statistical analysis methods to identify potential sources from long-term air pollution measurement data. *Environ. Model. Softw.* 24, 938–939. doi:10.1016/j.envsoft.2009.01.004

Wu, G., Wan, X., Gao, S., Fu, P., Yin, Y., Li, G., et al. (2018). Humic-like substances (HULIS) in aerosols of central Tibetan plateau (Nam Co, 4730 m asl): Abundance, light absorption properties, and sources. *Environ. Sci. Technol.* 52, 7203–7211. doi:10.1021/acs.est.8b01251

Wu, G., Wan, X., Ram, K., Li, P., Liu, B., Yin, Y., et al. (2020). Light absorption, fluorescence properties and sources of Brown carbon aerosols in the Southeast Tibetan Plateau. *Environ. Pollut.* 257, 113616. doi:10.1016/j.envpol.2019.113616

Xiang, Y., Zhang, T., Liu, J., Wan, X., Loewen, M., Chen, X., et al. (2021). Vertical profile of aerosols in the Himalayas revealed by lidar: New insights into their seasonal/diurnal patterns, sources, and transport. *Environ. Pollut.* 285, 117686. doi:10.1016/j.envpol.2021.117686

Xiao, Q., Saikawa, E., Yokelson, R. J., Chen, P., Li, C., and Kang, S. (2015). Indoor air pollution from burning yak dung as a household fuel in Tibet. *Atmos. Environ.* 102, 406–412. doi:10.1016/j.atmosenv.2014.11.060

Xu, J., Zhang, Q., Shi, J., Ge, X., Xie, C., Wang, J., et al. (2018a). Chemical characteristics of submicron particles at the central Tibetan plateau: Insights from aerosol mass spectrometry. *Atmos. Chem. Phys.* 18, 427–443. doi:10.5194/acp-18-427-2018

Xu, J., Zhang, Q., Wang, Z., Yu, G., Ge, X., and Qin, X. (2015). Chemical composition and size distribution of summertime PM_{2.5} at a high altitude remote location in the northeast of the qinghai–xizang (tibet) plateau: Insights into aerosol sources and processing in free troposphere. *Atmos. Chem. Phys.* 15, 5069–5081. doi:10.5194/acp-15-5069-2015

Xu, Q., Wang, S., Jiang, J., Bhattarai, N., Li, X., Chang, X., et al. (2019). Nitrate dominates the chemical composition of PM2.5 during haze event in Beijing, China. *Sci. Total Environ.* 689, 1293–1303. doi:10.1016/j.scitotenv.2019.06.294

Xu, X., Zhang, H., Lin, W., Wang, Y., Xu, W., and Jia, S. (2018b). First simultaneous measurements of peroxyacetyl nitrate (PAN) and ozone at Nam Co in the central Tibetan plateau: Impacts from the PBL evolution and transport processes. *Atmos. Chem. Phys.* 18, 5199–5217. doi:10.5194/acp-18-5199-2018

Xu, Y., Li, Q., Xie, S., Zhang, C., Yan, F., Liu, Y., et al. (2022). Composition and sources of heavy metals in aerosol at a remote site of Southeast Tibetan Plateau, China. *Sci. Total Environ.* 845, 157308. doi:10.1016/j.scitotenv.2022.157308

Yang, J., Kang, S., and Ji, Z. (2020). Critical contribution of south Asian residential emissions to atmospheric black carbon over the Tibetan plateau. *Sci. Total Environ.* 709, 135923. doi:10.1016/j.scitotenv.2019.135923

Yang, M., Howell, S. G., Zhuang, J., and Huebert, B. J. (2009). Attribution of aerosol light absorption to black carbon, Brown carbon, and dust in China – interpretations of atmospheric measurements during EAST-AIRE. *Atmos. Chem. Phys.* 9, 2035–2050. doi:10.5194/acp-9-2035-2009

Yao, T., Thompson, L. G., Mosbrugger, V., Zhang, F., Ma, Y., Luo, T., et al. (2012). Third Pole environment (TPE). *Environ. Dev.* 3, 52–64. doi:10.1016/j.envdev.2012.04.002

Zhang, X., Wang, Y., Zhang, X., Guo, W., and Gong, S. (2008). Carbonaceous aerosol composition over various regions of China during 2006. *J. Geophys. Res.* 113, D14111. doi:10.1029/2007jd009525

Zhang, N., Cao, J., Wang, Q., Huang, R., Zhu, C., Xiao, S., et al. (2018). Biomass burning influences determination based on PM 2.5 chemical composition combined with fire counts at southeastern Tibetan Plateau during pre-monsoon period. *Atmos. Res.* 206, 108–116. doi:10.1016/j.atmosres.2018.02.018

Zhang, L., Tang, C., Huang, J., Du, T., Guan, X., Tian, P., et al. (2021a). Unexpected high absorption of atmospheric aerosols over a western Tibetan plateau site in summer. *Geophys. Res. Atmos.* 126 (7). doi:10.1029/2020jd033286

Zhang, X., Liu, L., Chen, X., Gao, Y., Xie, S., and Mi, J. (2021b). GLC_FCS30: Global land-cover product with fine classification system at 30 m using time-series landsat imagery. *Earth Syst. Sci. Data* 13, 2753–2776. doi:10.5194/essd-13-2753-2021

Zhao, C., Yang, Y., Fan, H., Huang, J., Fu, Y., Zhang, X., et al. (2020). Aerosol characteristics and impacts on weather and climate over the Tibetan Plateau. *Natl. Sci. Rev.* 7, 492–495. doi:10.1093/nsr/nwz184

Zhao, Z., Cao, J., Shen, Z., Xu, B., Zhu, C., Chen, L. W. A., et al. (2013). Aerosol particles at a high-altitude site on the southeast Tibetan plateau, China: Implications for pollution transport from South Asia. *J. Geophys. Res. Atmos.* 118, 360. doi:10.1002/jgrd.50599

Zheng, H., Kang, S., Chen, P., Li, Q., Tripathee, L., Maharjan, L., et al. (2020). Sources and spatio-temporal distribution of aerosol polycyclic aromatic hydrocarbons throughout the Tibetan Plateau. *Environ. Pollut.* 261, 114144. doi:10.1016/j.envpol.2020.114144

Zheng, J., Hu, M., Du, Z., Shang, D., Gong, Z., Qin, Y., et al. (2017). Influence of biomass burning from South Asia at a high-altitude mountain receptor site in China. *Atmos. Chem. Phys.* 17, 6853–6864. doi:10.5194/acp-17-6853-2017

Zoller, W. H., Gladney, E. S., and Duce, R. A. (1974). Atmospheric concentrations and sources of trace metals at the South pole. *Science* 183, 198–200. doi:10.1126/science.183.4121.198

frontiers | Frontiers in Environmental Science

TYPE Original Research
PUBLISHED 06 January 2023
DOI 10.3389/fenvs.2022.1013875

OPEN ACCESS

EDITED BY
Longlei Li,
Cornell University, United States

REVIEWED BY
Chenglai Wu,
Institute of Atmospheric Physics (CAS), China
Yong Zhao,
Chengdu University of Information Technology, China

*CORRESPONDENCE
Hui Tang,
hui.tang@geo.uio.no

SPECIALTY SECTION
This article was submitted to Atmosphere and Climate, a section of the journal Frontiers in Environmental Science

RECEIVED 07 August 2022
ACCEPTED 19 December 2022
PUBLISHED 06 January 2023

CITATION
Tang H, Haugvaldstad OW, Stordal F, Bi J, Groot Zwaaftink CD, Grythe H, Wang B, Rao Z, Zhang Z, Berntsen T and Kaakinen A (2023), Modelling the 2021 East Asia super dust storm using FLEXPART and FLEXDUST and its comparison with reanalyses and observations.
Front. Environ. Sci. 10:1013875.
doi: 10.3389/fenvs.2022.1013875

Modelling the 2021 East Asia super dust storm using FLEXPART and FLEXDUST and its comparison with reanalyses and observations

Hui Tang[1,2,3]*, Ove Westermoen Haugvaldstad[1], Frode Stordal[1], Jianrong Bi[4], Christine D. Groot Zwaaftink[5], Henrik Grythe[5], Bin Wang[6], Zhimin Rao[7], Zhongshi Zhang[8,9,10], Terje Berntsen[1] and Anu Kaakinen[2]

[1]Department of Geosciences, University of Oslo, Oslo, Norway, [2]Department of Geosciences and Geography, University of Helsinki, Helsinki, Finland, [3]Climate System Research, Finnish Meteorological Institute (FMI), Helsinki, Finland, [4]College of Atmospheric Sciences, Lanzhou University, Lanzhou, China, [5]Norwegian Institute for Air Research (NILU), Kjeller, Norway, [6]School of Geography and Tourism, Shaanxi Normal University, Xi'an, China, [7]School of Electrical and Information Engineering, North Minzu University, Yinchuan, China, [8]Department of Atmospheric Science, School of Environmental Studies, China University of Geoscience, Wuhan, China, [9]School of Geographic Science, Nantong University, Nantong, China, [10]NORCE Norwegian Research Centre, Bjerknes Centre for Climate Research, Bergen, Norway

The 2021 East Asia sandstorm began from the Eastern Gobi desert steppe in Mongolia on March 14, and later spread to northern China and the Korean Peninsula. It was the biggest sandstorm to hit China in a decade, causing severe air pollution and a significant threat to human health. Capturing and predicting such extreme events is critical for society. The Lagrangian particle dispersion model FLEXPART and the associated dust emission model FLEXDUST have been recently developed and applied to simulate global dust cycles. However, how well the model captures Asian dust storm events remains to be explored. In this study, we applied FLEXPART to simulate the recent 2021 East Asia sandstorm, and evaluated its performance comparing with observation and observation-constrained reanalysis datasets, such as the Modern-Era Retrospective analysis for Research and Applications, Version 2 (MERRA-2) and CAMS global atmospheric composition forecasts (CAMS-F). We found that the default setting of FLEXDUST substantially underestimates the strength of dust emission and FLEXPART modelled dust concentration in this storm compared to that in MERRA-2 and CAMS-F. An improvement of the parametrization of bare soil fraction, topographical scaling, threshold friction velocity and vertical dust flux scheme based on Kok et al. (Atmospheric Chemistry and Physics, 2014, 14, 13023–13041) in FLEXDUST can reproduce the strength and spatio-temporal pattern of the dust storm comparable to MERRA-2 and CAMS-F. However, it still underestimates the observed spike of dust concentration during the dust storm event over northern China, and requires further improvement in the future. The improved FLEXDUST and FLEXPART perform better than MERRA-2 and CAMS-F in capturing the observed particle size distribution of dust aerosols, highlighting the importance of using more dust size bins and size-dependent parameterization for dust emission, and dry and wet deposition schemes for modelling the Asian dust cycle and its climatic feedbacks.

KEYWORDS

particle size distribution, PM10, extreme dust storm, dust emission, Lagrangian modelling

1 Introduction

Mineral dust aerosols have a large impact on climate, ecosystem functioning and human health (Huang et al., 2014; Li et al., 2022b). Dust can both scatter and absorb solar radiation (Li et al., 2022a), with a net negative radiative impact of dust being widely documented, especially over the dust source regions (Myhre and Stordal, 2001; Myhre et al., 2003). The direct radiation effect of dust accounts for a substantial fraction of the total dust aerosol feedback in the climate system (Li et al., 2021; Kok et al., 2018). Dust can also exert an indirect radiative effect by aerosol-cloud interactions. It can either serve as cloud condensation nuclei (CCN) that increase cloud cover and exert a net negative radiative impact (Jia et al., 2021), or modify the vertical profile of temperature and thus relative humidity and stability of the atmosphere, likely inducing less clouds and a net positive radiative impact (Huang et al., 2014). Better understanding the natural processes of the dust cycle is essential for estimating and projecting its climatic, ecological and societal impacts in the future, and providing guidance to alleviate the issues caused by severe dust storms.

Dust models describing dust emission, transport and deposition, are important tools for understanding the dust cycles. As part of the aerosol module, it has been implemented in many global and regional Earth system models or weather forecast models to describe complex dust aerosol feedbacks in the Earth system and provide a forecast of dust storms (Kok et al., 2014; Checa-Garcia et al., 2021). Most dust models capture the spatial patterns and seasonal cycles of global dust processes well. But large uncertainties and inter-model differences remain, particularly with regard to dust emission, and the dust seasonal cycles over North China and North America (Zeng et al., 2020; Zhao et al., 2022). Observations, especially remotely sensed aerosol optical depth, have been assimilated to improve dust modelling (Gong and Zhang, 2008; Benedetti et al., 2019; Randles et al., 2017). Nevertheless, dust emission and deposition are still poorly constrained in these models.

Off-line Lagrangian dispersion models that can trace the movement of an air parcel or particles in the atmopshere, provide an alternative way to study dust cycles. They do not include dust-climate feedbacks, and therefore can be focused on the dust emission and deposition processes (Sodemann et al., 2015). They can be run in both forward and backward modes and are particularly efficient for studying dust processes by comparing with site observations. Since these models use a numerically non-diffusive Lagrangian particle solver, they exhibit much less numerical diffusion than the grid-based Eulerian approach (Cassiani et al., 2016; Ramli and Esler, 2016) which is commonly employed in the weather prediction models or Earth system models. When the meteorological forcing data are available, these models require much less computing resources, and therefore allow for high-resolution representation of dust particle size bins in the simulation. However, there has been few Lagrangian trajectory models that implement dust emission and deposition schemes to properly describe the full dust cycle (Sodemann et al., 2015; Mallia et al., 2017). The Lagrangian particle dispersion model FLEXPART and the associated dust emission model FLEXDUST is one of the few models that can simulate the full global dust cycle and high-latitude regions in particular (Sodemann et al., 2015; Groot Zwaaftink et al., 2017, 2016; Zamora et al., 2022). The model has also been shown valuable in modelling regional dust events (Groot Zwaaftink et al., 2022), but its application to modelling extreme dust storms in specific regions, like East Asia, remains to be tested.

East Asia is one of the natural hot spots for dust storms (Shao and Dong, 2006; Chen et al., 2017). The emitted dust from the desert regions in central Asia, such as the Taklimakan and Gobi deserts, can give rise to strong episodic dust storms swiping over East Asia, and sometimes, even being transported to North America (Uno et al., 2009) and high Arctic regions (Huang et al., 2015). Asian dust storms mostly occur in spring, due to drier soil conditions, strong wind and cold surges in the season (Shao and Dong, 2006). The frequency of Asian dust storm events has decreased rapidly in the past decades, particularly over northern China, which has been attributed to the weakened temperature gradients and decreased zonal winds in spring and winter associated with the enhanced warming in the Arctic (Liu et al., 2019). In addition, the large-scale vegetation restoration projects in the arid regions of northern China have also contributed to the recent inhibition of dust emission (Wang et al., 2021).

Contrary to the long-term decline of the Asian dust storms, the 2021 East Asia sandstorm (Figure 1), beginning from the Eastern Gobi desert steppe in Mongolia on 14 March, and later spreading over North China and the Korean Peninsula, was the most severe sandstorm to hit China in a decade (Filonchyk, 2022). It has been found that the barer, drier and more loosened soil due to the anomalous early snow melting and a lack of precipitation in spring over the dust source region, together with the exceptionally strong Mongolian cyclone developed over the source region (i.e., central and eastern Mongolia), had triggered the emission and transport of enormous amounts of dust to East Asia during this event (Gui et al., 2022; Yin et al., 2022). The 2021 East Asia sandstorm has provided a unique testbed for dust modelling, particularly in regard to dust emission schemes which has the largest uncertainties (Jin et al., 2022; Wang et al., 2022). The ability of dust models in reproducing such extreme dust events will be critical for understanding the causes and projecting the occurrences of such extreme events in the future.

In this study, we applied FLEXDUST and FLEXPART to simulate the 2021 East Asia dust storm event. We focus on evaluating and improving the performance of FLEXDUST and FLEXPART in reproducing the strength and spatio-temporal pattern of the dust cycle during the event as shown by available observation and observation-constrained reanalysis data. In Section 2, we introduce the FLEXDUST and FLEXPART models and the observation and reanalysis data used in this study. In Section 3, we examine the ability of FLEXDUST and FLEXPART in depicting dust emission, concentration and deposition during the dust storm event. In Section 4, the consistency between forward and backward FLEXPART simulations in simulating dust concentration at individual sites are analyzed, followed by the discussion on the biases of FLEXDUST and FLEXPART in representing the spike of dust concentration during the dust storm event, and their comparison with the reanalysis data. The results of this study are expected to provide valuable insights into further development and application of FLEXDUST and FLEXPART for studying the Asian dust cycles on longer time scales.

2 Materials and methods

2.1 FLEXPART and FLEXDUST

We used a recent FLEXPART development branch (v10.4-36-g1228ef7) based on version 10.4 (Pisso et al., 2019) (access from: https://www.flexpart.eu/browser/flexpart.git). Compared to the previous model versions, FLEXPART version 10.4 has been

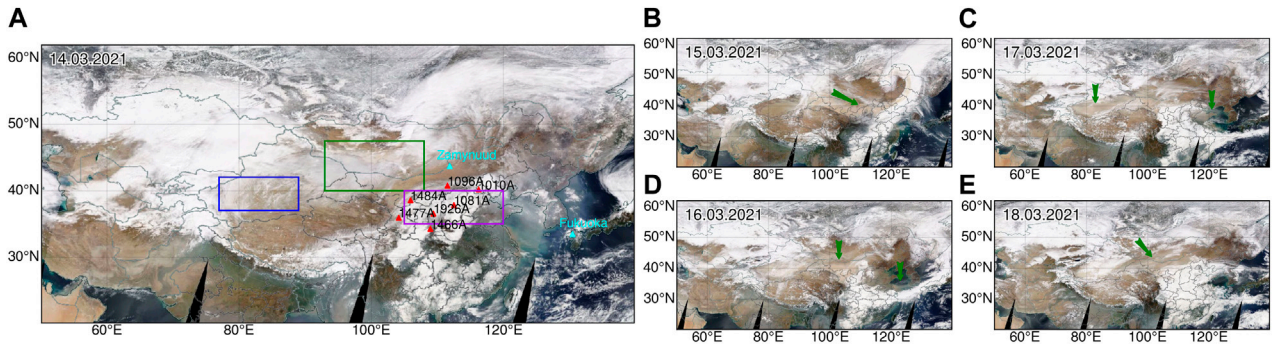

FIGURE 1
Terra MODIS true color image showing the 2021 East Asia dust storm event during March 14-18, 2021 **(A–E)** (from: https://worldview.earthdata.nasa.gov). The green arrows denotes the dust storm visible from the images. The red triangles in **(A)** denote the sites for the backward simulations of FLEXPART and the observation sites used in Figure 5. The blue triangles in **(A)** denote the observation sites used in Figure 6. The blue, green and purple boxes in **(A)** denote the Taklimakan Desert (TA), Gobi Desert (GB), and North China (NC) used in Table 2, respectively.

improved in several aspects, including a new turbulence scheme for the convective boundary layer considering the skewness in the vertical velocity distribution and vertical air density gradient, a new gravitational settling parameterization for aerosols, a rewritten wet deposition scheme based on cloud information from the meteorological input fields, and a new dust mobilization tool (i.e., FLEXDUST) to work with FLEXPART for simulating the full dust cycle. More details about these improvements and available options for these processes can be found in Pisso et al. (2019). In this study, the original FLEXPART code was only adapted for using new meteorological forcing.

FLEXDUST is a stand-alone dust emission model that can provide mineral dust emissions as gridded output or release files which contain the position and number of dust particles emitted at each time step that can be directly read by FLEXPART as input (Groot Zwaaftink et al., 2016). Depending on the types of FLEXPART simulations, FLEXDUST can be used as either a preprocessing tool providing release files for the forward simulation of FLEXPART, or a postprocessing tool yielding gridded output that can work together with the output of the backward simulation of FLEXPART to estimate dust concentration or deposition at a receptor point. The vertical dust flux in FLEXDUST is estimated based on Marticorena and Bergametti (1995) by default. A soil texture-dependent minimum threshold friction velocity for wind erosion according to Shao and Lu (2000) is assumed for dust emission to occur. The dust emission rate is further scaled by the erodibility of the surface, which is parameterized according to the bare ground fraction estimated using land cover data from Global Land Cover by National Mapping Organizations (GLCNMO), topographic depressions using Eq. 1 (Ginoux et al., 2001), as well as soil moisture and snow cover. We refer to Groot Zwaaftink et al. (2016) for more detailed description of FLEXDUST.

In this study, we used the most recent version of FLEXDUST (https://git.nilu.no/christine/flexdust, commit: e60cabd). For the default setting experiment (referred to as FLEXDUST-default hereafter), the model was only modified to use new meteorological forcing, and write specific output. In addition, soil texture data from World Soil Information (ISRIC) (Poggio et al., 2021) and land cover data from GLCNMO version 3 (Kobayashi et al., 2017) were used, following the study by Haugvaldstad (2021) who found that the update of soil texture data is necessary for capturing the dust source regions in Asia.

For the improved setting experiment (referred to as FLEXDUST-update), we further improved the model in the following aspects to reduce the biases in simulating dust emission.

(1) Default topographic scaling accounting for the potential influence of local topography on the erodibility of soil in FLEXDUST is based on Ginoux et al. (2001) (see Eq. 1).

$$S = \left(\frac{z_{max} - z_i}{z_{max} - z_{min}} \right)^5 \tag{1}$$

Here z_i is the local elevation, $z_{\max}$ and $z_{\min}$ are the maximum and minimum elevation in a 10° × 10° area. A 10° × 10° box is commonly used when topographical data are on coarse spatial resolution. But when topographical data have high spatial resolution, local depressions at finer scale can be missed by this definition. Therefore, we used different sizes of the box to derive a topographic scaling S similar to the approach proposed for creating global Sand and Dust Storms Source Base-map (https://maps.unccd.int/sds/).

$$S = \frac{(S_{9\times9} + S_{6\times6} + S_{3\times3} + S_{1.2\times1.2})}{4} \tag{2}$$

where $S_{9\times9}$, $S_{6\times6}$, $S_{3\times3}$ and $S_{1.2\times1.2}$ are topographic scaling factors using 9°, 6°, 3°, and 1.2°boxes, respectively.

(2) In FLEXDUST-default, the land cover types that could emit dust are limited to bare ground, and sparse vegetation types in GLCNMO classification scheme. It has, however, been widely observed that both herbaceous and crop land cover types in GLCNMO may have at least seasonal dust emission, especially in winter and spring. Hence, we expand the land cover types in GLCNMO that can contribute to bare ground fraction and thus dust emission in FLEXDUST-update. The total effect of the updates (1) and (2) on the erodibility is shown in Figure 2.

(3) In FLEXDUST, the threshold friction velocity u_{*t} is calculated using the expression from Shao and Lu (2000):

$$u_{*t}(d_p) = \sqrt{An\left(\frac{\rho_p}{\rho_a} g d_p + \frac{\gamma}{\rho_a d_p}\right)} \tag{3}$$

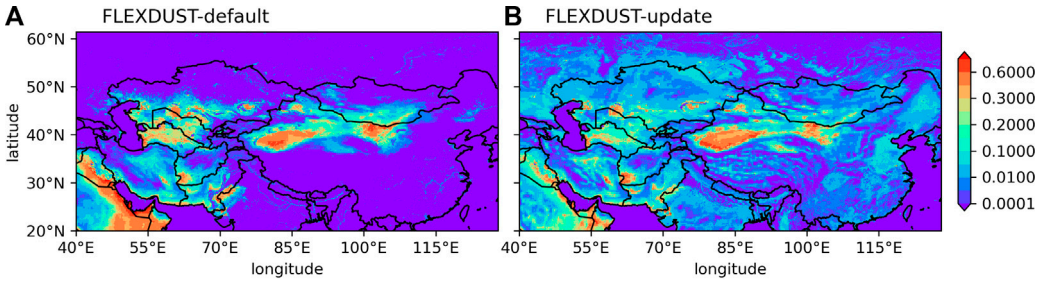

FIGURE 2
Erodibility of the default FLEXDUST (FLEXDUST-default) **(A)** and updated FLEXDUST (FLEXDUST-update) **(B)**.

TABLE 1 Summary of the settings for dust modelling in FLEXDUST and FLEXPART, MERRA-2 and CAMS-F.

	Resolution (lon × lat × lev)	Size bins (μm in diameter)	Density (kg/m^{-3})	Emission	Dry deposition	Wet deposition	Assimilation	References
FLEXDUST and FLEXPART	0.3° × 0.3° × 137L	0.04, 0.22, 0.71, 1.304, 2.057, 3.53, 6.1, 8.63, 12.25, 17.32	2500	TFV: Shao and Lu. (2000); **Vertical fluxes:** Marticorena and Bergametti. (1995) or Kok et al. (2014); Size **distribution:** Kok. (2011); **Erodibility:** Ginoux et al. (2001)	**Gravitational settling:** a function of particle size, density and dynamic viscosity of air Näslund and Thaning, (2007). **Dry deposition:** a function of gravitantional settling, surface type and meteorological conditions Wesely. (1989)	**In-cloud scavenging:** efficiencies increase with particle size Grythe et al. (2017). Below-cloud scavenging: a function of the sizes of both the aerosol and falling hydrometeors Kyrö et al. (2009); Laakso et al. (2003)	No	Pisso et al. (2019); Grythe et al. (2017); Groot Zwaaftink et al. (2016)
MERRA-2	0.5° × 0.625° × 72L	1.46(0.2–2.0), 2.8(2.0–3.6), 4.8(3.6–6.0), 9(6.0–12.0), 16(12–20)	2500, 2650, 2650, 2650, 2650	**TFV:** Marticorena and Bergametti. (1995); **Vertical fluxes:** Ginoux et al. (2001); **Size distribution:** Tegen and Lacis. (1996); **Erodibility:** Ginoux et al. (2001)	**Gravitational settling:** a function of particle size, density and viscosity of air Fuks. (1989). **Dry deposition:** a function of surface type and meteorological conditions Wesely. (1989)	**In-cloud scavenging:** Chin et al. (2000); Ginoux et al. (2001). Below-cloud scavenging: Chin et al. (2000); Ginoux et al. (2001)	AOD from MODIS Collection 5, AVHRR, MISR and AERONET.	Gelaro et al. (2017); Randles et al. (2017); Chin et al. (2002)
CAMS-F	0.4° × 0.4° × 137L	0.06–1.1, 1.1–1.8, 1.8–40	2610	**TFV:** Marticorena and Bergametti. (1995); **Vertical fluxes:** Marticorena and Bergametti. (1995); **Size distribution:** Kok. (2011); **Erodibility:** Ginoux et al. (2012)	Gravitational settling: a function of particle size, density and viscosity of air Morcrette et al. (2009). **Dry deposition:** a function of particle diameter, surface type and meteorological conditions Zhang et al. (2001)	**In-cloud scavenging:** fixed efficiencies for dust, the release of aerosol particles due to re-evaporation is considered. Below-cloud scavenging: fixed efficiencies for dust	AOD from MODIS collection 6, MODIS Dark Target and Deep Blue data; the MetOp Polar Multi-sensor Aerosol product (PMAp) provided by EUMETSAT	Rémy et al. (2022)

where ρ_p and ρ_a are density of dust particle and air, respectively. d_p is particle diameter, g is acceleration due to gravity. The parameters An = .0123 and γ = 2.9 × 10^4 kg/s^2 are from Shao and Lu (2000) in FLEXDUST-default. In FLEXDUST-update, we modified An to .0025 to lower the threshold friction velocity for dust emission.

(4) The default scheme describing vertical dust fluxes from the surface is based on Marticorena and Bergametti (1995) (referred to as MB95 scheme) and is used in FLEXDUST-default. In contrast, the scheme based on Kok et al. (2014) (referred to as KOK14) is used in FLEXDUST-update. We note that different global tuning factors have been used in the MB95 scheme (4.8×10^{-4}) and the KOK14 scheme (4.8×10^{-3}) to produce comparable results.

2.2 Model experiments

The 3-hourly meteorological forcings for both FLEXDUST and FLEXPART are derived from the fifth generation atmospheric reanalysis of the global climate (ERA5) produced by the European Centre for Medium-Range Weather Forecasts (ECMWF) (Hersbach et al., 2018) using Flex_extract (version 7.0.4, downloaded from: https://www.flexpart.eu/wiki/FpInputMetEcmwf), a pre-processing tool developed for preparing the GRIB files needed by FLEXDUST and FLEXPART from the ECMWF Meteorological Archival and Retrieval System (Tipka et al., 2020). The domain of the meteorological forcing in our application covers 10–160° east longitude and 10–80° north latitude with 30 km horizontal resolution (T639) and 137 vertical levels from surface to .01 hPa (80 km).

In this study, both FLEXDUST-default and FLEXDUST-update were run for the whole month of March in 2021 with spatial resolution of .1° covering the major dust source regions (20°–62° north latitude and 40°-128° east longitude), and temporal resolution of 1 h. The emitted dust particles are assumed to be spherical, and are represented by 10 size bins (see Table 1). The volume size distribution of the 10 size bins follows the brittle fragmentation theory according to Kok (2011) (see Supplementary Figure S1) and is assumed to be independent of soil texture and wind conditions as saltation and sand-blasting have been considered as the main mechanisms contributing to dust emission.

FLEXPART was run in both forward and backward modes in this study. Results are independent of whether the model is run forward or backward in time. Direction of modelling is therefore chosen based on what is numerically efficient and what analyses are desired. The forward simulation (referred to as FLEXPART-F) started on 01.03.2021 well before the dust storm events (14-18.03.2021) to capture the potential contribution of long-living dust aerosols (> 5 days) emitted prior to the event. We followed the default model settings as indicated in Pisso et al. (2019), except that the influence of sub-grid scale orographic variations on atmospheric boundary layer height was turned on, and the dust particles in the model have an age limit of 20 days. The output of FLEXPART-F, e.g., dust concentration, and dry and wet deposition, has a spatial resolution of .1°covering 20°–65°north latitude and 50°-140°east longitude and 25 vertical levels from near surface (100 m above surface) to the stratosphere (18 km above surface) to allow better comparison with different observation data. The original output of FLEXPART-F in a binary format was converted into a netcdf format using REFLEXIBLE (https://github.com/spectraphilic/reflexible) for further analyses.

Backward FLEXPART simulations (referred to as FLEXPART-B) were setup for specific receptor sites. In each simulation, computational dust tracer particles were released at hourly intervals throughout the dust storm event (from 10.03.2021 to 20.03.2021). Following the release at the receptor, the particles were traced backwards in time for 10 days (240 h), which has been shown to be sufficient for capturing the Asian dust cycle (Haugvaldstad, 2021). The output of FLEXPART-B is the emission sensitivity (*ES*) which corresponds to a distribution of all possible dust sources that could influence the dust concentration at the receptor location at a given time interval over the 10 days backward period. The predefined output region of *ES* is at a resolution of .1°covering 25°–65° latitude and 50°–128° longitude. The *ES* is then combined with the dust emission field from FLEXDUST with the same time stamp and summed up temporally over the 10 days backward period to yield a map of source contribution (SC) at a given time (see Eq. 4). Summing up the (SC) spatially over the output domain then gives the concentration at the receptor at specific time interval (1-hourly averaged). The details of the FLEXPART-B derivation and how it is related to FLEXPART-F are described in Seibert and Frank (2004).

$$SC_r(t,j,i) = \sum_{bt=0}^{-240}\left(ES_r(t+tb,j,i)\frac{E(t+bt,j,i)}{H}\right) \quad (4)$$

where ES_r is the emission sensitivity field (unit: s) for a receptor from FLEXPART-B simulation. E is the emission field from FLEXDUST (unit: $kgm^{-2}s^{-1}$). H = 100 is the hight (m) of the surface atmospheric level where ES_r is derived. SC_r is the source contribution (unit: kgm^{-3}) for a receptor. t and bt denote the time when particles are released from the receptor, and the backward tracing time (unit: hour), respectively. j and i are the indices of latitude and longitude of a grid cell, respectively.

In FLEXPART-B, the same 10 dust size bins as in FLEXPART-F were simulated individually to generate *ES* for each dust size bin. The emission of each dust size bin was derived by scaling the total emission with their volumetric fraction assumed in FLEXDUST (See Supplementary Figure S1), so that the variations of emission in space and time were taken into account equally in FLEXPART-B and FLEXPART-F simulations. Summing up the estimated dust concentration of each size bin at a receptor gives the total dust concentration and also the distribution of the 10 dust size bins at a receptor. There are in total 7 receptor sites across North China chosen for the FLEXPART-B simulations (see Figure 1), as they cover the area that experienced the most severe dust storm during the event, and also show certain differences in the timing and strength of the dust storm along the west-east and north-south gradient.

2.3 Reanalysis and observation dataset

2.3.1 MERRA-2 and CAMS-F

To evaluate the performance of FLEXDUST and FLEXPART in depicting the full dust cycle of the 2021 East Asia dust storm, the Modern-Era Retrospective Analysis for Research and Applications, version 2 (MERRA-2) produced by the NASA's Global Modeling and Assimilation Office (Gelaro et al., 2017) and the global atmospheric composition forecast (referred to as CAMS-F) produced by the Copernicus Atmosphere Monitoring Service (Inness et al., 2019) were used. MERRA-2 was generated using the Goddard Earth Observation System (GEOS-5) with a 3D variational data assimilation system that assimilates aerosol optical depth (AOD) from various ground- and space-based remote sensing platforms, improving estimates of aerosol properties over the simulations without AOD assimilation (Randles et al., 2017). MERRA-2 has an

hourly output on spatial resolution of .5° × .625° and 72 hybrid-eta levels from the surface to .01 hPa. The dust emission scheme in MERRA-2 is based on Ginoux et al. (2001) and Marticorena and Bergametti (1995) using five size bins (Table 1). The dry and wet deposition are based on the GOCART aerosol module (Ginoux et al., 2001; Chin et al., 2002). It has been demonstrated that MERRA-2 is capable of characterizing the three-dimensional evolution of dust aerosols in East Asia and Sahara (Buchard et al., 2017; Yao et al., 2020) comparing with satellite and ground-based observations.

CAMS-F uses the Integrated Forecasting System (IFS) that also produces ECMWF weather forecasts, but with additional modules enabled for aerosols, reactive gases and greenhouse gases that have been developed within CAMS (Rémy et al., 2022). It provides the estimation of dust aerosols with three size bins (Table 1) and the spatial resolution of .45° × .45° and 137 vertical levels. CAMS-F does not assimilate observations throughout the prediction period. It, however, starts every 12 h with initial conditions obtained by combining a previous forecast with the satellite retrievals of many atmospheric constituents including AOD from different remote sensing platforms through data assimilation. CAMS-F, in 48 h projection, has been shown to capture the Asian dust cycle (especially the dust AOD) better than the unconstrained model when comparing with observations (Benedetti et al., 2019). We use CAMS-F instead of the CAMS global reanalysis (known as EAC4) which assimilates observations at each time step, because CAMS-F does not only provide the dust aerosol mixing ratio and optical depth, but also emission, dry and wet deposition rates which are absent in EAC4. This allows us to better quantify the full dust cycle during the dust storm. Details of the dust emission, and dry and wet deposition schemes used in CAMS-F are summarized in Table 1.

2.3.2 Observation dataset

2.3.2.1 PM_{10} concentrations from the CNEMC network

Hourly averaged PM_{10} (Particle matter with an aerodynamic diameter smaller than 10 μ m) for different sites in northern China (Figure 1) were obtained from the air quality monitoring network operated by China National Environmental Monitoring Center (CNEMC). The dataset was created in 2013 and is constantly updated thereafter. The method for measuring PM_{10} is described by the National Environmental Protection Standards HJ 653–2013 (MEP, 2013). The air quality monitoring stations are located at least 50 m from any noticeable stationary sources of pollution, and instrument inlets were located at least 1 m above the roof of a building or wall.

2.3.2.2 Particle size distrisbution

At the Semi-Arid Climate and Environment Observatory of Lanzhou University (SACOL) (1477A in Figure 1), a GRIMM Optical Aerosol Spectrometer (model EDM180) has been devised to simultaneously measure dust particle size distribution and mass concentrations (e.g., PM_{10}, $PM_{2.5}$, and $PM_{1.0}$) based on the principle of light scattering with scattering angle of 0°–90°. It can provide 31 size bins ranging from .25 to 32 μm. The measurement range and accuracy of mass concentration are expected to be .1-6000 and .2 $\mu g.m^{-3}$, respectively. An automatic Nafion isothermal dehumidification system is installed inside the sampling tube, which could effectively retain some semivolatile aerosol compounds. The sample flow rate is 1.2 L/min and the measurement uncertainty of the dust size distribution is ±5% of the maximum range (Grimm and Eatough, 2009). Since the station is well selected to be representative of the region (Huang et al., 2008), we consider the uncertainties caused by spatial heterogeneity to be small. The size distribution of dust aerosol measured during the 2021 East Asia dust storm event was used in this study to compare with the modelled distribution of different dust size bins.

2.3.2.3 Ground-based lidar observation

The Asian dust and aerosol lidar observation network (AD-Net) (Shimizu et al., 2004) is a lidar network continuously monitoring the vertical profile of dust and other aerosols with high temporal (15 min) and vertical (30 m) resolution in real time. Over more than 20 sites in East Asia are included in AD-Net. The standard lidar system at each site is a two-wavelength (1,064 nm, 532 nm) polarization sensitive Mie-scattering lidar. In this study, we chose one site close to the dust source region (Zamynuud in Mongolia) and one site located in the deposition region (Fukuoka in Japan) to evaluate the vertical dust profile simulated by FLEXDUST and FLEXPART. The data was downloaded from: https://www-lidar.nies.go.jp/AD-Net/. The geographical locations of the two sites are shown in Figure 1. The variables used in this study were the 532 nm aerosol extinction coefficient and attenuated backscatter coefficient. For more details on the processing of lidar data from AD-Net and its quality control, we refer to the original data website.

3 Results

3.1 Dust source of the 2021 East Asia dust storm

Figure 3 shows daily averaged dust emission during the dust storm event (13-17.03.2021) simulated by FLEXDUST-update, along with MERRA-2 and CAMS-F. All the models show the strongest dust emission over the Gobi Desert (especially the Eastern Gobi desert steppe) at the start of the dust storm event (14.03.2021). Later on, the center of high dust emission moved westward with weakened dust emission in the Gobi Desert, but enhanced dust emission in the Taklimakan desert. FLEXDUST-default seriously underestimates dust emission compared to MERRA-2 and CAMS-F (Supplementary Figure S2). In particular, dust emissions from the Taklimakan desert and eastern Inner Mongolia are missing throughout the dust storm event. In comparison, FLEXDUST-update shows persistently high dust emission in both the Taklimakan desert and Qaidam basin (Figure 3), which is more consistent with MERRA-2 and CAMS-F. The strength of emission over the main dust source regions (e.g., Gobi and Taklimakan deserts) is the strongest in CAMS-F while FLEXDUST-update and MERRA-2 are similar to each other (Table 2). FLEXDUST-update still shows slightly lower emission over North China than CAMS-F and MERRA-2.

3.2 Dust concentration of the 2021 East Asia dust storm

Figure 4 illustrates vertically integrated total dust concentration simulated by FLEXPART-F using the emission from FLEXDUST-update. Similar to CAMS-F and MERRA-2, the highest total dust

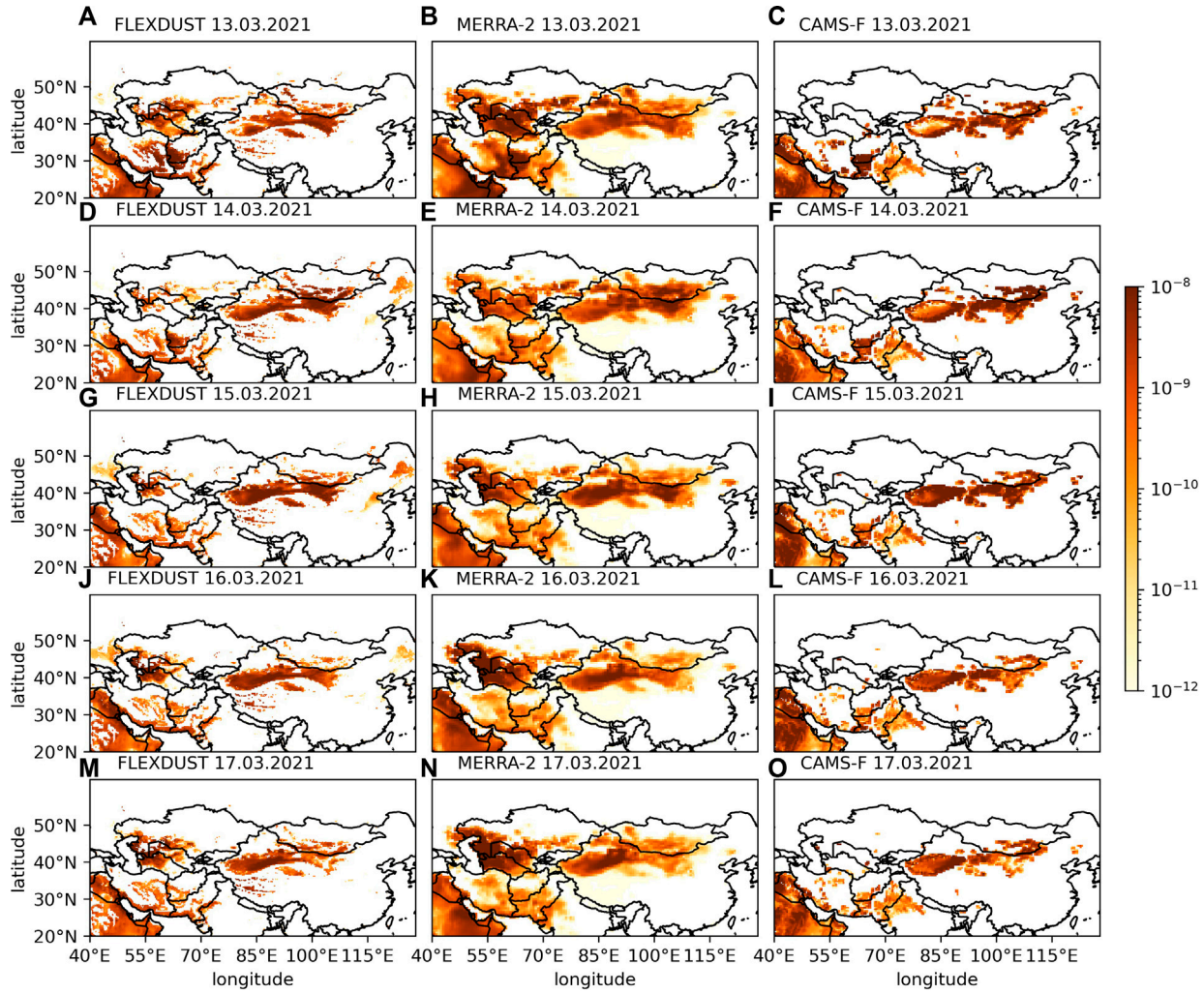

FIGURE 3
Daily average of dust emission (kg m^{-2} s^{-1}) during the dust storm event, each of the days from 13.03 to 17.03.2021. **(A,D,G,J,M)** FLEXDUST-update, **(B,E,H,K,N)** MERRA-2, **(C,F,I,L,O)** CAMS-F. Dust emission of FLEXDUST-default using MB95 scheme is shown in Supplementary Material.

concentration over the dust source region (Taklimakan and Gobi deserts) is well depicted in FLEXPART. In addition, the movement of the high dust concentration belt swiping from Mongolia at the beginning of the dust storm event to northern China and southern Japan in the later stage of the dust storm event (Figure 4), as observed in MERRA-2 and CAMS-F as well as the satellite image (Figure 1), is also captured in FLEXPART-F. In contrast, FLEXPART-F using the emission from FLEXDUST-default shows much lower total dust concentration than that in MERRA-2 and CAMS-F (Supplementary Figure S3). In general, the spatio-temporal pattern of total dust concentration in FLEXPART-F is more similar to that in CAMS-F than in MERRA-2. While MERRA-2 shows dust ($> 10^{-5}$ kg m^{-3}) all over the Asian domain during the dust storm event (Figure 4), both CAMS-F and FLEXPART-F indicate an absence or very low concentration of the dust aerosol in southern China, central Asia, and northern India.

To further evaluate the performance of FLEXDUST and FLEXPART in simulating surface dust concentration, we compared the modelled dust PM_{10} with the observed dust PM_{10} at individual sites over North China (Figure 5). The concentration estimated by FLEXPART-B are shown together with FLEXPART-F to test the consistency and robustness of the two approaches for estimating dust concentration at a site. All the models underestimate the dust PM_{10} peak as indicated by observation by an order of magnitude, except Xi'an (1466A), where the model and observation match well with each other. The dust PM_{10} simulated by FLEXPART-F and FLEXPART-B agrees well with each other and is also consistent with that from MERRA-2 and CAMS-F in terms of both timing and magnitude. Over the Beijing (1010A) and Hohhot (1096A) sites, CAMS-F exhibits a higher dust PM_{10} peak than MERRA-2 and FLEXPART, likely owing to the higher emission strength of CAMS-F over Mongolia and the eastern Inner Mongolia, which are the major dust source for the two sites. In contrast, at the more western and southern sites such as Xi'an (1466A), Yan'an (1926A) and Yinchuan (1484A), dust PM_{10} simulated by MERRA-2 and FLEXPART are generally higher than that in CAMS-F, especially for the dust PM_{10} peak during 19-20.03.2021.

Figure 6 shows the temporal evolution of the vertical profile of dust concentration over sites with lidar measurement of dust aerosols. At the Mongolian site (Zamynuud) which is in the dust source region, the

TABLE 2 Dust budget over the major dust source and deposition regions during the 2021 East Asia dust storm event (14/03/2021 00:00 - 18/03/2021 00:00, Beijing time). TA: Taklimakan desert (77–89°E, 37–42°N), GB: Gobi desert (93–108°E, 40–47.5°N), NC: North China (105–120°E, 35–40°N), AD: Asian domain (50–140°E, 20–65°N).

	Emission (kg/s)	Dry deposition (kg/s)	Wet deposition (kg/s)	Total deposition (kg/s)	Concentration change (kg/s)	Net transport (kg/s)
FLEXPART-F						
TA	2,238	1,070	92	1,162	1,340	264
GB	2,231	990	49	1,039	−27	−1,218
NC	85	121	52	173	145	233
AD	11,653	5,066	1,159	6,225	1,297	−41,31[a]
MERRA-2						
TA	2,273	1,496	23	1,511	1,102	340
GB	2,056	945	24	965	−239	−1,330
NC	133	163	41	203	−38	32
AD	16,104	12,752	3,483	15,533	4,937	4,366
Global[b]	50,545	35,610	15,379	50,989		
CAMS-F						
TA	6,820	6,935	219	7,154	1,627	1,961
GB	7,774	5,913	64	5,977	250	−1,547
NC	331	584	117	700	230	600
AD	25,494	24,487	4,623	29,110	4,764	8,380
Global[b]	51,497	144,216	65,005	209,221		

[a]The negative value arises because there is no dust transportation from the outside of the model domain in FLEXPART-F.
[b]Multiyear global average from Zhao et al. (2022).

starting of the dust storm (i.e., high local dust emission from the surface) on 14.03.2021 is visible in both attenuated backscatter coefficient and aerosol extinction coefficient at 532 nm (Figures 6A, C). The dust event is followed by a reduced local dust emission, but a salient high-level transport of dust from other source regions during 15-16.03.2021. The presence of high-level (as high as 10 km above surface) dust plume at the location, is consistent with the results from CALIPSO (Filonchyk, 2022). A second local dust emission occurred on 18.03.2021, but this dust event is mostly restricted to the lower and middle troposphere. FLEXPART-F captures these observed features well (Figure 6E), and the temporal-vertical structure is quite similar to that in CAMS-F, except that a strong local dust emission persists during 15-16.03.2021 in CAMS-F. Compared to FLEXPART-F and CAMS-F, MERRA-2 tends to overestimate dust concentration in the middle and upper troposphere (Figures 6G,I).

At the Fukuoka site in Japan which is far from the dust source regions, the influence of the dust storm event is clearly shown in both FLEXPART-F and CAMS-F (Figures 6F,J), and is also present but less obvious in the lidar observation and MERRA-2. The arrival of the dust plume first appears in the upper troposphere on 16.03.2021, while the majority of the dust transported through mid-troposphere arrived on 17.03 and 18.03.2021. As the location is at the coast, the constantly high extinction attenuated backscatter coefficient (Figure 6D) likely arises from the influence of sea salt aerosols. Both FLEXPART-F and the reanalysis data suggest low dust concentration in the lower troposphere for the entire period except the beginning of 17.03.2021.

The ability of FLEXPART in simulating the size distribution of dust aerosols at the surface is evaluated against the observation from the SACOL site (Figure 7). The fluctuation in dust size distribution mainly occurs on 14.03, 16.03, and 19.03.2021 with a sharp increase of coarse particles (> 10 μm), but a decrease of medium size particles (1–10 μm). The changes of the particle size distribution correspond well to the start of the local dust storm events (i.e., high PM_{10} peak) (cf. Figures 5E, 7). It is noticed that such changes in dust particle size distribution are hardly captured by MERRA-2 and CAMS-F, both of which show little variation throughout the dust storm event. Both FLEXPART-F and FLEXPART-B exhibit larger variation in the dust particle size distribution than MERRA-2 and CAMS-F, such as the decrease (increase) of 1–10 μm (0–1 μm) dust size bin on 19.03.2021. The size distribution derived from FLEXPART-F ($0.1 \times 0.1^\circ$ box) appears to be more fluctuated than FLEXPART-B during the dust storm event (Figure 7C). The spatial averaging ($1 \times 1^\circ$ box) of the results of FLEXPART-F significantly smoothes the variation and displays a better agreement with the results from FLEXPART-B.

To further analyze the cause of the variations in the dust particle size distribution at the SACOL site, the emission sensitivity and the source contribution for different dust size bins during individual episodes with a strong increase in coarse particles, i.e., 14.03, 16.03, 19.03.2021 are shown in Figures 8, 9 and Supplementary Figure S5, respectively. The major dust source regions on 14.03 and 19.03.2021 are quite different. On 14.03.2021, the dust, including coarse particles, was mainly from the west along the northern slope of the Tibetan Plateau, transported by energetic westerly and north westerly wind (Figure 8). In contrast, on 19.03.2021, the dust was mainly from the northern and northeastern source regions, and the

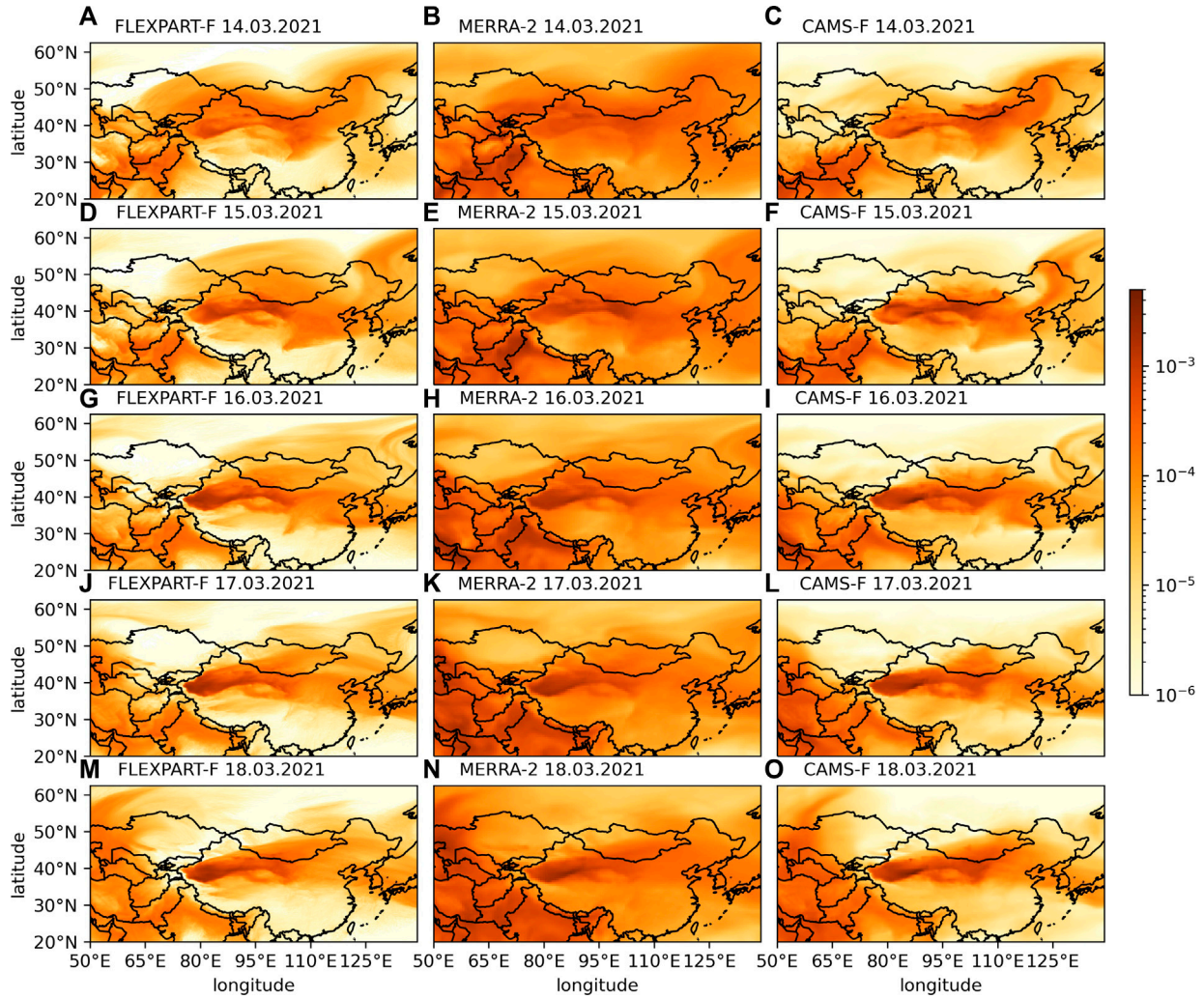

FIGURE 4
Daily average of vertically integrated dust concentration (kg m^{-2}) during the dust storm event. **(A,D,G,J,M)** FLEXPART-F using the emission from FLEXDUST-update, **(B,E,H,K,N)** MERRA-2, **(C,F,I,L,O)** CAMS-F.

transport of coarse dust particles to the SACOL site was much weaker than that of the finer dust particles (Figure 9). The difference in the dominant wind system and source regions may explain why the high proportion of coarse dust particles on 14.03.2021 are well captured in FLEXPART, but not on 19.03.2021. The coarse dust particles observed on 19.03.2021 were likely derived from the nearby regions northeast of the SACOL site (Figure 9C), where there is little dust emission in FLEXDUST.

3.3 Dust deposition of the 2021 East Asia dust storm

The spatio-temporal pattern of dry deposition is quite similar to that of the dust concentration (cf. Figures 4, 10). Both FLEXPART-F and reanalysis data show high dry deposition in dust source regions such as the Taklimakan and the Gobi deserts. On average, CAMS-F has the strongest dry deposition, while FLEXPART-F has lower dry deposition similar to MERRA-2.

The wet deposition in FLEXPART-F is also weaker than in CAMS-F and the strength is closer to MERRA-2 (Figure 11). The spatial pattern of wet deposition is closely related to precipitation in the model. The precipitation and cloud fields used in FLEXPART-F are derived from ERA5, which shares the same IFS modelling system as CAMS-F, and thus exhibits good similarity to CAMS-F in their spatial structures (see Supplementary Figures S6, S7). Accordingly, FLEXPART-F and CAMS-F display quite similar spatio-temporal pattern of wet deposition compared to that of MERRA-2. For instance, the presence of wet deposition in northern China on 16.03.2021 (Figures 11G–I), and the strong wet deposition over the Tibetan Plateau and the Taklimakan desert on 18.03.2021 (Figures 11M–O), are observed in both FLEXPART-F and CAMS-F, but not shown in MERRA-2 due to its different precipitation and cloud fields.

3.4 Dust budget of the 2021 East Asia dust storm

The total dust budget for the major source and deposition regions of the East Asia dust storm in FLEXPART-F is rather consistent with that in CAMS-F and MERRA-2 (Table 2). All the models indicate that

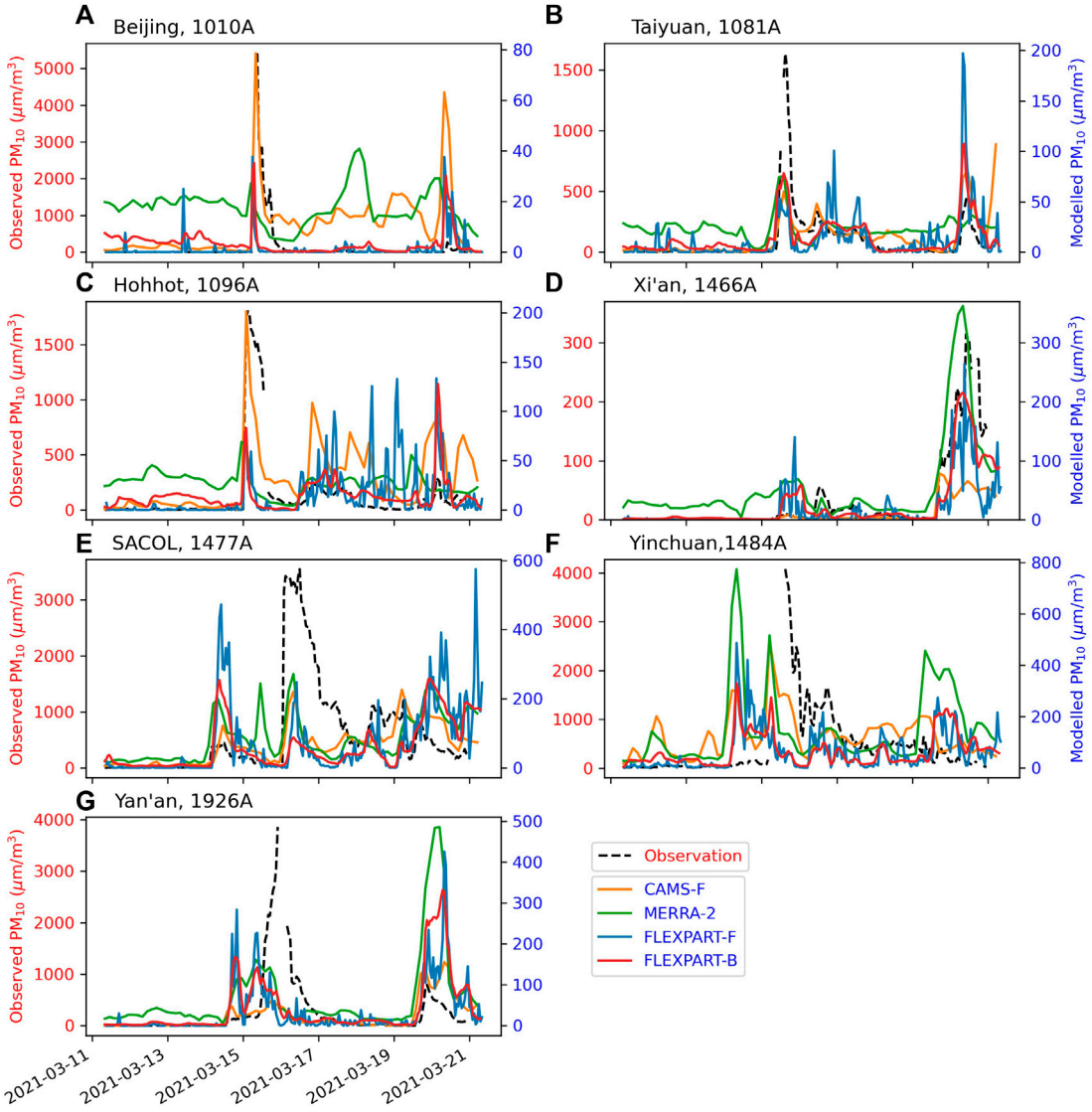

FIGURE 5
Comparison of modelled dust PM_{10} ($\mu g.m^{-3}$) at the surface (0–100 m) with observations over sites in China. **(A)** Beijing (1010A), **(B)** Taiyuan (1081A), **(C)** Hohhot (1096A), **(D)** Xi'an (1466A), **(E)** SACOL (1477A), **(F)** Yinchuan (1484A), **(G)** Yan'an (1926A). The names in brackets are the site codes used in the CNEMC network. The observed dust PM_{10} is derived from observed total PM_{10} scaled by dust:total PM_{10} ratio estimated by CAMS-F. The location of the sites are shown in Figure 1. How dust PM_{10} was derived for FLEXPART, MERRA-2 and CAMS-F can be found in the Supplementary Material. Note that local time (i.e., Beijing time) is adopted in this figure.

the Gobi Desert (GB) is the major dust source region for the dust storm, having a net outward transport of dust from the region. In contrast, although the Taklimakan desert (TK) is a dust region, it has a net dust transport into the region. North China (NC) is a major region for dust deposition, and hence has a net dust transport into the region. The net dust transport for the larger Asian domain (AD) is negative in FLEXPART-F (Table 2), while it is positive in CAMS-F and MERRA-2. This is because FLEXDUST and FLEXPART cover only the AD, and do not account for the dust transport from outside of the AD, as opposed to the global datasets of MERRA-2 and CAMS-F. Dusts from the middle East and eastern Europe were likely to be transported to the AD during the dust storm event. But they probably deposited in the western part of the AD (Figure 10), and had minor influence on the dust concentration over East Asia (see Figure 4). This explains why there are much higher dust deposition rate and greater increase of dust concentration over the AD in MERRA-2 and CAMS-F than in FLEXPART-F, while the dust budgets over TA, GB and NC in MERRA-2 and CAMS-F are more consistent with that in FLEXPART-F (Table 2).

4 Discussion

4.1 Consistency between backward and forward FLEXPART simulations

Numerous studies have shown that running FLEXPART in forward and backward mode to simulate aerosol concentration or deposition at a site yields consistent results, given the sources and parameter settings are the same (Seibert and Frank, 2004; Eckhardt

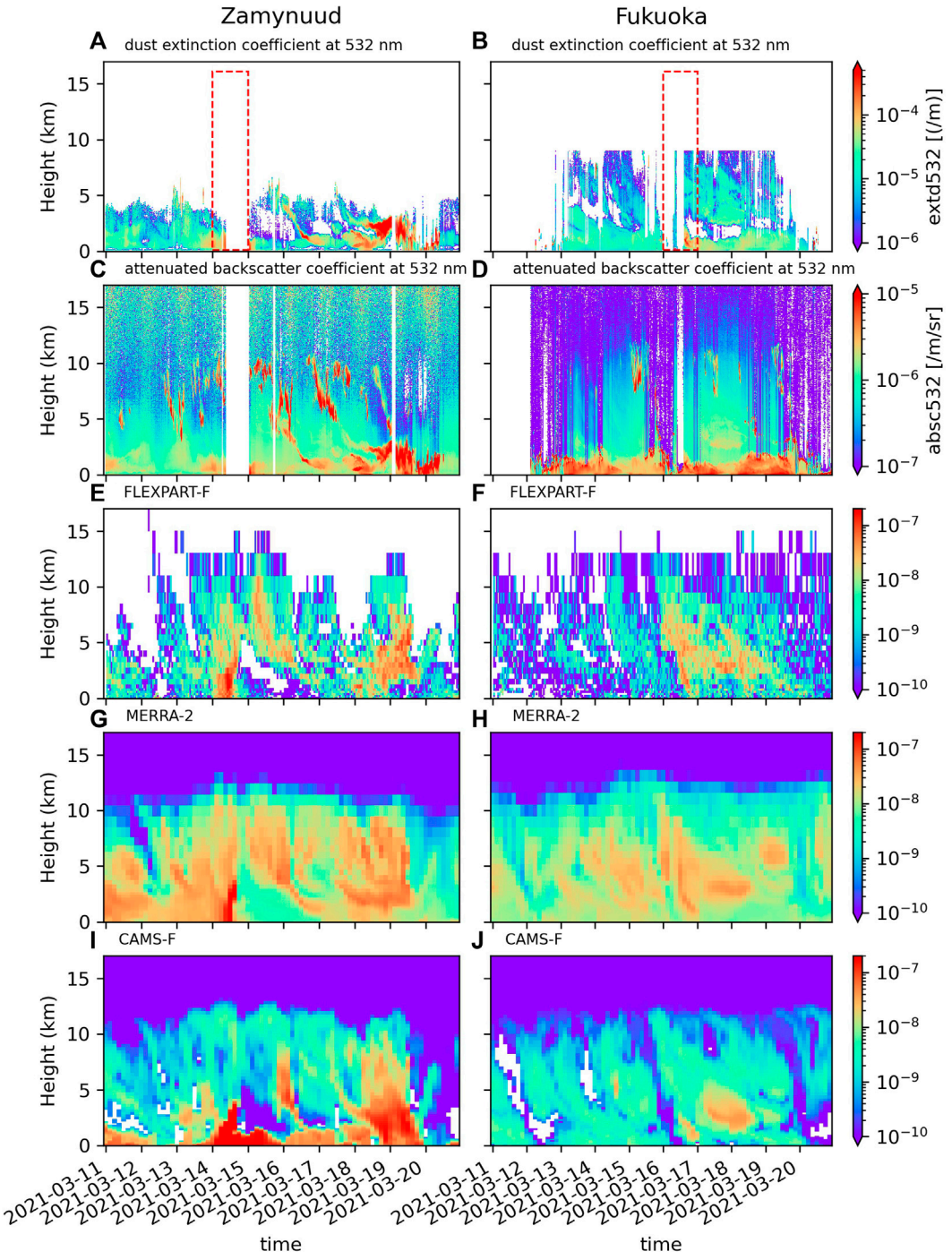

FIGURE 6
Modelled temporal-vertical profile of dust concentration (kg m^{-3}) and its comparision with lidar measurement over Zamynuud, Mongolia **(A,C,E,G,I)** and Fukuoka, Japan **(B,D,F,H,J)**. **(A,B)** Attenuated backscatter coefficient at 532 nm, **(C,D)** Dust extinction coefficient at 532 nm, **(E,F)** FLEXPART-F, **(G,H)** MERRA-2, **(I,J)** CAMS-F. The locations of the two sites are shown in Figure 1. The red boxes denote the dust storm event at the locations.

et al., 2017). Direction of modelling is therefore chosen based on what is numerically efficient and what analyses are desired. When the number of sources exceed the number of receptors it is generally more cost efficient to run backward simulations. Our results further confirm that both FLEXPART-F and FLEXPART-B can consistently depict dust concentration changes at a site during the 2021 East Asia dust storm event (Figures 5, 7). However, the results from FLEXPART-F are in general noisier than FLEXPART-B. We find that increasing backward tracing time and the number of particles released at each time in FLEXPART-B do not significantly improve the consistency between FLEXPART-F and FLEXPART-B. Instead, the spatial averaging of the results of FLEXPART-F from .1 × .1° to 1 × 1 ° can greatly reduce the discrepancies between forward and backward simulations (Figure 7). This implies that the particles reaching at the

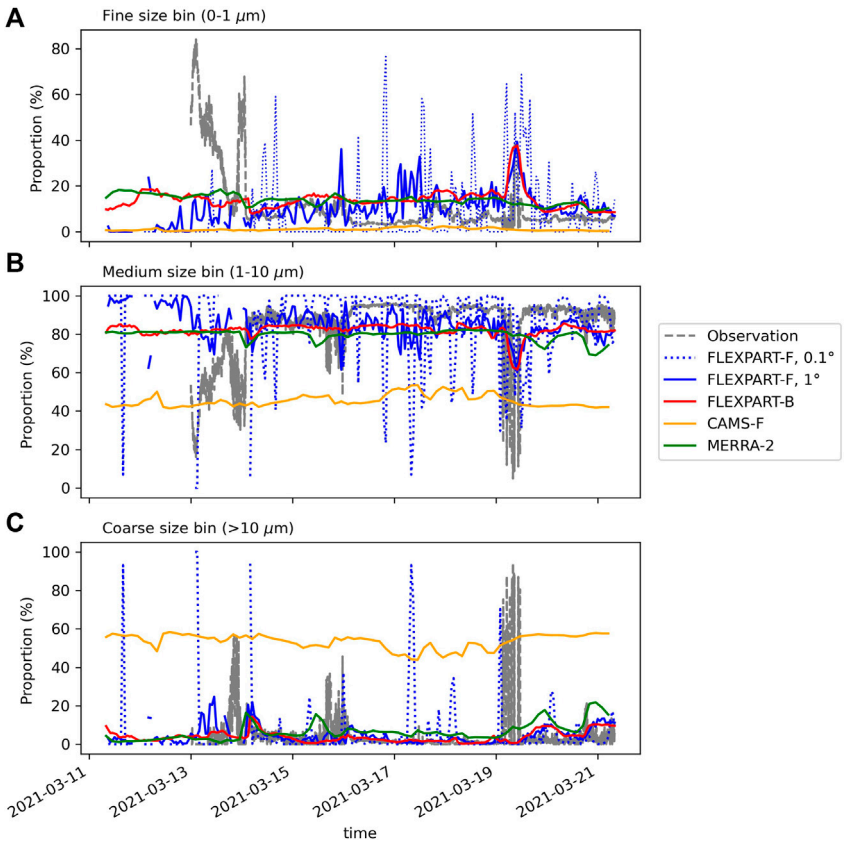

FIGURE 7
Observed and modelled particle size distribution at the SACOL site. **(A)** Fine size bin (0-1 μm), **(B)** Medium size bin (1-10 μ m), **(C)** Coarse size bin (> 10 μm). For FLEXPART-F, data from 0 to 100 m above surface is used. The time axis is in Beijing time.

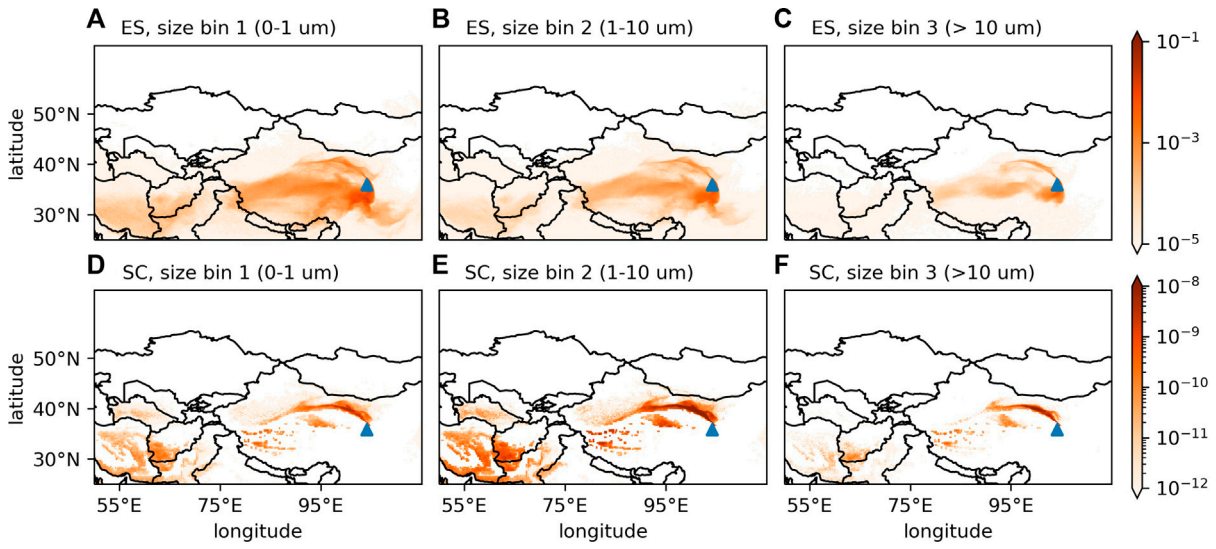

FIGURE 8
Emission sensitivity (ES, unit: s) **(A–C)** and source contribution (SC, unit: kgm^{-3}) **(D–F)** for the dust aerosol concentration near surface (0–100 m) at SACOL during 18:00 13.03-06:00 14.03.2021 (Beijing time) estimated by FLEXPART-B. The blue triangle denotes the location of the SACOL site.

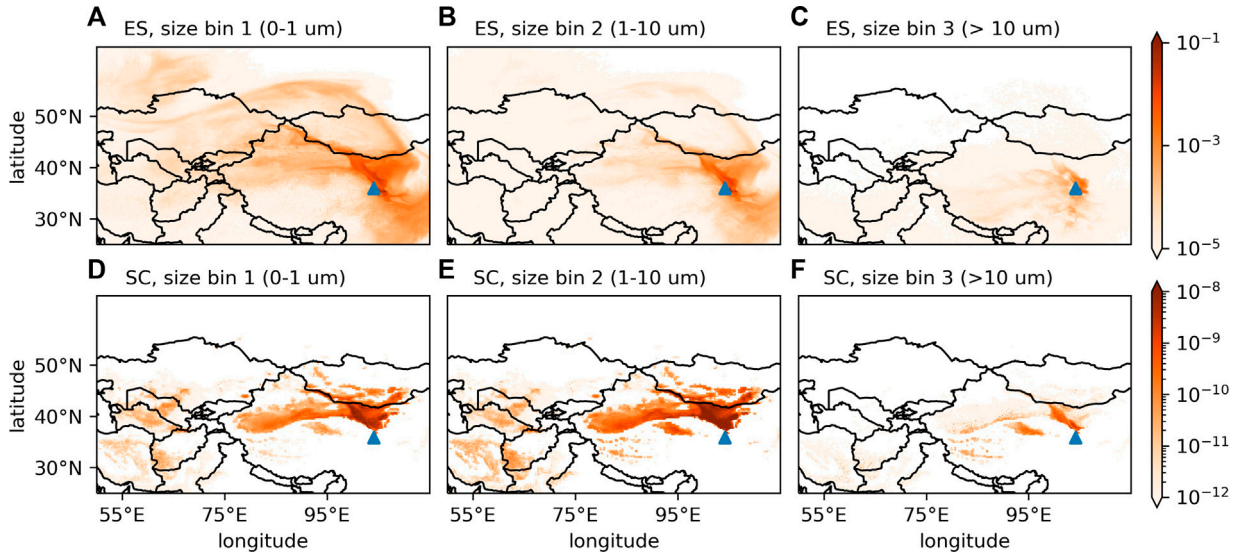

FIGURE 9
The same as Figure 8 but for 00:00-12:00 19.03.2021 (Beijing time).

site (namely .1 × .1° box) in the forward simulation may not be sufficient to achieve statistical robust results, even though the total number of particles released in FLEXPART-F is already quite high. The spatial resolution and representativeness of the forward simulation at a site are strongly limited by the number of particles reaching to the site, and therefore need to be tested for each individual cases.

4.2 Underestimation of dust emission and concentration in FLEXDUST and FLEXPART

It has previously been found that FLEXDUST and FLEXPART considerably underestimate monthly dust concentrations and annual dust deposition over an East Asian site (Cheju) (Groot Zwaaftink et al., 2016). Consistent to this study, we found that FLEXPART using the output of FLEXDUST-default underestimates the strength of the 2021 Asian dust storm compared to observations and reanalysis data (see Supplementary Figures S2, S3). This can be largely attributed to the underestimation of dust emission in FLEXDUST-default owing to the limited types of vegetation used to infer the bare soil fraction in FLEXDUST, and the coarse topographical scaling used to depict the erodibility of the surface (Figures 2, 12A,B). In addition, the threshold friction velocity (TFV) for dust emission is also overestimated, prohibiting dust emission during the dust storm event (Figure 12C). This is in line with previous studies showing that TFV parameterization is the main source of the uncertainties for accurate dust-emission forecasts (Jin et al., 2018). The parameters (e.g., A_n) used in Eq. 3 to estimate TFV were derived from wind tunnel experiments (Shao and Lu, 2000) using loosely spread spherical particles on a dry and bare surface. The finer the particles, the larger are the uncertainties of Eq. 3 in predicting TFV. We found that lowering A_n is necessary to increase the extent and strength of dust emission during this dust storm event, while the modification of γ in Eq. 3 has only a minor effect. According to Shao and Lu (2000), the deviation from default parameters in the equation would implies that dust particles emitted during the dust storm are likely to be finer or less spherical than that originally assumed when deriving the equation.

We also note that the KOK14 scheme in general performs better than the MB95 scheme in depicting the vertical dust flux from the surface during the strong Asian dust storm event. In particular, the KOK14 scheme simulates more (less) emission over Taklimakan desert (northeastern China) than the MB95 scheme (Figure 12D; Supplementary Figure S8), which is more consistent with MERRA-2 and CAMS-F. The better performance of the KOK14 scheme has been demonstrated in Kok et al. (2014) and has been shown in previous studies that the KOK14 scheme tends to predict more dust emission than the MB95 scheme during the Asian dust storm event (Wu et al., 2019; Zeng et al., 2020; Wang et al., 2022) and thus shows better agreement with observation. This can be linked to the high sensitivity of dust flux in the KOK14 scheme to the soil's threshold friction velocity, as it accounts for soil's increased ability to produce dust under continuous saltation bombardment, taking also into account an increased scaling of the vertical dust flux with wind speed (Kok et al., 2014). Moreover, soil texture (i.e., the fraction of soil clay content) exerts a linear influence on dust emission throughout its range (0%–100%) in the KOK14 scheme (Kok et al., 2014), while it has an exponential impact on dust emission, only within a limited range (0%–20%), in the MB95 scheme (Marticorena and Bergametti, 1995). The reduced sensitivity to the soil clay fraction in the KOK14 scheme enhances the dust emissions from the sandy deserts where the soil clay fraction is small, e.g the Taklimakan desert (Figure 12D).

FLEXPART using the output of FLEXDUST-update yields comparable results to MERRA-2 and CAMS-F, and similar to the two dataset, it still underestimates the observed peak of surface PM_{10} (by an order of magnitude at some sites) during the dust storm event (Figure 5). It is also noticed that studies using the meso-scale model WRF-CHEM and an offline chemical transport model CAMx also exhibit a similar magnitude of underestimation of surface PM_{10} during

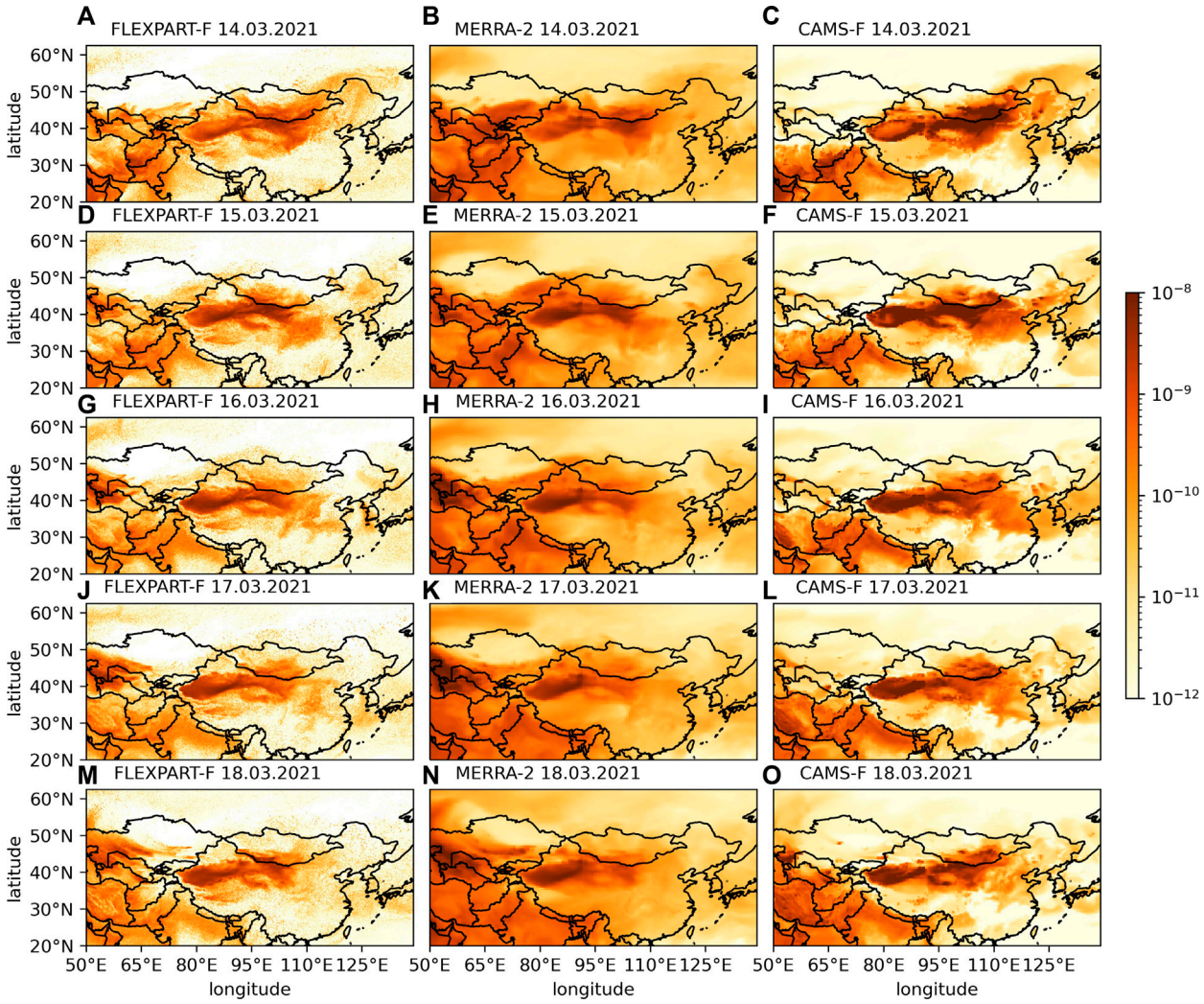

FIGURE 10
Daily average of total dry dust deposition (including gravitational settling) (kg m^{-2} s^{-1}) during the dust storm event. **(A,D,G,J,M)** FLEXPART-F using emission from FLEXDUST-update; **(B,E,H,K,N)** MERRA-2; **(C,F,I,L,O)** CAMS-F.

the East Asian dust storm events using their default settings (Song et al., 2019; Wang et al., 2022).

The underestimation of the observed surface PM_{10} peak during the dust storm event can be largely ascribed to the underestimation of the dust emission in the models. The analysis of global dust emission using inversion model constrained by available observation data reveals that current dust models on average underestimate the Asian dust emission (Kok et al., 2021). Consistently, a recent study applying data assimilation to derive dust emission suggests >15 million tons of dust emitted from the Chinese and Mongolian Gobi Desert during the 2021 East Asia dust storm event (Jin et al., 2022). This is much higher than that in FLEXDUST-update, MERRA-2 and CAMS-F, suggesting that the dust emission schemes used in these models may miss important processes that can invigorate extreme dust emission during the dust storm event. For instance, the soil might have become extremely susceptible with a lot of loose material at the surface when the storm started.

Moreover, the biases in surface wind speed, soil moisture and vegetation cover, which are critical for dust emission may also contribute to the underestimation. These data were all derived from ERA5. For surface wind speed and soil moisture, ERA5 has been shown to exhibit the least biases against station observations among the available reanalysis data (Li et al., 2020; Fan et al., 2021), hence is unlikely to be the main reason for the underestimation of dust emission in FLEXDUST. To further confirm this, we calculated the mean surface wind speed for the available observation stations (Dunn, 2019) over the TA (2.8 m/s), GB (4.5 m/s) and NC (2.8 m/s) regions during the 2021 East Asia dust storm event. ERA5 indeed exhibits small biases in the mean wind speed in TA (+.3 m/s), GB (−.2 m/s) and NC (+.1 m/s). On the other hand, Wang et al. (2022) has shown that the use of gusty wind to capture short-term variation in wind speed can increase dust emission and concentration by more than 50% for the 2021 dust storm. Using gusty wind instead of hourly-average wind speed in FLEXDUST may help reducing the underestimation of dust emission.

For vegetation cover, the data from ERA5 is low in the main desert areas (such as Taklimakan Desert, Gobi Desert and Qaidam basin) (Supplementary Figure S4). But other regions (e.g., North China),

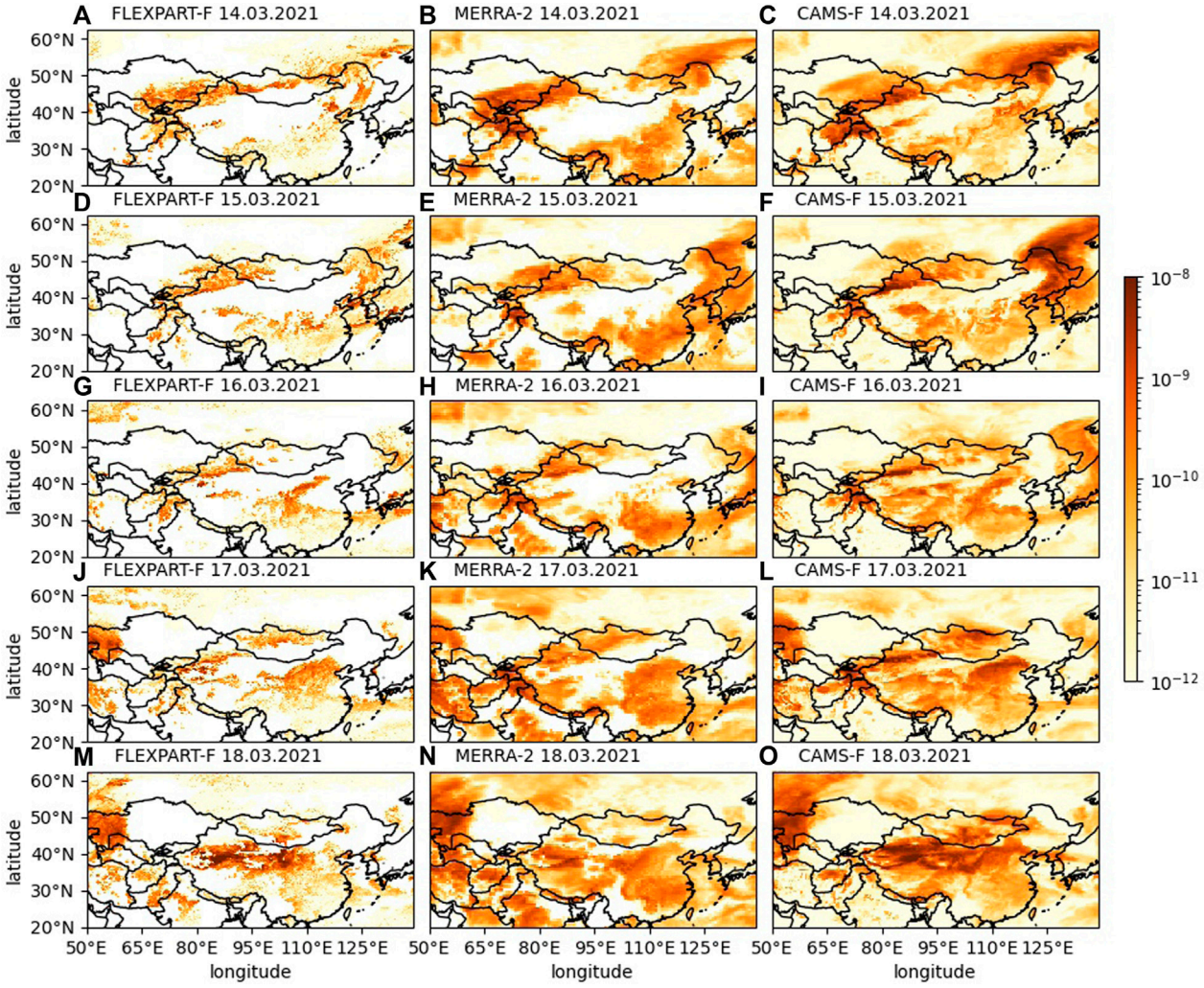

FIGURE 11
The same as Figure 10, but for wet deposition.

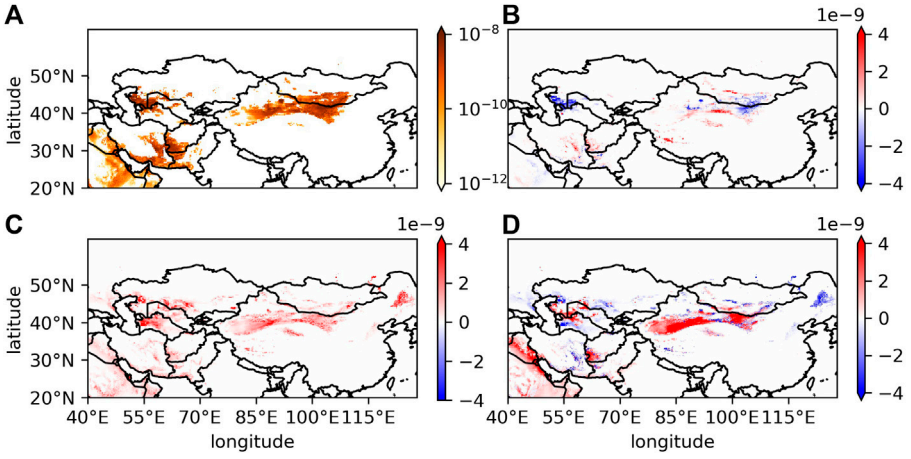

FIGURE 12
Average dust emission (kg m^{-2} s^{-1}) during the whole dust storm event (13.03.2021-17.03.2021) simulated by FLEXDUST-default with MB95 scheme **(A)**, and the changes in emission (kg m^{-2} s^{-1}) due to improved erodibity **(B)**, improved TFV **(C)**, and the switch from MB95 to KOK14 scheme **(D)**.

which can potentially be a seasonal dust source in spring, have quite high static vegetation cover throughout the year. The lack of seasonality in the vegetation cover data from ERA5 may explain the underestimation of the dust emission, especially over northern China, an important nearby local dust sources for the observation sites of surface PM_{10} in Figure 5. Further improvement, such as using leaf area index (LAI) instead of total vegetation cover from ERA5, to infer the seasonal variation in vegetation and its potential impact on dust emission, would be needed.

We also notice that with the strength and spatial distribution of dust emission similar to FLEXDUST-update, Wang et al. (2022) show that the use of the KOK14 scheme for dust emission in CAMx is sufficient to reproduce the observed peak of surface PM_{10} during the 2021 East Asia dust storm. This indicates that the underestimation of the observed surface PM_{10} in FLEXPART may result from the too short lifetime of dust particles in the atmosphere. A modelling study of the East Asian dust storm in 2017 (Song et al., 2019) also found that increasing the proportion of the finer dust particles emitted from the surface and thus longer lifetime in the atmosphere, can significantly alleviate the underestimation of the surface PM_{10} during the dust storm event. Following this study, we have tested different size distributions of the emitted dust in FLEXPART-B, but found little improvement in the predicted surface PM_{10} (Figure not shown). This suggests that further tuning of the dust transport and deposition parameters in FLEXPART seem to be necessary to fully resolve the underestimation of the observed strength of the extreme Asian dust storms.

4.3 Comparison with MERRA-2 and CAMS-F

Owing to the lack of observation data on dust emission and deposition, we have employed the state-of-the-art reanalysis data, such as MERRA-2 and CAMS-F to evaluate the performance of FLEXDUST and FLEXPART. We note that MERRA-2 and CAMS-F are still model results and may suffer from large potential biases compared to observation (e.g., Figure 5) when simulating the dust cycle, even though they have assimilated remote-sensed aerosol optical depth (AOD). The comparison with MERRA-2 and CAMS-F can only tell how much FLEXDUST and FLEXPART deviate from the observation-constrained dust cycle as represented in MERRA-2 and CAMS-F.

It is found that using FLEXDUST-update, FLEXPART-F can well capture the strength and spatio-temporal evolution of the dust storm consistent with that in MERRA-2 and CAMS-F. In general, the strength of the dust emission, concentration and deposition in FLEXPART-F resemble those in MERRA-2 (Table 2), likely due to the similarity in their emission and deposition schemes (Table 1). In contrast, the spatio-temporal pattern of the dust cycle in FLEXPART is more consistent with that in CAMS-F than in MERRA-2 (Figures 3, 4, 10, 11). This can result from the similarity in their atmospheric forcing fields, such as wind, temperature and precipitation, as FLEXPART-F uses forcings from ERA5, which is produced with the same IFS system as CAMS-F (see Supplementary Figures S4, S6, S7).

The stronger dust emission, and dry and wet deposition in CAMS-F during the dust storm event than that in MERRA-2 and FLEXPAR-F are consistent with the finding by Zhao et al. (2022) on global scale (Table 2). Due to the lack of observation data, it remains uncertain whether CAMS-F is better in capturing the full dust cycle during the dust storm event. Given that CAMS-F is better in capturing the magnitude and temporal changes of the observed surface PM_{10} (Figure 5), the high dust emission in CAMS-F might be more realistic than MERRA-2 and FLEXPART-F. However, the analyses on AEROVAL (https://aeroval.met.no/) reveal that CAMS generally overestimates PM_{10} in North China on seasonal and yearly scale. The higher dust emission in CAMS-F can be related to its use of a more recent observation-based approach to quantify erodibility, instead of the topographic scaling adopted in both MERRA-2 and FLEXDUST (Table 1). In addition, soil map (e.g. , soil texture) used in CAMS-F is different from MERRA-2 and FLEXDUST, which may also explain the differences in emission (Rémy et al., 2022).

We note that FLEXPART-F shows a noticeable weak wet deposition compared to CAMS-F and even MERRA-2 in some regions (Figure 11). This can be ascribed to the parameterization of wet deposition scheme in FLEXPART-F where dust particles are set up as very poor cloud condensation nuclei and thus are inefficiently removed by in-cloud scavenging (Grythe et al., 2017). Furthermore, there is initially very little precipitation close to the source, which gives time for dry deposition of the larger particles leaving mainly smaller particles that are less efficiently removed by below-cloud scavenging. Also the wet deposition in FLEXPLART-F displays a more "patchy" pattern compared to that in CAMS-F and MERRA-2. This can be related to the number of particles used in the simulation, but also to the issue of precipitation disaggregation using Flex_extract and the spatial interpolation of the variables (e.g., cloud water content and total cloud cover) required by the wet scavenging scheme, as pointed out by Hittmeir et al. (2018) and Tipka et al. (2020).

Our results reveal a high capability of FLEXDUST and FLEXPART in simulating the particle size distribution and its variation (Figure 7). Although a fixed size distribution of emitted dust (i.e., 10 dust size bins) has been assumed in FLEXDUST (see Supplementary Figure S1), FLEXPART is still able to reproduce the variation of the particle size distribution well during the dust storm event, owing to the particle-size dependent parameterization employed in both dry (e.g. gravitational settling) and wet deposition (e.g., below-cloud scavenging) in FLEXPART. Compared to FLEXDUST and FLEXPART, CAMS-F and MERRA-2 use less size-dependent parameterizations for dry and wet deposition (Table 1), and less dust size bins, namely 3 and 5 size bins for CAMS-F and MERRA-2, respectively. This can explains the lower performance of CAMS-F and MERRA-2 in simulating the particle size distribution and its changes during the dust storm event at the SACOL site. Further improvement of the dust emission, and dry and wet deposition in FLEXDUST and FLEXPART and other dust models with size-segregated/size-resolved schemes (e.g., Holopainen et al., 2020; Zeng et al., 2020), will likely help to better simulate the size distribution of the Asian dust aerosol and its climatic impact.

5 Conclusion

In this study, the performance of the Lagrangian trajectory model system FLEXDUST and FLEXPART in simulating the 2021 East Asia dust storm was evaluated against available observation data and observation-constrained reanalysis/forecast data of the atmospheric compositions (i.e., MERRA-2 and

CAMS-F). It is found that the default FLEXDUST underestimates dust emission during the event compared to MERRA-2 and CAMS-F. Modification of the parameterization of the topographic scaling, bare soil fraction as well as threshold friction velocity in FLEXDUST can reproduce the strength and spatial extent of the dust emission, and the resultant concentration, and dry and wet deposition comparable to MERRA-2 and CAMS-F. Both FLEXPART and the reanalysis data, however, underestimate the peak of surface dust PM_{10} over North China during the dust storm event, even though the timing of the peak is well reproduced. This can be attributed to various reasons, such as the lack of nearby natural or anthropogenic dust sources and positive feedback between soil erodibility and dust emission in the models, the biases in surface wind speed, and the size distribution of emitted dust, and other factors leading to the too-short lifetime of dust in the model. More studies are needed to improve the dust models to better represent the dust cycle during the extreme Asian dust storms without deteriorating the performance during normal conditions. FLEXDUST and FLEXPART can better represent the observed size distribution of dust aerosol than MERRA-2 and CAMS-F, highlighting the importance of using a high number of dust size bins (e.g., more than 10) and size-dependent dust emission and deposition schemes in depicting the Asian dust storms and its climatic, ecological and socio-economic impacts. This evaluation study provides not only a direction for futher improvements of FLEXDUST and FLEXPART in representing Asian dust cycle, but also a basis for employing FLEXDUST and FLEXPART in studying the spatio-temporal dynamics of Asian dust in the past, present and future conditions.

Data availability statement

The datasets presented in this study can be found in online repositories. The names of the repositories and accession number(s) can be found Supplementary Material.

Author contributions

HT, OH, FS, and AK designed the study. HT performed forward simulations of FLEXDUST and FLEXPART, while OH performed backward simulations for the study. JB, BW, and ZR provided observation data for this study. HG and CZ provided insights on the modelled processes in FLEXDUST and FLEXPART. HT led the writing and the analyses of the results. All the co-authors contributed to the analyses of the results and the writing of the manuscript.

Funding

The study is supported by Academy of Finland, grant no. 316799. JB, BW, and ZR are supported by the Natural Science Foundation of China (NSFC), grant no. 42075126, 42072208, and 42105140, respectively.

Acknowledgments

The authors would like to express special thanks to all staff of SACOL and AD-Net for supplying the ground-based observations. Lidar data were provided by courtesy of AD-Net (https://www-lidar.nies.go.jp/AD-Net). The simulations were performed on resources provided by Sigma2—the National Infrastructure for High Performance Computing and Data Storage in Norway. The MERRA-2 data used in this study have been provided by the Global Modeling and Assimilation Office (GMAO) at NASA Goddard Space Flight Center. CAMS data used in this study were generated using Copernicus Atmosphere Monitoring Service Information (2022). ERA5 data used in this study were downloaded using the Copernicus Climate Change Service (C3S) Climate Data Store. Neither the European Commission nor ECMWF is responsible for any use that may be made of the information it contains. We would also like to acknowledge the two reviewers for their valuable comments.

Conflict of interest

The authors declare that the research was conducted in the absence of any commercial or financial relationships that could be construed as a potential conflict of interest.

Publisher's note

All claims expressed in this article are solely those of the authors and do not necessarily represent those of their affiliated organizations, or those of the publisher, the editors and the reviewers. Any product that may be evaluated in this article, or claim that may be made by its manufacturer, is not guaranteed or endorsed by the publisher.

Supplementary material

The Supplementary Material for this article can be found online at: https://www.frontiersin.org/articles/10.3389/fenvs.2022.1013875/full#supplementary-material

References

Benedetti, A., Di Giuseppe, F., Jones, L., Peuch, V. H., Rémy, S., and Zhang, X. (2019). The value of satellite observations in the analysis and short-range prediction of Asian dust. *Atmos. Chem. Phys.* 19, 987–998. doi:10.5194/ACP-19-987-2019

Buchard, V., Randles, C. A., Silva, A. M. d., Darmenov, A., Colarco, P. R., Govindaraju, R., et al. (2017). The MERRA-2 aerosol reanalysis, 1980 onward. Part II: Evaluation and case studies. *J. Clim.* 30, 6851–6872. doi:10.1175/JCLI-D-16-0613.1

Cassiani, M., Stohl, A., Olivié, D., Seland, y., Bethke, I., Pisso, I., et al. (2016). The offline Lagrangian particle model FLEXPART-NorESM/CAM (v1): Model description and comparisons with the online NorESM transport scheme and with the reference FLEXPART model. *Geosci. Model Dev.* 9, 4029–4048. doi:10.5194/GMD-9-4029-2016

Checa-Garcia, R., Balkanski, Y., Albani, S., Bergman, T., Carslaw, K., Cozic, A., et al. (2021). Evaluation of natural aerosols in CRESCENDO Earth system models (ESMs): Mineral dust. *Atmos. Chem. Phys.* 21, 10295–10335. doi:10.5194/ACP-21-10295-2021

Chen, S., Huang, J., Qian, Y., Zhao, C., Kang, L., Yang, B., et al. (2017). An overview of mineral dust modeling over East Asia. *J. Meteorological Res.* 31 (31), 633–653. doi:10.1007/S13351-017-6142-2

Chin, M., Ginoux, P., Kinne, S., Torres, O., Holben, B. N., Duncan, B. N., et al. (2002). Tropospheric aerosol optical thickness from the GOCART model and comparisons with satellite and sun photometer measurements. *J. Atmos. Sci.* 59, 461–483. doi:10.1175/1520-0469(2002)059¡0461:taotft¿2.0.co;2

Chin, M., Rood, R. B., Lin, S. J., Müller, J. F., and Thompson, A. M. (2000). Atmospheric sulfur cycle simulated in the global model GOCART: Model description and global properties. *J. Geophys. Res. Atmos.* 105, 24671–24687. doi:10.1029/2000JD900384

Dunn, R. J. H. (2019). *HadISD version 3: Monthly updates*. Exeter, UK: Hadley Centre Technical Note.

Eckhardt, S., Cassiani, M., Evangeliou, N., Sollum, E., Pisso, I., and Stohl, A. (2017). Source-receptor matrix calculation for deposited mass with the Lagrangian particle dispersion model FLEXPART v10.2 in backward mode. *Geosci. Model Dev.* 10, 4605–4618. doi:10.5194/GMD-10-4605-2017

Fan, W., Liu, Y., Chappell, A., Dong, L., Xu, R., Ekström, M., et al. (2021). Evaluation of global reanalysis land surface wind speed trends to support wind energy development using *in situ* observations. *J. Appl. Meteorology Climatol.* 60, 33–50. doi:10.1175/JAMC-D-20-0037.1

Filonchyk, M. (2022). Characteristics of the severe March 2021 Gobi Desert dust storm and its impact on air pollution in China. *Chemosphere* 287, 132219. doi:10.1016/J.CHEMOSPHERE.2021.132219

Fuks, N. A. (1989). *The mechanics of aerosols*. Dover Publications.

Gelaro, R., McCarty, W., Suárez, M. J., Todling, R., Molod, A., Takacs, L., et al. (2017). The Modern-Era retrospective analysis for research and applications, Version 2 (MERRA-2). *J. Clim.* 30, 5419–5454. doi:10.1175/JCLI-D-16-0758.1

Ginoux, P., Chin, M., Tegen, I., Prospero, J. M., Holben, B., Dubovik, O., et al. (2001). Sources and distributions of dust aerosols simulated with the GOCART model. *J. Geophys. Res. Atmos.* 106, 20255–20273. doi:10.1029/2000JD000053

Ginoux, P., Prospero, J. M., Gill, T. E., Hsu, N. C., and Zhao, M. (2012). Global-scale attribution of anthropogenic and natural dust sources and their emission rates based on MODIS Deep Blue aerosol products. *Rev. Geophys.* 50, 3005. doi:10.1029/2012RG000388

Gong, S. L., and Zhang, X. Y. (2008). CUACE/Dust: An integrated system of observation and modeling systems for operational dust forecasting in Asia. *Atmos. Chem. Phys.* 8 (9), 2333–2340. doi:10.5194/ACP-8-2333-2008

Grimm, H., and Eatough, D. J. (2009). Aerosol measurement: The use of optical light scattering for the determination of particulate size distribution, and particulate mass, including the semi-volatile fraction. *J. Air & Waste Manag. Assoc.* 59, 101–107. doi:10.3155/1047-3289.59.1.101

Groot Zwaaftink, C. D., Aas, W., Eckhardt, S., Evangeliou, N., Hamer, P., Johnsrud, M., et al. (2022). What caused a record high PM10 episode in northern Europe in October 2020? *Atmos. Chem. Phys.* 22, 3789–3810. doi:10.5194/ACP-22-3789-2022

Groot Zwaaftink, C. D., Arnalds, l., Dagsson-Waldhauserova, P., Eckhardt, S., Prospero, J. M., and Stohl, A. (2017). Temporal and spatial variability of Icelandic dust emissions and atmospheric transport. *Atmos. Chem. Phys.* 17, 10865–10878. doi:10.5194/ACP-17-10865-2017

Groot Zwaaftink, C. D., Grythe, H., Skov, H., and Stohl, A. (2016). Substantial contribution of northern high-latitude sources to mineral dust in the Arctic. *J. Geophys. Res. Atmos.* 121, 13, 678–713, 697. doi:10.1002/2016JD025482

Grythe, H., Kristiansen, N. I., Zwaaftink, C. D., Eckhardt, S., Ström, J., Tunved, P., et al. (2017). A new aerosol wet removal scheme for the Lagrangian particle model FLEXPART v10. *Geosci. Model Dev.* 10, 1447–1466. doi:10.5194/GMD-10-1447-2017

Gui, K., Yao, W., Che, H., An, L., Zheng, Y., Li, L., et al. (2022). Record-breaking dust loading during two mega dust storm events over northern China in March 2021: Aerosol optical and radiative properties and meteorological drivers. *Atmos. Chem. Phys.* 22, 7905–7932. doi:10.5194/ACP-22-7905-2022

Haugvaldstad, O. W. (2021). *Aeolian dust sources, transport and deposition over the Chinese loess plateau during 1999-2019: A study using the FLEXDUST and FLEXPART models*. Oslo, Norway: Master Thesis, University of Oslo.

Hersbach, H., Bell, B., Berrisford, P., Biavati, G., Horányi, A., Muñoz Sabater, J., et al. (2018). ERA5 hourly data on pressure levels from 1959 to present. *Copernic. Clim. Change Serv. (C3S) Clim. Data Store (CDS)*. doi:10.24381/cds.bd0915c6

Hittmeir, S., Philipp, A., and Seibert, P. (2018). A conservative reconstruction scheme for the interpolation of extensive quantities in the Lagrangian particle dispersion model FLEXPART. *Geosci. Model Dev.* 11, 2503–2523. doi:10.5194/GMD-11-2503-2018

Holopainen, E., Kokkola, H., Laakso, A., and Kühn, T. (2020). In-cloud scavenging scheme for sectional aerosol modules - implementation in the framework of the Sectional Aerosol module for Large Scale Applications version 2.0 (SALSA2.0) global aerosol module. *Geosci. Model Dev.* 13, 6215–6235. doi:10.5194/GMD-13-6215-2020

Huang, J., Wang, T., Wang, W., Li, Z., and Yan, H. (2014). Climate effects of dust aerosols over East Asian arid and semiarid regions. *J. Geophys. Res. Atmos.* 119, 398–411. doi:10.1002/2014JD021796

Huang, J., Zhang, W., Zuo, J., Bi, J., Shi, J., Wang, X., et al. (2008). An overview of the semi-arid climate and environment research observatory over the loess plateau. *Adv. Atmos. Sci.* 25, 906–921. doi:10.1007/s00376-008-0906-7

Huang, Z., Huang, J., Hayasaka, T., Wang, S., Zhou, T., and Jin, H. (2015). Short-cut transport path for asian dust directly to the arctic: A case study. *Environ. Res. Lett.* 10, 114018. doi:10.1088/1748-9326/10/11/114018

Inness, A., Ades, M., Agustí-Panareda, A., Barr, J., Benedictow, A., Blechschmidt, A. M., et al. (2019). The CAMS reanalysis of atmospheric composition. *Atmos. Chem. Phys.* 19, 3515–3556. doi:10.5194/ACP-19-3515-2019

Jia, H., Ma, X., Yu, F., and Quaas, J. (2021). Significant underestimation of radiative forcing by aerosol–cloud interactions derived from satellite-based methods. *Nat. Commun.* 12 (12), 3649. doi:10.1038/s41467-021-23888-1

Jin, J., Lin, H. X., Heemink, A., and Segers, A. (2018). Spatially varying parameter estimation for dust emissions using reduced-tangent-linearization 4DVar. *Atmos. Environ.* 187, 358–373. doi:10.1016/J.ATMOSENV.2018.05.060

Jin, J., Pang, M., Segers, A., Han, W., Fang, L., Li, B., et al. (2022). Inverse modeling of the 2021 spring super dust storms in East Asia. *Atmos. Chem. Phys.* 22, 6393–6410. doi:10.5194/ACP-22-6393-2022

Kobayashi, T., Tateishi, R., Alsaaideh, B., Sharma, R. C., Wakaizumi, T., Miyamoto, D., et al. (2017). Production of global land cover data – GLCNMO2013. *J. Geogr. Geol.* 9, 1. doi:10.5539/JGG.V9N3P1

Kok, J. F. (2011). A scaling theory for the size distribution of emitted dust aerosols suggests climate models underestimate the size of the global dust cycle. *Proc. Natl. Acad. Sci. U. S. A.* 108, 1016–1021. doi:10.1073/pnas.1014798108

Kok, J. F., Adebiyi, A. A., Albani, S., Balkanski, Y., Checa-Garcia, R., Chin, M., et al. (2021). Contribution of the world's main dust source regions to the global cycle of desert dust. *Atmos. Chem. Phys.* 21, 8169–8193. doi:10.5194/ACP-21-8169-2021

Kok, J. F., Mahowald, N. M., Fratini, G., Gillies, J. A., Ishizuka, M., Leys, J. F., et al. (2014). An improved dust emission model – Part 1: Model description and comparison against measurements. *Atmos. Chem. Phys.* 14, 13023–13041. doi:10.5194/acp-14-13023-2014

Kok, J. F., Ward, D. S., Mahowald, N. M., and Evan, A. T. (2018). Global and regional importance of the direct dust-climate feedback. *Nat. Commun.* 9, 241–311. doi:10.1038/s41467-017-02620-y

Kyrö, E.-M., Grönholm, T., Vuollekoski, H., Virkkula, A., Kulmala, M., Laakso, L., et al. (2009). Snow scavenging of ultrafine particles: Field measurements and parameterization. *Boreal Environ. Res.* 4, 527–538.

Laakso, L., Grönholm, T., Rannik, l., Kosmale, M., Fiedler, V., Vehkamäki, H., et al. (2003). Ultrafine particle scavenging coefficients calculated from 6 years field measurements. *Atmos. Environ.* 37, 3605–3613. doi:10.1016/S1352-2310(03)00326-1

Li, J., Carlson, B. E., Yung, Y. L., Lv, D., Hansen, J., Penner, J. E., et al. (2022a). Scattering and absorbing aerosols in the climate system. *Nat. Rev. Earth Environ.* 3, 363–379. doi:10.1038/s43017-022-00296-7

Li, J., Hao, X., Liao, H., Yue, X., Li, H., Long, X., et al. (2022b). Predominant type of dust storms that influences air quality over Northern China and future projections. *Earth's Future* 10. doi:10.1029/2022EF002649

Li, M., Wu, P., and Ma, Z. (2020). A comprehensive evaluation of soil moisture and soil temperature from third-generation atmospheric and land reanalysis data sets. *Int. J. Climatol.* 40, 5744–5766. doi:10.1002/JOC.6549

Li, L., Mahowald, N. M., Miller, R. L., Pérez García-Pando, C., Klose, M., Hamilton, D. S., et al. (2021). Quantifying the range of the dust direct radiative effect due to source mineralogy uncertainty. *Atmos. Chem. Phys.* 21 (5), 3973–4005. doi:10.5194/ACP-21-3973-2021

Liu, J., Wu, D., Liu, G., Mao, R., Chen, S., Ji, M., et al. (2019). Impact of Arctic amplification on declining spring dust events in East Asia. *Clim. Dyn.* 54, 1913–1935. doi:10.1007/S00382-019-05094-4

Mallia, D. V., Kochanski, A., Wu, D., Pennell, C., Oswald, W., and Lin, J. C. (2017). Wind-blown dust modeling using a backward-Lagrangian particle dispersion model. *J. Appl. Meteorology Climatol.* 56, 2845–2867. doi:10.1175/JAMC-D-16-0351.1

Marticorena, B., and Bergametti, G. (1995). Modeling the atmospheric dust cycle: 1. Design of a soil-derived dust emission scheme. *J. Geophys. Res. Atmos.* 100, 16415–16430. doi:10.1029/95JD00690

MEP (2013). *Specifications and test procedures for ambient air quality continuous automated monitoring system for PM10 and PM2.5*. Beijing, China: The Ministry of Environmental Protection of People's Republic of China. HJ 653-2013.

Morcrette, J. J., Boucher, O., Jones, L., Salmond, D., Bechtold, P., Beljaars, A., et al. (2009). Aerosol analysis and forecast in the European Centre for medium-range weather forecasts integrated forecast system: Forward modeling. *J. Geophys. Res. Atmos.* 114, D06206. doi:10.1029/2008JD011235

Myhre, G., Grini, A., Haywood, J. M., Stordal, F., Chatenet, B., Tanré, D., et al. (2003). Modeling the radiative impact of mineral dust during the Saharan Dust Experiment (SHADE) campaign. *J. Geophys. Res. Atmos.* 108, 8579. doi:10.1029/2002JD002566

Myhre, G., and Stordal, F. (2001). Global sensitivity experiments of the radiative forcing due to mineral aerosols. *J. Geophys. Res. Atmos.* 106, 18193–18204. doi:10.1029/2000JD900536

Näslund, E., and Thaning, L. (2007). On the settling velocity in a nonstationary atmosphere. *Aerosol Sci. Technol.* 14, 247–256. doi:10.1080/02786829108959487

Pisso, I., Sollum, E., Grythe, H., Kristiansen, N. I., Cassiani, M., Eckhardt, S., et al. (2019). The Lagrangian particle dispersion model FLEXPART version 10.4. *Geosci. Model Dev.* 12, 4955–4997. doi:10.5194/GMD-12-4955-2019

Poggio, L., De Sousa, L. M., Batjes, N. H., Heuvelink, G. B., Kempen, B., Ribeiro, E., et al. (2021). SoilGrids 2.0: Producing soil information for the globe with quantified spatial uncertainty. *SOIL* 7, 217–240. doi:10.5194/SOIL-7-217-2021

Ramli, H. M., and Esler, J. G. (2016). Quantitative evaluation of numerical integration schemes for Lagrangian particle dispersion models. *Geosci. Model Dev.* 9, 2441–2457. doi:10.5194/GMD-9-2441-2016

Randles, C. A., Silva, A. M. d., Buchard, V., Colarco, P. R., Darmenov, A., Govindaraju, R., et al. (2017). The MERRA-2 aerosol reanalysis, 1980 onward. Part I: System description and data assimilation evaluation. *J. Clim.* 30, 6823–6850. doi:10.1175/JCLI-D-16-0609.1

Rémy, S., Kipling, Z., Huijnen, V., Flemming, J., Nabat, P., Michou, M., et al. (2022). Description and evaluation of the tropospheric aerosol scheme in the Integrated Forecasting System (IFS-AER, cycle 47R1) of ECMWF. *Geosci. Model Dev.* 15, 4881–4912. doi:10.5194/GMD-15-4881-2022

Seibert, P., and Frank, A. (2004). Source-receptor matrix calculation with a Lagrangian particle dispersion model in backward mode. *Atmos. Chem. Phys.* 4, 51–63. doi:10.5194/ACP-4-51-2004

Shao, Y., and Dong, C. H. (2006). A review on East Asian dust storm climate, modelling and monitoring. *Glob. Planet. Change* 52, 1–22. doi:10.1016/J.GLOPLACHA.2006.02.011

Shao, Y., and Lu, H. (2000). A simple expression for wind erosion threshold friction velocity. *J. Geophys. Res. Atmos.* 105, 22437–22443. doi:10.1029/2000JD900304

Shimizu, A., Sugimoto, N., Matsui, I., Arao, K., Uno, I., Murayama, T., et al. (2004). Continuous observations of Asian dust and other aerosols by polarization lidars in China and Japan during ACE-Asia. *J. Geophys. Res. Atmos.* 109, D19S17–36. doi:10.1029/2002JD003253

Sodemann, H., Lai, T. M., Marenco, F., Ryder, C. L., Flamant, C., Knippertz, P., et al. (2015). Lagrangian dust model simulations for a case of moist convective dust emission and transport in the Western Sahara region during Fennec/LADUNEX. *J. Geophys. Res. Atmos.* 120, 6117–6144. doi:10.1002/2015JD023283

Song, P., Fei, J., Li, C., and Huang, X. (2019). Simulation of an asian dust storm event in may 2017. *Atmosphere* 10 (10), 135. doi:10.3390/ATMOS10030135

Tegen, I., and Lacis, A. A. (1996). Modeling of particle size distribution and its influence on the radiative properties of mineral dust aerosol. *J. Geophys. Res. Atmos.* 101, 19237–19244. doi:10.1029/95JD03610

Tipka, A., Haimberger, L., and Seibert, P. (2020). Flex_extract v7.1.2 – A software package to retrieve and prepare ECMWF data for use in FLEXPART. *Geosci. Model Dev.* 13, 5277–5310. doi:10.5194/gmd-13-5277-2020

Uno, I., Eguchi, K., Yumimoto, K., Takemura, T., Shimizu, A., Uematsu, M., et al. (2009). Asian dust transported one full circuit around the globe. *Nat. Geosci.* 2, 557–560. doi:10.1038/ngeo583

Wang, J., Zhang, B., Zhang, H., Hua, C., An, L., Gui, H., et al. (2022). Simulation of a severe sand and dust storm event in March 2021 in Northern China: Dust emission schemes comparison and the role of gusty wind. *Atmosphere* 13, 108. doi:10.3390/ATMOS13010108

Wang, S., Yu, Y., Zhang, X. X., Lu, H., Zhang, X. Y., and Xu, Z. (2021). Weakened dust activity over China and Mongolia from 2001 to 2020 associated with climate change and land-use management. *Environ. Res. Lett.* 16, 124056. doi:10.1088/1748-9326/AC3B79

Wesely, M. L. (1989). Parameterization of surface resistances to gaseous dry deposition in regional-scale numerical models. *Atmos. Environ.* 23, 1293–1304. doi:10.1016/0004-6981(89)90153-4

Wu, M., Liu, X., Yang, K., Luo, T., Wang, Z., Wu, C., et al. (2019). Modeling dust in East Asia by CESM and sources of biases. *J. Geophys. Res. Atmos.* 124, 8043–8064. doi:10.1029/2019JD030799

Yao, W., Che, H., Gui, K., Wang, Y., and Zhang, X. (2020). Can MERRA-2 reanalysis data reproduce the three-dimensional evolution characteristics of a typical dust process in East Asia? A case study of the dust event in may 2017. *Remote Sens.* 12, 902. doi:10.3390/RS12060902

Yin, Z., Wan, Y., Zhang, Y., and Wang, H. (2022). Why super sandstorm 2021 in North China? *Natl. Sci. Rev.* 9, nwab165. doi:10.1093/NSR/NWAB165

Zamora, L. M., Kahn, R. A., Evangeliou, N., and Groot Zwaaftink, C. D. (2022). Comparisons between the distributions of dust and combustion aerosols in MERRA-2, FLEXPART and CALIPSO and implications for deposition freezing over wintertime Siberia. *Atmos. Chem. Phys. Discuss.* 2022, 1–25. doi:10.5194/acp-2022-124

Zeng, Y., Wang, M., Zhao, C., Chen, S., Liu, Z., Huang, X., et al. (2020). WRF-Chem v3.9 simulations of the East Asian dust storm in May 2017: Modeling sensitivities to dust emission and dry deposition schemes. *Geosci. Model Dev.* 13, 2125–2147. doi:10.5194/GMD-13-2125-2020

Zhang, L., Gong, S., Padro, J., and Barrie, L. (2001). A size-segregated particle dry deposition scheme for an atmospheric aerosol module. *Atmos. Environ.* 35, 549–560. doi:10.1016/S1352-2310(00)00326-5

Zhao, A., Ryder, C. L., and Wilcox, L. J. (2022). How well do the CMIP6 models simulate dust aerosols? *Atmos. Chem. Phys.* 22, 2095–2119. doi:10.5194/ACP-22-2095-2022

frontiers | Frontiers in Environmental Science

TYPE Original Research
PUBLISHED 10 January 2023
DOI 10.3389/fenvs.2022.1059292

OPEN ACCESS

EDITED BY
Zhiyuan Hu,
School of Atmospheric Sciences, Sun Yat-sen University, China

REVIEWED BY
Ming Chang,
Jinan University, China
Tianhe Wang,
Lanzhou University, China
Bing Pu,
University of Kansas, United States

*CORRESPONDENCE
Yuanjian Yang,
yyj1985@nuist.edu.cn

†These authors have contributed equally to this work and share first authorship

SPECIALTY SECTION
This article was submitted to Atmosphere and Climate, a section of the journal Frontiers in Environmental Science

RECEIVED 01 October 2022
ACCEPTED 06 December 2022
PUBLISHED 10 January 2023

CITATION
Zhou C, Duan Z, Ling X and Yang Y (2023), Effects of local aerosol and transported dust pollution on the surface energy balance over farmland in eastern China during spring. *Front. Environ. Sci.* 10:1059292. doi: 10.3389/fenvs.2022.1059292

Effects of local aerosol and transported dust pollution on the surface energy balance over farmland in eastern China during spring

Chuanru Zhou[1†], Zexia Duan[1†], Xinfeng Ling[2] and Yuanjian Yang[1*]

[1]Key Laboratory for Aerosol-Cloud-Precipitation of China Meteorological Administration, Climate and Weather Disasters Collaborative Innovation Center, School of Atmospheric Physics, Nanjing University of Information Science and Technology, Nanjing, China, [2]Shouxian Meteorological Bureau of Anhui Province, Shouxian, China

Compared with the urban boundary layer, air pollution–surface energy budget interactions in farmland areas are relatively sparse. To investigate the roles of local aerosol and transported dust pollution on the surface energy balance over farmland, a field experiment was conducted during spring 2016 in eastern China. The heavy pollution episodes during the measurement period were typically accompanied by easterly winds, low wind speeds, and high relative humidity. On polluted days, relative to clean days, both downward and upward shortwave radiation decreased by 46%, while downward and upward longwave radiation increased by 4% and 1%. The combined effects of the four radiation components resulted in a 33% reduction in net radiation on polluted days, and thus, the surface energy budget changed. Polluted days had 15% (58%) less sensible (latent) heat flux than clean days. This resulted in a higher daytime Bowen ratio on polluted days (0.83) compared to clean days (0.44). In a case analysis of dust pollution, high wind speeds and continuous high pressure induced the outbreak of the dust pollution episodes. Compared to local pollution events, the latent (sensible) heat flux was reduced more (less) than that in transported dust pollution events. Generally, this work has important implications for understanding the surface energy balance across land–atmosphere interactions over farmland regions, which are experiencing frequent aerosol pollution from local emissions and transboundary dust events.

KEYWORDS

dust pollution, aerosol, meteorological factors, surface energy balance, farmland

1 Introduction

Particulate matter (PM) air pollution poses a great threat to the environment, global climate change, and human health (Gu et al., 2018; Hamanaka and Mutlu, 2018; Yang et al., 2019; Wang et al., 2020a). Meanwhile, the process of heat exchange is one of the most important factors in the surface energy budget for understanding the formation, maintenance, and dissipation of PM pollutants (Guo et al., 2016; Wang et al., 2020b). Radiative transfer processes can be modulated by aerosols through the scattering, reflection, and absorption of shortwave radiation and through the reflection, absorption, and emission of longwave radiation, which further alter the surface energy balance (Jacobson et al., 2007; Brown et al., 2018). For example, Ding et al. (2013) pointed out that mixed agricultural burning plumes with fossil fuel combustion pollution in eastern China could result in the solar radiation intensity reducing by more than 70%. In a winter wheat field on the North China Plain, the daily mean shortwave (longwave) radiation on polluted days reduced (increased) by about 50% (20%) when compared to clean days, due to the radiative forcing of aerosols. Although the radiative forcing of aerosols has been intensively investigated, a thorough understanding of the surface energy budget under different pollution levels has yet to be realized, especially in the Huaihe River Basin (HRB) of eastern China. In addition, most observation stations are located in urban or suburban areas, with relatively little observational data available for the pure farmland background area, meaning there is a lack of knowledge on the effects of aerosols on surface energy budgets over farmland. In China, there is a large amount of farmland (accounting for 12.5%), which plays a key role in weather forecasting across the range of land–atmosphere interaction. At present, weather forecasting models rarely account adequately for the energy balance in cases of aerosol pollution, and thus studying the effects of aerosols on surface energy budgets over farmland can help to improve weather forecasting models. Also, more broadly, such work has important implications for understanding the surface energy balance across the land–atmosphere interactions that take place over farmland regions, which themselves are experiencing frequent aerosol pollution episodes, owing to local emissions and transboundary dust events.

The HRB (30°–36°N, 112°–122°E), a transitional belt between the subtropical and temperate climate regions in eastern China, is an area known to be sensitive to climate change (Jin et al., 2022). It belongs to the warm temperate semi-humid monsoon climate zone, with the mean annual precipitation varying between 600 and 1400 mm, and the average air temperature (T_a) ranging from 11°C to 16°C (Xu et al., 2021). Owing to the sufficient precipitation and suitable temperature, the HRB has become one of China's major grain-producing areas (Yang et al., 2020a). Recently, PM pollution episodes have started to occur frequently and intensively over the farmland area of the HRB. The aerosol composition and sources in the HRB are complex, including not only local anthropogenic pollutants (e.g., from crop straw burning, transportation, and industrial emissions) but also natural aerosols from regional dust storms in spring (Jin and Shepherd, 2008; Fan et al., 2010). In addition to the issue of air pollutant emissions, the formulation of PM pollution episodes is also closely related to the prevailing meteorological conditions [e.g., winds, temperature inversion, relative humidity (RH), and boundary layer height], and synoptic-scale circulation (Zhang et al., 2014; Li et al., 2018; Fan et al., 2019; Wang et al., 2019; Yin et al., 2019). To explore the air pollution–boundary layer dynamics, many atmospheric field experiments have been conducted in the HRB over the past few years (Gao et al., 2003; Tanaka et al., 2007; Chen et al., 2015; Duan et al., 2021). For example, Kang et al. (2013) analyzed a long-lasting haze episode in Nanjing and found that the formation of haze pollution was often accompanied by lower wind speeds, a stably stratified atmosphere and a lower planetary boundary layer depth. Moreover, dust pollution in Asia generally originates from remote areas, such as northern China or Inner Mongolia (Liu et al., 2009; Liu et al., 2011). Also, for eastern China specifically, Han et al. (2022) reported that the storms in spring transporting dust to the region mainly derive from the deserts of Northwest China, Central Asia, South Asia, and East Asia, based on spaceborne lidar measurements.

Previous studies have shown that aerosols can discernably decrease the surface net shortwave radiation in the HRB (Xiong et al., 2022), and this in turn can result in rice yields in East China reducing by around 6.74% on average (Wang et al., 2020c). In addition, air pollution caused by the combination of local sources and long-distance transport is prominent in the HRB (Hu et al., 2018; Shao et al., 2006; Zhu et al., 2011; Shen et al., 2015), where PM concentrations from regional transport are higher than the average typically observed for concentrations from local sources (Ding et al., 2017; Hu et al., 2018). However, few studies have focused on the effects of local aerosol and transported dust pollution on the surface energy balance over farmland in the HRB. Thus, this study seeks to quantify the differences in the meteorological conditions, radiation, and turbulent flux on days categorized according to three different pollution levels (background, clean, and polluted) at a farmland site in spring in eastern China. Following this introduction, Section 2 introduces the site, instruments, and data processing methods; Section 3 reports and discusses the results; and Section 4 provides conclusions.

2 Data and methods

2.1 Data

The data used in this study were obtained from the National Climatology Observatory (32.44°N, 116.79°E; 26.8 m above sea

TABLE 1 Type key technical specifications of sensors.

Sensor type	Measurement range	Accuracy	Sampling frequency (Hz)	Installation height (m)
CNR4	DSR and USR: 0.3–2.8 μm	DSR and USR: 10–20 μv W^{-1} m^{-2}	0.1 Hz	1.5
	DLR and ULR: 5–50 μm	DLR and ULR: 5–15 μv W^{-1} m^{-2}		
CSAT3A	u, v, w: ±65.6 m s^{-1}	±2% (wind vector within ±5° of horizontal)	10 Hz	2.5
	T_a: −50 to 60°C	±3% (wind vector within ±5° of horizontal)		
EC150	CO_2: 0–1,000 μmol mol^{-1}	±1%	10 Hz	2.5
		±2%		
GRIMM180	$PM_{2.5}$ and PM_{10}: 0–1,500 μg m^{-3}	±5%	0.1 Hz	At the top of a 3 m-high building

DSR, USR, DLR, and ULR, are the downward shortwave radiation, upward shortwave radiation, downward longwave radiation, and the upward longwave radiation. u and v are the horizontal wind velocity along the *x* and *y* axis. w is the vertical wind velocity. T_a is the air temperature.

level) in Shouxian County, Anhui Province, China. The site is located on the south bank of the Huaihe River and is influenced by the subtropical monsoon climate (Figure 1). The annual mean T_a in 2015–2018 was 16.4°C and the annual precipitation was 1116 mm (Duan et al., 2021). During the measurement period (March–May 2016), winter wheat was grown around the site. A 2.5 m eddy covariance flux tower, equipped with a three-dimensional sonic anemometer (CSAT3A, Campbell Scientific Incorporation, United States) and a CO_2/H_2O open-path gas analyzer (EC150, Campbell Scientific Incorporation, United States), was installed at the center of the wheat field to continuously monitor the surface turbulent flux. In addition, a net all-wave radiometer (CNR4, Kipp & Zonen Inc., Netherlands) was installed at 1.5 m a.g.l. (meters above ground level). The raw 10-Hz EC eddy covariance data were averaged over 60-min periods following the methods described in Duan et al. (2022). Additional sensors measuring coarse PM (PM_{10}) and fine PM ($PM_{2.5}$) (GRIMM180) were installed on top of a 3 m-high building, 100 m northwest of the flux tower. The PM concentration, radiation, and meteorological data were excluded according to the criterion of $X(t) < (\bar{X} - 4\sigma)$ or $X(t) > (\bar{X} + 4\sigma)$, where $X(t)$ is the observation value, $\bar{X}$ denotes the means over the interval, and σ is the standard deviation. Eddy fluxes of sensible heat and latent heat were calculated as: $Hs = \bar{\rho} C_p \overline{\omega' T'}$, $LE = L\bar{\rho}\overline{\omega' q'}$, where $\bar{\rho}, C_p$ and L are the density of air (kg m^{-3}), the specific heat of air (J kg^{-1} K^{-1}), and the latent heat of vaporization (J kg^{-1}), respectively. ω', T' and q' are the fluctuations in the vertical wind component (m s^{-1}), air temperature (K) and specific humidity, respectively (Gao et al., 2009). In addition, data collected on rainy days were discarded to minimize the effects of clouds and precipitation. More detailed information about the instruments can be found in Table 1.

2.2 Materials and methods

Based on the environmental air quality criteria proposed by the Ministry of Environmental Protection of China, the days on which pollution events occurred during the measurement period were categorized into three levels: 1) background days, 2) clean days, and 3) polluted days. The selected period covered 1 March–31 May, during which, as illustrated in Figure 2, pollution episodes occurred frequently, with some episodes (e.g., on 2 March) having daily maximum values of PM_{10} and $PM_{2.5}$ that reached as much as 414 and 320 μg m^{-3}. Background days represented the arithmetic means of variables during the measurement period apart from on days when precipitation events occurred and the 2 days for either side of those events. Daily mean PM_{10} concentrations higher than 150 μg m^{-3} for more than 48 consecutive hours and hourly $PM_{2.5}$ concentrations higher than 100 μg m^{-3} were regarded as polluted episodes. To reduce the impacts of solar altitude and seasonal changes, four polluted cases (i.e., 2–8 March, 13–15 March, 17–20 March, and 26–27 March) in the same month were selected. In addition, clean days were defined as when the daily mean PM_{10} was lower than 150 μg m^{-3} within 5 days before and after each polluted episode. Ultimately, 20 background days (background episodes, BEs), 6 clean days (clean episodes, CEs), and 6 polluted days (polluted episodes, PEs) were obtained during 3 months (Table 2). The daily mean PM_{10} ($PM_{2.5}$) concentrations for CEs, BEs, and PEs were 104, 124, and 234 μg m^{-3} (68, 91. and 184 μg m^{-3}), respectively. Moreover, four dust cases (i.e., 8–14 March, 18–23 March, 5–11 May, and 10–15 May) were identified in the study period from the dust records of weather phenomena at the weather station, in which the ratios of PM_{10} and $PM_{2.5}$ are combined and precipitation events are excluded.

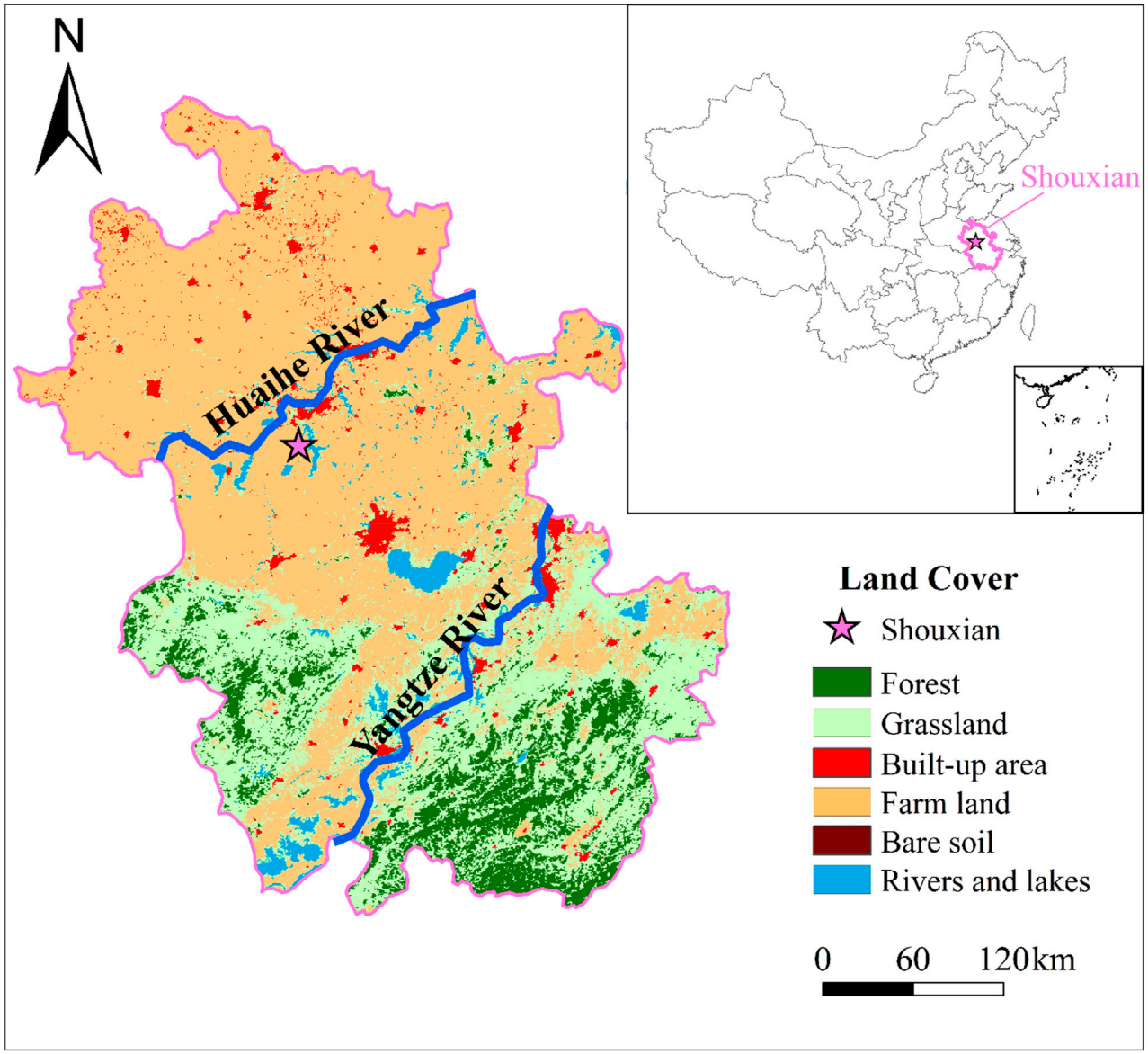

FIGURE 1
MODIS land use/land cover (resolution: 500 m) in eastern China in 2016.

3 Results and discussion

3.1 Meteorological conditions

As shown in Figure 3A, the wind speed and variance of vertical wind speed (σ_w^2) had consistent diurnal variations under different pollution conditions. The wind speed fluctuated between 1.5 m s^{-1} during 00:00–08:00 LST (local standard time), and then increased sharply to a relatively high value (about 2.5–3.5 m s^{-1}) at noon. After that, the wind speed began to decrease and kept at a stable value of about 1.5 m s^{-1} during 18:00–24:00 LST. The wind speed and σ_w^2 were markedly different on background, clean, and polluted days. For example, the wind speed on clean days was broadly higher than that on polluted days, especially in the middle part of the day (13:00 LST; difference could be up to 1 m s^{-1}), which was favorable for atmospheric diffusion. High-PM concentrations were mostly found under low wind speeds (about 1.7 m s^{-1}) from the east or southeast—around 20% lower than during CEs—indicating that local sources contribute to elevated loadings of PM_{10} at the observatory (Figures 3B, C).

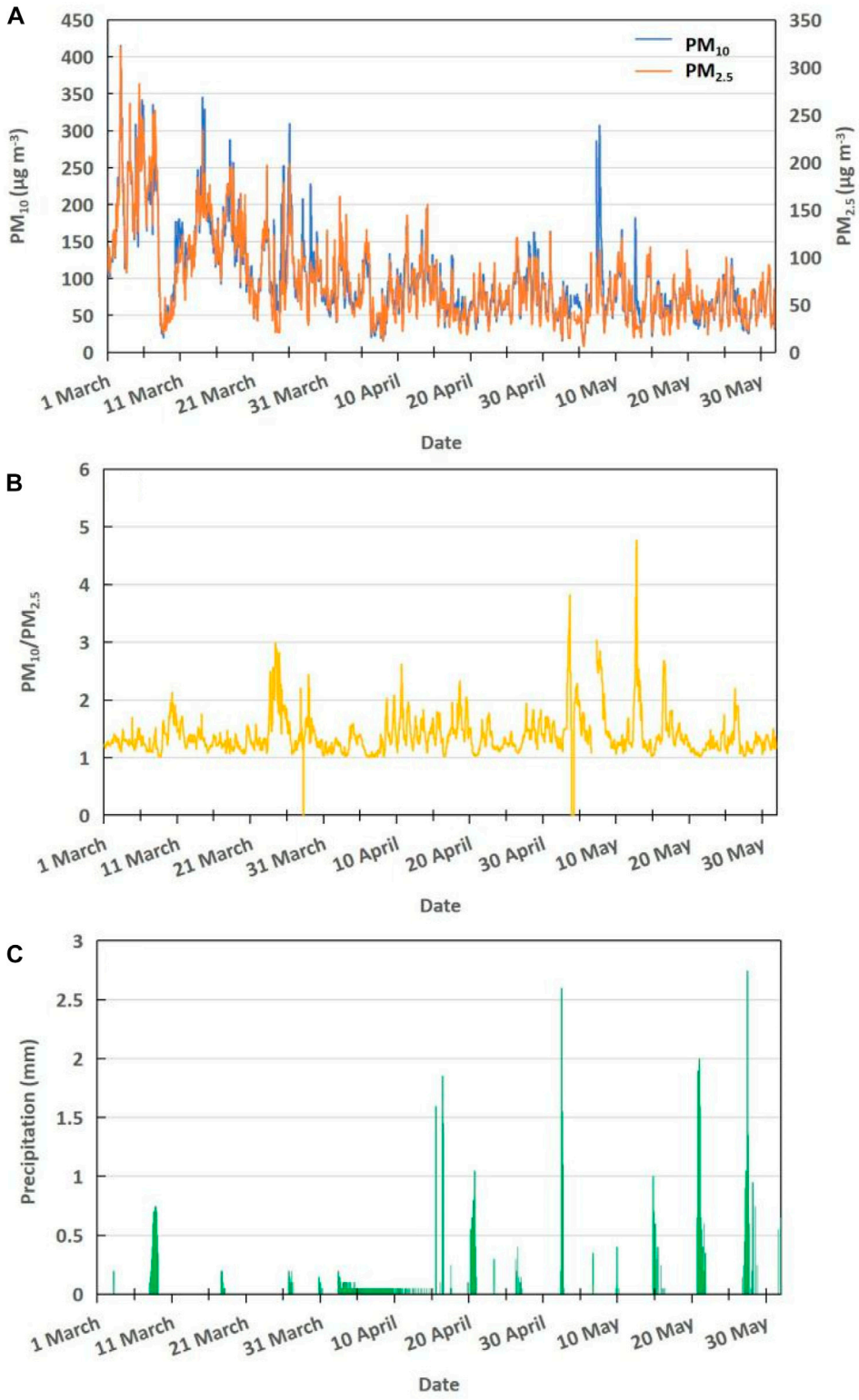

FIGURE 2
Hourly **(A)** mass concentrations of PM_{10} and $PM_{2.5}$, **(B)** ratio of PM_{10} to $PM_{2.5}$, and **(C)** precipitation during 1 March–31 May 2016.

TABLE 2 Typical pollution and clean days.

Type	Date	PM_{10} (μg m^{-3})	$PM_{2.5}$ (μg m^{-3})
Pollution days	2 March 2016	245	187
	4 March 2016	223	173
	5 March 2016	278	214
	6 March 2016	213	175
	7 March 2016	231	197
	14 March 2016	216	159
Clean days	11 March 2016	136	91
	21 March 2016	69	54
	23 March 2016	110	78
	24 March 2016	87	38
	28 March 2016	107	70
	29 March 2016	116	79

The PM concentration increased with increasing of T_a (Figure 4). High T_a was induced by southeasterly winds during PEs, which would bring warm and moist air to Shouxian. In addition, the radiative warming effect due to the absorption/reflection of longwave radiation by air pollutants can lead to a high T_a (Cao et al., 2016). The daily mean RH during PEs (40%) and BEs (23%) was much higher than during CEs, indicating that high RH was conducive to the growth of aerosol hygrosorption (Peter, 1988; Hara et al., 2018).

3.2 Surface energy budget

Aerosols modulate the climate by absorbing and scattering solar radiation to alter the energy budget of the earth–atmosphere system (Wang et al., 2019). Figure 5 shows the diurnal variations in surface radiation (Rn), sensible heat flux (Hs), and latent heat flux (LE) under the PEs, CEs, and BEs in Shouxian from March to May 2016. The downward shortwave radiation (DSR) and upward shortwave radiation (USR) during PEs were much lower than during CEs (Figure 5A). The DSR on PEs decreased by 15–287 W m^{-2} during the daytime (07:00–18:00 LST); the attenuation rate was 28%–84% and the daily average value was 123 W m^{-2}. Meanwhile, the USR during PEs decreased by 4–52 W m^{-2}, with an attenuation rate of 27%–80% during the daytime. In order to eliminate the interference of cloud cover, some typical polluted days with few or no clouds were selected (Tables 3, 4). The DSR and USR during PEs with few or no clouds were also lower than those during CEs; the DSR decreased by 6–75 W m^{-2} during the daytime (07:00–18:00 LST), with an attenuation rate of 1%–11% (Figure 6A). The downward longwave radiation (DLR) and upward longwave radiation (ULR) showed unimodal diurnal variation. The peak of ULR was delayed by 30 min–1 h compared with the peak of DLR, reflecting the response time of the underlying surface of farmland in Shouxian County to solar radiation heating during the diurnal cycle (Figures 5B, 6B). The DLR and ULR during PEs were higher than those during CEs, with daily average differences of 13 and 4 W m^{-2} between PEs and CEs, respectively (Figure 5B).

Under the three types of weather conditions, the trend of Rn was consistent with that of shortwave radiation (both DSR and USR), indicating that shortwave radiation was the main factor affecting Rn (Figures 5C, 6C). The Rn during the day was significantly lower during PEs than CEs with clouds (few clouds or clear days), with a peak difference of more than 100 W m^{-2} (61 W m^{-2}), approaching 32% (12.5%) and a mean daily difference of 115 W m^{-2} (20 W m^{-2}) (Figures 5C, 6C). In contrast, the difference in Rn between different weather conditions at night was very small, and the Rn during PEs was slightly higher than during CEs (Figures 5C, 6C). In the daytime, aerosols weakened the solar radiation reaching the ground and reduced the effective radiation at the surface. Under the combined effect of the two, the Rn was reduced, thus weakening the energy of the earth–atmosphere system and causing the ground to cool. Longwave radiation played a dominant role at night, and the existence of aerosols reflected the longwave radiation emitted by the ground and the lower atmosphere back to the surface, increasing the DLR and playing a role in thermal insulation (Figures 5B, 6B).

The diurnal variations of Hs and LE were similar to that of Rn, showing a consistent unimodal pattern (Figures 5D, 6D). The diurnal variation of Hs was comparable during BEs, PEs, and CEs with clouds (few clouds or clear days), with daytime mean values of 36, 33, and 39 W m^{-2} (36, 36, and 39 W m^{-2}), respectively. LE dominated the Rn during all three types of weather conditions with clouds (few clouds or clear days), with the daytime mean LE/Rn being 32%, 21%, and 28% (32%, 24%, and 28%) for BEs, PEs, and CEs, respectively. The LE during PEs with few clouds also increased by 13 W m^{-2} (Figures 5D, 6D). In the daytime, the mean Bowen ratio (β = Hs/LE) was about 0.36, 0.83, and 0.44 (0.36, 0.55, and 0.44) for BEs, PEs, and CEs with much cloud (few clouds or clear days) (Figures 5D, 6D). Therefore, through comparative analysis, the reduction in aerosols changed the distribution of Rn in Hs and LE, and the effect of aerosols on LE was greater than that of Hs. However, in the urban areas of the Yangtze River Delta, the situation is on the contrary. Hs dominates Rn and aerosols had deeper influence on Hs than that on LE (Ling and Han, 2019).

The diurnal variation of LE was more obvious than that of Hs (Figures 5D, 6D). Since the underlying surface of this area is farmland, crops transpire and vegetation interacts with the atmosphere, so there is a high rate of water vapor exchange. The LE was obviously larger than the Hs (Figures 5D, 6D), which indicated that the heat exchange in this area was mainly in the form of LE, and the heat exchange by moisture was

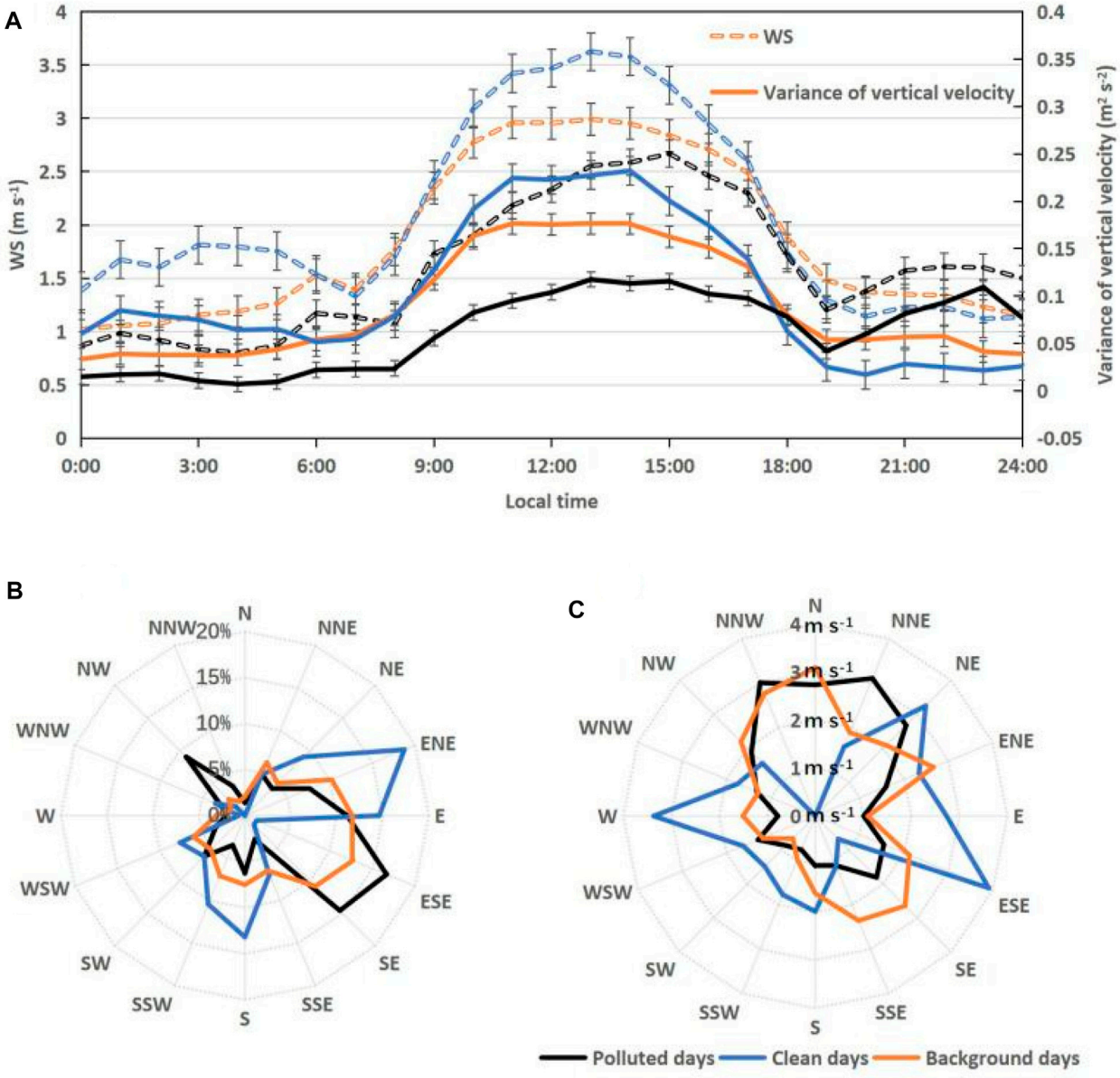

FIGURE 3
Diurnal variations of winds under three pollution levels (background, clean, and polluted days): **(A)** wind speed (WS) and variance of vertical velocity, **(B)** radar chart for wind direction, and **(C)** radar chart for wind speed.

stronger than the heat exchange caused by the change in surface temperature between land and atmosphere. This was because aerosols during PEs in Shouxian reduced the transpiration rate of crops, so the LE during PEs was much less than that during CEs (Wang et al., 2021). Meanwhile, the Hs had a similar range of variation and the same trend under the three types of weather conditions, so the influence of aerosols on LE during PEs was greater than on Hs (Figures 5D, 6D).

3.3 Case analysis

In order to deepen the level of understanding regarding the impact of transported dust pollution on the surface energy balance over farmland in eastern China, four cases (i.e., 7–8 May, 10–11 March, 20–21 March, and 12–13 March) were selected. Here, we focus on the evolution of the atmospheric boundary layer structure during a dust pollution period (7–8 May 2016).

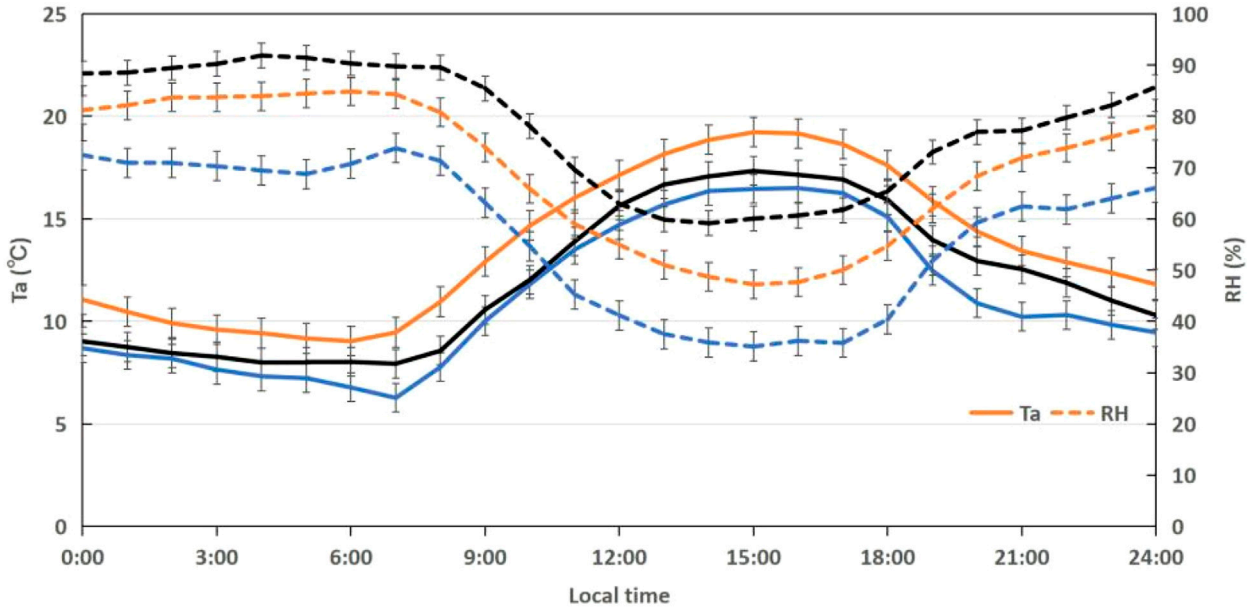

FIGURE 4
Diurnal variations of air temperature (T_a, solid lines) and relative humidity (RH, dashed lines) on heavily polluted days (black), clean days (blue), and background days (yellow).

3.3.1 Meteorological conditions

On 5 May, the surface PM_{10} concentration began to increase steadily. Starting from 13:00 LST 7 May, the PM_{10} concentration increased dramatically and reached up to 307 μg m^{-3} by 19:00 LST 7 May. The site was controlled by low pressure (~1,001 hPa) before the occurrence of the dusty pollution (5–6 May). However, the surface air pressure increased rapidly from 12:00 LST 6 May, and then remained at a high level of 1010 hPa during 7–8 May. Thereafter, the pressure oscillated and dropped, and the concentration also gradually fell back (Figure 7A1). Similar phenomena also occurred in other dusty pollution events (Figures 7A2–A4). In addition, high wind speeds transported a lot of regional aerosol, which caused the outbreak of the dust pollution (Figures 7B1–B4). The T_a was relatively low between 16:00 LST 7 May and 02:00 LST 8 May, when PM_{10} concentrations remained high (Figure 7C1). After that, the PM_{10} concentration gradually decreased as the T_a increased. High temperatures accelerate evaporation from rivers, resulting in high RH, which inhibits the occurrence of dust pollution. High RH can increase the viscosity of the near-surface air and sand, which further inhibits the occurrence of dust pollution (Chang et al., 2012). As shown in Figures 7D1–D4, RH at about 50% was able to inhibit the occurrence of dust pollution. Meanwhile, the RH was relatively low (daily mean: 69%) during the dust events (Figure 7C1). Therefore, high air pressure, low T_a, and low RH co-induced the formation, maintenance, and dissipation of dust pollutants.

3.3.2 Radiation and turbulent flux

As can be seen in Figure 8A1–A4, the shortwave radiation during the dust pollution periods was significantly lower than on clean days. For example, the downward radiation at noon on 7 May was approximately 481 W m^{-2}, lower than the value of 657 W m^{-2} on 6 May. During the process of dust pollution, the surface effective radiation decreased obviously under the effect of aerosol. The Rn at noon on 7 May had decreased by 385 W m^{-2} compared with the previous day. As can be seen from Figures 8B1–B4,C1–C4, the Hs and LE also weakened as the Rn decreased. Compared to the clean days beforehand, the Hs and LE decreased by 3 and 35 W m^{-2}, respectively, during dust pollution days. In addition, the proportion of Hs and LE in Rn also reduced, by 43% and 49%, respectively. Hence, an outbreak of dust pollution has a greater impact on LE. Dust pollution weakens crop photosynthesis and transpiration, which further reduces the surface–atmosphere exchanges of water, energy, and carbon dioxide.

3.3.3 Dynamic factors

Previous studies have reported that PM concentrations are closely related to dynamic factors in the near-surface layer (Zhang et al., 2015; Miao et al., 2018). Figure 9 shows the response of surface dynamic factors (vertical velocity and covariance of vertical velocity and horizontal wind components) during the dust pollution episodes. The variance of vertical velocity (σ_w^2) showed an obvious unimodal pattern of diurnal variation, and the diurnal maximum appeared at noon. The highest σ_w^2 (0.27 m^2 s^{-2}) occurred at 18:00 LST 6 May. Then,

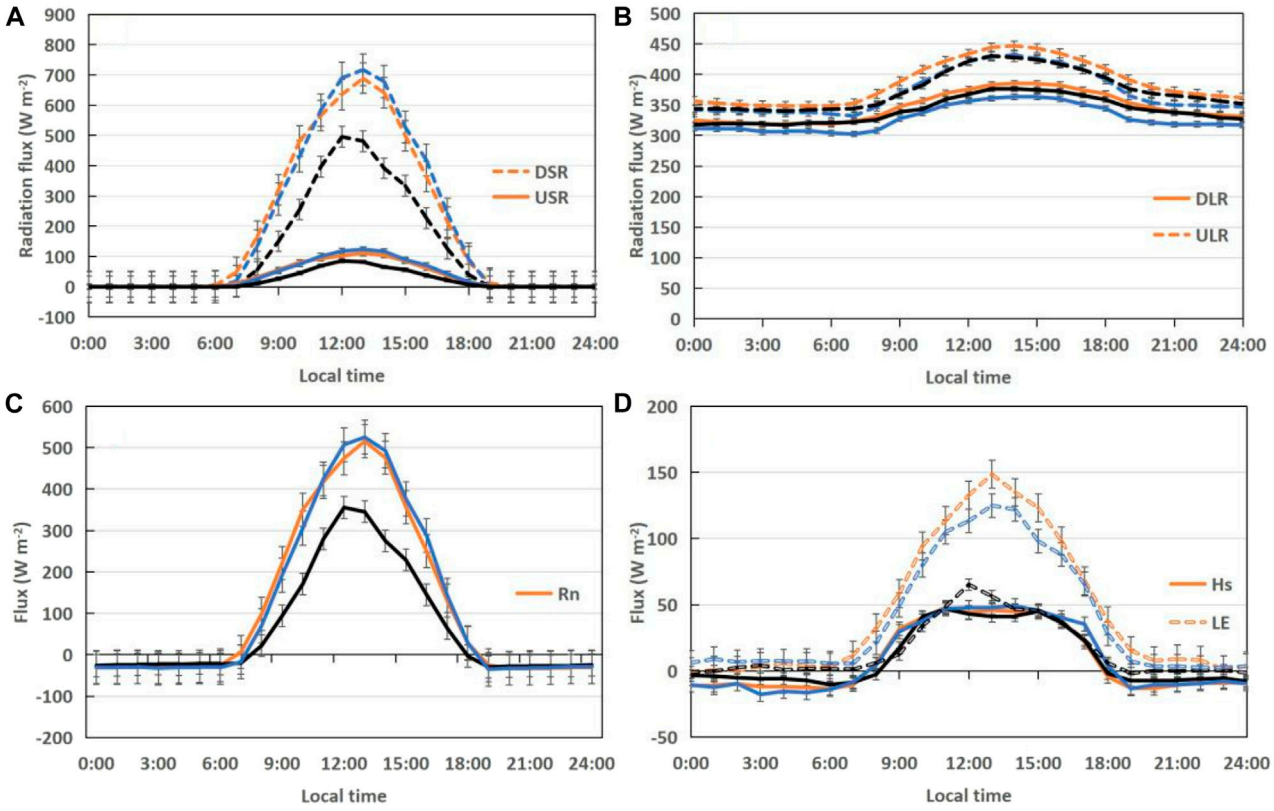

FIGURE 5
Diurnal variations in the four components of the surface energy balance under three pollution levels (background days: yellow, clean days: blue, and polluted days: black): **(A)** downward shortwave radiation (DSR) and upward shortwave radiation (USR), **(B)** downward longwave radiation (DLR) and upward longwave radiation (ULR), **(C)** net radiation (Rn), and **(D)** sensible heat flux (Hs) and latent heat flux (LE).

TABLE 3 Typical polluted days with clouds.

Date	Mean daily PM_{10} ($\mu g\ m^{-3}$)	Mean daily $PM_{2.5}$ ($\mu g\ m^{-3}$)	Mean daily cloud cover	Mean daily low cloud cover	Weather
2 March 2016	245	187	8	0	Cloudy
4 March 2016	223	173	10	0	Cloudy
5 March 2016	278	214	8.6	0	Cloudy
6 March 2016	213	175	6	0	Partly cloudy
7 March 2016	231	197	10	0	Cloudy
14 March 2016	216	159	2.8	0	Partly cloudy

σ_w^2 declined slowly until 8 May, with the maximum daytime value of 0.16 $m^2\ s^{-2}$ occurring at 19:00 LST (PM_{10} larger than 300 $\mu g\ m^{-3}$ during this period). This turbulence transported the PM accumulated in the residual layer downwards to the lower levels, resulting in the later cumulative stage of PM (Halios and Barlow, 2018).

Figure 9B shows the covariance of the vertical velocity and the horizontal wind component. There was a clear positive correlation between the southeasterly wind component and the vertical velocity before the outbreak of the pollution process. Southeasterly winds promoted the transport of pollutants to Shouxian. The enhanced downdraft and the

TABLE 4 Typical polluted days with few clouds or clear sky.

Date	Mean daily PM_{10} (μg m^{-3})	Mean daily $PM_{2.5}$ (μg m^{-3})	Mean daily cloud cover	Mean daily low cloud cover	Weather
1 March 2016	130	106	0.6	0	Clear day
6 March 2016	213	175	6	0	Partly cloudy
14 March 2016	216	159	2.8	0	Partly cloudy
16 March 2016	140	108	4.8	0	Partly cloudy
19 March 2016	155	130	0	0	Clear day
22 March 2016	148	120	5.6	0	Partly cloudy

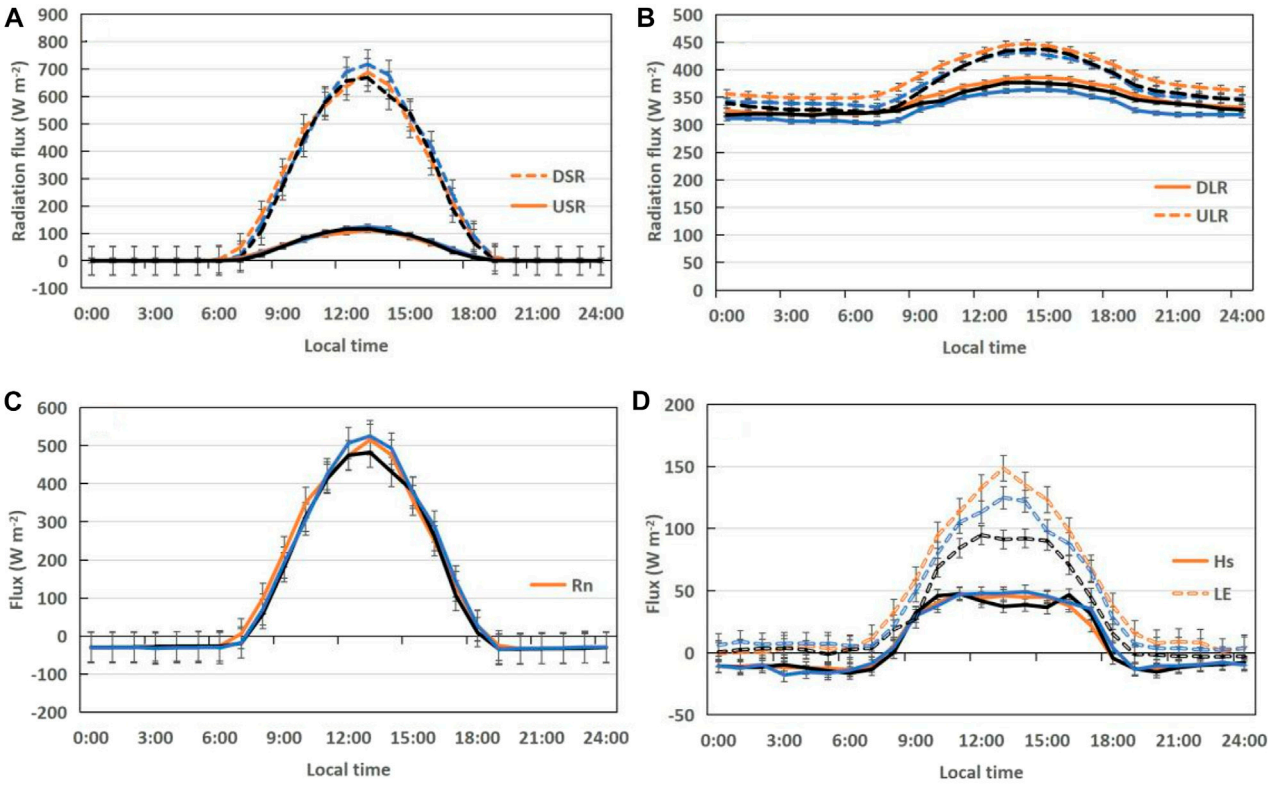

FIGURE 6
Diurnal variations in the four components of the surface energy balance under three weather conditions with less cloud or clear days (background weather—yellow, clean sky—blue, and polluted sky—black): **(A)** downward shortwave radiation (DSR) and upward shortwave radiation (USR), **(B)** downward longwave radiation (DLR) and upward longwave radiation (ULR), **(C)** net radiation (Rn), and **(D)** sensible heat flux (Hs) and latent heat flux (LE).

increased vertical momentum flux caused the downward transport of pollutants over Shouxian, leading to rapid accumulation and mixing of pollutants in the area (Figure 9B). The horizontal winds and vertical velocity jointly changed the aerosol concentration. From 7 to 8 May, the covariance of the vertical velocity and the horizontal wind component was negative (around $-0.05\ m^2\ s^{-2}$), indicating that the vertical velocity and horizontal wind component changed in

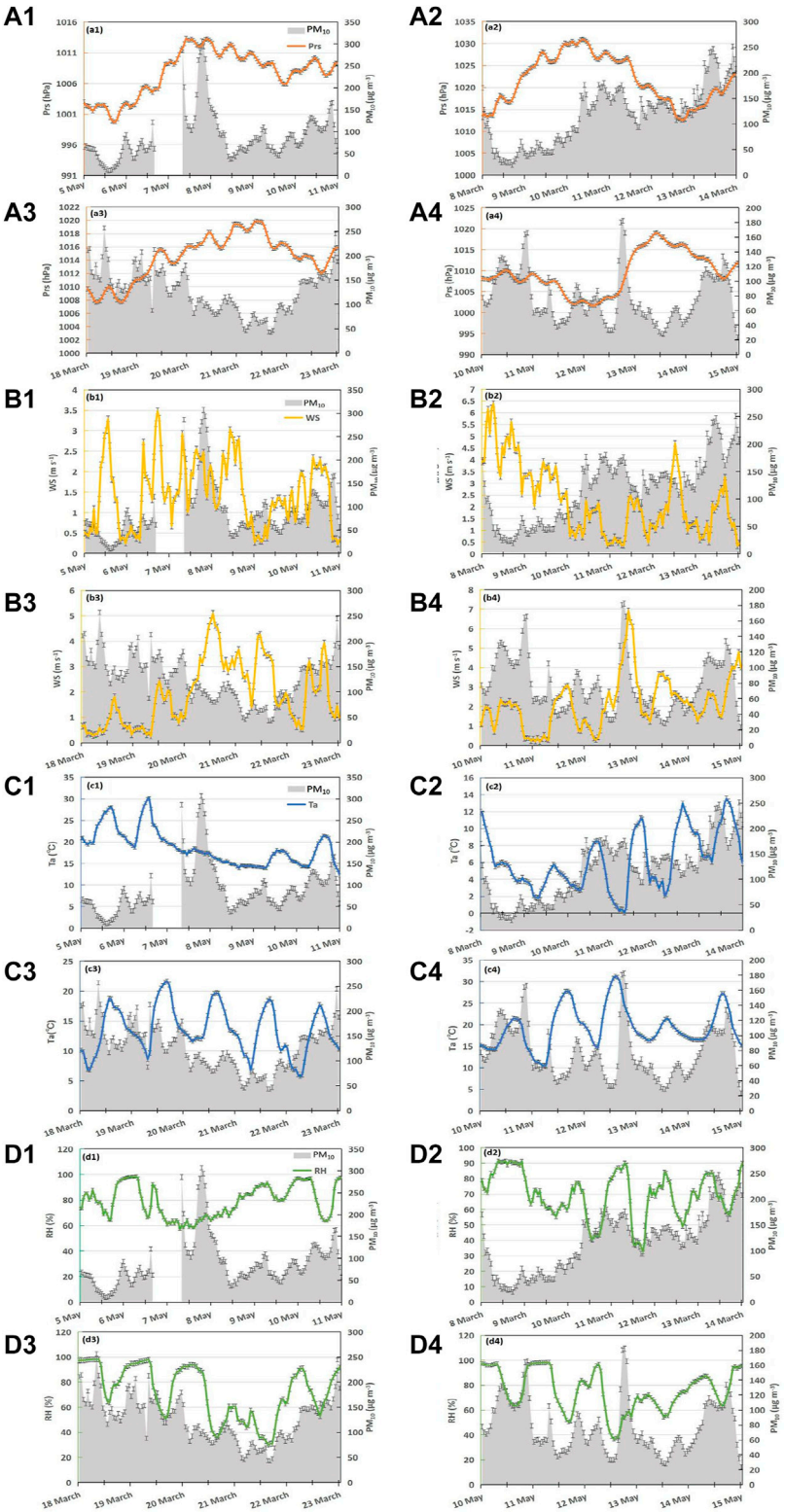

FIGURE 7
Daily variations in surface micrometeorological conditions during dust pollution periods: **(A1–A4)** air pressure (Prs), **(B1–B4)** wind speed (WS), **(C1–C4)** air temperature (T_a), and **(D1–D4)** relative humidity (RH). The gray-shaded region in each panel is the PM_{10} concentration.

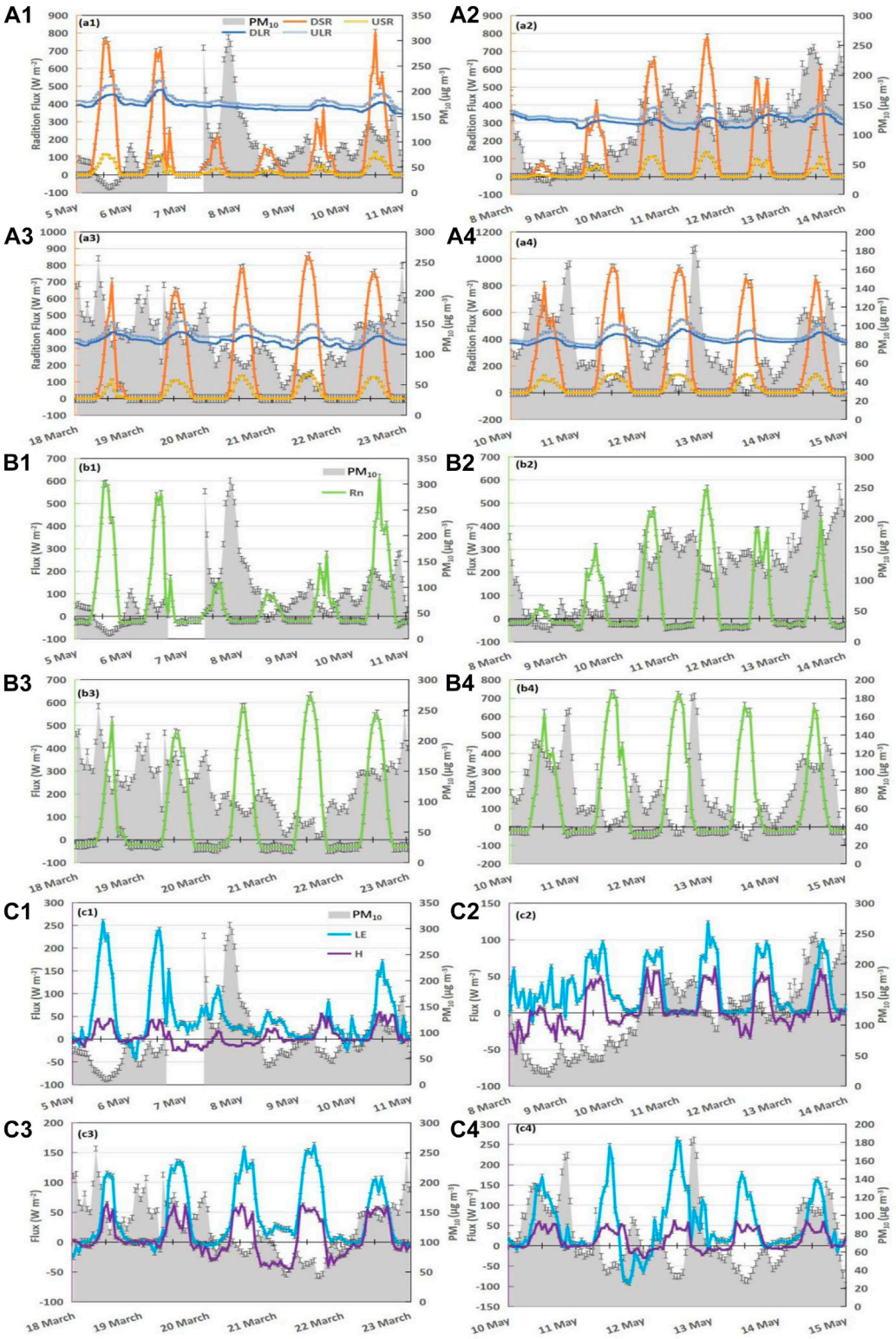

FIGURE 8
Daily variation in the surface energy budget during dust pollution periods: **(A1–A4)** the four radiation components (DSR, downward shortwave radiation; USR, upward shortwave radiation; DLR, downward longwave radiation; and ULR, upward longwave radiation), **(B1–B4)** net radiation flux (Rn), and **(C1–C4)** sensible heat flux (Hs) and latent heat flux (LE). The gray-shaded region in each panel is the PM_{10} concentration.

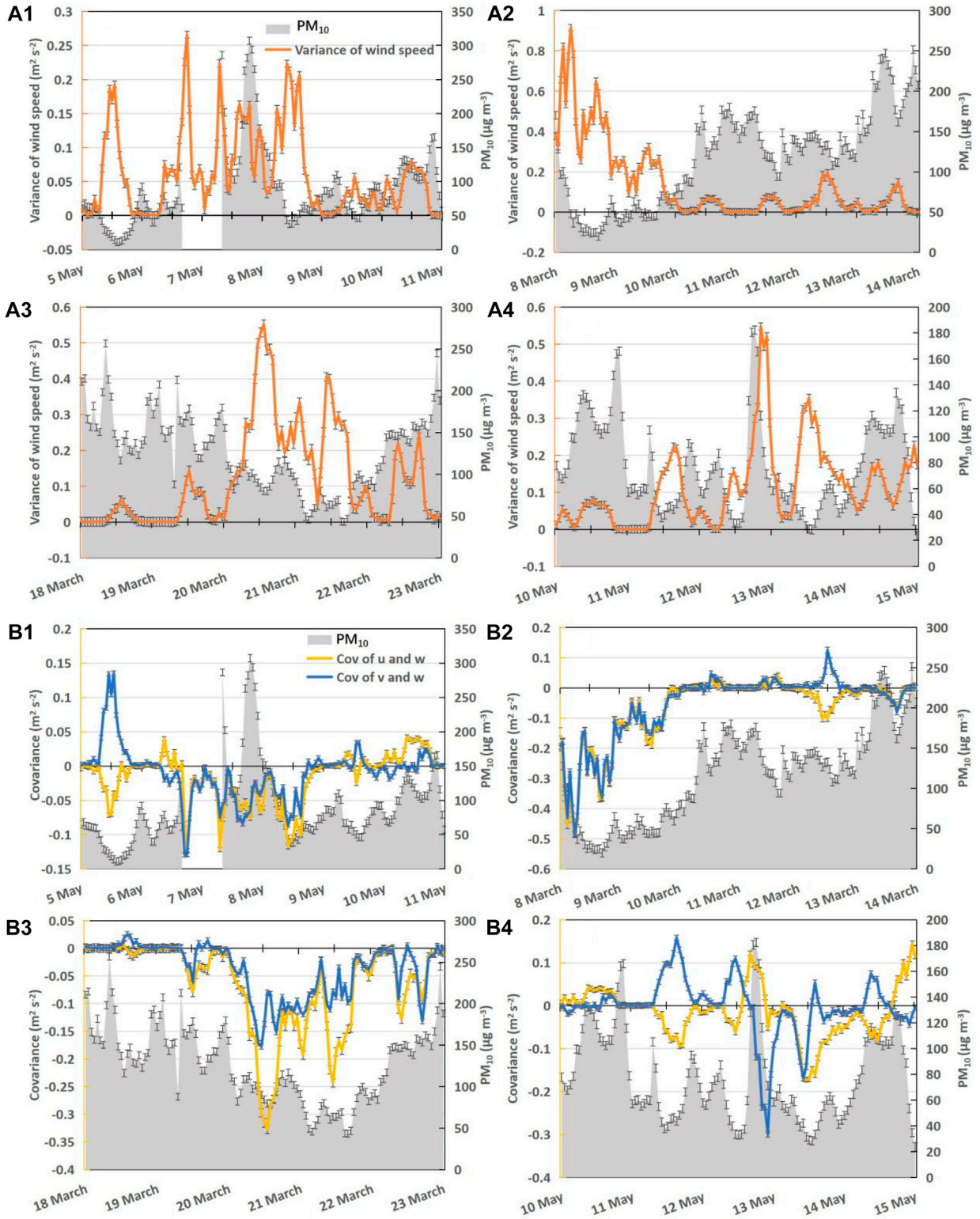

FIGURE 9
Daily variations in surface dynamic factors during dust pollution periods: **(A1–A4)** vertical velocity variance and **(B1–B4)** covariance of vertical velocity (w) and horizontal wind components (u, v). The gray-shaded region in each panel is the PM_{10} concentration.

the opposite direction. The horizontal wind component became larger and the vertical velocity became smaller. Eventually, these factors led to the occurrence of dust pollution in this area. The decrease in air pressure and wind speed led to a rapid decrease in the PM_{10} concentration on 8 May, which also resulted in a continuous decrease in the covariance between the horizontal wind component and the vertical velocity. At this moment, the degree of reversal in the vertical velocity and horizontal wind component became more pronounced. The rapid increase in vertical velocity and decrease in the horizontal component prompted dust floating in the air to be deposited downwards, and thus, the pollution process was weakened.

3.4 Limitations

There are differences in composition and size among different aerosol types. In terms of composition, absorptive and scattering aerosols differ in their effects on radiation and energy balance. For example, absorbing aerosol dominated by black carbon has strong absorbing properties, which induce both prominent surface cooling and near-surface warming. Scattering aerosols are dominated by sulfate, which has a strong scattering capacity and cools the surface to result in a weaker near-surface warming (Gu et al., 2006; Ding et al., 2016; Huang et al., 2018; Zhu et al., 2018; Yang et al., 2020b).

In addition, the size of aerosol particles also affects the radiation budget (Tegen and Lacis, 1996; Murphy et al., 2021), but there is no way to quantitatively distinguish the corresponding relationship between radiation and particle size when measuring radiation. Therefore, mainly, the differences in radiation and energy balance are compared by taking the $PM_{2.5}$ as the primary pollutant under the eastern region's background and the PM_{10} transported from a distance. However, the meteorological factors under the two different backgrounds also bear some differences, so they too will bring some errors to the contributions of different aerosol species to the effect on the surface energy balance over farmland. Sensitivity tests with more precise observations and numerical simulations will be conducted in the future.

4 Conclusion

Based on the meteorological observations, and measurements of radiation and turbulent flux in Shouxian between 1 March and 31 May 2016, meteorological factors and the surface energy balance were analyzed under different air pollution levels. The main conclusions can be summarized as follows:

1) Compared to clean days, polluted days had high RH, low wind speeds, and low air pressure. Weak wind speed had an inhibitory effect on the diffusion of pollutants. The high RH was conducive to the growth of aerosol hygroscopicity.
2) Compared with the DSR, USR, DLR, and ULR in the daytime during CEs, the attenuation ratios during PEs were about 46%, 46%, 4%, and 1%, respectively, which mainly caused a 33% reduction in Rn.
3) During the whole observation period, the range of diurnal variation of Hs and LE was diminished on highly polluted days. PEs had 15% (58%) less sensible (latent) heat flux than CEs. This resulted in a higher daytime Bowen ratio during PEs (0.83) than CEs (0.44).
4) In Shouxian, sandstorms occur frequently in spring. A sharp increase from low pressure to high pressure (1005–1010 hPa) and the continuation of high pressure cause outbreaks of dust pollution. On dust polluted days, Hs was reduced by 43% and LE by 49%. The influence of aerosol on LE was greater than that on Hs during both typical PEs and dust PEs.

The present study demonstrates that the aerodynamic and thermodynamic conditions in the atmospheric boundary layer are mainly modulated by local aerosol and transported dust pollution. This has important implications for the surface energy balance across the land–atmosphere interactions over farmland regions, which are experiencing frequent aerosol pollution from local emissions and transboundary dust events.

Data availability statement

The raw data supporting the conclusion of this article will be made available by the authors, without undue reservation.

Author contributions

Conceptualization: YY; methodology and software: CZ; formal analysis: CZ, ZD, XL, and YY; data curation: CZ, ZD, and XL; writing—original draft preparation: CZ; writing—review and editing: CZ, ZD, XL, and YY; supervision: YY; and funding acquisition: YY. All authors have read and agreed to the submitted version of the manuscript.

Funding

This study was supported by the National Natural Science Foundation of China (42222503).

Acknowledgments

The authors thank all the scientists, engineers, and students who participated in the field experiments, maintained the instruments, and processed the measurements. They acknowledge the High Performance Computing Center of

Nanjing University of Information Science and Technology for their support in this work.

Conflict of interest

The authors declare that the research was conducted in the absence of any commercial or financial relationships that could be construed as a potential conflict of interest.

Publisher's note

All claims expressed in this article are solely those of the authors and do not necessarily represent those of their affiliated organizations, or those of the publisher, the editors, and the reviewers. Any product that may be evaluated in this article, or claim that may be made by its manufacturer, is not guaranteed or endorsed by the publisher.

References

Brown, H., Liu, X., Feng, Y., Jiang, Y., Wu, M., Lu, Z., et al. (2018). Radiative effect and climate impacts of Brown carbon with the Community Atmosphere Model (CAM5). *Atmos. Chem. Phys.* 18 (24), 17745–17768. doi:10.5194/acp-18-17745-2018

Cao, C., Lee, X., Liu, S., Schultz, N., Xiao, W., Zhang, M., et al. (2016). Urban heat islands in China enhanced by haze pollution. *Nat. Commun.* 7 (1), 12509. doi:10.1038/ncomms12509

Chang, Z., Wang, Y., Han, F., and Zhong, S. (2012). Relationship between frequency of sandstorms and air humidity as well as plant phenology: A case study from the minqin desert area. *Acta eco. Sin.* 32, 1378–1386. doi:10.5846/stxb201101100041

Chen, C., Li, D., Gao, Z., Tang, J., Guo, X., Wang, L., et al. (2015). Seasonal and interannual variations of carbon exchange over a rice-wheat rotation system on the North China Plain. *Adv. Atmos. Sci.* 32 (10), 1365–1380. doi:10.1007/s00376-015-4253-1

Ding, A. J., Fu, C. B., Yang, X. Q., Sun, J. N., Petäjä, T., Kerminen, V. M., et al. (2013). Intense atmospheric pollution modifies weather: A case of mixed biomass burning with fossil fuel combustion pollution in eastern China. *Atmos. Chem. Phys.* 13 (20), 10545–10554. doi:10.5194/acp-13-10545-2013

Ding, A. J., Huang, X., Nie, W., Sun, J. N., Kerminen, V. M., Petäjä, T., et al. (2016). Enhanced haze pollution by black carbon in megacities in China. *Geophys. Res. Lett.* 43 (6), 2873–2879. doi:10.1002/2016GL067745

Ding, X., Kong, L., Du, C., Zhanzakova, A., Wang, L., Fu, H., et al. (2017). Long-range and regional transported size-resolved atmospheric aerosols during summertime in urban Shanghai. *Sci. Total Environ.* 583, 334–343. doi:10.1016/j.scitotenv.2017.01.073

Duan, Z., Gao, Z., Xu, Q., Zhou, S., Qin, K., and Yang, Y. (2022). A benchmark dataset of diurnal- and seasonal-scale radiation, heat, and CO2 fluxes in a typical East Asian monsoon region. *Earth Syst. Sci. Data* 14 (9), 4153–4169. doi:10.5194/essd-14-4153-2022

Duan, Z., Yang, Y., Wang, L., Liu, C., Fan, S., Chen, C., et al. (2021). Temporal characteristics of carbon dioxide and ozone over a rural-cropland area in the Yangtze River Delta of eastern China. *Sci. Total Environ.* 757, 143750. doi:10.1016/j.scitotenv.2020.143750

Fan, S., Gao, Z., Kalogiros, J., Li, Y., Yin, J., and Li, X. (2019). Estimate of boundary-layer depth in Nanjing city using aerosol lidar data during 2016-2017 winter. *Atmos. Environ.* 205, 67–77. doi:10.1016/j.atmosenv.2019.02.022

Fan, X., Chen, H., Xia, X., Li, Z., and Cribb, M. (2010). Aerosol optical properties from the atmospheric radiation measurement mobile facility at shouxian, China. *J. Geophys. Res.* 115 (D7), D00K33. doi:10.1029/2010JD014650

Gao, Z., Bian, L., and Zhou, X. (2003). Measurements of turbulent transfer in the near-surface layer over a rice paddy in China. *J. Geophys. Res.* 108 (D13), 2779. doi:10.1029/2002JD002779

Gao, Z., Lenschow, D. H., He, Z., and Zhou, M. (2009). Seasonal and diurnal variations in moisture, heat and CO_2 fluxes over a typical steppe prairie in Inner Mongolia, China. *Hydrol. Earth Sys. Sci.* 13 (7), 987–998. doi:10.5194/hess-13-987-2009

Gu, Y., Liou, K. N., Xue, Y., Mechoso, C. R., Li, W., and Luo, Y. (2006). Climatic effects of different aerosol types in China simulated by the UCLA general circulation model. *J. Geophys. Res.* 111 (D15), D15201. doi:10.1029/2005jd006312

Gu, Y., Wong, T. W., Law, C. K., Dong, G. H., Ho, K. F., Yang, Y., et al. (2018). Impacts of sectoral emissions in China and the implications: Air quality, public health, crop production, and economic costs. *Environ. Res. Lett.* 13 (8), 084008. doi:10.1088/1748-9326/aad138

Guo, J., Miao, Y., Zhang, Y., Liu, H., Li, Z., Zhang, W., et al. (2016). The climatology of planetary boundary layer height in China derived from radiosonde and reanalysis data. *Atmos. Chem. Phys.* 16 (20), 13309–13319. doi:10.5194/acp-16-13309-2016

Halios, C. H., and Barlow, J. F. (2018). Observations of the morning development of the urban boundary layer over london, UK, taken during the ACTUAL project. *Boundary-Layer Meteorol.* 166 (3), 395–422. doi:10.1007/s10546-017-0300-z

Hamanaka, R. B., and Mutlu, G. M. (2018). Particulate matter air pollution: Effects on the cardiovascular system. *Front. Endocrinol.* 9, 680. doi:10.3389/fendo.2018.00680

Han, Y., Wang, T., Tang, J., Wang, C., Jian, B., Huang, Z., et al. (2022). New insights into the Asian dust cycle derived from CALIPSO lidar measurements. *Remote Sens. Environ.* 272, 112906. doi:10.1016/j.rse.2022.112906

Hara, Y., Nishizawa, T., Sugimoto, N., Osada, K., Yumimoto, K., Uno, I., et al. (2018). Retrieval of aerosol components using multi-wavelength mie-Raman lidar and comparison with ground aerosol sampling. *Remote Sens.* 10 (6), 937. doi:10.3390/rs10060937

Hu, R., Wang, H., Yin, Y., Chen, K., Zhu, B., Zhang, Z., et al. (2018). Mixing state of ambient aerosols during different fog-haze pollution episodes in the Yangtze River Delta, China. *Atmos. Environ.* 178, 1–10. doi:10.1016/j.atmosenv.2018.01.032

Huang, X., Wang, Z., and Ding, A. (2018). Impact of aerosol-PBL interaction on haze pollution: Multiyear observational evidences in North China. *Geophys. Res. Lett.* 45 (16), 8596–8603. doi:10.1029/2018gl079239

Jacobson, M. Z., Kaufman, Y. J., and Rudich, Y. (2007). Examining feedbacks of aerosols to urban climate with a model that treats 3-D clouds with aerosol inclusions. *J. Geophys. Res.* 112 (D24), D24205. doi:10.1029/2007JD008922

Jin, H., Chen, X., Zhong, R., and Duan, K. (2022). Frequency analysis of extreme precipitation in different regions of the Huaihe River Basin. *Intl. J. Climatol.* 42 (6), 3517–3536. doi:10.1002/joc.7430

Jin, M., and Shepherd, J. M. (2008). Aerosol relationships to warm season clouds and rainfall at monthly scales over east China: Urban land versus ocean. *J. Geophys. Res.* 113 (D24), D24S90. doi:10.1029/2008JD010276

Kang, H., Zhu, B., Su, J., Wang, H., Zhang, Q., and Wang, F. (2013). Analysis of a long-lasting haze episode in Nanjing, China. *Atmos. Res.* 120-121, 78–87. doi:10.1016/j.atmosres.2012.08.004

Li, J., Sun, J., Zhou, M., Cheng, Z., Li, Q., Cao, X., et al. (2018). Observational analyses of dramatic developments of a severe air pollution event in the Beijing area. *Atmos. Chem. Phys.* 18 (6), 3919–3935. doi:10.5194/acp-18-3919-2018

Ling, X., and Han, X. (2019). Aerosol impacts on meteorological elements and surface energy budget over an urban cluster region in the Yangtze River delta. *Aerosol and Air Qual. Res.* 19 (5), 1040–1055. doi:10.4209/aaqr.2017.12.0602

Liu, J., Zheng, Y., Li, Z., Flynn, C., Welton, E. J., and Cribb, M. (2011). Transport, vertical structure and radiative properties of dust events in southeast China determined from ground and space sensors. *Atmos. Environ.* 45 (35), 6469–6480. doi:10.1016/j.atmosenv.2011.04.031

Liu, T. H., Tsai, F., Hsu, S. C., Hsu, C. W., Shiu, C. J., Chen, W. N., et al. (2009). Southeastward transport of Asian dust: Source, transport and its contributions to Taiwan. *Atmos. Environ.* 43 (2), 458–467. doi:10.1016/j.atmosenv.2008.07.066

Miao, Y., Guo, J., Liu, S., Zhao, C., Li, X., Zhang, G., et al. (2018). Impacts of synoptic condition and planetary boundary layer structure on the trans-boundary aerosol transport from Beijing-Tianjin-Hebei region to northeast China. *Atmos. Environ.* 181, 1–11. doi:10.1016/j.atmosenv.2018.03.005

Murphy, D. M., Froyd, K. D., Bourgeois, I., Brock, C. A., Kupc, A., Peischl, J., et al. (2021). Radiative and chemical implications of the size and composition of aerosol particles in the existing or modified global stratosphere. *Atmos. Chem. Phys.* 21 (11), 8915–8932. doi:10.5194/acp-21-8915-2021

Peter, W. (1988). The growth of atmospheric aerosol particles with relative humidity. *Phys. Scr.* 37 (2), 223–230. doi:10.1088/0031-8949/37/2/008

Shao, M., Tang, X., Zhang, Y., and Li, W. (2006). City clusters in China: Air and surface water pollution. *Front. Ecol. Environ.* 4 (7), 353–361. doi:10.1890/1540-9295(2006)004[0353:ccicaa]2.0.co;2:ccicaa]2.0.co;2

Shen, X. J., Sun, J. Y., Zhang, X. Y., Zhang, Y. M., Zhang, L., Che, H. C., et al. (2015). Characterization of submicron aerosols and effect on visibility during a severe haze-fog episode in Yangtze River Delta, China. *Atmos. Environ.* 120, 307–316. doi:10.1016/j.atmosenv.2015.09.011

Tanaka, H., Hiyama, T., Yamamoto, K., Fujinami, H., Shinoda, T., Higuchi, A., et al. (2007). Surface flux and atmospheric boundary layer observations from the LAPS project over the middle stream of the Huaihe River basin in China. *Hydrol. Process.* 21 (15), 1997–2008. doi:10.1002/hyp.6706

Tegen, I., and Lacis, A. A. (1996). Modeling of particle size distribution and its influence on the radiative properties of mineral dust aerosol. *J. Geophys. Res.* 101 (D14), 19237–19244. doi:10.1029/95JD03610

Wang, B., Wang, Z., Wang, C., Wang, X., Li, J., Jia, Z., et al. (2021). Field evidence reveals conservative water use of poplar saplings under high aerosol conditions. *J. Ecol.* 109 (5), 2190–2202. doi:10.1111/1365-2745.13633

Wang, H., Li, J., Gao, M., Chan, T.-C., Gao, Z., Zhang, M., et al. (2020a). Spatiotemporal variability in long-term population exposure to PM2.5 and lung cancer mortality attributable to PM2.5 across the yangtze river delta (yrd) region over 2010–2016: A multistage approach. *Chemosphere* 257, 127153. doi:10.1016/j.chemosphere.2020.127153

Wang, L., Fan, S., Hu, F., Miao, S., Yang, A., Li, Y., et al. (2020b). Vertical gradient variations in radiation budget and heat fluxes in the urban boundary layer: A comparison study between polluted and clean air episodes in beijing during winter. *JGR. Atmos.* 125 (14), e2020JD032478. doi:10.1029/2020JD032478

Wang, L., Liu, J., Gao, Z., Li, Y., Huang, M., Fan, S., et al. (2019). Vertical observations of the atmospheric boundary layer structure over Beijing urban area during air pollution episodes. *Atmos. Chem. Phys.* 19 (10), 6949–6967. doi:10.5194/acp-19-6949-2019

Wang, Y., Meng, Z., Lyu, R., Huang, G., He, Q., and Cheng, T. (2020c). Spatiotemporal changes of surface solar radiation: Implication for air pollution and rice yield in East China. *Sci. Total Environ.* 739, 140361. doi:10.1016/j.scitotenv.2020.140361

Xiong, C., Li, J., Liu, Z., and Zhang, Z. (2022). The dominant role of aerosol-cloud interactions in aerosol-boundary layer feedback: Case studies in three megacities in China. *Front. Environ. Sci.* 10, 2412. doi:10.3389/fenvs.2022.1002412

Xu, Y., Sun, H., and Ji, X. (2021). Spatial-temporal evolution and driving forces of rainfall erosivity in a climatic transitional zone: A case in Huaihe River Basin, eastern China. *CATENA* 198, 104993. doi:10.1016/j.catena.2020.104993

Yang, Y., Yim, S. H. L., Haywood, J., Osborne, M., Chan, J. C. S., Zeng, Z., et al. (2019). Characteristics of heavy particulate matter pollution events over Hong Kong and their relationships with vertical wind profiles using high-time-resolution Doppler lidar measurements. *J. Geophys. Res. Atmos.* 124 (16), 9609–9623. doi:10.1029/2019JD031140

Yang, Y., Zhang, M., Li, Q., Chen, B., Gao, Z., Ning, G., et al. (2020a). Modulations of surface thermal environment and agricultural activity on intraseasonal variations of summer diurnal temperature range in the Yangtze River Delta of China. *Sci. Total Environ.* 736, 139445. doi:10.1016/j.scitotenv.2020.139445

Yang, Y., Zheng, Z., Yim, S. Y. L., Roth, M., Ren, G., Gao, Z., et al. (2020b). PM2.5 pollution modulates wintertime urban heat island intensity in the beijing-tianjin-hebei megalopolis, China. *Geophys. Res. Lett.* 47 (1), e2019GL084288. doi:10.1029/2019GL084288

Yin, J., Gao, C. Y., Hong, J., Gao, Z., Li, Y., Li, X., et al. (2019). Surface meteorological conditions and boundary layer height variations during an air pollution episode in nanjing, China. *J. Geophys. Res. Atmos.* 124 (6), 3350–3364. doi:10.1029/2018JD029848

Zhang, H., Wang, Y., Hu, J., Ying, Q., and Hu, X. M. (2015). Relationships between meteorological parameters and criteria air pollutants in three megacities in China. *Environ. Res.* 140, 242–254. doi:10.1016/j.envres.2015.04.004

Zhang, R., Li, Q., and Zhang, R. (2014). Meteorological conditions for the persistent severe fog and haze event over eastern China in January 2013. *Sci. China Earth Sci.* 57 (1), 26–35. doi:10.1007/s11430-013-4774-3

Zhu, S., Zhang, H., Wei, X., and Yang, D. (2018). Simulation of aerosol influences on shortwave radiative flux under different pollution conditions (in Chinese). *Acta Meteorol. Sin.* 76 (5), 790–802. doi:10.11676/qxxb2018.031

Zhu, T., Shang, J., and Zhao, D. (2011). The roles of heterogeneous chemical processes in the formation of an air pollution complex and gray haze. *Sci. China Chem.* 54 (1), 145–153. doi:10.1007/s11426-010-4181-y

Frontiers in
Environmental Science

Explores the anthropogenic impact on our natural world

An innovative journal that advances knowledge of the natural world and its intersections with human society. It supports the formulation of policies that lead to a more inhabitable and sustainable world.

Discover the latest Research Topics

See more →

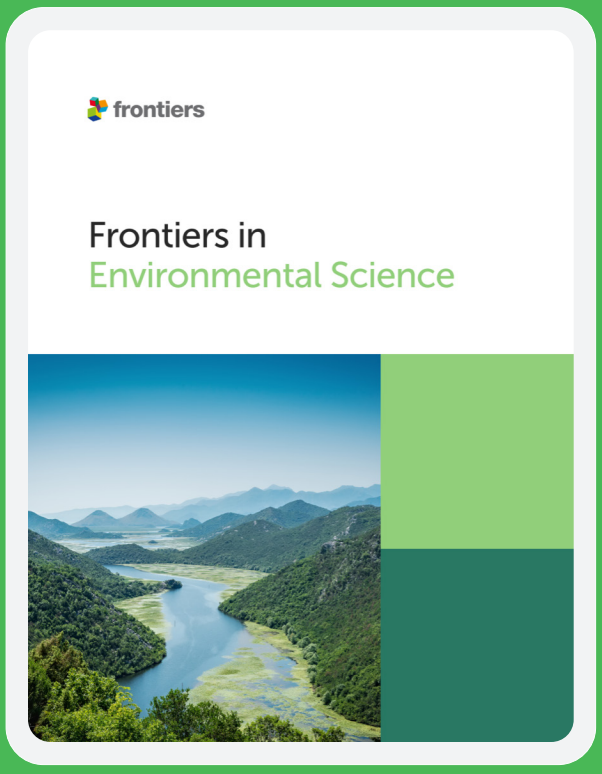

Frontiers

Avenue du Tribunal-Fédéral 34
1005 Lausanne, Switzerland
frontiersin.org

Contact us

+41 (0)21 510 17 00
frontiersin.org/about/contact